FOR FURTHER TRAN

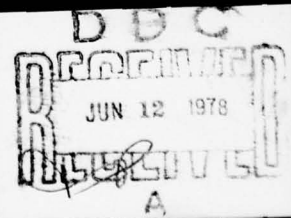*International Union of Theoretical and Applied Mechanics*
Symposium 1976

STRUCTURE OF TURBULENCE
AND
DRAG REDUCTION

Edited by

F. N. Frenkiel, M. T. Landahl, and J. L. Lumley

American Institute of Physics

STRUCTURE OF TURBULENCE
AND
DRAG REDUCTION

FOR FURTHER TRAN ~~~~

International Union of Theoretical and Applied Mechanics

STRUCTURE OF TURBULENCE
AND
DRAG REDUCTION.

Proceedings of an International Symposium

Held in Washington, D.C., U.S.A.
7—12 June 1976

N00014-76-C-0385

1976

NR-062-526

277 p.

Edited by

François N. Frenkiel, Mårten T. Landahl, and John L. Lumley

D D C
RECEIVED
JUN 12 1978
A

404 853

INTRODUCTION

During the General Assembly of the International Union of Theoretical and Applied Mechanics held in Moscow, USSR in August 1972 it was suggested that a symposium on structure of turbulence and drag reduction be sponsored by IUTAM. Immediately following the General Assembly an informal working group consisting of G. K. Batchelor (U.K.), F. N. Frenkiel (U.S.A.), M. T. Landahl (Sweden), and L. I. Sedov (U.S.S.R.) met at Moscow University and agreed to formally recommend that IUTAM plan a symposium with the following general outline: "The study of the structure of turbulence in shear flow with special emphasis on the changes brought about by the addition of polymers or other agents." The General Assembly of IUTAM held in September 1974 in Udine, Italy approved the scheduling of this Symposium in 1976 in the eastern United States.

The Scientific Committee appointed by IUTAM consisted of P. Bradshaw (U.K.), C. Elata (Israel), J. O. Hinze (Netherlands), M. T. Landahl (Sweden), J. L. Lumley (U.S.A.), J. C. Rotta (Fed. Rep. Germany), L. I. Sedov (U.S.S.R.), I. Tani (Japan), and F. N. Frenkiel (U.S.A.) Chairman.

The Scientific Committee agreed to devote the symposium to the study of the structure of shear flow turbulence and more particularly, to those aspects of the structure which are subject to modification associated with flows in which drag reduction occurs, such as the flow of dilute polymer solutions (Toms' effect), flow past compliant surfaces, etc. The study of drag reduction would emphasize the dynamic structure of turbulence with the purpose of contributing to a better understanding of the physical nature of turbulent phenomena.

The Symposium was held from June 7 to 12, 1976 and was hosted by the National Academy of Sciences in Washington, D.C. and the National Bureau of Standards in Gaithersburg, Maryland.

The Local Organizing Committee consisted of R. D. Cooper, Chairman, R. Y. Dow, A. J. Faller, P. S. Klebanoff, Joseph Sternberg, and M. P. Tulin.

About 90 participants and 30 observers took an active part in the discussions. Seven invited papers, largely of a review nature were presented including an after dinner speech by Professor A. B. Toms for whom the Toms Effect has been named. Forty shorter research contributions were presented (the program of the symposium is given as an Appendix). Adequate time was provided for discussion of the papers following the presentation as well as at several informal meetings.

After the morning session held at the National Bureau of Standards (on June 10) Dr. E. L. Brady addressed the Symposium on "NBS, The Nation's Measurement Laboratory" followed by a tour of the Fluid Mechanics Laboratory.

The authors of papers prepared for these Proceedings were requested to present their results in a form appropriate for publication in a scientific journal. The discussions of the papers during the Symposium are not included in the Proceedings; however, the authors were offered the opportunity to take the discussions, as well as the comments of the referees who reviewed their manuscripts into account, by making appropriate revisions in their papers.

Part A consists of the speech by Professor Toms. Part B includes papers whose authors were invited to prepare a review of their subject, although in some cases they include new research contributions. Part C consists of research papers based on shorter contributions, and Part D includes the abstracts of papers which were either not available at the time of publication of this volume or because the reported results are included in papers published (or to be published) elsewhere.

PROCEEDINGS OF AN INTERNATIONAL SYMPOSIUM ON STRUCTURE OF TURBULENCE AND DRAG REDUCTION

PART D: ABSTRACTS OF PAPERS NOT PUBLISHED IN FULL (These papers were either not available at the time of publication of the Proceedings or the reported results are included in papers published (or to be published) elsewhere)

APPENDICES

PART A

On the Early Experiments on Drag

Reduction by Polymers

Address

by

B. A. Toms

On the early experiments on drag reduction by polymers[a]

B. A. Toms

Department of Chemistry, University of Birmingham, Birmingham B15 2TT, England

Mr. Chairman, ladies and gentlemen,

This is a great occasion for me, one which I could never have foreseen or will ever forget. It is both an honor and a pleasure to be here, and I feel that the Organizing Committee has paid me a generous compliment by inviting me to attend the Symposium and to speak on this social occasion. I would like to express my sincere thanks for this friendly and hospitable gesture of recognition.

Since my contribution to the symposium program is intended to be personal and reminiscent, I may begin by recalling that my original experiments on drag reduction by polymers were done exactly thirty years ago, in the summer of 1946. The results I got were presented two years later at an international congress on Rheology which was held at Scheveningen, in Holland, and they were eventually published in 1949.[1]

I have to admit that that single paper was the only contribution I ever made to the study of turbulent fluid motion but, as things turned out, the agony of compressing it into the required 1500 words has been well rewarded. It has been very widely quoted and has helped (apparently) to set off a virtual explosion of research and development work in many countries; but, the "explosion" was delayed for something like a decade and most of the modern work has been done during the past 15 years.

The astonishing variety, complexity, and specialization of contemporary research makes it almost impossible for a bystander like myself to appreciate the present state of knowledge or even to comprehend all that is going on. I think it would be fair to say, quite simply and entirely without derogation, that in spite of all that has been achieved, and there have been several significant advances, both practical and theoretical, the phenomenon of turbulent drag reduction by additives remains an enigma today.

On this pleasant and relaxed occasion, near the end of a grueling week, it may be of some interest if I recall and explain briefly how it all began. After all, a modern mining engineer may still learn something from an early prospector who found a nugget and brought it back for everyone to see. Why did he go to that particular place, and did he just dig at random? My story is prosaic but I think it illustrates how scientists work and what can be involved in transforming a strange observation into an accepted discovery.

The background to my work was some experience in the mechanical degradation of polymers which I had gained during World War II in connection with the manufacture of polymer solutions. Among the technical problems encountered was that of securing constancy in the rheological properties of the finished product. It was soon established that a prime cause of variation was the actual breakage of linear macromolecules which accompanied vigorous stirring or shaking, but thirty years ago this phenomenon was less familiar than it is today. It then seemed almost unbelievable and was quite inexplicable since it was not always clearly associated with large nominal rates of shear and depended, somewhat capriciously, on the molecular size-distribution of the polymer. However, there was no time in those days for fundamental study and the practical problem was solved empirically; but, the occurrence of mechanical degradation intrigued me and I wanted to know more about it.

When the war ended, i joined the newly-opened Courtaulds Fundamental Research Laboratory at Maidenhead (in Berkshire, England) and was fortunate to be able to discuss the feasibility of investigating mechanical degradation with G. S. Hartley, who was my immediate boss. We agreed that there might be some connection between degradation and turbulence although neither of us, being mere chemists, understood turbulent fluid motion in precise hydrodynamical terms. After searching the literature, however, I realized that almost nothing was known about the characteristics of turbulence in polymer solutions and that I would have to determine some of the basic facts myself before I could seek a correlation with degradation.

I therefore settled down early in 1946 to find out what I could about the transition from laminar to turbulent flow when some typical polymer solutions passed through a straight narrow tube under increasing pressure. This work was done with dilute solutions of high molecular weight poly(methyl methacrylate) in monochlorbenzene mainly because I happened to have enough of both these materials for a lengthy investigation. (In those days, just after the war, there were frustrating shortages in Britain of both chemicals and ordinary laboratory equipment, so that one used whatever came to hand). My apparatus was very simple and quite crudely constructed, although I was lucky

---
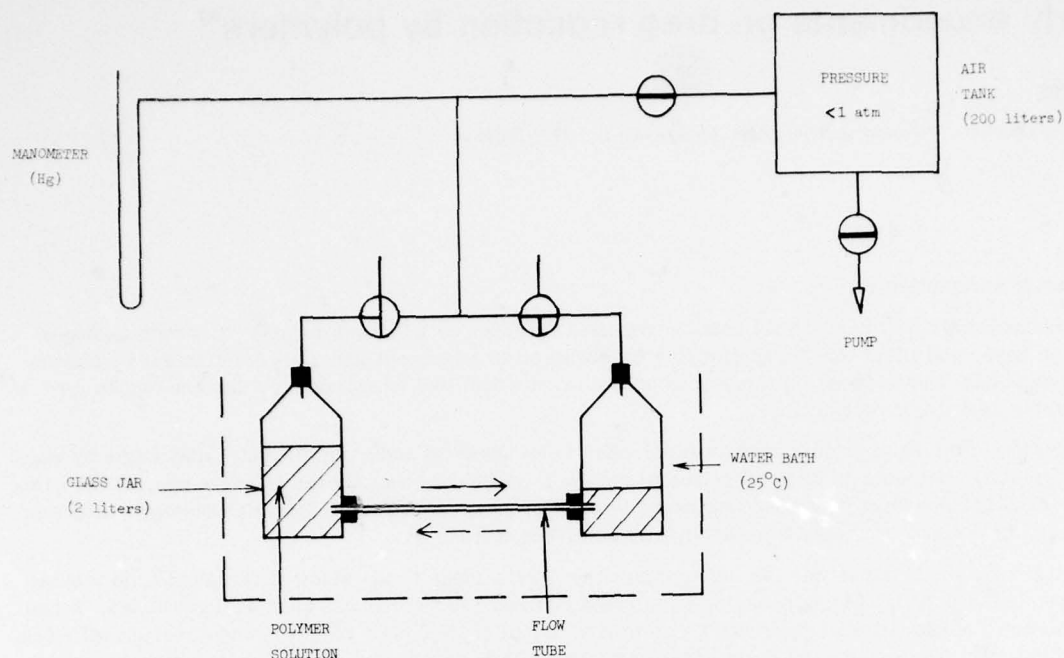
FIG. 1. Flow apparatus.

enough to obtain a single length of precision-bore brass tube which could be cut into pieces to produce a set of matching flow tubes of different lengths, including some with specially shaped entrances. Each flow tube was fitted with a pair of rubber bungs which were inserted into the base holes of two glass aspirator jars. This gave me a flow apparatus (Fig. 1) consisting of a horizontal tube with a reservoir at each end which could be immersed in a water bath kept at constant temperature. Two liters of polymer solution were used in an experiment, and each reservoir was about half-full when the air pressure was the same in both. Movement of the solution through the flow tube was achieved pneumatically by reducing the air pressure in one jar while the pressure in the other remained atmospheric. I was thus able to measure, quite accurately with a stop watch, the time required for one liter of solution to pass through the tube under a known pressure-head (shown by a mercury U-tube manometer), and I could vary the driving pressure over a fairly wide range.

When the relation between pressure head and rate of flow for a single solution was eventually plotted, it was usually obvious where a departure from laminar flow occurred. Indeed, this generally happened when the Reynolds number was between 2000 and 4000, as in Newtonian liquids. When however, I plotted the rate of flow at constant pressure against the polymer concentration, a remarkable anomaly appeared. In laminar flow the rate decreased as expected, but when the flow was not laminar, and could be regarded as turbulent, the rate of flow at constant pressure actually increased as more polymer was added. This only occurred over a narrow range of (low) polymer concentrations, and I could find no record of any similiar behavior in the published literature. The really astounding thing was that in the critical region of concentration, and under turbulent conditions, a polymer solution clearly offered less resistance to flow, under constant pressure, than the solvent itself. This, of course, is the essence of drag reduction, and it was first noticed about the middle of 1946.

When A. H. Wilson (now Sir Alan Wilson), who was in charge of Courtaulds research at that time, heard of these results he arranged for J. G. Oldroyd to visit Maidenhead and discuss their possible implications from the theoretical standpoint. Oldroyd was then working at Cambridge University. I had not previously met him, but he was interested in what I had found and agreed to consider the new evidence in the light of existing theories of nonlaminar flow. He later expressed the opinion that the anomaly which had been detected might conceivably be explained in terms of a wall effect, rather than as evidence of turbulence suppression, but that observations in a second tube of different diameter would be needed to resolve this fundamental question. I agreed to obtain the additional data while he undertook to devise a practical method for analyzing them which would disclose whether or not a wall effect existed in turbulent flow. In the event, as some of you will recall, it did appear that the polymer had introduced a wall effect which could be characterized by an effective coefficient of slip. This important conclusion was reached toward the end of 1946 or early in 1947.

About that time Oldroyd moved to the Maidenhead laboratory and we continued to collaborate. When the plan to hold a rheological conference in Holland in 1948 was announced, we decided to present our work there, in separate papers.[1,2] Thus, the first phase of my research on polymer degradation ended about the middle of 1947; but the

project was not resumed, partly because of laboratory reorganization and partly because the prospect of finding an unambiguous relation between degradation and turbulence now seemed more remote than when I started, and I was not inclined to pursue the study of turbulent flow indefinitely. Instead, Oldroyd and I embarked on a different rheological enterprise (measuring the elasticity of polymer solutions) and this was to engage us, separately and in association, for the next five years. After that I wanted to return to chemical research and did so.

When I recall the rheological congress at Scheveningen, I can remember that only a small number of people expressed interest in my experimental results. Some of them questioned whether the observed flow had really been turbulent while others disliked the proposition of a wall effect, but there was certainly no wild excitement, and very little speculation about possible applications of the phenomenon I had described. After publication of the Congress Proceedings in 1949 I received some requests for reprints of my paper; then, for a period of about 10 years, nothing at all seemed to happen until a trickle of papers appeared, extending my observations to other polymers and other solvents, notably water. By the mid-60's there was a stream of publications and by the end of the decade a small torrent, showing that the interest in drag reduction was not only intense but world wide.

Well, that is how the study of turbulent drag reduction by polymeric additives began, as I remember it, and I hope you may have found some points of interest in the story. The discovery of the phenomenon was accidental in the sense that it was wholly unexpected, but I would stress that it emerged from the performance of a proper scientific experiment in which a significant deviation from normality was detected by an observer who was sufficiently experienced to recognize it and sufficiently sure of his facts to justify reporting them to others.

In conclusion, I return to the present Symposium at which about 45 papers and some remarkable films have been presented and very thoroughly discussed by acknowledged experts from all over the world. I have already expressed my personal pleasure and privilege at being able to attend, but I feel sure that the other foreign visitors here tonight would wish me to convey their collective gratitude to our American hosts for the excellent and most enjoyable arrangements which they made for our reception in Washington, and also to congratulate them most warmly on the undoubted success of this important international scientific meeting.

[1]B. A. Toms, in *Proceedings of the International Congress on Rheology* (North-Holland, Amsterdam, 1949), Sec. II, p. 135.
[2]J. G. Oldroyd, in *Proceedings of the International Congress on Rheology* (North-Holland, Amsterdam, 1949), Sec. II, p. 130.

PART B

REVIEW PAPERS

This part includes papers whose authors were invited to prepare a review of their subject although in some cases they include new research contributions.

Survey and new measurements of turbulent structure near the wall

William W. Willmarth

Department of Aerospace Engineering, The University of Michigan, Ann Arbor, Michigan 48109

Thomas J. Bogar

Department of Physics, Westminister College, New Wilmington, Pennsylvania 16142

A survey of recent measurements of turbulent structure near the wall which are applicable to the phenomenon of drag reduction by polymer additives is presented. Knowledge of the vorticity in the wall region provides a framework for understanding turbulent structure and the effects of polymer additives. New measurements using a small, calibrated streamwise vorticity probe are described. Near the wall where the turbulent production and dissipation are a maximum the streamwise vorticity is a maximum and is highly intermittent. New measurements of the Reynolds stress have also been made with a very small, computer calibrated hot-wire array. Intermittent small scale structures producing rapid oscillations of the hot-wire signals are detected near the wall which are too small to be resolved by the array. Their spatial scale is much less than the Kolmogoroff length. It is suggested that they are associated with streamwise vorticity.

I. INTRODUCTION

The phenomenon of drag reduction by additives (known as the Toms' phenomenon) was reported by Toms[1] in 1948. He observed that the addition of a very small fraction of polymer to a fully turbulent pipe flow of solvent produced a substantial pressure drop below that of the solvent alone at the same flow rate. Since 1948 there have been numerous experimental investigations which provide quantitative information about the Toms' phenomenon in turbulent pipe and boundary layer flows. The effects produced by additives are well documented, but an understanding of the drag reduction mechanism is far from complete.

Lumley[2] reviewed the state of knowledge of drag reduction in 1969 and suggested that additional measurements were needed. The experiments have been found to be extraordinarily difficult because the rheological behavior of the fluid adversely affects the response of pressure and heat transfer probes placed in the flow. A noninvasive technique using the laser-Doppler anemometer has been developed which is now reliable for mean measurements, but still presents serious difficulties for measurements of fluctuating quantities.

The early measurements of Virk *et al.*[3] who used Pitot tubes and hot film sensors were followed by numerous investigations using laser-Doppler anemometers. The measurements reported by Rudd,[4] Reischman and Tiederman,[5] and by Mizushina and Usui in Ref. 6 provide examples of laser-Doppler anemometer measurements. The investigations all indicate that the primary effect of polymer additives during drag reduction in a turbulent flow is located in the region very near the wall where the mean velocity gradient is reduced. This region extends from the wall out to approximately 60 viscous lengths (i.e., $yu_\tau/\nu = y^+ \lesssim 60$, where u_τ squared is the ratio of wall shear stress to fluid density and ν is the kinematic viscosity). The mean flow and those fluctuating turbulent quantities that have been reliably measured are not significantly affected beyond $y^+ = 60$. This indicates that understanding of the mechanism of drag reduction by additives will require information about the structure of turbulence in the region near the wall.

Many investigations of the structure of wall turbulence in Newtonian fluids have been reported during the past 15 years. Experiments using hot wire probes, wall pressure transducers, and visual methods have produced background information applicable to a better understanding of turbulent structure. The extensive literature and new results have been summarized by Kovasznay,[7,8] Mollo-Christensen,[9] Laufer[10] and Willmarth.[11] In this paper a brief survey of the highlights of the present knowledge of turbulent structure near the wall is presented. Then, recent results that we have obtained in our efforts to measure extremely small scale turbulent structure near the wall are described.

II. SURVEY OF TURBULENT STRUCTURE NEAR THE WALL

A. Vorticity and a model for the intermittent turbulent structure

The essential features of turbulent structure near the wall are reviewed to provide background knowledge necessary for further understanding of the mechanism of drag reduction by additives. Let us begin by mentioning that one of the primary effects of turbulence is to promote mixing in the flow. Consider a boundary layer flow immediately after transition. Turbulent mixing brings high speed fluid very near the wall and carries low speed fluid far from the wall. The result is that the laminar and turbulent mean velocity profiles cross at some point near the wall and that the mean wall shear stress is much larger than the laminar value.

Turbulence in boundary layer or duct flows is self-sustaining and consists of a random distribution of vorticity, ω. The presence of turbulence in the boundary layer produces dramatic changes in the mean vorticity distribution. Figure 1 from Lighthill[12] shows approxi-
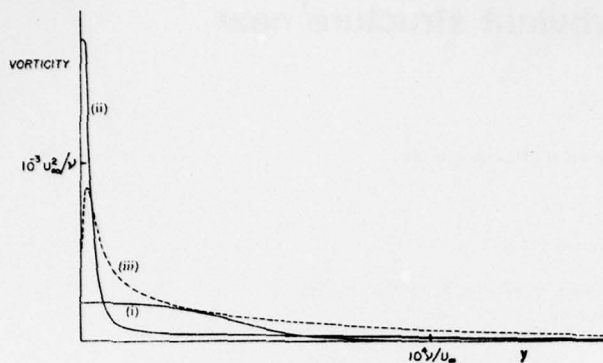
FIG. 1. Distribution of mean vorticity in a boundary layer with uniform external flow: (i) at beginning, (ii) at end of transition. Curve (iii) gives rough values of the root-mean-square vorticity at end of transition. From Lighthill. [12]

mate results from the measurements of Schubauer and Klebanoff. [13] Curve (i) is the laminar distribution of mean vorticity in a boundary layer just before transition at a Reynolds number, Re_x, based on distance, x, from the leading edge of 2.3×10^6. Curve (ii) is the distribution of mean vorticity just after transition at $Re_x = 3.3 \times 10^6$. The turbulence has redistributed the vorticity so that at the wall the mean vorticity, τ_w/μ, is many times the laminar value. A small portion (5% of the total) of the mean vorticity is also much farther from the wall in a region of intermittently turbulent flow. Curve (iii) gives approximate values of the root-mean-square vorticity fluctuations in the fully turbulent region after transition. Curve (iii) was apparently deduced by Lighthill from the relation for isotropic turbulence, $\overline{\omega^2} = \epsilon/\nu$, using Schubauer and Klebanoff's [13] measurements of the dissipation, ϵ. Later in the paper accurate measurements of the streamwise component of vorticity are described. The streamwise vorticity fluctuations attain a high maximum very close to the wall near the edge of the sublayer, where turbulent production and dissipation are also a maximum, and extend to the outer edge of the boundary layer.

It is remarkable that turbulence near the wall is able to maintain large gradients of mean and fluctuating vorticity in spite of the large viscous diffusion down the gradient. The processes that accomplish this are central to an understanding of the structure of wall turbulence and the mechanism of drag reduction produced by additives.

The vorticity in a Newtonian fluid obeys the equation

$$\partial \omega/\partial t + (\mathbf{q} \cdot \nabla) \omega = (\omega \cdot \nabla)\mathbf{q} + \nu\nabla^2\omega, \tag{1}$$

which states that the time rate of change of vorticity as one follows the fluid is produced by a nonlinear stretching (or contraction) of existing vorticity, $(\omega \cdot \nabla)\mathbf{q}$, plus diffusion of vorticity, $\nu\nabla^2\omega$. Lighthill [12] has discussed the fact that the wall itself is a source of vorticity. If one considers a flow in the x direction over a plane surface (the x, z plane) with pressure gradients in the x direction, the requirement of no slip at the wall and the Navier Stokes equations plus Eq. (1) yield the flow of z vorticity out of the surface [12]

$$-\nu \frac{\partial \omega_z}{\partial y} = \frac{1}{\rho} \frac{\partial p}{\partial x}, \tag{2}$$

where p is the pressure. The meaning of (2) is that the pressure gradient along a wall creates vorticity tangential to the surface in the direction of the surface isobars. The sense of rotation is that of a ball rolling down the line of steepest pressure fall and the magnitude of the vorticity source strength per unit area $(-\nu \partial\omega_z/\partial y)$ is $1/\rho$ times the pressure gradient.

The new vorticity tangential to the wall that is produced by mean and fluctuating wall pressure gradients is eligible for further modification in accordance with Eq. (1). The problem is highly nonlinear because the rotational part of the velocity field appearing in Eq. (1) is "induced" by the vorticity. The induced velocity field alters the vorticity, see Eq. (1), by convection, $(\mathbf{q} \cdot \nabla)\omega$, and stretching, $(\omega \cdot \nabla)\mathbf{q}$. The source of vorticity at the wall also provides a mechanism by which the outer flow in the boundary layer can influence the flow near the wall.

The concept of the wall as a source of vorticity, Eq. (2), which is produced by pressure gradients and then evolves in accordance with Eq. (1) provides a useful framework for further understanding of turbulent structure. Observations of this structure during the past decade using various methods of flow visualization have greatly stimulated turbulence research. Observations of the flow in the sublayer using dye injection methods by Hama and by Beatty et al. (see Corrsin [14]) revealed a strong orientation of the dye into streamwise filaments. Later, Kline et al. [15] used hydrogen bubbles produced by electrolysis at the surface of a fine wire to observe these filaments of alternating high and low speed flow in the sublayer. Figure 2 is a good example of what they have called the "streaky" sublayer structure. The filaments of increased bubble concentration in the low speed flow regions (the streaks) occur with an average transverse spacing of the order of 100 viscous lengths ($100\nu/u_\tau$).

Two-point correlation measurements of the sublayer structure using hot wires have been made by Gupta et al. [16] They showed that the streaky structure occurs intermittently in space and time and observed alternating large positive and negative transverse spatial correlations with a wavelength of approximately 100 viscous lengths ($\lambda^+ = 100$) during short time periods. Over longer time periods the two-point correlations with wavelength ($\lambda^+ = 100$) were completely smeared out by the randomness of the streaky sublayer structure.

Kline and his colleagues [15,17] also observed a recurring coherent pattern of events in the flow near the wall. The pattern of events consisted of a process of gradual lift up and rapid ejection in which low speed fluid containing sublayer streaks moved rapidly away from the wall. Figure 3 is an example of this process and shows a typical lift up and subsequent rapid ejection and contortion of a streak of dye previously injected into the sublayer of a fully turbulent boundary layer. [15] The intermittent process of lift up and contortion of the sublayer fluid was observed to occur randomly in space and
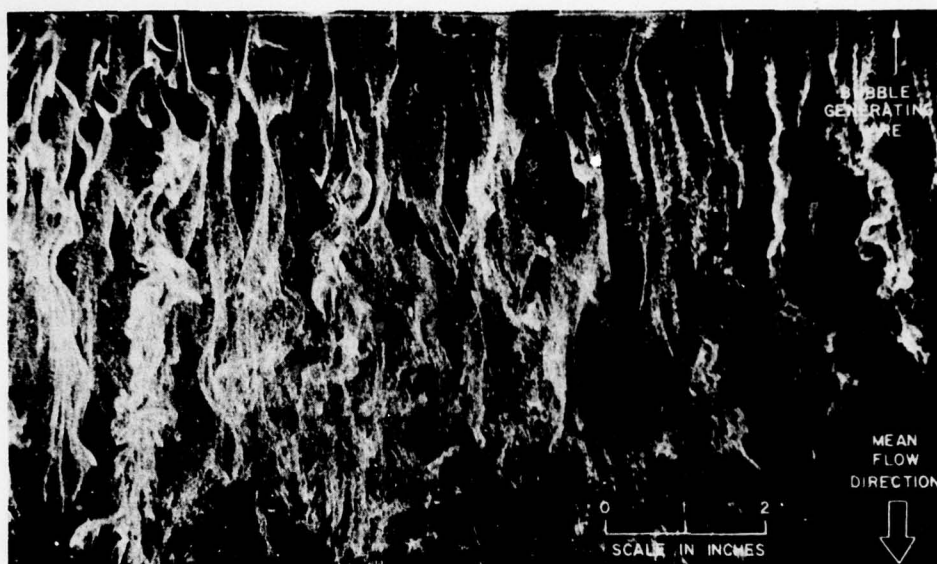
FIG. 2. Photograph of hydrogen bubbles in the sublayer showing "streaky" structure. Bubble generating wire parallel to wall at $y^+ = 8$. From Kline et al.[15]

time. Figure 4 shows the averaged trajectories of the ejected fluid obtained from motion pictures of many occurrences of the ejection process. Kim et al.[17] have termed the ejection process "bursting" probably because

the process appears to be quite rapid. Corrsin has pointed out that in 1957[14]; he used the term "burst" to describe the sudden increases in streamwise velocity accompanied by higher frequencies that were observed intermittently in the oscillograms of streamwise velocity measured by Ruetenik and Corrsin in a turbulent channel flow.
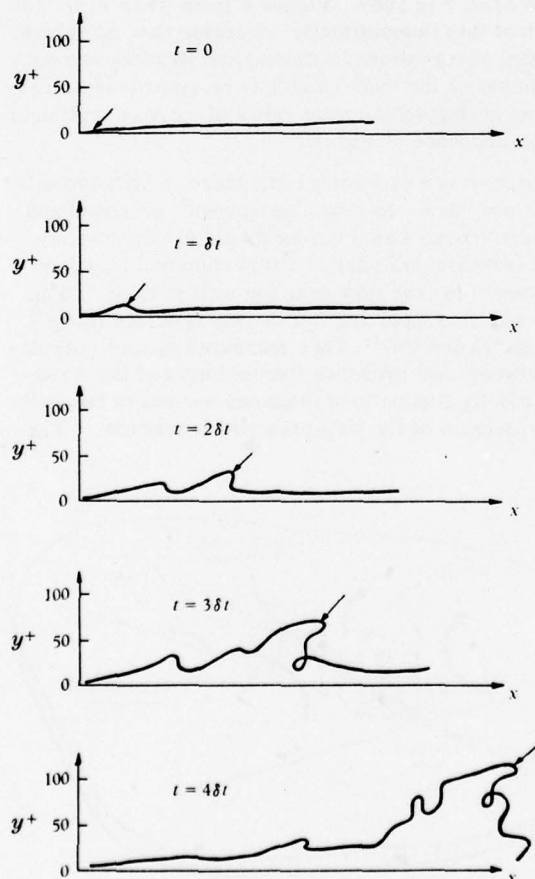
FIG. 3. Dye streak breakup during bursting; illustration as seen in side view. From Kline et al.[15]
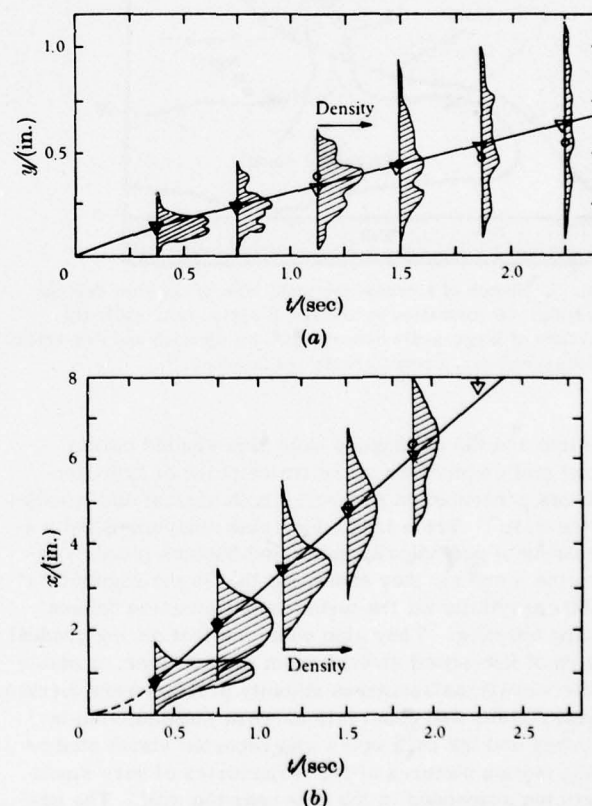
FIG. 4. Trajectories of ejected eddies during bursting, zero pressure gradient. From Kline et al.[15]
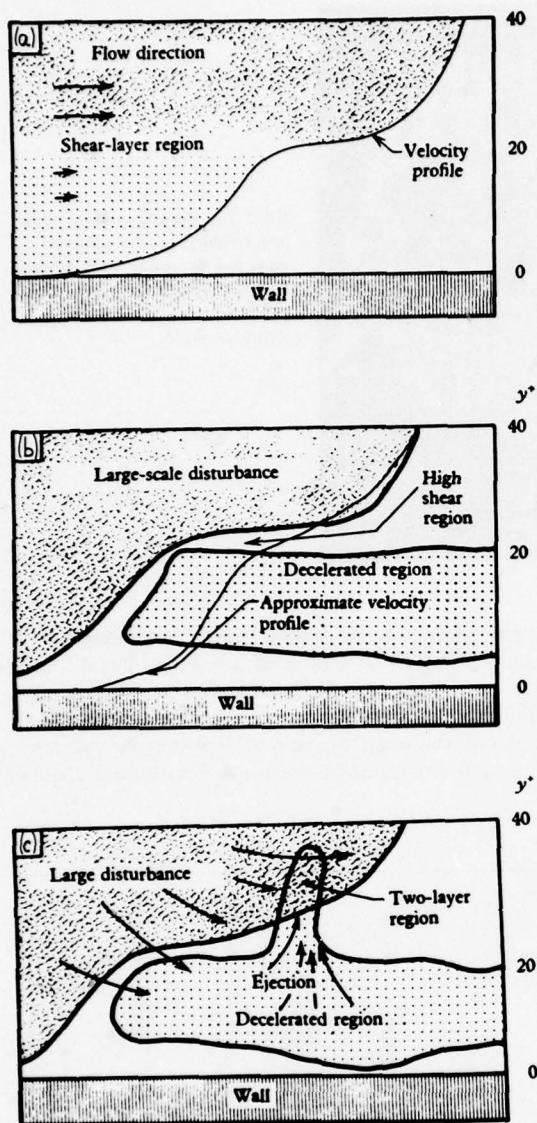
FIG. 5. Sketch of a cross-sectional view of the flow during bursting: (a) formation of low speed region near wall, (b) entrance of large-scale disturbance, (c) ejection and two-layer velocity region. From Corrino and Brodkey.[18]

Kline and his colleagues have also studied bursts using motion pictures of the trajectories of hydrogen bubbles generated on fine wires both normal and parallel to the wall.[17] From frame by frame analysis of the trajectories of periodically generated bubbles (used to determine u and v), they concluded that in the region $0 < y^+ < 100$ essentially all the turbulence production occurs during bursting. They also observed that during gradual lift up of low-speed streaks from the sublayer, unstable (inflectional) instantaneous velocity profiles were formed. These results and observations were substantiated by Brodkey and his colleagues who reported visual studies using motion pictures of the trajectories of very small particles suspended in the flow near the wall. The sequence of events before and after chaotic breakdown during the bursting process as reported by Corino and

Brodkey[18] began with the formation of a low speed parcel of fluid near the wall in the region $y^+ \leq 30$. After formation of a low speed region a much larger high-speed parcel of fluid came into view and by "interaction" began to accelerate the low speed fluid. Following this a small scale process of rapid ejection began in which the low speed fluid appeared to be ejected upward with intense, abrupt, and chaotic movements. This sequence of events is sketched in Fig. 5.

The ejection phase ended with the entry from farther upstream of fluid directed primarily in the stream direc with a velocity approximating the normal mean velocity profile. The entering high-speed fluid carried away the retarded fluid remaining from the ejecting process; this was called the sweep event. Both Corino and Brodkey[18] and Kim et al.[17] agree that the bursting phenomenon is an important process for turbulent energy production. Corino and Brodkey concluded that 70% of the Reynolds stress was produced during ejections.

Offen and Kline[19] also reported visual studies of bursting by photography of the flow near the wall using a combination of dye injection at various distances from the wall and hydrogen bubbles generated on a fine wire normal to the wall. They concluded that the severe flow disturbances near the wall that had been observed in previous work[15,17] were associated with just one type of flow structure, a stretched and lifted vortex described by Kline et al.[15] in 1967. Figure 6 from Kline et al.[15] is a sketch of this intermittently occurring flow structure. The visual observations of Corino and Brodkey are not contradicted by the model and may be visualized as randomly occurring streamwise views of a cross section of the burst sequence of Fig. 6.

The occurrence of a vortex structure in turbulence is hardly a new idea. In 1952 Theodorsen[20] proposed and sketched a "horse shoe" vortex model for the mechanism of turbulent transfer of momentum and heat. A vortex model for the flow near the wall similar to Fig. 6 and evidence supporting it was also reported in 1967 by Willmarth and Tu.[21] They measured spatial correlations between wall pressure fluctuations and the transverse velocity fluctuations in planes normal to the wall and downstream of the wall pressure transducer. The
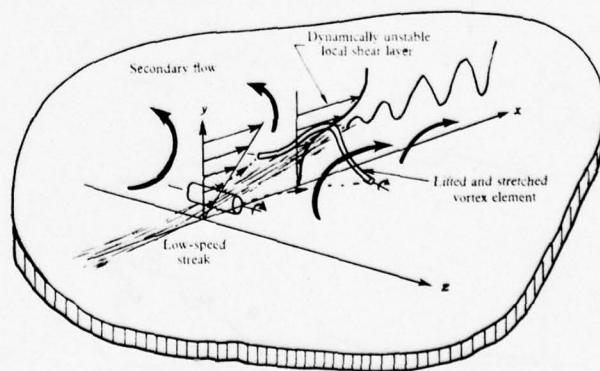
FIG. 6. The model of streak breakup that precedes bursting. From Kline et al.[15]
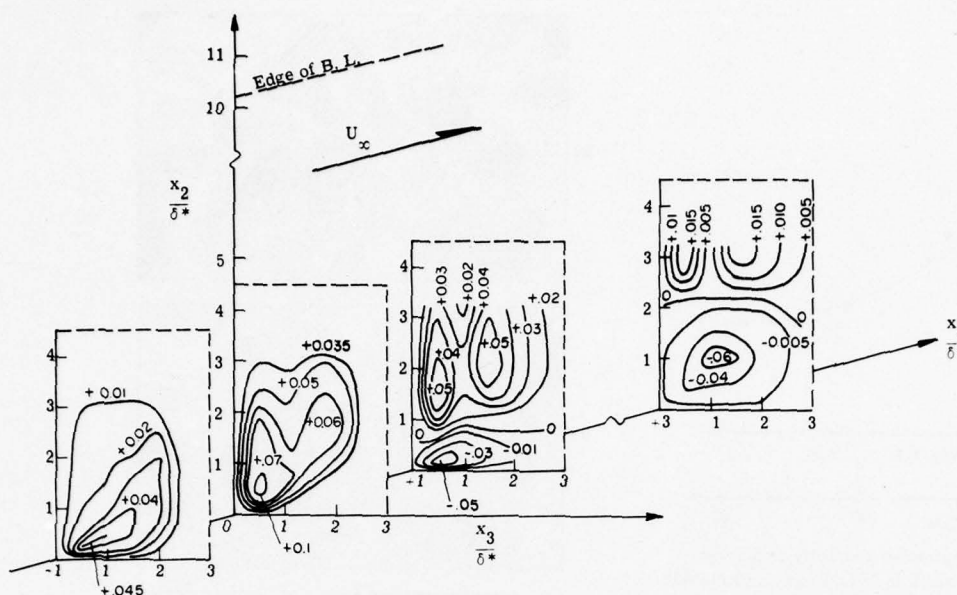
FIG. 7. Three-dimensional diagram of contours of constant wall pressure-spanwise velocity correlation coefficient $(R_{pw} = \text{const})$. From Willmarth and Tu.[21]

results are displayed in Fig. 7 and show the lift up with downstream distance of what must have been streamwise vorticity emanating from the wall. The vorticity produced a reversal of spanwise velocity and hence the sign of $\overline{pw}$ across the inclined plane of zero correlation.

Recently, Kastrinakis *et al.*[22] have reported measurements of streamwise vorticity fluctuations using very small, precisely constructed and calibrated hot wire arrays that can be placed very near the wall of a channel flow. The typical length of the wires and their spacing was 2 to 3 viscous lengths. Figure 8 shows an example of the intermittent nature of the streamwise vorticity and velocity fluctuations at $y^+ = 15$. Notice that the vorticity fluctuations are much more intermittent than the velocity fluctuations. In Figs. 9 and 10 the distribution of the root-mean-square and kurtosis of the streamwise vorticity is displayed. The kurtosis is large, of the order of 6, all across the channel. The root-mean-square vorticity attains a large maximum value of the order of one quarter of the mean wall vorticity at $y^+ \simeq 21$. This indicates the presence of large streamwise vorticity at the same distance from the wall that lift up followed by ejection occur in the model shown in Fig. 6. This is also the region in which turbulent energy production and dissipation are a maximum.

There are numerous measurements and observations by other investigators (see the reviews[7-11] mentioned

earlier) which support a model of an intermittently occurring vortical structure near the wall that is responsible for a large fraction of the observed Reynolds stress and turbulence production. Owing to the difficulty of the measurements the model is in a primitive state. Little more than has been described here is known about the structure of the flow field which is produced during bursting near the wall.

B. Evidence of small scale phenomena associated with turbulent structure

One of the primary difficulties presented by measurements of the structure of wall turbulence is the small scale of the turbulent fluctuations. There is considerable evidence (new results will be described in the next section) that the turbulent structure near the wall is of a much smaller scale than the size of probes used in its investigation. Corino and Brodkey[18] in their visual studies of fluid motions near the wall observed a two-layer phenomenon in which groups of particles were observed moving in different directions within a thin illuminated plane of fluid oriented parallel to the stream and normal to the wall. A sketch based on photographs of this phenomenon is shown in Fig. 5(c). The photographs[18] had a depth of field of the order of 20 viscous lengths. The two-layer phenomenon was commonly observed during bursting and this is direct evidence that severe velocity variations within a distance of less than
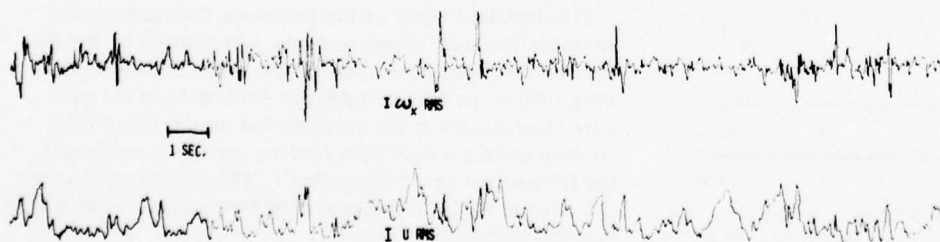
FIG. 8. Record of streamwise vorticity (upper trace) and streamwise velocity (lower trace) as function of time. *Probe in fully developed channel flow at $y^+ = 31$.* From *Kastrinakis et al.*[22]
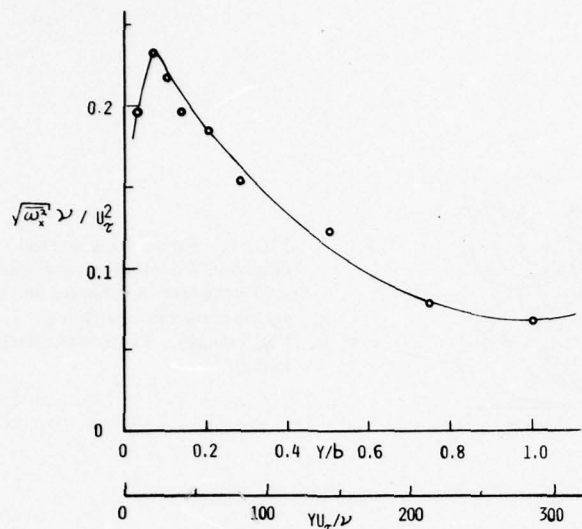
FIG. 9. Root-mean-square streamwise vorticity in a fully turbulent channel flow, channel width is $2b$. From Kastrinakis et al.[22]

20 viscous lengths are common during bursting.

Additional observations indicating that the structure of turbulence near the wall is of extremely small scale have been obtained from measurements of wall pressure fluctuations. Emmerling et al.[23] performed an experiment in which a section of the wall of an acoustically quiet and vibration free wind tunnel was used as one of the mirrors of a Michelson interferometer. The pressure fluctuations within the boundary layer deflected the mirror surface which was a thin reflecting membrane that covered an array of closely spaced holes drilled in the wall. Motion pictures of the fringe shift patterns on the membrane were analyzed to obtain instantaneous patterns of the wall pressure fluctuations. Figure 11 is an example of a sequence of four frames in which an intense
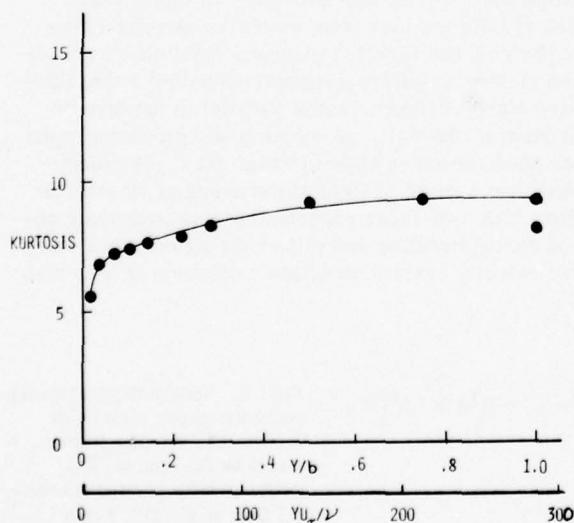
FIG. 10. Kurtosis of streamwise vorticity in a fully turbulent channel flow, channel width is $2b$. From Kastrinakis et al.[22]
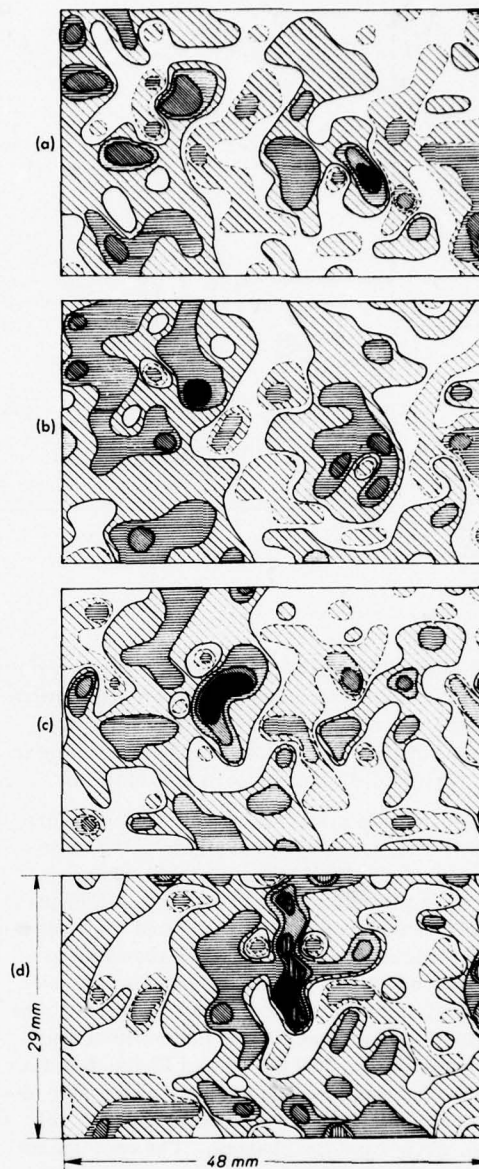
FIG. 11. Contours of instantaneous pressure fluctuations. The darker shading indicates large pressure changes. Positive fluctuations are outlined with solid lines and negative fluctuations with dashed lines. Stream velocity is from left to right. Time increases from (a) to (d): first frame (a) time = 17.57 msec; (b) time = 18 msec; (c) time = 19.14 msec; (d) time = 20.85 msec. From Emmerling.[23]

small scale increase in pressure is observed to form and move downstream.

The smallest scale of the pressure fluctuations observable in these measurements was limited by the diameter (55 viscous lengths) of the holes drilled in the wall. On some occasions large reversals in the pressure fluctuations could be observed on the membrane surface over a single hole (during pressure reversals the fringes became "S" shaped). This indicates that the transverse scale of the pressure fluctuations is less than half the membrane diameter.
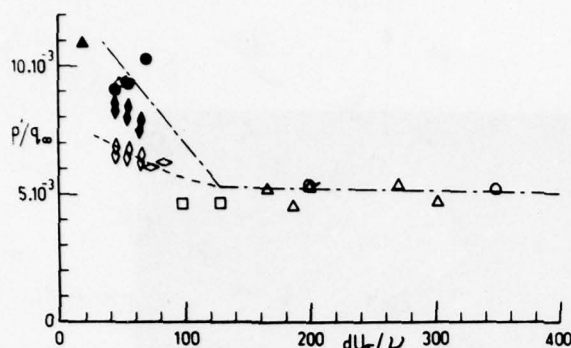
FIG. 12. Variation of measured rms wall pressure fluctuation with transducer size and type. Pinhole data: ●, Blake; ▲, Emmerling[23]; ♦, Bull and Thomas[24] flush-mounted-piezoelectric data: ◇, Lim; ○, Willmarth and Roos; △ Bull; □, Schloemer:, ◊, Bull and Thomas[24]; ▲, Emmerling[23] flush mounted capacitor microphone. From Bull and Thomas.[24]

Further evidence supporting the existence of intense small scale pressure fluctuations was obtained from the results of measurements by a number of investigators of wall pressure fluctuations using small "pinhole" microphones. Figure 12 shows the results of these measurements as summarized by Bull and Thomas.[24] Notice that for pinhole diameters less than 100 viscous lengths there is a dramatic increase in the root-mean-square wall pressure. Bull and Thomas[24] have shown that part of this increase is produced by the discontinuity in the surface caused by the pinhole. The open symbols in Fig. 12 show that the smaller, correct, values measured by very small flush transducers are of the order of 50% higher than the value at $d^+ \simeq 100$. This indicates that the smaller scale wall pressure fluctuations (with scales less than 100 viscous lengths) are of comparable intensity to those of larger scales. (The addition of two uncorrelated random signals of equal strength will result in an increase in the root-mean-square of their sum by a factor of $\sqrt{2}$.)

The wall pressure fluctuations must satisfy Poisson's equation (obtained from the divergence of the momemtum equation)

$$\partial^2(P+p)/\partial x_i^2 = -\rho \partial^2[(U_i+u_i)(U_j+u_j)]/\partial x_i \partial x_j. \quad (3)$$

The velocity gradient terms on the right-hand side of Eq. (3) can be regarded as the source terms in an integral representation for the pressure fluctuations in the flow. It is clear that the pressure at one point is produced by velocity contributions at many others and that the intensity of the pressure fluctuations must die off rapidly with distance from discrete sources. This suggests that the intense small scale wall pressure fluctuations must be produced very near the wall by equally intense and perhaps smaller scale velocity fluctuations. Further knowledge of these small scale flow fluctuations is necessary for a better understanding of the mechanism of drag reduction effects produced by additives.

III. NEW MEASUREMENTS OF SMALL SCALE STRUCTURE USING HOT WIRES

The evidence described here for the existence of small scale flow phenomena near the wall led us to de-

velop an extremely small hot wire array. We have constructed an "X" hot wire array, for measurements of the u and v velocities and the Reynolds stress, that has typical dimensions (wire length and spacing) of 100 μ (approximately 2.5 viscous lengths). The hot wire array was constructed from Wollaston wire with a core of 90% platinum–10% rhodium and a nominal diameter of 0.5 μ. The tapered wire supports were formed by etching the silver coating of the Wollaston wire as described by Bogar.[25] The X array was so small that it could not be made with a precisely aligned and oriented arrangement of the hot wires. To compensate for the lack of precision of the X array geometry a unique calibration scheme that will be described was developed to interpret the two electrical signals produced by the hot wire array. Figure 13 is a photograph of the probe and Fig. 14 is a drawing of the probe showing it positioned near the wall.

The hot wires were operated at 50% overheat. This required only a few milliamperes and was supplied by specially constructed constant temperature hot wire anemometer circuits patterned after the circuit described by Wyngaard and Lumley.[26] The frequency response of the hot-wire anemometer system was uniform up to frequencies of 20 kHz. This was determined by exposing the wires to an intense acoustical sound field.[25] The calibration of the array for the combined response to u and v velocities was accomplished with the aid of a digital computer. The probe to be calibrated was mounted on a mechanical device which slowly pitched it through angles of ± 75° in the free stream flow in the wind tunnel. A potentiometer was used to measure the pitch angle, θ, of the probe and a propellor anemometer
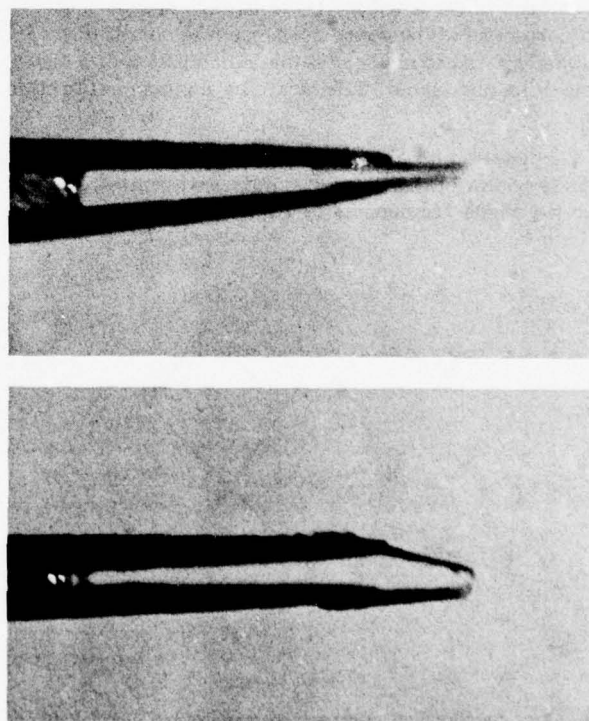
FIG. 13. Small X probe. Photographs of top and side view.
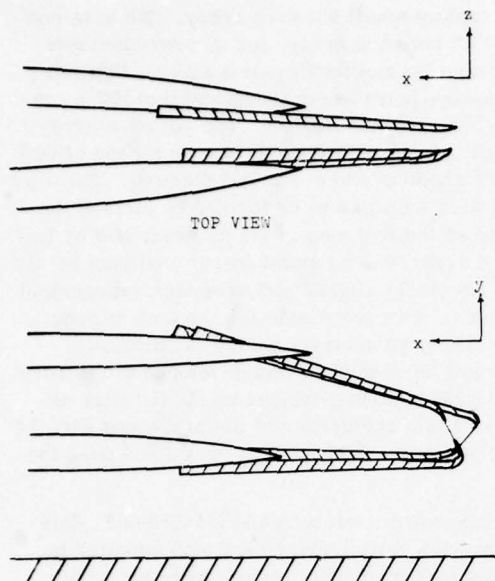
FIG. 14. Small X probe. Drawing of sensitive region; top and side view.

(R. M. Young Co.) was used to measure the mean-free-stream speed in the tunnel. The voltage outputs of the constant temperature anemometers and the voltage corresponding to the pitch angle of the probe and the free stream speed were then recorded on magnetic tape using a frequency modulated system (Honeywell 5600C). As the voltage signals were recorded the pitch angle of the probe was varied periodically and the free stream speed was slowly decreased from speeds greater than any encountered in the boundary layer to zero speed. In this way a record of the probe response was obtained when it was exposed to every possible combination of u and v velocities obtainable in the spatially uniform calibration flow.

The notation for the probe geometry during calibration is shown in Fig. 15. The output voltages from the two hot wires are denoted by EL and EU. The calibra-
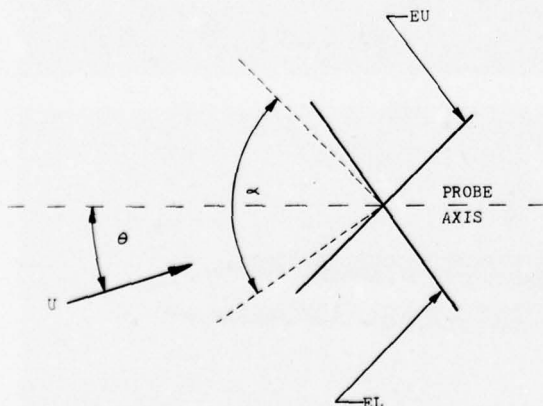
FIG. 15. Geometrical arrangement and symbol definitions for X probe.
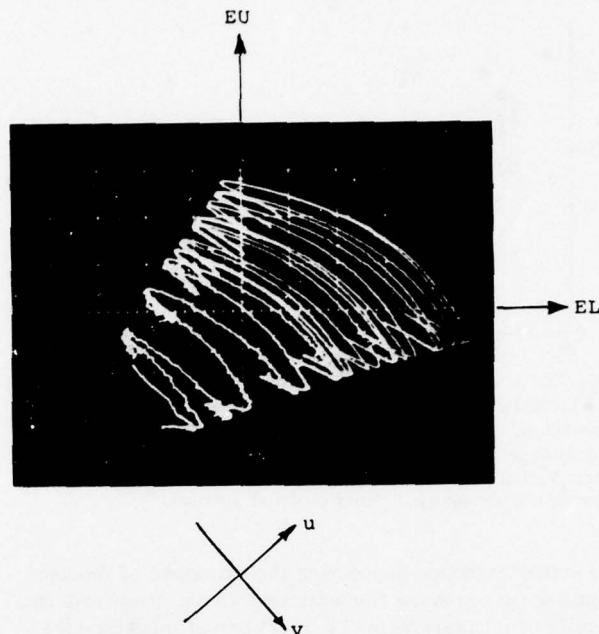
FIG. 16. Photograph of variation of voltages EL and EU displayed on a screen of storage oscilloscope during calibration for turbulence measurements at $y^+ = 335$.

tion of the X wire makes use of the concept that there is a unique pair of voltages EL and EU for each velocity pair u and v. This is true when the velocity is uniform over the X wires, the spanwise velocity is zero, and the velocity vector lies within the angle, α, formed either by the normals to the two wires or by the two wires themselves, whichever angle is the smaller. In Fig. 15 the angle, α, is that between the normals to the two wires. Obviously, α, is a maximum of 90° when the wires are ideally oriented at right angles. If the inclination of the velocity vector exceeds the range denoted by, α, the wires will produce a nonunique voltage pair that corresponds to more than one velocity pair.

The geometry of the probe used for these measurements allowed angles of attack, θ, in the range from +38° to −51°. Figure 16 is an example of voltage pairs EL and EU resulting from a typical calibration displayed on the screen of a storage oscilloscope. The points where ambiguity of the voltage pairs was produced by exceeding the range, α, of the probe can be clearly discerned at the edges of the calibration grid. The EL, EU traces appear to curl under producing the same pairs of EL and EU voltages for different pairs of u and v velocity components.

The four tape recorded channels of calibration data were reproduced and digitized with the aid of a Data General Minicomputer System using a 12 bit analog-to-digital converter with simultaneous sample and hold input amplifiers. A computer program was written to process only the unique voltage pairs of calibration data within the range, α, and to construct a relatively coarse (20 ×20) calibration table or "grid" with 400 discrete points. The velocity pairs, u and v, and the four partial derivatives of u and v with respect to EL and EU were com-

TABLE I. Properties of the actual and ideal turbulent boundary layer.

	Present work	Coles' ideal boundary layer
U_∞ (m/sec)	9.14	...
Re_θ	11 700	11 700
δ/cm	17.8	...
δ^*/cm	2.4	...
θ/cm	1.78	...
δ^*/θ	1.349	1.337
u_T/U_∞	0.0350	0.0351
$Re_x/10^{-6}$	3.7	7.9

puted at each of the 400 entry points of the table and stored in the computer.

Measurements were made in a fully turbulent boundary layer with a free stream velocity of 9.1 m/sec. The boundary layer was that developed on the smooth floor of the 1.52×2.13 m wind tunnel at the University of Michigan. The properties of the boundary layer at Re_θ =11 700 are given in Table I.

Figure 17 shows storage oscilloscope traces of the calibration grids superimposed upon the EL, EU traces produced by the probe when it was immersed in the turbulent boundary layer. In Fig. 17(a), at $y^+ \simeq 650$, the EL, EU traces were all well within the range of values produced during the calibration of the probe. The EL and EU voltages were digitized and stored on magnetic tape. A computer program was used to "look up" and interpolate from the calibration table data the pair of u and v velocity components appropriate for each pair of digitized EL and EU voltages. The results for y^+ greater than approximately 600 ($y/\delta > 0.15$) were in good agreement with those obtained classically in many other investigations. Figures 18 and 19 display the measured values of root-mean square velocities u and v and the Reynolds stress as a function of y. When the probe was nearer the wall, $y/\delta < 0.15$, the measured root-mean-square velocities u and v and also the Reynolds stress were larger than the values measured in classical investigations.

As the probe was moved much closer to the wall, below values of $y^+ = 120$, not only were the root-mean-square velocities u and v and the Reynolds stress too large, but the EL, EU voltage traces obtained in the boundary layer went beyond the valid boundaries of the corresponding calibration grid at that location. Figures 17(b) and 17(c) show typical results at $y^+ \simeq 65$ and at $y^+ \simeq 3$ (the smallest distance from the wall that could be obtained with the small X probe). The EL, EU traces began to exceed the bounds of the calibration grid first on the lower, outflow ($v > 0$) portion of the grid and then also on the upper, inflow ($v < 0$) portion of the grid. The excursions from the grid were characteristically rather intense and rapid voltage fluctuations. As the probe approached the wall the excursions from the grid became more numerous. Very near the wall at $y^+ \simeq 10$ the excursions were so frequent that 19% of the time the voltage pairs were off the grid. Furthermore, 40% of the

time that the velocity was lower than the mean and outward from the wall the EL, EU traces were off the grid.

The occurrence of excursions from the calibration grid made it impossible to assign the correct velocity pairs u and v to the voltage pairs EL and EU that were off the grid. Furthermore, even when the voltage pairs were within the calibration grid there is no way to guarantee the accuracy of the assignment of velocity pairs to voltage pairs using the calibration data. Figures 18 and 19 show values of the root-mean-square velocity components of u and v and values of the Reynolds stress $\overline{uv}$ as well as the measurements of these quantities using conventional techniques by Klebanoff,[27] Schubauer[28] and Lu and Willmarth.[29] When the voltage pairs were off the grid, in the present measurements, the velocity pair at the point of departure from the grid was assigned to each voltage pair thereafter until the voltage pairs again returned to the grid. The present data of Figs. 18 and 19 are, therefore, seriously in error near the wall for $y/\delta < 0.15$ or $y^+ < 600$.
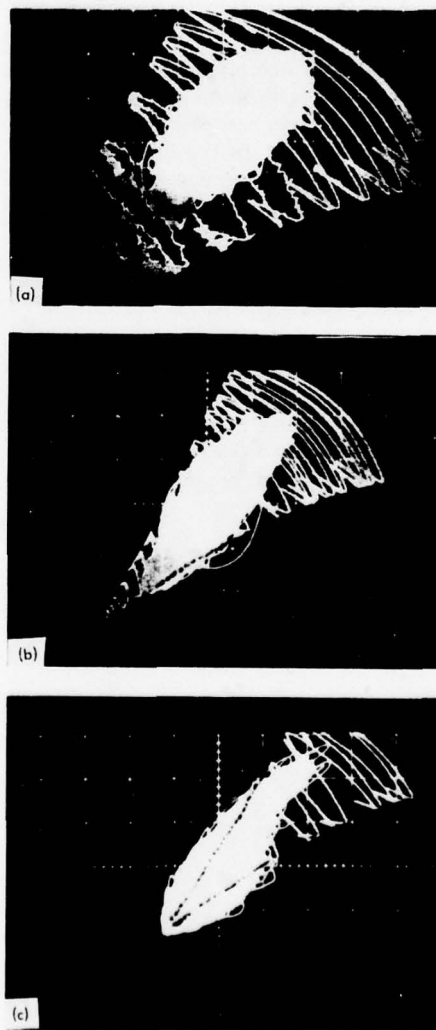
FIG. 17. Photographs of EL and EU voltages during turbulence measurements and calibrations displayed on screen of storage oscillosocpe. (a) $y^+ = 670$; (b) $y^+ = 65$; (c) $y^+ = 3$.
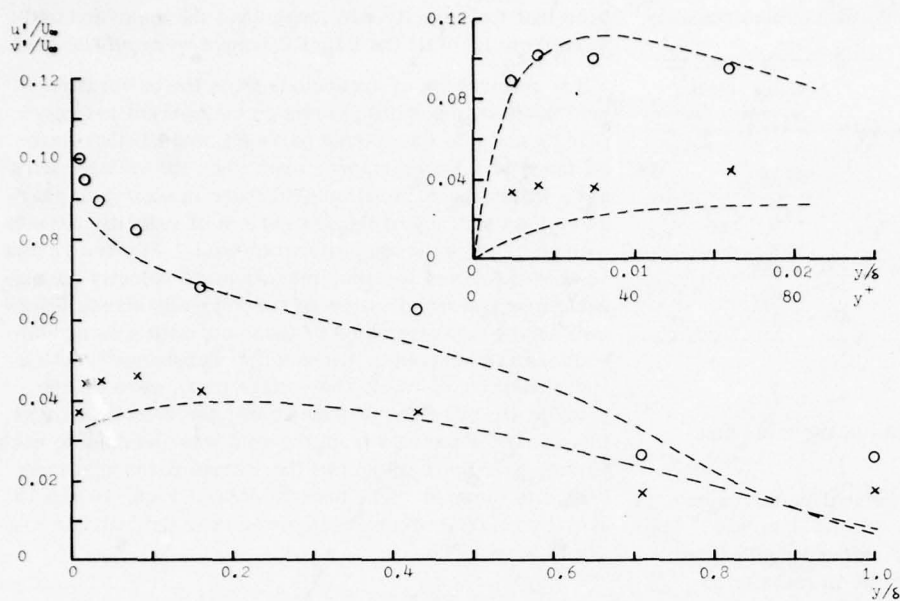
FIG. 18. Profiles of rms velocity fluctuations in the streamwise direction, u', and normal to the wall v'. o, u'/U_∞; ×, v'/U_∞; --- data of Klebanoff.[27]

A number of hypotheses which might explain the cause of the excursions from the calibration grid include aerodynamic or thermal interaction between the hot wires or their supports, the presence of the transverse velocity component, w, the presence of free convection effects and motion or vibration of the hot wires. A detailed discussion and analysis of the effect that each of these phenomena would have on the EL, EU voltage traces is presented in Bogar.[25] The result of the analysis was that the presence of a transverse velocity acts to bring the EL, EU trace back on the grid. The thermal effects are confined to a wake region which is thin compared with the spacing between the wires, and thus could not cause large excursions from the grid. The effect of transverse velocity and heated wake interactions were checked in the wind tunnel by calibrating a yawed probe.

Large differences in the calibration grid were not encountered, and it was concluded that transverse velocities and thermal effects did not cause large excursions from the grid. Free convection effects were negligible at the speeds at which large excursions were observed. Motion of the hot wires under the influence of the local flow in the streamwise and spanwise directions would have similar effects on each wire and would not tend to take the EL, EU traces off the grid. Greater motion of one wire than the other could be caused by local flow normal to the wall, but this would tend to put the EL, EU traces back on the grid. The result was that none of these phenomena were found capable of producing large excursions from the grid similar to those observed when the X array was near the wall. The only remaining explanation for the excursions from the calibration grid is
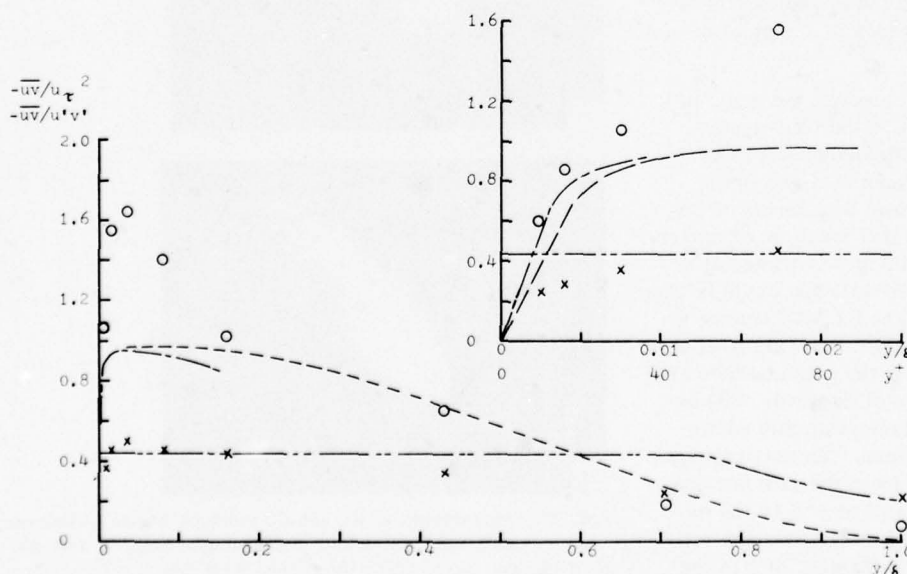
FIG. 19. Profiles of Reynolds stress normalized with rms velocities and wall shear stress. o, $\overline{uv}/u_\tau^2$. ×, $\overline{uv}/u'v'$; ---, data of Klebanoff[27]; ― ― ―, data of Schubauer[28]; ―··―, data of Lu and Willmarth[29]; ―·―, profile calculated from mean profile.[25]
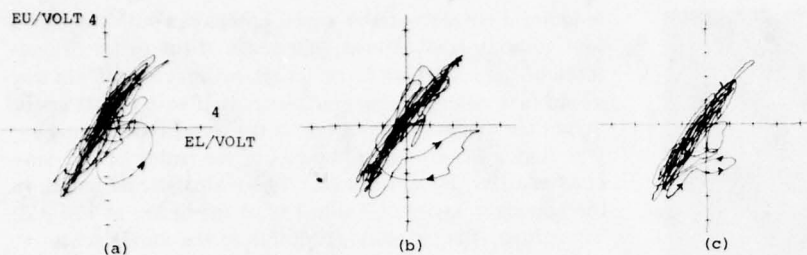
FIG. 20. EL and EU traces of individual high intensity excursions from the calibration grid. (a) $y^+ = 8$; (b), (c) $y^+ = 10$.

that one wire of the array was exposed to flow with a velocity different (in both magnitude and direction) from the velocity to which the other wire in the array was simultaneously exposed. This will occur if the probe encounters severe velocity gradients associated with turbulence of a scale smaller than the probe dimensions. A directly observable example is the two-layer phenomena reported by Corino and Brodkey,[18] see Fig. 5(c), which has a scale less than 20 viscous lengths.

In support of this explanation one should note that during an excursion neither of the voltages EL or EU was one that was not produced during probe calibration. The significant observation is that the *pair* of voltages produced during exposure to the small scale turbulence near the wall was not encountered during calibration of the probe in a uniform flow. Thus, during an excursion one wire of the probe encounters fluid with a velocity different in magnitude and direction from the velocity of the fluid which the other wire encounters. The X array is then not capable of determining the u and v velocity at a point and the excursions from the calibration grid are simply an indication that turbulent structure of a scale smaller than the distance between the hot wires of the X array has been encountered.

The conclusion that is drawn from these results is that the measurements of the root-mean-square velocities $\sqrt{\overline{u^2}}$ and $\sqrt{\overline{v^2}}$ and of the Reynolds stress $\overline{uv}$ for $y^+ < 500$

using a small hot wire X array with 100 μ length, l, ($l^+ = 2.5$) and spacing, s, ($s^+ = 2.5$) are not correct. Thus, the data points shown on Figs. 18 and 19 are in error for $y/\delta < 0.15$ ($y^+ < 500$).

An important question which one must ask is: What does a conventional size X wire array measure in the boundary layer near the wall? For simplicity, let us assume that the wires are very straight, of large aspect ratio, have $\alpha = 90°$, and obey the classical cosine law. Then, one can state that the use of the conventional sum and difference of linearized hot wire output voltages EL and EU to obtain the velocity components u and v will not give correct results when small scale turbulent structures encounter the hot wire array. However, one will not be able to determine when the velocity components u and v determined by the conventional sum and difference technique are in error. Furthermore, since a conventional X array is of the order of ten times as large as the small X array described here much of the effect of the small scale structure will be smeared out by the excessive length of each of the hot wires. This should surpress the excursions from the calibration grid.

To check these conclusions we purchased the smallest commerical available hot wire, X array (Thermosystems Inc. Model 1248T1.5) and calibrated it using the same EL, EU grid technique that was used for our 100
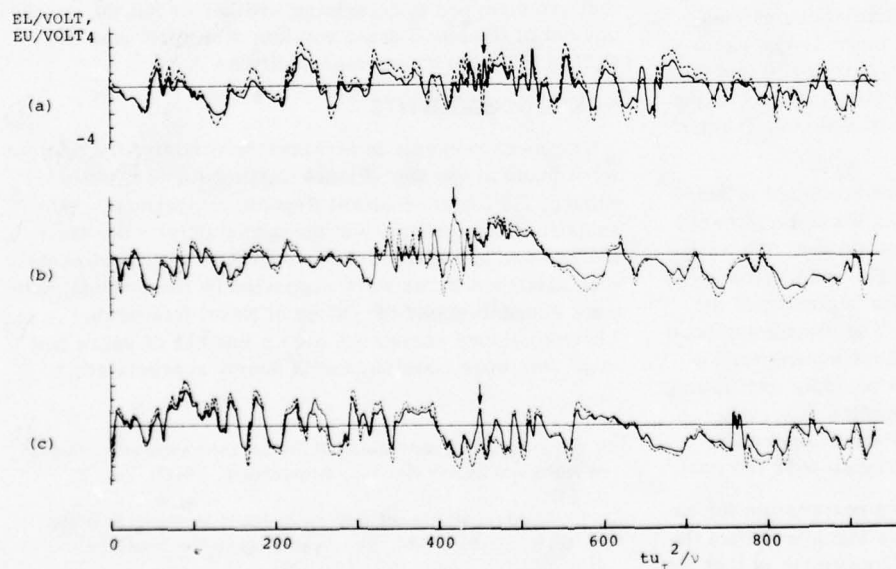
FIG. 21. EL and EU as a function of dimensionless time before and after excursion of Fig. 20. Arrow indicates excursion of Fig. 20. —, EL; ---, EU.
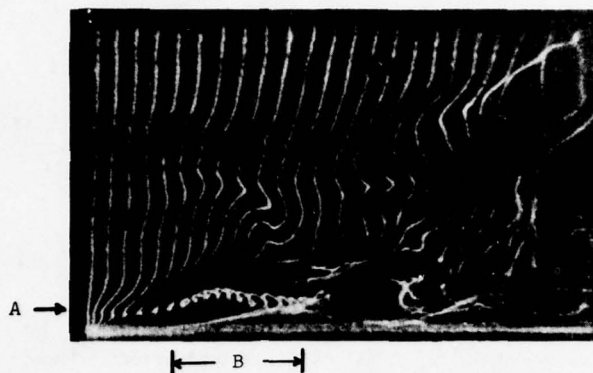
FIG. 22. Growing streamwise vortex near the wall terminating in breakup. Vortex extends from line A over zone B. Note inflectional profile near the normal bubble wire. From Kline *et al.*[17]

μ X array. The wire length, l, was 1200 μ ($l^+ = 30$) and the spacing between the wires, s, was 500 μ ($s^+ = 12.5$). When placed in the boundary layer near the wall, the EL, EU traces were almost always on the grid. However, near the wall with the center of the X array at a distance $y = 800$ μ ($y^+ = 20$) from the wall occasional excursions off the calibration grid were observed. At $y^+ = 20$, only 0.05% of the data pairs EL and EU were off the grid. Furthermore, the excursions were smaller than those measured with the small X array. Although the excursions of the grid were surpressed, the root-mean-square values of the velocity components u and v determined from the calibration grid were 15 to 20% higher than the classical values and the Reynolds stress $\overline{uv}$ was between 50% to 100% higher than the mean shear at the wall for $20 \le y^+ < 600$.

These results indicate that severe excursions from the calibration grid were suppressed by the spatial averaging of the small scale structure along the length of the larger X array hot wires and by the greater spacing between the wires. They also demonstrate that measurements with conventional X wire arrays are inaccurate when small scale structure is present. Serious measurement errors can occur even if there are no excursions from the calibration grid. This is consistent with the results of measurements of the wall pressure using small transducers, see the results of Bull and Thomas[24] in Fig. 12.

A few of the largest excursions were studied in more detail. Figure 20 shows three examples of large excursions from the calibration grid at points near the wall. Figure 21 shows the corresponding EL and EU traces as a function of time, the location of the beginning of the excursion is marked by an arrow. The interesting feature of this data is that when an excursion occurred a few cycles of high amplitude almost periodic oscillations of the hot wire voltage signals were often observed. This suggests the association of the excursions with small scale oscillatory flow in the region near the wall.

The scale of the velocity gradients responsible for excursions from the calibration grid is much less than the hot wire length or spacing. A rough estimate is that the

velocity changes may be small compared with the turbulent velocity fluctuations on a scale of the order of one-tenth of the small hot wire length or spacing. This suggests that velocity changes associated with small scale structure are small relative to the amplitude of turbulent fluctuations over distances of the order of 0.2 viscous lengths (10 μ) or less. The Kolmogoroff length in the boundary layer of Table I is of the order of 170 μ. Therefore, the velocity gradients in the small scale structure near the wall will only become small over a distance that is less than approximately 1/20 of the Kolmogoroff length.

It is important to know more about the nature of the small scale structure near the wall. Our observations suggest that the small scale turbulent flow is energetic and contains definite periodicity when the small scale structure causes excursions of the X array voltage pairs from the calibration grid.

Kim *et al.*[17] have observed intermittent small scale streamwise vortices in bubble traces near the wall. When the vortices occurred, they also observed a few cycles of energetic oscillations of the streamwise velocity. Figure 22 is an example of a bubble trace observed when these oscillations occurred and shows the swirling flow pattern produced by a typical small intense streamwise vortex whose transverse scale is of the order of 2 viscous lengths near its origin. Small scale streamwise vortices were often observed by Kim *et al.*[17] during bursting. We suggest that the streamwise vortical flow structure is primarily responsible for intense small scale gradients in the turbulent flow near the wall.

When drag reduction occurs in practical water flows, the flow speeds are of the order of 1 to 10 m/sec. The transverse scale of the streamwise vortices near the wall is then in the range of 5 μ to 50 μ. We suggest that the size of the small scale flow structures near the wall is comparable to the typical length scale of the shear waves in fluids with polymer additives,[30] or of extended polymer molecules as discussed by Tulin[31] and by Hinch[32] at this symposium. Experiments should be performed that are designed to determine whether or not the development of the small scale vortical structure near the wall is inhibited by polymer additives.

ACKNOWLEDGMENTS

[1] B. A. Toms, in *Proceedings of the 1st International Congress on Rheology* (North Holland, Amsterdam, 1948), Vol. 2, p. 135.
[2] J. L. Lumley, in *Annual Review of Fluid Mechanics*, edited by W. R. Sears and M. Van Dyke (Annual Reviews, Palo Alto, Calif., 1969), Vol. 1, p. 367.

[3]P. S. Virk, E. W. Merril, H. S. Mickley, K. A. Smith, and E. L. Mollo-Christensen, J. Fluid Mech. **30**, 305 (1967).

[4]M. J. Rudd, J. Fluid Mech. **51**, 673 (1972).

[5]M. M. Reischman and W. G. Tiederman, J. Fluid Mech. **70**, 369 (1975).

[6]T. Mizushina and H. Usui, Phys. Fluids **20**, S100 (October, Part II, 1977).

[7]L. S. G. Kovasznay, Phys. Fluids Suppl. **10**, S25 (1967).

[8]L. S. G. Kovasznay, in *Annual Review of Fluid Mechanics*, edited by M. Van Dyke, W. G. Vincenti, and J. V. Wehausen (Annual Reviews, Palo Alto, Calif., 1970), Vol. 2, p. 95.

[9]E. L. Mollo-Christensen, AIAA J. **9**, 1217 (1971).

[10]J. Laufer, in *Instituto Nazionale Di Alta Mathematica*, Symposia Mathematica (Monograf, Bologna, 1972), Vol. IX, p. 299.

[11]W. W. Willmarth, in *Advances in Applied Mechanics*, edited by C. S. Yih (Academic, New York, 1975), Vol. 15, p. 159.

[12]M. J. Lighthill, in *Laminar Boundary Layers*, edited by L. Rosenhead (Oxford University Press, Oxford, 1963), Chap. II.

[13]G. B. Schubauer and P. S. Klebanoff, NACA Report 1289 (1956).

[14]S. Corrsin, in *Naval Hydrodynamics*, Publication 515 (National Academy of Sciences, National Research Council, Washington, D.C., 1957), Chap. XV.

[15]S. J. Kline, W. C. Reynolds, F. A. Schraub, and P. W. Runstalder, J. Fluid Mech. **30**, 741 (1967).

[16]A. K. Gupta, J. Laufer, and R. E. Kaplan, J. Fluid Mech. **50**, 493 (1971).

[17]H. T. Kim, S. J. Kline, and W. C. Reynolds, J. Fluid Mech. **50**, 133 (1971).

[18]E. R. Corino and R. S. Brodkey, J. Fluid Mech. **37**, 1 (1969).

[19]G. R. Offen and S. J. Kline, J. Fluid Mech. **62**, 233 (1974).

[20]T. Theodorsen, 50 *Jahre Grenzschichtforschung*, edited by H. Görtler and W. Tollmien (Vieweg, Braunschweig, 1955), p. 55.

[21]W. W. Willmarth and B. J. Tu, Phys. Fluids Suppl. **10**, S134 (1967).

[22]L. Kastrinakis, J. M. Wallace, and W. W. Willmarth, Bull. Am. Phys. Soc. **20**, 1422 (1975).

[23]R. Emmerling, G. E. A. Meier, and A. Dinkelacker, in *AGARD Conference Proceedings* 131 *on Noise Mechanism*, (Advisory Group for Aerospace Research and Development, North Atlantic Treaty Organization, Paris, 1973), paper No. 24; see also A. Dinkelacker, M. Hessel, G. E. A. Meier, and G. Schewe, Phys. Fluids **20**, S216 (October, Part II, 1977).

[24]M. K. Bull and A. S. W. Thomas, Phys. Fluids **19**, 597 (1976).

[25]T. J. Bogar, Ph. D. thesis, University of Michigan (1975).

[26]J. C. Wyngaard and J. L. Lumley, J. Sci. Instrum. **44**, 363 (1967).

[27]P. S. Klebanoff, NACA Technical Note 3178 (1954).

[28]G. B. Schubauer, J. Appl. Phys. **25**, 188 (1954).

[29]S. S. Lu and W. W. Willmarth, J. Fluid Mech. **60**, 481 (1973).

[30]M. Tulin, Bull. Am. Phys. Soc. **10**, 267 (1965).

[31]M. Tulin, in *Sixth Symposium on Naval Hydrodynamics* (Government Printing Office, Washington, D.C., 1966), p. 3.

[32]E. J. Hinch, Phys. Fluids **20**, S22 (October, Part II, 1977).

Mechanical models of dilute polymer solutions in strong flows

E. J. Hinch

Department of Applied Mathematics and Theoretical Physics, University of Cambridge, Cambridge, England

In strong flows, such as turbulence, it is suggested that randomly coiled macromolecules might become nearly fully extended. To investigate this extended state, four models are considered which show the importance of the inextensibility of the polymer chain and the variation of the friction coefficient with the extension. The rheological consequences of these processes are then explored in an appropriately modified dumb-bell model. A dilute polymer solution is predicted to have a high extensional viscosity but a low shear viscosity, a stress hysteresis, and a slow stress relaxation. The action of the novel rheology is shown in two simple flows. Finally, speculations are made on the possible way dilute polymer solutions can modify turbulence.

I. STRESS LEVEL

Before attempting to explain the reduction of turbulent drag by very dilute polymer solutions, it is necessary to understand a little about both turbulent drag and dilute polymer solutions. This paper is concerned solely with the polymer side. Those features of the rheology of polymer solutions which I consider important in drag reduction will be reviewed. A complete historical review of the development of the subject has not been attempted.

For me the most amazing feature of drag reduction is that dramatic effects on the drag can be achieved with exceedingly small quantities of polymer additive, just a few parts per million by weight. How so little can be so effective is one question we can answer. Let me start by producing some estimates of the change in the levels of stress caused by suspending some small particles in a solvent.

A suspension of small particles can be treated as an effective continuum, albeit non-Newtonian and different from the solvent, as long as the particles are smaller than the smallest length scale of the flow. Often the length scale of the flow is simply the dimension of the apparatus, but in a turbulent boundary layer the required scale is the thickness of the viscous sublayer. A randomly coiled polymer is sufficiently small, typically being one hundredth the size of the smallest eddy. I should perhaps note here that this is not the situation in drag reduction by dusty gases and fiber suspensions. In these cases the relevant particle size, the stopping distance of the dust particles and the fiber length, usually exceeds the smallest eddy size by a large factor. Hence, dusty gases and fiber suspensions cannot be regarded as continua when studying turbulent drag reduction.

An immediate consequence of the ratio of the flow scale and the polymer size being large is that this non-dimensional group has no dynamical significance. By measuring the properties of a continuum, it is not possible to determine the size of its microstructure. Thus, the "length hypothesis" for the onset of drag reduction, however good it might appear as an experimental correlation, can have no physical basis.

When a suspension of particles acts as an effective continuum, the typical stress levels can often be estimated by applying Einstein's effective viscosity calculation. Einstein[1] showed that, for a dilute suspension of rigid inert spheres, the fractional change in the viscosity was two and a half times the volume fraction of the spheres. Before applying this result one needs to know that in low-Reynolds-number flows (the flow around the small polymers has a Reynolds number less than 10^{-4}) the effective hydrodynamic size of a particle is its largest linear dimension, e.g., the drag on a falling rod is crudely given by Stokes' law based on the half-length of the rod, with a very weak logarithmic dependence on the shape and thickness of the rod. Thus, to estimate the viscosity of dilute polymer solutions we use the volume fraction of those spheres which just enclose the separate polymer molecules.

Three things can go wrong with this procedure for estimating the stress levels in the suspension. First the particles can deform and thus not carry the same stress as a rigid particle which fully resists the straining. When polymers deform, however, they can avoid only a fraction of the rigid particle stress. Second, rod-like particles can sometimes align in a direction in which there is no component of strain, and this leads to a reduction in the apparent viscosity. This directionality effect occurs, however, only in simple shear flow which is not typical of turbulent motions. Finally, the effective hydrodynamic volume fraction can be large and thus break the diluteness restriction used in the Einstein calculation. In fact, this occurs in our application, even though the true volume fraction of the particles is minute. Fortunately, we are saved here by a recent theory of Batchelor[2] verified in some experiments by Mewis and Metzner[3]: in the case of fibrous particles the dilute formula still holds with very weak modifications.

As an illustration which will be continued through the paper, I will take a 100 ppm solution in water of Polyox of molecular weight 10^6. The relevant dimensions are then 0.3 μm for the separation of the polymers in solution, 0.03 μm for the rms size of the coiled (equilibrium) polymer in which each monomer is joined to the preceding one at a random angle and the chain thus executes a random walk (in a θ solvent), and 7 μm for the length
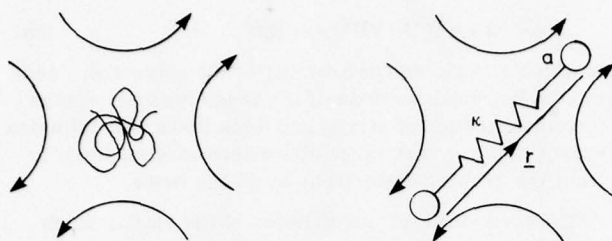
FIG. 1. The elastic dumb-bell model of a distorting polymer in the linear velocity field $\mathbf{u}(\mathbf{x}, t) = \mathbf{x} \cdot \nabla \mathbf{U}(t)$.

of the chain when it is stretched straight. If the polymers are coiled, the viscosity is estimated to change by a few percent, which is consistent with observation, while if the polymers are fully stretched the procedure suggests the viscosity increases by a factor of ten thousand.

The preceding illustration shows that if the polymers were all fully stretched then large changes in the rheology of a dilute solution can be expected, changes sufficient to effect turbulent drag. Clearly, the polymers need not be fully extended; significant rheological changes occur when the polymer coil is extended by a factor of ten (a hundred being fully stretched). If one believes that turbulence is moderately robust and can only be modified by major dynamical changes, then one must conclude that in drag reduction the randomly coiled polymers are stretched substantially. How the polymers can become stretched is tackled in the next section.

Why drag reduction can be achieved with only a little polymer has now been answered. Weight is simply an inappropriate measure of the added polymer. A better measure is the effective hydrodynamic volume fraction, i.e., the volume fraction of spheres just enclosing the separate polymers, and this measure shows a large concentration if the polymers are highly stretched.

Finally, I would like to criticize the agglomeration theories of drag reduction for not producing estimates of the effectiveness of aggregates. In order to produce a large rheological effect in turbulence but a negligible effect in a viscometric flow, the effective size of the aggregates must be ten times larger in turbulence. I fear that the implied levels of stress within an extended aggregate far exceeds the weak binding forces.

II. STRONG FLOWS

About the simplest representation of a distorted polymer is the elastic dumb-bell, introduced by Kuhn and Kuhn.[4] While, this limited model cannot answer many questions about macromolecular behavior, it does expose most clearly the key issues which determine how much distortion can be expected when the polymer is placed in a particular flow.

The gross distortion of the random walk of the chain, e.g., the separation of the monomers at the end of the chain, is represented by a single vector $\mathbf{r}$ which becomes the extension of a spring separating two beads, see Fig. 1. Now Brownian fluctuations in the chain con-

figuration produce a relaxation of the distortion. This entropic desire to return to the most probable, spherically symmetric, randomly coiled state is modeled by the elasticity of the spring. The linearized spring constant κ is usually taken to be $3kT/Nb^2$, in which kT is the Boltzmann temperature, N is the number of monomers, and b is their length. This spring law corresponds to the force which must be applied at the opposite ends of a single independent bond in order to produce an expected alignment of $\mathbf{r}/N$, the calculation closely following the theory of magnetic susceptibility. When $r/N \ll b$ the (inverse Langevin) spring law can be linearized.

The polymer chain is distorted by a flow with a velocity gradient because there is a velocity difference between the two sides of the random walk. In the elastic dumb-bell model this stretching is represented by the hydrodynamic drag on the spherical beads, with friction constants $6\pi\mu a$, according to Stokes' law. As I noted in the preceding section, the effective hydrodynamic size of the polymer chain is its linear dimension and so in this gross model one should take $a = b(N/6)^{1/2}$ (known as the impermeable case).

To derive the evolution equation of the dumb-bell, a force balance is made on each bead, resulting in

$$\dot{\mathbf{r}} = \mathbf{r} \cdot \nabla \mathbf{U}(t) - \lambda \mathbf{r} , \tag{1}$$

where $\lambda = \kappa/6\pi\mu a$. Also, one concludes that the polymer is advected by the local bulk flow, so that the velocity gradient tensor should be evaluated as a function of time in a Lagrangian frame. The two terms on the right-hand side of (1) express, as any simple model of the microstructure of a fluid inevitably must, the flow-induced distortion and its relaxation, with only the relaxation rate depending on the details of the model. For the continuing illustration of the Polyox solution referred to earlier, the relaxation time is estimated to be a little shorter than a millisecond, which is consistent with observations of the dynamic viscosity.

The question of how much distortion can be expected when the polymer is placed in a particular flow can now be answered by solving (1). For simplicity, we consider flows with constant histories, i.e., the $\nabla \mathbf{U}$ seen by the polymer advected by the bulk flow is independent of time. Under such circumstances the solution of the linear evolution equation (1) is the sum of three exponential functions of time. Denoting $|\nabla \mathbf{U}|$ as the largest real part of an eigenvalue of the tensor $\nabla \mathbf{U}$, the behavior of the polymer can be divided into two classes. If $|\nabla \mathbf{U}| < \lambda$ (a weak flow), the restoring force wins and the distortion decays. If $|\nabla \mathbf{U}| \geq \lambda$ (a strong flow), the stretching flow wins, and within this crude model, the distortion increases in time without bound. The next section will examine the development of the very large distortions more carefully. For the present we only need the suggestion that large distortions exist in strong flows. The first indication of the existence of strong flows was Takserman-Krozer's[5] study of the related Rouse–Zimm model in uni-axial straining motion.

From the discussion of the preceding section relating the levels of stress to the distortion of the polymers,

dramatic rheological effects are to be expected in strong flows. The condition that the flow is strong leads[6] to the "time hypothesis" for the onset of drag reduction: that the turbulent wall strain rate u_*^2/ν, should exceed the principal polymer relaxation time $0.4\, kT/\mu N^{3/2} b^3$. Experimentally, the two time scales are found to be of the same order of magnitude, but there is wide scatter in the data. I think the reason for the poor practical correlation is that both time scales need some refinement. It is becoming increasingly clear that the polymers respond more to the peak strain rate rather than the rms level represented by u_*^2/ν. The peak levels will have a weak Reynolds number dependence because of the intermittency within the turbulence. The molecular time scale employed can be faulted as depending too much on a poor theory, even when expressed in the less sensitive form $[\eta]\, \mu M/RT$. Direct observation of the relaxation time, e.g., from the dynamic viscosity, would be preferable. The influence of polydispersivity also needs to be understood.

Using the classification of flows into weak and strong, an unsatisfactory feature of viscometric testing is exposed. Simple shear flow has the property that $|\nabla U|$ vanishes whatever the magnitude of the flow. Viscometric measurements may thus not be relevant to strong flows such as those found in turbulence.

The strange property of simple shear, that it is weak whatever the magnitude of the flow, is very rare in the class of all possible types of flow; in fact, those flows with this property have the zero measure of a point on a plane. Lumley's[7] study of two-dimensional flows is misleading on this matter because two-dimensional flows are weak if the vorticity exceeds the strain rate. The trouble stems from his special orthogonality of the vorticity vector to the only two principal axes of strain. If the vorticity is sufficiently large, the polymer molecule spins roughly with the vorticity and this spinning averages out the oscillating strain-rate that it sees in the plane orthogonal to the vorticity. Thus, in two-dimensional flows the spinning molecule sees an average strain rate of zero once the vorticity is large enough. In three-dimensional flows, however, it is most unusual for the component of the straining in the direction of the vorticity to vanish, i.e., for the average strain rate in the orthogonal plane to vanish.

Before passing on to some models of polymers at large distortions, I should briefly mention some classical improvements in the crude elastic dumb-bell model. By adding Brownian motion to the beads, the undesirable feature of the distortion vanishing althogether in weak flows can be avoided; instead the distortion tends to a small nonzero equilibrium. With the polymer state now described by the expected second moment of the distortion $\langle \mathbf{r}\,\mathbf{r}\rangle$ the evolution equation becomes

$$\frac{D}{Dt}\langle \mathbf{rr}\rangle = \langle \mathbf{rr}\rangle \cdot \nabla\mathbf{U} + \nabla\mathbf{U}^T \cdot \langle \mathbf{rr}\rangle - 2\lambda\left(\langle \mathbf{rr}\rangle - \frac{r_0^2}{3}\mathbf{1}\right),\quad (2a)$$

in which r_0 is the equilibrium radius of gyration. The constitutive equations for the dilute polymer solution are completed (in this extension of the elastic dumbbell) by an expression for the bulk stress,

$$\sigma = -p\mathbf{1} + \mu\,(\nabla\mathbf{U} + \nabla\mathbf{U}^T) + n\kappa\,\langle \mathbf{rr}\rangle\,,\qquad (2b)$$

in which n is the number density of the polymers. Adding the Brownian motions of the beads does not change the classification of strong and weak flows, for diffusion cannot produce very large distortions in weak flows or limit the growing distortions in strong flows.

A second standard modification of the elastic dumbbell is the model Rouse[8] and Zimm[9] in which the polymer chain is represented by a necklace of beads and springs, with some form of hydrodynamic interaction between the beads. The necklace allows some internal distribution of the distortion to be represented in addition to the gross distortion. This internal distribution shows itself in the dynamic viscosity, but only modifies the strong and weak flow classification by changing the critical flow strength, λ, to the relaxation rate of the slowest mode.

Finally, there are a number of complicated effects which make the radius of gyration of the equilibrium random walk differ from the ideal result $r_0 = b(N/6)^{1/2}$. These effects are the hindered rotation of the bond angle between monomers, the finite volume of the monomers and adjacent solvent molecules, and short and long range electrostatic interactions between subgroups. All these effects are usually lumped into a modified value of r_0, sometimes ten times the ideal value. Changes in these effects with distortion are not normally considered.

III. LARGE DISTORTIONS

So far we have seen that large distortions of the polymer molecules are needed for dilute solutions to have dramatic flow properties and that the crude elastic dumb-bell model suggests such large distortions can be expected in strong flows. In this section the dynamics of polymers with large distortions are explored. Four models are presented which exhibit in a simple way different aspects of the dynamics. I think a full model incorporating all conceivable effects would not necessarily be an improvement because it would be intractable and cloud our understanding of the mechanics underlying the phenomena.

Two important effects enter when the distortion becomes large. As soon as the distortion becomes comparable with the radius of gyration, the hydrodynamic shielding of parts of the chain by other parts is altered. At very much larger distortions the finite extensibility of the polymer chain becomes relevant. I am going to concentrate on these two effects, even though in practice excluded volume, ionic charges and knotting of the chain may not be negligible. These other effects are, however, auxiliary factors in the essential competition between the bulk flow creating the distortion and the entropic restoring mechanism.

A. Elastic ellipsoid

The first nonlinear effect to be considered then is the dependence of the stretching by the bulk flow on the distortion. A suitable model to exemplify this effect is the elastic ellipsoid model, introduced by Cerf[10] before the necklace generalization of the bead-and-springs and ex-

S24   Phys. Fluids, Vol. 20, No. 10, Pt. II, October 1977

E. J. Hinch   S24

plored later by Roscoe.[11] In the model the deformed polymer is represented by an ellipsoidal shaped particle of constant volume. The solvent flow around the particle exerts distorting surface tractions. For the entropic restoring forces the particle is given a simple Hookean elasticity. Resistance to changes in shape due to the chain moving in a viscous solvent and also due to the chain entangling with itself is represented by an internal viscosity of the particle which exceeds the solvent value.

It should be noted that the elastic ellipsoid is again a gross distortion model; the internal distribution of the chain distortion is not represented. The model further suffers the use of an *ad hoc* relation between its elastic modulus and the molecular origin of the restoring force. The beauty of the model, however, is that if the particle starts as a homogeneously stressed ellipsoid, e.g., a sphere at rest, then it always remains an ellipsoid. The development of the distortion can therefore be tracked into the nonlinear regime using just five variables. Even so the mathematics is too complex to be presented here. From the details two new effects emerge.

The first and more important conclusion from the elastic ellipsoid model is that the frictional grip of the flow increases with the distortion. As pointed out in the first section of the paper, the effective hydrodynamic size of a particle is its maximum linear dimension. The detailed mathematics must therefore reflect this basic fact with a friction coefficient for the stretching motion increasing roughly in proportion to the distortion. A consequence of this increasing frictional grip is that large distortions can be maintained by some weak flows so long as the initial distortion is large enough. Because the nonlinear hydrodynamics only widens the difference between the stretching and restoring forces in strong flows, the growing distortion can only be limited by the finite extensibility of the polymer chain (or the finite duration of the strong flow). Finite extensibility will be taken up in the next model.

The second conclusion from the model, which is less important in dilute solutions, is that the particle spins with a sum of the full vorticity but only part of the straining motion. The inefficiency of the straining motion in spinning the particle is due to the "rigidity" of the particle provided by the internal viscosity. It appears that this internal rigidity leads to several rheological phenomena absent in the elastic dumb-bell, namely, a shear thinning viscosity, second normal stress differences, and, in flows starting from rest, a nonzero initial stress and oscillatory overshoots. None of these effects would have a large magnitude in a dilute solution.

B. Inextensible flexible thread

The preceding model has shown that in strong flows (of sufficient duration) the distortion will grow until it is limited by the finite extensibility of the polymer chain. To examine the combined effects of hydrodynamic stretching and the inextensibility, I have investigated a new flexible thread model.[12] For slender bodies such as
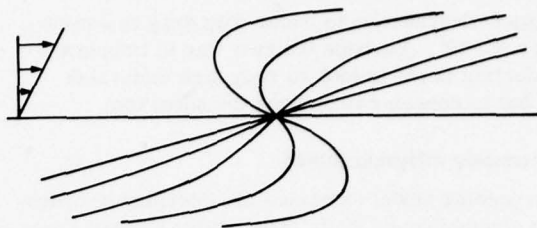
FIG. 2. The straightening of a flexible inextensible thread in a shear flow, starting from the S shape. The configuration $\mathbf{x}(s, t)$ is plotted as a function of s at $\gamma t = 0$, 1, 2, 3, 4.

a thread, there is an asymptotic theory for the flow of the solvent around a thread. With the thread described by a vector function of arc length s and time t, $\mathbf{x}(s, t)$, and with $\mathbf{T}(s, t)$ the tension in the thread, the governing equations can be found as

$$\dot{\mathbf{x}} = \mathbf{x} \cdot \nabla \mathbf{U} + \frac{\log}{2\pi\mu}(\mathbf{T}'\mathbf{x}' + \tfrac{1}{2}\mathbf{T}\mathbf{x}'') \tag{3a}$$

$$\mathbf{T}'' - \tfrac{1}{2}(\mathbf{x}'')^2 \mathbf{T} = -(2\pi\mu/\log)\mathbf{x}' \cdot \nabla \mathbf{U} \cdot \mathbf{x}', \tag{3b}$$

where the primes denote differentiation with respect to arc length and the argument of the logarithm is the ratio of the length to the breadth of the thread. These equations can be solved by perturbation methods for nearly straight threads, and more generally on a computer. Figure 2 is an example of a numerical solution for simple shear flow starting from an initial S shape.

The main conclusion of the study of the flexible thread is that nearly always the thread rapidly straightens as shown in Fig. 2. First, the thread tends to an orientation in which it is in tension. This tension then snaps the thread straight. An exceptional flow is simple shear in which the tension vanishes in the eventual orientation, but here the bends of the thread are found to decay more rapidly than the approach to the final orientation, so that a straight thread still results.

From this model something can be said about the possibility of mechanical degradation of polymers in drag reduction. If one accepts the premise that some polymers may be fully stretched in the turbulence, then (3b) enables the tension at the center of the chain to be estimated as $2\pi\mu |\nabla \mathbf{U}| N^2 b^2 / \log N$. If our standard illustration of Polyox is placed in a flow with $|\nabla \mathbf{U}| = 10^5$ sec^{-1}, corresponding to a friction velocity of 0.3 m/sec this tension is 10^{-8} N. To estimate the binding force of the carbon atoms along the backbone, I have taken the binding energy of $\mathcal{E} = 120$ kcal/mol and divided this by the atomic separation of 3 A. The resulting estimate of the binding force is 10^{-8} N. Thus, one would expect the polymer to break into two in a flow with a strain rate as strong as 10^5 sec^{-1}. This prediction is consistent with general experience of degradation. It is interesting to note the variation with molecular weight of the onset point for drag reduction $|\nabla \mathbf{U}| \gtrsim kT/\mu N^{3/2} b^3$, and the onset point for mechanical degradation $|\nabla \mathbf{U}| \gtrsim \mathcal{E}/\mu N^2 b^3$. Making the degree of polymerization, N, larger may insure an earlier onset of drag reduction, but my modeling suggests that it may be more effective at lowering the start of degradation. Crudely speaking, I

would expect degradation to occur with drag reduction whenever $N > 10^5$. Perhaps the best way to improve drag reduction is not to look to very high molecular weights but to consider improving the solvation.

C. Transversely diffusing thread

The preceding model examined the interplay of hydrodynamic stretching and finite extensibility. When these two effects dominate, I concluded that the polymer chain would be stretched out almost straight. A question now naturally arises as to how strong the flow need be for these two effects to dominate. To answer the question the Brownian motion of the chain must be reintroduced, so that the conditions under which the Brownian coiling of the stretched chain is ineffective can be found.

In a second thread model,[13] I have included some weak Brownian motions. Weak Brownian motions acting on a straight thread cause small transverse distortions which can be described by a diffusion process in the *deformation space. So that the continuum thread represents the small but finite bonds of the polymer backbone, the degrees of freedom of the transverse distortions must be truncated.* This truncation also avoids an "ultraviolet catastrophe."

Some straightforward analysis yields the probability distribution of the distortions. There is less transverse displacement at the center compared with the ends of the thread, because there the tension is largest and it is the tension which snaps out the Brownian distortions. The rms transverse displacement is $0.2 (kT \log (kT \log N/\mu Nb |\nabla U|)^{1/2}$, a result insensitive to the truncation. Associated with the transverse distortions is a small coiling effect: the ends of an inextensible thread must come closer when the thread is not straight. This shortening is found to have a magnitude $kT \log N/ \mu Nb^2 |\nabla U|$, with a precise value which depends critically on the truncation. In some sense each degree of freedom of the transverse distortions brings $\frac{1}{2}kT$ potential energy; energy stored as the tension multiplied by the shortening. Thus, the shortening is roughly proportional to the number of degrees of freedom, i.e., dependent on the truncation. Also note that the shortening varies as the small strength of the weak Brownian motion multiplied by the large number of degrees of freedom, a result exploited in the following model.

For the Brownian motions to have a small effect, it is necessary that the transverse distortions and the associated shortening should both be small compared with the length of the thread, Nb. The second condition is the more stringent, $|\nabla U| \gtrsim kT \log N/\mu N^2 b^3$. Note that the flow strength needed to maintain the stretched polymer is $N^{-1/2}$ times weaker than the flow required to produce the initial large distortion of the random coil. This result simply reflects the increased frictional grip on the polymer.

D. Elastic rod

In the transversely diffusing thread model we saw that, except in extremely strong flows, the shortening is an order of magnitude larger than the transverse dis-

placements, although both were restricted to be small in the analysis. This result opens the possibility of a further regime for less strong flows, in which it is envisaged that the thread executes a noticeable random walk contained within a long slender envelope. To examine this regime, I present my final model of an elastic rod. The distorting forces of the bulk flow are still calculated using the slender-body theory for Stokes' flow, but are now applied to the envelope rather than directly to the thread. The Brownian motions of the polymer chain are included by treating the envelope as an elastic rod with an entropic longitudinal elasticity related to the local coiling of the thread.

To describe the coiling of the polymer chain in the elastic rod, the position r along the straight rod is specified as a function of the arc length s along the thread, i.e., $r(s, t)$. The local stretching of the random walk is thus $\partial r/\partial s$. Using similar arguments as for the elastic dumb-bell, the longitudinal tension $\mathbf{T}$ in the elastic rod is related to this local stretching by the Langevin spring law,

$$\mathbf{T} = (kT/b) \mathcal{L}^{-1}(\partial r/\partial s) \quad .$$

The drag of the bulk flow on the stretching rod yields

$$\frac{\partial r}{\partial t} = r |\nabla \mathbf{U}| + \frac{\log}{2\pi\mu} \frac{\partial \mathbf{T}}{\partial s} / \frac{\partial r}{\partial s} \quad .$$

Careful consideration must be given to the moving ends of the rod where the tension vanishes. There are many similarities between my elastic rod model and the fully nonlinear Rouse–Zimm model.

Steady equilibria are found if the flow is strong enough, $|\nabla \mathbf{U}| \gtrsim kT \log^2 N/4\pi\mu N^2 b^3$. In such an equilibrium the chain is at least half fully stretched. The model shows that in the central region the chain is more fully stretched. An asymptotic concentration of the coiling in regions near the ends never dominates in practice because of its mere logarithmic dependence.

The elastic rod model shows two effects in time dependent flows: Depending on the circumstances, the polymer can respond much slower or much faster than the relaxation time of the randomly coiled polymer. If the flow is strong, say strong enough to create the large distortions of the random coil, then in equilibrium the polymer is virtually fully extended, hard against the stops of the nonlinear spring. The polymer then responds very quickly and often almost as a rigid rod. If little of the polymer is fully stretched, then its response time is much longer, $N^{1/2}\lambda^{-1}/\log^2 N$, which is longer than that of random coil. Here, the nonlinearity of the spring is unimportant and it is the second effect of the $\sqrt{N}$ enhanced friction which is significant. At large distortions the polymer relaxes slowly against the large frictional resistance.

IV. RHEOLOGICAL FUNCTIONS

Large distortions were examined in the preceding section. In strong flows of sufficient duration the polymer was found to become virtually fully extended. The simple models also revealed two basic physical processes; a frictional grip increasing with the distortion and a

rate of coiling rapidly increasing as the distortion is limited by the finite extensibility of the chain. These basic results now need more careful study by refined models. Experimental testing of some of the associated predictions is also necessary.

Instead of considering more refined models here, we now turn to the other direction for development, namely, the rheological response of a dilute solution of polymers with large distortions. If complex flows, such as those thought to be present in turbulence are to be analyzed using a rheology representing polymer solutions, then the rheological constitutive equations employed must be simple. The constitutive equations describing any of the partial models of the preceding section are far too complicated for such purposes. A realistic approach to interesting flows, I think, must involve highly simplified constitutive equations which symbolically represent, rather than accurately describe, the microstructural dynamics. I therefore propose to modify the simple elastic dumb-bell constitutive equations (2) so as to incorporate, at least at some crude level, the two basic physical processes revealed in Sec. III. In this section the modification will be made and the standard rheological functions evaluated. In the following section we will see how the rheology affects some flows. As first suggested by Peterlin,[14] the finite extensibility can be incorporated into the elastic dumb-bell model by changing the spring constant κ of the linear spring to $\kappa/(1 - r/Nb)$, where the length of the spring r is extracted from $\langle \mathbf{rr} \rangle$ by $r^2 = \mathrm{Tr}\langle \mathbf{rr} \rangle$. While some arguments can be put forward for using the inverse Langevin spring, I prefer the above nonlinear elastic law for its simplicity. In addition, the bonds are not in reality fully independent as required for the Langevin law. My elastic law shares with the correct one, whatever it is, three general features; a linear region vanishing at zero deformation, an infinite force restricting extensions to $r < Nb$, and variations on a length scale of Nb rather than $N^{1/2}b$. If the ignored effects of excluded volume and charge repulsion were taken into account, then there might be variations in the details of the elastic law on the length scale of $N^{1/2}b$.

The improved frictional grip at large distortions can be included by making the bead size, a, change with r. Perhaps the most appropriate dependence for the bead size, and certainly the simplest, is just to replace a by r so that the friction coefficient was the largest linear dimension. This modification of the elastic dumb-bell was introduced by de Gennes[15] and independently by Hinch.[16] Slender-body theory for Stokes' flow suggests that the linear increase with r should be reduced by a weak logarithmic factor, $\log(r/N^{1/2}b)$, but we shall ignore this possible refinement.

In addition to the two basic physical processes in large distortions, I wish to include further the rigidity effect found in the elastic ellipsoid model. This third effect has little influence on genuinely large distortions, but apparently it is essential in insuring an acceptable behavior in simple shear flow, which probably stretches the random coil at most by a factor of three. The rigidity effect modifies the constitutive equations in two

places. In the evolution equation for $\langle \mathbf{rr} \rangle$, the velocity gradient ∇U is first split into the antisymmetric part, Ω the vorticity tensor, and the symmetric part, E the strain rate tensor. Then, the symmetric part is multiplied by an "inefficiency factor" $r^2/(3r_0^2 + r^2)$. Note at large distortions the efficiency increases to unity. The second part of the rigidity modification is to include an additional term in the bulk stress $10\mu n r_0^3 E\, r^2/(3r_0^2 + r^2)$. Without an adequate study of polymer behavior in simple shear flow, there is necessarily an arbitrariness in my modification and this is unsatisfactory. Thus, the detailed predictions for simple shear should not be trusted.

The constitutive equations for the elastic dumb-bell with the modifications noted herein are

$$\frac{D}{Dt} \langle \mathbf{rr} \rangle = (\langle \mathbf{rr} \rangle \cdot \Omega - \Omega \cdot \langle \mathbf{rr} \rangle)$$

$$+ \frac{r^2}{3r_0^2 + r^2} (\langle \mathbf{rr} \rangle \cdot E + E \cdot \langle \mathbf{rr} \rangle)$$

$$- 2\lambda \frac{aNb}{r(Nb - r)} \left(\langle \mathbf{rr} \rangle - \frac{r_0^2}{3} \mathbf{1} \right) ,$$

$$\sigma = -p\mathbf{1} + 2\mu \left(1 + 5nr_0^3 \frac{r^2}{3r_0^2 + r^2} \right) E + n\kappa \frac{Nb}{Nb - r} \langle \mathbf{rr} \rangle ,$$

with $r = \mathrm{Tr}\langle \mathbf{rr} \rangle)^{1/2}$. (Note that these constitutive equations are not in the familiar form in which stress is given as a functional of the strain rate; instead stress depends on the strain rate and the microstructural dynamics. To display the rheological response of this pair of constitutive equations, in this section I will take $N = 10^4$, $a = r_0 = N^{1/2}b$ and $nr_0^3 = 10^{-3}$, values corresponding very roughly to the 10^6 Polyox at 100 ppm.

Most rheological tests are performed with simple shear flow. As discussed earlier, the constitutive equations were not carefully designed for this weak flow which probably does not produce large distortions. Only the most qualitative features of the response in shear flows are therefore worth noting. The viscosity of the dilute solution differs little from that of the solvent; there is an undetectable shear thinning between a zero shear rate viscosity 0.2% above the solvent value and a high shear rate limit 0.13% above the solvent value, half the thinning occurring by $\gamma = 2\lambda$. The second normal stress difference is negative and about half the magnitude of the primary difference, although both are less than one thousandth of the shear stress. At low shear rates the normal stress differences vary quadratically in the shear rate, while at high shear rates they level off to constant values as the polymer tends to a small finite distortion aligned with the flow.

The prototype strong flow is axisymmetric straining motion. Plotted in Fig. 3 as a function of strain rate is the polymer contribution to the viscosity for this flow in steady state conditions. Most striking is the high value, $6 \times 10^3 \mu$, of the extensional viscosity in the stronger flows which stretch out the polymer; a good illustration of the discussion of the levels of stress in Sec. I. In the simplified constitutive equations this high value of the extensional viscosity is $2\pi\mu nN^3 b^3$. Refinements from a slender-body analysis would reduce this
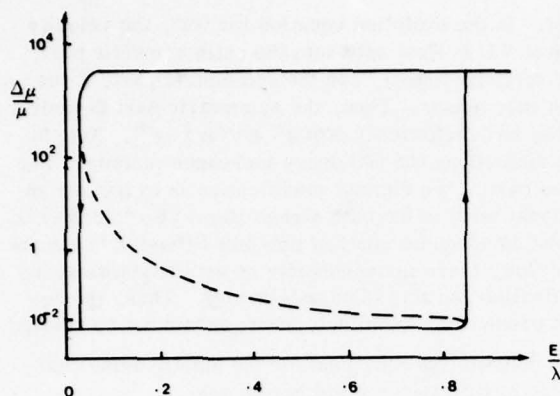
FIG. 3. The polymer contribution to the viscosity as a function *of the axisymmetric strain rate.*

by $18 \log(nN^2b^3)$. The solution viscosity does not differ significantly from that of the solvent until $r > 6r_0$.

The extensional viscosity exhibits a hysteris in the range $0.02\lambda < E < 0.84\lambda$, the dotted part of the curve corresponding to unstable equilibria. At $E = 0.84\lambda$ the polymer *extension jumps from* $r = 1.2r_0$ *up to* $r = 0.99Nb$, if E is increased, while at $E = 0.02\lambda$ the extension drops from $r = 0.5Nb$ down to $r = 1.00003r_0$ if E is decreased. The hysteresis occurs because the frictional grip increases with the distortion and thus a weaker flow, $2\lambda N^{-1/2}$, is required to maintain a large distortion once it has been created. Tanner[17] noted that most phenomenological theories of constitutive equations are unable to represent a hysteresis.

Steady state conditions in axisymmetric straining motions are difficult to achieve experimentally. It is therefore pertinent to consider the transient problem. This also reveals some further rheological properties. Plotted in Fig. 4 is the polymer contribution to the time dependent stress in an axisymmetric straining motion which is suddenly applied and later removed. A flow strength of $E = 2\lambda$ was used, and this exceeds the critical value of 0.84λ necessary to create large extensions. Initially, the stretching is retarded by the restoring force, an extension of only $r = 2.7r_0$ being produced by $\lambda t = 1.5$. Then follows a phase of duration $\log N/4E$ in which the polymer is stretched like a fluid element with virtually no elastic resistance. During this phase, at $\lambda t = 2.1$, *the polymer contribution to the stress becomes* comparable with, and then very quickly dominates, the solvent stress. Finally, the nonlinear elasticity abruptly arrests the stretching $r_0E/8$ short of the full extension on a time scale of $\lambda/N^{1/2}E^2$. When the flow is removed, there is a very fast initial decay on the time scale $\lambda/N^{1/2}E^2$ in which the nonlinear elasticity factor $1/(1 - r/Nb)$ drops from $N^{1/2}E/\lambda$ to $O(1)$, thus reducing *the stress by a similar amount. There then follows a* long relaxation of duration $N^{1/2}/\lambda$ which is made slow by the high friction associated with the large distortions.

The transient response illustrates several important rheological features. Time is needed for the polymers to become sufficiently stretched for them to contribute to bulk stress. Before this happens the solution differs imperceptibly from the pure solvent, but once the polymers begin to contribute they soon overwhelm the solvent (assuming that the straining motion can be maintained in the presence of the very large stresses). The transients also exhibit a fast relaxation process accelerated by the highly nonlinear elasticity, and also a slow relaxation process retarded by the enhanced friction.

V. TWO FLOW STUDIES

The high extensional viscosity must clearly be relevant to drag reduction, especially when potentially assisted in intermittent conditions by the hysteresis. Before continuing to more detailed comments on drag reduction, I wish to present two flow phenomena associated with the rheology of the preceding section. The first phenomenon is an anisotropy involving only polymers which are fully extended, and the second is the inhibition of a stretching flow by the large stresses which would occur if the flow were not checked.

In the first study we suppose the flow is strong everywhere and remains so. Therefore, after a short time the polymers are virtually fully extended and in a regime where the nonlinear elasticity produces a fast response to changes. Under these conditions the polymer solution behaves much the same as a suspension of rigid rods, with some useful simplification of the constitutive equations. Evans[18] has studied the flow of a dilute suspension of rigid rods in several simple geometries, solving the constitutive equations and the momentum equation together. (Note the constitutive equations include one for the reorientation of the rods, an effect omitted from papers about similar problems presented at this Symposium on Structure of Turbulence and Drag Reduction).

The principal rheological property of a suspension of rigid rods is a high viscous resistance to any extensional motion in the direction of the rods, and a low resistance to other motions, i.e., a high extensional viscosity with a low shear viscosity. This anisotropy of the suspension influences the structure of flows which are combinations of straining and shear. Such a combination occurs in flow in a tapered channel or flow through an orifice. Simple similarity solutions show that the material anisotropy reduces the transverse length scale of the flow relative to the scale in the stream direction
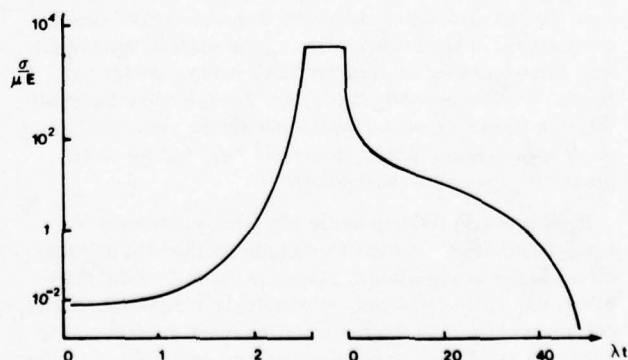
FIG. 4. The build up and relaxation of the polymer contribution to the stress.

S28   Phys. Fluids, Vol. 20, No. 10, Pt. II, October 1977

E. J. Hinch   S28

(the direction of the rods), the ratio of the length scales becoming the square root of the ratio of the extensional and shear viscosities. The compression of the transverse scale in the two converging flows has the effect of introducing backflow regions at smaller angles of convergence than occur in the isotropic Newtonian case. Evans has taken these simple ideas generated from the similarity solution and looked at the more realistic flow in the contraction between two channels. Figure 5 shows that the suspension has larger recirculating eddies and a convergence with a slightly greater streamwise extent.

While considering the rheological functions in Sec. IV and also in the first flow study, I have implicitly assumed that the *strong flow can be maintained* when the polymers have been greatly extended and thus are producing large stresses. The second flow study examines the conflict between these large stresses resisting the very flow which creates them. A flow with a limited stretching effort, and which can easily be analyzed, is the time dependent stretching of a column of the polymer solution under a constant tension and neglecting inertia. This is an oversimplification of the nylon spinning problem. Figure 6 shows typically how the thickness of the column changes in time. Initially, the polymers contribute little to the bulk stress and the thickness follows the Newtonian curve. Just before the moment when the Newtonian column would have zero thickness the polymers become sufficiently stretched for their contribution to the bulk stress to be important. A *new dynamical regime is then entered*, with the unsupportably large stresses being avoided by a sudden drop in the strain rate. This drop in the strain rate leaves
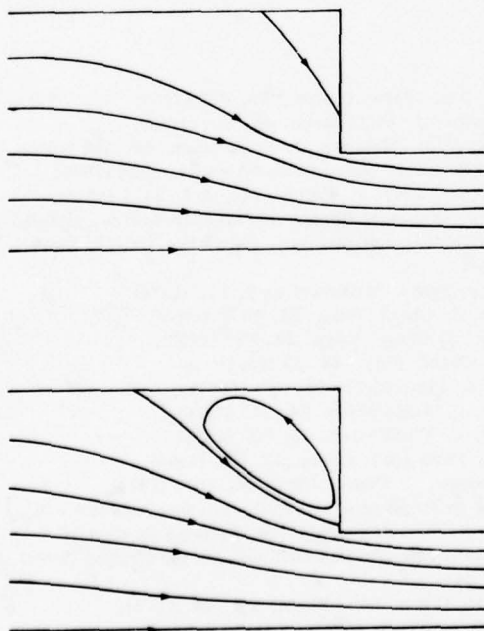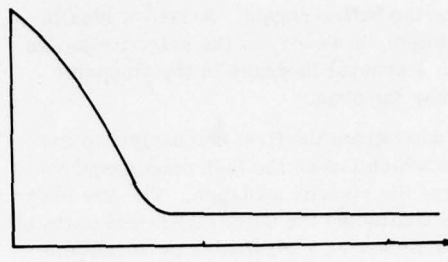
FIG. 6. The thickness as a function of time of a column of polymer solution under constant tension.

the bulk stress dominated by the polymer contribution. To stop the polymers collapsing some stretching is required, but the necessary strain rate is just the polymer relaxation rate for large distortions $\lambda/N^{1/2}$. Thus, the new regime lasts a long time, and the "saturation" dynamics are independent of the magnitude of the tension. This latter feature may be relevant to the well-known persistence of polymer threads and the good stability in spinning. The regime eventually ends, with the polymers fully extended and the column thickness simultaneously vanishing. For the related nylon spinning problem, Petrie[19] found that several phenomenological constitutive equations show a similar limitation of the strain rate.

VI. DRAG REDUCTION

I wish to conclude the paper with a few speculative *comments on drag reduction*. There is no doubt in my mind that the high extensional viscosity in strong flows is the principal instrument in reducing the drag, but I do not find such a plain statement a satisfactory level of explanation. The phenomenological theories of turbulence, which can sometimes predict drag reduction by tampering with a length scale or with the turbulence intensities (in conflict with observed intensity changes?), may not, I fear, be able to provide a satisfactory link between the change in rheology and the change in drag. Fortunately, the improving picture of the detailed structures in shear flow turbulence reported at the Symposium does offer an opportunity to contemplate the mechanisms of drag reduction, although certainly more understanding of the turbulence is required before a complete explanation can be presented. With the present picture of turbulence there appear to me to be four different ways the polymers might affect the turbulence, each an aspect of the high extensional viscosity.

A simple mechanism for drag reduction, suggested several years ago, supposes that turbulent shear flows are comprised of many flow structures. The high extensional viscosity then selectively dissipates some of these structures, and it happens that the eliminated structures are more efficient than average at transporting momentum (producing drag). While many different features have been observed in turbulence, evidence is emerging, particularly at this Symposium, that perhaps the different features are organized as parts of a single grand structure. There seems to be little support for the availability of several unrelated transport processes

FIG. 5. The converging flow from a channel to one a third of the width, upper for a Newtonian fluid and lower for a suspension of rigid rods with an extensional viscosity fifty times the shear viscosity.

especially within the buffer region. A salient idea in this first mechanism, however, is the selective action of the polymers: a general increase in the viscosity must just increase the drag.

It is a small move from the first mechanism to the second and third which invoke the high extensional viscosity to stabilize the viscous sublayer. The low shear viscosity leaves unaffected the quiet shear-like parts of the sublayer, but selectively dissipates perturbations which must have an extensional component. Using the constitutive equations for a suspension of rigid rods, Bark[20] found that inflectional velocity profiles could be strongly stabilized, and at the Symposium, Tiederman's films convincingly show signs of a stabilized sublayer. There are two ways of completing the mechanism and relating the stabilization to drag reduction. For the second mechanism one argues that larger perturbations would be needed for the sublayer to break down, and this might just mean waiting longer before a burst which can transport momentum (assuming the transport by a single burst changes little). Less frequent bursting is usually observed in drag reduction. For the third mechanism one argues that the scales of the successful instability might adjust, with adjustments possible both in the overall scale and in the interal ratio of the scales such as shown in the first flow study, and these changes lead to less efficient transport. Observations of drag reduction always show increases in length scales, while it is not yet clear whether the ratio of the spanwise, streamwise and perpendicular lengths change. A variation on the third mechanism omits the stabilization of the sublayer and just changes the length scales of the bursts. The violence of the bursts may, however, mean that they are inertially controlled and thus beyond the influence of the rheology.

The fourth way the polymer could affect the turbulence is to limit the strain rate,[21] as in the second flow study of Sec. V. If this were the only mechanism, I would expect it to be found in the later stages of the bursts after the polymers had been stretched in the earlier stages. Strain rate limitations within the bursts would reduce the rate they transport momentum. Unfortunately, there are no observations of the effect of polymers on the strain rate within bursts. The only relevant observation is that the duration of the bursts appears to be unchanged in drag reduction. This would contradict the fourth mechanism if one supposed that the strain rate limitation terminated the bursts early.

My discussion of possible drag reduction mechanisms raises many questions for further consideration, both experimental and theoretical. Two other questions are worth listing. Almost all rheologists share the view put forward in this paper that the polymers are highly stretched in drag reduction. Yet no direction observation has been made of the extension of the polymers in turbulence. Light scattering measurements in some laminar flows have shown polymers extending, although the extensions found are small because laminar flows cannot maintain high strain rates for long in the Lagrangian frame. Despite the severe technical difficulties of light scattering in a turbulent boundary layer, the ab-

sence of such an observation can only become increasingly embarrassing. Once a suitable experimental technique is available many points could be examined: Are the distortions just moderately large or are the polymers virtually fully extended, do the stretched polymers exist everywhere or just in the buffer region, is it the bursts which stretch the polymers, does the hystersis and slow relaxation help to maintain the large distortions? While waiting for this experimental breakthrough, theoreticians can contribute by assessing the important flow variables in the polymer stretching processes, thereby avoiding the need to measure all nine components of the velocity gradient as functions of (Lagrangian) time.

The second outstanding problem concerns the onset of drag reduction. Verification of the "time hypothesis" would be improved with better monodisperse polymers and a direct measurement of the polymer relaxation time, e.g., by the dynamic viscosity. In view of practical applications a systematic study of polydispersity would also be useful. We should now, however, be turning to the challenging regime just beyond onset. Theoreticians can contemplate how the stretching of the polymers varies with the distance from the onset: Are the polymers stretched more, do the stretched polymers exist in a larger part of the flow, and does the flow adapt so the strain rate is limited by the value at onset? Experiments which find the appropriate molecular variables beyond onset can provide useful insights: Is the polymer concentration best nondimensionalized as $[\eta]c$ or nN^3b^3 (based on the coiled and stretched sizes, respectively), is the ratio of the coiled to stretched size important in addition to the concentration and the relaxation rate, and do all the changes in the turbulence depend on the same variables and thus sale with the drag reduction?

[1]A. Einstein, Ann. Phys. (Leipz.) **19**, 289 (1906).
[2]G. K. Batchelor, J. Fluid Mech. **46**, 813 (1971).
[3]J. Mewis and A. B. Metzner, J. Fluid Mech. **62**, 593 (1975).
[4]W. Kuhn and H. Kuhn, Helv. Chim. Acta **28**, 1533 (1945).
[5]R. Takserman-Krazer, J. Polym. Sci. A **1**, 2477 (1963).
[6]J. L. Lumley, in *Annual Review of Fluid Mechanics*, edited by M. Van Dyke (Annual Reviews, Palo Alto, Calif., 1969), Vol. I, p. 367.
[7]J. L. Lumley, Symp. Mathematica **9**, 315 (1972).
[8]P. E. Rouse, J. Chem. Phys. **21**, 1272 (1953).
[9]B. M. Zimm, J. Chem. Phys. **24**, 169 (1956).
[10]R. Cerf, J. Chim. Phys. **48**, 59 (1951).
[11]R. Roscoe, J. Fluid Mech. **28**, 273 (1967).
[12]E. J. Hinch, J. Fluid Mech. **74**, 317 (1976).
[13]E. J. Hinch, J. Fluid Mech. **75**, 765 (1976).
[14]A. Peterlin, Pure Appl. Chem. **12**, 273 (1966).
[15]P. G. de Gennes, J. Chem. Phys. **60**, 5030 (1974).
[16]E. J. Hinch, in *Proceedings of Colloques Internationaux du Centre de la Recherche Scientifique* (Editions du Centre National de la Recherche Scientifique, Paris, France, 1974), No. 233, p. 241.
[17]R. I. Tanner, Trans. Soc. Rheol. **19**, 557 (1975).
[18]J. G. V. Evans, Ph.D. thesis, Cambridge University (1975).
[19]C. J. S. Petrie, J. Non-Newtonian Fluid Mech. **2**, 221 (1977).
[20]F. H. Bark, Ph.D. thesis, Kungl. Tekniska Högskolan, Stockholm (1975).
[21]F. A. Seyer and A. B. Metzner, AIChE J. **15**, 424 (1969).

Effect of compliant wall motion on turbulent boundary layers

Dennis M. Bushnell and Jerry N. Hefner

Langley Research Center, National Aeronautics and Space Administration, Hampton, Virginia 23665

Robert L. Ash

Old Dominion University, Norfolk, Virginia 23508

A critical analysis of available compliant wall data which indicated drag reduction under turbulent boundary layers is presented. Detailed structural dynamic calculations suggest that the surfaces responded in a resonant, rather than a compliant, manner. Alternate explanations are given for drag reductions observed in two classes of experiments: (1) flexible pipe flows and (2) water—backed membranes in air. Analysis indicates that the wall motion for the remaining data is typified by short wavelengths in agreement with the requirements of a possible compliant wall drag reduction mechanism recently suggested by Langley.

I. INTRODUCTION

The current energy shortage places additional emphasis upon research to increase the efficiency of transportation, including aircraft.[1] Since, for long-haul aircraft, the viscous drag is approximately 40–50 percent of the total drag, any sizable decrease in turbulent skin friction translates directly into an appreciable fuel saving. Reference 2 provides a discussion of various techniques for reducing viscous drag, as well as drag-due-to-lift. A more detailed review of various C_f (skin friction coefficient) reduction approaches[3] concluded that five techniques (laminar flow control, slot injection, particle injection, polymers, and compliant skins) were worthy of further detailed research.

The laminar flow control technology is quite mature, and most of the remaining important problems are in the practical areas of maintainability and reliability. Further research is, however, still required for optimization of suction rate and distribution. Skin friction reduction due to injection of low momentum air near the wall (slot or porous injection) can definitely cause large local C_f reductions,[4] but recent studies[5] have shown that, as one might expect, the penalties for collecting and ducting the slot air outweigh the expected drag reduction benefits on aircraft; therefore, this method is presently suitable only for local regions where excess air, perhaps from a laminar flow control system, might be available. Particle injection can also provide a drag reduction,[6] but applying this technique to aircraft (particularly considering the various anti-pollution regulations) is not currently feasible. Polymer injection produced large C_f reductions,[7–10] but the effect is limited to liquids.

The remaining technique, compliant walls, is the subject of the present critical review. Blick[11] discussed the field, with primary emphasis upon the University of Oklahoma research. The introduction sections of Refs. 12, 13, and 14 provide fairly up-to-date synopses.

The purpose of the present paper is to investigate the entire subject for both the transitional and the turbulent flow cases and discuss possible correlations between computed wall motion and observed drag reduction. The paper also presents alternate explanations for "drag reductions" observed in several cases reported in the literature.

Considering the demonstrated success with laminar flow control on the X-21 aircraft[15] one might reasonably ask why anything further (another drag reduction technique) is needed for aircraft. There are two responses. First, laminar flow control has thus far been applied on wings, and not fuselages. On the present wide body transports, approximately one-half of the surface area is on the fuselage. Since the fuselage boundary layer is relatively thick and generally has small pressure gradients, it may be much more suitable for applying compliant walls rather than for laminar flow control (although there has been no concentrated effort to apply laminar flow control to the fuselage). The second and more serious comment concerns the high altitude operating conditions necessary for laminar flow control. The low unit Reynolds numbers required for a successful laminar flow control system (primarily dictated by roughness and radiated noise from the fuselage) are only available at altitudes above 35 000 ft and, ideally, over 40 000 ft. However, most operational flights (and 60% of aircraft fuel) are for stage lengths less than 1500 miles and therefore considerable fuel is burned at altitudes below the levels required for laminar flow control. The application of laminar flow control is optimal for high altitude, long range aircraft, but something else (perhaps compliant walls) is needed for the considerable traffic in the shorter stage length, lower altitude cases. With these considerations, and because there does not seem to be any other potentially viable viscous drag reduction scheme, compliant wall research should obviously be pursued until the potential for drag reduction under turbulent boundary layers is either conclusively proved or disproved.

The current state of compliant wall technology can best be described as confusing and inadequate. Although the mechanism for altering the drag must be connected with the flow induced wall motion, to the present authors' knowledge, except for some recent attempts at

Langley, only the study by Grosskreutz[16] measured wall motion for either successful, or unsuccessful, compliant wall experiments. Extensive wall motion measurements must be made, particularly in cases where drag reduction is obtained, before any theoretical approach to the problem (or derived design methodology) can be reasonably validated. The problem is obviously one of fluid-structural dynamic interaction, and yet the structural side has been somewhat ignored by the experimentors. Another confusing issue is the various options available for eventual application to aircraft, i.e., (1) delaying/stretching out transition vs reducing C_f in fully turbulent flow and (2) use of truly compliant (flow perturbation following) walls vs resonant (excited eigenmode) walls. Also, theoretical research indicated that compliant walls with low damping were required for flow stabilization whereas practical applications and experiments necessarily utilize resonant walls with appreciable damping. Studies are available for practical application of the transition-retarding option.[17]

An additional use for compliant walls is reduction of turbulent boundary layer noise. Both analytical[18] and experimental[19,20] work are available, but this option has not yet received extensive study. Reference 12 discusses the possible application of compliant walls for drag reduction in other modes of transportation besides aircraft.

Compliant wall research evidently originated from consideration of the drag of dolphins.[21-25] However, the possible presence of such walls on dolphins is problematical. In an article in *Scientific American*[21] Gray surmised, based upon the observed 22 mph speed of dolphins and their (then) known physiological propulsion efficiency, that the dolphin must have some means of producing extensive regions of laminar flow (although it was not mentioned, lower drag can obviously also be due to considerably reduced transitional/turbulent drag levels as well as to more extensive regions of laminar flow). Kramer,[22] in 1961, published a suggestion as to how extensive regions of laminar flow might be produced on the dolphin. He based his suggestion, which he termed "distributed flow damping" or compliant walls, upon a detailed examination of porpoise skin. He found that the skin is quite pliable and contains a considerable quantity of absorbed water. His initial tests (starting in 1956) of man-made coatings simulating porpoise skin did indeed yield lower drag in sea water. In a later paper[22] Kramer estimated that the porpoise could obtain up to a 40% drag reduction just due to the favorable pressure gradient influence on transition Reynolds number (body shaping); he further concludes that an additional drag reduction is necessary to explain the porpoise speed and again advances the compliant skin concept as a method for stabilizing the boundary layer fluctuations by supplying distributed damping. However, tests conducted by Lang et al.[24,25] indicate that, while the porpoise can indeed reach high speeds (on the order of 22 knots), the animal does so only for relatively short time periods, and this may be accomplished by running the muscles into "oxygen deficit." Lang's studies of porpoises observed during relatively controlled "open

water" tests yielded drag coefficients in approximate agreement with fully turbulent predictions during high speed coasting (where the drag coefficient may be determined more accurately than, but may not be a true representation of, the propulsive case).

Therefore, whether the porpoise uses a compliant skin still seems to be somewhat a matter of contention, but an important result of this line of inquiry is the drag reduction obtained by Kramer on periodic "porpoise-like" skins where evidently, the wall motion induced in the surface by the boundary layer disturbance field caused a lower drag. It is not entirely clear from Kramer's results whether the lower drag is a result of (a) delaying transition, (b) reducing the intensity of bursts in the transitional region, or (c) reducing the turbulent skin friction. The present authors' conjecture that at least the latter two effects [(b) and (c)] may have occurred. As a footnote to the porpoise skin discussion there is available a hydrophilic coating for use on boats. The surface of this coating evidently becomes somewhat similar to a compliant wall when water-saturated. Some details concerning the coating are available in Ref. 11. The coating was tested both in the laboratory[26] and on ships.[27] Some drag reduction is observed, but the mechanism involved has not been studied and the reduction is evidently not large.

The present critical review first briefly considers the structural dynamics and flow stability areas. The major portion of the paper concerns the theory and experiments for compliant walls under turbulent boundary layers.

II. STRUCTURAL DYNAMIC CONSIDERATIONS FOR COMPLIANT WALLS

The compliant wall problem is one of fluid-structural dynamic interaction. Considerable structural dynamics and fluid-structural interaction research is available,[28,29] but many compliant wall experimenters have not used this technology to design their walls. Although this may be stating it somewhat strongly, the usual approach seems to have been, "this feels soft, let's try it."

The problem is not straightforward. The walls are exposed to a relatively wide-band spectral loading and the formulation must include the influence of wall-motion-induced aerodynamic forces. The prime variables are multitudinous and include: (a) flow parameters such as speed, Reynolds number, boundary layer thickness, and state (laminar, transitional, or turbulent), pressure gradient and flow medium (air or water, etc.); (b) structural configuration (vertical and/or horizontal layers, two or three dimensions, with or without pretensioned members) and the possibility of nonlinear effects such as caused by membranes backed with small air gaps; and (c) material property parameters such as density, modulus, damping, degree of anisotropy, and the possible variation of these properties with temperature, vibration frequency, and aging. Given a set of flow parameters and a stable of available materials, the type of structure is dictated by the surface response desired.

For the case of a simple two-dimensional convected

surface wave, the fundamental wall motion parameters are wavelength, wave amplitude, and wave speed or frequency. However, since the structure is continuous, the surfaces will, in general, react over a whole range of amplitudes, wave speeds, and wave lengths. In addition, since the forcing field is three-dimensional, the induced motion could also be three-dimensional, depending upon the degree of "compliance." It is also possible that favorable alteration of the turbulence field demands the presence of unsymmetric surface waves having particular wall curvature or pressure gradient distributions.

Some attempts have been made[12,13,30-33] to utilize structural dynamics technology, of varying sophistication, to design compliant walls according to various assumed aerodynamic (or disturbance damping/alteration) criteria. One such criterion ("roughness" effect) is quite obvious from difficulties encountered in the experiments. The amplitude of the motion must be kept low enough to avoid causing a "roughness" effect which would increase, rather than decrease, the drag. The occurrence of static divergence conditions (large standing waves) have commonly been observed in compliant wall experiments[34-36] at high flow speeds and generally lead to drag increases. For application to the turbulent case one could use the common roughness height rule-of-thumb of $k^+ \leq 6$ to determine an allowable wave amplitude, where k^+ equals the wave or roughness height in usual law of the wall coordinates. [A superscript (+) is used throughout this paper to denote law of the wall units where one unit is given by ν/u_τ, kinematic viscosity divided by frictional velocity.] For most turbulent flows this limits the maximum wave height to less than 0.5 mm. However, except for the static divergence case, the Langley experience is that it is quite difficult, for air flows, to excite practical walls to amplitudes even the order of 0.02 mm (based upon both surface amplitude measurements and structural dynamic calculations).

There is another design criteria which is probably correct, the waves must move or at least have fairly high frequency. Most experiments with fixed wavy walls[37] (and the zero wave speed results of Ref. 38) used wave amplitudes which exceed the roughness criteria just mentioned and thus measured increases in drag. Reference 38 indicates that a fixed wavy wall has a pressure drag due to the phase shift between the surface contour and the wave-induced pressure field. Unpublished experiments at Langley with fixed waves smaller than those of Ref. 38 indicated, within an accuracy of $\simeq \pm 3$ percent, no net change in drag for low-speed turbulent flow. These latter data seem to suggest that drag reduction requires moving or relatively high frequency waves. Aerodynamic design criteria which might be used for compliant walls is discussed more fully in the theoretical sections of this paper.

One basic structural dynamics consideration that should be emphasized is the difference between the "compliant" walls dictated by stability theory[39,40] and the usual flexible walls employed in experiments. The successful compliant wall, according to stability theory, has extremely small damping and modulus of elasticity

and can therefore respond, with little phase lag, to the wall forcing function produced by the flow disturbance field. However, such surfaces are practically impossible to construct. Therefore, the experimental data are taken with structures which are not optimal in the stability theory sense, but are actually "resonant surfaces" in that the flow-disturbance forcing function excites wall vibration modes.

Compliant wall experiments must, practically speaking, be conducted using resonant walls. The design of structures to provide the desired wall motion is complex and requires design techniques based on aerodynamic wall motion criteria obtained either from wall motion measurements during successful experiments or from rather sophisticated theory.

III. INFLUENCE OF WALL MOTION ON STABILITY/TRANSITION

Although the major purpose of the present paper concerns the influence of wall motion upon the drag in turbulent boundary layers, in this section a brief review of the laminar/transitional results (which are primarily theoretical) is provided for later theoretical application in the turbulent case. In particular, the turbulent wall burst formation and pre-burst flow may involve a relatively brief region (brief in time and space) where stability theory applies in the near wall region. Influencing this portion of the flow may be sufficient to break the feed-back loop which allows the turbulence to be self-sustaining (see also Ref. 40, p. 126).

A. "Conventional compliant" walls

Pelt[41] reviewed the various approaches to the stability theory of compliant walls through approximately 1964, including the results of Benjamin,[42] Landahl,[39] Betchov,[43] Boggs and Tokita,[44] Hains and Price,[45] Nonweiler,[46] and Linebarger.[47] Theoretical research since the Pelt review comprises further work by Benjamin,[48] (including an excellent summary paper[40]), Landahl and Kaplan,[49] Kaplan,[50] Takematsu,[51] Burden,[52] and Amfilokhiyev et al.[53] From the number of authors cited, this has obviously been a popular problem, with most of the work accomplished in the early sixtys (primarily due to the stimulus of Kramer's results[22,23]). However, attempts to experimentally validate the theoretical calculations generally used either resonant surfaces, which do not correspond to the theoretical assumptions employed, or active walls.[54] In fact, Landahl[39] concludes that the Kramer surfaces were so far removed from the conditions necessary for stabilization according to the theory that the Kramer drag reduction must be due to a favorable modulation of the later stages of transition or turbulent portions of the body.

Burden[52] suggests the following compliant wall characteristics as necessary for stabilization of oscillations in the early stages of transitional flow (see also Kaplan[50]): (a) wall density the order of the fluid density (obviously out of the question for air); (b) shear modulus the order of the fluid dynamic pressure; (c) small wall dissipation; and (d) impervious wall. He further states, in agreement with earlier authors, that too much flexi-

bility, or too much dissipation will allow the growth of instabilities not otherwise found in the zero-pressure-gradient rigid wall case. The definitive review of research in this area is that of Benjamin.[40] It should be noted that all of these approaches used steady state stability theory in the sense that the wall motion was not allowed to "back react" upon the assumed mean profile. For moderate to large wall displacements the surface motion induces a traveling pressure signal[38] which can modulate the mean profile and this invalidates a key assumption in the conventional stability theory approach to compliant walls. The relaxation of this assumption is discussed in a subsequent section of this paper.

Although Wehrmann[54] had to use an "active" or driven wall to simulate the compliant surface assumed in the theories, he was able to show, experimentally, that, depending upon the phase between the driven wall wave and the Tollmien-Schlichting wave generated by a vibrating ribbon, large reductions in velocity fluctuation intensity could be obtained. The largest reduction occurred near the wall.

In summary, there is a large body of theoretical research (which is probably correct, judging by the available checks on rigid wall stability theory and the results of Ref. 54) which suggests that certain types of compliant walls can (a) increase the lower critical Reynolds number, and (b) reduce the spatial and temporal amplification rates of unstable waves. The problem, particularly for the air case, is that the walls required to produce these effects evidently cannot be constructed with current technology. Consequently, we have a possible drag reduction effect of highly compliant walls which, while intriguing, is probably not practical, especially for air flows.

B. Stability with resonant walls

The Kramer surfaces[22] are obviously more resonant than compliant due to their large damping. In the present review, we treat the Kramer data[22,55-57] as primarily indicating an alteration of the transitional and turbulent burst frequency/structure rather than a delay of the onset of transition, because of the amount and slope of the drag reduction obtained with the surface at large Reynolds numbers (up to 15×10^6).[22] Therefore, the detailed discussion of the Kramer data is deferred until the section on turbulent experiments.

There is essentially no applicable theory for the influence of resonant (excited structural eigenvalue, fairly wide-band motion, random phase) walls on transition except perhaps for piecewise application of the fairly large, and recent, effort on stability in modulated or periodic boundary layer flows. These latter efforts (theory and available experiments) are discussed in the next section since they were developed primarily for active or driven oscillations (wall or stream); the present discussion focuses on passive walls.

An experimental study was conducted at MIT[58] to simulate a compliant wall by a series of streamwise-connected Helmholtz resonators. "The vertical motions of plugs of air adjacent to the flow was intended to model the oscillations of a flexible membrane." These experimental results indicate earlier (increased instability), rather than retarded transition primarily because of the fairly large size and discrete nature of the surface perturbations. Attempts to duplicate Kramer's work by delaying transition in ground facilities during the early sixtys were also unsuccessful.[59,60]

The major investigations on the influence of resonant surfaces on stability were conducted by Babenko. This work included porpoise skin studies[61] and experimental stability investigations using a wide variety of surfaces.[62-64] These studies concentrated quite heavily upon the characterization of the structural dynamic parameters for the surfaces tested. The experimental results indicate that for compliant surfaces the wave number corresponding to initial loss of stability was larger than for rigid surfaces. Measurements of neutral stability curves provided Reynolds numbers for the loss of stability (lower critical Reynolds number) for wide variations in surface design and material parameters. Variables include surface material, damping, density, modulus, and tension (for those surface using membranes).

The data indicate that significant changes in critical Reynolds number occurred for resonant walls, with measured values both above and below the conventional Blasius value, depending upon the surface parameters. On the basis of the Babenko results, it seems that not only compliant walls but resonant walls as well, can favorably alter the stability boundaries of laminar flows. Considerably more experimental and theoretical research is required in this area, but the results may have eventual practical application, particularly for water flows, where one can build resonant walls over a wide range of wall motion parameters (e.g., frequency, amplitude, wave speed, spectra). This research further suggests that Kramer's assertions that he delayed transition with his fairly high damping surfaces may be correct. As a final note to this section there are also the data of Karplus,[65] who measured a decrease in Reynolds number for transition, and a lengthening of the transition region itself; the results are of a preliminary nature.

C. Stability of periodic boundary layers

As already stated, the modulation produced by a resonant wall can be sufficient to significantly alter the effective mean velocity profile under investigation. There are two effects; one is the obvious influence of alternately increasing and decreasing, through profile modification, the disturbance amplification rate, so that the integrated amplitude ratio may be greater (or less) depending upon the amplitude, frequency, and wave speed of the imposed oscillation. The second influence involves the timewise dynamics of the modulated boundary layer in that the application of ordinary stability theory in a quasi-steady sense is not sufficient, and one must include time derivatives of the mean profile parameters in the theory. It is the present authors' contention that this timewise modulation of the mean flow and the subsequent influence upon stability may be the key to fur-

ther theoretical understanding of the experimental re-
sults obtained using resonant walls for both laminar and
turbulent flows.

Several types of modulations are possible. The free
stream (or wall) velocity can be varied primarily in the
in-plane or stream direction.[66] This imposes a cyclic
variation which diffuses in a viscous manner through
the profile. On the other hand, one can impose a pres-
sure gradient modulation upon the flow, in which case
the entire profile is modified. This pressure modula-
tion can be imposed either upon the flow as a whole
(i.e., vary the imposed pressure drop in a Poiseuille
flow with time) or can be generated locally at the wall
by the use of traveling surface waves. This latter meth-
od probably occurs for the resonant or active wall
case.[13]

As noted earlier, the rigid wavy wall does not seem
to produce a favorable effect, one needs moving sur-
face waves, or at least stationary, nodal time-depen-
dent surface motion. The stability theory calculation
for a rigid wavy wall (with parallel flow assumption[67]),
indicates a destabilization effect.

There are two recent, and quite excellent, reviews
in this area of stability for modulated viscous flows,[68,69]
the latter being an outgrowth of work in Refs. 70–72.
These reviews are highly recommended by the present
authors as entry points for this relatively new, and quite
exciting, technology. It appears to be important to ac-
count for the true time-dependent nature of the complete
problem; a quasi-steady stability analysis of the modu-
lated flow[73] is not sufficient in many cases. For in-
stance, if one examines a flow containing an inflection
point during some portion of the cycle, this instanta-
neous profile will generally have a reduced lower criti-
cal Reynolds number compared with the unmodulated
profile. The initial reaction is to brand the modulation
as destabilizing, since, somewhere in the cycle, the
lower critical Reynolds number is reduced. Such a con-
clusion could be erroneous. A more satisfactory ap-
proach (but incorrect for high frequency) is to use the
quasi-steady analysis to generate local amplification
rates and then integrate these over complete cycles of
the modulation.[69] For stabilization, the trick seems to
involve using modulations which are not so large that
they trigger enormous amplification during part of a
cycle. Therefore, one needs small-to-moderate ampli-
tude modulations but not so small as to have little or no
measurable effect upon the flow, a problem with reso-
nant surfaces in air flows where an extremely low wall
modulus is required to produce any reasonable surface
amplitude. Another requirement for stabilization, al-
though this varies with the particular type of flow,[68] is
a relatively high frequency modulation. Theoretical pa-
pers of particular interest include Refs. 74 and 75.
Some of the limited experimental backup data (using ac-
tive or driven disturbances) are given in Refs. 76–79.

In summary, the results of both theoretical and ex-
perimental studies in time-modulated flows indicate that
it may be possible to stabilize boundary layer flows us-
ing low-to-moderate amplitude/relatively high frequency
oscillations. In the compliant wall case these oscilla-

tions, in the form of pressure modulations due to travel-
ing surface waves, could result from the use of resonant
walls. Further research is obviously needed to deter-
mine whether or not these indications are correct.

IV. THEORETICAL C_f REDUCTION MECHANISMS FOR TURBULENT FLOWS WITH MOVING WALLS

Based upon Refs. 80 and 81, it is probable that the
turbulent drag reduction mechanisms to be discussed in
this section are also applicable to the later (turbulent
burst) stage of transition, and therefore, one or more
of these mechanisms could cause a stretch-out and re-
duction of drag for the transition region as well as a
turbulent skin friction reduction. This postulation is
further bolstered by the common sensitivity of transi-
tional and turbulent flow regions to changes in boundary
conditions (other than wall motion) such as pressure
gradient, wall suction/blowing, and longitudinal curva-
ture.

The influence of wall modulation upon shear flows is
part of the general problem of the behavior of turbulent
flows subjected to periodic disturbances. This question
is investigated in some detail in Refs. 82 and 83, but
the pertubation amplitudes are relatively small, and the
studies do not consider the possibility of altering the
basic turbulent structure via this approach. Experi-
mental attempts to introduce substantial periodic dis-
turbances into turbulent wall layers (other than by wall
motion) are documented in Refs. 84 and 85. Reference
84 describes the influence of large (up to 34%) narrow-
band fluctuations in free stream velocity at Strouhal
numbers less than 1 (based on boundary layer thickness
and free stream velocity). This is a low frequency in
terms of the modulations required by unsteady stability
theory to increase stability (as described in the previous
section). No appreciable alteration of the turbulence
structure was observed. In Ref. 85 a turbulent boundary
layer was subjected to an imposed sound field over a
wide frequency range. The experimental trends ob-
served are in agreement with the unsteady stability the-
ory results in that high frequency sound caused a reduc-
tion in surface heating and lower frequency sound caused
an increase. However, the effects are not large, only
of the order of 4%.

This experiment, along with the compliant wall burst
modulation theory and interpretations of compliant wall
data (both described later in this paper) as well as the
unsteady stability theory, indicate that a reduction in
the turbulence transport rate requires a high frequency
modulation (of moderate amplitude). The present auth-
ors suggest that future experiments in the area of tur-
bulence control for wall flows concentrate on the high
frequency range to prove or disprove this evidentiary
material.

A. Sublayer models

1. Analysis by J. E. Ffowcs Williams

Ffowcs Williams[86] uses the assumption of two-dimen-
sional disturbances and linearized (sublayer) equations
to derive an expression for shear stress near a compli-

ant membrane. From examination of this expression he concludes that moving waves in a surface with low wave speed can produce a region of "negative Reynolds stress" which could "starve the turbulent eddies" and "may lead to a reduction in the turbulent level." Therefore, for a shear stress decrease, this approach seems to indicate the use of surfaces designed to generate low speed waves (less than about eighty percent of the free stream velocity, the convection speed of the gross wall pressure fluctuations). The approach of Blick[87] is quite similar.

2. The sublayer approach of Semenov

Semenov[88] provides an alternate sublayer type analysis, using equations similar to those of Sternberg.[89] He predicts that the Reynolds stress could decrease, or increase, depending upon the characteristics of the surface motion, and is careful to point out the importance of the surface wave phase angle. Comparisons between the predictions of Ref. 88 and the data of Ref. 90 (shown in Fig. 3 of Ref. 88) indicate quite reasonable agreement for the change in Reynolds stress as a function of frequency due to a resonant wall. Both hot-wire data[90] and theory give a reduction due to the wall motion at low frequency (region of "energy containing eddies") and an increase for higher frequencies. To the present authors' knowledge the theory has not yet been extensively applied, evidently due to the lack of the necessary empirical input for cases other than Ref. 90. The approach probably could be used in parametric studies to predict the type of surface motion necessary for drag reduction (and thus provide design data for experimental surfaces).

3. A mixing length approach

Amfilokhiyev[91] assumes that the elasticity of a surface (wall motion) reduces the Prandtl wall slope ($K \simeq 0.4$ for rigid walls) and indicates skin friction values as a function of the assumed decrease in K. This approach does not agree with the data of Ref. 90, where K was still $\simeq 0.4$ in the drag reduction case. In Ref. 90 the sublayer thickness was increased, thereby indicating, in terms of mixing length turbulence closure, an increase in the Van Driest wall damping constant, A^+.

4. Analysis of Zimmermann[14]

He considers the surface motion as a small disturbance to the basic turbulent flow, which is assumed known in detail. Further assumptions include low damping in the surface and small thickness, an approach to the surface dynamics which is similar to that used in the conventional stability theory of compliant walls. The Navier–Stokes equations are then linearized using the small disturbance assumption and solved by a Green's function approach. He uses measured pressure-velocity correlation data from rigid walls to estimate the change in shear stress due to the flexible surface and predicts only a small reduction for air, but a measurable ($\simeq 5\%$) reduction for water where the coupling is greater between the fluid and flexible wall.

5. Reynolds stress at surface

Hueristic arguments concerning the possibility of producing an altered Reynolds stress condition simply due to the horizontal and vertical velocity fluctuations, u' and v' associated with the surface motion itself are available in Refs. 92 and 93.

B. Drag reduction mechanisms based upon turbulent burst modulation

The "sublayer" theoretical approaches just described for the problem of the wall motion effect upon turbulence were based upon traditional modeling of sublayer flow and use of Reynolds averaging. Analysis of the more recent research on the detailed structure of wall turbulence, particularly the flow visualization and conditional sampling data, yields an alternate theoretical approach,[13] based upon the possible modulation of the pre-burst flow. The implications from the detailed data on rigid walls are first summarized briefly and then the possible modification of the turbulence production process using high frequency wall motion is discussed.

1. Coherent structures and a possible feedback mechanism for turbulent wall flows

There is considerable evidence that a "quasi-ordered" or "coherent" series of fluid dynamic events are responsible for the production of turbulence in wall flows. These events occur randomly in time and space and originate above the surface in the near wall ($y^+ < 100$) region. Several excellent reviews are available which analyze and summarize this relatively recent information,[94–96] especially Ref. 97. Reference 81 attempts to model turbulent flows using this information. Stated briefly, a low speed streak occurs very near the wall; this streak undergoes retardation with increases in time and space with a "burst" or eruption of the low speed fluid occurring for the more severe retardations. This burst and subsequent sweep provides the bulk of the Reynolds stress and turbulence production. The flow between events and the pre-burst retardation region is relatively quiescent (low $u'v'$). This latter statement is important for theoretical calculations of these events, because in order to reproduce the retardation one should not use the fully developed or time-averaged Reynolds stress level in the flow, but instead a rather small fraction of that level. There is still considerable controversy as to the relationship between the retardation and the burst or ejection. Many authors suggest that the (retardation-influenced) pre-burst profile undergoes an instability growth/amplification in a fashion similar to the burst formation in transitional flows. Landahl (see Sec. 7 of Ref. 80) suggests that the burst may be due to space-time focusing of instability waves, leading to the observed catastrophic growth. Both experiment and theory indicate the existence of a highly inflected retarded profile (inflection point at $y^+ \simeq 25$, Fig. 31 of Ref. 97) as the required pre-burst condition. (In Landahl's theory the inflection is a necessary, but not sufficient, condition.) This near wall turbulence production, through discrete bursts, bears remarkable resemblance to the earlier theories.[98,99]

A logical question is, what sets up the requisite pre-burst profile, why does the profile become retarded? It has long been known (Ref. 100 and others) that the larger scale, more intense portion of the wall pressure spectrum has a convection speed the order of 0.7 to $0.8U_\infty$ and appears to originate at $y^+ > 100$. There is evidence[97,101,102] that the retardation is caused by this portion of the wall pressure field, which in turn is probably due to the growth and interaction of old bursts produced upstream. In fact, Burton[94] measured a strong correlation between the occurrence of a burst and the imposition on the wall flow of a large moving adverse pressure gradient signal with a magnitude of the order of three times the rms wall pressure intensity. This adverse pressure gradient was followed by a favorable gradient, perhaps at least partially responsible for the sweep portion of the event cycle. It should be noted that recent evidence appears to show more high frequency energy in the wall pressure fluctuation spectra than was originally indicated, perhaps associated with the burst process (see Fig. 9 of Ref. 97 and Ref. 103). However, the burst initiation seems to involve the lower frequency portion of the spectrum. It should be noted that not all outer-flow imposed, low frequency wall pressure fluctuations produce bursts. Evidently, only the large amplitude, long lasting pulses can cause sufficient retardation to produce the necessary pre-burst conditions. Preliminary quasi-steady retarded near wall calculations, using low levels of Reynolds stress and the burst-producing pressure pulses measured by Burton,[94] indicated that the pressure gradients involved are sufficient to cause severe retardation of the near wall flow.[13] The recognition of the low Reynolds stress condition of the pre-burst flow is critically important to the success of such calculations. Further, much more detailed and complete calculations of the pre-burst flow (with and without resonant wall motion) are currently underway by Orszag in collaboration with Langley Research Center, National Aeronautics and Space Administration.

Therefore, there exists a possible feedback mechanism in which older bursts, which have grown and migrated up to the law of the wall and outer portions of the boundary layer, interact and produce a pressure field which contains pulses of sufficient duration and amplitude to induce new bursts in the near wall flow. This near wall region contains a high level of background turbulence but fairly low levels of $\overline{u'v'}$ during the non-burst periods.

It is interesting that an effort to artificially induce bursts using a stationary pressure pulse[104] did not seem to alter the characteristic burst frequency of a turbulent wall flow.

2. Burst modulation due to wall motion

One approach to a theory of drag reduction due to wall motion is to postulate that certain types of surface motion can alter or interrupt some portion of the feedback process just described. The portion of the process most available for alteration by wall motion is the pre-burst, near wall retardation region. Other drag reducing procedures, such as the injection of polymers, may alter this or some other part of the feedback loop.

Reference 13 suggests that the moving surface waves associated with a resonant wall can produce a modulation of the pre-burst retarded flow. The details of this modulation are a function of the wavelength, wave speed (or frequency), and amplitude of the surface motion; however, for short, steep traveling waves the wall motion can produce a modulated pressure gradient, (modified for viscous effects and wave speed as per the Kendall[38] data) alternately positive and negative. This modulation is superimposed upon the adverse gradient signal which normally triggers the bursts. The suggestion[13] is that this modulation, if it has high frequency and moderate amplitude (see the section on stability theory for periodic flows), can delay the burst formation. Considering the expected stabilizing influence of the following favorable gradient portion of the outer flow generated signal, only a small delay may be sufficient to completely obviate the burst. Longer waves (lengths in excess of 500 wall units) would presumably trigger as many extra bursts (due to the long adverse gradient portion of the wave) as the number of bursts eliminated by the stabilizing influence of the favorable gradient part of the wave train. An alternate approach to a similar mechanism is to analyze the pre-burst flow using the breakdown mechanism of Landahl.[105,106] As a minimum, the wall frequency required is probably the order of 50 times the fundamental burst frequency ($\lambda^+ \sim 100$, $C/U_\infty \sim 0.5$).

The burst alteration mechanism just described is only a suggestion; further, more detailed calculations and experiments are necessary to either prove, or disprove, this approach. However, it is known that small surface waves can alter much larger scales of turbulence in the atmosphere over a sea surface[107,108] and the high frequency surface motion dictated by the mechanism is in general agreement with wall motions computed for successful drag reduction experiments (next section of report). Detailed calculations using this burst modulation model are underway.

V. CRITICAL ANALYSIS OF RESONANT WALL EXPERIMENTS UNDER TURBULENT BOUNDARY LAYERS

In this section we attempt to examine the available data with the following two questions in mind: (1) Is there another possible, (and defensible) explanation for the drag reduction observed, and (2) for the successful cases which survive the filter of question 1, what is the computed wall motion, is it high or low frequency (Strouhal number much greater than, or less than, one)? We also mention, for completeness, some of the experiments on drag over resonant water waves in air and the unsuccessful compliant wall experiments, which are discussed first.

A. "Unsuccessful" (small reduction, no change or C_f increase) experiments

It should be noted beforehand that this class of experiments has not received the detailed study by the present authors which it perhaps deserves. We have spent most

of our efforts trying to understand the successful experiments, in an attempt to infer the type of wall motion responsible for the observed drag reduction (if no other cause for the reduction other than wall motion input could be found). On the basis of the theoretical and experimental results thus far, it is reasonable to conjecture that a favorable influence (reduction) on C_f, if indeed such a thing can occur, is probably only possible over a relatively narrow range of wall motion conditions. Without an attempt to control, measure or widely vary the wall motion, hitting the correct combination in an experiment is a pure happenstance. Nevertheless, there are a few obvious comments which can be made concerning these unsuccessful studies.

1. Ritter and Porteous[109]

This water experiment used the original Kramer surface material (periodic, "stubbed" rubber—discussed in considerable detail in Sec. VD). A pertinent comment from Ref. 110 on these data is that the free stream turbulence level was probably too high to constitute a valid test of the laminarizing properties of the surface. The speed was limited due to the formation of local blisters in the coating at high dynamic pressure. Skin friction was estimated from measured values of momentum thickness, a procedure which is not always sufficiently accurate.[12] Problems with the fairing at the leading edge of the coating caused premature transition.

What is fascinating about these data is (1) the use of a periodic surface (spatially repeated substructure, although the modulus of the rubber may have been somewhat high considering the reduced speed range of the tests), and (2) the data in Fig. 5 of Ref. 109 which indicate that drag levels at various distances back along the body have a premature turbulent-like variation with Reynolds number, *and this distribution is below the developed turbulent level*. The amount of this drag reduction is greater farther forward on the body, but due to the later transition on the rigid body (better surface finish) the compliant wall drag levels are generally above the rigid case (and therefore, the authors of Ref. 109 did not consider the data as indicating a drag reduction). The present authors strongly suggest that the fact that these compliant data, obtained using a periodic surface, have a turbulent-like variation with Reynolds number (but at a lower C_f level) may be highly significant. Based on the discussion in the paper thus far, a single stub spacing would not be expected to work well over a wide Reynolds number range, and also the well-known peak in P'_w/q_∞ (ratio of root mean square wall pressure to free stream dynamic pressure) associated with the end of transition may help explain the apparent variation of performance with body distance. This experiment should probably be redone, with more complete instrumentation, to higher speeds, and using a series of periodic surfaces designed over a range of wavelength, wave amplitude, and wave speed (or frequency).

2. Ritter/Messum[111]

This is a continuation of the research of Ref. 109, but using small flat plates rather than cylindrical bodies.

Again, the stream turbulence levels were quite high, and Kramer's stubbed coatings were used. The data, taken only for turbulent boundary layer flow on six different skins, exhibit considerable scattering, but two types of skins gave a drag reduction. One skin showed a consistent 7–14% drag reduction, again exhibiting a variation with Reynolds number parallel to, but below, the rigid turbulent case. A second skin gave a drag reduction (7–15%) except at high speed where standing waves (roughness) may have occurred.

3. Laufer and Macstrello[112]

From Ref. 113, one of the problems in this experiment was the possible reflection of flow-induced surface waves from the downstream end of the channel. Periodic surfaces were used (in some of the tests). A further difficulty in this experiment is that air (rather than water) was used as the test medium. Therefore, the velocity of the flow must be considerably higher to provide a level of wall pressure fluctuation (forcing function) necessary to excite the fairly stiff surfaces used. However, when the flow speed is increased the frequency requirements which the surface waves must meet also increase and therefore, a very careful surface structural design effort is needed. The Langley experience with the design of periodic surfaces for air flows shows that one can get reasonable amplitudes with long wave length (low frequency), but as one tries to increase the frequency of the surface response the amplitude of the motion is considerably reduced, even using very low modulus materials. The periodic surface design problem for air flows is not straightforward. The general conclusion from Ref. 112 is that the surfaces used were too rigid, except for one case, and in that case the duct cross-section changed, due to the pressure loading on the flexible surface, thus invalidating the results.

4. Smith[114]

This is a pipe flow experiment using a nonperiodic (gel-coated) surface and diesel fuel as the test fluid. Only drag increases were measured, and these were ascribed to the roughness of the gel coating. For the higher Reynolds number data, long wave instabilities may have occurred, giving increased roughness. There are several other pipe experiments besides Ref. 114, but these gave substantial drag reductions, and therefore, the discussion of the main portion of the pipe data is postponed until Sec. VB.

5. Dinkelacker[115, 116]

This is one of the most carefully conducted of the compliant surface tests. Water was the test medium and the facility was a pipe inlet flow. In particular, Dinkelacker attempted to determine, for his experiments (a) the repeatability of the rigid tube data, (b) influence of small steps in the tube walls (found to be significant), and (c) possible occurrence/effect of organ pipe acoustic modes, along with studies of other possible influences upon his experimental results. In his own words,[115] "The main outcome of this investigation was the establishment of a detailed picture of the difficulties which

S38   Phys. Fluids, Vol. 20, No. 10, Pt. II, October 1977

Bushnell, Hefner, and Ash   S38

may occur in experiments with flexible walls." Some results of the study seemed to indicate a reduction in drag.

6. Taneda/Honji [117]

This study measured drag on towed flat plates in water, using non-periodic surfaces. The drag of the flexible surface covered plates was generally greater than the rigid ones (due perhaps to early transition). Also, the turbulent levels for the flexible data were generally equal to, or greater than, the rigid levels.

7. Mattout [118]

A fairly detailed study using both resonant and active (driven) walls in water. For the driven wall case a 25% drag reduction and a thrust[122] is obtained. For the flexible wall, only a 7% reduction was observed. For the driven wall case, the waves were quite long (4.2 to 50 cm) compared with the boundary layer thickness which was on the order of 2 cm. The passive walls were membrane covered foams, which are not really periodic surfaces for the relatively small pore size used. Mattout invested considerable effort in determing the modulus of his passive surfaces and used both Polyvinyl chloride and Mylar membranes. Prime variables included membrane tension and flow velocity. Figure 39 of Ref. 119 provides a thumbnail review of the compliant wall results up to 1970.

8. Grosskreutz [16, 93, 123]

This was an attempt to build nonisotropic effects into the wall and is one of the very few studies with wall motion data. The basic concept was to preload the surface so that the surface motion always produced a positive correlation of Reynolds stress, i.e., u and v at the surface were either both positive or both negative. Therefore, the surfaces (which were periodic due to the discrete pre-loading used) directly controlled the Reynolds stress at the wall. The tests were conducted in water, and the surfaces used are somewhat similar to Kramer's (see Fig. 2 of Ref. 93) except that the periodicity length is greater than in the Kramer case. Grosskreutz measured a reduction in momentum thickness on one of the surfaces for the low velocity (low unit Reynolds number) cases. The present authors speculate that there is a possibility that the favorable low unit Reynolds number results may have been due to thicker sublayers where the periodic spacing used was closer to the wavelengths required for burst modulation.

9. Hansen/Hunston [34]

These experiments were run on a rotating disk in water using layered (nonperiodic) surfaces. There is insufficient conditional sampling data for the three-dimensional boundary layers on rotating disks to determine the type of wavelengths and three-dimensional waveforms which might be required for burst modulation. The results of the experiment[34] were null in that no drag reduction occurred. At high speeds, where static divergence waves formed, the drag increased. One should probably stay with zero pressure gradient, two-dimen-

sional, turbulent flows for testing of wall motion effects and prove/disprove the case for drag reduction there, before considering three-dimensional and pressure gradient effects.

10. Kawamata et al. [124]

This study used a floating element model on the wall of a water tunnel. Material properties such as damping coefficient and stiffness are given for several of the surfaces used, which were fairly thick rubber or Neoprene membranes backed by either air or olive oil. Due to the nonperiodicity of the surfaces, the wavelengths were probably quite large. The authors claim large drag reductions, but there are more drag increase data than drag reduction. The most worrisome point is that sizable reductions are observed in the fully laminar case, perhaps indicating possible problems with accuracy using the floating element balance (flow/pressure gradients in the gap, etc.) or other experimental problems. These experiments should be carefully analyzed and perhaps repeated.

11. McAlister and Wynn [125]

This was an attempt to confirm the results of Blick et al. at the University of Oklahoma (Refs. 36, 90, 126–132, reviewed in Ref. 11). In Sec. VC the present authors suggest, based upon recent Langley analysis and experimental results, a possible alternative explanation for the drag reductions observed during the Oklahoma liquid-backed membrane tests. This alternate explanation may account for the difficulty which McAlister and Wynn and also Lissaman and Harris[35] experienced in reproducing the liquid-backed Oklahoma results. McAlister and Wynn used an airfoil type model mounted on flexures for direct force measurements and tested in air. There may be an absolute accuracy problem in these experiments associated with the combination of pressure and skin friction drag sensed by the load cells and the percentage of overall surface area covered with compliant surface. The flexible surfaces used were layered and non-periodic and were probably too stiff to respond well to the relatively low dynamic pressure of the air flow. No drag reduction was observed.

In summary, even though labeled "unsuccessful," several of these studies did observe some drag reduction ($\approx$ 5–15 percent) particularly for conditions condusive to small wavelength, steep waves (low unit Reynolds number, water flow, periodic surfaces with small cell size).

B. Flexible pipe experiments

Successful drag reduction experiments with turbulent flows in flexible pipes have been reported by Pelt,[41] Teslo and his co-workers,[133,134] and Klinzing et al.[135] All of these investigators have reported significant reductions in the pressure drop for a flexible pipe when compared with a rigid pipe. However, these data should be questioned because of the extreme sensitivity of pressure drop to changes in diameter. A theoretical model is discussed which indicates that significant drag reductions can be attributed directly to changes in tube shape

rather than a compliant effect (see also Ref. 136 for possible effects of geometry change).

Hydrostatic displacement of the tubes employed in Pelt's experiments has been studied in some detail.[137] Although that analysis does not apply directly here, an important result was that, for the materials and geometry employed in Pelt's experiments, the radial tube displacement, $w(x)$, could be well approximated by

$$w(x) = (R_0/\alpha)[R_0 P(x) - \nu_T N_x(x)]$$

for axial (x) locations away from the ends. In this equation, R_0 is the tube radius, P is the local fluid pressure, ν_T is Poisson's ratio, N_x is the axial load, and α is a constant given by

$$\alpha = E\delta_T \left(1 + \frac{\delta_T^2}{12 R_0^2 (1 - \nu_T^2)}\right) ,$$

where E is Young's modulus for the tube and δ_T is the tube thickness. The tube was modeled as a shell, the influence of end conditions on the tube deformation was restricted to very small regions in the vicinity of each end (less than two diameters). These approximations are also valid for the flexible tube employed by Teslo et al.[133,134] By assuming quasi-parallel flow, the tube deformation can be coupled with the flow-induced pressure drop in a straightforward manner.

Assuming that the rigid pipe friction factor, $\bar{\lambda}$ can be employed locally for the flexible pipe (quasi-parallel flow) and that γ varies with Reynolds number, R_e according to

$$\bar{\lambda} = C R_e^{-\beta} = 0.3164 R_e^{-1/4}$$

which is related to the local pressure gradient by

$$\frac{dP}{dx} = \frac{\bar{\lambda}}{D} \frac{1}{2} \rho V^2 ,$$

where D is the local pipe diameter, ρ is the fluid density, and V is the local mean velocity, the local pressure gradient can be developed as a function of diameter. If γ_0 is the rigid pipe, fully developed pressure gradient, dP/dx_r, given by

$$-\gamma_0 = \frac{dP}{dx_r} = -\frac{\bar{\lambda}_0}{D_0} \frac{1}{2} \rho V_0^2 ,$$

it can be incorporated in the last equation along with the conservation of mass requirement

$$VD^2 = V_0 D_0^2 ,$$

to write

$$dP/dx = -\gamma_0 \left(\frac{D_0}{D}\right)^{5-\beta} .$$

Furthermore, the local diameter is given by

$$D(x) = D_0 + 2w = D_0 \left(1 + \frac{R_0 P(x) - \nu N_x}{\alpha}\right)$$

and the axial load, N_x is related to the applied tension, T and local fluid pressure, $P(x)$ by

$$N_x = T + (R_0/2) P(x) ,$$

when the pressure at the end of the tube $(x = L)$ is zero. Combining the last three equations

$$\frac{dP}{dx} = \frac{-\gamma_0}{\left\{\left[1 - \frac{\nu}{\alpha} T + \frac{R_0}{\alpha}\left(1 - \frac{\nu}{2}\right)P\right]^{5-\beta}\right\}^{-1}}$$

which can be integrated between $x = 0$ and L to yield

$$\left[1 - \frac{\nu}{\alpha} T + \frac{R_0}{\alpha}\left(1 - \frac{\nu}{2}\right)P_0\right]^{6-\beta}$$
$$= \left(1 - \frac{\nu}{\alpha} T\right)^{6-\beta} + \frac{1}{\alpha} R_0 (6-\beta)\left(1 - \frac{\nu}{2}\right)\gamma_0 L$$

or

$$P_0 = \frac{\alpha}{R_0} \frac{1}{1 - \frac{\nu}{2}} \left\{\left[\left(1 - \frac{\nu}{\alpha} T\right)^{6-\beta}\right.\right.$$
$$\left.\left. + \frac{1}{\alpha}\left(6 - \beta\right)\left(1 - \frac{\nu}{2}\right)\gamma_0 R_0 L\right]^{1/(6-\beta)} - \left(1 - \frac{\nu}{\alpha} T\right)\right\} ,$$

where P_0 is the pressure at $x = 0$, which in this case corresponds to the estimated pressure drop.

Using the flexible pipe data in Table I, the pressure

TABLE I. Flexible pipe data.

Pipe material	Thick rubber[a]	Thin rubber[a]	Tygon[a]	Texin[a]	Polyethlene[b]
L, m	2.79	2.79	2.79	2.79	2.80
R_0, mm	4.8	4.8	4.8	4.0	25.0
δ_T, mm	5.6	3.6	1.6	0.8	0.16
E, N/cm^2	140	70	250	1000	15 000
ν_T	0.49	0.49	0.45	0.45	0.45
T, N/cm^c	5.2	2.4	3.8	3.3	NA
measured pressure drop, N/cm^2	18.1	12.8	18.6	22.0	0.110
$P_0(T=0)$, N/cm^2	20.3	12.2	13.4	24.8	0.128
pressure drop for a rigid pipe, N/cm^2	24.7	18.0	18.0	31.1	0.128

[a]Data from Pelt, Ref. 21.
[b]Data from Teslo and Zhoga, Ref. 37.
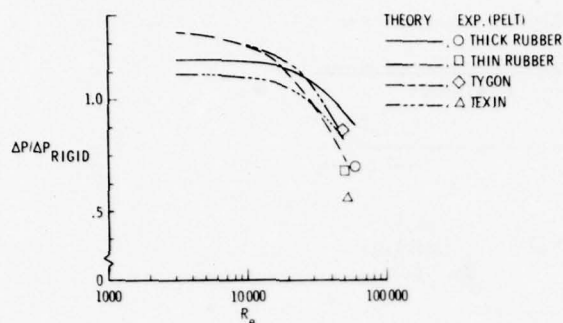[c]Tension estimation based on reported elongation.

FIG. 1. Variation of flexible pipe pressure drop with Reynolds number.

drop has been calculated from this last equation for various Reynolds numbers and is shown in Fig. 1. Since the effect of gravity (which was important in Pelt's[41] vertical flow experiments) has been ignored, the calculated pressure drops cannot agree with Pelt's measurements, particularly at low Reynolds numbers where hydrostatic effects dominate. However, at Reynolds numbers of 50 000 the calculated pressure drop agrees with the measured data to within about 10% in all cases except for tygon tubing where the theoretical prediction was about 30% lower than the measured value.

The close agreement between theory and experiment may be fortuitous because end effects and viscoelastic effects have not been considered. End conditions would generally increase the pressure drop whereas viscoelastic creep would likely result in diametral increases and subsequent reductions in pressure drop. The latter effect may be responsible for the 25% drag reduction reported in Teslo et al.[133,134] Teslo and Filipchuk[134] note that a 3% increase in diameter occurred in their experiments, which is not predicted by the current theory. A 3% increase in diameter will cause a 15% reduction in pressure drop. Conversely, a 25% reduction can be caused by a 5% change in diameter which may be within the uncertainty of their measurements. Although the present investigation cannot show positively that the data of Teslo et al. are a result of pipe deformations, it appears very likely that creep may have occurred during those tests.

C. Re-evaluation of compliant wall experiments in air with water substrates

A large portion of the successful compliant wall air data (which indicate drag reductions to 50%) were obtained at the University of Oklahoma during the years 1966 through 1969.[126-132] A re-evaluation of the Oklahoma experiments with water substrates (most of the data) was conducted at the Langley Research Center and is presented in Ref. 138.

The Oklahoma experiments, conducted on compliant surfaces in air at subsonic speeds with foam and/or fluid substrates, measured, directly, the skin friction drag on floating panel models which were mounted flush with the tunnel floor. The models, shown schematically in Fig. 2, were mounted on a long, vertical, single-col-

umn beam. Weights were attached to the upstream portion of the models to counterbalance bending moments caused by the surface skin friction. This arrangement permitted very low drag forces to be measured on the compliant model panels (e.g., forces as small as 0.5% of the hard plate drag could be detected).

The models for Ref. 127 had a compliant surface 63.8 cm long by 18.1 cm wide whereas the model surface for Ref. 128 was 38.1 cm long 24.1 cm wide. Various fluid substrates with different viscosities (i.e., air, water, and solutions of water and Polyox) were explored in the investigation of Ref. 127 which was conducted at a free stream velocity of 11.6 m/sec. Skin friction drag reductions up to 50% were reported for these tests. Reference 128 explored the effect of free stream velocity (i.e., $U_\infty \approx 5.2 - 67.1$ m/sec) on the compliant wall drag reduction for porous polyurethane foam substrates (some of which were saturated with water), and drag reductions up to 38% were achieved. Both investigations used thin polyvinyl chloride sheets, either 0.0064 or 0.0089 cm thick, for the compliant wall skins.

The following re-evaluation of the Oklahoma water-backed membrane tests stems from thus-far unsuccessful attempts at the Langley Research Center to experimentally verify the University of Oklahoma experiments. As noted previously, Ref. 35 and 125 were also unable to reproduce the liquid-backed Oklahoma experiments. No drag reductions were obtained in Langley experiments conducted in a small subsonic wind tunnel on floating panel compliant wall models with liquid substrates. The size of the models tested, the fluid substrates, and the flow conditions were similar to those reported in Refs. 127 and 128, and are summarized in Table II. The major difference between the Langley experiments and those at the University of Oklahoma was the method of obtaining the direct skin friction drag measurements. Whereas the University of Oklahoma experiments used the single-column, cantilever beam type of arrangement, the Langley experiments supported the floating panels by thin wires attached to each of the four corners of the test panels outside the air stream (see Fig. 3). The drag force was then obtained by determining the amount of weight necessary to null the test plate to the original windoff position.

In the Langley attempts to duplicate the University of Oklahoma experiments, small standing waves were measured on the compliant surface as the free stream velocity was increased from 15 to 30 m/sec. These waves
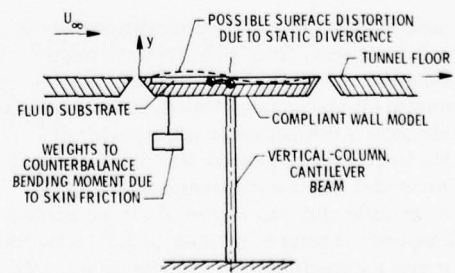

FIG. 2. Typical University of Oklahoma experiment.

TABLE II. Comparison of Langley Research Center and University of Oklahoma experiments in air with water substrates.

| | | University of Oklahoma | |
	Langley research center	Looney/Blick	Chu/Blick
Stream velocity	9–30 m/sec	11.6 m/sec	5–67 m/sec
Model surface			
Length	66 cm	63.8 cm	38.1 cm
Width	20.3 cm	18.1 cm	24.1 cm
Depth	1.27 cm	0.79 cm	1.27 cm
Membrane			
Material	PVC	PVC	PVC
Thickness	0.0064 cm	0.0064 and 0.0089 cm	0.0064 cm
Longitudinal tension	3.5 N/m	4–111.7 N/m	55.3 N/m
Lateral tension	3.5 N/m	1.9–55.5 N/m	53.6 N/m

resembled sine waves with half of the wave protuding over the upstream portion of the model and the other half of the wave being recessed over the downstream end of the model. Reference 128 and private communications with Dr. Edward F. Blick of the University of Oklahoma acknowledged the existence of small standing waves in the Oklahoma tests at certain free stream velocities. It is concluded that this information, coupled with the results of the Langley drag reduction experiments, suggest that standing waves in the University of Oklahoma experiments could have caused a shift in the model center of gravity and this shift may have created a bending moment on their single column balance that was interpreted as a reduction in the skin friction drag.

Reference 138 analytically determined the amplitude of a simple sine wave necessary to produce a center of gravity shift and resulting bending moment large enough to account for an apparent 40 percent reduction in skin friction drag on a single-beam balance. The assumed wave shape is shown in Fig. 2. Based on a hard plate average skin friction coefficient of 0.00389 for the tests of Ref. 127, the apparent drag reduction was approximately 1.9 g. For the balance moment arm of 85.7 cm in the University of Oklahoma tests, this apparent drag reduction could have generated a bending moment of 1.63 g-m. The maximum amplitude of a sine wave necessary to shift the model center of gravity upstream and to create this bending moment was only 0.013 cm (assuming that the compliant wall skin was always in contact with the water substrate). As Ref. 138 points out, surface motion this small would obviously be very difficult to detect with the unaided eye and could probably have been overlooked.

To check the analytically determined magnitude of the possible surface deflections, Ref. 138 presents measured surface deflections for the Langley experiments of Fig. 3 on a compliant wall model with 0.0064 cm thick polyvinyl chloride skin stretched over a water-filled cavity. The tests were representative of those reported in Ref. 127. The model had a compliant surface 66.0 cm long by 20.3 cm wide and was tested at a free stream velocity of 16.2 m/sec. Uniform tension ($\approx$3.5 N/m) was applied laterally and longitudinally to the compliant wall membrane with a vacuum-tensioning device. During the

Langley drag reduction tests the tension was actually varied over a wide range, and no drag reduction was observed. The value of 3.5 N/m for tension applies to the data runs for surface deformation measurements. An optical system developed by Weinstein at Langley, was used to measure the compliant wall surface deflections. The system used two photo detectors, 1.37 cm apart, driven on a track over the full length of the model surface. Each photodetector measured the instantaneous surface angle over a spot 0.13 cm in diameter to within 0.002 of a degree. However, for the data of Ref. 139, only one detector was used to obtain a time-average surface angle. The original wind-off and then the wind-on surface angles were measured, and the differences between the two were integrated to obtain the flow-induced change in surface position.

The surface position measurements of Ref. 138 on the polyvinyl chloride compliant skin model with water-filled substrate are presented in Fig. 4 for three longitudinal pressure gradients. Pressure gradients of these magnitudes were found in Refs. 127 and 128. References 127 modified the upper tunnel wall in an attempt to eliminate or reduce the gradients whereas Ref. 128 corrected the drag measurements by calculating the bending moment induced by action of the measured variation in the surface pressures on the edges of the balance. In the study of Ref. 138, the gradients were obtained by moving the tunnel side walls ±0.318 cm from the mean zero pressure
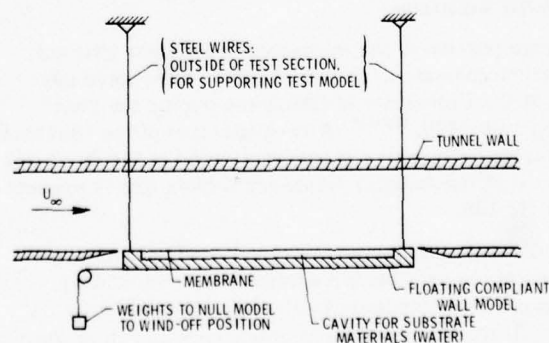

FIG. 3. Air flow over water-backed membranes. Langley attempted redo of typical University of Oklahoma experiments.
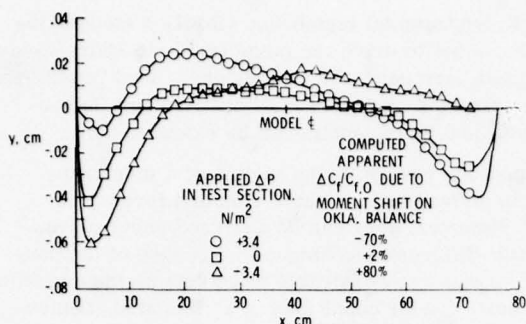
FIG. 4. Surface position measurements for compliant surface with water substrate in Langley experiments. $U_\infty = 16$ m/sec, static divergence mode.

gradient position. These changes produced a 1.1% variation in the steam velocity with a 2.2% variation in static pressure. The corresponding changes in the static pressure (Δp) over the 76.2 cm long model were approximately ± 3.4 N/m².

Reference 138 showed the large effect of only small pressure gradients on the formation of standing waves on the compliant wall surface (see Fig. 4). For the nearly zero pressure gradient the surface protruded outward by approximately 0.009 cm. The positive gradient created a bulge over the upstream portion of the model whereas the negative gradient caused the bulge to shift to the downstream portion of the surface. The model fairing plate around the compliant surface caused the surface to dip over the first 7.6–16.5 cm for all three gradients; the surface dipped over the last 23 cm for the zero and slightly positive gradients.

The water volume under each of the three waves in Fig. 4 was integrated in the study of Ref. 138 to determine the bending moment caused by the transfer of the water mass. The slightly positive gradient shifted the center of gravity upstream of the model centerline and generated a 3 g-m bending moment. The near zero and negative pressure gradients shifted the model center of gravity downstream of the model centerline and generated 0.1 g-m and 3.3 g-m bending moments, respectively. As Ref. 138 showed, these bending moments in each situation would be sufficient to significantly alter the drag reductions reported in Ref. 127 and 128 and hence compromise the validity of the data (e. g., the 3 g-m bending moment for the positive gradient could have indicated an apparent 70% drag reduction). A further problem with tests of this type is that, from the Langley experiments, the balance reading is quite sensitive to even small air leaks in the enclosure surrounding the tunnel and balance system. An excellent seal is mandatory for accurate data.

1. Structural dynamics analysis of water-backed membranes

Having suggested that drag reduction did not occur for air flow over water-backed membranes, it is of interest to determine whether their characteristic surface response is in agreement with the arguments thus far which

indicate that high frequency surfaces are necessary for drag reduction. The influence of water-backing on membrane surface motion has been studied by Blick[87] and Ash and Balasubramanian.[32] Those analyses are similar, but the somewhat more detailed calculations of Ash and Balasubramanian[32] are extended in the present work. Details of their calculations are given in Ref. 32 and only the salient features of the model are discussed here.

Membrane motion has been assumed driven by three pressure force contributions: a direct turbulent wall pressure field and two reaction pressure fields induced by wall motion. The turbulent wall pressure was assumed to obey Taylor's "frozen pattern" hypothesis so that individual wave number pressure contributions could be analyzed one at a time. The turbulent wall pressure spectrum was modeled using Bull's[139] data, but modified for very low frequencies (Strouhal numbers based on displacement thickness and free stream velocity, $\omega\delta^*/U_\infty$, below 0.05) by assuming the spectrum level fell off with the fourth power of the wavenumber (ω/U_∞). A potential flow model was employed to estimate the induced pressure field resulting from membrane motions over the water backing, and a subsonic acoustic wave equation could be solved to estimate the induced pressure on the turbulent air boundary layer side of the membrane when wave velocities were different from the flow velocity.

Membrane deflection was developed using a normal mode expansion approach. Subsequently, surface motion calculations were obtained for individual turbulent wall pressure frequency contributions, which included the two induced pressure effects, and a spectrum of expected surface motion values was generated from the compilation of those frequencies. Calculation results are shown in Fig. 5 for a typical case corresponding to the Langley data. It is obvious from these results that the surface motion is at quite a low frequency, having very little motion at frequencies larger than the Strouhal number one level. This indicates that surface wavelengths are larger than the boundary layer thickness, and therefore more than an order of magnitude larger than values necessary for drag reduction according to the burst modulation mechanism described herein. Therefore, the null result (no drag reduction) on these surfaces is, in a sense,
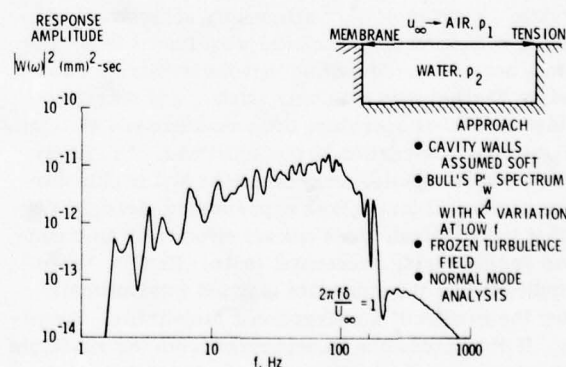

FIG. 5. Predicted surface motion of water-backed membranes. Typical Langley experiments, $U_\infty = 16$ m/sec.
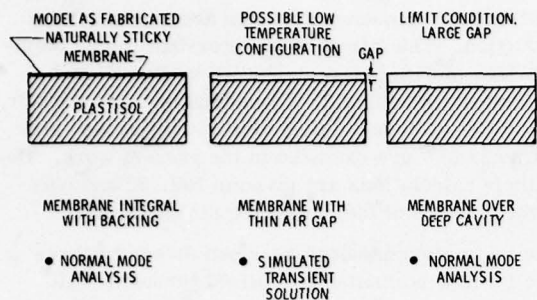
FIG. 6. Possible geometric configurations. Langley membrane/Plastisol model.

somewhat encouraging as far as verification of this theory is concerned.

D. High frequency/periodic surfaces

The turbulence modification model (modulation of pre-burst flow) discussed previously requires short wavelength, high frequency surface motions for effective compliant wall interaction. Since that motion does not normally occur on structural panels, it is important to determine whether such motion could have been present during previously reported highly successful experiments. Three sets of such experiments cannot at this point be dismissed by alternate explanations: (1) Kramer's experiments[55-57] in water, (2) Walter[90] experiments in air, and (3) the experiment of Fischer et al.[12] at low temperature (on the order of 0 °C) in air. Aside from being in air, the experiments of Walters[90] and Fischer et al.[12] have marked similarities and will be discussed first.

In these experiments in air, both investigators employed thin rectangular membrane surfaces stretched over a soft elastic substrate. Walters[90] employed a thin polyvinyl chloride skin stretched over a porous polyurethane foam, while Fischer et al.[12] used a Mylar skin stretched over a sticky, gelatinous layer of polyvinyl chloride plastisol. It should be noted that even though these substrates were structurally soft, both were very rigid from the standpoint of the available turbulent pressure forces. Walters[90] found that no drag reduction occurred when the membrane skin was attached to the substrate by means of a spray adhesive, but drag reduction did occur when the membrane simply rested against the substrate. Fischer et al.[12] apparently achieved significant drag reduction only when the wind tunnel temperature was near 0 °C. Recalling that the substrate employed by Fischer was naturally sticky, and noting further that a 20 °C temperature drop would result in significant thermal contraction of the substrate, it is likely that the substrate pulled away from the Mylar skin during the successful test. Both experiments strongly suggest that the substrate does not act effectively as a continuous spring during successful tests. Rather, those data indicate that the substrate may act intermittently to alter the motion of a conventional membrane. Specifically, if the membrane is separated from the substrate by a thin air gap, as shown in Fig. 6, it is likely that the substrate functions as a "wavelength chopper." That is, by interfering with the downward displacement of long

wavelength fundamental membrane vibration modes, the substrate can act to drive the membrane into short wavelength higher harmonic vibration modes. That possibility has been examined by Ash et al.[13] and Ash and Balasubramanian[32] and their results can be extended here.

The equations governing the motion of a membrane over a thin air gap are, in their simplest form, nonlinear.[13] However, they can be analyzed using conventional finite-difference techniques. Because of the nonlinearity, it was very desirable to determine the dynamic surface motion under conditions of a simulated, nonfrozen, turbulent wall pressure loading. Details of the turbulence simulation are discussed briefly by Ash and Balasubramanian[32] and simulated surface motion histories are also shown.

Again referring to Fig. 6, the membrane substrate system employed by Fischer et al.[12] could change from (1) an integral system of a membrane attached to a continuous elastic spring, to (2) a membrane separated from its substrate by a thin gap, and finally (3) to a membrane over a cavity which is deep enough to eliminate contact between the membrane and substrate. Those three configurations have been subjected to the same simulated turbulent wall pressure to show the influence of those structural changes on the response amplitude spectra and are shown in Fig. 7. It can be seen that the integral system produces a smoother, lower amplitude response, whereas the narrow air gap case yields a higher frequency motion.

Recently, unpublished experiments have been performed at Langley Research Center in which attempts were made to control the thin air gap behind a membrane in a low speed air flow. The major finding of those tests was that a specified gap cannot be maintained beneath a membrane with any reasonable tolerance over a large surface. (Small localized "bubbles" did however occur and produced drag reductions of 10–15%.) That work is continuing, but alternate methods for producing short wavelength, high frequency surface motion are being examined. The most direct method for producing short wavelength motion is to employ a ribbed periodic substructure beneath a thin skin. The rib spacing can be used to control the surface wavelength and frequency.
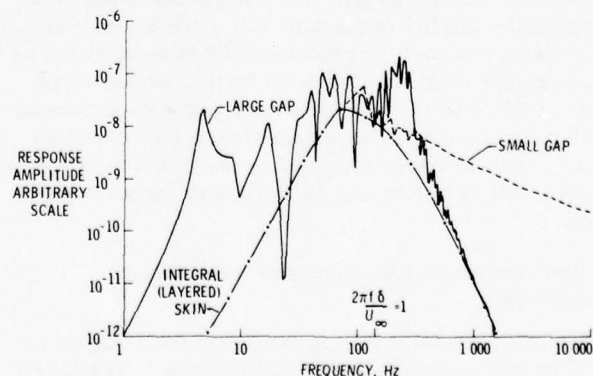

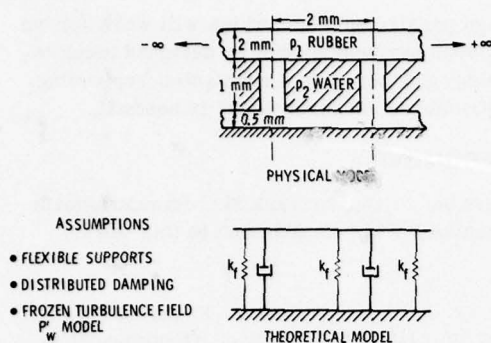FIG. 7. Predicted response of Langley membrane/Plastisol model.

FIG. 8. Predicted surface motion—Kramer's periodic structure.

FIG. 10. Resonant compliant wall structural concepts.

However, analysis has shown that in the low speed, turbulent, air boundary layers currently available for testing, reasonable amplitudes of surface motion cannot be achieved. That would not be the case in water and since Kramer's[55] original model designs employed the types of periodic structures just suggested, a reexamination of his experiments is appropriate.

A cross section of one of Kramer's[55] successful compliant surfaces is shown in Fig. 8, where the structural elements are periodic, i.e., repeated with the same dimensions. If one assumes that Kramer achieved his drag reduction beneath a fully turbulent boundary layer, the reported average skin friction coefficients can be used to estimate a turbulent wavelength, λ^*, for the compliant surface. The variation of λ^* was found to be between 200 and 500 wall units over the velocity range (7 to 18 m/sec) of his successful tests.

It has been rather commonplace to discount Kramer's results, for many reasons. First, because the tests were performed by towing test models behind a motor boat in Long Beach Harbor, it has been reasoned that the tests may not have been as closely controlled as most laboratory facility experiments. Kramer acknowledges that his experiments were affected by the season (experiments in summer were less encouraging than at other times of the year) and attempts to duplicate his results in towing tanks[59] and water tunnels[109] were unsuccessful or inconclusive.

FIG. 9. Steady-state response of Kramer stubbed periodic surface. $U_\infty = 18$ m/sec, water flow.

The structural dynamics response of Kramer's model has been examined recently at Langley Research Center assuming interaction with a fully turbulent boundary layer. For a two-dimensional model of the configuration shown in Fig. 8, an approximately equivalent spring-dashpot (also shown) has been used to study the system, employing the method of space harmonics.[29] A frozen turbulence pattern was assumed with the same spectrum employed in the water-backed membrane analysis. The spectrum of surface motion is displayed in Fig. 9 for the test conditions just mentioned and it is observed that significant high frequency motion can be developed by that surface adding further support to a high frequency requirement and, by inference, the turbulence modification explanation.

To conclude this section, there is sufficient evidence in support of the turbulent burst modulation theory for compliant wall drag reduction to merit further investigation of high frequency surfaces. Furthermore, surface motion measurements during successful tests are crucially needed, as are reliable numerical predictions of expected surface motion for a particular design (which also must be verified by experimental data). To date, the surface design concepts shown in Fig. 10 have been examined on the basis of high frequency surface motion potential. Of these concepts only the membrane over the thin air gap and the periodic structures are considered promising at this time for significant modification of low speed turbulent air boundary layers.

VI. AIR-SEA INTERFACE AS A PROBLEM OF WALL MOTION INFLUENCE UPON TURBULENCE

As final note on the influence of wall motion on wall turbulence structure we briefly discuss the air-sea interface problem. As already mentioned, Refs. 107 and 108 indicate that the suppression of small (capillary) waves on the ocean surface can alter much larger scales of turbulence in the atmosphere above the surface. In the absence of capillary waves, the air boundary layer appears to lose coherence with the ocean waves. The usual influence of the large ocean waves on skin friction is to increase drag[140] (evidently due to a roughness effect for traveling waves,[41] and also zero wave speed case[37]). Although there is still controversy, the wind generated waves on this resonant surface (air-sea interface) can evidently become large enough to separate the air flow

between waves.[142] Nevertheless, the present authors suggest that the information on the air-sea interface problem can at least be used to indicate regions in the three space of wavelength, wave speed, and wave amplitude (normalized in law of the wall coordinates) which one should stay away from (drag-increasing) in the design of resonant walls.

VII. SUMMARY

In this paper we have reviewed the following subjects pertinent to the use of walls with moving waves for drag reduction:

(a) The need, in aeronautics, for drag reduction research using moving walls under turbulent boundary layers.

(b) Simple structural dynamic considerations which indicate that practical walls must be of the resonant type and also periodic for control of wavelength.

(c) The influence of wall motion upon boundary layer stability for highly compliant and also resonant walls and the stability of periodic flows. Recent Soviet experimental research indicates that resonant walls can also influence transition.

(d) Theoretical models of the drag reduction mechanism for moving walls under turbulent boundary layers. The current best strategy, in the opinion of the present authors, is to further investigate an approach based upon modulation of the pre-burst flow. This modulation may result in delay of burst formation and the subsequent elimination of a reasonable percentage of the total number of bursts. This mechanism requires considerable further research but does provide a crude guideline for future experiments (small wavelength, steep wave high frequency surfaces).

(e) A critical analysis of the available compliant wall data (resonant walls under turbulent boundary layers) indicates that the best performance has been obtained using high frequency response surfaces. Alternate explanations (other than alteration of the turbulence structure) are given for the drag reductions observed in pipe flows and also for liquid-backed membranes in air.

As a suggestion, further experiments should be conducted in water using both periodic and active (driven) surfaces, but over a much wider range of wavelength than used in past experiments, particularly at the low end (smaller wavelengths). Due to the low dynamic pressures associated with air tests for velocities much less than transonic, subsequent air tests should initially concentrate on driven surfaces, especially with small wavelengths. All experiments should measure surface motion and, if a drag reduction is observed, the influence of the wall motion upon the bursting process should be determined. Also, redundant drag measurements should be mandatory.

The purpose of the active wall research is to provide controlled experiments to determine what type of wall motion (wave speed, length, amplitude, etc.) is required to produce a drag reduction. These criteria can then be used to design passive surfaces which will work (or we find out that such surfaces cannot be designed using today's technology and therefore a substantial supporting materials/structures research effort is needed).

ACKNOWLEDGMENT

[1]A. L. Nagel, W. J. Alford, Jr., and J. F. Dugan, Jr., presented at AIAA 11th Annual Meeting, Washington, D.C. (1975), AIAA Paper No. 75-316.
[2]R. E. Bower, NASA CR-142559 (1974), also NASA TMX-72659 (1975).
[3]M. C. Fischer and R. L. Ash, NASA TM X-2894 (1974).
[4]I. E. Beckwith and D. M. Bushnell, NASA TN D-6221 (1971).
[5]A. Marino, C. Economos, and F. G. Howard, NASA CR-132718, ATL TR 216 (1975).
[6]R. Pfeffer and S. J. Rossetti, NASA CR-1894 (1971).
[7]J. L. Lumley, J. Polym. Sci. Macromol. Rev. 7, 263 (1973).
[8]F. H. Bark, E. J. Hinch, and M. T. Landahl, J. Fluid Mech. 68, 129 (1975).
[9]P. S. Granville, Naval Ship Research and Development Center Report SPD 569-03 (1975).
[10]N. G. Coles, Editor, *Proceedings of International Conference on Drag Reduction* (BHRA Fluid Engineering, Cranfield, England, 1974).
[11]E. F. Blick, in *Proceedings of International Conference on Drag Reduction*, edited by N. G. Coles (BHRA Fluid Engineering, Cranfield, England, 1974) paper F2.
[12]M. C. Fischer, L. M. Weinstein, D. M. Bushnell, and R. L. Ash, presented at the AIAA 8th Fluid and Plasma Dynamics Conference (1975), AIAA Paper No. 75-833.
[13]R. L. Ash, D. M. Bushnell, L. M. Weinstein, and R. Balasubramanian, presented at the Fourth Biennial Symposium on Turbulence in Liquids, University of Missouri, Rolla (1975).
[14]G. Zimmermann, Max-Planck-Institut für Strömungsforschung, Göttingen Report 10a/1974 (1974).
[15]P. P. Antonatos, Astronaut. Aeronaut. 4, 32 (1966).
[16]R. Grosskreutz, Max-Planck-Institut für Strömungsforschung, Göttingen, Federal Republic of Germany, No. 53 (1971).
[17]D. Gyorgyfalvy, J. Aircr. 4, 186 (1967).
[18]Y. S. Pan, presented at the AIAA 2nd Aero-Acoustics Conference (1975), AIAA Paper No. 75-507.
[19]W. A. Von Winkel and J. E. Barger, J. Acoust. Soc. Am. 33, 836 (1961).
[20]C. R. Nisewanger, Naval Weapons Laboratory, China Lake, Report 8518, NOTS TP-3510 (1964).
[21]Sir James Gray, Sci. Am. 197, 29 (1957).
[22]M. O. Kramer, Am. Soc. Nav. Eng. 73, 103 (1961).
[23]M. O. Kramer, in *Advances in Hydroscience*, edited by V. T. Chow (Academic, New York, 1965), Vol. 2, p. 111.
[24]T. K. Lang, and K. Pryor, Science 152, 531 (1966).
[25]T. G. Lang, presented at the Symposium on Swimming and Flying in Nature, California Institute of Technology (1974).
[26]T. M. Pemberton, Naval Ship Research and Development Center Test and Evaluation Report No. P-351-H-01 (1969).
[27]A. M. van Londen, presented at the Third International Congress on Marine Corrosion and Fouling, Gaithersburg, Maryland (1972).
[28]E. Naudascher, editor, *IUTAM-IAHR Symposium Karlsruhe (Germany)* (Springer-Verlag, Berlin, 1972).
[29]D. J. Mead and K. K. Pujara, Sound Vib. 14, 525 (1971).
[30]E. F. Kerkman and E. M. Kerwin, Jr., Bolt-Beranek and Newman, Inc., Rpt. No. 2374 (1972).
[31]N. Tokita and F. W. Boggs, U.S. Rubber Company Research Center Report, Wayne, N. J. (1962).

[32]R. L. Ash and R. Balasubramanian, presented at the American Society of Chemical Engineers National Water Resources and Ocean Engineering Conference, San Diego, California (1976), Report 2726.

[33]M. O. Kramer, Rand Corporation Memo RM-3018-PR (1962).

[34]R. J. Hansen and D. L. Hunston, J. Sound Vib. 34, 1 (1974).

[35]P. B. S. Lissaman and G. L. Harris, presented at the AIAA 7th Aerospace Science Meeting (1969), paper 69-164.

[36]E. F. Blick, R. R. Walters, R. Smith, and H. Chu, presented at the AIAA 7th Aerospace Sciences Meeting (1969), AIAA Paper 69-165.

[37]C. Cancelli and F. Vatta, Accademia della Scienze, Classe di Scienze Fisiche, Matematiche Naturali, Memorie No. 20, p. 1 (1974) [NASA IT F-16 (1975), p. 525].

[38]J. M. Kendall, J. Fluid Mech. 41, 259 (1970).

[39]M. T. Landahl, J. Fluid Mech. 13, 609 (1962).

[40]T. B. Benjamin, in *Proceedings of the Eleventh International Congress of Applied Mechanics*, Munich, Germany (1964), edited by H. Görtler, (Springer-Verlag, Berlin, 1966), p. 109.

[41]R. J. Pelt, Ph.D. thesis, University of Pittsburgh (1964).

[42]T. B. Benjamin, J. Fluid Mech. 9, 513 (1960).

[43]R. Betchov, Douglas Aircraft Report No. ES-39174 (1959).

[44]F. W. Boggs and N. Tokita, in *Third Symposium on Naval Hydrodynamics*, edited by S. W. Doroff (Superintendent of Documents, U. S. Government Printing Office, Washington, D. C., 1960) p. 451.

[45]F. D. Hains and J. F. Price, Phys. Fluids 5, 365 (1962).

[46]T. Nonweiler, Aeronautical Research Council Report No. CP622 (1963).

[47]J. H. Linebarger, M. S. thesis, Massachusetts Institute of Technology (1961).

[48]T. B. Benjamin, J. Fluid Mech. 16, 436 (1963).

[49]M. T. Landahl and R. E. Kaplan, AGARDograph 97, (1965), p. 363.

[50]R. E. Kaplan, Massachusetts Institute of Technology, Report ASRL TR-116-1 (1964).

[51]M. Takematsu, Rep. Res. Inst. Appl. Mech., Kyushu Univ. 16, 109 (1968).

[52]E. W. Burden, Ph.D. dissertation, University of Pennsylvania (1969).

[53]V. B. Amfilokhiyev, V. V. Droblennov, and A. S. Zavorokhina, Zh. Prikl. Mekh. Tekh. Fiz. 13, 137 (1972) [J. Appl. Mech. Tech. Phys. 13, 253 (1974)].

[54]O. H. Wehrmann, Phys. Fluids 8, 1389 (1965).

[55]M. O. Kramer, Am. Soc. Nav. Eng. 72, 25 (1960).

[56]M. O. Kramer, Am. Soc. Nav. Eng. 74, 341 (1962).

[57]M. O. Kramer, *Jahrbuch der Deutschen Gesellschaft für Luft-und Raumfahrt* (Hermann Blenk and Werner Schulz, Köln, Federal Republic of Germany, 1969), p. 102.

[58]P. B. Rhines and E. L. Mollo-Christensen, Phys. Fluids 10, 916 (1967).

[59]F. W. Puryear, David Taylor Model Basin, Hydromechanics Laboratory of Research and Development Report 1668 (1962).

[60]R. D. Galway, M. S. thesis, Queens University, Belfast, Ireland (1963).

[61]V. V. Babenko, Bionika No. 5, 109 (1971).

[62]V. V. Babenko, Bionika No. 7, 71 (1973) [NASA TT F-16, 392].

[63]V. V. Babenko, and L. F. Kozlov, Izv. Acad. Nauk. SSSR Mekh. Zhid. Gaza 8, 122 (1973).

[64]V. V. Babenko, Gidromekhanika No. 24, 3, (1973).

[65]H. B. Karplus, Illinois Institute of Technology Research Institute Report No. IITRI 1205-4 (1963).

[66]J. Kestin, P. F. Maeder, and H. E. Wang, Appl. Sci. Res. A 10, 1 (1960).

[67]V. Ya Levchenko and A. S. Solov'ev, Izv. Akad. Nauk. SSSR Mekh. Zidk. Gaza, 7, 11 (1972) [Fluid Mech. 7, 884 (1974)].

[68]S. H. Davis, in *Annual Review of Fluid Mechanics*, edited by M. Van Dyke, W. G. Vincenti, and J. V. Wehauser (Annual Reviews, Palo Alto, Calif., 1976), Vol. 8, p. 57.

[69]R. I. Loehrke, M. V. Morkovin, and A. A. Fejer, J. Fluids Eng. 97, 534 (1975).

[70]H. J. Obremski and A. A. Fejer, J. Fluid Mech. 29, 93 (1967).

[71]H. J. Obremski and M. V. Morkovin, AIAA J. 7, 1298 (1969).

[72]R. I. Loehrke, M. V. Morkovin, and A. A. Fejer, presented at the Fluid Dynamics Symposium, McMaster University Hamilton, Ontario (1970) AFOSR 70-1586TR.

[73]Y. Kobashi, M. Hayakawa, and K. Nakagawa, presented at the Symposium on Unsteady Aerodynamics, sponsored by the U. S. Air Force-Air Force Office of Scientific Research and the University of Arizona (1975).

[74]C. von Kerczek, and S. H. Davis, J. Fluid Mech. 62, 753 (1974).

[75]C. E. Grosch, and H. Salwen, J. Fluid Mech. 34, 177 (1968).

[76]S. I. Sergeev, Izv. Acad. Nauk. SSSR Mekh. Zhid. Gaza 1, 168 (1966).

[77]R. G. Finucane and R. E. Kelly, Int. J. Heat Mass Transfer 19, 71 (1976).

[78]R. J. Donnelly, Proc. R. Soc. London Ser. A 281, 130 (1964).

[79]R. J. Donnelly and H. Suhl, Phys. Rev. Lett. 9, 363 (1962).

[80]M. T. Landahl, in *Proceedings of Thirteenth International Congress of Theoretical and Applied Mechanics*, edited by E. Becker and G. K. Mikhailov (Springer-Verlag, Berlin, 1973), p. 177.

[81]L. D. Loudenback and D. E. Abbott, Purdue University Technical Report CFM TR-73-1 (1973).

[82]R. E. Davis, J. Fluid Mech. 63, 673 (1974).

[83]A. Hussain and W. C. Reynolds, J. Fluid Mech. 54, 263 (1972).

[84]S. K. F. Karlsson, J. Fluid Mech. 5, 633 (1959).

[85]P. Gougat, Centre National de la Recherche Scientifique, Meudon (France), Laboratoire d'Aerothermique, Report 70-8 (1970), [NASA TT F-15, 852].

[86]J. E. Ffowcs Williams, Bolt-Beranek and Newman Inc., Report No. 1138 (1964).

[87]E. F. Blick, in *Viscous Drag Reduction* (Plenum, New York, 1969), p. 409.

[88]B. N. Semenov, Zh. Prikl. Mekh. Tekh. Fiz. 12, 58 (1971) [J. Appl. Mech. Tech. Phys. 12, 393 (1973)].

[89]J. Sternberg, J. Fluid Mech. 13, 241 (1962).

[90]R. R. Walters, Ph.D. dissertation, The University of Oklahoma (1969).

[91]V. B. Amfilokhiyev, Bionika No. 3, 46 (1969).

[92]R. L. Ash, NASA CR 2387 (1974).

[93]R. Grosskreutz, Univ. Sci. J. (Dar es-Sallam University) 1, 65 (1975).

[94]T. E. Burton, Massachusetts Institute of Technology Report 70208-10 (1974).

[95]G. R. Offen and S. J. Kline, J. Fluid Mech. 70, 209 (1975).

[96]J. Laufer, in *Annual Review of Fluid Mechanics*, edited by M. Van Dyke and W. G. Vincenti (Annual Reviews, Palo Alto, Calif., 1975), Vol. 7, p. 307.

[97]W. W. Willmarth, in *Advances in Applied Mechanics* (Academic, New York, 1975), Vol. 15, p. 159.

[98]H. A. Einstein and H. Li, ASCE Proc. 82, 945 (1956).

[99]T. J. Black, in *Proceedings of Heat Transfer Fluid Mechanics Institute*, edited by M. A. Saad and J. A. Miller (Stanford University, Stanford, California, 1966), p. 366.

[100]W. W. Willmarth, NASA Memorandum 3-17-59W (1959).

[101]W. C. Cliff and V. A. Sandborn, NASA TM X-64935 (1975).

[102]R. Blackwelder and L. S. G. Kovasznay, Johns Hopkins University Technical Report, DA-31-124-ARO-D-313 (1970).

[103]M. K. Bull and A. S. W. Thomas, Phys. Fluids 19, 597 (1976).

[104]R. F. Blackwelder and H. H. W. Woo, Phys. Fluids 17, 515 (1974).

[105]M. T. Landahl, J. Fluid Mech. 56, 775 (1972).

[106]F. H. Bark, The Royal Institute of Technology, Department of Mechanics, Stockholm, Sweden, TRITA-MEK-74-01,

(1974); also J. Fluid Mech. 70, 229 (1975).

[107] W. R. Barger, W. R. Garrett, E. L. Mollo-Christensen, and K. W. Ruggles, J. Appl. Meterol. 9, 396 (1970).

[108] E. Mollo-Christensen, in *Annual Review of Fluid Mechanics*, edited by M. Van Dyke, W. G. Vincenti, and J. V. Wehausen (Annual Reviews, Pal Alto, Calif., 1973), Vol. 5, p. 101.

[109] H. Ritter and J. S. Porteous, Admirality Research Laboratory Report N3/G/HY/9/7 (1965).

[110] M. O. Kramer (private communication).

[111] H. Ritter and L. T. Messum, Admirality Reserach Laboratory Report N1/G/NY/9/7 (1964).

[112] J. Laufer and L. Maestrello, The Boeing Company Document No. DY-9708 (1963).

[113] L. Maestrello (private communication).

[114] L. L. Smith, M. S. thesis, University of Washington (1963).

[115] A. Dinkelacker, J. Sound Vib. 4, 187 (1966).

[116] A. Dinkelacker, Deutsche Versuchsanstalt für Luft–und Raumfahrt Report FB–66–78 (1966).

[117] S. Taneda and H. Honji, Rep. Res. Inst. Appl. Mech., Kyushu Univ. XV, 1 (1967).

[118] R. Mattout, Association Technique Maritime et Aéronautique, Bulletin No. 72, 207 (1972).

[119] R. Mattout, Societé Bertin & Cie, Note Technique 71/61/08 (1971).

[120] R. Mattout and B. Cottenceau, Societé Bertin and Cie, Note Technique No. 71–C1–09 (1972).

[121] J. P. de Loof, in *Proceedings of International Conference on Drag Reduction*, edited by N. G. Coles (BHRA Fluid Engineering, Cranfield, England, 1974), paper F3.

[122] M. Botman, presented at 1st AIAA Annual Meeting (1964), AIAA Paper 64-461.

[123] R. Grosskreutz, Navships Translation No. 1320, Max-Planck-Institut für Strömungsforschung und der Aerodynamischen Versurhsanstalt, Nr. 53, Göttingen (1971).

[124] S. Kawamata, T. Kato, Y. Matsumura, and T. Sato, *Theoretical and Applied Mechanics*, (University of Tokyo Press, Tokyo, 1973), Vol. 21, p. 507.

[125] K. W. McAlister and T. M. Wynn, NASA TM X-3119 (1974).

[126] E. F. Blick and R. R. Walters, J. Aircraft 5, 11 (1968).

[127] W. R. Looney and E. F. Blick, J. Spacecraft 3, 1562 (1966).

[128] H. H. Chu and E. F. Blick, J. Spacecraft 6, 763 (1969).

[129] W. R. Looney, M. E. thesis, University of Oklahoma (1966).

[130] D. H. Fisher and E. F. Blick, J. Aircraft 3, 163 (1966).

[131] E. F. Blick, United States Army Research Office Final Report DA-31-124-AGROD-349 (1974).

[132] H. H. Chu, Ph.D. thesis, University of Oklahoma (1971).

[133] A. P. Teslo and V. A. Zhoga, Gidromekhanika No. 24, 18 (1973); Joint Publication Research Service 60785 (1974).

[134] A. P. Teslo and V. Ye Filipchuk, Gidromekhanika 29, 45, (1974) [NASA TT F-16, 555 (1975)].

[135] G. E. Klinzing, R. J. Kubovcik, and J. F. Marmo, Ind. Eng. Chem. Process Design Develop. 8, 112 (1969).

[136] U. P. Ivlev, Bionika No. 6, 39 (1972).

[137] R. L. Ash, Old Dominion University Technical Report 76-Tl (1976).

[138] J. N. Hefner and L. M. Weinstein, AIAA J. Spacecr. Rockets 13, 502 (1976).

[139] M. K. Bull, J. Fluid Mech. 28, 719 (1967).

[140] R. H. Stewart, J. Fluid Mech. 42, 733 (1970).

[141] E. J. Plate and G. M. Hidy, J. Geophys. Res. 72, 4627 (1967).

[142] P. C. Chang, E. J. Plate, and G. M. Hidy, J. Fluid Mech. 47, 183 (1971).

Dilute polymer solutions in elongational flow

C. Elata, J. Burger, J. Michlin, and U. Takserman

Ben-Gurion University of the Negev, Beer Sheva, Israel

A series of experiments is described using solutions of various concentrations of Polyox coagulant flowing through porous beds of spherical particles. Results are reported, similar to those obtained by James and McLaren, which show a substantial increase in drag. The onset of this drag increase from solvent flow seems to occur at a constant Deborah number multiplied by the square root of the concentration. The flow in a bundle of symmetrical convergent-divergent channels which may serve as a model for a porous medium is analyzed. The presence of elongated particles in the fluid will alter the flow pattern in such a channel from that given by the Stokes' solution. Assuming the particles to be aligned parallel to the mean flow direction, this flow re-arrangement will attenuate the effect of the particles on the dissipation of mechanical energy. Extended molecules may be misaligned with the streamlines in the diverging section of the channel, which could explain the large increase in drag observed with dilute polymer solutions in porous beds.

INTRODUCTION

Drag reduction in turbulent shear flow of dilute polymer solutions seems to be associated with the ability of the dissolved molecules to be extended appreciably. Such extensions will occur at sufficiently high strain rates. In simple shear flow, the molecules will extend only slightly and therefore do not significantly alter the shear viscosity.

These basic assumptions led to many studies of the effect of dissolved polymers on the characteristics of elongational flows. In the following, some experiments carried out with dilute Polyox solutions in a porous bed of spherical particles are described. Some preliminary results of the analyses of the flow through a periodically divergent–convergent channel assumed to be representative for a porous medium will also be presented.

Flows in expanding jets, through orifices and between rotating cylindrical rollers have been described and analyzed, as reported in an already extensive literature.[1-3] The experiments suggest that the resistance to elongational deformation may be increased by several orders of magnitude by dissolving long chain molecules in a fluid. Our aim is to study elongational flows under laminar flow conditions, in a field in which the flow may be analyzed, and preferably at small enough Reynolds numbers so that inertial effects may be neglected. One is typically looking for flows, with Reynolds numbers of the order 1, and with Deborah numbers of the order 1 or larger, conditions for which we could expect stretching to occur. One possible experimental way which meets these conditions is the flow through porous media.

Experiments and analyses of such flows of more concentrated polymer solutions, carried out over the last fifteen years, have been presented in the literature[4,5] and were reviewed by Savins up to 1969.[6]

After earlier work by Dauben and Menzie,[7] with the flow of dilute polymer solutions through a porous medium, a first systematic presentation of experimental data was made by James and McLaren.[8] Experiments similar to theirs were carried out and are presented in the following section. Results paralleling ours were also

obtained in Karlsruhe by Naudascher and Killen.[9] Although the experiments are difficult to carry out and the scattering of data is wide, the agreement between the trend of our results and that of others gives confidence in their veracity.

THE EXPERIMENTS

The experimental apparatus is shown in Fig. 1. The fluid stored in an overhead tank flows through a porous bed of glass beads, contained by screens in a 30 mm tube and is discharged to the atmosphere and discarded. Piezometric pressure taps, located upstream from and along the porous bed, are connected to a water or a mercury manometer.

A series of measurements of pressure drop versus rate of flow was made for water and dilute water solutions of Polyox coagulant. Measurements were made in beds of spherical particles of either 0.5 or 1.0 mm diam, and concentrations of Polyox coagulant ranging between 10–150 ppm (weight). Typical results of the hydraulic gradient $\Delta H/L$ versus superficial velocity V_0 (defined as the ratio between rate of flow Q and total cross-sectional area A) are shown in Fig. 2, for experi-
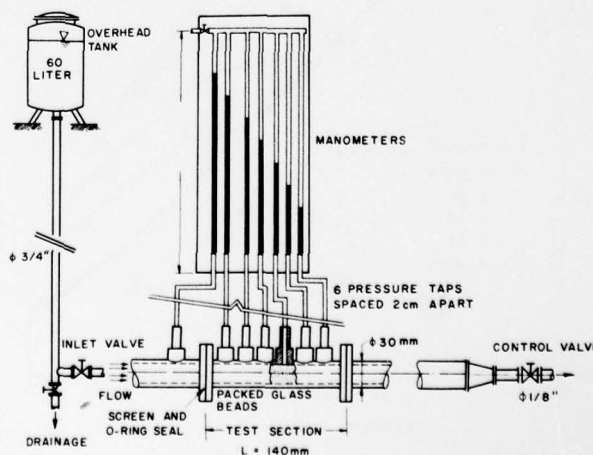
FIG. 1. The experimental setup.
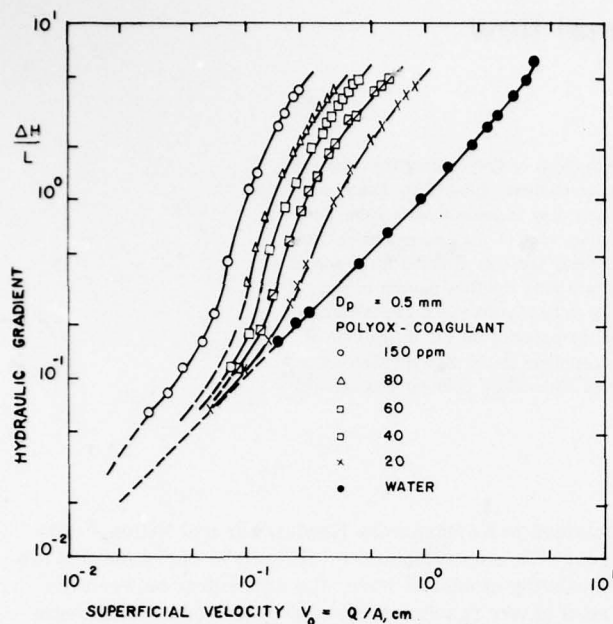
FIG. 2. Head losses of Polyox solutions in a porous bed.

ments with the 0.5 mm particles.

The usual way to plot such results is on nondimensional Ergun coordinates, relating the friction factor f versus Reynolds number Re, defined for a porous medium as

$$f = g \frac{\Delta H}{L} \frac{D_p}{V_0^2} \frac{n^3}{1-n} \quad , \tag{1}$$
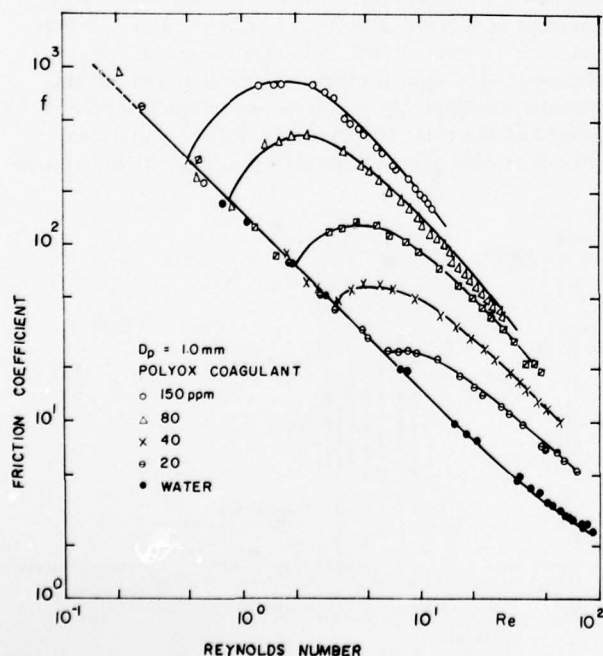
FIG. 3. Dependence of friction factor on Reynolds number of Polyox solutions in a porous bed.
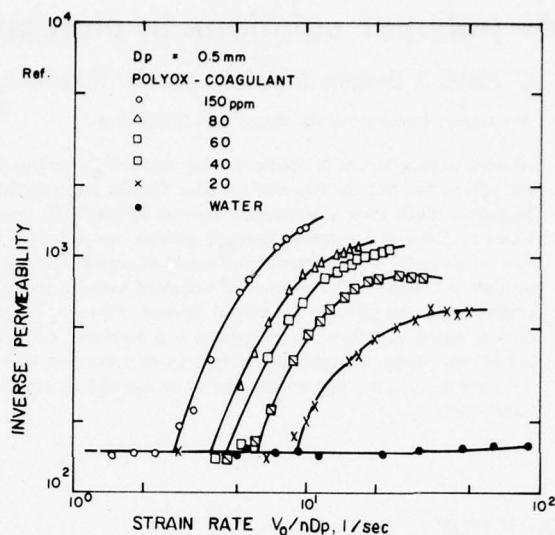
FIG. 4. Inverse permeability versus strain rate for different concentrations of Polyox in solution.

$$\text{Re} = \frac{D_p V_0}{\nu} \frac{1}{1-n} \quad , \tag{2}$$

where g is the gravitational acceleration, D_p is the particle diameter, n is the porosity of the medium, and ν is the kinematic viscosity of the fluid. Such a presentation for the results with the 1.0 mm particles is shown in Fig. 3. The data for experiments with water or any other Newtonian fluid in a porous bed with spherical particles follow the unique relationship

$$\text{Re} f = 150 \tag{3}$$

for Re < 5. For larger values of the Reynolds number, the friction factor deviates somewhat from Eq. (3). Re f represents a nondimensional inverse permeability, or resistance coefficient.

It may be seen from Fig. 3 that up to a particular value of the Reynolds number, the friction factor for flows of dilute polymer solutions is equal to that of the solvent. Beyond this "critical" Reynolds number there is an increase in drag and the value of f for the solution becomes much larger. At slightly higher Reynolds numbers this increase in drag reaches a maximum and subsequently seems to drop off. A similar trend is obtained for the different concentrations of Polyox in solution. The larger the concentration, the smaller the "critical" Reynolds number at onset and the larger the increase in friction factor.

In comparing the data for different sizes of the particles making up the porous medium, it was found that the "critical" Reynolds number seemed to scale with the square of the particle size at each Polyox concentration. This led to a clearer way of plotting the results, namely on coordinates of Re f versus strain rate: V_0/nD_p, where V_0/n represents the actual average velocity in the pore spacings. On such a graph, as shown in Fig. 4, the data for water all fall on a horizontal line.

From the data as presented in Fig. 4, the experimen-
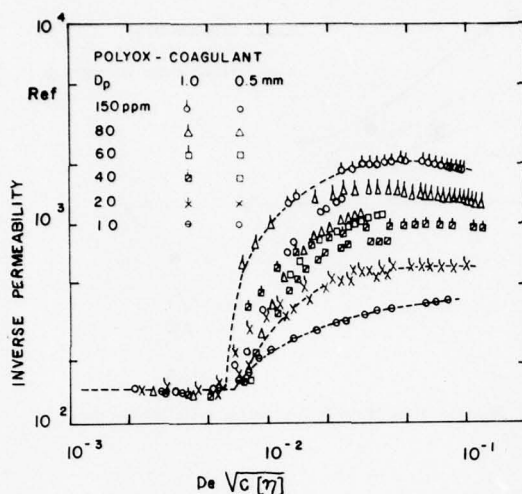
FIG. 5. Nondimensional plot of inverse permeability for solutions of Polyox coagulant.

FIG. 7. Nondimensional plot of inverse permeability for solutions of Polyox WSR 301 (data from James et al.[8]).

tal relation between the strain rate at onset and concentration was found to be

$$(V_0/nD_p)_t \propto C^{-1/2} \ ,$$

where the subscript t denotes conditions at onset.

This suggested a presentation of the data on a graph of Re f versus De$(C[\eta])^{1/2}$, where De is the Deborah number defined by De $= V_0 \tau/nD_p$. τ is the maximum relaxation time of the molecules given by

$$\tau = 6\mu_s[\eta]M/\pi^2 RT \ ,$$

where μ_s is the dynamic viscosity of the solvent, M is the molecular weight of the molecules, and $[\eta]$ is the intrinsic viscosity of the solution also used in conjunction with C to obtain a nondimensional presentation.

The use of De as a correlating parameter was shown to be sometimes appropriate for flow of more concen-
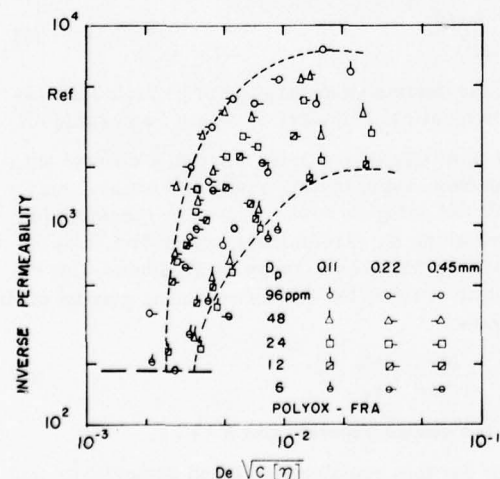
FIG. 6. Nondimensional plot of inverse permeability for solutions of Polyox FRA (data from James et al.[8]).
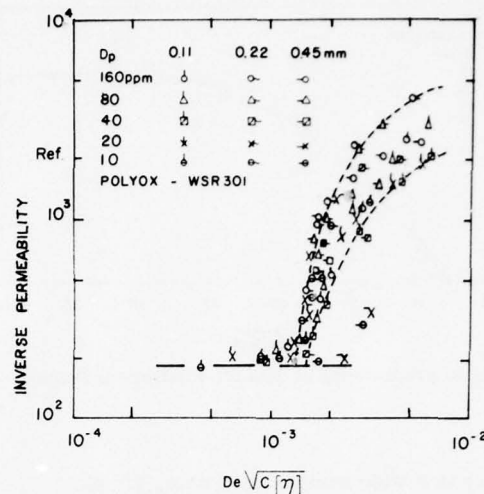
trated polymer solutions, as well.[10,11]

For Polyox coagulant, $[\eta]$ was found experimentally to have a value of 23 (100 cc)/g, from which the value of τ was estimated to be 0.0041 sec. Correspondingly, the values of the Deborah number at onset are of the order of 10^{-2}, much smaller than anticipated. James has pointed out, however, that the representative pure strain rate may be larger by a factor of 150 than V_0/nD_p due to the particular configuration of the pore spacings. Such a strain rate would lead to onset Deborah numbers larger than 1, as expected.

The data for Polyox coagulant plotted in the manner suggested (Fig. 5) show a unique value of De$(C[\eta])^{1/2}$ at onset of 6×10^{-3} nearly independent of particle size and polymer concentration. The data of James and McLaren were similarly plotted with the results as shown in Figs. 6 and 7. Experimental points for data beyond the maximum values of Re f are deleted from these graphs to focus attention on the collapse of the onset points to close to constant values of De$(C[\eta])^{1/2}$. The difference in onset values for Polyox coagulant (present data), Polyox FRA and Polyox WSR 301[8] may be due to the polydispersivity of the molecular weight distribution. The value of $[\eta]$ is representative of some average value of the molecular weight of the polymer while the onset may be partially dependent on the highest fraction.

The maximum drag increase was found to be dependent on concentration as well and seems to follow the relation (Re $f)_{max} \propto (C)^{1/2}$. This suggests that the data may be made to collapse with a vertical ordinate of the form

$$[\Delta \text{Re} f/(\text{Re} f)_0](C[\eta])^{-1/2} \ ,$$

where the subscript 0 denotes the value for water flow. Examples of data presented in this manner are shown in Figs. 8 and 9. In Fig. 8 the present data for $D_p = 0.5$ mm are presented on a linear scale, while Fig. 9 shows the data of James et al. for WSR 301 on a logarithmic scale.

FIG. 8. Unifying presentation of data for solutions of Polyox coagulant.

FIG. 10. Stokes' flow field in a channel with sinusoidal boundaries.
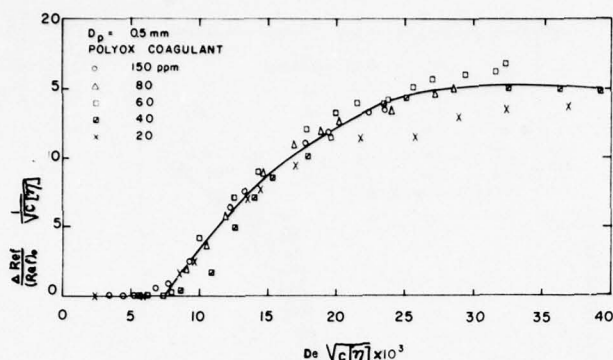
While there is a wide scattering of data, the plot seems to fit best for the points up to maximum drag increase. The divergence seems to be highest for data with the 0.45 mm particles where an extensive degree of degradation of the polymer solution was observed.

The maximum drag increases vary greatly for the different types of Polyox, approximately according to $[\eta]^{3/2}$ rather than $[\eta]^{1/2}$, used here to nondimensionalize the concentration.

A MODEL FOR PORE FLOW

The most simplistic model for a porous medium is a bundle of parallel uniform capillaries. From such a model the general form of the permeability or Darcy coefficient can be derived with a correction coefficient symbolizing the apparent increase in capillary length.

Such a model is inevitably unsuited for flow of dilute polymer solutions since it is required that the convergent–divergent characteristics of the flow be represented. This led to the choice of a more sophisticated model for porous media in the form of a bundle of capillaries with sinusoidal boundaries.[12]

FIG. 9. Unifying presentation of data for solutions of Polyox WSR 301 (data from James et al.[8]).

A typical picture of such a flow is presented in Fig. 10. The flow length constitutes one-half of the wavelength $2L$ of a two-dimensional channel with sinusoidal boundaries which have an average distance $2h$ and a wave amplitude a. At values of $a/L > 0.35$, the flow will separate and secondary vortices will form in the outer corners. The solution presented in Fig. 10 was found by solving the Stokes' equations in the given boundaries.

It has been postulated that the drag reduction effects in turbulent shear flow and the drag increase in laminar elongational flows are due to the increased resistance to pure strain deformation of solutions with dilute polymers. The increase in resistance is assumed to be due to the work expended in stretching the dissolved polymer molecules and to the high extensional viscosity found, even for dilute solutions, with stretched molecules. The appropriate expression of the stresses due to stretched (rigid) particles was derived by Batchelor.[13] The normal stress in the mean flow direction is expressed by

$$\sigma_{11} = -P + \mu e_{11}(2 + \kappa) , \qquad (4)$$

where P is the isotropic pressure, e_{11} is the streamwise strain rate, and

$$\kappa = \frac{4}{3} c \, \frac{l^2/R_0^2}{\log(\pi/c)} , \qquad (5)$$

where c is the volume concentration of particles all assumed to be identical cylinders of length l and radius R_0.

The flow of elongated particles through a channel with wavy boundaries, representing a porous medium, may now be analyzed using Eq. (4). Assuming the particles to be aligned along the streamlines, which to a first approximation may be taken to mean an alignment with the main direction of flow, the Stokes' equation may be modified to become

$$\frac{\partial^4 \psi}{\partial x^4} + 2K \frac{\partial^4 \psi}{\partial x^2 \partial y^2} + \frac{\partial^4 \psi}{\partial y^4} = 0 \qquad (6)$$

where ψ is the stream function and $K = 1 + \kappa$.

A solution for this equation was found numerically and is presented in Fig. 11. It can be seen from this figure that the increase in elongational resistance represented
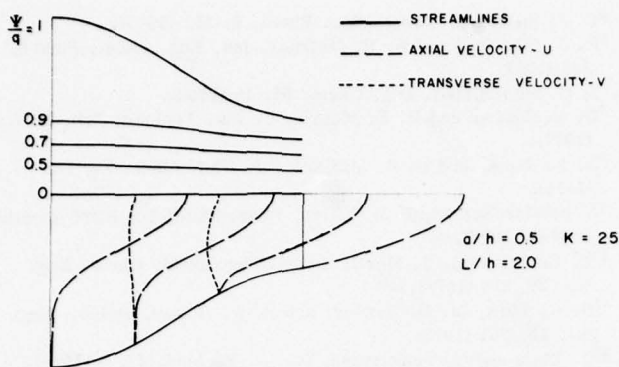
FIG. 11. Flow field of fluid with augmented extensional viscosity in sinusoidal channel.

by the parameter K causes a change in the flow pattern such that the streamlines become more parallel and most of the flow occurs in the central part of the channel. This re-arrangement of the flow is also apparent from a calculation of the total flow dissipation.

In Fig. 12 the nondimensionalized dissipation ϕ is presented as a function of K. It can be seen from this figure that the dissipation increases only slightly (solid line). Apparently at infinite K, the streamlines become parallel to the main direction of flow. The increase in dissipation will be due to the increase in shear stresses of the parallel flow, now seemingly confined to a uniform flow channel with a half-width corresponding to $h-a$. As a comparison, the broken line in Fig. 12 represents the hypothetical case for which the flow pattern is frozen as for the case $K=1$; without flow re-arrangement, the dissipation increases significantly due to the increasing resistance to pure strain deformation.

DISCUSSION

The puzzling phenomenon observed from the experimental data is the abruptness of the onset point and its dependence on concentration.

The sudden deviation from the solvent flow characteristics could be interpreted by assuming an instantaneous unfolding of the molecules at critical stress levels which is consistent with present molecular theories.[14]

Daoudi[15] following such an assumption found the onset strain rate to be independent of concentration, in contradiction to the experimental evidence.

Another difficulty arises from the fact that the polymer molecules can stretch only by the degree that the fluid particles, in which they are imbedded, are elongated. It is hard to envision stretch ratios of 10–100 necessary in order for the molecules to affect the stress field appreciably, especially since in the larger cavities of the passages in the porous medium, laminar separation may occur. Strain rates sufficiently large for unfolding of the molecules to occur may be present, however, at the upstream section of the porous medium where pure strain rates in the converging fluid will be maximal. Following the theory of Hinch,[14] it may be

assumed that the molecules unfolding when entering the porous medium may remain stretched by much smaller forces necessary for that purpose.

In the previous section, we have seen that extended molecules aligned in the flow direction will alter the flow pattern, causing only marginal changes in dissipation. The direction of the major strain will be much closer to the direction of the streamlines in the convergent than in the divergent passages. Thus, the extended molecules may very well become misaligned with the direction of flow in the diverging part of the flow channels. Such an effect, which would cause longitudinal asymmetry, would actually result in a flow pattern much closer to that of the solvent (Fig. 10) than to the one for aligned particles (Fig. 11). As a result, the dissipation would be closer to the dashed curve in Fig. 12 than to the solid one. This could explain the large dissipations observed for flow in a porous medium as well as the effect of concentration on the onset of drag increase.

It is now evident that the large increases in flow resistance, observed with dilute polymer solutions in porous media cannot be explained simply by assuming molecules stretched and aligned with the flow direction. A solution should be found for the flow simultaneously with the angles of the major axis of the stretched molecules relative to the chosen coordinate system. Such angles, which should depend on the flow history of the molecules and on the relative magnitude and direction of the local rates of strain and rotation, will greatly affect the local dissipation.

The strong polymer-flow interaction, assumed to occur in laminar flow in channels with nonuniform cross sections, may be absent in turbulent shear flow, explaining the nonexistent (or small) influence of polymer concentration on the onset of drag reduction. Changes in the flow pattern due to a particle-flow interaction could also result in the flow instability observed by James et al.[8] whereby at the same pressure drop different
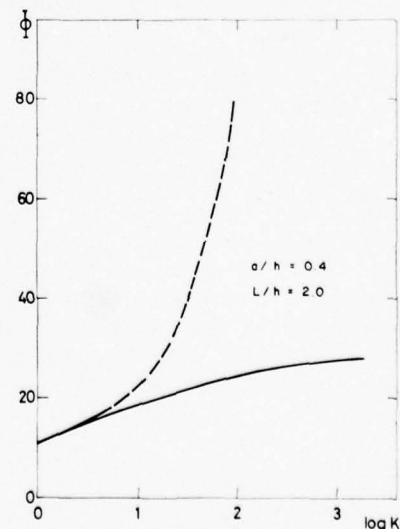
FIG. 12. Dissipation in flow through a sinusoidal channel as a function of extensional viscosity.

S53   Phys. Fluids, Vol. 20, No. 10, Pt. II, October 1977

Elata, Burger, Michlin, and Takserman   S53

rates of flow could be obtained.

The approach presented here may lead to a relevant description of laminar flow of dilute polymer solutions. Only when that is accomplished, can a beginning be made in understanding the drag reduction phenomenon in turbulent shear flow. In conclusion, it should be pointed out that to date there is no experimental confirmation of appreciable stretching of polymer molecules in pure straining flow and that all the available evidence is circumstantial.

[1] A. B. Metzner and A. P. Metzner, Rheol. Acta 9, 174 (1970).
[2] E. Bilgen, J. Mec. 12, 375 (1973).
[3] L. S. G. Kovasznay and J. T. Kuo, Phys. Fluids 20, S 291 (October, Part II, 1977).

[4] T. J. Sadowski, Trans. Soc. Rheol. 9, 251 (1965).
[5] R. J. Marshall and A. B. Metzner, Ind. Eng. Chem. Fund 6, 393 (1967).
[6] J. G. Savins, Ind. Eng. Chem. 61, 18 (1969).
[7] D. L. Dauben and D. E. Menzie, J. Pet. Technol. 240, 1065 (1967).
[8] D. F. James and D. R. McLaren, J. Fluid Mech. 70, 733 (1975).
[9] A. Naudascher and J. M. Killen, Phys. Fluids 20, S 280 (October, Part II, 1977).
[10] Z. Kemblowski, J. Mertl, and M. Dziubinski, Chem. Eng. Sci. 29, 213 (1974).
[11] H. C. Park, M. C. Hawley, and R. F. Blanks, Polym. Eng. Sci. 15, 761 (1975).
[12] C. Elata and U. Takserman. Isr. J. Technol. 14, 6 (1976).
[13] G. K. Batchelor, J. Fluid Mech. 46, 813 (1971).
[14] J. Hinch, Phys. Fluids 20, S 22 (October, Part II, 1977).
[15] S. Daoudi, J. Phys. (Paris) –Lett. 37, 1 (1976).

Dynamics of boundary layer turbulence and the mechanism of drag reduction

M. T. Landahl

*Massachusetts Institute of Technology, Cambridge, Massachusetts
and The Royal Institute of Technology, Stockholm, Sweden*

The dynamics of the fluctuating velocity field in a turbulent boundary layer is discussed on the basis of a simplified analysis of localized unsteady perturbations in a parallel shear flow. Three classes of such disturbances may be distinguished, namely: (i) large-scale propagating disturbances which may be represented by a superposition of shear waves; (ii) convected disturbances which decay only slowly through the action of viscosity; and (iii) small-scale disturbances resulting from the secondary instability of the large-scale motion. Coupling between large and small scales is incorporated in a two-scale model in which the large scales are considered driven by the Reynolds stresses produced by the small scales. Shearing by the mean flow is shown to cause intensification of internal shear layers in the flow and could lead to local inflection in the instantaneous velocity profile, thus making secondary instability possible. Drag reducing additives, as modeled by some simple constitutive relations are found to be able to inhibit secondary instability, and would hence lower turbulent stress production according to the model employed.

I. INTRODUCTION

The problem of explaining cause and effect relationships for the organized flow structures observed in turbulent boundary layers and other shear flows is surely one of the most challenging tasks faced by fluid mechanicists in recent times. The existence of such structures with recognizable and repeatable patterns in space and time points to the possibility of unraveling the mechanism of turbulence production from detailed analysis of localized flow disturbances in a shear flow without turning to statistical theory, a path that so far has proven itself a dead-end street. Such detailed analysis is, of course, extremely difficult in that a nonlinear problem involving unsteady, three-dimensional, and viscous flow need be considered, which may seem as difficult as a calculation of the complete instantaneous turbulent flow field. However, the observations of the bursting sequence give certain indications of what properties may be the essential ones for the construction of simplified models. (For a review of the relevant experimental information, we refer to the excellent recent one by Willmarth.[1]) The motion is found to be gentle and laminar-like during most of the time with the abrupt break-up stage perhaps occupying less than 10% of the time. This indicates that a strongly nonlinear interaction mechanism may be involved in the production of turbulent mixing and its associated stress, with the remainder of the motion governed by linear or weakly nonlinear mechanisms. One also finds that the scales of motion involved are usually much greater in the streamwise and spanwise directions than in the direction normal to the wall, which suggests that a viable model could perhaps be based on the idea of perturbations of a slowly varying almost parallel shear flow. Therefore, parallel-flow stability theory with appropriate consideration given to the effect of nonhomogeneities with slow variation in time and space should be a useful tool. Such ideas underlie previous efforts by this author[2-4] to model the fluctuating field. The waveguide theory[2] was originally applied to the pressure fluctuations, and interaction with the mean shear was found to make these propagate as waves. The waves were found to be damped for all frequencies, and all scales decayed in a length of travel proportional to their own streamwise length. A further extension by Bark[5] for the fluctuating velocities in the wall layer region gave evidence that the u component is predominantly wave-like as well, and that the characteristic streamwise and spanwise scales could be estimated from a linear problem in which point-like turbulence production "sources" are assumed to excite perturbations of the mean shear flow. In order to analyze the effect of localized turbulence production on a large scale field, a two-scale[4] model was proposed in which the small-scale motion produced by secondary inflectional instability was treated as the driving mechanism for the large-scale one through the creation of localized Reynolds stresses resulting from the small-scale mixing. The strong nonlinear interaction was assumed to result from the wave breakdown mechanism[3] proposed as an explanation for the appearance of low velocity "spikes" in a boundary layer undergoing transition. The two-scale model was applied in a preliminary study of the burst regeneration mechanism, i.e., how a previous burst could set up conditions for the appearance of a new one farther downstream. Another application[6,7] of the model was to the phenomenon of drag reduction due to additives; it was found that on the basis of simple rheological models for the fluid-additives systems the additives considered all had strong stabilizing effects on inflectional instability, with one exception, namely, that of a flexible surface, which would only have a substantial effect in the case of walls with such extreme lightness and flexibility as to be unrealistic for practical use.

In the present paper, the exploration of the two-scale model is carried farther with particular emphasis on such properties of the large-scale field as would be important for burst regeneration, and a tentative model is offered for the ejection and sweep mechanisms.

II. THE TWO-SCALE MODEL

The two-scale model proposed and tentatively explored earlier[4,6,7] will be reviewed briefly since it is the basic

foundation upon which the extensions to be presented are built. Adopting the parallel-flow assumption for the mean flow by setting

$$U_i = U(y)\,\delta_{1i} + u_i(x_j, t) \tag{1}$$

$(x_1 = x,\ x_2 = y,\ x_3 = z)$, where the fluctuating components $u_1 = u,\ u_2 = v,\ u_3 = w$ have zero mean, one obtains from the Navier–Stokes equations,

$$\frac{\partial u_i}{\partial t} + U\frac{\partial u_i}{\partial x} + vU'\delta_{1i} = -\frac{1}{\rho}\frac{\partial p}{\partial x_i} + \nu\nabla^2 u_i + \frac{\partial \tau_{ij}}{\partial x_j}\ , \tag{2}$$

$$\partial u_i/\partial x_i = 0\ , \tag{3}$$

where the fluctuation turbulent stress terms τ_{ij} are given by

$$\tau_{ij} = \overline{u_i u_j} - u_i u_j\ . \tag{4}$$

An equation formally relating $u_2 = v$ to the stresses τ_{ij} is obtained by eliminating the pressure[2]

$$\frac{D}{Dt}(\nabla^2 v) - U''v_x - \nu\nabla^4 v = q\ , \tag{5}$$

where

$$\frac{D}{Dt} = \frac{\partial}{\partial t} + U\frac{\partial}{\partial x}$$

and

$$q = \frac{\partial}{\partial x_j}\left(\frac{\partial^2 \tau_{ij}}{\partial x_i \partial x_2} - \frac{\partial^2 \tau_{2j}}{\partial x_k \partial x_k}\right)\ . \tag{6}$$

The left-hand side of (5) is recognized as the Orr–Sommerfeld operator in space-time. The purpose of writing the equations of motion in this way was to bring out the importance of the interaction of the disturbance field with the mean shear, as manifested primarily by the term $U''v_x$, acting qualitatively as a restoring elastic force making possible the appearance of oscillatory, i.e., wave-like, disturbances in the system. The quadratic terms will cause coupling between different scales of motion; the formulation of the two-scale model represents an attempt to single out, in a schematical and qualitative way, the mechanism of interaction between disturbances of disparate scales. That very small scales of motion appear intermittently in the wall layer region is indicated by many of the experimental investigations of the bursting phenomenon, first in the visual observations by Kline et al.,[8] who found scales of motion during the oscillatory and ejection stages smaller than the wall layer thickness, i.e., less than $l^+ \sim 20$ (plus refers to wall units). The bursting motion was found to affect a region of typical dimensions 1000 and 200 wall units in the streamwise and spanwise directions, respectively. We shall discuss a conceptually simple mechanism through which fluctuations of small scales could be created by dynamical instability of the internal shear layers formed by the large-scale motion and intensified by the shearing action of the mean flow on the large eddies, an effective process in strong shear flows of low viscosity. Because of the nonuniformity of the "stress" term, q, in (6), all scales larger than the smallest will be excited, as can be seen, e.g., by a Fourier analysis of (5). The dynamical coupling between large and small scale motion may be formally brought

out in an asymptotic theory by assuming the existence of two disparate scales $\bar{\lambda}$ and λ', where

$$\lambda'/\bar{\lambda} = O(\epsilon)\ . \tag{7}$$

(In the original formulation,[4] the small-scale activity was considered to be spread out over a horizontal patch of a typical dimension $\bar{\lambda}$, but this is not an essential assumption.) The velocity field is then subdivided into a large-scale (primary) and small-scale (secondary) field by the introduction of

$$u_i = \bar{u}_i + u_i'\ , \tag{8}$$

whereupon substitution into (5) and (6) gives, to lowest order in ϵ, a set of equations of the form

$$\frac{D}{Dt}(\nabla^2 \bar{v}) - U''\bar{v}_x - \nu\nabla^4 \bar{v} = \bar{q}\ , \tag{9}$$

$$\frac{D}{Dt}(\nabla^2 v') - U'' v_x' - \nu\nabla^4 v' = q'\ , \tag{10}$$

where the tilde (~) denotes averages taken over the large scales, and

$$q' = q - \bar{q}\ . \tag{11}$$

Because the source term q involves triple spatial derivatives, a formal expansion in ϵ shows that the largest contribution to $\bar{q}$ will come from the small scales, in particular, from those terms involving the highest y derivatives. The large-scale field will thus be governed by a formally linear problem with the turbulent stresses due to small-scale motion providing the driving mechanism. The source term, q', for the small-scale motion contains both linear and nonlinear terms in u_i', the most essential linear ones representing the convection of the small-scale motion by the large-scale field.[4] Hence, for this motion the role of the mean parallel flow is taken over by the large-scale velocity field, and it is basically nonlinear. The mean flow is found to be stable to small disturbances, and the energy transfer from the mean field to the fluctuations must then involve finite-amplitude processes. The one singled out in the two-scale model is secondary instability of the large-scale ("primary") field due to the appearance of local inflectional velocity profiles in the perturbed flow. Strong secondary instability can be expected when an additional kinematical condition[3] is fulfilled, namely, when the group velocity of the secondary disturbance becomes equal to the propagation velocity (phase velocity) of the primary field. When this condition is met, the secondary disturbance will be strongly enhanced by space-time focusing in a localized region leading to breakdown of the primary field. As the breakdown condition can be expected to hold only locally and intermittently in the flow field, the nonlinear excitation terms in (5) are likely to be large only in localized regions of space and time. This leads to considerable simplification of the analysis, since the linearized equations of motion may then be used almost everywhere with the nonlinear effects acting only in highly localized source regions. Hence, one is led naturally to the study, on the basis of the linearized equations, of the behavior of a single localized disturbance with initial conditions set by the nonlinear forcing terms. This approach was initiated
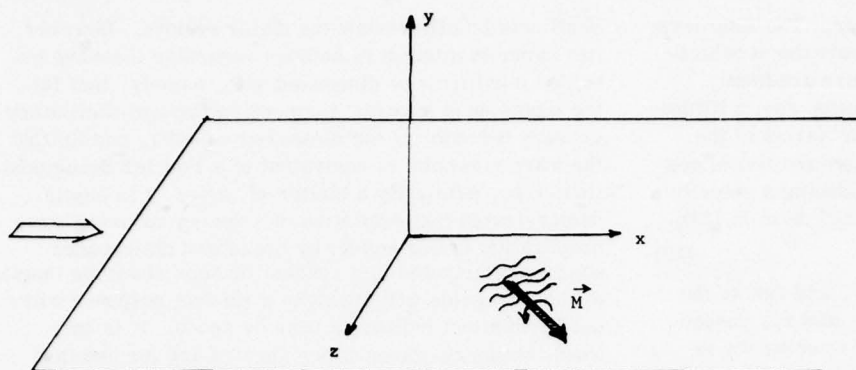
FIG. 1. Overall effect of localized disturbance.

earlier[4] and some tentative conclusions drawn. By considering the limit of vanishing viscosity, it was found[4] that for the fluctuation velocity component u (and also for w), two disturbance modes appear, a decaying wave mode (as for v and p) and a nondecaying eddy mode (in Ref. 4 referred to as a "permanent scar") convected downstream by the mean velocity field. The convective mode has (in the linear approximation) no pressure field associated with it. Thus, it may be regarded as essentially passive, and it is nonpropagating in the sense that each fluid element involved retains its original horizontal velocity unchanged with time (in the inviscid approximation). In contrast, the wave mode has associated with it a disturbance pressure field, which gives rise to propagation of disturbances across fluid elements.

III. PROPERTIES OF A LOCALIZED DISTURBANCE

Some basic properties of a localized disturbance in a parallel shear flow were discussed in the earlier paper.[4] We shall review these briefly and present some extensions of the earlier analysis.[4] First, one can show that the average effect on the large-scale motion of a localized nonlinear "source" on an inviscid flow is that of a moment impulse with components (Fig. 1)

$$M_1 = -2\rho \iint vw \, dV \, dt \, ,$$

$$M_2 = -2\rho \iint uw \, dV \, dt \, , \tag{12}$$

$$M_3 = -2\rho \iint uv \, dV \, dt \, .$$

This result is obtained by taking the cross product of the position vector with the Euler vector equation and then integrating over volume and time assuming the disturbance to be localized so that the velocities die out sufficiently quickly to make the integrals converge. (This result holds irrespective of the two-scale assumption.) The moment impulse is imparted on the flow by the induced surface pressure. Since there is no vertical surface for the pressure to act on, it follows that M_2, and hence the integrated contribution to the shear stress component uw, must be zero. A contribution to uv of the usual sign (negative) will be associated with an overpressure downstream of the localized disturbance and an underpressure upstream of the disturbance. For

disturbances originating from breakdowns that are oblique to the mean flow direction, there will be a contribution to vw and hence an induced pressure distribution on the wall tending to tilt the flow to the right or left depending on the sign of the integral of vw. The details of the initial motion set up by the strong nonlinear activity can be obtained only by a difficult nonlinear analysis, but the large-scale portion can be expressed directly in terms of the instantaneous turbulent stresses.[4] The subsequent linear motion is most conveniently analyzed by taking the space Fourier transform of the equation for the v component, whereupon the solution of the resulting initial value problem is expressed as an expansion in terms of the eigenfunctions of the Orr–Sommerfeld problem. Numerical studies[2,5] show that the eigenvalues for the turbulent mean flat-plate profile are damped. Furthermore, the eigenvalue of the most damped mode (few results have become available for the higher ones) gives a decay rate which is very nearly the same for all wavelengths so that all waves decay in a distance of travel approximately proportional to their length. This means that short-wave components of the initial v disturbance will die out much more quickly than the long-wave ones, so that after some time has passed, the details of the initial distribution will have been smeared out, and the disturbance region will appear to lengthen in the streamwise direction as it decays. Also, the eigenvalues show very little dependence on the spanwise wavenumber, which means that there will be very little dispersion of the disturbance in this direction. The pressure is directly related to the v component through the y component of the linearized perturbation equations and will therefore exhibit a similar behavior. The u perturbation has a more complicated behavior as can be seen by considering the inviscid equation for the u component

$$\frac{Du}{Dt} = -\frac{1}{\rho}\frac{\partial p}{\partial x} - vU' \equiv f \, , \tag{13}$$

which may be directly integrated to give

$$u = \int_0^t f \, Dt_1 \equiv \int_0^t f[x - U(t - t_1), \, t_1] \, dt_1 \, , \tag{14}$$

where the initial disturbance in the following is assumed to be zero. For a stable flow, p and v will decay with time, but not necessarily u, since the integral may tend to a limiting nonzero value for large time. We shall

consider the consequences of this later. The first term on the right-hand side of (13) represents the acceleration of a fluid element due to a pressure gradient, whereas the second gives the contribution due to liftup of a fluid element, the "mixing-length" terms of the turbulence. It is of interest to compare the two to see which is the most effective one in producing a velocity defect or excess. Set, for the "driving" term in (13),

$$f = f_p + f_l \ , \tag{15}$$

where $f_p = -(1/\rho)(\partial p/\partial x)$ and $f_l = -vU'$, and denote the corresponding contributions to u by u_p and u_l, respectively. For comparison purposes it is necessary to express the two terms in the same quantity, the most convenient one being the pressure. By taking the horizontal gradient of the linearized Euler equations, and using continuity, one finds that

$$\nabla_h^2 p \equiv \frac{\partial^2 p}{\partial x^2} + \frac{\partial^2 p}{\partial z^2} = -\rho \left[\frac{D}{Dt} \left(\frac{\partial v}{\partial y} \right) - U' \frac{\partial v}{\partial x} \right] \ . \tag{16}$$

This may be solved for v subject to the boundary condition $v = 0$ at the wall, and then $u_l = \int_0^t f_l \, Dt$ determined. It is found that

$$u_l = -\frac{U'}{\rho} \int_0^y dy \left[\int_0^t (t - t_1) \nabla_h^2 p \, Dt_1 \right] \ . \tag{17}$$

For the pressure gradient term one finds

$$u_p = -\frac{1}{\rho} \int_0^t p_x \, Dt_1 \ . \tag{18}$$

From these, one can estimate that the ratio of the lift-up to the pressure gradient contributions is of order

$$u_l/u_p \sim U' t y / l_h \ , \tag{19}$$

where l_h is the typical horizontal scale of the eddy taken to be of the same order in the spanwise and the streamwise directions. It follows that the lift-up contribution is small for short times after the onset of the pressure disturbance, and in regions very near the wall. For longer times, and in regions farther out from the wall, the contribution due to lift-up becomes appreciable and is likely to be the dominating one. In particular, this will be true for pressure regions having very small spanwise dimensions compared with streamwise ones.

For large times, viscosity will become of increasing importance, particularly in the regions close to the wall, so that the contributions due to lift-up and to pressure will become considerably modified, especially that due to pressure gradient, since the inviscid solution gives a nonzero value of u at the wall for this contribution. It is not likely that this will substantially alter the conclusion that the contribution due to lift-up will be important for large times. If anything, the lift-up contribution could be expected to become relatively more important, since it would be expected to be influenced less by viscosity, because the inviscid solution for u_l satisfies the no-slip condition on the wall.

IV. THE WAVE CHARACTER OF THE FLUCTUATIONS

The wave aspects of the large-scale fluctuating field have been explored in earlier papers[2,5] and here we shall only briefly review the major results. However, two common misunderstandings regarding the wave behavior must first be dispensed with, namely, that (a) the waves need manifest themselves through oscillatory or wavy behavior of the measured velocity, and (b) that the wave viewpoint is equivalent to a Fourier decomposition, i.e., primarily a matter of taste. It is easily demonstrated that excitation of a system allowing wave propagation (a waveguide) by broadband disturbance sources distributed in a random manner along the length of the waveguide will result in a random response without any distinct pattern in time or space. It is only when frequency-wavenumber spectra are formed that the wave-like character is brought out. If the excitation of an infinite waveguide with propagation characteristics given by the dispersion relation

$$\omega = \omega^{(0)}(k_x, k_z) = k_x c^{(0)}(k_x, k_z) \ , \tag{20}$$

where $c^{(0)} = c_R + i c_I$ is the phase velocity for the damped waves (assumed independent of x), and k_x, k_z the horizontal wavenumber components, the frequency-wavenumber spectrum for the fluctuating quantity q ($q = u$, v, w, p) considered will have the form

$$S_{qq} = C_{qq} / |\omega - k_x c^{(0)}|^2 \ , \tag{21}$$

where C_{qq} is the spectrum of the excitation, which is assumed to vary only slowly with frequency and wavenumber. What is characteristic for a system with marked wave propagation (i.e., with lightly damped waves) is thus a strongly peaked distribution with a variation around the peak typical of the spectrum of a system with lightly damped resonant response. A system without wave propagation will not show such a peak. Thus, the spectral representation will reveal important quantitative dynamical properties of the system studied which are not so directly available in other statistical representations, such as space-time correlations.

According to the two-scale model the large-scale normal velocity component and pressure should be predominantly of a wave-like nature, whereas the u and w components could show both wave-like and eddy-like behavior. The first application[2] of the wave model to a turbulent shear flow dealt with the pressure fluctuations, and it was verified that the measured spectra behaved fairly close to those predicted by Eq. (21). An extension to the u-fluctuation spectra in the wall region has recently been presented by Bark.[5] He determined spectra essentially on the basis of (21), assuming the nonlinear driving terms to be a random distribution of delta functions in x, z, and t with a variation with y inferred from the experimental data of Kim et al.[9] The computed spectra were found to have peaks for frequencies and wave numbers which were in reasonable agreement with the measured data of Morrison and Kronauer,[10] but the computed peaks were considerably narrower than the measured ones. Bark[5] also showed that the wave propagation modes provided the dominating contribution to the spectra in the wall region, a result that will be further commented upon.

Perhaps the most significant finding in Bark's[5] study was that the wave propagation constants computed on the basis of the Orr–Sommerfeld problem for the mean
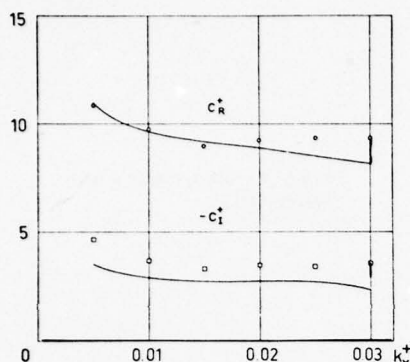
FIG. 2. ○ measured values of $S_{uu}(\omega^+, k_x^+)$ for $k_x^+ = 0.01$ from Morrison and Kronauer.[10] —three parameter fit according to (21), from Bark.[5]

velocity distribution were in good agreement with those inferred from the experimental spectra.[10] The experimental propagation constants are obtained by fitting a curve of the form (21) to the measured spectra, assuming C_{qq} to be approximately constant. His curves are reproduced in Figs. 2 and 3. The comparison between the computed values of c_R and c_I with those obtained from the experimental data indeed shows very good agreement, lending strong support to the wave model.

V. THE CONVECTED EDDY

That it becomes necessary to consider a convected eddy mode in addition to the wave propagation mode follows by taking the limit of the inviscid solution (14) for large times. Provided the disturbances vanish sufficiently fast (faster than t^{-1}), the integral in (14) will tend to a limiting value which is a function of the convected variable $\xi = x - U(y)t$, only, but not of x and t separately, namely,

$$\lim_{t \to \infty} u = \int_0^\infty f[\xi + Ut_1, t_1]dt_1 \equiv u_\infty(\xi, y, z) . \qquad (22)$$

Thus, the eddy will have a velocity distribution in each plane $y = \text{const}$, which will remain unchanged as the eddy is convected downstream by the mean velocity $U(y)$. Associated with u_∞, there will also be a z component of velocity, $w = w_\infty(\xi, y, z)$, to satisfy continuity. Of some interest is the vorticity of the convected eddy. From (22), it follows that

$$\gamma_1 \equiv \frac{\partial w}{\partial y} - \frac{\partial v}{\partial z} = w_{\infty y} - tU'w_{\infty\xi} , \qquad (23a)$$

$$\gamma_2 \equiv \frac{\partial u}{\partial z} - \frac{\partial w}{\partial x} = u_{\infty y} - w_{\infty\xi} , \qquad (23b)$$

$$\gamma_3 \equiv \frac{\partial v}{\partial x} - \frac{\partial u}{\partial y} = -u_{\infty y} + tU'u_{\infty\xi} = -u_{\infty y} - tU'w_{\infty z} , \qquad (23c)$$

the second version of (23c) being a consequence of continuity. The perturbation shear will thus intensify linearly with time due to the shearing of the eddy by the mean flow (or, equivalently, through the stretching of spanwise vorticity, an effect that will be present only

for a three-dimensional flow field with $w_{\infty z} \neq 0$), but viscosity and nonlinearity will act to set a limit for large times. Estimates of the times needed for viscosity and nonlinearity to have substantial effects can easily be obtained from simple kinematical considerations. Assume that the convected eddy has initially x and y dimensions of l_1 and l_2, respectively, with $l_2/l_1 = 0(1)$ (see Fig. 4). After a long time, shearing of the perturbed region will have given it an overall streamwise dimension of $U'tl_2$ and a thickness of

$$\delta \sim l_1/U't . \qquad (24)$$

Viscous diffusion will become important after a time $t = t_v$, where

$$t_v \sim \delta^2/\nu . \qquad (25)$$

Combination of (24) and (25) gives

$$t_v \sim (l_1^2/\nu U'^2)^{1/3} \qquad (26)$$

and a minimum attainable shear layer thickness of

$$\delta_{\min} \sim (\nu l_1/U')^{1/3} . \qquad (27)$$

(This is recognized as the parameter combination appearing in the estimate of the thickness of the "critical layer" in hydrodynamic stability theory.) For streamwise scales in the range of $l_1^+ = 100 - 1000$, which may be typical of the large eddies in the wall layer, the smallest shear layer thickness produced would be 5–10 in wall units. Typical associated time scales would be 25–100 in wall units. Such values could be compared to the decay time for the wave-like eddies, which is given by

$$t_d \sim l_1/c_I . \qquad (28)$$

With $c_I^+ \sim 3$, according to Bark's[5] calculations, this gives values of t_d^+ in range 30–300. Thus, near the wall the waves of large wavelengths will generally have a longer lifetime than the convected eddies and may, therefore, provide the dominating contribution to statistical averages, as was indeed found to be the case for the u spectrum in Bark's[5] calculations. Farther out from the wall, in the log region, the reverse is likely to be true, due to the U' factor in (27), and the convected eddies would probably dominate.
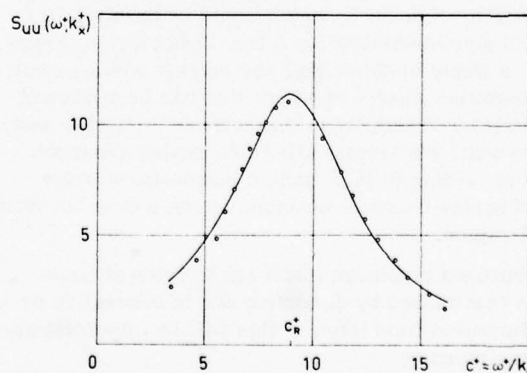

FIG. 3. Real and imaginary part of the downstream phase velocity. ○, □ computed from (21) and measurements by Morrison and Kronauer.[10] —computed from the Orr-Sommerfeld equation, from Bark.[5]
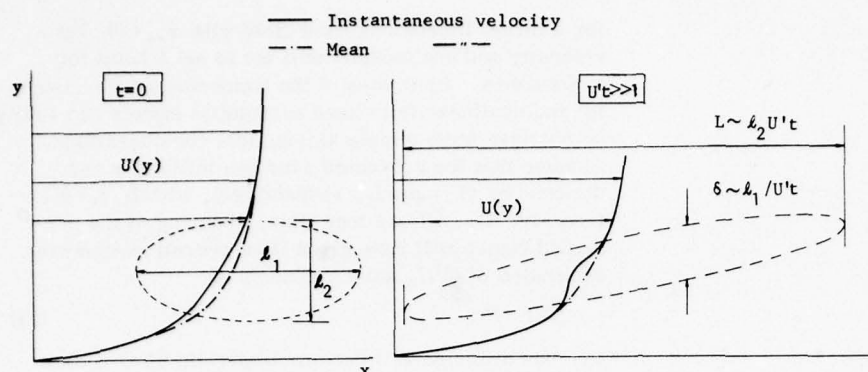
— Instantaneous velocity
—·— Mean   — " —

FIG. 4. Shearing of a convected eddy.

Strong nonlinear effects set in when the shearing has produced a local inflection with associated secondary instability. The time to reach inflection is determined from

$$\partial^2 u/\partial y^2 + U'' = 0 , \tag{29}$$

or, for

$$u/\delta^2 \sim |U''| , \tag{30}$$

which will occur after a time

$$t_i \sim l_1 \left| \frac{U''}{u} \right|^{1/2} \frac{1}{U'} . \tag{31}$$

Viscosity will prevent inflection if $t_v < t_i$, i.e., for eddies of a streamwise scale greater than

$$l_{1\,max} \sim \left| \frac{u}{U''} \right|^{3/2} \frac{U'}{\nu} . \tag{32}$$

The smallest value given by this expression is found for $y^* \simeq 15$ to be about 100 in wall units (setting $u \sim u_*$). Hence, inflection in this region can only be produced by fairly small eddies of streamwise scales in the range of those typical of the observed low-speed streaks. The low limit on scale is set by the requirement that the inflectional profile is unstable, which requires that the Reynolds number based on the shear layer thickness δ and the velocity difference across the layer must not be too small. For $l_1^* \sim 100$ and $u \sim u_*$, one obtains a Reynolds number of about 5, which would be barely large enough to give instability for a free shear layer. Hence, $l_1^* \sim 100$ is likely to define both the largest and the smallest streamwise scales of eddies that can be sustained by inflectional instability in this manner. Farther away from the wall, the largest allowable scales are much greater according to (32), and an increasingly wider range of scales becomes possible as one moves out from the wall region.

An additional nonlinear effect apt to arise at large times is that caused by distortion due to convection by the perturbation field itself. This will be important after a time given by

$$t_{nc} \sim l_1 / u . \tag{33}$$

For the scale ranges considered, this time is likely to be much larger than the viscous diffusion time.

VI. THE PROCESS OF BREAKDOWN TO SMALL SCALES

It was demonstrated that large velocity defects or excesses result from the combined effect of pressure gradient and lift-up, with the latter being particularly effective for large times after the birth of a localized disturbance. From a three-dimensional disturbance, there will then result an eddy convected downstream with the local mean velocity which will have a u- and w-perturbation field which will change very slowly in each plane $y = $ const under the action of viscosity and nonlinearity. The shearing of this convected eddy will lead to strong intensification of the shear so that local inflection could arise after passage of a sufficiently long time. This shear layer is immersed in the large-scale decaying wave field coming from disturbances created by bursting motions originating father upstream. According to the breakdown model,[3] strong localized instability of the thin shear layer will set in for any wavenumber of the unstable secondary wave

$$c_g' = c_0 , \tag{34}$$

where c_g' is the group velocity of the secondary wave and c_0 is the phase velocity of the large-scale primary field. For a primary field of arbitrary time and space variation, the equivalent phase velocity is defined (in the two-dimensional case) by[3]

$$c_0 = - (c_g')_t / (c_g')_x , \tag{35}$$

where the index means the partial derivative holding the wavenumber constant. This condition, when applied to the transition problem, was found to predict, well, the onset of the first low-speed spike as well as the frequency of the small-scale disturbances in the multiple-spike stage. The tentative hypothesis put forward here is that the observed ejection and sweep motions during bursting in a turbulent boundary layer are quite similar to the one-spike stage of transition. To give a quantitative assessment of the correctness of this conjecture is quite difficult at this time since verification of the breakdown condition (34) would require the calculation of secondary group velocities for a series of instantaneous velocity profiles appearing just before breakdown, as was done in the test of the model for the transition case.[3] However, some very tentative qualitative conclusions may be drawn with the aid of crude approxima-
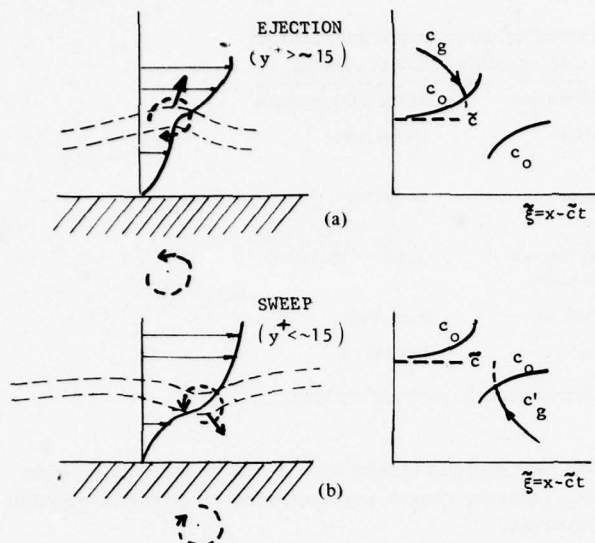
FIG. 5. (a, b) Proposed conceptual breakdown model for the ejections and sweeps.

tions based on the assumption that the shear layer has a thickness which is much smaller than the scale of the primary motion causing the shear layer breakdown. For a very thin shear layer, the phase velocity, and hence, the group velocity of the secondary wave, will be near the velocity of the inflection point. Let this velocity be U_i, which is composed of the mean velocity, U, the velocity perturbation due to the convected eddy, u_∞, plus a wave part, $\tilde{u}$. Taking only the convected part into account one finds from (35) that

$$c_0 = U , \tag{36}$$

so that the focusing condition will not be satisfied by the convected eddy alone, since $c'_g \simeq U + u_\infty$. We must therefore also consider the wave contribution. One may set, very approximately, neglecting the eddy contribution,

$$c'_g \simeq U + \tilde{u} \simeq U + \tilde{f}(x - \tilde{c}t, t) , \tag{37}$$

where $\tilde{c}$ is the phase velocity of the wave. For a non-decaying wave, $\tilde{f}$ would be a function of the phase variable

$$\tilde{\xi} = x - \tilde{c}t \tag{38}$$

alone, but for a decaying wave there is also a dependence with t explicitly such that $\tilde{f}_t/\tilde{f} < 0$. Application of (35) then gives

$$c_0 \simeq \tilde{c} - \tilde{f}_t/\tilde{f}_{\tilde{\xi}} . \tag{39}$$

For a nondecaying wave with $\tilde{f}_t = 0$, one would thus have $c_0 = \tilde{c}$, as expected. For finite, but small decay rates, the second term of (39) will become important near points of the traveling wave for which $\tilde{f}_{\tilde{\xi}} \simeq 0$, usually near the crest or trough of the wave. The variation of the equivalent phase velocity c_0 with the phase variable $\tilde{\xi}$ will thus be qualitatively as illustrated in Fig. 5 with an asymptote at a position $\tilde{\xi}$ corresponding to that of the extremum of $\tilde{f}$. It follows from Bark's[6] analysis that $\tilde{c}$ (which is the real part of the eigenvalue $c = c_R$

$+ ic_I$) will have a value near $c^*_R \simeq 9$ over a wave number range typical of that found in the wall region for the maximum spectral contribution. This corresponds to the mean velocity at $y^+ \simeq 15$. For shear layers with velocities at the point of inflection greater than $U_i^* \simeq 9$, most large-scale waves will travel more slowly than the velocity at the inflection point and will be overtaken by the secondary wave group. This is illustrated schematically in Fig. 5(a), and was the situation found in the boundary layer case just upstream of the point of breakdown. The breakdown theory, being essentially linear, would not distinguish between the individual secondary crests and trough, but as pointed out[3], one can expect a nonlinear filtering mechanism to set in at large amplitudes which will preferentially select that type of disturbance which has the lowest propagation velocity. This will be so if the first half-wave is upward, away from the wall. The deformation of the shear layer by a single upward kink would be kinematically similar to a perturbation vorticity of negative (in the opposite sense of the mean vorticity) sign. By placing an image vortex to make the condition of zero normal velocity on the wall be satisfied, one sees that the induced vortex has the effect, for this case, of slowing down the disturbance in the shear layer and hence tends to make it focus earlier than that associated with a downward kink. Thus, for $y^+ > 15$, one would expect to see an upward kink, leading to ejection, more often than a downward kink, leading to a sweep. For shear layers originating below $y^+ \simeq 15$, the converse would be true [Fig. 5(b)]. This might explain the experimental result[1] that ejections dominate in the outer region ($y^+ > 15$) and sweeps in the inner ($y^+ < 15$). However another, and perhaps more likely, explanation for the domination of the sweeps in the near-wall region could be that sharp internal shear layers cannot form in the immediate neighborhood of the wall so that a point there will be subjected to fewer ejections, which always originate from shear layers located *below* the measurement point as compared to sweeps, which originate from shear layers lying *above* the point of measurement.

The idea that the low velocity spikes appearing in a boundary layer undergoing transition are due to kinks formed on the internal intense shear layer was put forward originally by Kovasznay *et al.*,[12] and here we thus propose that a similar mechanism may be at work in a turbulent boundary layer, with the addition that downward kinking may also occur, especially in the region very close to the wall.

VII. THE MECHANISM OF DRAG REDUCTION

The mechanism of drag reduction due to additives was considered in an earlier paper,[7] and it was suggested there that the major dynamical effect of additives would be to cause stabilization of secondary inflectional instability and thereby inhibit turbulence production. In the original paper, two very simple rheological models were employed, believed to represent, in a qualitative manner, the effects of polymer additives and fibers. They were a convected Maxwell model (the simplest model for a viscoelastic fluid) and a suspension of rigid,

TABLE I. Effects of fluid additives on secondary instability.

Fluid-additive system	Rheological model	Effect on inflectional stability	Effect on drag
Polymer solution	Convected Maxwell	Marginal destabilization	Marginal increase
Polymer solution fiber suspension	Rigid-rod suspension (Ref. 13)	Strong stabilization	Reduction
Solid-particle suspension	Dusty gas (Ref. 16)	Strong stabilization	Reduction
Flexible wall	Stretched membrane	Stabilization only for extremely small mass	None or increase
Porous wall	Darcy's law	Strong destabilization	Increase
Magnetohydrodynamic flow	Longitudinal magnetic field.	Strong stabilization	Decrease

aligned rods, [13] the latter thought to model, in a very approximate way, the effect of stretched molecular coils for flow conditions beyond drag reduction onset. Some additional rheological models intended for *other* drag reducing fluid systems have since then been studied in the same manner. Since most of the results have been published elsewhere, [6,7,14,15] we shall simply summarize them in a short table (Table I) and add a few comments:

In these stability calculations, [6] a schematic inflectional boundary layer velocity profile[6] was employed, and not the actual measured instantaneous velocity profiles because such were not available. Since the results are only used for qualitative comparisons, however, the specific choice made should not be too important as long as the velocity profile employed is unstable over a range of wavenumbers in the Newtonian case.

The table demonstrates that, on the basis of the rheological models used, there is a strong secondary stabilization for all cases where there is clear experimental evidence of drag reduction. Viscoelasticity modeled in the most simple way was found to have a slight and fairly insignificant destabilizing effect, so it does not seem, on the basis of this model, that viscoelasticity as such is the key fluid property responsible for drag reduction due to polymeric additives. A more likely candidate is the anisotropic stress caused by the extension of the molecular coils (or molecular aggregates) in a turbulent flow of sufficiently high wall stress. If stretched strongly by the mean shear flow, such structures will have an overall effect on unsteady perturbations qualitatively similar to that of almost rigid elongated particles suspended in the fluid. In a pure shear flow the particles will tumble, but if they are much elongated, they will tend to spend most of their time oriented in or near the mean-flow direction. Thus, according to the model, the rheological effect of polymer additives would be qualitatively the same as that of fibers. The Batchelor[13] model for a suspension of rigid rods shows that very high values of elongational viscosity without any substantial increase in shearing viscosity can be obtained in a dilute suspension solution if the rods are very slender. Thus, an additive of this kind can have a substantial dynamical effect on the unsteady flow without causing much additional shearing stresses, as would be required for true drag reduction to arise.

The calculations indeed show very strong stabilization in parameter ranges corresponding to effective polymer additives.

Suspended solid spherical particles can have a strong stabilizing effect on inflectional instability for particles in certain density and size ranges. This is primarily due to the time lag between acceleration of a fluid element and its inertial reaction caused by the suspended particles. The detailed calculations[7,14] which were based on Saffman's "dusty gas" model, [16] show that the stabilization effect by such particles can be quite as strong as with rigid rods for a realistic combination of parameters. Typical of these are mass loadings of order unity and particle sizes of typically 0.001 of the boundary layer thickness. From comparisons between results based on the rigid-rod model and those for the suspension of heavy spheres, one may conclude that drag reduction from the presence of small heavy particles suspended in the flow could be of roughly the same magnitude as is attained with polymers and fibers. Experiments by Rosetti and Pfeffer[17] on flow in vertical pipes with glass spheres suspended in air give, indeed, such large values of drag reduction.

Calculations by Gustavsson[15] for incompressible conducting fluids gave results indicating strong stabilization of two-dimensional disturbances in a shear flow subjected to a longitudinal magnetic field. Experiments such as those of Fraim and Heiser[18] show that substantial drag reduction can be obtained when a magnetic field is applied.

Flexible surfaces constitute a controversial subject since in some instances[19,20] they have been reported to lower the drag, in other cases to cause no substantial change. [21] The stability calculations show that substantial stabilization of the inflectional velocity distribution can be achieved only with extremely light and flexible surfaces having a mass per unit area equal to or less than that of the boundary layer fluid affected. Such surfaces would be impractical for engineering uses, or even for testing in the laboratory, and the surfaces used in the reported successful tests appear to be too rigid to have any substantial effect on the short-wave secondary instability. Most likely, the mechanism of drag reduction is different for this case than for others con-

sidered here, possibly involving modifications of the large-scale field.

For the purpose of testing the turbulence model, cases for which the drag will increase are also of interest. Such a case is that of a porous wall, for which results for pipe flows which give a strong drag increase have been reported.[22] The stability calculations based on a boundary condition at the porous wall derived from the application of Darcy's law for the flow in the wall in fact show a strong destabilizing influence of the wall porosity, thus giving additional indirect support to the model.

VIII. CONCLUSIONS

The picture emerging for the burst sequence from the conceptual model proposed is the following: A bursting motion produces, through the excitation of the mean shear flow caused by the strong mixing, decaying wave-like disturbances propagating downstream. As the v and p perturbations decay, there will remain a u perturbation in the form of a convected eddy. Shearing of this eddy by the mean flow will further intensify the shear and produce a thin internal shear layer which will develop an inflection point and thus become locally unstable. While this is going on, the shear layer is intermittently bombarded with large-scale propagating disturbances originating upstream in other bursting events. These disturbances will give the group velocity of the small-scale secondary instability waves a large-scale variation in space and time. When the secondary group velocity becomes locally equal to the phase velocity of a wave-like disturbance, focusing of the secondary disturbance on the primary wave will lead to rapid buildup of secondary wave energy. The first strong secondary disturbance would be likely to appear more or less as a half-wave in the form of a "kink" of the shear layer. The shear layer will kink upward or downward leading to either an ejection or a sweep.

The u-velocity defects in the large-scale motion near the wall giving rise to inflection are primarily the result of the combined effect of two different mechanisms; the deceleration due to the pressure gradient and the perturbation arising because of lift-up or depression of a fluid element. For short instances after the initiation of the disturbance, and near the wall, the first mechanism will contribute most of the u perturbation, whereas for long times, and farther out from the wall, the lift-up effect would dominate. For the creation of a large velocity defect near the wall in combination with an excess farther out to cause a strong inflection, the lift-up is probably the most important effect, whereas the pressure gradient is likely to be primarily responsible for supplying the large-scale time and space variations required to produce breakdown.

On the basis of the model proposed the phenomenon of turbulent drag reduction due to additives of various kinds appears most easily explained as being caused by stabilization of the inflectional velocity profile due to the additive. Flexible walls constitute an exception since they do not seem to have a substantial stabilization effect for realistic values of wall mass density and flexibility. Thus, the reported drag reduction observations for such surfaces do not seem to fit the model proposed, and a different explanation must be sought for these.

[1]W. W. Willmarth, in *Advances in Applied Mechanics*, edited by C.-S. Yih (Academic, New York, 1975), Vol. 15, p. 159.
[2]M. T. Landahl, J. Fluid Mech. **29**, 441 (1967).
[3]M. T. Landahl, J. Fluid Mech. **56**, 775 (1972).
[4]M. T. Landahl, SIAM, J. Appl. Math. 28, 735 (1975).
[5]F. H. Bark, J. Fluid Mech. 70, 229 (1975).
[6]M. T. Landahl, in *Proceedings of the Thirteenth IUTAM Congress*, edited by E. Becker and G. K. Mikhailov (Springer-Verlag, Berlin, 1973), p. 177.
[7]M. T. Landahl and F. H. Bark, in *Actes du Colloque International Nr 233: Polymeres et Lubrification*, edited by Cl. Wolff (Centre National de la Recherche Scientifique, Paris, 1975), p. 249.
[8]S. J. Kline, W. C. Reynolds, F. A. Schraub, and P. W. Runstadler, J. Fluid Mech. 30, 741 (1967).
[9]H. T. Kim, S. J. Kline, and W. C. Reynolds, J. Fluid Mech. 50, 133 (1971).
[10]W. R. B. Morrison and R. E. Kronauer, J. Fluid Mech. 39, 117 (1969).
[11]H. Eckelmann, J. Fluid Mech. 65, 439 (1974).
[12]L. S. G. Kovasznay, H. Komoda, and B. R. Vasudeva, in *Proceedings of the* 1962 *Heat Transfer and Fluid Mechanics Institute*, edited by F. E. Ehlers, J. Kauzlarich, C. A. Sleicher, Jr., and R. Street (Stanford University, Stanford, Calif., 1962), p. 1.
[13]G. K. Batchelor, J. Fluid Mech. 41, 545 (1970).
[14]F. H. Bark, The Royal Institute of Technology, Department of Mechanics Report TRITA-MEK 74-01 (1974).
[15]H. Gustavsson, B. S. thesis, The Royal Institute of Technology, Stockholm (1973).
[16]P. G. Saffman, J. Fluid Mech. 13, 120 (1962).
[17]S. J. Rosetti and R. Pfeffer, AIChE J. 18, 31 (1972).
[18]F. W. Fraim and W. H. Heiser, J. Fluid Mech. 33, 397 (1968).
[19]M. O. Kramer, J. Aerospace Sci. 27, 69 (1960).
[20]R. L. Smith and E. F. Blick, J. Hydronaut. 3, 100 (1969).
[21]K. W. McAlister and T. M. Wynn, NASA TM X-3119 (1974).
[22]Y. Chu and L. W. Gelhar, Ralph M. Parson's Laboratory for Water Resources and Hydrodynamics, Massachusetts Institute of Technology Report 148 (1972).

Drag reduction in two phase and polymer flows

John L. Lumley[a]

The Pennsylvania State University, University Park, Pennsylvania 16802

The basic dynamics of turbulent boundary layers of several media is described qualitatively: suspensions of several types and polymer solutions. Despite the considerable differences in these media, it is argued that a number of the flows are affected only in the buffer layer, and drag reduction can result if behavior in the sublayer and buffer layer differ. In polymer solutions, it is argued that molecular expansion is responsible for the difference, and experimental evidence of this expansion is presented, and compared with calculations.

INTRODUCTION

Skin friction drag in turbulent flow can be reduced below that of the clear fluid (or solvent) alone by the addition of several substances.[1] For example, in a horizontal boundary layer above a surface, particles for which inertia may be neglected, but fallout may not, can reduce the drag in certain flow regimes. In a different situation, particles for which fallout may be neglected, but inertia may not, can also reduce the drag, but by a different mechanism. Particles for which both may be neglected can also reduce the drag if they are large enough. Polymer additives can make very substantial reductions in the drag. A detailed examination of the mechanisms involved[1] (in some cases highly speculative) suggests that while the heavy particle case may be explained by the effect of a stable density stratification, the other cases appear to have a basic mechanism in common: the addition of the substance affects only the dissipative scales of the turbulence, suppressing the dissipative eddies, and increasing the scale of dissipation. At the same time, the effective viscosity in steady shear is only slightly affected so that the sublayer scaling remains unchanged. In a turbulent boundary layer it is argued that such a change in dissipative scale cannot affect the momentum transport throughout most of the flow, which will, hence, have a logarithmic region with the classical slope. In the buffer zone, however, where the scales of the dissipative and energy containing eddies are roughly the same, the energy containing eddies will be suppressed, resulting in reduced momentum transport, an effectively thickened sublayer and reduced drag. The idea that a change in dissipative structure does not affect the energy containing eddies away from the wall is supported by measurements in media as disparate as slurries and polymer solutions. In polymer solutions, in particular, there is evidence that the structure of the sublayer remains essentially unchanged except in scale, leaving the mechanism of turbulence production unchanged.

The case of polymer solutions is characterized by the so-called onset phenomenon[2]: below a certain value of the flow parameters there is no apparent effect of the polymer. It is now clearly established that onset is well correlated with polymer terminal relaxation time[3] (see

Lumley[2] for other contributing evidence). Polymers are predicted to expand in a suitable velocity field when a criterion based on the relaxation time is exceeded[4] and this expansion process is felt to be responsible for drag reduction.[5,6] Polymer expansion in turbulent flow has been predicted, and the threshold for expansion correlates well with that for onset.[7] Indirect evidence[8] for the molecular expansion has been found in connection with Pitot tube errors, but no direct measurements have previously been reported. Here, we report direct measurements of molecular size in a two-dimensional pure strain. The molecular expansion measured, although not large due to limitations of the experimental apparatus, is that predicted[7] within experimental error, lending credence to other predictions regarding molecular expansion in turbulent flows and its relation to onset.

DYNAMICS OF TURBULENT TWO-PHASE AND POLYMER FLOWS

An earlier version of some of the following material, presented from a different viewpoint, has appeared in Ref. 1. We restrict discussion to media which display little non-Newtonian behavior in steady simple shear. We adopt the position that the basic structure of turbulent boundary layers of such media (flows with suspended particles, foams, polymer solutions, etc.), with a few exceptions such as the effect of buoyancy, is similar to that of Newtonian boundary layers, although the different regions may scale differently. That is, regardless of the fine structure of the medium, and hence of the dissipative mechanism, there will be a linear region[9] next to the wall in which the dissipative forces dominate (the sublayer); the central part of the flow will be dominated by inertia; there will be a logarithmic region with the usual slope[9]; and in the buffer layer (between these two latter parts) and extending into the sublayer there will be large eddies essentially similar to those found in Newtonian flows, the form of which is determined primarily by inertial forces and kinematics,[10] and which produce little Reynolds stress, but do produce inflectional profiles leading to secondary instabilities and the production of Reynolds stress. Within this conceptual framework, the only question is the scaling of the various regions, which will differ in different media. Hence, our position is that a detailed, mathematical, theory for turbulent boundary layers in these media is not necessary, since their structure is so similar to that of Newtonian boundary layers, and indeed is not

---

[a]Present address: Sibley School of Mechanical and Aerospace Engineering, Cornell University, Ithaca, N. Y. 14853.

possible, since in fact Newtonian boundary layers are not sufficiently well understood to permit the construction of such a theory.

This conceptual framework is intended to give structure to the discussion which follows, and according to Townsend.[11] "...provide targets for criticism...." It is probably an over-simplification, and should be qualified in various ways. Support for this framework is fragmented and is somewhat negative, in the sense that the most that can be said is that the supportive bits and pieces do not seem to be a variance with the framework proposed. It has the advantage of being the simplest framework with that property, i.e., the smallest change from the Newtonian boundary layer capable of explaining the observations, which does not assume things about non-Newtonian boundary layers that are not known about the Newtonian layer.

Let us leave aside the case of heavy particles for which inertia may be neglected; this case is treated extensively in Lumley, where it is shown that the basic mechanism is a pseduo-buoyancy resulting from the drag and fallout. The pseudo-stable stratification suppresses the vertical motion, resulting in a reduction of drag relative to a single phase fluid of the same density. Whether the drag is reduced relative to the clear fluid depends on the relative contributions to the Reynolds stress of the increased density and the reduced vertical motions; for increasing stability (controlled by the ratio of terminal velocity to shear velocity) drag reduction is possible. It is evident that this mechanism is quite different from the mechanism described in the preceding paragraphs.

Let us consider particles for which fallout may be neglected, but inertia may not. This corresponds roughly to a high-speed, relatively low Reynolds number flow.[1] In such a flow, the particles nearly follow the motion, following well at large scales and poorly at small. We may use an essentially Lagrangian estimate for the rate at which work is done by the fluctuating relative velocities induced by the particle inertia. A crude integration[1] gives for the additional energy dissipation per unit total mass (particles included)

$$1.18\epsilon(2 - 1/0.74sa)\mathcal{L}/(1 + \mathcal{L}), \quad 0.74sa > 1 , \tag{1}$$

where s is the (Kolmogoroff) cutoff frequency of the Lagrangian spectrum, which would ordinarily be $(\epsilon/\nu)^{1/2}$. a is the particle time constant, equal to V_T/g for small particles, and $\mathcal{L}$ is the loading, or mass ratio of particles. We are considering values of $\mathcal{L}$ of the order of unity, with particle/fluid density ratios of the order of 10^3 and volume concentrations of the order of 10^{-3}, so that particle-particle interactions may be neglected.

It is well known in turbulence that the presence of an additional mechanism for energy dissipation at high frequencies does not imply that the over-all dissipation of energy is increased. It is an experimentally observed property of turbulence that so long as the dissipation is confined to the small scales, the large scales are dominated by inertia. Hence, if the efficiency of the dissipative mechanism is increased (still being confined to

small scales), the scale at which the dissipation occurs will be increased so as to keep the total amount dissipated the same.

In expression (1), the ϵ is the rate at which energy is being cascaded down the spectrum, which will not be changed by the presence of the particles. The cutoff frequency s will be reduced by the presence of the particles, and the purely viscous dissipation will be given by νs^2, where ν is the value of the kinematic viscosity with particles. Note that the *dynamic* viscosity is essentially unchanged by the presence of the particles, the ratio being $1 + 5C/2$,[12] where C is the volume concentration; with $C = 10^{-3}$, this can safely be ignored.

Since the viscous dissipation plus the dissipation associated with the particles must dissipate all of ϵ, we may write

$$\epsilon = \nu s^2 + 1.18\epsilon(2 - 1/0.74sa)\mathcal{L}/(1 + \mathcal{L}) \tag{2}$$

which provides an equation to determine s.

We may simplify expression (2) by defining $\hat{s} = s(\nu_f/\epsilon)^{1/2}$ where ν_f is the kinematic viscosity of particle-free fluid; thus, $\hat{s}$ is the ratio of the cut-off frequency with and without particles. Also, it is convenient to define a parameter $\gamma = 0.74a(\epsilon/\nu_f)^{1/2}$, which is the product of the particle time scale and the cut-off frequency in the particle-free fluid (with a numerical factor included for convenience). Then, (2) becomes

$$\mathcal{L} = (1 - \hat{s}^2)/(1.36 - 1.18/\gamma\hat{s}) . \tag{3}$$

The cut-off viscous wave number is more relevant to turbulence dynamics. We may form a nondimensional cutoff wavenumber by normalizing by its value when $\mathcal{L} = 0$, which is proportional to $(\epsilon/\nu_f^3)^{1/4}$, and designate it by $\hat{k}_d$. Then, we have

$$\hat{k}_d = [\hat{s}(1 + \mathcal{L})]^{1/2} . \tag{4}$$

We have two conflicting phenomena here: the increased density due to the presence of the particles reduces the effective ν and tends to increase k_d, while the increased dissipation tends to reduce it. From (3) and (4) we find that there is a relatively narrow range of values of $\mathcal{L}$ in which, for sufficiently large values of γ modest reductions in k_d occur (see Fig. 1).[1]

In the wall region of a particle-free turbulent shear flow, the occurence of turbulence may be plotted as in Fig. 2.[2] The abscissa is wavenumber, scaled with the friction velocity and the kinematic viscosity of the fluid with particles, while the ordinate is distance from the wall scaled in the same way. The turbulence is con-
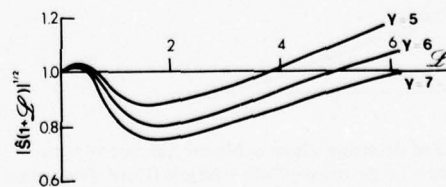

FIG. 1. Variation of dimensionless cutoff wavenumbers with loading, for various values of the particle/fluid time scale ratio.[1]
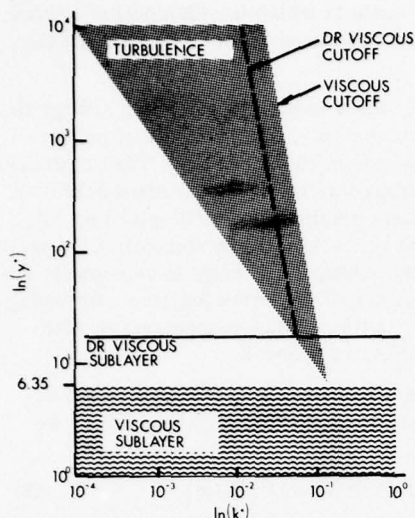
FIG. 2. Scaling relations in the viscous and inertial sublayers with and without polymers.[2] DR refers to drag reduction: the DR viscous cutoff and sublayer indicated correspond to an increase in viscosity in the turbulent part of the fluid, without a corresponding increase in the viscous sublayer.[1]

tained in the shaded region. That is, the peak of the energy containing eddies lies on the left-hand edge, while the peak of the dissipative region lies on the right-hand edge. As the wall is approached, the two scales approach each other, the turbulence Reynolds number dropping progressively, and *in the viscous sublayer the two scales are of the same order.*

It may be objected that a plot such as Fig. 2 ignores all the detailed information which we have about the form of the anisotropic eddies in the vicinity of the wall. Certainly, there are the large eddies to which we have already referred, which do not scale according to Fig. 2. In this figure we are referring, however, to the small scale eddies that are produced by the secondary instability of the inflectional profile produced by the big eddies, the eddies responsible for the Reynolds stress; these do scale according to Fig. 2, and they are the ones responsible for profile changes. According to Lumley,[10] the big eddies are essentially parasitic, in the sense that their size and intensity is determined by the mean velocity profile, while they carry little Reynolds stress.
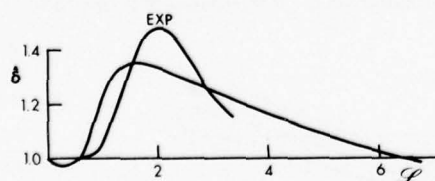

FIG. 3. Variation of dimensionless sublayer thickness with loading, for a rather large value of the particle/fluid time scale ratio.[1] The curve labeled EXP is from Kane et al.[13] for 36 μ glass beads, and corresponds to a value of the time scale ratio considerably beyond the range for which the present analysis is valid.
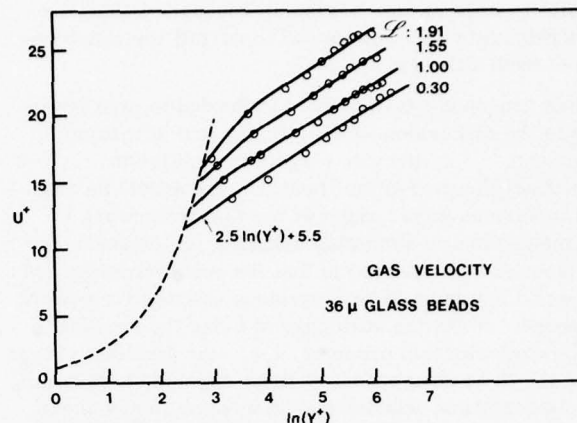

FIG. 4. Mean gas velocity profile in flows with the indicated loading of 36 μ glass beads from Kolansky et al.[14]

They are also essentially inertial, losing energy primarily at the bottom of the viscous sublayer.

According to Fig. 1, the presence of particles can, in the right parameter range, reduce the value of k_d. Away from the wall a reduction of k_d will have no effect on the energy containing eddies, and hence will leave the momentum transport and the slope of the mean velocity profile unchanged. Just outside the viscous sublayer, however, this reduction in k_d will cause the apex of the shaded region to move farther from the wall, killing the energy-containing eddies there, and effectively thickening the viscous sublayer. It is not hard to show that a thickening of the viscous sublayer at constant friction velocity corresponds to a reduction in drag, since the mean velocity at the sublayer edge increases. For small changes, the percentage change in wall shear stress is about the same as the percentage change in sublayer thickness. Of course, if the sublayer is thicker than for a clear fluid of the same density, drag has not necessarily been reduced; this will happen only if the sublayer is thicker than for the fluid without particles.

Hence, we will define $\hat{\delta}$ as the ratio of the sublayer thickness to that in the clear fluid. We will take as the definition of sublayer thickness the point of intersection of the right- and left-hand edges in Fig. 2. We obtain

$$\hat{\delta} = [\hat{s}(1 + \mathcal{L})]^{-2/3} . \tag{5}$$

This is plotted in Fig. 3[1] for a value of $\gamma = 7$, γ being evaluated at a distance from the wall corresponding to the sublayer thickness (as defined herein). For a qualitative comparison, we have included a measured reduction in drag due to particles.[13] The value of the parameter γ is too large (roughly 50) for our analysis to be applicable, but the general shape and range of $\mathcal{L}$ is qualitatively similar.

There are very few detailed measurements of profiles in particle-laden flows, and none to our knowledge of turbulent structure; certainly there are none in our parameter range. In Fig. 4 we present measurements of Kolansky et al.,[14] which clearly show the unchanged logarithmic region and drag reduction relative to a clear

fluid of the same density, despite the too-large value of γ. In corroboration we can also offer profile measurements in pipe flows of slurries, which are observed to have a logarithmic region with the classical slope.[15]

We may extend these ideas to neutrally buoyant particles, which neither fall out nor dissipate extra energy through inertia; however, flows of these particles display drag reduction.[16] Based on our reasoning here, if the particles are in every dimension small relative to the Kolmogoroff microscale everywhere in the flow we would expect no influence, and experiment bears this out. Anomalous effects are observed only in flows in which at least one dimension of the particle exceeds the Kolmogoroff length scale near the wall. For particles smaller than the Kolmogoroff microscale, only the effect on viscosity will be important, and this will be the same both in the turbulent part of the flow and in the viscous sublayer. Hence, a diagram such as Fig. 2 will remain unchanged, and no drag reduction will occur. Some drag reduction could occur if the particles migrated out of the wall layer,[17] since then there would be an increase in viscoity in the turbulent fluid and not in the sublayer; however, this would require a relative Reynolds number of order unity or greater, which cannot occur if the particles are smaller than the Kolmogoroff microscale (the relative Reynolds number based on velocity differences across the particle is $(l/\eta)^2$, where l is the particle dimension). For particles larger than the Kolmogoroff microscale, two effects are possible: migration out of the wall layer, causing a lower viscosity there, and suppression of the small eddies that are smaller than the particles. That is, a vertical line in Fig. 2 will represent particles of a constant size; the energy containing eddies will not be affected until the vertical line crosses the left-hand boundary of the shaded part. Below this point, the energy containing eddies will be suppressed, with a reduction in Reynolds stress, causing a thickening of the sublayer and reduction of drag. The suppression of the small eddies is in addition to the increase in viscosity; otherwise, the diagram would not be affected. If the effective viscosity in the sublayer remains Newtonian, the profile slope in the logarithmic region will not change; data indicate, however, that the slope usually increases. As Tennekes[9] has explained, a change in slope in the log region indicates a change in the viscous stress-strain rate relation in the sublayer; most likely migration is responsible for this. It is also possible that particle interaction or particle flexibility is responsible; recent measurements in blood[18] indicate that flexibility is the most important contributor to non-Newtonian behavior of particulate fluids in laminar flow.

Again, we do not have measurements of detailed turbulence structure, but the observed gross behavior is at least consistent with our simple model.

In polymer drag reduction we have more information than in any of the particulate flows. The mechanism that has been proposed is the expansion of the polymers in relatively rotation-free straining flows. In the next section we shall present the evidence that exists for this ex-

pansion. Here, we will summarize briefly what is presumed to happen.

Molecules exist in solution as tangled balls, mostly filled with solvent. Thermal agitation is responsible for keeping them in this partially contracted shape, providing an effective spring constant for return to their equilibrium diameter. Under the action of a pure strain, the molecules are pulled out into an ellipsoidal shape; when the strain rate exceeds the restoring force, the molecule expands as far as it can, until it is essentially fully extended. This picture is qualitative, being complicated by the fact that the effective restoring force changes as the molecule is expanded, so that the expansion does not happen all at once. If the molecule is in a shear, so that it is rotating as well as being subjected to the straining, a greater strain rate is required to produce the same effect, since the molecule remains aligned with the principal axes of strain rate for a shorter time. If the rotation rate is too great, in fact, the expansion produced is quite limited no matter how great the strain rate. In Fig. 5[7] we show the behavior of an isolated molecule in various combinations of vorticity and strain rate. In particular, in a shear, vorticity is equal to strain rate, and the expansion obtainable is quite limited.

The whole picture is complicated by the fact that there is evidence[19] that interaction of the molecules is an important part of the drag reduction process, and by the fact that any sample of polymers contains a spectrum of molecular weights, and hence of spring constants and relaxation times. Nevertheless, it is felt that the preceding paragraph provides a crude qualitative picture of behavior of polymer molecules in drag reducing flows. In the turbulent part of the flow, at high Reynolds number, vorticity and strain rate are uncorrelated with each other, and can occur in virtually any combination; they both have distributions with long tails, so that large and small values of each are more probable than for a Gaussian distribution. Hence, there is a substantial probability of finding regions of relatively large strain rate and relatively small vorticity. Under these circumstances, the molecules can expand, if the level of strain rate is sufficiently large. This discussion is oriented primarily toward large Reynolds numbers. If we consider turbulence at low Reynolds numbers, such as that
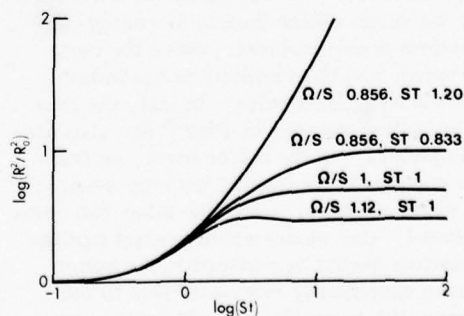

FIG. 5. Mean square molecular radius as a function of time in a two-dimensional flow, for various values of vorticity and strain rate (relative to the relaxation time T) from Lumley.[2]

near a wall, there are also regions of relatively large strain rate and low vorticity; Abernathy[20] has shown that in the field of flow of the large counter-rotating eddy pairs in the sub- and buffer layers such regions exist.

On the other hand, in the viscous sublayer, the vorticity is equal to the strain rate, and the molecules cannot expand significantly. The diffusion coefficient for molecules of this size is so large, that by the time expanded molecules from the turbulent part of the flow have diffused down into the sublayer, they will have collapsed.

When the molecules expand, the viscosity of the solution increases dramatically. Essentially, the increased dissipation due to the presence of the molecules is dependent on the velocity differences occurring over a molecule. The more the molecule expands, the greater the velocity difference. Since the mean square diameter of the molecule can expand by a factor of the number of submolecular units, and this can be of the order of 10^5, the increase in viscosity can be correspondingly great. Hence, we can have a substantial increase in viscosity in the turbulent part of the flow, and virtually no increase in viscosity in the viscous sublayer.

Again, this increase in viscosity in the turbulent part, and not in the viscous sublayer, suppresses the eddies which carry the Reynolds stress in the buffer layer, resulting in a thickening of the sublayer, and a reduction of drag. Since the majority of the turbulent part of the flow is dominated by inertia, we expect the slope of the mean velocity profile to remain unchanged, so long as the stress-strain rate relation in the viscous sublayer remains Newtonian. Since the drag reduction phenomenon occurs at concentrations so low that, if the molecules are not expanded, the total change in viscosity is of the order of 1%, the sublayer will remain Newtonian, and the slope of the mean velocity profile will be classical. This is exactly what is observed.[5]

In these polymer flows the form of the large eddy structure near the wall has been inferred from measurements of fluctuating wall shear stress.[21] It is found that the large eddies are essentially the same as in a Newtonian flow, but that the scale of the large eddies has expanded to fit the expanded sublayer. This is consistent with the predictions of Lumley[10] that the large eddy structure is parasitic, and determined primarily by the mean velocity profile; it is also consistent with the statement there that the large eddies lose their energy primarily at the bottom of the sublayer, where the molecules are contracted, and the viscosity is essentially unchanged from the Newtonian value. In fact, the measurements of fluctuating velocity by Rudd[22] are also consistent with this picture. In the buffer layer, he finds the streamwise component increasing with the mean velocity (at fixed shear velocity), while the other two components are reduced. Our model would predict that the turbulence intensities should be reduced in the buffer layer, but we have specifically restricted this to the small scale eddies that carry the Reynolds stress there. In fact, a major contributor to the streamwise fluctuating velocity are the large scale fluctuations in the mean velocity profile[23] induced by the big eddies. If the big

eddies extend farther from the wall, the net velocity difference over their height is greater, and the fluctuations in streamwise velocity induced will be greater. Hence, we expect the peak value of the streamwise fluctuating velocity to scale up as the sublayer thickness increases, as observed by Rudd.

The model predicts several other qualitative phenomena. For example, at low concentrations, the molecules will essentially expand fully, so that the net relative change in viscosity will be proportional to the concentration. Using our same definition for change in sublayer thickness with change in viscosity, we find drag reduction proportional to concentration for small concentrations.[2] Unfortunately, although early data appeared to show this, recent unpublished measurements of Berman indicate a progressive drop in drag reduction per unit concentration as concentration decreases for low concentrations, at constant flow time scale. This suggests that interaction is important and that effective intrinsic viscosity vanishes at zero concentration, implying that interaction with other molecules is necessary to expand a molecule. For larger concentrations, we have a feedback mechanism: as the molecules expand, the increased viscosity causes a reduction in the strain rate, since the dissipation must remain constant; the reduction in the strain rate stops the expansion. The equilibrium state is one of partially expanded molecules, producing an increase in viscosity just sufficient to hold them at that expansion.[2] The result is a saturation of drag reduction with concentration. If more polymer is added, the average expansion is reduced, to hold the effect about the same. The saturation for large concentrations is observed.[24]

EVIDENCE FOR MOLECULAR EXPANSION

Our explanation for the behavior of polymer solutions in turbulent flow is based on the idea that polymer molecules expand under the right circumstances. Evidence for such expansion has been either calculations based on various models[4] or indirect evidence from other phenomena. For example, the calibration curve for a hot film set at an angle to the free stream,[25] Fig. 6, can be explained on the basis of molecular expansion in irrotational flow.[2] When the film is normal to the free stream, the molecules are expanded in the irrotational flow near the stagnation region, causing an increase in viscosity and boundary layer thickness and a decrease in heat transfer. As the film is placed at an increasing angle relative to the free stream, the flow along the stagnation line becomes a shear flow, in which vorticity is equal to strain rate, the molecules tumble, and contract, resulting in a reduction in viscosity and boundary layer thickness, and an increase in heat transfer. The behavior of Pitot tubes[8] provides similar indirect evidence. Attempts have previously been made to measure molecular size directly, in circular Couette flow[26]; since the flow is a shear, only relatively small molecular expansion would be expected, and the experimental measurements were in agreement with this expectation.

Recently, Dennison[27] has completed a series of measurements of molecular size of poly(ethylene oxide)
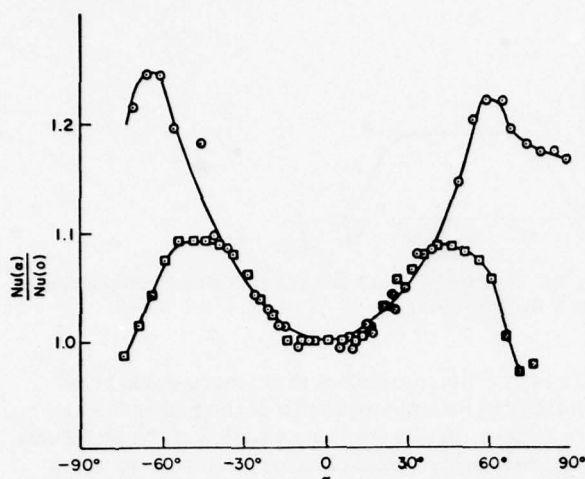
FIG. 6. Plot of angular calibration of a hot film probe at two mean speeds. ○, 300 ppm J-100, 25 cm/sec; □, 300 ppm J-100, 57 cm/sec.[25]

FIG. 8. Distribution of strain rate along centerline of two-dimensional contraction.[28]

(Union Carbide Polyox WSR-301) by light scattering in a two-dimensional, irrotational contraction, using a modified recording goniophotometer supplied by the Shell Pipeline Division, Houston. The contraction is shown in Fig. 7,[28] where all dimensions are in inches. The flow region was 0.2 in. thick, the top and bottom surfaces being glass. The cell of the goniophotometer was replaced with this contraction, the beam of the light source (a He–Ne laser) passing through the contraction normal to the plane of the figure, at several points along the centerline. The upstream end of the contraction was fed from a 2.0 in. circular pipe in which the flow was laminar, the two being joined by a round-to-rectangular smooth transition.

The flow in the contraction was extensively analyzed by finite difference.[28] Figure 8 is a plot of strain rate along the centerline, (all values nondimensionalized by entrance velocity and entrance half-width). The analysis of the flow field for the solvent alone and for the
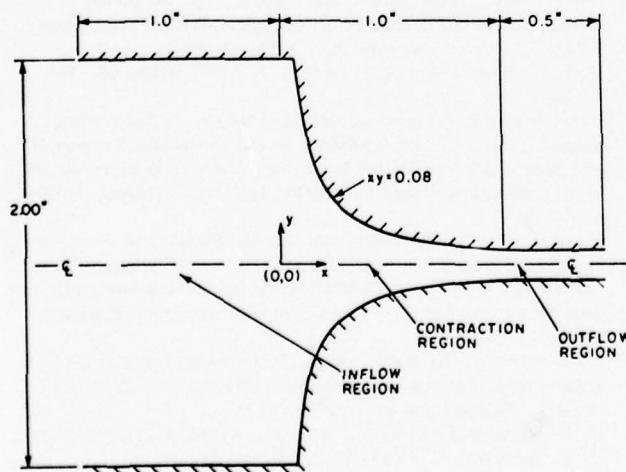
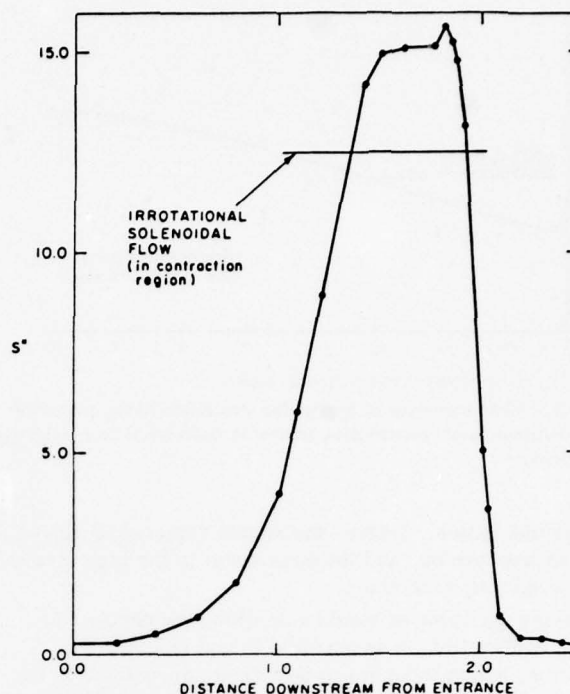polymer solution indicated that there was no appreciable difference. The increase of the strain rate in the contraction above the value predicted for irrotational flows is due to viscous boundary layers, which effectively reduce the dimensions of the contraction. The viscosity is computational, in the calculations of Gatski.[28] In the real experiment, the Reynolds number at the exit (based on width) is about 25 600, so that the flow is almost certainly turbulent. A crude estimate of turbulent boundary layer thickness, based on boundary layers in the stagnation region[29]; that is, proportional to $(\nu_f/S)^{1/2}$, where the turbulent viscosity is based on the local boundary layer thickness and free-stream velocity, and the strain rate S is that of the contraction) indicates a turbulent boundary layer of approximately the same thickness as the computational laminar boundary layer, so that Fig. 8 may be taken to be representative of the real flow. Because of its small size, of course, the real nozzle suffers from geometrical inaccuracies, which almost surely cause differences in the flow field.

The difficulty in the design of such a flow is to retain the polymer molecule in the flow field for a time great enough for it to be significantly extended. In the entrance region, the flow does not begin to follow the contraction for a distance which is probably a nearly constant fraction of the entrance width. Hence, widening the entrance region does not significantly increase the time spent by the polymer molecule in the high strain rate region. Lengthening the down stream end does not add much, first because of the difficulty of accurately machining the increasingly parallel section, and second because of the great increase in length necessary for a moderate increase in time, since the flow is traveling
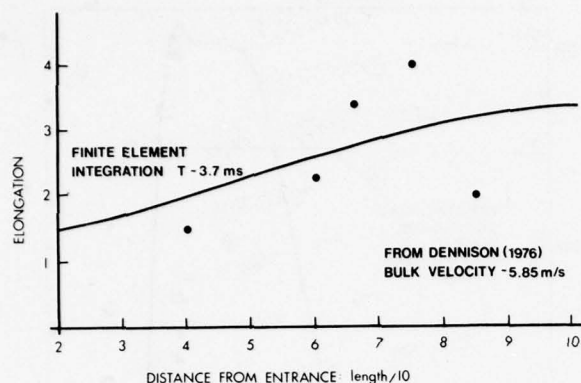

FIG. 7. Two-dimensional contraction.[28]

FIG. 9. Measurements of molecular expansion along centerline of two-dimensional contraction (curve is calculated from Oldroyd equation).[27]

FIG. 10. Hypothetical terminal relaxation time distribution for fresh Polyox WSR-301.[3]

faster and faster. Hence, the nozzle depicted is difficult to improve on, and the time spent in the high strain rate region is quite short.

Having the value of strain rate along the center line of the contraction, it is possible to use the Oldroyd equation, which is known to be a first approximation to the constitutive relation for a polymer solution,[30,31] to calculate molecular size.[28] Close to the critical value of the dimensionless strain rate, the finite difference technique suffers severe instabilities; we have obtained solutions in this range by finite element techniques, using eight unequal regions of stepwise constant strain rate through the contraction. In Fig. 9 we show the measured values of streamwise molecular size obtained by Dennison, together with the calculated values of molecular size from the Oldroyd equation. The terminal relaxation time has been selected to give the best fit to the data. This relaxation time is of the order of the largest times measured for this polymer by Berman et al.[8] using the observed onset of drag reduction to infer a time. It is also near the upper edge of the postulated relaxation time distribution suggested by these authors for this molecule (see Fig. 10).

The molecular expansions were measured at a concentration of 1600 ppm. Although this is substantially higher than the concentrations which are of interest in drag reduction, it was necessary to go to this concentration because of the small scattering cross section of the polymer molecule. The total light scattered by the molecules at lower concentrations was not reliably perceptable over instrumental noise. Although such a high concentration would certainly affect the behavior of this polymer in a drag reducing flow, it should have relatively little influence on its behavior in an irrotational contraction.

Although the total increase in size displayed by the molecules in this flow is necessarily limited due to the short time spent in the high strain rate region, the fact that the expansions measured agree so well with those predicted by the Oldroyd model suggests that our understanding of the behavior of such molecules in irrotational flows is substantially correct. The values observed are in good agreement with those reported by
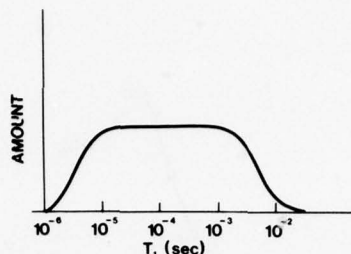
Smith et al.[32] In a turbulent flow, there would be no such limitation on the expansion of the molecules as there is here, because a finite fraction of the molecules would presumably remain in a strain rate field which was substantially rotation free for a sufficient time to expand, if the flow parameters exceed the threshold values.

ACKNOWLEDGMENTS

[1]J. L. Lumley, in *Topics in Applied Physics*, edited by P. Bradshaw (Springer-Verlag, Berlin, 1976), Vol. 12, Chap. 7.

[2]J. L. Lumley, J. Polymer Sci.: Macromol. Rev. **7**, 263 (1973).

[3]N. S. Berman and W. K. George, Jr., Phys. Fluids **17**, 250 (1974).

[4]A. Peterlin, Pure Appl. Chem. **12**, 563 (1966).

[5]J. L. Lumley, in *Annual Reviews of Fluid Mechanics*, edited by W. R. Sears and M. Van Dyke (Annual Reviews, Inc., Palo Alto, Calif., 1969), Vol. 1, p. 367.

[6]A. Peterlin, Nature **227**, 598 (1970).

[7]J. L. Lumley, in *Symposia Mathematica* (Academic, New York, 1972), Vol. 9, p. 315.

[8]N. S. Berman, G. B. Gurney, and W. K. George, Phys. Fluids **16**, 1526 (1973).

[9]H. Tennekes, Phys. Fluids **9**, 872 (1966).

[10]J. L. Lumley, in *Developments in Mechanics* (University of Notre Dame, Notre Dame, Ind., 1971), Vol. 6, p. 63.

[11]A. A. Townsend, *Structure of Turbulent Shear Flows* (Cambridge University, Cambridge, 1956), p. xi.

[12]G. K. Batchelor and J. J. Green, J. Fluid Mech. **56**, 401 (1972).

[13]R. S. Kane, S. Weinbaum, and R. Pfeffer, in *Proceedings, Second International Conference on the Pneumatic Transport of Solids in Pipes* (British Hydromechanics Research Association Fluid Engineering, Cranfield, Bedford, England, 1973), p. C3-29.

[14]M. S. Kolansky, S. Weinbaum, and R. Pfeffer, in *Proceedings Third International Conference on the Pneumatic Transport of Solids in Pipes* (British Hydromechanics Research Association Fluid Engineering, Cranfield, Bedford, England, 1976), p. C1-1.

[15]W. C. Mih, C. K. Chen, and J. F. Orsborn *Bibliography of Solid-Liquid Transport in Pipelines* (Washington State University, Pullman, Wash., 1971), p. 9.

[16]R. C. Vaseleski and A. B. Metzner, AIChE J. **20**, 301 (1974).

[17]P. G. Saffman, J. Fluid Mech. **22**, 385 (1965).

[18]M. Belzer, M. S. thesis, The Pennsylvania State University (1976).

[19]N. Berman (private communication).

[20]F. Abernathy (private communication).

[21]L. D. Eckelman, G. Fortuna, and T. J. Hanratty, Nature Phys. Sci. **236**, 94 (1972).

[22]M. J. Rudd, J. Fluid Mech. **51**, 673 (1972).

[23]H. P. Bakewell, Jr., and J. L. Lumley, Phys. Fluids 10, 1880 (1967).

[24]P. R. Kenis and J. W. Hoyt, Naval Undersea Research and Development Center Report TP-240 (1971).

[25]C. A. Friehe and W. H. Schwarz, in *Viscous Drag Reduction*, edited by C. S. Wells (Plenum, New York, 1969), p. 281.

[26]F. R. Cottrell, E. W. Merrill, and K. A. Smith, J. Polym.

7, 1415 (1969).

[27]G. Dennison, M. S. thesis, The Pennsylvania State University (1976).

[28]T. Gatski, Ph. D. thesis, The Pennsylvania State University (1976).

[19]H. Schlichting, *Boundary Layer Theory* (McGraw-Hill, New York, 1960), p. 81.

[30]H. Giesekus, Rheol. Acta **2**, 50 (1962).

[31]J. L. Lumley, Phys. Fluids **14**, 2282 (1971).

[32]K. A. Smith, E. W. Merrill, H. H. Peebles, and S. H. Banijamali, in *Polymeres et Lubrification* (Centre National de la Recherche Scientifique, Paris, 1975), p. 341.

PART C

RESEARCH PAPERS

(Abstracts of papers not published in full in these Proceedings are given in Part D)

Effects of elongational viscosity of polymer solution on Taylor–Görtler vortices

Y. Tomita and T. Jotaki

Mechanical Engineering Department, Kyushu Institute of Technology, Kitakyushu 804, Japan

Based on an assumption that drag reduction occurs due to the interaction of an elongational type of secondary flow with an elongational viscosity of a polymer solution, the effect of a polymer additive on Taylor–Görtler vortices was calculated. The results indicate that the Görtler parameter for the neutral stability always increases by increasing elongational viscosity and that the critical wavenumber decreases.

INTRODUCTION

Addition of a small amount of long chain linear polymer in water flow may result in drag reduction when the shear flow is turbulent. It may possibly delay transition from laminar to turbulent flow. Even under laminar flow conditions, drag reduction can be obtained for flows such as those in curved pipes,[1] in the boundary layer on a rotating disk,[2] or past spheres.[3] It is assumed that the flows affected by the addition of polymers are accompanied by secondary flows. These secondary flows are composed of pairs of counter-rotating vortices and these represent an elongational flow where the velocity has a significant longitudinal gradient. These secondary flows are, for example, the intense circulation in laminar flows in curved pipes, the logarithmic spiral vortices in laminar boundary layer flows around a rotating disk,[4] Taylor vortices in rotating cylinder flows,[5-7] the sublayer eddies in turbulent boundary layer flows,[8] Kármán vortices in flows behind a body,[9] and so on. Moreover, these effects appear only when the velocity of the undisturbed flow exceeds some threshold value. The crucial mechanical property of the polymer solution which affects these phenomena is presumed to be the elongational viscosity, which is additional viscosity in the elongational flow, as pointed out by Lumley,[10] and Seyer and Metzner.[11] According to a theory of Peterlin,[12] the elongational viscosity rapidly increases with the elongational deformation rate, then tends to saturate at a certain large value when the elongation rate exceeds the inverse of the molecular relaxation time. In addition, when the effects are brought about by a small amount of polymer, it is suggested that the effect on the flows by the addition may be a secondary one, that is, the elongational viscosity affects only the elongational type of secondary flows. In regions of sharply converging streamlines due to the pairs of counter-rotating vortices, the polymers may experience elongational deformation rates and then the secondary flows may be resisted. Thus, the effects of polymer additives are considered to be due to the interaction of the elongational type of secondary flow with the elongational viscosity of the solution.

In flows along concave walls, instability with respect to three-dimensional disturbances occurs before actual transition to turbulence. These disturbances, called Taylor–Görtler vortices, also represent elongational flows. In this paper, we shall be concerned with the model calculations of the stability characteristics for Taylor–Görtler vortices of a drag reducing polymer solution.

THEORY

It will be assumed that the profile of the basic two-dimensional laminar flow depends only on the distance from the wall and the Blasius profile is taken as the basic velocity distribution. In this case, the basic flow is simple shear flow and the elongational viscosity cannot directly affect the assumed basic flow. In a dilute polymer solution, its viscosity in simple shear varies little with shear rate which is close to that of the solvent. Thus, the stress tensor for the basic flow is substantially unchanged from that of the solvent. On the other hand, the disturbance flow due to the Taylor–Görtler vortices is essentially elongational, although it is not a pure elongational flow. We may suppose that the vortices extend the polymers, and the elongational viscosity is applicable to the vortices. Then, one further assumes that the contribution to the disturbance stress tensor due to the elongational viscosity is superposed only on the diagonal terms of the ordinary Newtonian stress tensor and the total disturbance stress tensor τ'_{ij} due to the vortices will be modified as follows:

$$\tau'_{xx} = -p' + (\mu + \gamma)\mathbf{e}'_{xx}, \quad \tau'_{xy} = \tau'_{yx} = \mu\mathbf{e}'_{xy},$$
$$\tau'_{yy} = -p' + (\mu + \gamma)\mathbf{e}'_{yy}, \quad \tau'_{yz} = \tau'_{zy} = \mu\mathbf{e}'_{yz}, \qquad (1)$$
$$\tau'_{zz} = -p' + (\mu + \gamma)\mathbf{e}'_{zz}, \quad \tau'_{zx} = \tau'_{xz} = \mu\mathbf{e}'_{zx},$$

where p' is the disturbance hydrostatic pressure, $\mathbf{e}'_{ij}$ is the disturbance strain rate tensor, μ is the conventional shear viscosity, and γ, the elongational viscosity which we use is the value given by pure elongational flow. The basic flow $U(y)$ is measured in the direction of the curvilinear coordinate x along the concave wall, y is the distance from the wall, and z is perpendicular to both x and y. The radius of curvature of the wall is R and is assumed to be constant.

The linearized equations governing the neutral stability of the Taylor–Görtler vortices are

$$[D^4 - 2(1 + \lambda^2)\sigma^2 D^2 + \sigma^4]\bar{v} = -2G^2\sigma^2\bar{U}\bar{u},$$
$$(D^2 - \sigma^2)\bar{u} = (D\bar{U} - \beta\bar{U})\bar{v}, \qquad (2)$$

and the boundary conditions are

$$\bar{u} = \bar{v} = D\bar{v} = 0 \quad \text{at } \eta = 0,$$
$$\bar{u} = \bar{v} = D\bar{v} = 0 \quad \text{at } \eta = \infty, \qquad (3)$$
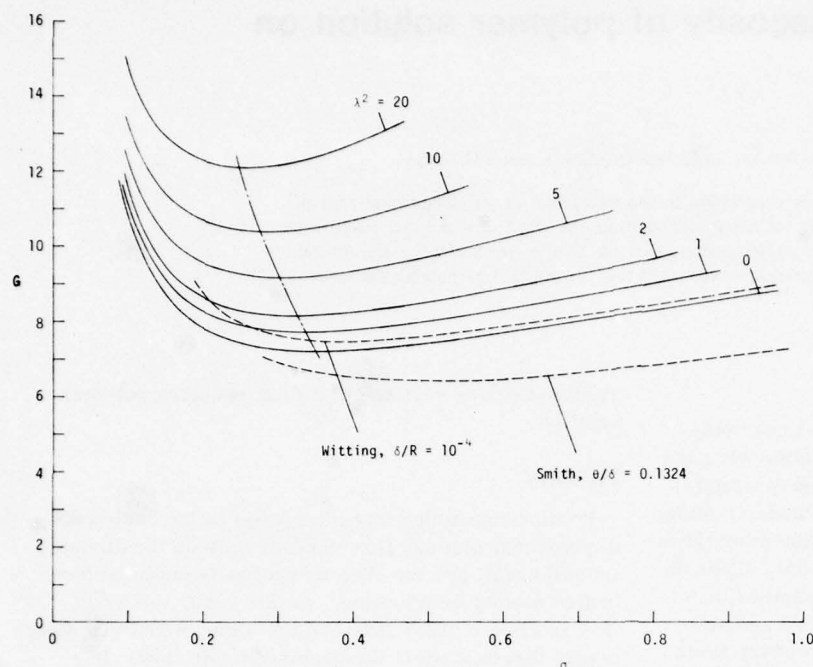
FIG. 1. Curves of neutral stability of Taylor–Görtler vortices for $\delta/R = 10^{-4}$ for various values of the viscosity ratio.

where it is assumed that the elongational viscosity is constant and that the radius of curvature of the wall is significantly larger than the boundary layer thickness δ. Equations are nondimensionalized by using the boundary layer thickness and the free stream velocity U_∞. The nondimensional variables are

$$G = R_e \beta^{1/2}, \quad \lambda^2 = \frac{2\gamma}{\mu}, \quad \sigma = \alpha\delta, \quad \beta = \frac{\delta}{R}, \quad R_e = \frac{\rho U_\infty \delta}{\mu},$$

$$\bar{u} = \frac{u_1}{U_\infty}, \quad \bar{v} = R_e \frac{v_1}{U_\infty}, \quad \bar{U} = \frac{U}{U_\infty}, \quad D = \frac{d}{d\eta}, \quad \eta = \frac{y}{\delta},$$

where ρ is the density, $u_1(y)$ and $v_1(y)$ are the disturbance functions, and α is the wavenumber. Solutions can be obtained by a method similar to that of Hämmerlin.[13]

RESULTS OF CALCULATIONS

The results of the calculations are shown in Fig. 1, where for the nondimensional curvature $\beta = 10^{-4}$, the Görtler parameter G is plotted against the nondimensional wavenumber σ with the viscosity ratio λ^2 as a parameter. The results of $\lambda^2 = 0$ due to Smith[14] and Witting[15] are also indicated and the present calculation for $\lambda^2 = 0$ agrees fairly well with those curves. Smith considered the streamwise growth of a boundary layer. By the action of the elongational viscosity, the limit of neutral stability is enlarged over the wide range of the nondimensional wavenumber and in particular, its effect is noted in the high wavenumber range. At the same time, the wavenumber of the critical condition at the onset of Taylor–Görtler vortices is also reduced, suggesting that the lateral scale of the vortices also becomes larger.

Figure 2 shows streamwise patterns of the Taylor–

Görtler vortices viewed from downstream plotted for the wavenumber near the critical condition for different values of the viscosity ratio. The form of the patterns is not strongly altered by the elongational viscosity, but the position of the neutral point, where the velocity in the plane vanishes, moves to the center of curvature of the wall with an increase in the elongational viscosity, suggesting that together with the decrease in the critical wavenumber the spatial scale of the vortices becomes larger.

Figure 3 shows the disturbance functions plotted for the wavenumber near the critical condition. A scale of velocity is so chosen that the maximum value of the
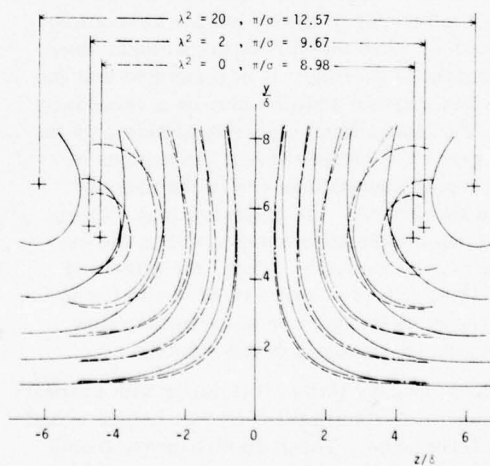

FIG. 2. Streamline patterns for various values of the viscosity ratio near the critical condition at the onset of Taylor–Görtler vortices.
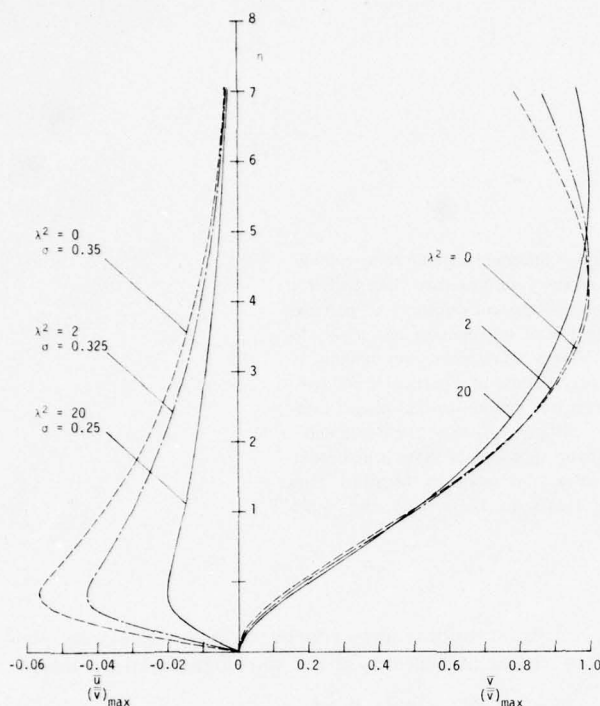
FIG. 3. Curves of the disturbance functions $\bar{u}$ and $\bar{v}$ for various values of the viscosity ratio near the critical condition at the onset of Taylor–Görtler vortices.

transverse component of the disturbance velocity becomes unity. The distance from the wall of the position of the maximum value of the streamwise component of the disturbance velocity is not dependent on the elongational viscosity. The ratio of the maximum value of the streamwise component of the disturbance velocity to that of the transverse component decreases considerably with an increase in the viscosity ratio, suggesting that the elongational viscosity may greatly affect the pitch of the spirals of the Taylor–Görtler vortices. The curvature of the streamlines in the central plane of the vortices may strongly decrease with an increase in the viscosity ratio.

If one believes that the Taylor–Görtler vortices and sublayer eddies in turbulent boundary layer are analogous structures, it is inferred that the addition of polymers in turbulent boundary layer flows would also increase the stability of the sublayer eddies and suppress the production of energy dissipating eddies.

According to the measurements of the elongational viscosity for polyacrylamide by Metzner and Metzner,[16]

a viscosity ratio as high as $\lambda^2 = 1020$ is the most conservative estimate for a 100 ppm solution. According to a theory of Peterlin, the viscosity ratio λ^2 near zero shear elongation rate is proportional to a product of the concentration and the zero-shear intrinsic viscosity for simple shear. When the elongation rate exceeds the inverse of the terminal relaxation time of the molecule, the ratio of λ^2 to the value at the zero elongation rate is roughly equal to the number of monomer units in the polymer chain. Thus, theoretically it may be concluded that when the elongation rate due to the vortices is small, the effects of the additives are expected only in high concentration solutions, but when the elongation rate exceeds the inverse of the molecular relaxation time the effects are expected even in a dilute solution. In all calculations, the elongational viscosity was assumed to be constant. Unfortunately, even after this calculation the effects of additives on the Taylor–Görtler vortices remains quantitatively undetermined.

CONCLUSIONS

From this study we may conclude that when the drag is changed by polymer additives the basic flow will have an elongational type of secondary flow and that the elongational viscosity will act on this secondary flow. In laminar boundary layer flows along concave walls by the addition of polymers the beginning of Taylor–Görtler vortices may be delayed and the spatial scale of the vortices will be increased with an increase in the elongational viscosity.

[1]H. A. Barnes and K. Walters, Nature **216**, 366 (1967).
[2]D. D. Kale, R. A. Mashelkar, and J. Ulbrecht, Nature **242**, 29 (1973).
[3]M. A. Ruszczycky, Nature **206**, 614 (1965).
[4]E. Bilgen, J. Basic Eng. D **93**, 85 (1971).
[5]H. Rubin and C. Elata, Phys. Fluids **9**, 1929 (1966).
[6]B. J. Bailey, Nature **222**, 373 (1969).
[7]M. M. Denn and J. J. Roisman, Am. Inst. Chem. Eng. J. **15**, 454 (1969).
[8]L. D. Eckelman, G. Fortuna, and T. J. Hanratty, Nature **236**, 94 (1972).
[9]G. E. Gadd, Nature **211**, 169 (1966).
[10]J. L. Lumley, in *Annual Review of Fluid Mechanics* (Annual Reviews, Palo Alto, Calif., 1969), Vol. 1, p. 367.
[11]F. A. Seyer and A. B. Metzner, Am. Inst. Chem. Eng. J. **15**, 426 (1969).
[12]A. Peterlin, Pure Appl. Chem. **12**, 563 (1966).
[13]G. Hämmerlin, J. Rat. Mech. Anal. **4**, 279 (1955).
[14]A. M. O. Smith, Q. Appl. Math. **13**, 233 (1955).
[15]H. Witting, Arch. Rat. Mech. Anal. **2**, 243 (1958).
[16]A. B. Metzner and A. P. Metzner, Rheol. Acta **9**, 174 (1970).

Drag reduction scale-up criteria

J. G. Savins

Mobil Research and Development Corporation, Dallas, Texas

F. A. Seyer[a)]

University of Alberta, Edmonton, Alberta, Canada

Available drag reduction correlations are presented and their utility for engineering scale-up to a scale-up from a correlation based on friction velocity and the availability of some turbulent flow data with the process fluid of interest is compared. A further purpose is to investigate the consequences of polymer modification of the mean flow profile in the outer layer. Emphasis is placed on accuracy and ability to portray the drag reducing activity of complex systems. In the case of very dilute polymeric systems in large conduits, very accurate predictions may be needed to assess the performance of a particular additive. Similarly, equations capable of detailed predictions of observed behavior can provide needed insight into the mechanism of drag reduction. Inasmuch as the semi-logarithmic resistance law, e.g., the Seyer and Metzner model of turbulent viscoelastic flow, provides a scale-up criterion significantly more complicated to use than a number of other models, an engineering approximation to this model is described. It is shown that for accurate predictions to be made at modest levels of drag reduction activity, the model must be modified to compensate for thickening of the sublayer.

INTRODUCTION

Interpretation and ultimately application of turbulent flow drag reduction may involve comparisons or scale-up to systems which differ in scale by more than an order of magnitude. Unfortunately, percentage reductions in drag may be much smaller in large scale systems as compared with laboratory scale systems. Consequently, ability to portray detail quantitatively may be extremely important, while on the other hand engineering and interpretive utility may be seriously hampered by complexity or the need to deal with large numbers of parameters. As noted, scale-up to practical sized systems results in much less drag reduction than in the laboratory sized apparatus. In applications with very dilute solutions the predicted decrease in drag from that for a Newtonian fluid may involve the difference between two numbers of equal magnitude, so that small uncertainties in scale-up may result in very large uncertainty in the decrease of drag to be expected. Owing to the complex rheology of the drag reducing fluids and our current inability to precisely define or even measure the rheological properties at conditions of interest, it is also of importance to develop criteria which may be independent of detailed rheological measurements.

It is the purpose of this paper to explore some of the approximations involved with use of the familiar semilogarithmic representations of the gross flow, and to show that a much simpler relation gives a practically indistinguishable scale-up criteria. Given turbulent flow data obtained with the process fluid of interest, scale-up can be effected without measurement of rheological properties.

THEORETICAL

The general features of drag reduction, correlations, and possible mechanisms have been reviewed recent-

ly.[1,2] Most studies have represented mean velocity profiles with modifications of the semilogarithmic relation:

$$u^+ - C(\xi, f) = A \ln y^+ + B , \qquad (1)$$

where u^+ is dimensionless velocity $(u^+ = \bar{u}/u^*)$, y^+ is dimensionless distance from the pipe wall $(y^+ = y u^*/\nu)$, $\bar{u}$ is the mean velocity at distance y from the wall, u^* is the friction velocity $(u^* = (\tau_w/\rho)^{1/2})$, τ_w is the wall shear stress, ρ and ν are the mass density and kinematic viscosity, R and V are pipe radius and bulk velocity, and $A = 2.46$ and $B = 5.6$ are acceptable values for these constants for Newtonian fluids. The empirical correction factor $C(\xi, f)$, where ξ is a dimensionless distance from the tube wall $(\xi = y/R)$ and $f = 2\tau_w/\rho V^2$ is the friction factor, has been estimated by several investigators, and will be taken from Ref. 3, so that

$$C(\xi, f) = 0.05 \sqrt{2/f} \exp[-(\xi - 0.8)^2/0.15] . \qquad (2)$$

Figure 1 shows typical velocity profiles obtained with an optical technique[4] for Newtonian fluids (a) and 100 wppm Dow polyacrylamide in water at various Reynolds numbers. For the drag reducing solution the solid lines (b)–(d) drawn parallel to the Newtonian line indicates that an increase in the intercept B, with slope A held constant, provides a fit which is equivalent to that obtained with Newtonian fluids. Alternatively, if the function $C(\xi, f)$ is ignored, Rollin's earlier study has shown that for equal precision a larger value of A is required to describe velocities outside the sublayer region. In extreme cases of drag reduction, either at high concentration or in sufficiently small tubes, the portion of the velocity profile describable by Eq. (1) shrinks to zero and data points tend to cluster around the asymptote

$$u^+ = 11.7 \ln y^+ - 17.0 \qquad (3)$$

proposed by Virk.[2] Equation (3) is also shown in Fig. 1 as the solid line (e). Equation (3) has been the basis, in some studies, for approximating the entire profile by three regions described successively by $u^+ = y^+$, Eq. (3), and finally Eq. (1). In one study,[5] the flow has been

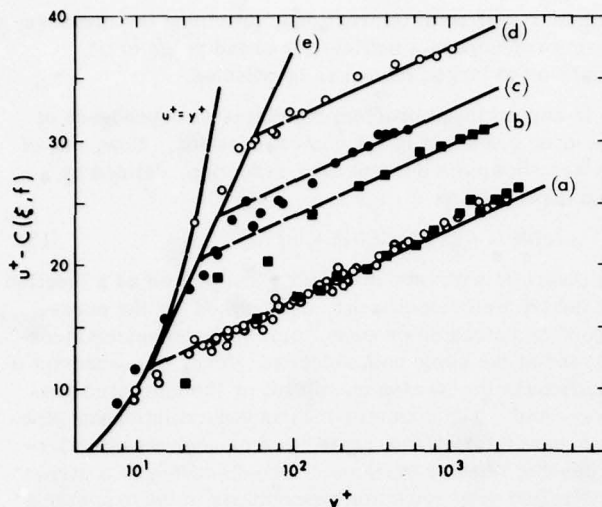[a)]Present address: Syncrude Canada Limited, Edmonton, Alberta, Canada.

FIG. 1. Typical velocity profiles for: Newtonian fluids (a) in 2.54 cm, 0, and 6.98 cm, ∎, tubes. 100 wppm polyacrylamide, (b) $N_{Re} = 97800$, 6.98 cm tube, (c) $N_{Re} = 34400$, 2.54 cm tube, (d) $N_{Re} = 80400$, 2.54 cm tube, and (e) Virk's maximum drag reduction asymptote.

divided into four sections, which in the case of tube flow amounts to use of the correction function given by Eq. (2) for points near the centerline.

If it is assumed drag reduction is controlled by viscoelastic properties, a minimum of one time scale is necessary to provide a description of the fluid properties. If the characteristic time for the drag reducer system is defined by θ_p, then dimensional considerations show for drag reduction that

$$B \rightarrow B(\theta_p u_p^{*2}/\nu_p) = B(t_p) , \qquad (4)$$

where all quantities are as previously defined and the subscript p represents the drag reducer system. It is important to note that irrespective of the rheological point of view taken, that is, whether θ_p and ν_p are taken as shear dependent or constants for example, the function in (4) is solely determined for a given polymer solvent system by the friction velocity, u_p^*. Of course, for a given system the shape of the function B with respect to values of t_p will depend on the particular definitions of θ_p and ν which are employed.

By integration of Eq. (1) to determine the bulk velocity, the friction law can be obtained. For internal flow of Newtonian fluids and assuming a negligible contribution from the sublayer, integration with minor adjustment of the constants results in

$$1/\sqrt{f} = 1.74 \ln N_{Re} \sqrt{f} - 0.4 , \qquad (5)$$

where $N_{Re} = 2RV/\nu$ is the Reynolds number and here the natural logarithm is used. Equation (5) is asymptotically valid at large N_{Re} for $\xi \rightarrow 0$. As shown by the velocity profiles for drag reducers, the portion of the flow actually described by Eq. (1) is somewhat less than for Newtonian fluids and is dependent on the scale of the system. Most generalizations to relate the velocity profiles to the gross flow characteristics have ignored these possi-

ble effects as is done in arriving at Eq. (5). It has been shown[6,7] that if the profile is approximated by Eq. (1) to the intersection with $u^+ = y^+$ and integrated piecewise, then

$$\sqrt{2/f} = A(1 - \xi_l)^2 \ln N_{Re}\sqrt{f} + (1 - \xi_l)^2 [B(t_p) - A \ln 2\sqrt{2}] - G \qquad (6)$$

in which

$$G = 3.60 - F(\xi_l) - \frac{2Ru_p^*}{\nu_p}\left(\frac{\xi_l^2}{2} - \frac{\xi_l^3}{3}\right), \qquad (7)$$

and $\xi_l = (y/R)_l$ at the intersection of Eq. (1) with the linear relation

$$y_l^+ = A \ln y_l^+ + B(t_p) . \qquad (8)$$

For a sublayer thickness $\xi_l = 0.1$, there is a considerable modification of the terms in Eq. (6). For Newtonian fluids, $\xi_l = 0.1$ occurs at $N_{Re} \simeq 3100$ while for drag reducing systems this may occur at much larger N_{Re} and is dependent on the amount of drag reduction as shown by Eq. (8). In the earlier work the variation of G with ξ_l was ignored and, based on data for Reynolds numbers in excess of 10^4, it was shown that $G = \text{const} = 3.0$ gave an adequate approximation of the available data. With this approximation, however, one of us has noticed that Eq. (6) gives unrealistic predictions at low Reynolds numbers, even for Newtonian fluids.

Figure 2 illustrates the resulting discrepancy for Newtonian friction factors. The solid curve (a) is Eq. (5), the accepted Nikuradse relation. Equation (6) with $G = 3.0$ is given by the dashed curve (b). At low Reynolds numbers there is considerable deviation from Eq. (5). It is of interest to note at $N_{Re} = 2000$, $\xi_l \simeq 0.15$ so that terms such as $(1 - \xi_l)^2$ amount to multiplication by
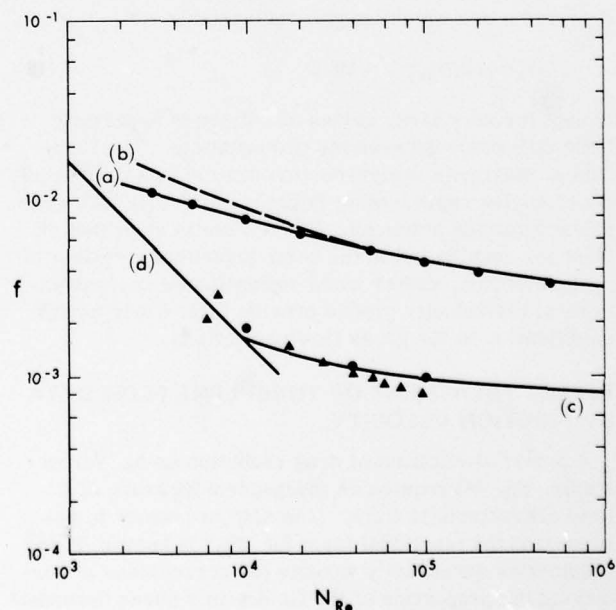

FIG. 2. Illustration of effect of sublayer thickness on predicted friction factors: (a) Eq. (5), (b) Eq. (6) with $G = 3.0$, (c) Eq. (12) maximum drag reduction, (d) laminar flow, ▲ data on 1000 wppm polyacrylamide, ● Eq. (6) with $G = $ variable.

J. G. Savins and F. A. Seyer   S79

72% in Eq. (6). Judging by available data for drag reducers this value for $\xi_l = 0.15$ may be a reasonable rule of thumb in estimating the limit for which the fully developed turbulence can be sustained. For drag reduction along the so-called maximum asymptote this would occur at $N_{Re} \simeq 3 \times 10^4$.

To generalize (7) it is noted[7] that the function $F(\xi_l)$ from Eq. (7) is, by definition,

$$F(\xi_l) = 2 \int_0^{\xi_l} (1 - \xi) f_3(\xi) \, d\xi , \qquad (9)$$

where

$$f_3(\xi) = (U_m - \bar{u})/u^* = -A \ln \xi + [C(1, f) - C(\xi, f)] \qquad (10)$$

and U_m is the centerline velocity. To a close approximation[3] for $\xi_l < 0.2$, which is within the range of interest, $C(1, f) - C(\xi, f) \cong 0.8$. Thus, integrating Eq. (9)

$$F(\xi_l) = \tfrac{1}{2} A (4\xi_l - \xi_l^2 + 2\xi_l^2 \ln \xi_l - 4\xi_l \ln \xi_l) + 0.8 \xi_l (2 - \xi_l) . \quad (11)$$

The circles lying on curves (a) and (b) in the upper portion of Fig. 2 indicate the predicted friction factors with G variable, from Eqs. (7) and (11) in Eq. (6). There is excellent agreement with the accepted equation over the entire range of N_{Re} so that the modified equation properly accounts for the sublayer. Noting that if the sublayer thickness is fully accounted for in Eq. (6), the predictions are quite indistinguishable from that of the simpler Eq. (5), it is of interest to compare with the equivalent calculations for a drag reducer. Considering the case for which maximum drag reduction occurs provides the largest values for ξ_l, as shown by Eq. (8). A close approximation for this case is with $B(\xi_l) = 32$. In the lower portion of Fig. 2 is a comparison of results for G variable shown as circles from Eq. (6) and curve (c), representing the simpler equation for maximum drag reduction which ignores the variable ξ_l,

polymer system of interest and, providing the measurements encompass a sufficiently broad range of u^*, scale-up to larger tubes can be effected.

In any scale-up problem the diameter dependence of the drag reduction is the central question. Now, one of us has shown the percent drag reduction, defined by γ and expressed as

$$\gamma = 100 (1 - f_p / f_0) = 100 [1 - (u_p^*/u_0^*)^2] \qquad (13)$$

is invariant with tube diameter when plotted as a function of the friction velocity, u_0^*, determined for the corresponding untreated process fluid, with the same viscosity and at the same bulk velocity. Here, the subscript 0 represents the Newtonian solvent or the untreated process fluid. The diameter invariant correlation for pipe flow has its origins in prior work on aqueous micellar-type drag reducer systems.[8] The discovery of a stress controlled drag reduction phenomenon in these systems suggested correlating the data in the form $[(u_0^*)^2, \gamma]$. Since solvent friction velocity is readily obtained from standard correlations, determination of drag reduction activity is readily achieved for conditions of interest once the correlation of (u_0^*, γ) has been established. This is a simpler and more direct procedure than using the more complex semi-logarithmic relations which require a description of the rheological properties of the fluid. These more sophisticated resistance laws would find greater use if it were not so difficult to provide, experimentally or theoretically, a realistic description of viscoelastic properties over a broad range of turbulent flow conditions for a system usually containing a few weight parts per million of additive. A version of the (u_0^*, γ) correlation was applied by Astarita et al.[9] and more recently applied by Lee et al.[10] to pipe flow data acquired under turbulent viscoelastic flow conditions. Less direct correlations, e.g., the method used by Whitsitt et al.[11] correlate a parameter labeled "fraction laminarized" with friction velocity, and intermingle the measured drag reduction effect with fluid rheological properties. The result is that γ, the parameter which is derived from a scale-up must be determined by a trial-and-error procedure.
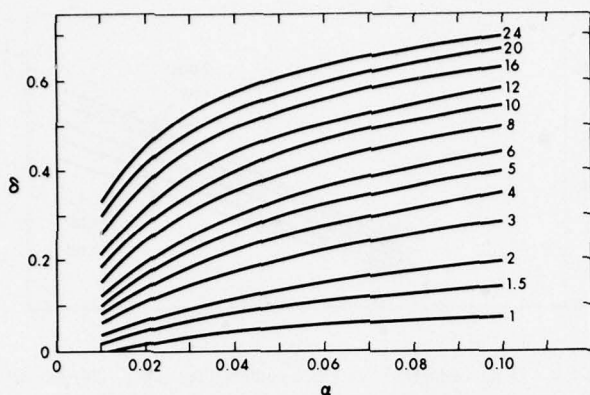
FIG. 3. Engineering approximation to Eq. (14), using Eq. (25) with $\beta = 1.0$. The indicated parameter is t_0 from Eq. (27).

is the basis for developing the engineering correlation. Here,

$$B(t_p) = Kt_p + B(0), \qquad 0 \le t_p < 18, \tag{15}$$

$$= 32.0, \qquad t_p \ge 18 \tag{16}$$

$$t_p = \theta_p(u_p^*)^2/\nu_p, \tag{17}$$

$$x_p = (N_{Re}\sqrt{f})_p, \tag{18}$$

$$G^* = P - (\xi_l) - \xi_l^2 Z + \tfrac{2}{3}\xi_l^3 Z, \tag{19}$$

$$P = 3A/2 + C_3, \tag{20}$$

$$Z = Ru_p^*/\nu_p, \tag{21}$$

and the function $S(\xi_l)$ is given by the relation

$$S(\xi_l) = 2A[(\xi_l^2/2)(\ln\xi_l - \tfrac{1}{2}) - (\ln\xi_l - 1)\xi_l] + 2C_3(\xi_l - \xi_l^2/2). \tag{22}$$

On neglecting terms in ξ_l and higher, and setting $A = 2.46$, $B(0) = 5.6$, $C_3 = 0.8$, and $K = 1.454$, Eq. (14) becomes

$$1/\sqrt{f_p} = 4.0 \log_{10}(x_p) + 1.0282 t_p - 1.023 . \tag{23}$$

Combining Eq. (23) with the resistance law for Newtonian fluids

$$1/\sqrt{f_p} = 4.0 \log_{10}(x_p) - 0.40 \tag{24}$$

and rearranging, there results an engineering correlation for turbulent viscoelastic flow, where the fractional drag reduction, ζ, is given by the relation

$$\zeta = 1 + 1/72 - \cdots \tag{25}$$

where

$$\cdots \tag{26}$$

$$\cdots \tag{27}$$

$$\cdots \tag{28}$$

$$\cdots \tag{29}$$

agreement between the engineering approximation, Eq. (25), and the modified Seyer–Metzner resistance law, Eq. (14), which includes all terms in ξ_l as given by Eq. (22), and with $B(0) = 5.6$, $K = 1.454$, and $P = 4.49$ is illustrated in Fig. 4, with u_0^* expressed here and in later examples in units of m/sec. For a pipe diameter of 2.54 cm the approximate solution predicts a higher level of drag reduction activity at low solvent friction velocity; for a pipe diameter of 50.8 cm, both solutions yield the same predicted level of activity. The degree of invariance of the (u_0^*, γ) correlation predicted by the assumed model of turbulent viscoelastic flow improves with increased friction velocity. The treated process fluid used in this example is characterized by the following assumed combination of viscous and elastic properties: $\beta = 1$, $\nu_p = 0.0518$ cm^2/sec, and $\theta_p = 1.25$ msec.

The solution conformation of the additive in the treated process fluid and its concentration will determine the kinematic viscosity of the resulting drag reducer system and the effects of this viscous loading on activity. Through Eq. (25), the fractional drag reduction correlation predicts an increase in kinematic viscosity from ν_0 to ν_p will depress the drag reduction effect, and the results illustrated in Fig. 5 indicate that viscous loading will be appreciable for small values of the parameter t_0.

DISCUSSION

The direct method of scale-up is useful when some turbulent flow data are available over the range of u_0^* of practical interest for a given process fluid. An experimentally derived correlation is shown in Fig. 6. Note that the diameter invariance of the (u_0^*, γ) correlation is considerably better than that of the model prediction shown in Fig. 4 for comparable levels of drag reduction activity and the same range in u_0^*. This particular cor-
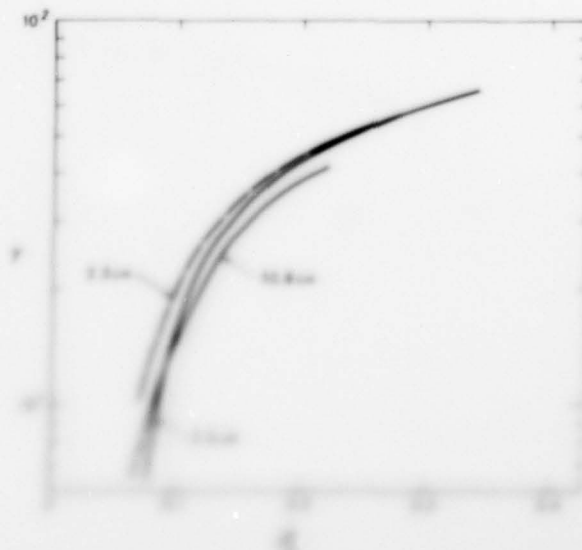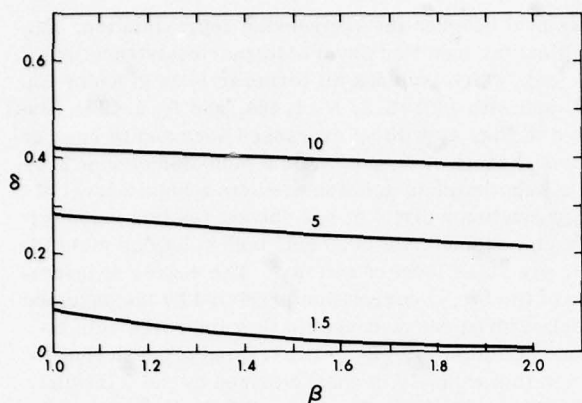
FIG. 5. Effect of viscosity ratio on drag reduction activity as predicted from Eq. (25) with $\alpha = 0.045$. The indicated parameter is t_0 from Eq. (27).

FIG 7. Drag reduction activity predicted from Eq. (25) for a pipe diameter of 20.82 cm and a kinematic viscosity of 0.041 cm^2/sec, and with different fluid characteristic times in msec.

relation was reconstructed from published data[12] comparing the turbulent friction losses developed on pumping water at different rates in tubing and annuli, against that of an aqueous solution containing 600 weight parts per million of a fracturing fluid additive. Such materials are commonly employed in the stimulation of oil and gas wells by a process described as a "hydraulic fracturing treatment." The correlation includes data from seven pipe diameters: 4.09, 5.05, 6.20, 10.2, 12.6, and 16.2 cm, and three annuli ratios: 0.451, 0.479, and 0.594. Within the scatter of both pipe and annuli data there is generally good correspondence, and diameter invariance is evidenced over a broad range of friction velocities corresponding to a wide range of turbulent flow conditions. The practical engineering utility of the friction velocity method is also illustrated for the first time in the correlation of turbulent viscoelastic

flow data from both tubing and annuli.

In general, the particular characteristics of a (u_0^*, γ) correlation reflect the functional dependence of the fluid characteristic time on flow conditions. Additionally, the correlation is only a partial measure of the performance of a drag reducer. The onset of viscoelastic activity in turbulent flow, the level of drag reduction produced, and viscous loading effects are determined by the particular combination of additive and solvent and the resulting solution conformation and intermolecular interactions. Thus, correlations of different characteristics can result between different process fluids treated with identical concentrations of the same additive. Depending upon the experimental configuration used to generate the data, "performance" with respect to shear induced degradation may not be obvious from the (u_0^*, γ) correlation.

The friction velocity method can also be used to produce a diameter invariant correlation for complex systems which do not exhibit drag reducing properties in turbulent flow. To effect a scale-up of turbulent flow behavior for these systems, replace fractional drag reduction by the "drag ratio," defined by Eq. (30).

Often a planning or econo-engineering group interfacing with this technology area will want to conduct scoping and process simulation studies to develop a perspective and broadly define opportunities for exploiting drag
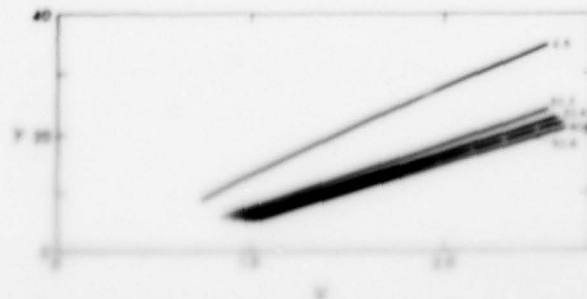
TABLE I. Flow conditions typical of certain pipeline systems.

Kinematic viscosity (cm^2/sec)	Pipe diam (cm)	Flow rate (m^3/sec)	Reynolds number	Velocity (m/sec)	u_0^* (m/sec)	α
0.0518	50.80	0.46	231 000	2.45	0.1066	0.0435
0.0421	50.80	0.46	274 000	2.27	0.0972	0.0428
0.0421	40.64	0.276	206 000	2.12	0.0938	0.0441
0.0421	30.48	0.147	146 000	2.01	0.0920	0.0456
0.0421	20.32	0.0736	220 000	2.27	0.1066	0.0469
0.0489	20.32	0.0736	95 000	2.27	0.1082	0.0476
0.025	15.49	0.046	154 000	2.42	0.1097	0.0453
0.0356	15.24	0.046	108 000	2.50	0.1185	0.0469

reduction technology in a problem area. Under these circumstances, Eq. (25) is useful for assessing the magnitude of drag reduction activity which might be expected under ideal conditions for combinations of pipe size, flow conditions, and assumed flow properties. In applying Eq. (25), (α), the normalized velocity parameter is computed from Eq. (29) and (β, θ_p) estimated for the drag reducer-process fluid combination of interest. Some examples applying the fractional drag reduction correlation are illustrated in Figs. 7 and 8. A sensitivity study of the influence of fluid characteristic time on drag reduction activity is presented in Fig. 7 where predictions are expressed as percent drag reduction versus bulk velocity expressed in units of m/sec. The pipe diameter is 20.8 cm, $\beta = 1$, and $\nu_p = 0.0418$ cm^2/sec for all examples, and $\theta_p = 1.0$, 1.25, 1.5, 1.75, and 2.0 msec. The so-called "diameter effect" is evident in Fig. 8 where simulations are presented for pipe diameters of 2.54, 20.3, 30.5, 40.6, and 50.8 cm. The assumed fluid properties are $\beta = 1$, $\nu_p = 0.0418$ cm^2/sec, and $\theta_f = 1.0$ msec. A correlation of the form (u_0^*, γ), in contrast to bulk velocity and drag reduction, clearly shows it is the magnitude of the friction velocity which determines the influence of size on drag reduction activity. In this regard, the information given in Table I suggests that for pipelines handling relatively low viscosity products, typical u_0^* values lie between 0.0914 and 0.1219 m/sec for sizes from 15.2 through 50.8 cm, and for fluid properties such that the Reynolds numbers are in the range from 90 000 to 300 000. From Table I, the corresponding average value of the normalized velocity parameter is $\alpha = 0.045$.

Noting that the correlation derived from the direct scale-up of turbulent flow data involves only the parameters (u_0^*, γ), and the solution to the fractional drag reduction correlation involves these same parameters, the known parameters (β, γ), and θ_p, a correlation of the form of Fig. 6 may be combined with the engineering approximation, Fig. 3, to obtain estimates of the functional dependence of the fluid characteristic time on flow conditions.

SUMMARY AND CONCLUSIONS

Detailed representation of the velocity profiles for drag reducing flows requires rather major modifications of the conventional relationships for Newtonian fluids. These, in principle, are ultimately related to structural

modifications of the flow. When these are manipulated to interpret the gross pressure drop or drag, attention to the internal details will usually provide little improvement over rather more simple relationships. As a result, gross flow measurements will generally be incapable of providing a severe test for discriminating between possible mechanisms.

A simple correlation of fractional drag reduction and solvent friction velocity is shown to be both diameter invariant for pipe flow and diameter ratio invariant for flow in an annular channel. That is, for a given combination of drag reducer additive and process fluid, superposition onto one master correlation can be achieved for turbulent viscoelastic flow in pipes and annuli. This friction velocity method is of practical value since from a limited comparison of experimental measurements of friction losses, with and without additive in the process fluid, one may scale up turbulent viscoelastic behavior by a direct and simple procedure to other flow conditions, pipe sizes, and annuli ratios without knowledge of viscoelastic properties. Experimentally, the diameter invariance of an experimentally determined correlation is found to be superior to the degree of superposition predicted from more complex semi-logarithmic resistance laws. The method will also yield a diameter invariant correlation of turbulent flow data on inelastic but rheologically complex systems on replacing the drag reduction parameter by the drag ratio. An approximation to the modified Seyer–Metzner resistance law is described which facilitates engineering scoping-type predictions of drag reduction activity using simple estimates of viscous and elastic properties and a graphical solution method. Scale up predictions derived from the approximation are in excellent agreement with those obtained from the more complicated semi-logarithmic equation.

G. C. Liddle, J. W. Hoyoos, D. L. Houston, H. Kim, D. L. Patterson, and R. T. Fang, Ind. Eng. Chem. Fund. **16,** 231

(1975).

[2]P. S. Virk, Am. Inst. Chem. Eng. **21,** 625 (1975).

[3]D. C. Bogue and A. B. Metzner, Ind. Eng. Chem. Fund. **2,** 143 (1963).

[4]A. Rollin and F. A. Seyer, Can. J. Chem. Eng. **50,** 714 (1972).

[5]T. T. Huang, Phys. Fluids **17,** 298 (1974).

[6]F. A. Seyer, and A. B. Metzner, Am. Inst. Chem. Eng. **15,** 426 (1969).

[7]F A. Seyer, Ph. D. thesis, The University of Delaware (1968).

[8]J. G. Savins, Rheol. Acta **6,** 323 (1967).

[9]G. Astarita, G. Greco, and L. Nicodemo, Am. Inst. Chem. Eng. **15,** 564 (1969).

[10]W. K. Lee, R. C. Vaseleski, and A. B. Metzner, Am. Inst. Chem. Eng. **20,** 128 (1974).

[11]N. F. Whitsitt, L. J. Harrington, and H. R. Crawford, in *Viscous Drag Reduction*, edited by C. S. Wells (Plenum, New York, 1969), p. 265.

[12]*Friction Loss Data in Oilfield Tubular Goods*, Technical Report, Dowell Division of the Dow Chemical Company (1967).

Laser Doppler velocimetry studies of early turbulence

J. L. Zakin,[a] C. C. Ni, and R. J. Hansen

Naval Research Laboratory, Washington, D.C. 20375

M. M. Reischman

Naval Ocean Systems Center, San Diego, California 92152

Laser Doppler anemometry is employed to measure the mean velocity and turbulence intensity in the early turbulence regime of the flow of a dilute polymer solution through a small-diameter tube. (This regime is initiated at an onset Reynolds number in the subcritical range, above which the polymer additive increases drag, and continues through the transitional Reynolds number range, where a continuous transition to turbulent flow with reduced drag is observed.) When the onset flow rate for early tubulence is exceeded, the mean velocity profile becomes progressively flatter with increasing flow rate. That is, a gradual transition from a laminar profile at onset to a more "turbulent-like" profile takes place. Turbulence intensities at the tube centerline are about one half those of a fully developed turbulent flow. The inference is drawn from these results that the onset of eary turbulence corresponds to the flow becoming hydrodynamically unstable due to viscoelastic effects introduced by the polymer additive and that the character of the flow is intermediate between laminar and fully developed turbulent flow.

I. INTRODUCTION

The drag-reducing effect of certain high-molecular-weight polymer additives in turbulent flows of Newtonian liquids has been thoroughly documented by experiments of the past three decades.[1-4] More recently, experiments at the Naval Research Laboratory[5-8] and elsewhere[9] have shown that small concentrations of these same additives can affect pipe flows at Reynolds numbers in the laminar and transitional range. This phenomenon, which has been called "early turbulence," occurs when the pipe diameter is sufficiently small and the solvent viscosity sufficiently large so that large shear rates are realized at subcritical Reynolds numbers. Under these circumstances the polymer solution exhibits laminar flow hydrodynamic drag behavior up to a fairly well-defined onset flow rate in the subcritical Reynolds number range. Above this onset condition the hydrodynamic drag exceeds that for laminar flow, the magnitude of the effect increasing with flow rate. As the flow rate is progressively increased a continuous transition from early turbulence to turbulent flow with reduced drag is observed. No transition region to turbulent flow with large pressure drop fluctuations is indicated by the pressure drop-flow rate measurements, in contrast to the behavior of a Newtonian liquid over the same Reynolds number range.

Previously reported experiments[8] established that early turbulence is unaffected by the inlet geometry of the tube, suggesting that it is not an entrance phenomenon. A small number of measurements of pressure drop at different distances from the inlet gave comparable results, lending further evidence to this conclusion.[6] The earlier experiments also indicated that the onset wall shear rate for early turbulence is, in general, only weakly dependent on solvent viscosity, polymer concentration, and polymer species.[6-8] An average value of about 1200 sec⁻¹ was observed for a number of solutions for a tube diameter of about 7.7 mm.

Since the deviations from predicted laminar pressure drops must be associated with deviations from the steady laminar profile, laser Doppler anemometry studies of early turbulence flows have been conducted. Measurements were made of velocity profiles, of the ratio of centerline to bulk velocity, of apparent centerline turbulence intensities, and of pressure gradients. Data were obtained for a polyethylene oxide additive (Union Carbide Polyox Coagulant) and a polyacrylamide additive (Dow Separan AP273). The measurements establish that early turbulence has characteristics intermediate between those of fully developed laminar and fully developed turbulent pipe flows.

II. APPARATUS AND PROCEDURES

A. Flow system

A schematic diagram of the apparatus is shown in Fig. 1. The flow system consisted of an upstream pressure reservoir from which liquid passed in a 25.4 mm i.d. tube to a settling chamber and then into the test pipe through a 68:1 area ratio tapered entrance. The pipe consisted of a 1.31 m long section of 7.7 mm i.d. brass tubing followed by two 1.27 m long sections of precision bore 7.94 mm ± 0.013 mm i.d. glass tubing. The sections were connected by butt joints. A measuring segment 25.4 mm long was located 3.41 m (430 diam) from the upstream end. The outside diam-
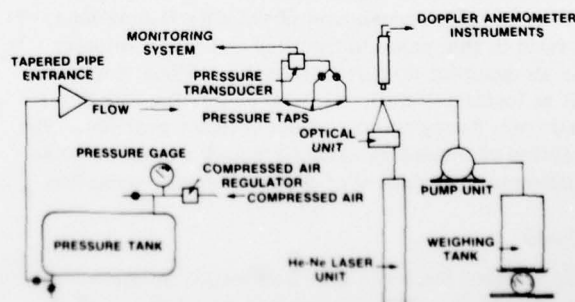

FIG. 1. Schematic pipe flow apparatus.

[a]Present address: University of Missouri-Rolla, Rolla, Mo. 65401.

eter of this segment was machined to have the same variations as the inside diameter, i.e., ±0.013 mm. The tube sections were secured in a straight position by notched mounts on a continuous aluminum (I-beam) rail. Movements of the rail were accomplished by vertical and horizontal tranversing devices and displacements were measured with micrometer gauges which could be read accurately within 0.005 mm.

For single-pass operation the liquid passed from the upstream pressure reservoir, through the test section and then through a Moyno positive displacement, progressing cavity, low internal shear rate (< 650 sec^{-1}) pump, which served as the flow rate controller. Flow rates were then measured with a weighing tank and stop watch. Upstream tank pressure was controlled by a pressure regulator on the feed line of the compressed air source. Recirculating operation was used when mechanical degradation of the polymer could be tolerated or when no additive was present. Under these circumstances the pump was placed between an open tank and the tapered entrance.

Three pressure taps were located 736.6, 431.8, and 127.0 mm upstream of the measuring segment. Tap holes were made by ultrasonic drilling which produced small size holes flush with the internal wall surface. Pressures were measured by a Celesco model P7D differential pressure transducer and carrier demodulator with a range of 1.3 psi full scale and an accuracy of ±0.0013 psi. Within the flow rate range of the experiments, constant gradients from different tapping points were observed, indicating that the flow was fully developed.

B. Laser anemometer

The laser anemometer used was DISA model 55L with a 50 mw He–Ne laser having a wavelength of 6328 Å. The optical components were arranged in the differential forward scatter mode. The 15.8° beam intersection angle and a laser beam diameter of 2.0 mm gave scattering volume dimensions of 0.38 mm length in the radial direction and 0.06 mm in diameter, both at the $1/e^2$ intensity points.

The electronic signal processing was accomplished by a standard DISA 55L tracker using both manual and the tracking modes. These methods were compared whenever possible. Both digital and analog readouts of frequency (velocity) were available. In addition, connection of the analog tracking signal to a DISA rms meter allowed the measurement of velocity fluctuations. The ratio of this value to the time-averaged velocity gives an apparent turbulent intensity. Since it was difficult to locate the wall, the tube centerline was determined from the symmetry of the velocity profiles. The centerline occasionally varied a small amount because of inadvertent movement of the micrometer mounting.

C. Fluid

The working fluid was a 59% by weight solution of glycerine in water. The solution was well mixed and allowed to attain thermal equilibrium prior to the mea-
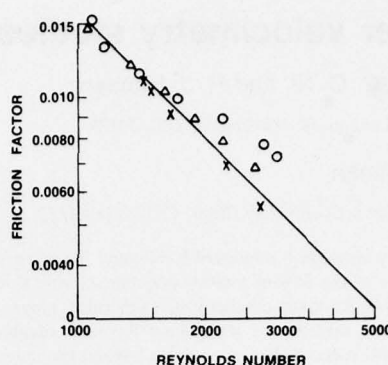
FIG. 2. Friction factor as a function of Reynolds number for a Newtonian liquid and solutions of two polymer additives: $-16/$ Reynolds number (Poiseuille Flow); × glycerine–water mixture; △ 50 ppm Separan AP273; ○ 50 ppm polyox coagulant.

surements. All make-up water was passed through a 0.1 μm cellulose filter and subsequently seeded with uniform polystyrene spheres of 1800 Å diam.

Polymer solutions were prepared by dispersing the polymer in pure isopropanol and adding the dispersion with stirring to water. The resultant concentrates were diluted to about 450 ppm of polymer and allowed to stand overnight before adding to the glycerine–water mixture from which the appropriate amount of water had been held out. Careful stirring insured uniform dispersion of the polymer. The refractive indices of the resultant solutions were close to 1.4150 at 77 °F.

III. RESULTS

A series of experiments were carried out using 50 ppm of Separan AP273, a polyacrylamide polymer of about 7×10^6 molecular weight and 50 ppm of Polyox Coagulant, a polyethylene oxide polymer of about 5×10^6 molecular weight dissolved in glycerine–water mixtures. Measurements were made of pressure gradients, centerline velocities, velocity profiles, and turbulence intensities.

A. Pressure drop measurements

The rise in pressure drop to a level above that predicted for laminar flow was observed with both polymers at a Reynolds number of about 1400 (see Fig. 2). This corresponds to a wall shear rate of about 1400 sec^{-1}, close to the value of 1200 reported previously.[6-8] For the glycerine–water solutions containing no polymer, no such effect in a number of experiments up to Reynolds number of over 3400 was observed. Transition for these flow conditions began at 3450–3700 for glycerine–water mixtures without polymer. The increase in pressure drop is substantially larger for the Polyox coagulant than for the Separan, a result which parallels the greater effectiveness of the former in a drag reduction experiment conducted in a small diameter tube at approximately equal polymer concentrations (see Fig. 3).
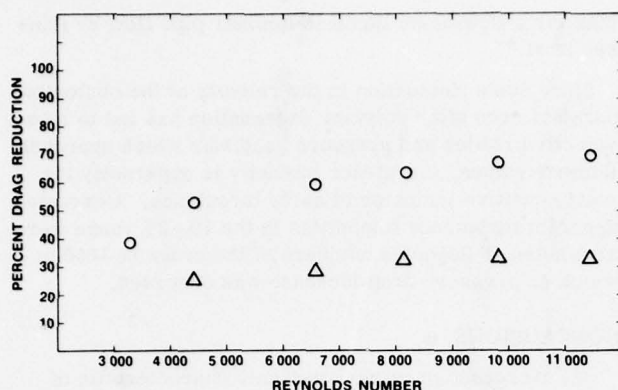
FIG. 3. Relative drag reduction effectiveness of two polymers in a 1.575 mm capillary tube flow: ○ 10 ppm Polyox coagulant; △ 12.5 ppm Separan AP273.

B. Velocity profiles

Measurements of velocity profiles were carried out to observe any changes in laminar profiles for the same conditions where increased pressure drops were obtained. Profiles at Reynolds numbers near 1800 of a fresh 50 ppm Polyox Coagulant solution and of a solution degraded by several hours of recirculation pumping are shown in Fig. 4. The mean velocity, V, of the fresh solution was 0.5% greater than the degraded solution but the higher temperature of the degraded solution gave it a slightly higher Reynolds number (1870 vs 1800).

Ratios of centerline to mean velocities in these runs were 1.82 for the fresh polymer solution compared with 1.91 for the degraded polymer solution. The lower value is a measure of the flatter profile and the higher one indicates a laminar profile. Typical values obtained with pure glycerine-water solutions were 1.90. Values in the range of 1.87–1.92 were obtained for many measurements of pure glycerine-water or degraded polymer solutions. The deviation from the expected value of two for laminar flow in a pipe is probably due to small errors in the calibration of the electronics and of the optical system.

The effects of Reynolds number on the friction factor and the ratio of U_{max}/V are shown in Tables I and II. f_m denotes the measured friction factor and f_c is the value calculated from the quotient $16/N_{Re}$. There is a consistent pattern of decrease in velocity ratio as the pressure gradient ratio increases. The velocity ratios are

TABLE I. Effect of Reynolds number on the centerline velocity and pressure drop for a glycerine-water mixture with 50 ppm Separan AP 273 in a 7.94 mm tube.

N_{Re}	U_{max}/V	f_m/f_c
1050	1.85	0.98
1335	1.85	1.01
1600	1.84	1.04
1875	1.83	1.05
2165	1.80	1.08
2610	1.78	1.11

TABLE II. Effect of Reynolds number on centerline velocity and pressure drop for a glycerine-water mixture with 50 ppm Polyox Coagulant in a 7.94 mm tube.

N_{Re}	U_{max}/V	f_m/f_c
1075	1.83	1.05
1150	1.83	0.96
1390	1.80	1.00
1715	1.78	1.06
2175	1.78	1.22
2720	1.75	1.32
2920	1.74	1.33

close for the two polymers although the Polyox Coagulant has a much larger effect on the pressure gradient.

C. Fluctuating velocity levels

Measurements of the rms fluctuating velocity voltage fed to the tracker were recorded for positions near the centerline for many of the solutions tested. The measured values were dependent on the band width setting of the tracker. (The 1% setting gave rms voltages 50%–100% greater than the 0.5% setting.) Values of rms voltages were normalized with mean velocity voltage measurements giving an apparent turbulent intensity. Values of apparent turbulence intensity of about 0.6% were observed at a Reynolds number of 1400 for glycerine-water mixtures and decreased to about 0.5% at 2100 (both measured at 0.5% bandwidth). For these laminar flows, a value of zero would be expected and the measured values reflect the finite size of the probe volume and noise in the measuring system. The latter is much larger than the former.

Intensity measurements made with a 50 ppm solution of Polyox coagulant are shown in Table III. A value of about 2.7% was obtained at a Reynolds number of about 2500 (1% bandwidth). This value decreased to about 1.5% at a similar Reynolds number after 7 passes through the system and to 0.9% after complete degrada-

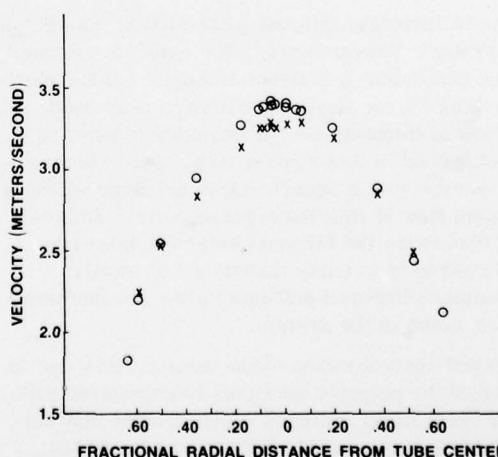FIG. 4. Velocity profiles for a glycerine-water mixture with 50 ppm Polyox coagulant in a 7.94 mm tube at a Reynolds number of 1800; × fresh solution ($U_{max}/V = 1.82$); ○ degraded solution ($U_{max}/V = 1.91$).

Zakin, Ni, Hansen, and Reischman

TABLE III. Effect of polymer degradation on the apparent centerline turbulence intensity for a glycerine-water mixture with 50 ppm Polyox Coagulant in a 7.94 mm tube at a Reynolds number of 2500.

Polymer solution condition	% Apparent turbulence intensity (1% bandwidth) setting	$\frac{U_{max}}{V}$	$\frac{f_m}{f_c}$
Fresh	2.7	1.80	1.22
Partially degraded (7 passes through system)	1.5	1.91	0.97
Degraded (20 passes through system)	0.9	1.90	0.95

tion (0.6% at 0.5% bandwidth). Also shown in this table are values of U_{max}/V and f_m/f_c. It is interesting to note that high values of apparent turbulence intensity (1.5%) were observed after the measured velocity and pressure gradient ratios reached apparently normal laminar values. Thus, the fluctuations in center-line velocity caused by the polymer persist even when the effect of the polymer on velocity profile and on pressure drop cannot be detected.

IV. DISCUSSION OF RESULTS

The velocity measurements show that the increased pressure drops associated with early turbulence are accompanied by a flattening of the velocity profile. The profiles lie between laminar and turbulent profiles. In the central core they are more like laminar profiles than turbulent. Their slopes close to the walls can only be inferred from the increased hydrodynamic drag.

Flattening of laminar velocity profiles can also occur if the fluid is shear thinning. The ratio of maximum to bulk mean velocity, U_{max}/V, is equal to $n+1/3n+1$. Thus, if the power law index, n, was 0.9 the ratio would be 1.95. However, shear thinning behavior is not expected at the low concentration studied here. Measurements of the effect of shear rate on viscosity in the range of 100 to 400 reciprocal seconds showed no significant deviation of n from unity.

The apparent turbulent intensities are lower than those observed in fully turbulent flows. For example, Pennell et al.[10] show centerline turbulence intensity values which are greater than 5% for Reynolds numbers near 3000. Similar values of intensity near a Reynolds number of 3000 were observed in this system with a pure glycerine-water solution with a square-edged entrance which gives turbulent flow at this Reynolds number.[8] This value is more than twice the largest centerline intensity values observed here in early turbulence at similar Reynolds numbers (tapered entrance) after corrections are made for noise in the system.

The observed destablization of the laminar flow due to the presence of the polymer additives is consistent with a number of theoretical analyses which predict that viscoelastic fluids are less stable than Newtonian fluids. Kundu[11] for example, predicted that the critical Reynolds number in plane Poiseuille flow would be lowered by a polymer additive. The rate of decay of damped disturbances was found to be less for a polymer solution

than for a Newtonian liquid in laminar pipe flow by Hansen et al.[8]

Since some fluctuation in the velocity at the centerline persists even after polymer degradation has led to mean velocity profiles and pressure gradients which approach laminar values, turbulence intensity is apparently the most sensitive indicator of early turbulence. Corrected apparent turbulence intensities in the 1%-2% range were also noted at Reynolds numbers of the order of 1000 at which no pressure drop increase was observed.

CONCLUSIONS

(1) Increased pressure gradients characteristic of early turbulence are accompanied by a flattening of the velocity profile and high turbulence intensities and flow character is intermediate between laminar and turbulent.

(2) Polymers which are more effective as drag reducers are also more effective in increasing early turbulence effects. Thus, polymer solution characteristics which enhance drag reduction may be the same ones which promote early turbulence.

(3) High turbulence intensity and flattened profiles are observed at low flow rates where pressure increases are not detected.

(4) At higher Reynolds numbers, where pressure increases are larger, higher intensities persist even after most of increased pressure loss is lost due to polymer degradation.

[1] G. K. Patterson, J. L. Zakin, and J. M. Rodriguez, Ind. Eng. Chem. **61**, 22 (1969).
[2] J. W. Hoyt, J. Basic Eng. **94**, 258 (1972).
[3] R. C. Little, R. J. Hansen, D. L. Hunston, O. K. Kim, R. L. Patterson, and R. Y. Ting, Ind. Eng. Chem. Fund. **14**, 283 (1975).
[4] P. S. Virk, AIChE J. **21**, 625 (1975).
[5] R. C. Little and M. Wiegard, J. Appl. Polym. Sci. **14**, 409 (1970).
[6] P. C. Forame, R. J. Hansen, and R. C. Little, AIChE J. **18**, 213 (1972).
[7] R. J. Hansen, R. C. Little, and P. C. Forame, J. Chem. Eng. Jpn. **6**, 310 (1973).
[8] R. J. Hansen, R. C. Little, M. M. Reischman, and M. D. Kelleher, in *Proceedings of the First International Conference on Drag Reduction*, edited by N. G. Coles (BHRA Fluid Engineering, Cranfield, United Kingdom, 1974), p. B4-45.
[9] A. Ram and A. Tamir, J. Appl. Polym. Sci. **8**, 2751 (1964).
[10] W. T. Pennell, E. M. Sparrow, and E. R. G. Eckert, Int. J. Heat Mass Transfer **15**, 1067 (1972).
[11] P. K. Kundu, Phys. Fluids 15, 1207 (1972).

Turbulence structure in drag reducing polymer solutions

Gary K. Patterson, Jack Chosnek, and J. L. Zakin

University of Missouri-Rolla, Rolla, Missouri 65401

Longitudinal turbulence intensities measured by split-film anemometry in degraded polymer solutions in pipe flow peaked much farther from the wall than longitudinal turbulence intensities in a Newtonian oil at the same Reynolds numbers. The peak values were at about the same level for the degraded solutions as for the oil, but were higher and nearer the wall for fresh polymer solutions. Radial turbulence intensities were lower for the polymer solutions at all locations under all conditions. Drag reduction for the polymer solutions ranged from 1 to 21% based on Newtonian fluid of equal viscosity. For the fresh solutions the Reynolds stresses dropped to zero or low values much farther from the wall than normal, indicating a region of almost complete turbulence shear strain recovery near the wall (positive uv excursions balanced negative uv excursions). Numerical computations with a turbulence model involving balance equations for turbulence energy and turbulence energy dissipation rate (the k-ϵ model) show that the location of the peak turbulence intensity (energy) is sensitive to the model for Reynolds stress production. It was possible to model the velocity and turbulence intensity profiles and predict the correct level of drag reduction using the k-ϵ model with an eddy viscosity as a function of shear relaxation time.

INTRODUCTION

Turbulence measurements in drag reducing polymer solution flows have led to various, seemingly conflicting, interpretations of the phenomenon. On the one hand some investigators have made such measurements with only one polymer solution and one Reynolds number[1-3] or for a very narrow Reynolds number range,[4] leading, in most cases, to interpretations based on only one type of behavior. On the other hand, other investigators have encountered quite different types of turbulence behavior, measured by the same method in each case, for either different polymer solutions or wide Reynolds number ranges spanning weak to strong drag reduction.[5-7] All these differing results have resulted in considerable confusion.

The intent of this paper is to show that all of these turbulence measurements may, in fact, be valid and that diverse effects of the viscoelastic properties of the polymer solutions on the various terms of the Reynolds equations of the mean flow, turbulence energy, and turbulence energy dissipation rate may be responsible for the variety of behavior types.

Review of previous experimental results

Early measurements of turbulence in drag reducing polymer flows included those of Patterson,[5] Rodriguez,[6] Rodriguez *et al.*,[7] and Seyer and Metzner.[8] Patterson and Rodriguez made measurements with wedge-type hot-film probes and because of the geometry of these probes *were not able to measure close to the wall*, where it is generally agreed that the effects causing drag reduction occur. Those measurements, in a variety of polymer solvent systems and a wide range of flow rates in a 2.5-cm smooth pipe, yielded longitudinal turbulence intensities which were in some cases higher and in other cases lower than the equivalent u^*-reduced intensities in a Newtonian fluid. For a given polymer solution, the intensities depended on flow rate (Reynolds number) as shown by each of the curves in Fig. 1. Where intensity profiles were measured, intensities in the entire profile were higher than normal or lower than normal. (The

measurements were to within 0.25R of the wall, so they did not include the near wall turbulence production region.) These data illustrate that, like friction factor, turbulence intensity does not correlate with Reynolds number alone for drag reducing solutions. In fact, as shown in Fig. 2, the data may be organized roughly into classes of behavior by plotting intensity versus fraction *friction reduction*. The significance of the three classes shown in Fig. 2 is not known, but each polymer always seems to relate to a given class regardless of concentration or level of degradation. This seems to indicate a relationship of behavior class to molecular structure.
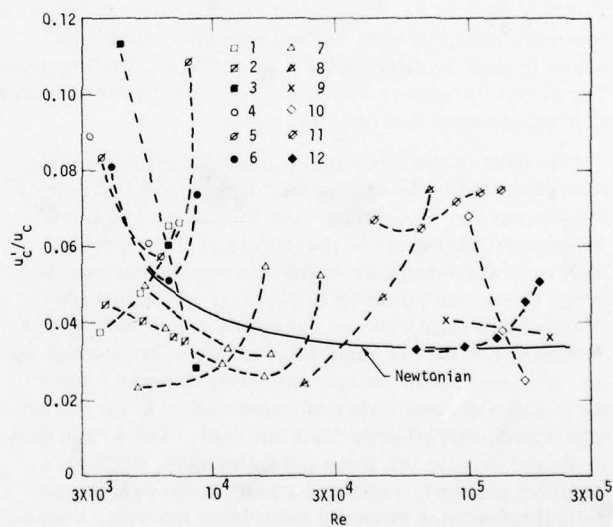
FIG. 1. Longitudinal turbulence intensities for a variety of polymer solutions at the center of the pipe. Data point indentification: 1, 2, and 3—fresh, intermediate, and degraded 0.2% polyisobutylene (PIB L-200) in oil, respectively; 4, 5, and 6—fresh, intermediate, and degraded 0.4% PIB L-200 in oil, respectively; 7—intermediate 0.4% PIB L-200 in cyclohexane; 8—fresh 0.1% PIB L-200 in cyclohexane; 9—degraded 0.05% PIB L-200 in toluene; 10—degraded 0.02% polyisoprene in toluene; 11—fresh 0.08% polyisoprene in toluene; 12—fresh 0.2% polyethylene oxide (WSR 201) in benzene.
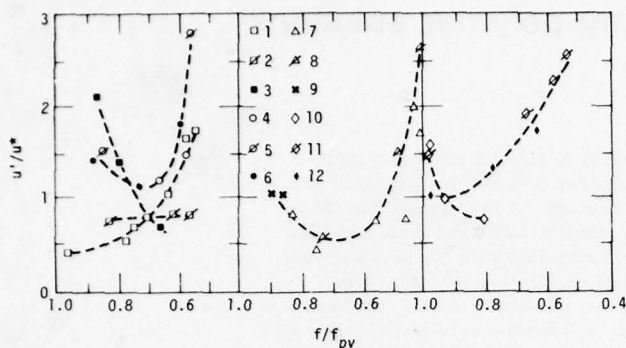
FIG. 2. Longitudinal turbulence intensities as a function of fraction friction factor reduction. Data point identification as in Fig. 1.

These data might suggest a viscoelastic interaction between the solution and the hot-film probe; however, that is not likely because of tests conducted by Rodriguez *et al.*[9] Oscillation of a wedge probe in the longitudinal direction in high velocity flows of drag reducing polymer solution through a 2.5-cm pipe showed that the hot-film anemometer measured essentially correct intensity values throughout the energy containing range of frequencies.

The Seyer and Metzner[7] data were obtained by streak photography for two widely different flow rates in 2.5-cm smooth pipe for two concentrations of a polyacrylamide. The lower concentration produced considerable drag reduction at the higher flow rate but not much deviation of turbulence measurements from Newtonian values at either flow rate. The higher concentration solution, however, caused a shift in the longitudinal turbulence intensity peak away from the wall at the higher flow rate. The radial turbulence intensities were much lower than Newtonian values for both flow rates.

This shift in the longitudinal intensity peak has also been observed by Rudd,[1] Logan,[2] Kumor and Sylvester,[3] Reischman and Tiederman,[4] and Mizushina and Usui.[10] There are differences in the details of these profiles, however, which indicate more than simply various degrees of viscous sublayer thickening, which has frequently been mentioned as a possible cause of drag reduction. The data of Rudd were obtained by laser-Doppler anemometry in an approximately 2.5-cm square duct, and indicated highly elevated values of turbulence with a peak shifted away from the wall. The Logan data in almost exactly the same geometry duct, but with a different polymer, exhibited a shift in the peak longitudinal turbulence intensity away from the wall, a small increase in peak level, and a reduction in the transverse turbulence intensity. The Kumor and Sylvester data for flow over a flat plate seemed to yield about the same longitudinal turbulence results as the Rudd data. In both cases only one flow rate was used.

The Reischman and Tiederman data indicated behavior quite different from the Rudd and Logan data, but the former used a channel with a large aspect ratio in order to avoid the secondary flow patterns of square ducts.

Reischman and Tiederman claimed that the measurements in square ducts showed effects of the polymer solution viscoelasticity on both turbulence intensities *and* secondary flows, making the effects of drag reduction very hard to interpret. Their data showed a much greater displacement of the longitudinal turbulence peak from the wall, but only a slight increase in friction velocity-normalized values. Centerline values were about the same as for a Newtonian fluid.

The velocity profile data for drag reduction measured by several investigators have indicated a thickened viscous sublayer because the $u^+ = y^+$ curve was followed to a higher value of y^+, but the data of Reischman and Tiederman did not. The logarithmic outer portion of the profiles was higher than for Newtonian fluid, and the buffer portion showed increased slope from $y^+ = 5$ outward. If there is no $\overline{uv}$-Reynolds stress, the velocity profile must follow $u^+ = y^+$, but if Reynolds stresses are only partly suppressed, the velocity profile slope will lie between $u^+ = y^+$ and that for the Newtonian buffer region.

As pointed out by Virk,[11] the Reynolds stresses measured by Logan were substantially reduced below those for Newtonian fluid for the region $5 < y^+ < 60$. This was discussed at length by Logan,[12] and he presented the same velocity profile behavior for his solution as reported by Reischman and Tiederman. In other words, since the Reynolds stresses were only reduced, not zero, in the buffer region starting at $y^+ = 5$, the velocity profile slope was lower than that for $u^+ = y^+$. Most data reported,[11,13] however, indicate completely suppressed Reynolds stresses to y^+ values greater than 5, since $u^+ = y^+$ to those y^+ values.

TURBULENCE MODELS FOR DRAG REDUCTION

It has long been expected that modification of the fluid response to locally changing rates of shear rate in turbulence by the viscoelasticity of polymer solutions is in some way responsible for drag reduction.[14–16] This idea was incorporated into a drag reduction model based on the estimated reduction of turbulence energy dissipation rate by viscoelastic response by Patterson and Zakin.[15] In this model, the ratio of turbulence energy dissipation rate for a viscoelastic fluid to that for a Newtonian fluid was given as

$$\frac{\epsilon}{\epsilon_s} = \frac{\nu \int_0^\infty \{n^2 F(n) dn / [1 + An^2 (u'/\overline{u})^2 T^2]\}}{[\nu_s \int_0^\infty n^2 F(n) \, dn]} ,$$

where $n^2 F(n)$ is interpreted as the turbulence energy dissipation spectrum, T is the solution relaxation time, A is a constant, and the subscript s refers to the solvent. A number of assumptions were necessary to obtain this relationship, the most severe being the assumption of isotropic turbulence energy dissipation rates in the numerator and the denominator. An empirical relationship between peak turbulence energy dissipation rate and wall shear stress (momentum transport rate) was used to obtain

$$\tau_w / \tau_{w_s} \approx (\epsilon/\epsilon_s)^{0.8} (\nu/\nu_s)^{0.6} .$$

This relationship was reasonably successful in predict-

ing levels of drag reduction for solutions for which the relaxation time T was calculated from normal stress difference measurements. The success of the model did not prove a particular mechanism but confirmed the link between viscoelasticity and drag reduction. The model also illustrated that turbulence intensities in the presence of drag reduction could be greater than those for a Newtonian fluid, but it provided no means of estimating the turbulence intensities during drag reduction. A complete turbulence energy balance would be necessary to estimate turbulence intensity profiles.

Virk[11] applied ideas from his elastic sublayer model to the turbulence energy balance problem in order to estimate the profiles of turbulence energy for low and high levels of drag reduction. He hypothesized that the gradient transport of turbulence energy must be reduced during the drag reduction to a degree similar to the momentum transport rate (shear stress). This led to an approximate picture of the changes in turbulence energy profile for drag reduction. With low drag reduction a raised peak in turbulence intensity results only in the near wall region, because the elastic sublayer is very thin. With high drag reduction the peak turbulence intensities are extended well outward from the wall in accordance with the thickened elastic sublayer. Virk's model predicts a maximum ratio of drag reduction turbulence peak intensity to Newtonian peak intensity of 2.2 at maximum drag reduction.

In an effort to explain several of the phenomenological aspects of drag reduction; i.e., "onset," drag reduction in very dilute solutions, the "Newtonian plug," occurrence of a highest effective concentration, and the maximum drag reduction asymptote; Lumley[17] formulated a qualitative model of turbulence in polymer solution drag reduction based on the unbounded expansion of polymer molecules in unsteady vorticity fields. Unbounded expansion which would produce orders-of-magnitude increases in elongational viscosity, was hypothesized to occur when $2\overline{S^2}\tau_L T - 1 \approx 2u_\tau^2 T/\nu - 1 \geq 0$, where T is a polymer molecular relaxation time, τ_L is the Lagrangian time scale of strain rate, and $\overline{S^2}$ is the mean-square strain rate. The second form using boundary layer variables is an onset criterion for drag reduction. In order for drag reduction to occur, the relaxation time T must be sufficiently increased over low shear rate values by unbounded molecular expansion. Lumley felt that unbounded expansion could explain very low concentration drag reduction.

According to the model unbounded expansion of polymer molecules may only occur in the turbulent region of flow. When this happens (and the criterion in the preceding paragraph is met), the molecules in the turbulent region expand and increase viscosity in their immediate locality. If k_d (peak dissipation wavenumber) $\approx 0.2(\epsilon/\nu^3)^{1/4}$ and $\epsilon \approx u_\tau^3/0.4y$ and if k_e (peak turbulence energy wavenumber) $\approx 1/y$ and turbulence can only exist when $k_d > k_e$,[18] Lumley showed that an increase of viscosity in the turbulent region could shift the k_d curve in such a way as to force the turbulent region farther from the wall. This would explain the thickening of the viscous sublayer observed in many cases and, since the turbu-

lence in the outer layer would be essentially unchanged, a "Newtonian plug" could exist. When $k_d \geq k_e$ at the pipe centerline or boundary layer edge, maximum drag reduction should result. Lumley also showed the possibility of a highest effective concentration (where concentration increase does not increase drag reduction) and increased turbulence intensities to be consistent with the unbounded expansion model. He hypothesized that the so-called "large eddies," which produce little Reynolds stress, can grow to higher intensities when viscous sublayer thickness is increased.

An interesting observation can be made with the Lumley model. If the rate of turbulence energy dissipation is decreased by viscoelastic response (as in the Patterson–Zakin model), essentially all the conclusions from the Lumley model remain the same. This would require, of course, that the effective polymer solution relaxation time T be related to concentration in the same way as viscosity in the unbounded expansion model. Another interesting observation is that the unbounded viscosity increase due to unbounded polymer molecule expansion may be the same phenomenon as the very high elongational viscosity predicted for drag reducing solutions. It has been hypothesized that such elongational viscosities can inhibit rapid fluid ejections from the viscous sublayer.[7,19,20]

EXPERIMENTAL MEASUREMENTS

Anemometry. In order to make further measurements of turbulence profiles closely approaching the pipe wall at a variety of drag reducing conditions, the split-film anemometer was used. A diagram of the sensing element of the probe is shown in Fig. 3. The probe is cylindrical with each of the two half-cylinder films connected independently to an anemometer circuit.

Development work on response equations and methods of measurement with this probe has been done by Olin and Kiland,[21] Shaw,[22] Spencer and Jones,[23] and Blinco and Sandborn.[24] Spencer and Jones formulated a response equation of the form

$$Q_i \approx (A_i + B_i U_e^n)(1 + \alpha_i V/U_e),$$

where Q_i is the rate of power dissipation from film i, U_e is the effective velocity, and α_i is a geometrical sensitivity factor related to the angular sensitivity of the sensor.
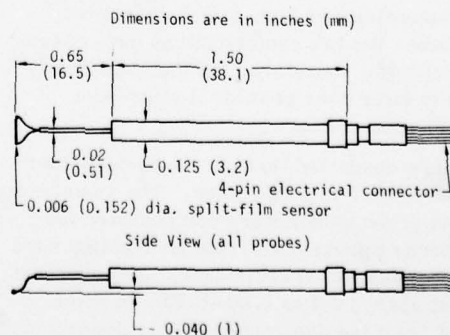

FIG. 3. Diagram of split-film anemometer probe.

If the probe is used without linearizing either channel, the following equations relating u' and v' to sum and difference voltages from the anemometers result:

$$u'/\overline{U} = 2(e_1 + e_2)'/(n_1 B_1 \overline{U}_1^n/\overline{E}_1 + n_2 B_2 \overline{U}_2^n/\overline{E}_2) \,, \tag{1}$$

$$v'/\overline{U} = 2(e_1 - e_2)'/[\alpha(\overline{E}_1 + \overline{E}_2)] \,, \tag{2}$$

where the apostrophe means rms value and $\alpha = \alpha_1 = -\alpha_2$. If the signal from each of the anemometers is linearized to give

$$(E_1)_l = C_l U_e \,, \tag{3}$$

then choosing $C_1 = C_2 = C$ for both linearizers we can obtain simple expressions for the rms values of the axial and radial intensities:

$$u' = (e_1 + e_2)'/2C \,, \tag{4}$$

$$v' = (e_1 - e_2)'/C\alpha(1/n_1 + 1/n_2) \,. \tag{5}$$

In both cases the angular sensitivity α has to either be measured by azimuthal yaw calibration or its value assumed from semi-empirical considerations. Spencer and Jones[23] obtained a value of 0.65, but in measurements with the probe used in these investigations α was adjusted to a value of 0.25 to obtain radial turbulence intensities near accepted values when a Newtonian liquid was used.

Three conventional hot-film probes and three different split-film probes were used in the anemometry measurements. All probes used were manufactured by Thermo Systems, Inc. (TSI). The conventional, single channel probes were: a parabolic probe model 1235; a cone probe model 1230W; and a cylindrical probe 0.0025 cm in diameter, model 1212-10.

Two split-film probes 0.015 cm in diameter, both model 1288AW, were used to obtain most of the split-film anemometry results. One of the probes belonged to the Max-Planck-Institut für Strömungsforschung in Göttingen, West Germany, where part of the work was done. The probes were designed with prongs bent so that the sensors could be placed as close as possible to the wall of the pipe. A third probe of the same design, but without a quartz coating, model 1288, was used for the final runs with the polymer solution after the first probe was damaged during a run (most probably a small piece of undissolved polymer collided with the sensor).

The anemometers used in each case were two DISA model 55D01 units operated in the constant temperature mode. They could be used with two bridge configurations, for high sensitivity or high-power operation. Comparison between the two configurations gave essentially the same results; therefore, the high sensitivity one was chosen in later runs because it afforded a greater signal-to-noise ratio.

The probes were connected through the probe holder to the anemometers by 5 m long cables. The resistances of the cables and probe holder were compensated for after using a shorting probe built from gold-plated wire to measure the compensation resistance. The overheat ratio was almost always set to 1.08–1.10. In some cases the output from the anemometers was linearized with DISA model 55D10 linearizers.
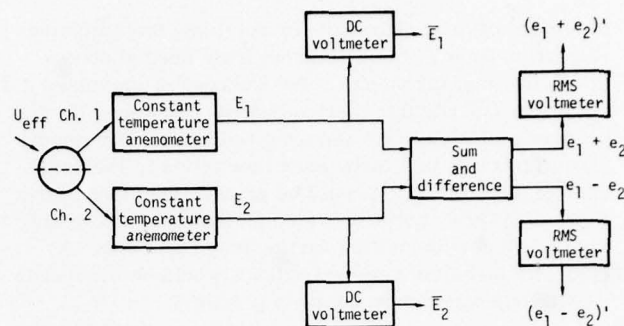
FIG. 4. Schematic of electronic equipment used for turbulence intensity measurements with the split-film probe.

The dc voltages from the anemometers were read by a Hewlett–Packard model 5326B integrating digital voltmeter using an integrating time of 10 sec. Four or five consecutive readings per velocity setting were taken, with their average determining the value used. The ac voltages were read on a DISA model 55D35 RMS meter, using an integrating time of 3 or 10 sec. Since for the split-film measurements we were interested only in the instantaneous sum or difference of the ac voltages, the outputs of the anemometers were connected to a DISA model 55A06 Random Signal Correlator. This apparatus provided the sum and difference at two of its outputs, which could then be read on the rms meter or recorded simultaneously on magnetic tape. The recorder used for this purpose, and for recording the direct output of the anemometer for single channel probes, was a Lyrec model TR-60 tape recorder (sold in the U.S. by DISA). All recordings were made at a tape speed of 6 ips with recording times ranging from 20 to 50 sec. Spectrum analysis of these recordings was carried out either with a Krohn–Hite model 3323 variable filter or with a Hewlett–Packard model 8064 spectrum analyzer. Figure 4 is a schematic of the basic electronics and their arrangement for making the velocity and turbulence measurements. It was found that significant ground loops could be avoided only if all ground connections but one were removed.

Two types of experimental runs were made: calibrations and velocity-turbulence profiles. The procedure and description of quantities measured follow.

(1) *Calibration runs.* A calibration run consisted of between 18 to 24 readings of voltage versus velocity at the pipe axis. The velocity was varied at random, instead of in an ascending or descending pattern in order to detect any shifts in voltage caused either by deposition of impurities on the probe (which was found to be of major consequence) or by anemometer drift (which was found to be negligible). When working with the polymer solutions, pressure drop readings were also taken at each velocity in order to determine the drag and friction factor ratios. (The drag ratio is the solution friction factor over solvent friction factor at the same flow rate; the friction factor ratio is the solution friction factor over solvent friction factor at the same Reynolds number.)

FIG. 5. Schematic of pipe system used at University of Missouri-Rolla. (The Max-Planck Institut system was very similar, except that the measuring tube was Plexiglas instead of stainless steel.)

Besides the calibration curve itself, values of centerline turbulence intensities versus Reynolds number were obtained during a calibration run.

(2) *Velocity profile runs.* Between 15 to 22 (usually 16) readings at different distances from the wall were taken for each run of this type. Half the number of readings was taken first by traversing the probe from the center of th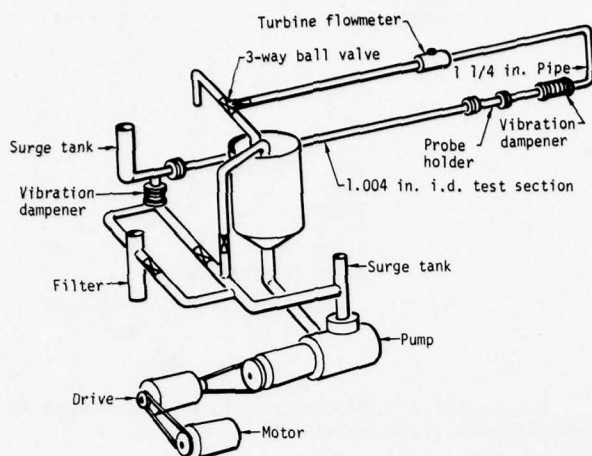e pipe to the wall, thereafter returning the probe to a position near the center of the pipe and taking the other half of the readings at points located between the points of the first traverse.

During these runs mean velocity profiles and turbulence intensity profiles were obtained. Tape recordings of the outputs of the anemometers were made at a minimum of four locations. From these recordings energy spectra were obtained. During several runs the Reynolds stress $\overline{uv}$ was also measured at every radial location by using a correlator to determine the correlation between the sum and difference signals. This was done on-line for the fresh solutions without tape recording.

EQUIPMENT AND MATERIALS

Axial and radial turbulence intensities and energy spectra were obtained for mineral oil and for a 0.2% by weight solution of polyisobutylene in the same oil. One of these oils, designated Stock 244, was donated by the Mobil Oil Company. Its kinematic viscosity was measured using a standard Ubbelohde viscometer and was found to be $3.43 \pm 0.4\%$ cst at $30.0\,^\circ$C. Its density was measured as a function of temperature and can be described, in the range 21–30 °C, by the equation

$$\rho(\text{g/cm}^3) = 0.863675 - 6.77687 \times 10^{-4} T\,(^\circ\text{C}).$$

The other oil was a Shell mineral oil of unknown designation with viscosity of 4.8 cp and density of 0.85 g/cm³ at 30 °C.

The polyisobutylene, Vistanex L-200 was obtained from the Enjay Corp., Baton Rouge, Louisiana, and had

an estimated molecular weight of $M_v = 4.7 \times 10^6$.[5] The polymer solution was prepared by dissolving the proper amount of polymer in a 0.038 m³ Pyrex vessel using a slow stirrer. This solution was then added to the oil already present in the pipe system and pumped for a short period of time in order to attain uniform concentration. Before and after each run with the polymer solution, samples of the liquid were taken and its viscosity determined as a function of shear rate by using a Fann model 35A viscometer.

Figure 5 is a schematic of the pipe system used at the University of Missouri-Rolla.[31] The test section was constructed of a 3.3 m length of nominal 2.5 cm i.d. stainless steel tubing. Three pressure taps separated by 45.7 cm lengths were bored beginning 67 diam from the tube entrance. The taps were bored with a No. 72 drill and then the entire length of the tube was honed to eliminate any burrs or irregularities and to insure a hydraulically smooth test section. The pressure drop measurements were made with an inverted oil manometer for the high and medium pressure drops, and with an oil-over Meriam fluid (No. D-2930, nominal specific weight 1.0) manometer for the low pressure drops. The system at the Max-Planck-Institut was very similar except that the pipe for measurement was made of Plexiglas.

Fluid from a 0.227 m³ stainless steel tank was pumped by a Viking model Q-124 rotary pump, driven by a 10-hp hydraulic variable speed transmission. Surge volumes were placed at the outlet of the pump and at the entrance to the test section to eliminate pulsations in the flow. The test section was isolated from the rest of the system by Teflon expansion joints, used to eliminate vibrations. A bypass line allowed diversion of flow so that it would pass through a cartridge-type filter. Two different filters were used; a Hayward filter having a cartridge to which a stainless steel cloth with a nominal opening of 43 μm was attached, and a Filterite model LM0205-1 having a cartridge of sintered stainless steel with a nominal opening of 10 μm.

The flow rate was constantly monitored by using a Brooks model HP-24N turbine flowmeter. The output of the flowmeter was read on a Transistor Specialties Inc. model 361 digital counter. The flowmeter was calibrated by diverting the flow into a weighing tank. The resulting calibration was a straight line for counts versus flow rate in the range of 0.68 to 3.78 kg/sec. Flow rates could be determined to within ±1%.

The pipe system was designed to maintain a constant temperature of 30.0 °C. The temperature could be controlled to ± 0.05 °C. This was accomplished by having two copper tubing coils immersed in the tank in one of which continuously ran a trickle of hot water, and in the other ran cooling water controlled with the aid of a thermoregulator, relay and solenoid valve.

The traversing holder for the anemometer probes was located at the end of the test section in such a way that the tip of the probe was inside the test section about 3 pipe diam from its end. The resulting entrance length-to-diameter ratio (L/D) was therefore equal to about 117
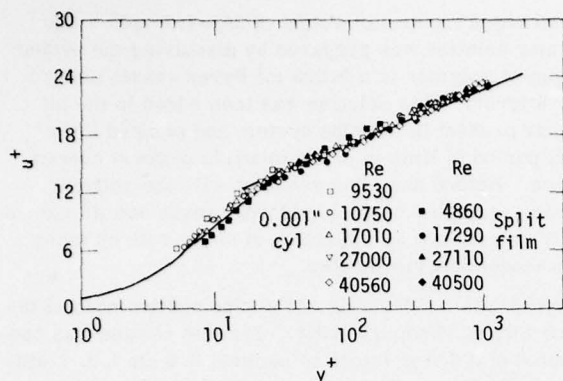
FIG. 6. Velocity profiles measured in a Newtonian oil.

FIG. 8. Longitudinal turbulence intensities in a Newtonian oil measured with a 0.015-cm split-film probe.

for the anemometry measurements. The probe holder could position the probe with a precision of 0.0025 cm.

DATA WITH NEWTONIAN FLUID

Data were obtained with the Newtonian oils in both pipe systems in order to ascertain proper operation of the equipment. The data obtained in each case, both for the Newtonian oils and the polymer solutions, were velocity profiles, turbulence intensity profiles (longitudinal and radial), energy spectra, and in some cases the Reynolds shear stress.

In the cases of the Newtonian oils the data obtained with both ordinary cylindrical and split-film probes were generally in accord with data obtained previously in pipe flows. The velocity profile results obtained are shown in Fig. 6 for a Reynolds number range of 4860 to 40 560. These data match the established inner variable correlation very well. Figures 7 and 8 show the longitudinal turbulence intensity data measured with the 0.0025-cm cylindrical probe and the split-film probe, respectively.

Figures 7 and 8 show the behavior of the longitudinal turbulence intensity profiles with various Reynolds numbers for measurements with the 0.0025-cm cylinder and split-film probes, respectively. The curves start at about the same turbulence-intensity level at the center

of the tube, intersect as the wall is approached, and reach a lower maximum value with increasing Reynolds number. The dashed line in Fig. 7 represents the probable level of the intensities if there had not been eddy shedding for the 40 560 Reynolds number. Figure 8 shows the data of Laufer[25] for comparison. The data reported here peak to lower values. The discrepancy will be discussed in greater detail in the following paragraphs.

Similar turbulence intensity variations with Reynolds number were obtained by Perry and Abell[26] in their turbulence measurements in air in a 111-mm (4.37-in.) pipe. Their Reynolds-number range was much higher, from 80 000 to 350 000 and only for the lowest Reynolds number do their turbulence intensities show a peak, with all the other data reaching only a little farther toward the wall from the intersection point. Their data show a region of constant turbulence which they call the region of overlap between the "inner flow region" ($y/R < 0.1$) and the "outer flow region" ($y^+ > 100$). Since the y^+ value which corresponds to a given y/R value is dependent on the pipe Reynolds number and increases as pipe Reynolds number increases, overlap of the inner and outer flow regions occurs only at higher Reynolds numbers. For instance, in the data obtained in this work the overlap region exists only at the highest Reynolds number (40 560) and even then is extremely small ($100 < y^+ < 106$). If the data at even higher Reynolds numbers followed the trend shown in Fig. 7 and 8, part of the intensity profile curve would probably be horizontal, so these results appear to agree with those of Perry and Abell.

Besides following the same trend, the longitudinal intensities measured with the split film were in close agreement with those measured with the 0.0025 cm cylinder probe as has been seen. Near the wall the split-film probe seems to give lower intensities in the region of up to 6 or 7 probe diam from the wall. This is probably due to interference to the flow by the small cylinder and its supports. The probe used for most of the oil results had relatively large "knobs" at the joints of the supports and sensing cylinder formed by a too heavy protective coating of epoxy, and they probably were the cause of this interference.
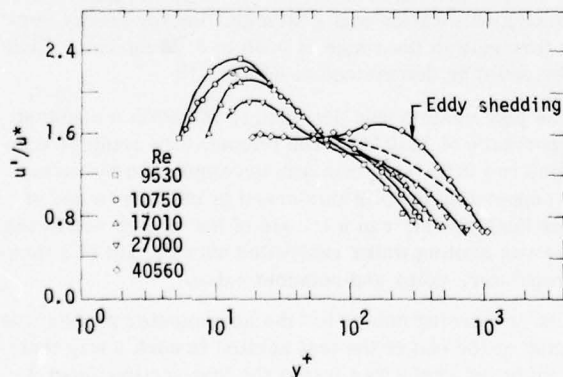

FIG. 7. Longitudinal turbulence intensities in a Newtonian oil measured with a 0.0025-cm cylinder probe.

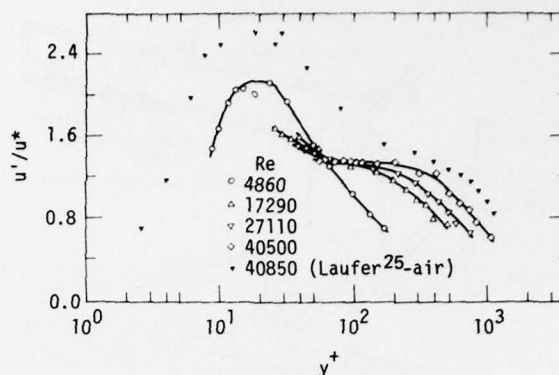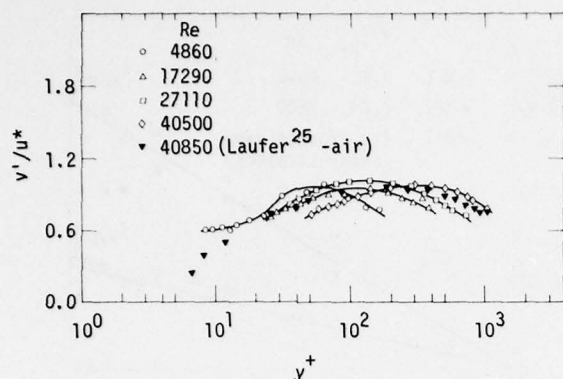FIG. 9. Radial turbulence intensities in a Newtonian oil measured with a 0.015-cm split-film probe ($\alpha = 0.25$).

Both the 0.0025 cm cylinder and split-film probe results peak lower near the wall than the data of Laufer[25] and Burchill[27] at the same Reynolds numbers. Since the present data were obtained in a small pipe, there may have been some scale effects. Also great efforts were made in these measurements to eliminate ground loops, which were shown to be responsible for 10%–20% increases in measured intensity when multiple grounding points were used.

The radial turbulence intensities as measured by the split-film probe are shown in Fig. 9 compared with the Laufer air pipe flow data. The α in Eqs. (2) and (5) was adjusted to a value of 0.25 to cause the Newtonian data to match the Laufer data. This was done because no *independent method* was used to obtain the value of α for the split-film probes used in this investigation. The value of α that was used by Burchill[27] was 0.65 (as measured by Spencer and Jones[23] for that probe).

One-dimensional turbulence energy spectra for both the longitudinal and radial turbulence were measured in the Newtonian oils and were found to be essentially normal as compared with comparable spectra measured by other investigators.

DATA WITH POLYMER SOLUTIONS

Velocity profiles measured with split-film probes in the polymer solutions are shown in Fig. 10. Designa-
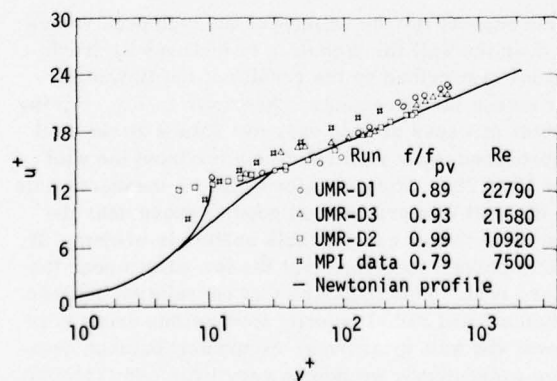
FIG. 10. Velocity profiles for polymer solutions.

FIG. 11. Longitudinal turbulence intensities for polymer solutions at low velocities (comparison of fresh and degraded behavior with Newtonian oil).

tions D1, D2, and D3 indicate relative extent of degradation for degraded solutions, D3 being most degraded. Since the levels of drag reduction in each of these cases was not high, the deviations of the velocity profiles from Newtonian were not great. The highest level of drag reduction for the fresh solution used at the Max-Planck-Institut für Strömungsforschung ($f/f_{pv} = 0.79$) caused the greatest elevation of u^+ values, as would be expected, and also showed some evidence of viscous sublayer thickening, which has been demonstrated by many investigations.

Longitudinal intensity profiles at low Reynolds numbers are shown in Fig. 11. One of the profiles is for the fresh solution and the other for the degraded solution. They are both at similar velocities, but the viscosity of the oil used in the fresh solution was higher, so the Reynolds number was lower. The intensities remain lower than those in oil all the way to the near-wall region instead of having higher values at an intermediate distance. The fresh solution profile peaked at a high intensity value very near the wall ($y^+ \approx 4$). The degraded solution profile did not reach a peak for $y^+ > 7$, the extent of the data, but the values are much lower than for the fresh solution. At the center, the fresh solution intensities were lower than normal.

Longitudinal intensity profiles at higher Reynolds numbers are presented in Fig. 12. The intensities for the degraded solution show a peak at $y^+ > 100$, well into the turbulent core, and have higher levels than in oil throughout most of the turbulent core, becoming smaller than in oil toward the buffer zone. The velocity for the fresh solution was about 20% lower than for the degraded solution. The fresh solution intensities show a tendency to peak very near the wall and much higher than normal. The centerline intensity for the degraded solution was much higher than for the Newtonian oils, while for the fresh solution it was much lower.

Radial turbulence intensity profiles are presented in Fig. 13 which shows that the radial intensities across the tube are lower for the polymer solution than for oil. The drag reducing data do not seem to have a peak value at about y^+ of 100 as do the oil data. For degraded solutions the peak is nearer the center, and for fresher

S95   Phys. Fluids, Vol. 20, No. 10, Pt. II, October 1977

Patterson, Chosnek, and Zakin   S95
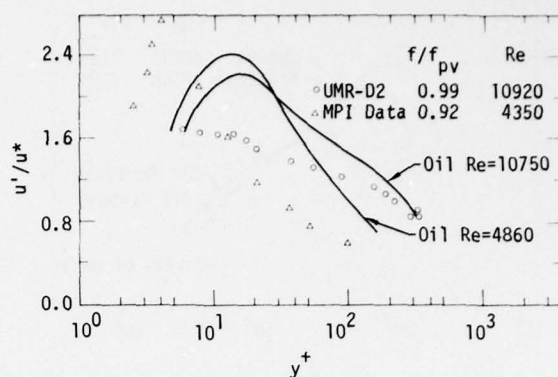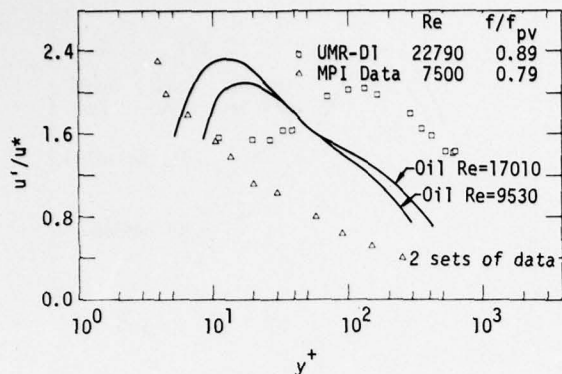
FIG. 12. Longitudinal turbulence intensities for polymer solutions at high velocities (comparison of fresh and degraded with Newtonian oil).

FIG. 14. Reynolds stress measurements for fresh solution drag reduction.

solutions there is no peak. The size of the decrease in the intensities diminishes as the degree of degradation of the polymer increases. This can be seen in Fig. 13 where the deviations from oil intensities decreased as degradation increased. The high value of f/f_{pv} for run UMR-D2 is due to a low Reynolds number and not to degradation. The low intensity values for this run at y^+ > 100 are characteristic of low Reynolds number data which peak at low values of y^+.

Increased longitudinal turbulence intensities were also found by Rudd[1] and Logan,[2] with the latter obtaining decreased radial intensities too. Rudd and Logan also obtained a shift in the peak of the axial intensities toward the center of the pipe, although not as marked as in this work, with their peak still being in the buffer zone. No extensive comparisons of this work to theirs can be made though, because of their use of square ducts in which secondary flows were present. Both increased and lowered axial intensities were obtained by Rodriguez et al.,[8] as shown in Figs. 1 and 2. In light of the profile data presented here, the high intensity values at

low levels of drag reduction are the result of intensity peaks far from the wall. The low values at the center at intermediate levels of drag reduction probably resulted from the close wall peak as in the fresh solutions illustrated here. The high values at the center at high levels of drag reduction are not yet explained, because intensity profiles at such high levels of drag reduction have not yet been measured except by Mizushina and Usui[10] for one polymer solution.

The longitudinal turbulence intensity peak nearer the wall than $y^+ = 12$ for fresh solution drag reduction is so far unreported by other investigators. Probe location and other obvious sources of error were carefully checked and rechecked. The possibility of probe effects is not ruled out, but, as mentioned herein Rodriguez et al.[9] could not find significant probe effects from viscoelastic solutions with a vibrating probe. It is unlikely that the peaks near the wall were caused by eddy shedding because the probe Reynolds numbers near the wall were too low (Re$_p \approx 6$ at $y^+ = 5$ for Re $= 7500$). The precision of probe positioning was approximately ± 0.002 cm, and the precision of turbulence measurements was about $\pm 5\%$ of value.

Some support for the validity of the high peak values very near the wall for high drag reduction with fresh solutions is provided by the results of the Reynolds shear stress measurements. As shown in Fig. 14, the Reynolds stresses drop to very low values as the wall is approached while still relatively far from the wall (y^+ of 10 to 20). The precision of the uv measurements near the wall was probably as good as those near the center even though considerable scatter is evident. It is fairly certain therefore that the low values near the wall are real. This indicates that correlation between longitudinal and radial velocity fluctuations drops very low near the wall (positive uv excursions balance negative uv excursions), producing very little eddy viscosity. This opens the possibility of having very large longi-

FIG. 13. Comparison of radial turbulence intensities in polymer solutions to those in a Newtonian oil.
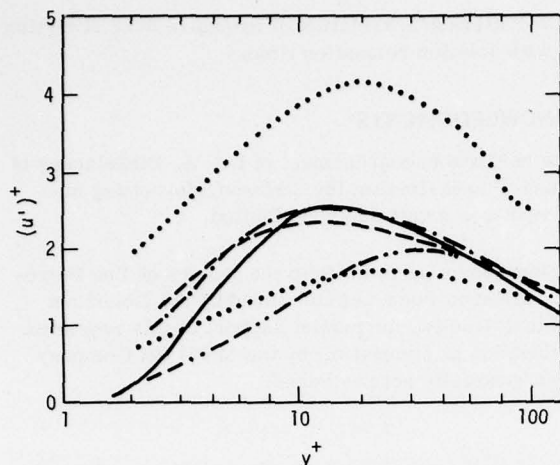
FIG. 15. Comparison of transport model turbulence intensity behavior for drag reducing behavior for two relaxation times.

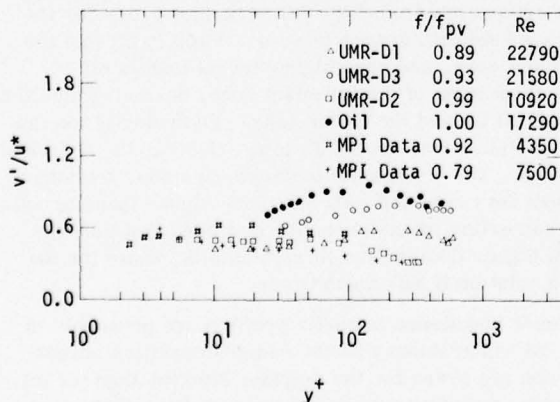|	f/f_{pv}	$(f/f_{pv})_m$	τ, sec	σ_k
. . . . (upper)	0.52	0.40	0.39	2.0
. . . . (lower)	0.53	1.00	0	0.5
— . — .	0.67	0.70	0.095	1.0
— — . .	0.36	0.40	0.39	1.0
— — — —	1.00	1.00	.0	1.0
————	Accepted Newtonian			

$(f/f_{pv})_m$ = value measured at given value of τ.

tudinal velocity fluctuations (or more likely shear strain fluctuations) near the wall. Of course, this reduction in $\overline{uv}$ requires extension of the viscous sublayer further from the wall, as has been shown in most velocity profile data. Much more detailed data very near the wall would have to be obtained to prove this hypothesis.

RESULTS OF MODELING DRAG REDUCTION

Turbulent flow in a pipe may be modeled by the $k - \epsilon$ (turbulence energy-dissipation rate) model as developed by Jones and Launder.[28] The basic equations contained in the model are as follows:

stream function:

$$0 = \frac{\partial^2 \psi}{\partial x_1^2} + \frac{\partial^2 \psi}{\partial x_2^2} + \frac{\omega}{\rho} \; ;$$

vorticity:

$$\frac{\partial}{\partial x_1}\left(\omega \frac{\partial \psi}{\partial x_2} \right) + \frac{\partial}{\partial x_2}\left(\omega \frac{\partial \psi}{\partial x_1} \right) = \frac{\partial}{\partial x_1}\left(\nu_e \frac{\partial \omega}{\partial x_1} \right) + \frac{\partial}{\partial x_2}\left(\nu_e \frac{\partial \omega}{\partial x_2} \right);$$

turbulence energy:

$$\frac{\partial}{\partial x_1}\left(k \frac{\partial \psi}{\partial x_2} \right) + \frac{\partial}{\partial x_2}\left(k \frac{\partial \psi}{\partial x_1} \right) = \frac{\partial}{\partial x_1}\left(\frac{(\nu_e + \nu)}{\sigma_k} \frac{\partial k}{\partial x_1} \right)$$

$$+ \frac{\partial}{\partial x_2}\left(\frac{(\nu_e + \nu)}{\sigma_k} \frac{\partial k}{\partial x_2} \right) + \nu_e \omega^2 - \epsilon \; ;$$

turbulence energy dissipation rate:

$$\frac{\partial}{\partial x_1}\left(\epsilon \frac{\partial \psi}{\partial x_2} \right) + \frac{\partial}{\partial x_2}\left(\epsilon \frac{\partial \psi}{\partial x_1} \right)$$

$$= \frac{\partial}{\partial x_1}\left(\frac{(\nu_e + \nu)}{\sigma_\epsilon} \frac{\partial k}{\partial x_1} \right) + \frac{\partial}{\partial x_2}\left(\frac{(\nu_e + \nu)}{\sigma_\epsilon} \frac{\partial k}{\partial x_2} \right)$$

$$+ C_1 \nu_e \omega^2 \epsilon / k - C_2 \epsilon^2 / k,$$

where $C_1 \approx 1.44$, $C_2 = 1.92$, and $\sigma_\epsilon = 1.3$. The parameter σ_k was varied as shown in Figs. 15 and 16.

In order to simulate the altered eddy viscosity, ν_e, in drag reducing flow it is necessary to use an altered eddy viscosity function. Hassid and Poreh[29] used

$$\nu_e = c_m (k^2/\epsilon)[1 - \exp(-A_m R_k)],$$

where c_m and A_m are constants and $R_k = k^2/\epsilon \nu$. A_m is a function of the level of drag reduction.

In modeling done in conjunction with the experimental work reported here, an eddy viscosity function of the polymer solution viscoelasticity, expressed as shear relaxation time, τ, was used. The expression was

$$\nu_e = \frac{k^2}{\epsilon}\left(\frac{c_m}{1 + 0.035^2 \pi^2 U^2 k \tau^2 / d^2 \overline{u}^2} \right),$$

where τ is the polymer shear relaxation time in solution, U is the bulk-mean velocity, and d is the pipe diameter.

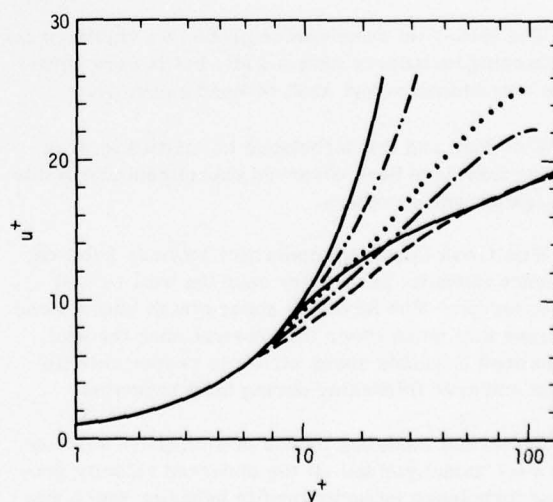

FIG. 16. Comparison of transport model velocity profile behavior for drag reducing behavior for two relaxation times (curve identification as for Fig. 15).

A near wall Reynolds stress attenuation function of the form $\exp[-10/(1+y^+)]$ was used for both Newtonian and drag reducing flows. Figures 15 and 16 show the result of using this relationship ($U = 20$ fps, $d = 0.0833$ ft, $C_m = 0.09$) with about the same values of the other constants as used by Hassid and Poreh for the velocity profiles and turbulence intensity for three levels of drag reduction. The noteworthy result of this eddy viscosity relationship is that for $\sigma_k = 1.0$ the predicted levels of drag reduction correspond very well to the empirical correlation of extensive drag reduction data with solution relaxation time by Rodriguez et al.[30] By use of the eddy viscosity modification alone, the near wall peak of the turbulence energy (intensity) was not obtained. That phenomenon is most likely a viscoelastic interaction of the fluid with the wall for the fresh solutions and will require modeling of the elastic contribution to the shear strain fluctuations near the wall.

Figures 15 and 16 show results of two different combinations of τ and σ_k (the ratio of kinematic viscosity to turbulence energy diffusivity) which produce almost the same levels of drag reduction (0.52 and 0.53). The velocity profiles are the same, but the profiles of turbulence intensity are quite different. In one case the intensities are very high, and in the other case the intensities are much lower than normal. Either of these cases is a possible mode of drag reducing turbulent behavior; however, the case for $\tau = 0$ does not correspond to observed drag reduction. In general, cases for $\sigma_k = 1.0$ are in best agreement with drag reduction data.

A much greater level of drag reduction generated by the model (0.36) yielded low turbulence intensities which peaked far from the wall ($y^+ > 40$). This behavior corresponds to that measured by Reischman and Tiederman,[4] but is not necessary for drag reduction to occur.

CONCLUSIONS

(1) The split-film anemometer probe is a viable means of measuring turbulence near a wall, but is very sensitive to contamination and must be used carefully.

(2) Both high and low turbulence intensities in drag reducing flow have been observed experimentally in this investigation and by others.

(3) With fresh (highly viscoelastic) polymer solution, turbulence intensity peaks very near the wall ($y^+ < 4$) were observed. The Reynolds shear stress under these conditions was much lower than normal near the wall. The lowered Reynolds shear stress is responsible for viscous sublayer thickening during drag reduction.

(4) Numerical modeling by use of a modified version of the $k - \epsilon$ model yielded all the observed velocity profile and turbulence intensity profile behavior which was experimentally observed except the intensity peak very near the wall. The $k - \epsilon$ model modification also yielded drag reduction levels corresponding to the Rodriguez–Zakin–Patterson correlation of extensive drag reduction data with solution relaxation time.

[1]M. J. Rudd, J. Fluid Mech. **51**, 673 (1972).
[2]S. E. Logan, AIAA J. **7**, 962 (1972).
[3]S. M. Kumor and N. D. Sylvester, in *Drag Reduction in Polymer Solutions* (American Institute of Chemical Engineers, New York, 1973), p. 1.
[4]M. M. Reischman and W. G. Tiederman, J. Fluid. Mech. **70**, 369 (1975).
[5]G. K. Patterson, Ph. D. thesis, University of Missouri-Rolla (1966).
[6]J. M. Rodriguez, Ph. D. thesis, University of Missouri-Rolla (1969).
[7]J. M. Rodriguez, G. K. Patterson, and J. L. Zakin, presented at the Fluid Mechanics Symposium, Hamilton, Ontario (1970).
[8]F. A. Seyer and A. B. Metzner, AIChE J. **15**, 426 (1969).
[9]J. M. Rodriguez, G. K. Patterson, and J. L. Zakin, in *Proceedings of the Symposium on Turbulent Measurements in Liquids*, edited by J. L. Zakin and G. K. Patterson (University of Missouri-Rolla, Rolla, Mo., 1971), p. 122.
[10]T. Mizushina and H. Usui, Phys. Fluids 20, S100 (October, Part II, 1977).
[11]P. S. Virk, Phys. Fluids **18**, 415 (1975).
[12]S. E. Logan, in *Proceedings of the Third Symposium on Turbulence in Liquids*, edited by G. K. Patterson and J. L. Zakin (University of Missouri-Rolla, Rolla, Mo., 1975), p. 91.
[13]J. W. Hoyt, J. Basic. Eng. **94**, 289 (1972).
[14]G. Astarita, Ind. Eng. Chem. Fund. **4**, 354 (1965).
[15]G. K. Patterson and J. L. Zakin, AIChE J. **14**, 424 (1968).
[16]M. C. Kohn, J. Polym. Sci., Polym. Phys. Ed. **11**, 2339 (1973).
[17]J. L. Lumley, J. Polym. Sci., Macromol. Rev. **7**, 263 (1973).
[18]H. Tennekes and J. L. Lumley, *A First Course in Turbulence* (M.I.T. Press, Cambridge, Mass., 1972), p. 248.
[19]R. J. Gordon, J. Appl. Polym. Sci. **14**, 2097 (1970).
[20]G. L. Donahue, W. G. Teiderman, and M. M. Reischman, J. Fluid Mech. **56**, 559 (1972).
[21]J. G. Olin and R. B. Kiland, presented at the Symposium on Aircraft Wake Turbulence, Seattle, Wash. (1970).
[22]R. H. Shaw, Pd. D. thesis, University of Guelph, Canada (1972).
[23]B. W. Spencer and B. G. Jones, in *Proceedings of the Second Symposium on Turbulence in Liquids*, edited by J. L. Zakin and G. K. Patterson (University of Missouri-Rolla, Rolla, Mo., 1972), p. 7.
[24]P. H. Blinco and V. A. Sandborn, in *Proceedings of the Third Symposium on Turbulence in Liquids*, edited by G. K. Patterson and J. L. Zakin (University of Missouri-Rolla, Rolla, Mo., 1975), p. 403
[25]J. Laufer, NACA TR 1174 (1953).
[26]A. E. Perry and C. J. Abell, J. Fluid Mech. **67**, 257 (1975).

[27]W. E. Burchill, Ph. D. thesis, University of Illinois (Urbana) (1970).

[28]W. P. Jones and B. E. Launder, Int. J. Heat Mass Transfer **16**, 1119 (1973).

[29]M. Poreh and S. Hassid, Phys. Fluids 20, S 193 (October, Part II, 1977).

[30]R. M. Rodriguez, J. L. Zakin, and G. K. Patterson, Soc. Pet. Eng. J. 7, 325 (1967).

[31]J. Chosnek, Ph. D. thesis, University of Missouri-Rolla (1975).

Reduction of eddy diffusion for momentum and heat in viscoelastic fluid flow in a circular tube

Tokuro Mizushina and Hiromoto Usui[a]

Department of Chemical Engineering, Kyoto University, Kyoto 606, Japan

The velocity profile, longitudinal turbulent intensity profile, and bursting period in drag reducing pipe flow were measured using a laser Doppler technique. The temperature distribution and heat transfer coefficient were measured with thermocouples in the same system. The results of the decrease in eddy diffusivities of momentum and heat near the wall, the gross flow measurements, and the velocity distribution were shown to be in a good agreement with the predictions of the eddy diffusivity model for viscoelastic fluids previously proposed. A simple method based on the eddy diffusivity model to calculate the rate of heat transfer in the fully developed pipe flow of viscoelastic fluids is proposed, and is ascertained to be effective by the previous experiments.

I. INTRODUCTION

Turbulent drag reduction by dilute polymer solutions, known as the Toms phenomenon, has been investigated by many workers. A few years ago, Lumley[1] summarized the work on the Toms phenomenon up to that time. Recently, Virk[2] has published a review of drag reduction. The gross flow behavior in drag reducing systems seems to have been clearly revealed by these papers, and the existence of the maximum reduction asymptote and many effects in the polymeric region were ascertained. However, the turbulence structure measurements, which are inevitable in the discussion of the Toms effect, are not sufficient because of the difficulty of the experimental technique. The most reliable method of measuring velocities in polymer solutions is the laser Doppler technique, which was previously employed by Rudd,[3] Logan,[4] and Chung *et al.*[5] for the measurement of the turbulent structure in polymer solutions. The first two papers used 1.25×1.25 cm^2 square pipes. The authors[6] used a 1×10 cm^2 duct and showed that the gross flow behavior was considerably different from that of circular pipe flow. The corner effect of the square duct seems to noticeably alter the turbulence structure in drag reducing flow. Chung *et al.* used a 1.19 cm i.d. pipe of Plexiglas. Their results are reliable only in the center portion of pipe flow because of the refraction effect. The test pipes were made of very thin polyester film in this work, and the measurements of velocity profile and fluctuating velocity near the wall were done using a laser Doppler meter.

One of the other reliable methods in drag reducing system is time-averaged temperature measurements. Although it has been known that the heat transfer rate around a blunt body in the cross flow of viscoelastic fluids was decreased in comparison with the Newtonian case,[7] the correct value of the time-averaged temperature in viscoelastic fluids must be known. Therefore, the temperature distribution and heat transfer coefficient in fully developed turbulent pipe flow were measured.

The authors previously reported that the damping ef-

fect of viscoelasticity on turbulent eddies might be the reason for drag reduction, and proposed an eddy diffusivity model for viscoelastic fluids. The experimental results of this work will be discussed on the basis of this model.

II. EXPERIMENTS

A. Velocity distribution and drag reduction

The laser Doppler technique was employed to measure the instantaneous and time-averaged velocity distribution in pipe flow of viscoelastic fluid. In this section, the laser Doppler meter used for this work and the flow system will be described.

1. Laser Doppler meter

The optical system employed in this work was the reference-scatter mode. The output of a helium–neon laser (JEOL, model JLG-H10) was 25 mW and the wavelength was 6328 Å. The reason for taking the reference-scatter mode (not the fringe mode) was:

(i) The scattering angle was not as large as to cause restrictions in the optical arrangement and test pipe.

(ii) The output of the laser beam was large enough to obtain a good signal-to-noise ratio even in the reference-scatter mode.

The optical system was constructed on the traversing device and the profile of longitudinal velocity was measured. The scattering angle was 6.76° and the scattering volume was about $0.15 \times 0.2 \times 0.8$ mm^3. To avoid having the signal drop out and to provide a good signal-to-noise ratio, 300 wppm of fresh milk was added to the test fluids as a scattering particle.

The data acquisition system was a pulse-averaging process similar to that of George and Lumley.[8] The range of measurable velocity was 10^{-4} to 10 m/sec. The schematic diagram of the signal processor is shown in Fig. 1. The time-averaged velocity was recorded by a laboratory recorder (YEW, LER-12A) and the root-mean-square value of the fluctuating velocity was read by a root-mean-square meter (Kanomax, model 21-

P.T.M. (R-453)

beat signal →

A-V Converter
(I.C. 741)

Preamplifier
(I.C. LM 301A)

B.P. Filter
(NF-FV 624 or) — B.P.F.
(NF-AE 921)

Comparator — Compa.
(NF-AE 921)

Buffer Amp.
(I.C. SN 7400)

Monostable
Multivibrator — M.M.
(I.C. SN 74121)

Buffer Amp.
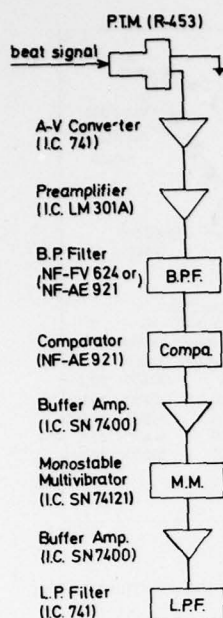(I.C. SN 7400)

L.P. Filter
(I.C. 741) — L.P.F.

FIG. 1. Data acquisition system.

1211). The mean bursting period $\overline{T}_b$ was determined from the time between peaks on the autocorrelation of the fluctuating velocity near the wall. This method was first ascertained by Kim *et al.*[9] in comparison with the visual study, and has been employed by many successive investigators. For this purpose, the output signal of the fluctuating velocity was recorded by a data recorder (TEAC, R-400), and the autocorrelation was obtained by a correlator (TEAC, C-100).

2. Flow system and preparation of polymer solution

The gravity flow system (not the pumping system) was used to avoid mechanical degradation of the polymer. The test tube had a 2.53 cm i.d. and 4.5 m length. The detailed sketch of the test section is shown in Fig. 2. The test tube was constructed of a polyester film (35 μ thickness), and a compensator attached around the pipe was filled with the test solution. The conjunction between polyester pipe and polyvinyl-chloride pipe was carefully adjusted to obtain smooth continuity. The refraction effect caused by the tube wall of polyester film was negligible except for the region very near the wall ($y < 0.05$ mm). The pressure drop of the flow was measured between two points 1.5 m apart by a U tube manometer with CCl_4. Another test tube with 1.99 cm i.d. and 3.5 m length was constructed for the measurements of velocity distributions in the higher Reynolds number range. The flow rate was measured by using a weighing scale and stop watch.

The polymer species used in this study was polyethyleneoxide (trade name ALCOX, E-160). The intrinsic viscosity of polyethylene oxide in water solution was determined experimentally as 16.1 dl/g. The molecular weight M of polyethylene oxide was calculated by means of Shin's equation[10] as $M = 4.57 \times 10^6$.

B. Temperature distribution and heat transfer rate reduction

The flow system was the same as that described in the previous section except for the test section. The heat transfer section was a copper tube with 2.6 cm i.d. and with a heated length of 4.2 m. The temperature distribution and Nusselt number in the fully developed region were measured under the condition of constant heat flux. The polymer species used in this experimental work was also polyethylene oxide. The intrinsic viscosity of the polymer solution was 13.5 dl/g and the molecular weight was determined to be 3.64×10^6.

The details concerning the experimental apparatus, procedure, and the results may be found in Ref. 11 and Ref. 6.

III. DAMPING FACTOR MODEL

A damping factor model for viscoelastic fluids was previously developed[12] using a procedure similar to that of van Driest[13] with the use of the Maxwell model as a constitutive equation. In this section the outline of this model will be described briefly.

For the first step of this development, the second problem of Stokes was solved for the case of a viscoelastic fluid. By an argument similar to van Driest's damping factor model, the solution of the amplitude of oscillation gives the damping factor, for momentum transfer, D_m, in turbulent pipe flow of viscoelastic fluids as

$$D_m = 1 - \exp\{-(y^+/A^+)[-\alpha + (\alpha^2 + 1)^{1/2}]^{1/2}\} , \qquad (1)$$

where $\alpha = (2\lambda/\nu)(u^*/A^+)^2$ and y^+ is the nondimensionalized distance from the wall, u^* is the friction velocity, λ is the relaxation time of the Maxwell model, and ν is the kinematic viscosity. If λ is put equal to zero, Eq. (1) must coincide with that of van Driest (Newtonian case),
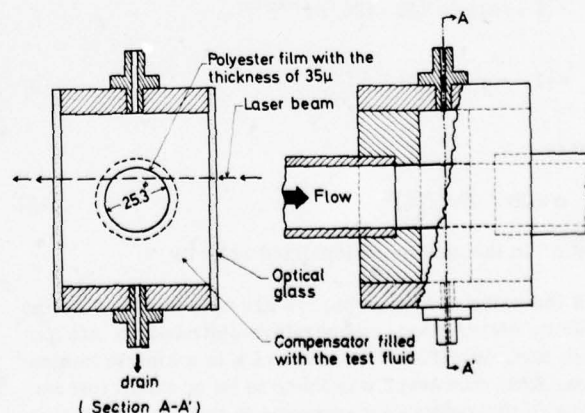
$$D_m = 1 - \exp(-y^+/26) ; \qquad (2)$$

FIG. 2. Detailed sketch of the test section.

Polyester film with the thickness of 35μ

Laser beam

25.3

Flow

Optical glass

Compensator filled with the test fluid

drain

(Section A-A')

accordingly, the value of A^+ is assumed to be 26.

On the other hand, the damping factor for heat transfer in Newtonian fluid flow is expressed as

$$D_h = 1 - \exp[-y^+(42 + 120/\mathrm{Pr}^{1/2})^{-1}] \quad , \tag{3}$$

where Pr is the Prandtl number.

As the ratio of the eddy diffusivities for heat and momentum, ϵ_h/ϵ_m, is equal to that of the mixing lengths, l_h/l_m, and approaches the value of 1.5 in the turbulent core of Newtonian fluid, the mixing lengths for momentum and heat transfer, l_m and l_h are expressed as;

$$l_m = fn(y^+, R^+)D_m \tag{4}$$

$$l_h = 1.5 fn(y^+, R^+)D_h \quad , \tag{5}$$

where

$$fn(y^+, R^+) = 0.4y^+ - \frac{0.44y^{+2}}{R^+} + \frac{0.24y^{+3}}{R^{+2}} - \frac{0.06y^{+4}}{R^{+3}} \tag{6}$$

and R^+ denotes the nondimensionalized radius of the tube. The ratio of eddy diffusivities for Newtonian fluid is given by

$$\epsilon_h/\epsilon_m = 1.5\{1 - \exp[-y^+(42 + 120/\mathrm{Pr}^{1/2})^{-1}]\}$$
$$\times[1 - \exp(-y^+/26)]^{-1} \quad . \tag{7}$$

Assuming that the eddy diffusivity ratio in viscoelastic fluids flow is approximately equal to that of a Newtonian fluid, the expressions for eddy diffusivities in viscoelastic fluids are finally given by

$$\frac{\epsilon_m}{\nu} = fn(y^+, R^+)^2 \left(1 - \exp\left\{-\frac{y^+}{26}[-\alpha + (\alpha^2 + 1)^{1/2}]^{1/2}\right\}\right)^2 \frac{dU^+}{dy^+} , \tag{8}$$

$$\frac{\epsilon_h}{\nu} = 1.5 fn(y^+, R^+)^2 \left(1 - \exp\left\{-\frac{y^+}{26}[-\alpha + (\alpha^2 + 1)^{1/2}]^{1/2}\right\}\right)^2$$
$$\times \{1 - \exp[-y^+(42 + 120/\mathrm{Pr}^{1/2})^{-1}]\}$$
$$\times [1 - \exp(-y^+/26)]^{-1} \frac{dU^+}{dy^+} , \tag{9}$$

where

$$\alpha = (2\lambda/\nu)(u^*/26)^2 \tag{10}$$

and U^+ is the nondimensionalized velocity.

If the value of λ is given, we are able to calculate the velocity distribution, temperature distribution, etc., from Eqs. (8)–(10). The value of λ in a simple laminar shear flow, however, was found to be so small that no effect of viscoelasticity appeared in the damping factor. It is expected that the value of the relaxation time in
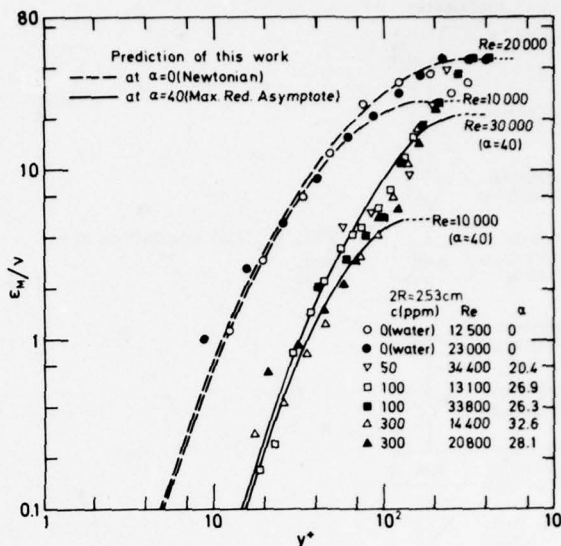
FIG. 3. Eddy diffusivity of momentum at the maximum reduction asymptote.

turbulent flow may be different from that of laminar flow. Thus, from the experimental results of the pressure drop of the turbulent flow of the dilute solutions of polyethylene oxide and polyacrylamide, the relaxation time in turbulent pipe flow was calculated using Eqs. (8) and (10). The relaxation time obtained in this way was defined as the turbulent relaxation time, λ_t. The correlation of λ_t in the polymeric region was obtained as

$$\lambda_t/\lambda_l = 3.76 \times 10^8 \, \mathrm{We}^{1.34}, \tag{11}$$

where

$$\mathrm{We \ is \ the \ Weissenberg \ number} = \lambda_l \langle U \rangle / 2R \tag{12}$$

and λ_l, $\langle U \rangle$, and R are the relaxation time for simple laminar shear flow, cross section-averaged velocity, and radius of the tube, respectively. The relaxation time for a simple laminar shear flow was calculated by the following equation, which was derived by James and Acosta[14] from the linear viscoelastic theory of Rouse,

$$\lambda_l = \frac{2}{5} \frac{\eta_s[\eta]^2 Mc}{kT} \quad , \tag{13}$$

where k is the gas constant, and η_s, $[\eta]$, c, T are the solvent viscosity, intrinsic viscosity (cm^3/g), concentration of polymer, and absolute temperature, respectively.

At the maximum reduction asymptote, the damping effect seemed to be saturated, and the value of α in Eq. (10) was found to be 40. So, for the maximum reduction asymptote

$$\alpha = 40. \tag{14}$$

The predicted values using Eqs. (8)–(14) will be compared with the experimental results in the following sections.

FIG. 4. Eddy diffusivity of heat at the maximum reduction asymptote.
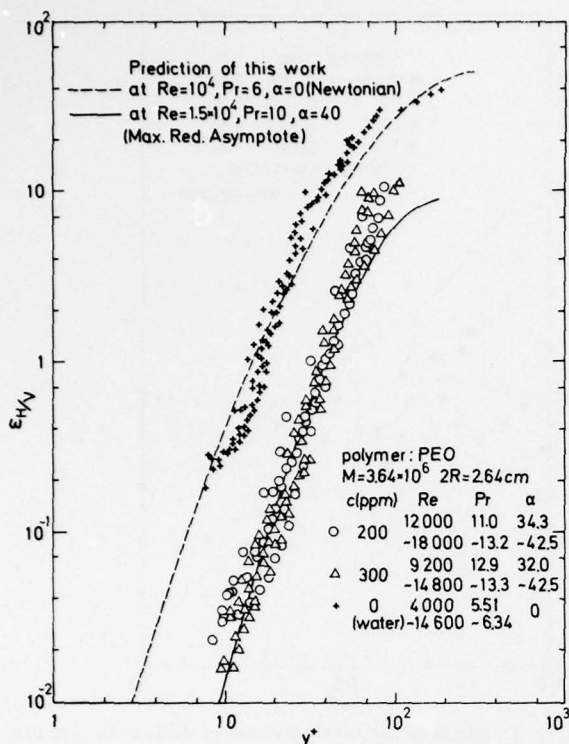
FIG. 6. Velocity distributions (2.53 cm i.d. tube).

IV. EXPERIMENTAL RESULTS

A. Eddy diffusivity

The experimental results of the eddy diffusivity of momentum obtained by the laser Doppler technique at the maximum reduction asymptote are compared, in Fig. 3, with the prediction of this model. The agreement between the predicted curves and the experimental results is good. The comparison of eddy diffusivity of heat at the maximum reduction asymptote is successfully shown in Fig. 4. These experimental results were presented and discussed in Ref. 11. The good agreement be-

tween the prediction of this model and the experimental results was also obtained in the polymeric region. Figures 3 and 4 show that the reduction of the turbulent eddy diffusivity of viscoelastic fluid near the wall is especially remarkable.

B. Friction factor

The results of the gross flow measurements are shown in Fig. 5. The solid lines in Fig. 5 are calculated by the eddy diffusivity model of this work. The agreement between the predicted curves and experimental results is good. This diagram shows the concentration effect in the polymeric region and the maximum reduction asymptote. The other effects on drag reduction, i.e., pipe diameter effect, molecular weight effect etc., were discussed in the previous paper.[12]

C. Time smoothed-velocity distribution

Time smoothed-velocity distributions were measured both in the polymeric region and at the maximum reduction asymptote. In Fig. 6 the results of velocity distribution measurements in a 2.53 cm i.d. tube are compared with the prediction of this work. The velocity profiles of the polymer solutions are shifted upward with the increase in polymer concentration and Reynolds number, and show good agreement with the predictions. The ultimate profile given by Virk[15] is also indicated in Fig. 6 by the broken line. Virk's asymptote means that at the maximum reduction, the turbulent core disappears and the whole region except for the laminar sublayer becomes "the elastic sublayer." The results of this work, however, show that the turbulent core remains even in the high drag reduction region. To observe the existence of the turbulent core at the maximum reduction, the

FIG. 5. Friction factor versus Reynolds number.
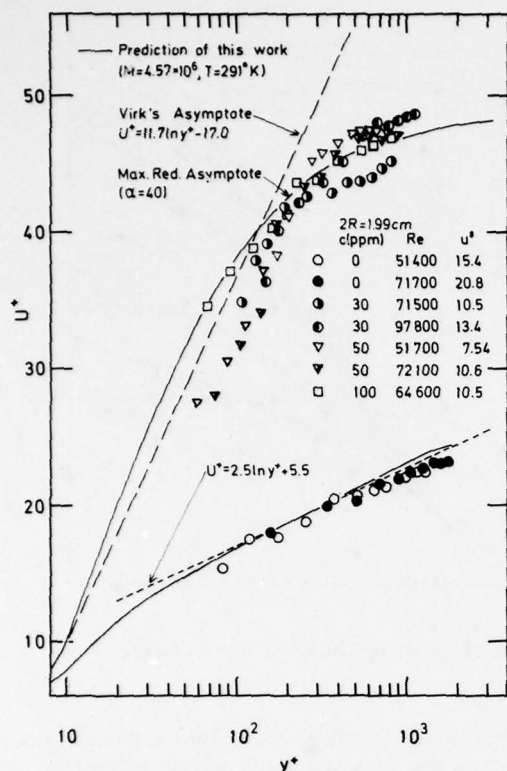
FIG. 7. Velocity distributions (1.99 cm i.d. tube, at higher Reynolds number range).
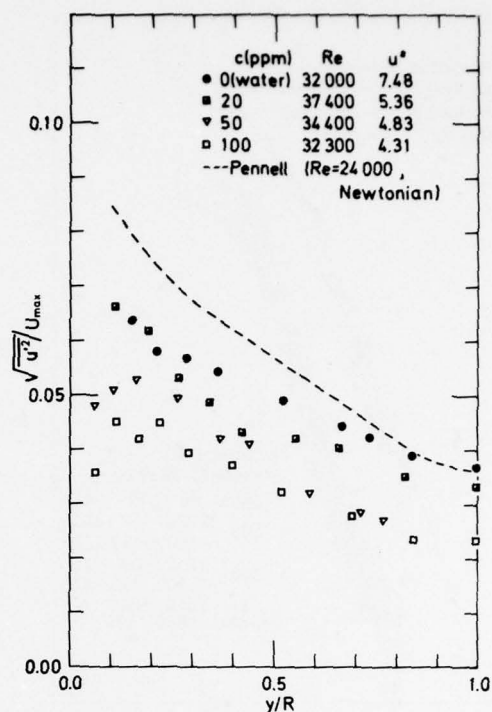
FIG. 9. Longitudinal turbulent intensity profiles at Re ≃ 33 000.

measurements in the higher Reynolds number range were carried out with the 1.99 cm i.d. tube. The results are shown in Fig. 7, which shows that the turbulent core does not disappear even at the maximum reduction asymptote.

D. Longitudinal turbulent intensities

At the present stage of development of the optical system in this work, the lateral turbulent intensity cannot

FIG. 8. Longitudinal turbulent intensity profiles at Re ≃ 11 000.
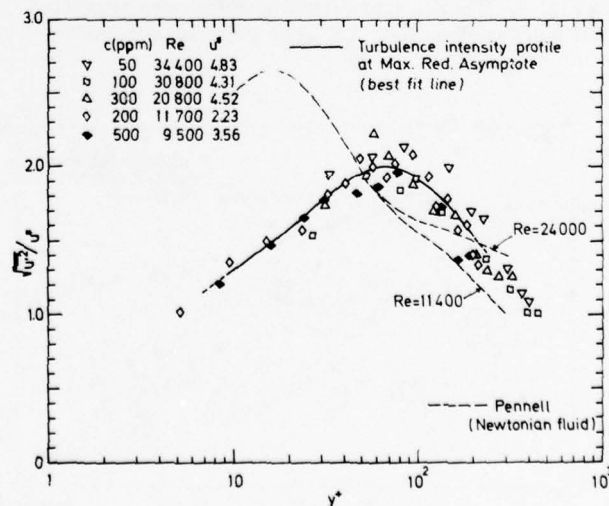
FIG. 10. Universal profile of longitudinal turbulent intensity at the maximum reduction asymptote.

TABLE I. Summary of mean bursting periods, $\bar{T}_b$.

c = 10 ppm $\nu=0.0109$ cm²/sec			c = 20 ppm $\nu=0.0108$ cm²/sec			c = 50 ppm $\nu=0.0115$ cm²/sec		
Re	u^*	$\bar{T}_b$	Re	u^*	$\bar{T}_b$	Re	u^*	$\bar{T}_b$
4640	1.50	0.35	6430	1.56	1.72	5260	1.40	1.82
8260	2.16	1.30	8310	1.82	1.68	8380	1.82	1.59
11500	2.74	1.40	10400	2.13	1.42	11000	2.23	1.42
15200	3.30	1.04	14400	2.62	1.18	13900	2.63	1.41
20800	4.07	0.92	19800	3.31	0.88	17700	3.07	1.09
25700	4.71	0.73	26000	3.95	1.06	23600	3.59	0.87
32000	5.39	0.91	38300	5.10	1.05			
37900	5.77	0.84						

c = 100 ppm $\nu=0.0119$ cm²/sec			c = 200 ppm $\nu=0.0148$ cm²/sec			c = 300 ppm $\nu=0.0177$ cm²/sec		
Re	u^*	$\bar{T}_b$	Re	u^*	$\bar{T}_b$	Re	u^*	$\bar{T}_b$
3940	1.10	1.81	6110	1.62	1.74	4620	1.56	1.71
4550	1.18	1.95	7470	1.85	1.57	5810	1.51	1.51
5770	1.37	1.73	9260	2.20	1.29	6990	2.15	1.33
7780	1.65	1.62	11600	2.57	1.54	8320	2.44	1.20
9370	1.88	1.51	14200	3.00	1.47	9370	2.69	1.52
11900	2.22	1.17	18800	3.57	1.58	12700	3.32	1.41
15300	2.60	1.06	24600	3.99	1.23	15700	3.75	0.94
19100	3.15	1.16				19800	4.30	1.04

c = 300 ppm $\nu=0.0142$ cm²/sec			c = 0 (water) $\nu=0.00984$ cm²/sec		
Re	u^*	$\bar{T}_b$	Re	u^*	$\bar{T}_b$
4700	1.24	2.58	5150	1.36	1.83
8700	2.01	2.23	6820	1.74	1.5_
10900	2.49	2.17	9050	2.22	1.02
13700	2.84	1.85	10800	2.59	0.84
18800	3.57	1.43	15600	3.57	0.60
			23700	5.16	0.50
			29300	6.21	0.34
			35900	7.42	0.36

FIG. 12. Dimensionless mean bursting period versus Reynolds number (nondimensionalized by wall parameter).

be measured. Only the profiles of the longitudinal turbulent intensities are obtained, and are shown in Figs. 8 and 9. These diagrams show the turbulent intensity profiles based on the centerline velocity $\overline{(u'^2)}^{1/2}/U_{max}$ at $Re \simeq 11\,000$ and $Re \simeq 33\,000$, respectively. The profiles in the solvent (Newtonian fluid) flow are in fairly good agreement with the results measured by Pennell *et al.*[16] using the hot wire anemometer, except for the region near the wall. The smaller values of the Newtonian intensity profiles obtained in the region near the wall seem to be caused by the finite scattering volume of this optical system. The longitudinal turbulent intensities of polymer solutions in the center portion of the pipe are not very different from those of Newtonian fluids; however, in the wall region, they are damped in proportion to the rate of drag reduction in the polymeric region, and the damping effect ceases to increase at the maximum reduction asymptote.

The results of the longitudinal turbulent intensity profiles based on the friction velocity $\overline{(u'^2)}^{1/2}/u^*$ at the maximum reduction asymptote are shown in Fig. 10. This profile seems to be independent of the Reynolds number and concentration of the polymer, and has a peak at $y^+ = 60$. The location of the peak, i.e., $y^+ = 60$, is in reasonable agreement with the prediction of the location of the largest turbulent energy production calculated[17] by

$$E^+ = \left[\left(1 - \frac{y^+}{R^+}\right) \Big/ \left(1 + \frac{\epsilon_m}{\nu}\right)\right]^2 \left(\frac{\epsilon_m}{\nu}\right) \qquad (15)$$

using the eddy diffusivity of this work. E^+ in Eq. (15) is the nondimensionalized production rate of turbulent energy. Since no reliable result of the intensity profile at the maximum reduction asymptote in pipe flow is seen in previous work, the best fit in Fig. 10 will be proposed as the universal profile of longitudinal turbulent intensity at the maximum reduction asymptote.

E. Bursting period

The bursting period was determined by a short-sampling-time autocorrelation method proposed by Strickland and Simpson.[18] In this study the experimental time was limited by the volume of the reservoir tank, and accordingly, the time of one run for the measurement of bursting periods was only a few minutes. So, the short-sampling-time autocorrelation method was most ade-
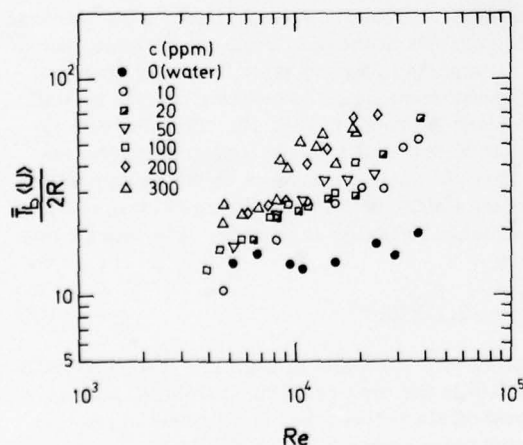

FIG. 11. Dimensionless mean bursting period versus Reynolds number (nondimensionalized by bulk parameter).

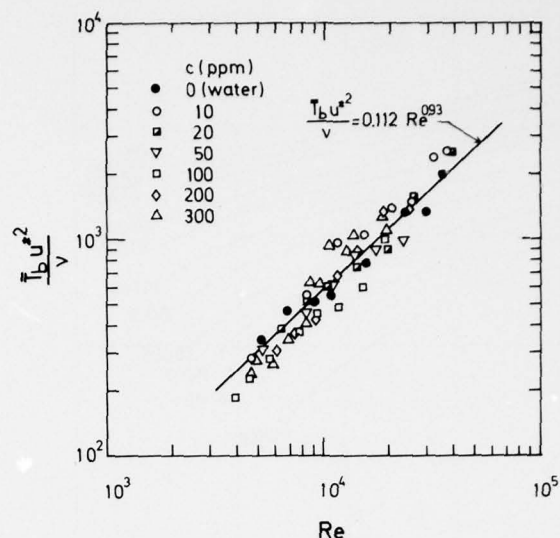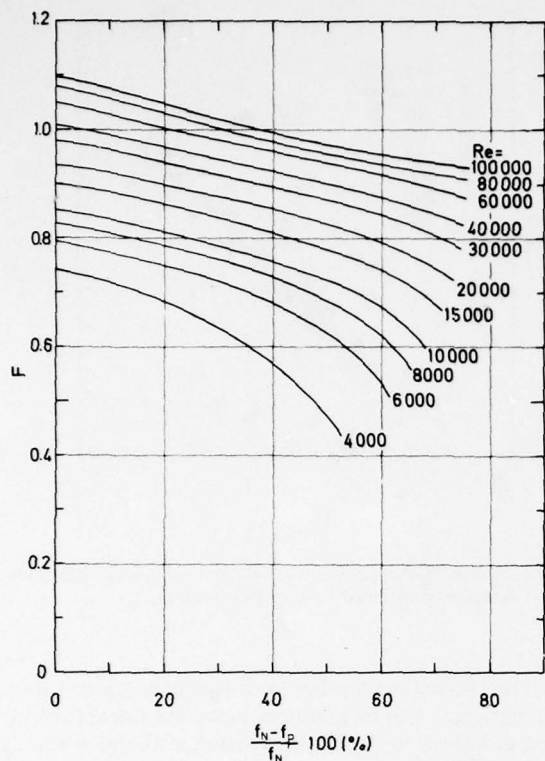FIG. 13. The dependence of correction factor on Reynolds number and the rate of drag reduction.

FIG. 14. Comparison of experimental values of the j factor with those predicted by Colburn's analogy.
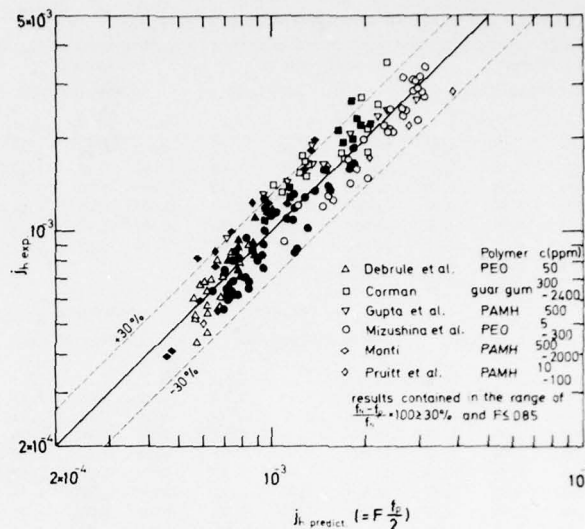
FIG. 15. Comparison of experimental values of the j factor with those predicted with the proposed method.

quate for this experiment. Strickland *et al.* showed that the average time of only 26 individual bursting times gave a reasonable value for the mean bursting period, $\overline{T}_b$. The authors ascertained that the average value of 20 individual points agreed well with that of 100 individual points. Thus, the average value of 20 individual

bursting times obtained by the short-sampling-time auto-correlation method was employed as the mean bursting time. Since it is very difficult to set the measuring point at a fixed location of y^+ beforehand because of the experimental error in the measurement of the friction velocity, the results of $\overline{T}_b$ were obtained at about $y^+ = 20 \sim 40$. However, the authors ascertained that $\overline{T}_b$ obtained in the region of $10 < y^+ < 100$ had the same value for a given Reynolds number.

The results of $\overline{T}_b$ are summarized in Table I. Figure 11 shows the dependence on Reynolds number of $\overline{T}_b$ normalized by the bulk parameter. The results for a New-tonian fluid show a nearly constant value, which corresponds to the results summarized by Laufer[19] for turbu-lent boundary layer flow. The results at the maximum reduction asymptote also have a nearly constant value $(\overline{T}_b \langle U \rangle / 2R = 60)$ in the higher Reynolds number range $(\mathrm{Re} > 10^4)$. The results obtained in the polymeric region show a transitional behavior from the lower constant level of Newtonian fluid to the upper constant level of maximum drag reduction. Figure 11 shows the increase in bursting periods in the drag reducing systems, but it is difficult to come to a conclusion from this diagram. Thus, the nondimensionalized bursting periods by wall parameter are indicated in Fig. 12. This diagram in-dicates that the bursting periods based on the friction velocity have the same dependence on Reynolds number as Newtonian fluids, both in the polymeric region and at the maximum reduction asymptote. The best fit line is given by

$$\overline{T}_b u^{*2}/\nu = 0.112 \, \mathrm{Re}^{0.93} \qquad (16)$$

and indicated by a solid line in Fig. 12. The universali-ty of Eq. (16) in the drag reducing system is interpreted as the counterbalance between the decrease in friction velocity and the increase in bursting period.

After all, the value of $\overline{T}_b$ increases up to two to three

times as large as those of Newtonian fluid flows, so that the scale of turbulence in the wall region is expected to become much larger than that of Newtonian fluids. This fact agrees with the experimental results of damping effects on the axial turbulent intensity shown in Figs. 8 and 9.

F. Simple method for the prediction of the heat transfer coefficient in drag reducing system

The predicting equations for fully developed turbulent heat transfer in pipe flow were previously proposed by Wells,[20] Gupta, Metzner, and Hartnett,[21] and Poreh and Paz.[22] etc. All of these equations have the disadvantages that not only the information on the friction factor, but also the information on the correct velocity profile, are needed to make use of them. Thus, the eddy diffusivity model given by Eqs. (8)–(14) was used to calculate the heat transfer coefficient. The results of computations showed that Colburn's analogy would not hold except in the higher Reynolds number range of the low drag reduction region. Thus, the deviation from Colburn's analogy, indicated by the correction factor F in Eq. (17) for the j factor of heat transfer,

$$j_h = F f_p / 2 \qquad (17)$$

was calculated for the case of various Reynolds number $(4 \times 10^3 < \text{Re} < 10^5)$, polymer concentration $(0 < c < 500$ ppm), molecular weight of polymer $(2.4 \times 10^6 < M < 4.3 \times 10^6)$, and pipe diameter $(1.3 \text{ cm} < 2R < 2.6 \text{ cm})$. The results of the calculation showed that the correction factor F depended only on Reynolds number and the rate of drag reduction defined by $(f_N - f_p)/f_N$, where f_N and f_p denote friction factors of Newtonian and polymer solutions, respectively. Then, a chart of F depending on $(f_N - f_p)/f_N$ and Re was drawn. The result is shown in Fig. 13. The comparisons with the experimental results (Ref. 11, Ref. 21, and Refs. 23–26) are shown in Figs. 14 and 15. Since all of the investigators referred to in Figs. 14 and 15 have measured both the friction factor and the Nusselt number, the experimental values of f_p were used in these diagrams. Figure 14 shows the correlation of the experimental results under the assumption that Colburn's analogy is valid in polymer solutions, i.e., $j_h = f_p / 2$. The solid symbol in Fig. 14 shows the data contained in the range $100 \times (f_N - f_p)/f_N \geq 30\%$ and $F \leq 0.85$, which correspond to those of the low Reynolds number range and high drag reduction range. The solid symbols are clearly not correlated by Colburn's analogy. Figure 15 shows the comparison of the j_h factor predicted by Eq. (17) and Fig. 13 with the experimental results. It is shown that the predicting method proposed in this work is effective even in the low Reynolds number range and the high drag reduction range.

V. CONCLUSIONS

(1) The measurements of the distribution of velocity and turbulent intensity in drag reducing flow in a round tube both in the polymeric region and at the maximum reduction asymptote were carried out by means of the laser Doppler technique.

(2) Although the physical meaning of the turbulent relaxation time has not been clarified and although its generality for the other polymers has not been examined, not only the friction factors, but also the eddy diffusivities and the velocity profiles of drag reducing flow can be predicted well, with the proposed damping factor model applying the turbulent relaxation time.

(3) Although the velocity profiles of polymer solutions are shifted upward and the turbulent core region becomes smaller with the increase in polymer concentration and Reynolds number, the turbulent core exists even in the high drag reduction region.

(4) The damping of the longitudinal turbulent intensity by viscoelasticity is highly effective in the wall region. In the center portion of the pipe, however, the turbulent intensity of polymer solutions has almost the same value as in the Newtonian case.

(5) There exists a universal profile of axial turbulent intensity at the maximum reduction asymptote.

(6) The mean bursting periods in drag reducing systems become larger than those of Newtonian fluid flows. In the maximum reduction region, its values become about two to three times as large as that of a Newtonian fluid at the same Reynolds number.

(7) A universal dependence of $\overline{T}_b$ on Reynolds number is obtained when it is normalized by wall parameters.

(8) From the eddy diffusivity model for heat transfer, the simple predicting method of the j_h factor was derived. This method was ascertained to be effective by previous experimental results.

[1]J. L. Lumley, J. Polym. Sci. **7**, 263 (1973).
[2]P. S. Virk, AIChE J. **21**, 625 (1975).
[3]M. J. Rudd, J. Fluid Mech. **51**, 673 (1972).
[4]S. E. Logan, AIAA J. **10**, 962 (1972).
[5]J. S. Chung and W. P. Graebel, Phys. Fluids **15**, 546 (1972).
[6]H. Usui, Ph.D. thesis, Kyoto University (1975).
[7]T. Mizushina and H. Usui, J. Chem. Eng. Jpn. **8**, 393 (1975).
[8]W. K. George and J. L. Lumly, J. Fluid Mech. **60**, 321 (1973).
[9]H. T. Kim, S. T. Kline, and W. C. Reynolds, J. Fluid Mech. **50**, 133 (1971).
[10]H. Shin, Sc. D. thesis, Massachusetts Institute of Technology (1965).
[11]T. Mizushina, H. Usui, and T. Yamamoto, Lett. Heat Mass Transfer **2-1**, 19 (1975).
[12]T. Mizushina, H. Usui, and T. Yoshida, J. Chem. Eng. Jpn. **7**, 162 (1974).
[13]E. R. van Driest, J. Aeronaut. Sci. **23**, 1007 (1956).
[14]D. F. James and A. J. Acosta, J. Fluid Mech. **42**, 269 (1970).
[15]P. S. Virk, J. Fluid Mech. **45**, 417 (1971).
[16]W. T. Pennel, E. M. Sparrow, and E. R. G. Eckert, Int. J.

Heat Mass Transfer **15**, 1067 (1972).

[17]J. Laufer, NACA Report No. 1174 (1956).

[18]J. H. Strickland and R. L. Simpson, Phys. Fluids **18**, 306 (1975).

[19]J. Laufer and M. A. B. Narayanan, Phys. Fluids **14**, 182 (1971).

[20]C. S. Wells, AIChE J. **14**, 406 (1968).

[21]M. K. Gupta, A. B. Metzner, and J. P. Hartnett, Int. J. Heat Mass Transfer **10**, 1211 (1967).

[22]M. Poreh and U. Paz, Int. J. Heat Mass Transfer **11**, 805

(1968).

[23]P. M. Debrule and R. H. Sabersky, Int. J. Heat Mass Transfer **17**, 529 (1974).

[24]J. C. Corman, Ind. Eng. Chem. Process Des. Dev. **9**, 254 (1970).

[25]R. Monti, *Progress in Heat and Mass Transfer* (Pergamon, Oxford, England, 1972), Vol. 5, p. 239.

[26]G. T. Pruitt, N. F. Whitsitt and H. R. Crawford, *Turbulent Heat Transfer to Viscoelastic Fluids* (Western Co., Dallas, Tex., 1966).

Additive effects on free turbulent flows

Marshall P. Tulin

Hydronautics, Inc., Laurel, Maryland 20810

Jin Wu

College of Marine Studies, and Department of Civil Engineering, University of Delaware, Newark, Delaware 19711

A theory is presented which predicts the spreading in time of a cylindrical turbulent cloud, allowing an estimation of the interface entrainment coefficient. In light of the theory, previously published experiments are analyzed and the effect of polymer concentration on entrainment is deduced; the entrainment is substantially reduced by concentrations as low as 25 ppm. It is suggested that this reduction accompanies a thickening of the interfacial superlayer of the same magnitude as the sublayer thickening which accompanies substantial drag reduction.

INTRODUCTION

The effect of polymer additives in dilute solution on friction reduction of flow in pipes and over plates is now generally agreed to be due largely to a change in the effective thickness of the viscous sublayer. This change arises in some way, still unknown, but seemingly related to changes in the flow occurring in a region close to the wall where small eddy phenomena are primary, and where the characteristic flow times are shorter than the relaxation time of the polymer. The latter requirement gives rise to the well-known onset criterion for drag reduction, first demonstrated by Elata *et al.*[1] The primacy of the wall region has been demonstrated by Wu and Tulin[2] in experiments where *normal drag reduction* on a flat plate was measured although the additive solution was injected only into a thin layer on the scale of the sublayer and buffer layer thicknesses. Do the changes in the flow near the wall depend critically for their presence on the wall itself? This question remains unanswered.

It is natural, in connection with this question, to think of the viscous "superlayer" separating free turbulent flows and nonturbulent flows in their exterior, and to query whether these superlayers are affected by polymer additives and in what way. It is the purpose of this brief paper to show evidence that superlayers are so affected and in some way suggestive of the wall effect in boundary layers. The evidence involves the growth of cylindrical turbulent clouds, created in the laboratory and observed photographically. The results would seem important not only for a better understanding of additive effects but also of the superlayer, a flow region poorly understood at the present time.

FREE TURBULENT FLOWS

Free turbulent flows, as in jets, wakes, and clouds of turbulence are characterized by a region of turbulent flow imbedded in a nonturbulent fluid on which the former encroaches through entrainment; the two regions are roughly demarcated. It is generally believed, following Corrsin and Kistler,[3] that entrainment proceeds through the diffusion of unsteady vorticity across a very thin moving interface ("superlayer"). Nothing is known experimentally about the thickness of this interface, although its large scale shape has been observed in various cases. On the other hand, the mean speed with which the turbulent region spreads can be readily measured, and it is known to scale with the intensity of the energetic turbulence behind the front.[4]

In particular, if q is the characteristic turbulent intensity in a particular flow cross section and v is the spreading speed, then

$$v = \beta q , \qquad (1)$$

where β is, in normal flow, a constant for the entire flow, but may vary from flow to flow; that is, it may differ somewhat for jets, wakes, boundary layers, and turbulent clouds. In fact, self-similarity (from one lateral cross section to another) of jets and wakes implies the existence of a constant β, and these flows, assuming sufficiently high Reynolds numbers, are well-known to be self-similar; they spread according to power laws. If δ is a cross-sectional dimension, u is a characteristic mean velocity in the downstream direction and x is the downstream distance, then

$$\delta \propto x^{\gamma}; \qquad u \propto x^{\alpha}$$

where (three dimensions)

	γ	α
Jets	1	-1
Wakes	$\frac{1}{3}$	$-\frac{2}{3}$

These laws, experimentally verified, follow from conservation of momentum flux and self-similarity. It is especially notable that the exponents γ and α do not depend at all on the value of the entrainment coefficient β, only on its existence as a constant.

TURBULENT CLOUDS

Turbulent clouds do not possess net momentum and this fact puts them in a different category than jets and wakes and renders them particularly important for the study of additive effects as we shall show.

We assume that the cloud motion in an incompressible fluid of density ρ is self-similar and characterized at
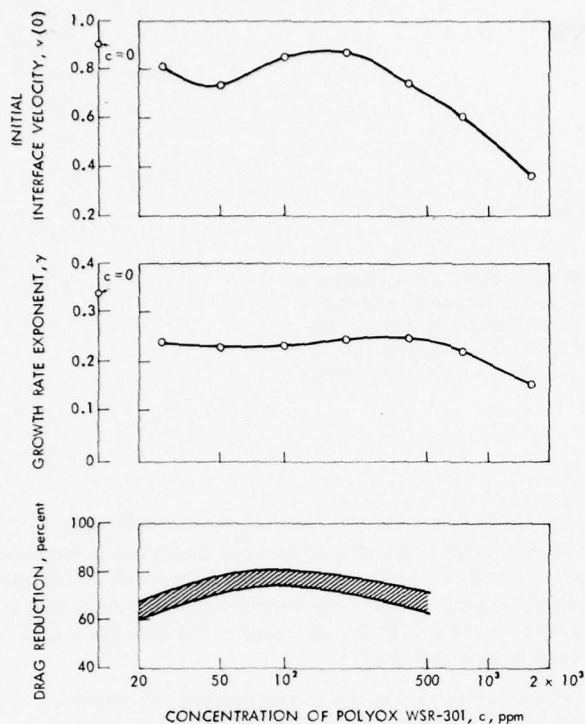
FIG. 1. Effects of polyox on initial growth rate (top), growth law exponent (middle), and drag reduction (bottom).

any time by the cloud radius, r, and q, the characteristic turbulent intensity within. The energy of the cloud, E, resides in the turbulent motion and q is conveniently defined through it (we deal with a cylindrical cloud)

$$E = (\rho q^2/2)\pi r^2 . \tag{2}$$

This energy continually declines through dissipation, which for sufficiently large Reynolds numbers may be expected to depend on the large scale turbulence in the usual way (λ is an appropriate length scale, proportional to r)

$$D = (k\rho q^3/\lambda)\pi r^2 = a\pi\rho q^3 r, \tag{3}$$

where $a = kr/\lambda$, and D is the rate of dissipation. Of course, the constant a will depend somewhat on the distribution of the turbulent energy and its integral scale and thus on the way in which the cloud is created.

There is no kinetic energy in mean motion to feed the cloud turbulence; so that

$$dE/dt = -D . \tag{4}$$

The growth of the cloud is assumed to depend on the large scale turbulence in the same way as for jets and wakes

$$dr/dt = v = \beta q . \tag{5}$$

These relations, (2)–(5) lead to a nonlinear differential equation for the radius

$$\ddot{r}r = -(1 + a/\beta)\dot{r}^2 . \tag{6}$$

The solutions $r(t)$ depend on the initial conditions, $[r(0); v(0)]$, and the single nondimensional parameter a/β, and

are given exactly by

$$\frac{r(t)}{r(0)} = \left(1 + \frac{(2 + a/\beta)v(0)t}{r(0)}\right)^{(2+a/\beta)^{-1}} \tag{7}$$

and for large times by

$$r(t)/r(0) = [t/t(0)]^\gamma , \tag{8}$$

where

$$\gamma = (2 + a/\beta)^{-1} . \tag{9}$$

Notice that γ is *not* given as a condition of self-similarity as in the case of jets and wakes, but depends essentially on the ratio, a/β, or dissipation coefficient/entrainment coefficient. Nor is β further constrained by energy considerations as Townsend showed in the case of jets and wakes. [5]

We carried out experiments at Hydronautics on the spreading of cylindrical turbulent clouds. [6] These clouds were generated in a transparent tank (120 cm high, 90 cm wide, 22 cm thick) by a spiral mesh paddle, 5 cm diam, driven by a weight and pendulum so that the net angular momentum introduced by the forward and backward swing of the paddle was virtually nil. Dye placed on the paddle caused the turbulent cloud so created to be visible and its spread was observed photographically. The clouds so created were generally cylindrical in shape. While the driving motion and paddle were unchanged, the fluid in the tank was altered from test to test by the addition of various amounts of Polyox WSR-301 so as to vary the weight concentrations in the tank over a range of 0–1250 ppm. The turbulent Reynolds numbers varied over the range 10^3–10^4.

The cloud growth was in all cases observed to be linear for early times (the first few seconds) and to follow a power law growth for later times (5–30 sec), all as predicted by the preceding analysis, Eqs. (7) and (8). In the case of pure water a value $\gamma = \frac{1}{3}$ was measured. The values of γ and $v(0)$ quoted here and shown in Fig. 1 have been taken directly from Wu. [6]

The data show that changes in initial spreading rate (upper Fig. 1), spreading exponent (middle Fig. 1), and drag reduction observed elsewhere (lower Fig. 1) follow similar trends. This is especially true in that each shows a significant effect at low concentrations and a peaking at around 50 ppm.

There is no way to be certain in these experiments that the initial turbulence intensity, $q(0)$, was quite unchanged throughout the tests, otherwise the data for $v(0)$ in the upper figure could be used to determine β, as well as the data for late spreading. Nevertheless, the general trend of the β variation deduced on the basis that $v(0)$ was constant is very similar to that shown in Fig. 1 and deduced from the spreading exponent according to Eq. (9).

If the additive does not affect the large scale turbulent motion, then a will not be affected, and Fig. 2 may then be interpreted to show how the entrainment coefficient *is generally reduced* with increasing additive concentration.
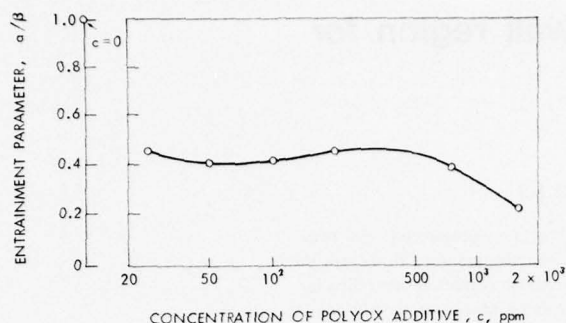
FIG. 2. Effect of polymer additive on entrainment parameter.

mogoroff microscale or the size of the smallest eddies

$$l = A(\nu/\zeta)^{1/2} , \tag{13}$$

where ζ is the strain rate amplitude behind the interface. In this case an increase of l would correspond to a reduction in straining rates due to the presence of the additive.

SUMMARY AND CONCLUSIONS

(1) The self-similar spreading of turbulent clouds leads to a power law variation for the radius with time according to the present theory and this has been observed experimentally for cylindrical clouds in both water and dilute additive solutions.

(2) The value of the spreading rate exponent, γ, is related to the entrainment coefficient, β, according to the theory presented here, and the dependence of β on additive concentration has been determined experimentally by measuring γ.

(3) Should the superlayer Reynolds number, vl/ν, be constant, as follows from a balance of the diffusion and convection of vorticity in the superlayer, then the reduced entrainment coefficient corresponds to a thickened superlayer; the observed variations in this thickness are similar to those measured in the viscous sublayer accompanying drag reduction by polymer additives.

(4) Should the superlayer thickness scale with the Kolmogoroff microscale, as suggested earlier, then the thickened superlayer corresponds to reduced straining rates behind the interface.

ACKNOWLEDGMENT

THE INTERFACE

We may speculate on the meaning of these data in terms of phenomena near the superlayer.

The production, convection, and diffusion of vorticity, ζ, must balance, in each plane, at a distance y from and parallel to the interface. The first of these terms depends on nonlinear effects and we neglect it in the interface where the vorticity is small. This simplification leads to a balance between diffusion (left-hand side) and convection (right-hand side) of vorticity

$$\nu(\partial^2 \zeta/\partial y^2) = -v(\partial \zeta/\partial y) \tag{10}$$

which has a solution for which

$$vl/\nu = R \tag{11}$$

(where l is the superlayer thickness, ν is the kinematic viscosity, and R is a Reynolds number) as may be seen from the form of the equation.

This result is equivalent to

$$ql/\nu = R/\beta \tag{12}$$

implying that a reduction in β corresponds to a thickening of the superlayer. The Reynolds number on the left is the superlayer equivalent of the sublayer Reynolds number $u*\delta'/\nu$, where $u*$ is the friction velocity and δ' is the sublayer thickness. The value $\beta/\beta_0 = 0.4$ corresponds to an increase in the superlayer Reynolds number by a factor of 2.5, quite similar in magnitude to the increased values of the sublayer Reynolds number which have been measured at maximum drag reduction.

It has been earlier suggested by Corrsin and Kistler[3] that the superlayer thickness should scale as the Kol-

[1] C. Elata, J. Lehrer, and A. Kahanovitz, Isr. J. Technol. 4, 87 (1966).

[2] J. Wu and M. Tulin, J. Basic Eng. 94, 749 (1972).

[3] S. Corrsin and A. Kistler, NACA Technical Report 1244 (1953).

[4] O. M. Phillips, J. Fluid Mech. 51, 97 (1972).

[5] A. A. Townsend, J. Fluid Mech. 26, 255 (1966).

[6] J. Wu, AIChE J. 17, 1408 (1971).

M. P. Tulin and J. Wu   S111

Turbulent fluctuations in the viscous wall region for Newtonian and drag reducing fluids

Thomas J. Hanratty, Larry G. Chorn, and
Dimitrios T. Hatziavramidis

Department of Chemical Engineering, University of Illinois, Urbana, Illinois 61801

An electrochemical method, which is the mass transfer analog of the hot film anemometer, has been developed to study flow fluctuations in the immediate vicinity of a wall. Electrodes mounted flush with the wall are the cathode of an electrolysis cell. At high enough voltages, the electric current is controlled by the rate of mass transfer to the cathode and the concentration of the reacting species at the surface is zero. These techniques allow the measurement of two components of the fluctuating velocity gradient at the wall. Results have been obtained on the structure of turbulence close to a wall and on the influence of drag reducing polymers on this structure.

I. INTRODUCTION

We have used electrochemical techniques which are the mass transfer analog of the hot film anemometer for a number of years to study the limiting behavior of a turbulent field very close to a wall. A chemical reaction is carried out on the surface of a small electrode mounted flush with the wall at a rapid enough rate so that it is mass transfer controlled. Under these conditions, the concentration of the reacting species at the electrode surface is kept at a constant value, $C_w \cong 0$. The current, I, flowing in the electrochemical circuit is then related to the mass flux of reacting species, N, by the equation

$$N = (I/n_e A_e F)(1 - T), \tag{1}$$

where n_e is the number of electrons involved in the reaction, A_e is the area of the electrode, and F is Faraday's constant. The transference number, T, which is a measure of the influence of the electric field on the mass flux is kept approximately equal to zero by using a large excess of neutral electrolyte.

Because the concentration boundary layer is very thin, the mass transfer rate to the electrode surface is influenced by the flow in the immediate vicinity of the wall. The current flowing to a circular electrode or to a rectangular electrode with the long side perpendicular to the direction of mean flow is a measure of the x component of the velocity gradient at the wall, s_x. The sum and the difference of the currents to a pair of electrodes in the chevron arrangement shown in Fig. 1 gives both components of the velocity gradient, s_x and s_z.

The use of an array of electrodes such as shown in Fig. 1 allows the determination of the velocity field at a number of wall locations; i.e., the "footprint" of the large eddies on the wall. More recently, we have been making turbulence measurements simultaneously at a single location in the fluid and at multiple wall locations. This has allowed us to check inferences regarding the eddy structure made from previous studies with electrodes at multiple locations on the wall.

These electrochemical techniques have been particularly useful for studying drag reducing flows since they have allowed the determination of changes of the structure of turbulence caused by the addition of polymers

without using probes that interfere with the flow. In previous work by Fortuna[1] we had difficulties since the electrolyte accelerated the degradation of the polymer. More recently, we have been able to overcome these difficulties by using a different electrochemical system and to put Fortuna's work on a firmer basis.

Much of our earlier work using electrochemical techniques to study turbulence has been summarized in Ref. 2. In this paper we present recent results. Particular emphasis is given to our measurements at multiple locations, to our measurements with drag reducing polymers and to the implications of these studies with respect to the structure of turbulence close to a wall.

II. DESCRIPTION OF THE EXPERIMENTS

The experiments were carried out in two different loops designed to provide a fully developed flow in a pipe. One of these[3] has a test section with a diameter of 19.34 cm, the other,[4] a diameter of 2.54 cm. The test electrodes are fabricated by gluing a platinum wire or a platinum sheet in the wall of a pipe and sanding it until it is flush with the wall. The resulting platinum circles or rectangles on the wall are the cathodes of an electrolysis cell. The anode is located downstream of the cathode and has a much larger area so that the current flowing in the electrolysis cell is controlled by the cathodic processes. In earlier work the electrolyte was a dilute solution of potassium ferri- and potassium ferrocyanide in a strong solution of sodium hydroxide. The reactions for this system are:
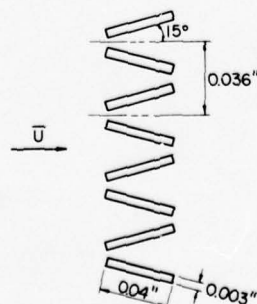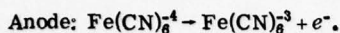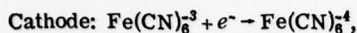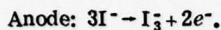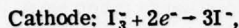

FIG. 1. Array of wall electrodes used to measure the two components of the fluctuating velocity gradient at a number of locations.

Cathode: $Fe(CN)_6^{-3} + e^- \rightarrow Fe(CN)_6^{-4}$,

Anode: $Fe(CN)_6^{-4} \rightarrow Fe(CN)_6^{-3} + e^-$.

More recently,[5] we have been using iodine dissolved in a potassium iodide solution for which the following reactions occur:

Cathode: $I_3^- + 2e^- \rightarrow 3I^-$,

Anode: $3I^- \rightarrow I_3^- + 2e^-$.

The anode is kept at ground potential and the test electrode is controlled at a large enough negative potential to insure that the reaction is mass transfer controlled but not at so large a potential that side reactions occur. The current is measured by determining the voltage drop across a feedback resistor on an operational amplifier that is connected to the test electrode. Details regarding the electronic circuitry are described in a previous paper.[4]

The methods used to fabricate the multiple wall electrodes shown in Fig. 1 are described in theses by Eckelman[6] and Lee[7] and in a paper by Lee et al.[8] The experiments in which measurements in the bulk fluid and at the wall were made simultaneously were done using an X-hot-film probe with its plane perpendicular to that of the wall located at a dimensionless distance $y^* = 13$.[7] In order to facilitate the handling of measurements made at multiple locations, the equipment is directly coupled with an IBM 1800 computer. The data are digitalized and stored on cards or on a magnetic tape for future analysis.[6,7]

The polymer solutions used in the drag reduction studies were prepared by slowly premixing the required amount of Separan AP-30, a high molecular weight polyacryamide, in ten liters of de-ionized water. The resulting solution was added to the electrolyte. This process avoided the formation of agglomerates and excessive mechanical degradation of the polymer. The concentration of the polymer solutions used ranged from 100 to 500 ppm by weight. Each solution was analyzed using a Brookfield cone and plate viscometer to determine the shear stress-shear rate relationship. All solutions exhibited a weak pseudo-plastic response.

III. THEORY

A. Linear analysis

Our first attempt to analyze measurements with single electrodes was to use linearized momentum equations to relate the frequency spectrum of the x and z components of the fluctuating velocity gradient, s_x and s_z, to the frequency spectrum of the pressure fluctuations at the wall. The pressure is assumed to be independent of y in the viscous wall region and to be given as

$$p = \hat{p}\exp[i(k_x x + k_z z - \omega t)], \tag{2}$$

where k_x and k_z, are the wavenumbers in the x and z directions, ω is the circular frequency, t is the time, and $\hat{p}$ is the amplitude of the pressure fluctuation.

The equations defining the flow are

$$\frac{\partial u}{\partial t} + \overline{U}\frac{\partial u}{\partial x} + v\frac{d\overline{U}}{dy} = -\frac{1}{\rho}\frac{\partial p}{\partial x} + \nu\left(\frac{\partial^2 u}{\partial y^2} + \frac{\partial^2 u}{\partial z^2}\right), \tag{3}$$

$$\frac{\partial w}{\partial t} + \overline{U}\frac{\partial w}{\partial x} = -\frac{1}{\rho}\frac{\partial p}{\partial z} + \nu\left(\frac{\partial^2 w}{\partial y^2} + \frac{\partial^2 w}{\partial z^2}\right), \tag{4}$$

$$\frac{\partial u}{\partial x} + \frac{\partial v}{\partial y} + \frac{\partial w}{\partial z} = 0. \tag{5}$$

Here u, v, and w are the three components of the fluctuating velocity field, $\overline{U}(y)$ is the time-averaged axial velocity, and ρ and ν are the density and kinematic viscosity, respectively. These are to be solved using the boundary conditions that u, v, and w are zero at $y = 0$ and that u and w are finite at large y. The solutions give

$$s_x = \hat{s}_x \exp[i(k_x x + k_z z - \omega t)] \tag{6}$$

$$s_z = \hat{s}_z \exp[i(k_x x + k_z z - \omega t)], \tag{7}$$

where $\hat{s}_x$ and $\hat{s}_z$ are functions of $\hat{p}$, k_x, k_z, and ω.

Sirkar[9] and Lee[7] examined truncated forms of Eqs. (3), (4), and (5) and concluded that linear theory can be used to calculate the high frequency part of the spectral function, W_{s_x}.

$$\overline{s_x^2} = \int_0^\infty W_{s_x}\, dn, \tag{8}$$

where n is the frequency in cycles per second. More recently, Hatziavramidis[10] solved the complete linear equations and extended the range of frequencies over which linear theory describes W_{s_x}. In this solution the pressure spectrum of Blake[11] was used and the wave properties of the flow were obtained from the frequency-wavenumber spectra measured by Morrison et al.[12] close to a wall. These indicate that the disturbances are wavelike in the x direction in that

$$ck_x = \omega, \tag{9}$$

where $c/u^* \cong 8$, and u^* is the wall friction velocity. The wavelike character was not so clear in the z direction so Hatziavramidis[10] used the ridge line, r, of the frequency-wavenumber spectra to define k_z

$$\left(\frac{k_z}{k_x}\right)_r = f\left(\frac{\omega\nu}{u^{*2}}\right). \tag{10}$$

The application of the linear momentum equations to describe turbulent flow in the viscous wall region has also been explored by Sternberg,[13] by Schubert and Corcos,[14] and by Kader.[15] The chief difference between these previous works and our own is that we have used linear theory only to describe a portion of the frequency spectrum and not the complete fluctuating velocity field. There are also some minor differences in the method of solution.

B. Pseudo-steady state approximation

The spectral function for s_x calculated by Hatziavramidis is compared with measurements in Fig. 2. This work supports the previous suggestion by Sirkar and by Lee that linear theory does a good job in describing the high frequency velocity fluctuations close to the wall, but that it is not adequate to describe the energy containing eddies. In order to introduce nonlinear effects,
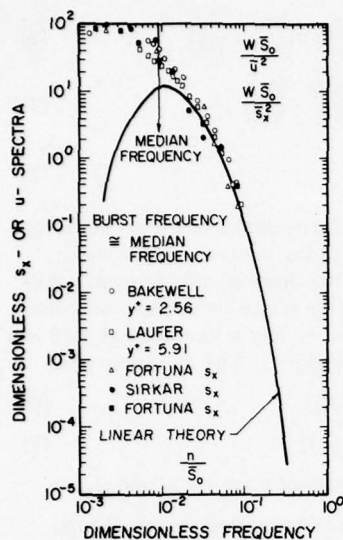
FIG. 2. Comparison of linear theory with measurements of the spectral density function of the component of the turbulent velocity fluctuations in the direction of mean flow, $\bar{S}_0 = u^{*2}/\nu$.

it is necessary to make a more detailed statement about the kinematics of the energy containing eddies in the viscous wall region. An approach along these lines was taken by Fortuna[16] to explain his results on the relation of the amount of drag reduction to the lateral wavelength, λ, of the flow oriented eddies in the immediate vicinity of the wall. This work was largely motivated by results obtained with multiple electrodes that will be presented later.

The flow close to the wall is assumed to be dominated by eddies of the simple form shown in Fig. 3(a). These are periodic in the z direction and are in a plane perpendicular to the direction of the mean flow. The transverse velocity associated with these eddies is given by a function, homogeneous in the flow direction, which varies harmonically in the z direction and randomly in magnitude with time t,

$$w = \hat{w}(t) f(y) \sin(2\pi z/\lambda). \tag{11}$$

This type of flow pattern would indicate a variation of s_z of the form shown in Fig. 3(b).

Fortuna visualized a fluid with a large component of x momentum being convected to the wall by these eddies. The fluid exchanges momentum with the wall and therefore, the fluid moving from the wall is deficient in x momentum. This would give rise to a spatial variation of s_x of the type shown in Fig. 3(b).

The variation of the x component of the velocity in this simple eddy is calculated by solving the equations

$$\frac{\partial U}{\partial t} + w\frac{\partial U}{\partial z} + v\frac{\partial U}{\partial y} = \nu\left(\frac{\partial^2 U}{\partial y^2} + \frac{\partial^2 U}{\partial z^2}\right), \tag{12}$$

$$\frac{\partial w}{\partial z} + \frac{\partial v}{\partial y} = 0, \tag{13}$$

with the boundary conditions

$U = 0$ at $y = 0$,

$U = U_L$ at large y. (14)

From this solution, an average velocity at a given distance from the wall, $\langle U \rangle$, can be defined as an average over z and over t. Then, the velocity fluctuation in the x direction obtained from this solution is given as $u = U - \langle U \rangle$.

Fortuna carried out his calculations by using the pseudo-steady state assumption that $\partial U/\partial t = 0$ and by neglecting $\nu \, \partial^2 U/\partial z^2$ compared with $\nu \, \partial^2 U/\partial y^2$. He used a simple form of (11) to describe the y variation close to the wall; i.e., $f(y) = y$. Equations (12) and (13) can then be solved using a similarity transform to give $U(y)$ provided $\hat{w}(t)$, λ, and U_L are specified.

Fortuna assumed that $\hat{w}(t)$ is given by a Gaussian distribution and he specified the mean square of $\hat{w}$ by using the following empirical fit to the turbulence measurements of Laufer[17] and of Fowles[18] in the region $0 < yu^*/\nu < 20$

$$(\overline{w^2})^{1/2}/u^* = 0.077(yu^*/\nu). \tag{15}$$

From the measurements of the flow oriented eddies close to a wall presented in a number of laboratories, he used $\lambda u^*/\nu = 100$. The value of U_L was selected so that in the limits of $y \to 0$

$$\overline{U}(y)/u^* = yu^*/\nu. \tag{16}$$

A comparison of the calculated $\overline{U}(y)$ with Laufer's measurements is given in Fig. 3, where U_L/u^* was taken as equal to 13.5 in order to satisfy condition (16). The good agreement between the calculations and the measurements seems to support the assumption made by Fortuna that the Reynolds stresses are associated with convective motions of the dimensions of observed flow oriented eddies close to the wall.

Fortuna carried out this calculation mainly to show that the increase in $\lambda u^*/\nu$ that he observed in drag re-
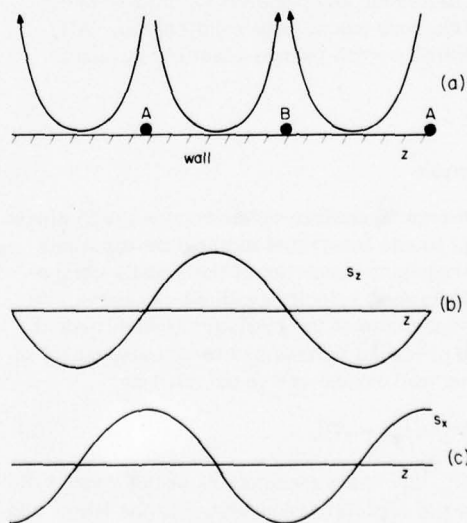

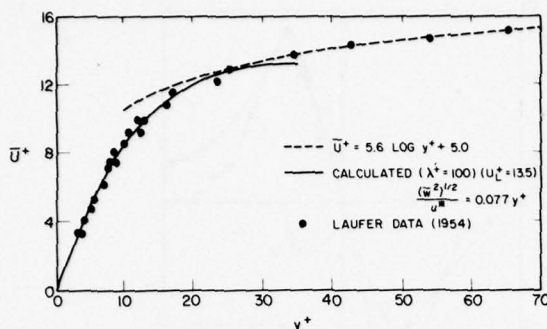FIG. 3. Idealized eddy pattern used in the pseudo-steady state analysis.

FIG. 4. Comparison of velocity profile calculated from pseudo-steady state solution with measurements.

FIG. 6. Comparison of measurements of $\overline{s_x^2}$ and $\overline{s_z^2}$ with determinations $\overline{u^2}$ and $\overline{w^2}$ close to a wall.

ducing polymer solutions is consistent with the magnitude of the measured decrease in the friction factor. For this purpose he matched the velocity profile in Fig. 4 with the following logarithmic relation assumed to hold for large y

$$\overline{U}/u^* = 5.60 \log(yu^*/\nu) + B. \qquad (17)$$

For a Newtonian fluid, with dimensionless lateral wavelength of $\lambda^+ = 100$ and $\overline{w^2}$ given by (15), B is evaluated as equal to 5.0. An increase of the value of λ^+ or a decrease of the coefficient in (15) require larger values of U_L^+ to satisfy condition (16), and therefore give larger values of B. Since the friction factor is related to the value of B, the magnitude of the decrease in the friction factor associated with increases in λ^+ and with decreases in the transverse component of the turbulent velocity fluctuations close to the wall can be calculated. Fortuna found this calculated decrease to agree with measurements for small amounts of drag reduction, as shown in Fig. 5.

IV. THE INTENSITY, SCALE AND SPECTRAL DENSITY FUNCTION OF THE FLUCTUATING VELOCITY GRADIENT

Measurements of $\overline{s_x^2}$ and of the frequency spectrum of s_x obtained with wall electrodes are compared with turbulent velocity measurements close to the wall obtained

FIG. 5. Comparison of calculated relation between λ^+ and percent drag reduction with measurements.

by other techniques in Fig. 6. Hot wire measurements of $(\overline{u^2})^{1/2}$ normalized with the local average velocity $\overline{U}$ extrapolate to a finite limit approximately equal to the value of $(\overline{s_x^2})^{1/2}/\overline{S}_x = 0.30 - 0.35$ determined with wall electrodes. These results indicate that for $y^+ < 7$

$$(\overline{u^2})^{1/2}/u^* = 0.32 y^+. \qquad (18)$$

Furthermore, it is found that the spectral function for s_x agrees with the spectral function for measurements of u at $y^+ < 7$, provided the measurements are normalized using wall parameters u^* and ν. This conclusion differs from our previous assessment of available measurements made at the IUTAM Symposium in Kyoto.[2]

These results support the suggestion made by Corrsin[19] that the viscous sublayer can be pictured as a Couette flow extending from a fixed wall at $y^+ = 0$ to an oscillating wall at $y^+ \cong 6$. An extrapolation of Laufer's anemometer measurements suggests, in agreement with this model, that transverse velocities become quite small close to the wall (see Hinze,[20] p. 523). However, the measurements with wall electrodes disagree with this picture in that the magnitude of the s_z fluctuations is found to be about one third the magnitude of the s_x fluctuations. This shows that the strong transverse velocities associated with the "streaky" structure observed by a number of investigators extend right to the wall. This conclusion is also supported by the recent measurements of velocity fluctuations close to a wall obtained by Sherwood et al.,[18] using visual techniques (see Fig. 6).

Measurements of the spatial correlation coefficient of s_x in the z and x directions are presented in Fig. 7. These show that the eddies close to the wall are greatly elongated in the x direction. The ratio of the dimensionless macro or integral scales, $\Lambda_{xx}^+/\Lambda_{xz}^+$, is approximately equal to 40. This result is consistent with the streaky structure close to the wall disclosed in visual experiments from a number of laboratories.

V. MEASUREMENTS WITH MULTIPLE WALL ELECTRODES

Measurements with multiple wall electrodes of the type shown in Fig. 8 can be more directly related to the
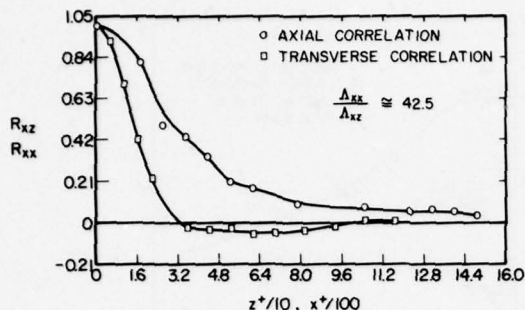
FIG. 7. Spatial correlation function s_x in the x and z directions.

FIG. 9. Spatial correlation coefficient of s_x at z with s_x at $z + \Delta z$.

spacing of the streaks observed by Kline and Runstadler[21] when they injected dye at a wall. If the dye streaks are associated with updrafts, then the indicated dimensionless streak spacings λ^+ are obtained. Lee et al.,[8] have analyzed a large number of these patterns to obtain an average value of $\lambda^+ = 75$ for both s_x and s_z. This value is close enough to the value of λ^+ reported in the literature to suggest that the pattern of the variation in wall velocity gradients corresponds to the streaky wall structure discussed in the literature.

Results of the type shown in Figs. 7 and 8 are consistent with the simple model of the flow close to the wall used by Fortuna, Eq. (11). The correlation measurements in Fig. 7 support the assumption of eddies which are approximately homogeneous in the x direction. An analysis of patterns of the type shown in Fig. 8 reveals an "approximate periodicity" in the z direction and does not show any difference in regions of inflow or outflow with reference to the spatial variation s_z or s_x.

An examination of simultaneous measurements of s_x and of s_z also seem to support the pseudo-steady state model outlined in Sec. IIIB. One of the striking features of these measurements is that for a large fraction of the time the phase difference of the spatial variation of s_x and s_z is as depicted in Fig. 3.

A more quantitative evidence for the frequent occurrence of these patterns can be obtained from measurements of spatial correlation between the longitudinal

and transverse components of the velocity gradient shown in Fig. 9. The correlation coefficients reveal a large positive and a large negative peak separated by a dimensionless distance of $z^+ = 53$. The idealized eddy pattern shown in Fig. 3 would give a periodic correlation coefficient with positive and negative peaks separated by a distance $\lambda/2$.

VI. MEASUREMENTS OF PHASE SHIFTS IN THE VELOCITY FIELD

The results presented in the previous section as well as the good agreement of the calculated average velocity field with measurements would seem to support the model for the flow oriented eddies in the viscous wall region outlined in Sec. IIIB. However, recent experiments,[7] which combined measurements of the turbulent velocity field at $y^+ = 13$ with measurements from multiple wall probes, are not consistent with the use of a pseudo-steady state assumption in that they show appreciable phase shifts between the velocity fields detected by the wall probes and by probes in the fluid.

Figure 10 presents measurements of the correlation between s_x and the component of the velocity fluctuations in the direction of mean flow, u_x, at $y^+ = 13$. The com-

FIG. 8. Determination of eddy structure from instantaneous velocity measurements, Re = 35 900.
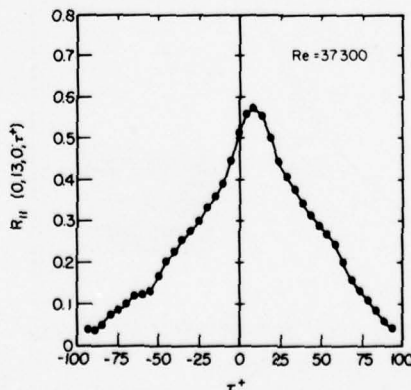
FIG. 10. Correlation between s_x and delayed $u(y^+ = 13)$.
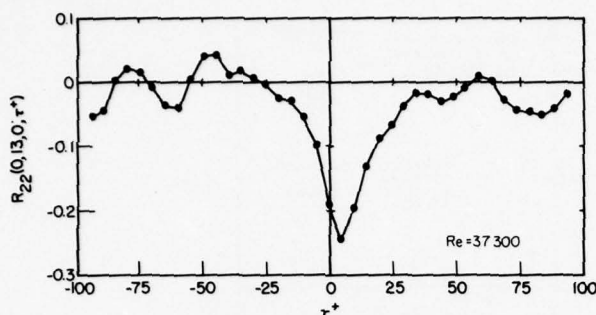
FIG. 11. Correlation between q and delayed $v(y^+ = 13)$.

ponent u_x, was delayed by time τ, plotted in Fig. 10 in the dimensionless form $\tau^+ = \tau u^{*2}/\nu$. It is noted that velocity fluctuations lead the fluctuations by a period of $\tau^+ \cong 10$. This is in line with results presented previously by Eckelmann.[22]

Even larger phase changes are obtained for the velocity fluctuations normal to the wall. From the equation of conservation of mass the following equation is obtained for the normal velocity fluctuations in the immediate vicinity of the wall

$$\frac{-\partial v}{\partial y} = y\frac{\partial s_x}{\partial x} + y\frac{\partial s_z}{\partial z}. \tag{19}$$

If the flow is approximately homogeneous in the direction of flow $\partial s_x/\partial x \ll \partial s_z/\partial z$, and (19) can be integrated to give
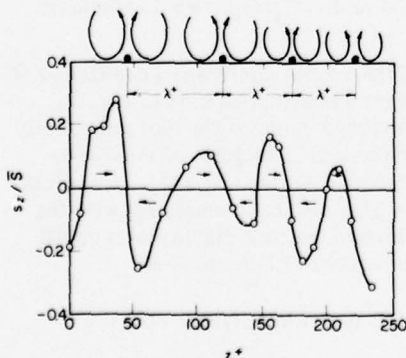
$$v_{y\to 0} = -y^2 q, \tag{20}$$

where

$$q \cong \tfrac{1}{2}(ds_z/dz). \tag{21}$$

We have obtained an approximate determination of q by measuring the difference of s_z at two wall locations. The correlation of these measurements of q with delayed measurements of v at $y^+ = 13$ are given in Fig. 11. It is
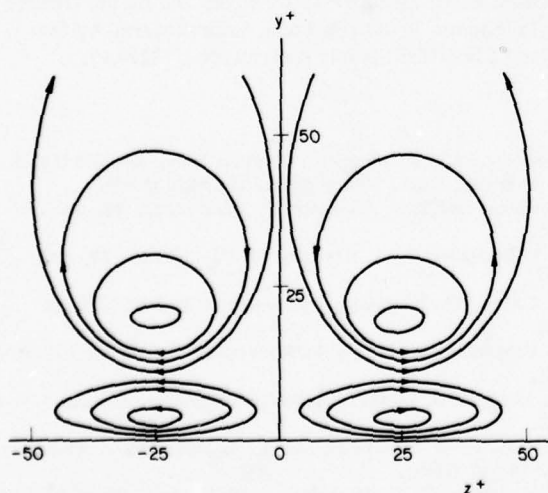
FIG. 12. Speculation regarding eddy patterns consistent with observed phase change of the fluctuating velocity close to a wall.
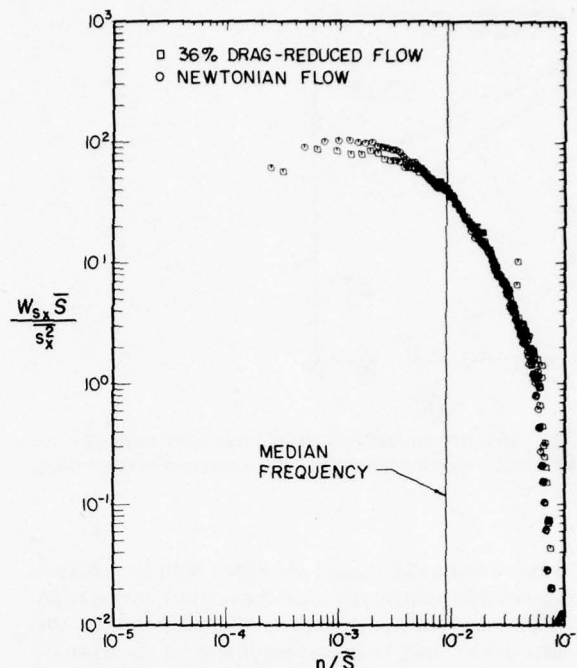
FIG. 13. Frequency spectrum to s_x for a drag reducing fluid.

noted that negative values are obtained at $\tau^+ = 0$. This would indicate that on the average the flow changes direction in a short distance from the wall. An eddy pattern of the type shown in Fig. 12 is one possible representation of the average structure of the flow oriented eddies consistent with these results. We would visualize the form of these eddies to be continually changing with time so that the extent of the closed eddy close to the surface might show considerable variation and, at times, not be present.

VII. INFLUENCE OF DRAG REDUCING POLYMERS

A comparison of the flow field close to a wall for a polymer solution and a Newtonian fluid at the same volumetric flow shows that drag reduction is accompanied by a decrease in the frequency and magnitude and an increase in the scale of the velocity fluctuations. We have taken the viewpoint, however, that the comparison should be made at the same friction velocity. A slightly different picture emerges.

Figure 13 shows data on the spectral density function of s_x obtained by Chorn[5] for a drag reducing fluid. It is noted that when normalized with wall parameters, the data are the same as that obtained for a Newtonian fluid. This indicates that the median frequency scales as u^{*2}/ν, or the average velocity gradient at the wall, $\overline{S}_x$. The decrease in frequency observed for drag reducing fluids is proportional to the decrease in the velocity gradient.

Figure 14 shows data for mean squared values of s_x and of s_z. It is noted that these decrease slightly more than does the velocity gradient after adding drag reducing polymers.
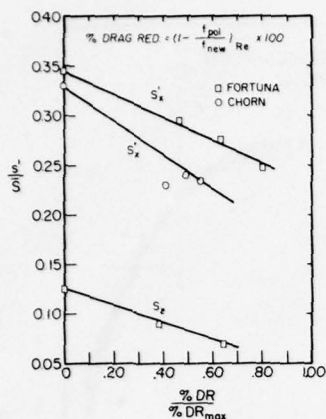
FIG. 14. Relative intensity of shear stress fluctuations versus percent drag reduction relative to the maximum percent drag reduction.

The most dramatic change observed with the addition of drag reducing polymers is in the spatial correlation coefficients and turbulent scales. Fortuna[1] estimated the influence of drag reducing polymers on the wavelength λ^* of the flow oriented eddies by determining the value of z^+ for the first zero crossing of the spatial correlation coefficient. This turned out to be an unreliable method since with increasing drag reduction the zero crossings became more poorly defined. Fortuna and Eckelman, [23] therefore, used a direct method which involved the analysis of signals from multiple wall electrodes as outlined in Sec. V. More recently, Chorn[5] has measured the ratio of the scales of drag reducing fluids and a Newtonian fluid by determining the integral of the lateral spatial correlation coefficient, Λ_{xz}^+.

The measurements of Fortuna and Eckelman and of Chorn are given in Fig. 15. These show a large increase in the ratio of the lateral scales of drag reducing and Newtonian fluids with increasing drag reduction.

It is convenient to think of the parameter λ as a measure of the small scale disturbances in the lateral direction in the same sense that the scale B of the wavenumber spectrum shown in Fig. 16 would correspond to the length characterizing the second zero crossing of its

FIG. 16. Comparison of hypothetical wavenumber spectra with their Fourier transforms.

Fourier transform. The measurements presented in this section then suggest that the role of the drag reducing polymers is to dampen the high wavenumber disturbances close to the wall. This gives rise to a less pronounced drop off of the wavenumber spectral density function at large wavenumbers as evidenced by the change in the form of the correlation function. The increase in the average distance between zero crossings (equal to $\lambda^*/2$) of the signal characterizing the lateral variation of the fluctuating velocity is then an indication of the damping of the large wavenumber components of the spectral function.

The apparent insensitivity of the shape of the frequency spectrum to the addition of drag reducing polymers shown in Fig. 13 is quite surprising in view of the observed variations of the spatial correlation function or the wavenumber spectrum. The reason for this is not understood but does seem to suggest that the high wavenumber components are not characterized by any particular range of frequencies.

ACKNOWLEDGMENTS

FIG. 15. Ratio of scales versus percent drag reduction relative to maximum drag reduction.

[1]G. Fortuna and T. J. Hanratty, J. Fluid Mech. **53**, 575 (1972).

[2]T. J. Hanratty, Phys. Fluids Suppl. **10**, S126 (1967).

[3]K. K. Sirkar and T. J. Hanratty, J. Fluid Mech. **44**, 605 (1970).

[4]J. E. Mitchell and T. J. Hanratty, J. Fluid Mech. **26**, 199 (1966).

[5]L. G. Chorn, Ph.D. thesis, University of Illinois, Urbana (1977).

[6]L. D. Eckelman, Ph.D. thesis, University of Illinois, Urbana (1972).

[7]M. K. Lee, Ph.D. thesis, University of Illinois, Urbana (1975).

[8]M. K. Lee, L. D. Eckelman, and T. J. Hanratty, J. Fluid Mech. **66**, 17 (1974).

[9]K. K. Sirkar and T. J. Hanratty, J. Fluid Mech. **44**, 589 (1970).

[10]D. T. Hatziavramidis, Ph.D. thesis, University of Illinois,

S118   Phys. Fluids, Vol. 20, No. 10, Pt. II, October 1977

Hanratty, Chorn, and Hatziavramidis   S118

Urbana (1978).

[11]W. K. Blake, J. Fluid Mech. **44**, 637 (1970).

[12]R. B. Morrison, K. J. Bullock, and R. E. Kronauer, J. Fluid Mech. **47**, 639 (1971).

[13]J. Sternberg, J. Fluid Mech. **13**, 241 (1962).

[14]G. Schubert and G. M. Corcos, J. Fluid Mech. **29**, 113 (1967).

[15]B. A. Kader, Fluid Mech. -Sov. Res. **1**, No. 3, 53 (1972).

[16]G. Fortuna, Ph.D. thesis, University of Illinois, Urbana (1971).

[17]J. Laufer, NACA TN 1053 (1951); NACA TN 1174 (1954).

[18]T. K. Sherwood, K. A. Smith, and P. E. Fowles, Chem. Eng. Sci. **23**, 1225 (1965).

[19]S. Corrsin, in *Symposium on Naval Hydrodynamics* Publication 515, (National Academy of Sciences-National Research Council, Washington, D. C., 1957), p. 373.

[20]J. O. Hinze, *Turbulence* (McGraw-Hill, New York, 1959), 523.

[21]S. J. Kline and P. W. Runstadler, J. Appl. Mech. (Trans. A.S.M.E.) **26**, 166 (1959).

[22]H. Eckelmann, J. Fluid Mech. **65**, 439 (1974).

[23]L. D. Eckelman, G. Fortuna, and T. J. Hanratty, Nature Phys. Sci. **236**, 94 (1972).

Drag reduction experiments with polystyrene with some implications for the mean velocity profile

L. H. Gustavsson

Department of Mechanics, The Royal Institute of Technology, Stockholm, Sweden

Results from drag reduction experiments with polystyrene in toluene are presented. Measurements were performed with a polymer sample with a molecular weight of 2×10^6 at different concentrations (c). Assuming a new sublayer portion of the velocity profile of the same form as that proposed by Virk in his elastic sublayer model, it is found that the thickness of this layer is proportional to $c^{0.76}$. The dependence of the onset wall shear stress on molecular weight was investigated for molecular weights of 2×10^6, 4.1×10^6, and 7.1×10^6. Because of degradation, the molecular weight range used was not sufficient to determine whether onset of drag reduction correlates with length or time scale.

I. INTRODUCTION

Virk[1] found that, for the turbulent boundary layer in a fluid containing drag reducing polymer additives, the mean velocity profile exhibits a new logarithmic region between the viscous sublayer ($u^+ = y^+$) and the ordinary logarithmic portion ($u^+ = 2.5 \ln y^+ + 5.5$). He denoted this part an "elastic sublayer." On the basis of an extensive set of measurements, Virk suggested that this extended sublayer is a part of the ultimate velocity profile with a velocity profile given approximately by $u^+ = 11.7 \times \ln y^+ - 17.0$. Since the turbulent energy production is known[2] to have its maximum at $y^+ \sim 10-15$ and since it has been observed that the polymers need to be close to the wall to give drag reduction,[3] one would expect the polymers to affect the flow strongly in the region close to the wall. It is of interest therefore to know how the thickness of this new wall layer depends on polymer parameters such as concentration, molecular weight, etc. This can be determined from measurements of the friction factor versus Reynolds number if one assumes that the variations of the velocity profile in the different regions are known. In the measurements presented here polystyrene with a molecular weight (M) of 2×10^6 was used and the concentration was varied to determine the dependence of the thickness of the new wall layer on concentration. Using Polyox in glycerine-water solutions, Berman and George[4] showed that the onset of drag reduction correlates better with time than with length scales. Since the expression for the terminal relaxation time of Rouse–Zimm also contains the temperature and the molecular weight, it would be useful to change these parameters, as well, in order to have an independent check for the onset correlation. In the present experiment an unsuccessful attempt was made to use three molecular weights (2×10^6, 4.1×10^6, 7.1×10^6) to determine whether onset of drag reduction correlates with length or time scales.

II. DESCRIPTION OF EXPERIMENTAL SETUP

The flow system used in the experiments is shown schematically in Fig. 1. The system was of a recirculating type with an impeller pump working at a speed of 700 rpm. The pressure drop over the test pipe was held constant by a pressure regulator, the total head being 1.5 atm. A differential pressure transducer measured the pressure drop over the test section of the pipe and the signal was displayed on a digital volt meter. The flow rate was measured by taking the time of rise to the liquid surface between two horizontal lines on a glass pipe connected to the measurement tank. The temperature was held constant to within $\pm 0.5\,^\circ$C by using a contact thermometer, a relay, and a magnetic valve (not shown in the figure). All runs were made at a nominal temperature of 30 °C. Pipe diameters used were 3 and 4 mm in the experiments to determine the thickness of the polymer dominated wall layer and 5 mm for the on set experiments. Polystyrene of the following three molecular weights were available:

$$M = 2 \times 10^6 \qquad (M_w/M_n < 1.2, \text{ Pressure Chemicals}),$$

$$M = 4.1 \times 10^6 \qquad (M_w/M_n = 1.1, \text{ Duke Standards}),$$

$$M = 7.1 \times 10^6 \qquad (M_w/M_n = 1.1, \text{ Duke Standards}).$$

The polymers were dissolved in toluene and each batch consisted of 4.5 kg of liquid.
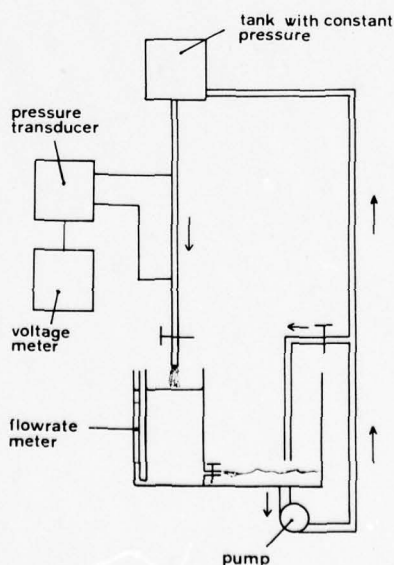
FIG. 1. Experimental setup.
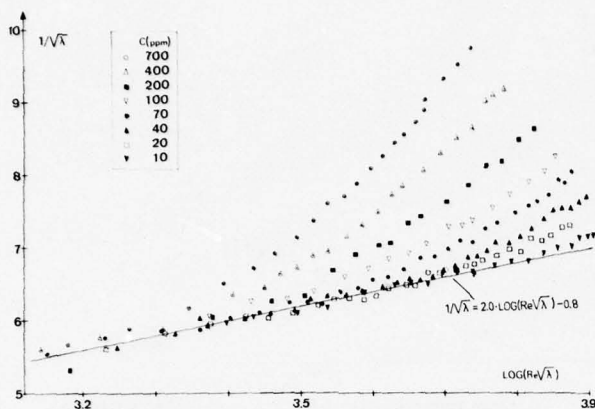
FIG. 2. Drag reduction for different concentrations. $M = 2 \times 10^6$, $\phi = 3$ mm.

III. EXPERIMENTAL RESULTS

The drag of a solution of polystyrene of a molecular weight of 2×10^6 was measured at different concentrations and in two different pipes, 3 and 4 mm. The results are shown in Figs. 2 and 3 plotted in Prandtl coordinates. The curves show the typical slope increment behavior, and one way to quantify the data is to correlate the slope increment with the concentration. An alternative way, which was used here, is to calculate from the data the increase in thickness of the polymer dominated wall layer. The following velocity variations, suggested by Virk,[1] were used:

$$u^+ = y^+, \qquad\qquad y^+ < 11.6,$$
$$u^+ = 11.7 \ln y^+ - 17.0, \qquad 11.6 \leq y^+ \leq y_e^+,$$
$$u^+ = 2.5 \ln y^+ + B, \qquad y_e^+ \leq y^+.$$

B is a constant which is coupled to y_e^+. By integrating the velocity profile over the cross section the thickness of the polymer dominated wall layer, $y_e^+ - y_0^+$ ($y_0^+ = 11.6$) was calculated. The results are plotted in Figs. 4 and 5 as a function of the wall shear stress (τ_w). It is seen that the thickness goes to zero for a specific value of τ_w which obviously is the onset wall shear stress (τ_w^*). This gives an alternative way of determining the onset

FIG. 4. Thickness of polymer dominated wall layer as a function of wall shear stress. $M = 2 \times 10^6$, $\phi = 3$ mm.

point. After onset the thickness appears to vary nearly linearly with τ_w which suggests a relationship between $y_e^+ - y_0^+$ and τ_w of the type

$$y_e^+ - y_0^+ = k(\tau_w/\tau_w^* - 1) \qquad \tau_w^* \leq \tau_w \ .$$

The slope, k, of these curves should then be a dimensionless function of concentration, molecular weight, etc. It is plotted versus concentration in Fig. 6. The results display a power dependence with an exponent of approximately 0.76. The closeness to the fractional power of $\frac{3}{4}$ may be suggestive when setting up models for the polymer dominated wall region.

It has been suggested[5] that the high molecular weight tail of a molecular weight distribution has a dominating effect on drag reduction, and it has been claimed that even with a value of M_w/M_n of as small as 1.2 the tail could be important.[6] Since higher molecular weights give larger drag reduction, one could argue that these results are representative not for $M = 2 \times 10^6$, but for the whole molecular weight distribution. Unfortunately, there are no complete measurements of drag reduction as a function of molecular weight available in the literature which makes it difficult to estimate the effect of the molecular weight distribution on these results. How-

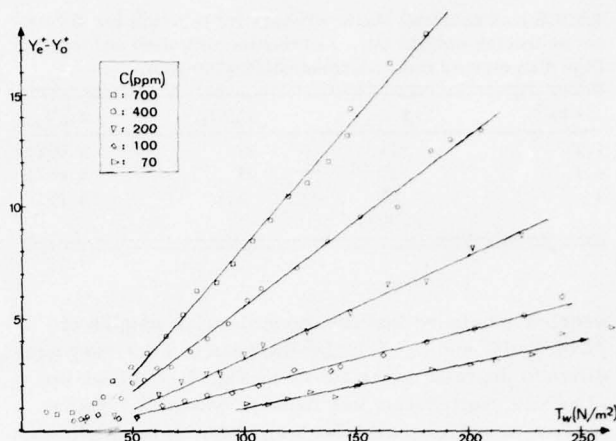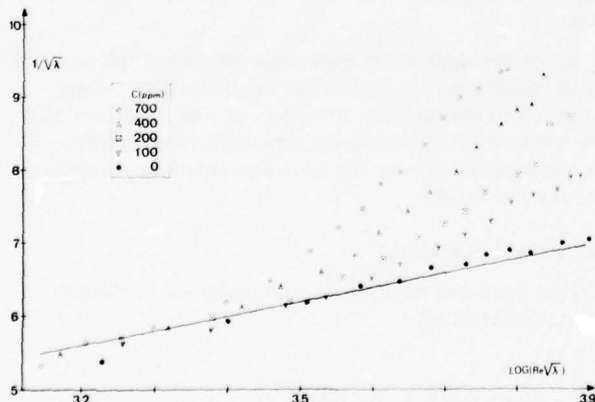FIG. 3. Drag reduction for different concentrations. $M = 2 \times 10^6$, $\phi = 4$ mm.
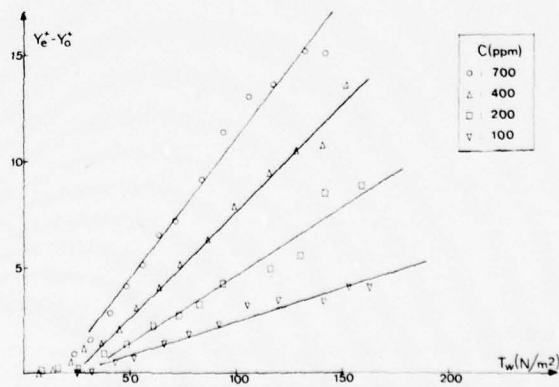
FIG. 5. Thickness of polymer dominated wall layer as function of wall shear stress. $M = 2 \times 10^6$, $\phi = 4$ mm.

TABLE I. Onset wall shear stresses (τ_w^* in N/m^2) for different molecular weights (M). Correlation with time and length. Pipe diameter = 5 mm. Concentration = 100 ppm.

$M \times 10^{-6}$	τ_w^*	T_m/T_w	L_m/L_w
7.1	11	27	0.0020
4.1	22	21	0.0021
2	23	6.5	0.0014
	($\pm 30\%$)		

ever, it was found that for the molecular weights of $M = 4.1 \times 10^6$ and $M = 7.1 \times 10^6$ the results were very sensitive to degradation as shown in Fig. 7, whereas for $M = 2 \times 10^6$ degradation was found to be small. Therefore, a very high molecular weight tail is not likely to be important for the drag reducing properties of the 2×10^6 sample since it would degrade rather quickly.

From Fig. 7 one can also estimate the variation of the onset wall shear stress, τ_w^*, with molecular weight. The results are shown in Table I, where correlations have been made with both time and length scales. The time scales used were

wall time: $T_w = \mu/\tau_w^*$;

terminal relaxation time[7]: $T_m \approx \mu[\eta]M/RT$.

The length scales employed were:

wall length: $L_w = \nu/u_\tau$;

radius of gyration[8,9]: $L_m \approx 1.42 \times 10^{-12} M^{0.57}$,

where μ is the dynamical viscosity, ν is the kinematical viscosity, M is the molecular weight, $[\eta]$ is the intrinsic viscosity, u_τ is the wall velocity, T is the absolute temperature, and R is the gas constant.

Table I shows that the time scales agree better than do the length scales. However, the formulae given are only approximate so the relevant comparisons are made vertically. For the two largest molecular weights degradation has certainly affected the results so that the "true" values of τ_w^* should probably be lower than the ones ob-
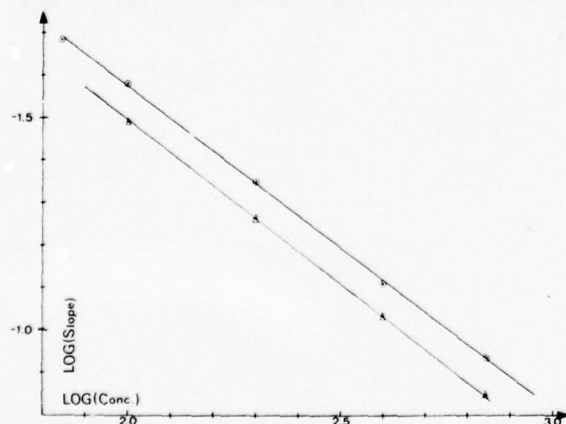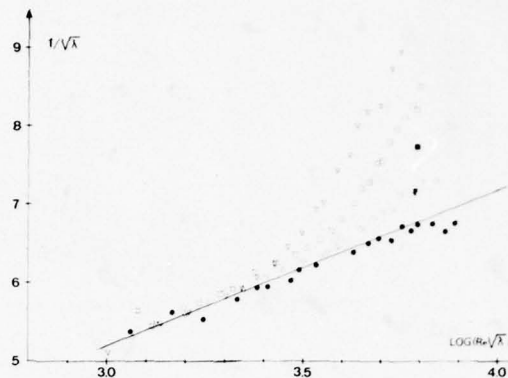
FIG. 7. Drag reduction for different molecular weights at 100 ppm. Pipe diameter $\phi = 5$ mm, ∇: $M = 7.1 \times 10^6$, $\square$: $M = 4.1 \times 10^6$, $\circ$: $M = 2 \times 10^6$, $\bullet$: solvent $\blacksquare$: $M = 4.1 \times 10^6$, 33 min running time. $\blacktriangledown$: $M = 7.1 \times 10^6$, 44 min running time.

tained. From the expressions for T_w and L_w it follows that a change in τ_w^* will affect T_w more strongly than L_w so that with a lower value of τ_w^* the time correlation would become much improved. Therefore, it is concluded that the present data do not necessarily contradict the time hypothesis. From a strict correlation point of view it is not possible to determine from these experiments whether the onset is governed by time or length scales. The molecular weights used in the experiments did not have a large enough range to yield the relevant correlation. In particular, it would have been desirable to have data on onset for lower molecular weights than those presented. Unfortunately, no onset could be observed for the next lower molecular weight available, $M = 6.7 \times 10^5$, at the maximum τ_w of 380 N/m^2 obtainable with the present apparatus.

IV. CONCLUSIONS

In the drag reduction experiments with polystyrene of molecular weight $M = 2 \times 10^6$ dissolved in toluene it was found, using the logarithmic variation of the velocity with distance from the wall for the polymer dominated regime of the wall regime proposed in Virk's[1] elastic wall layer model, that the thickness of this layer grows linearly with wall shear stress from the onset point, the slope being proportional to the concentration to the 0.76 power.

Measurements of the wall shear stress at the onset of drag reduction as a function of the molecular weight were also carried out. However, it was concluded that the range of molecular weights used was not sufficient to distinguish between the time and length scale hypothesis for the onset.

FIG. 6. Slope k of curve of polymer dominated wall layer thickness versus concentration $[(y_c^+ - y_0^+) = k(\tau_w/\tau_w^* - 1)]$. $\circ$: $\phi = 3$ mm, $\triangle$: $\phi = 4$ mm.

ACKNOWLEDGMENT

[1]P. S. Virk, AIChE J. 21, 625 (1975).
[2]A. A. Townsend, *The Structure of Turbulent Shear Flow* (Cambridge University, Cambridge, England, 1956), p. 219.

[3]C. S. Wells, Jr., and J. G. Spangler, Phys. Fluids **10**, 1890 (1967).

[4]N. S. Berman and W. K. George, Jr., Phys. Fluids **17**, 250 (1974).

[5]R. W. Paterson and F. H. Abernathy, J. Fluid Mech. **43**, 689 (1970).

[6]D. L. Hunston and M. M. Reischman, Phys. Fluids **18**, 1626 (1975).

[7]J. D. Ferry, *Viscoelastic Properties of Polymers* (Wiley, New York, 1970), 2nd ed., p. 200.

[8]J. Brandrup and E. H. Immergut, *Polymer Handbook* (Wiley, New York, 1966), p. IV-12.

[9]H. Morawetz, *Macromolecules in Solution* (High Polymers, 21) (Wiley, New York, 1966), Vol. 21, p. 305.

S123   Phys. Fluids, Vol. 20, No. 10, Pt. II, October 1977

H. Gustavsson   S123

Coherent motions in the outer region of turbulent boundary layers

R. E. Falco[a]

Department of Engineering, Cambridge University, Cambridge, England

The technique of simultaneous hot-wire anemometry and flow visualization has been used to determine the average characteristics of two important scales of motion in the outer region of turbulent boundary layers: large scale motions (average length 1.6δ), and "typical eddy" motions (average streamwise length approximately $200 \, \nu/u_\tau$). Results showed that the Reynolds number dependent "typical eddies" produced most of the Reynolds stress in the outer half of the layer at $R_\theta \approx 1200$, and that they are formed on the upstream side of large scale motions at all Reynolds numbers investigated. This phase relationship explains the scaling of the frequency of occurrence of outer layer bursts (which are identified with "typical eddies") on the free stream velocity and overall boundary layer thickness, although it is found that the lengths of the "typical eddies" scale on inner layer variables. In the log region, roughly one-half of the large scale motions sampled had zone-averaged streamwise velocity defects. Ensemble averaged results showed that they were associated with significant Reynolds stress contributions. A structural model showing the phase relationship of "typical eddies" and large scale motions is presented.

I. INTRODUCTION

Careful examination of the time series of the product of the streamwise and normal velocity fluctuations, i.e., of the instantaneous Reynolds stress, shows that significant contributions to the long time average value, i.e., the Reynolds stress, $-\rho\overline{uv}$, occur over relatively short intervals. A large fraction of the time there is a very small contribution. Observations of this kind have been made in both the outer and wall regions of turbulent boundary layers.[1-6]

Three important facts have emerged from detailed analysis of the fluctuating signals, where special attention has been paid to the intervals wherein large fluctuations occur. These intervals are generally called bursts. First, it has been found that the frequency of occurrence of sublayer bursts, which have a lateral dimension proportional to the sublayer thickness, scales on U_∞ and δ. This was pointed out by Rao *et al.*[1] Laufer and Badri-Narayanan[2] confirmed this and further noted (the second point) that the nondimensional period of occurrence of sublayer bursts, $U_\infty T_B/\nu \simeq 5$ was proportional to the period for the passage of outer region bulges measured by Corrsin and Kistler,[7] $U_\infty T_B/\nu \simeq 2.5$. Ueda and Hinze[6] have also recently found that the period of occurrence of outer region bursts is $U_\infty T_B/\nu \simeq 2.5$. Third, examination of the uv signal over the outer part of the layer, $y^+ > 30$, showed it to be intermittent, with the width of the peaks a small fraction of the layer. Lu and Willmarth[3] measured the duration of these peaks of high uv across the outer region and found that it increased by roughly a factor of two as the measurement position was moved across the layer, and that the period of occurrence changed little with increasing distance from the wall, over the outer region (also see Ref. 1).

A partial explanation of these facts relies on a now classical suggestion (which is being challenged in this

paper) that the large eddies (which are Reynolds number independent) produce most of the Reynolds stress.[8] It appeared possible that the large eddies, which scale on U_∞ and δ, upset the sublayer on average once every other passage, causing a sublayer burst. Since it is known that most of the production of turbulence occurs near the edge of the sublayer, and that this occurs as the result of the erupting sublayer fluid,[9] by suggesting that these sublayer eruptions grew into the large eddies, a cycle of events was hypothesized.[10]

However, there are many problems with this picture. The most obvious is the difference in size between the sublayer bursts and the bulges of the layer, a difference which increases with Reynolds number. The second problem is the higher frequency of occurrence of the bulges; there are roughly twice as many bulges as sublayer bursts. Furthermore, direct evidence suggesting that large scale motions are not the most important stress producing motions, has been obtained by Lu and Willmarth.[3] They showed that about 40% of the Reynolds stress at $y/\delta = 0.823$ was associated with small scale motions ($\sim \delta/10$ at $R = 4230$) that produced large intermittent contributions (peaks $> 10 \, \overline{uv}$). Falco[11] following the evolution of a smoke marked turbulent boundary layer observed a repetitive family of motions, called "typical eddies." They appeared to be highly coherent. Their movement relative to the surrounding marked fluid, suggested that they produced an important fraction of the Reynolds stress. These motions were strongly Reynolds number dependent. Observations of the motion of large scale features indicated that they were much less coherent. Falco and Newman[12] using the technique of combined simultaneous flow visualization/ hot-wire anemometry, observed the passage of all features of the turbulent boundary layer past an x wire at $y/\delta = 0.87$. They found that significant uv and v signals occurred when Reynolds number dependent "typical eddies" passed. The average "typical eddy" scale was 0.25δ (δ is the height of the boundary layer at which $U = 0.99 U_\infty$). Furthermore, large magnitude uv peaks
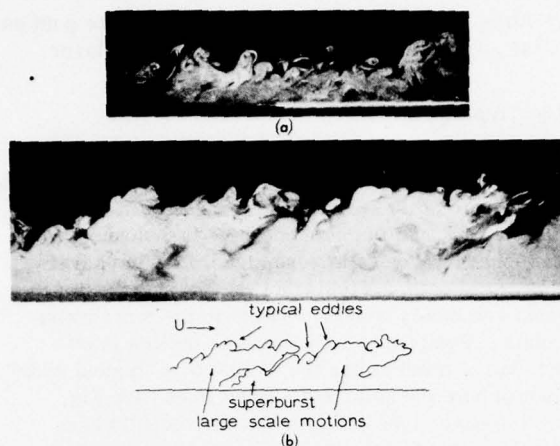
FIG. 1. Visualized turbulent boundary layers. Light plane is normal to the wall and parallel to the stream direction. (a) $R_\theta \approx 1000$: "typical eddies" are a large fraction of the boundary layer thickness. (b) $R_\theta \approx 4000$: "typical eddies" are a smaller fraction of the layer thickness and large scale motions (see sketch) are more easily definable. A superburst is also noted.

with length scales approximately the size of the bulges were never observed.

Falco[11] had earlier noted that the bulges of the boundary layer, which are defined by the boundary between marked and unmarked fluid at the edge of the boundary layer, continue to be defined in the interior of the layer by a boundary between the high smoke concentration of the fluid in the bulge and adjacent fluid of lower concentration. These regions, defined by the bulge at the top of the layer, and by concentration gradients that extend from the smoke-no smoke interface deep into the layer are called large scale motions (see Fig. 1). The combined smoke/hot-wire technique allows a single large scale motion to be isolated and its signal examined in the intermittent as well as the fully turbulent part of the layer. Because the motions can be isolated, these signals can be nondimensionalized to a common length, and ensemble-averaged large eddy signatures can be obtained.

The investigation reported herein had several goals in mind. The first was to provide further details of the "typical eddy" motions. An association between the average length scale of the "typical eddies" and that of the bursts measured by Lu and Willmarth[3] in the outer part of turbulent boundary layers was noted in Ref. 11. Clearly, the bursts are *not* large scale motions; thus, the fact that their frequency of occurrence scales on U_∞ (the free stream velocity) and δ, needs explaining. The second objective was the examination of the large scale motions with the combined smoke/hot-wire technique to obtain a quantitative measure of their fluctuating velocity and Reynolds stress, particularly in the fully turbulent part of the layer. Additional aims were: to examine the visual records of turbulent boundary layers for evidence of classes of motion other than these two in the outer region of the layer; to determine if there was a link between the "typical eddy" and large scale

motions; and if possible, to relate these motions to the structural data described here.

II. EXPERIMENTAL TECHNIQUE

The low Reynolds number experiments were made in the turbulent boundary layer that developed along the test section floor of a low speed tunnel capable of continuous flow visualization. The floor was 0.91 m wide and 12.2 m long. The boundary layer was visualized by introducing a fog of oil droplets (mean droplet diameter was approximately 5 μ) into the flow. The droplets were introduced into the flow through a row of holes which spanned the tunnel width, using an overpressure small enough that the laminar boundary layer above the holes remained stable. The laminar boundary layer with the oil fog in the lower part was then tripped. The resulting turbulent boundary layer was almost completely filled with the oil fog, hereafter called smoke. Quantitative measurements were taken 5.8 m downstream of the trip. When a sheet of light was passed through the smoke filled layer the droplets of oil in the light plane scattered the light. Thus, details of the smoke concentration patterns in any chosen plane in the flow field could be examined. Planes normal to the wall and parallel to the stream, and normal to the wall and cross stream were used in the present investigation. Using a cine camera, the evolution of details outlined by concentration gradients could be followed at all positions within the boundary layer. By moving a cine camera along with the flow the life cycle of various smoke marked features could be investigated (over the time interval in which they remained in the light plane).

Flow visualization, while providing the most efficient means of determining spatial relationships and scales, is an inefficient and inaccurate tool for measurement of velocities. Clearly, for the investigation of coherent motions, in which strong spatial relationships are implied, combining the point measurement capability provided by hot-wire anemometers and the spatial information obtained from flow visualization would be advantageous. This has been done in the present investigation. It was found that a standard DISA 55 A 38 miniature cross-wire probe, when operated at a resistance ratio of 1.8 exhibited no trends in the mean and rms response when operated in the smoke, compared with the response in clean air over the speed range of the low speed tunnel (0.8–2 m/sec). More accurately, any trends that may have existed were masked by the scatter of the data (a report documenting the changes over a wide range of Reynolds number and smoke concentration is in preparation).

The hot wires have been used to record data along a line in the illuminated plane of the boundary layer. By simultaneously recording the hot-wire signals and cine records of the smoke marked layer, conditional sampling of the hot-wire signals to specific flow features was performed. Thus, ensemble averages of the fluctuating velocities and instantaneous Reynolds stress associated with repetitive patterns in the smoke pictures were obtained.
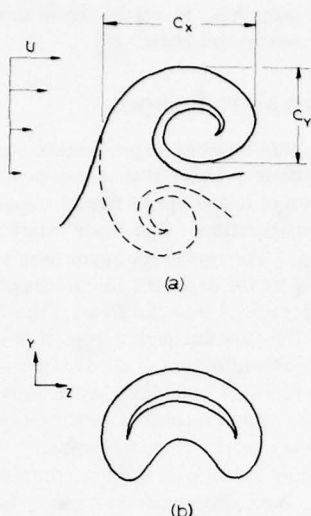
FIG. 2. Sketches of the "typical eddy." (a) The two common views seen when the light plane is parallel to the stream and normal to the wall. Solid outline represents one view, solid plus dashed the other. (b) One of the views seen with the light plane normal to the stream direction and normal to the wall (called the "crescent" view). The other view commonly seen with the light plane in this orientation is similar to the sketch in (a) with dashed plus solid lines, only rotated so the top of the "mushroom" is generally away from the wall.

III. RESULTS

An overall impression of the motion in the smoke marked turbulent boundary layer was gained by analyzing cine films. These were basically Lagrangian observations of the motions in light planes parallel to the stream and normal to the wall. In some experiments the camera was stationary, and thus features could be followed only over the field of view which was 3.5δ, but experiments were also performed with the camera following the flow at approximately $0.5U_\infty$ and U_∞. The intent of these experiments was twofold: first, to understand the extent to which the patterns resulted from wave-like phenomena, and second to be able to more completely follow the evolution of features of interest.

The results of extensive Lagrangian observations of the movements of the visualized boundary layer at $R_\theta \simeq 1000$ indicate that two basic families of motions exist. The term "family of motions" is meant to suggest a set of smoke marked features of similar appearance, which undergo (at least) part of a describable sequence of events. These are called the "typical eddy" family, and the large scale motion family. For a given flow, each family of motions has a distribution of scales, the mean value of each distribution defines the characteristic length scale of the respective family of motions. Attempts to identify other repetitive coherent motions (i.e., motions which appeared at least once every 5 to 10δ), in the outer part of the boundary layer were unsuccessful. A feature which appeared considerably less frequently, but which had a dramatic effect is briefly described later. Figure 1 shows pictures of turbulent boundary layers at $R_\theta \simeq 1000$ and 4000. "Typical ed-

dies," large scale motions, and a superburst are pointed out in the accompanying sketch of the $R_\theta \approx 4000$ layer.

A. The "typical eddies"

"Typical eddies" are highly coherent three-dimensional eddies. (The name "typical eddy" has resulted from the appearance of these motions throughout wakes, jets, turbulent spots, and in grid generated turbulence, as well as boundary layers in zero, favorable and adverse pressure gradients.) Figure 2(a) shows sketches of the two most commonly observed views in the streamwise light plane. Sometimes only the solid outline is observed, but at other times the outline of a "typical eddy" consists of both the solid and dashed lines [see Fig. 1(a)]. The lower lobe of this view has recently been more frequently observed as a result of the use of a very thin sheet of light obtainable with a laser. Figure 2(b) shows a sketch of one of the two commonly observed cross-stream views which appears crescent shaped. The other cross-stream view is the mushroom-like appearance similar to the above-mentioned streamwise view when the outline comprises both solid and dashed lines (although the top of the mushroom is generally pointing away from the wall). When this was discovered, it became apparent that typical eddies often look like distorted laminar vortex rings. The "crescent" shape in Fig. 2(b) which is seen in the cross-stream light plane, is precisely what a slice through a vortex ring looks like, for a ring orientated as in Fig. 2(a). The streamwise and normal length scales are defined in Fig. 2(a).

By measuring the length scales C_x and C_y at different Reynolds numbers, it was found[11] that "typical eddies" are strongly Reynolds number dependent. At very low Reynolds numbers their scales are the order of the boundary layer thickness, and they appear to be the important "large scale motions," i.e., in the slow motion movies, their appearance dominates the field of view as they move relative to the remaining smoke marked boundary layer fluid. As the Reynolds number is increased, the family of "typical eddies" continue to be observed, but the average scale is a smaller fraction of the boundary layer thickness, and it becomes clearer that the "typical eddies" constitute only part of the bulges of the outer part of the layer. Furthermore these smaller scale "typical eddies" can be clearly identified at various heights. They are not associated exclusively with the outer edge of the layer, nor do they appear to have evolved from the sublayer. Observations[11] have clearly shown the formation of a limited number near the middle of the layer. At high Reynolds numbers they would be considered small scale in the outer region. Falco[11] showed that the average "typical eddy" scale was close to the Taylor microscale over a decade of Reynolds number.

The average Reynolds stress produced by "typical eddies" has been measured, using the technique of simultaneous flow visualization and hot-wire anemometry, for the (low) Reynolds number $R_\theta \simeq 1200$, at $v/\delta = 0.87$. By conditionally sampling the signals from an x-wire arrangement, u, v, and uv due to the passage of a "typi-
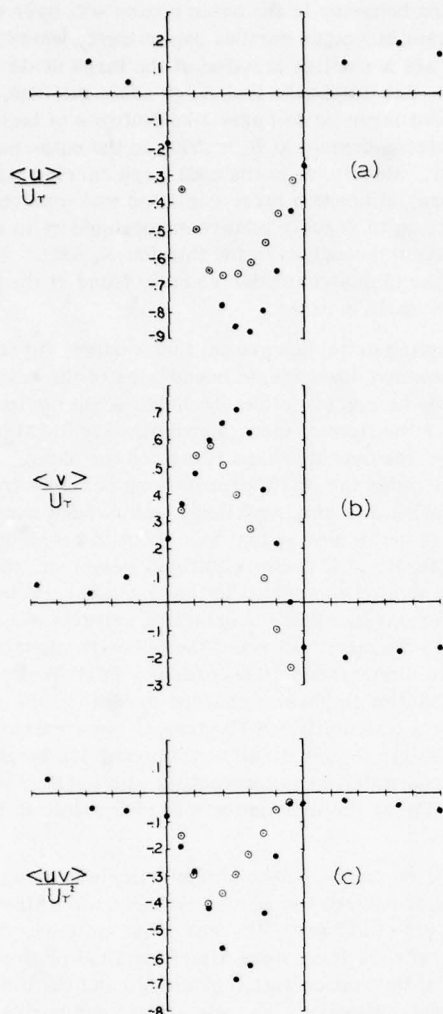
FIG. 3. Ensemble averaged distributions of $\langle u \rangle/U_\infty$, $\langle v \rangle/U_\infty$, $\langle uv \rangle/U_\infty^2$. Filled symbols are the "typical eddy" results at $y/\delta_{99} = 0.87$. Ensemble size = 33. Circles are the results of Antonia[13] for all turbulent regions at $y/\delta = 0.95$. Ensemble size is 132. Both "typical eddy" lengths and the lengths of the turbulent regions detected by Antonia have been nondimensionalized to fit between the vertical lines. Flow is from left to right.

cal eddy" were obtained. Thirty-three eddies were sampled. By nondimensionalizing the eddies to a unit length, the ensemble averaged signatures shown in Fig. 3 were obtained.

It is instructive to compare these results with ensemble averages of all of the turbulence detected inside the turbulent-nonturbulent interface. Antonia[13] used the time derivative of the uv signal as a turbulence detector to examine the nature of the turbulent regions in the outer intermittent part of a turbulent boundary layer (i.e., to examine the bulges). All regions in which the detector value exceeded some threshold level were called turbulent, and the distributions of u, v, and uv across these regions were recorded. One hundred and thirty-two regions were nondimensionalized to a unit length and the results ensemble averaged. If the instantaneous

uv derivative detector were a perfect turbulence detector, Antonia's results would represent the average distributions, $\langle u \rangle$, $\langle v \rangle$, and $\langle uv \rangle$ in the turbulent bulges at his measurement position of $y/\delta = 0.95$. Significantly, the average length of the detected regions in Ref. 13 was approximately 0.25δ. This suggests that his trigger signal was above the threshold level for only a small fraction of the average bulge length, determined from visual observations. From visual information, the average lengths of "typical eddies" have been measured over approximately two decades of Reynolds number.[11] From a curve fit of this data, it was found that the average "typical eddy" length at the Reynolds number used by Antonia is approximately 0.22δ. The similarity in the average lengths of the turbulent regions measured in Ref. 13 and the "typical eddy" scale suggests that a comparison of the u, v, and uv signatures is warranted.

If Antonia's detector was primarily sensing the "typical eddy" portion of the bulges, we would expect the signatures to look similar, when nondimensionalized so as to remove the Reynolds number effects; Antonia's data are at $R_\theta = 2160$ and the "typical eddy" data are for $R_\theta \approx 1200$. For the purposes of comparison it is assumed that nondimensionalization by u_τ will eliminate the Reynolds number dependence, since it accurately collapses the rms u and rms v as well as $\overline{uv}$ distributions over a much wider range of Reynolds number. When the results are compared (see Fig. 3) we see that the average "typical eddy" contribution for all three quantities is larger than the results of Antonia. Thus, we conclude that the "typical eddies" are very important parts of the turbulent boundary layer motions.

It is found that the variation of "typical eddy" scales with R_θ over a decade from $R_\theta = 1000$ to $10\,000$ can be effectively removed by nondimensionalizing the lengths using u_τ and ν as indicated in Fig. 4. Over this range $C_x u_\tau/\nu$ is approximately 200 and $C_y u_\tau/\nu$ grows slowly from a value of approximately 100. Lu and Willmarth[3] have measured the duration of bursts of intense intermittent Reynolds stress in the *outer* region of turbulent boundary layers at $R_\theta = 4230$ and $38\,000$. If we convert
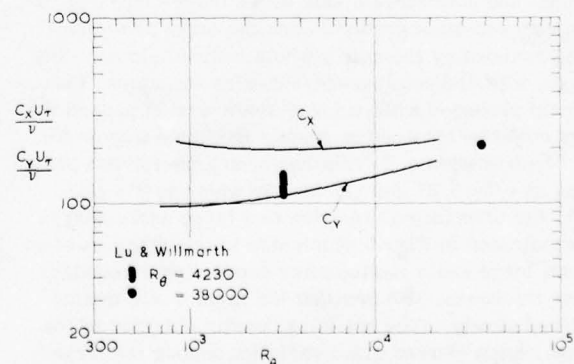
FIG. 4. "Typical eddy" streamwise (C_x) and normal (C_y) length scales nondimensionalized by ν and u_τ, as a function of R_θ. The data of Lu and Willmarth[3] for duration of bursts (converted to burst lengths using local mean velocities) in the outer part of turbulent boundary layers is shown for comparison.
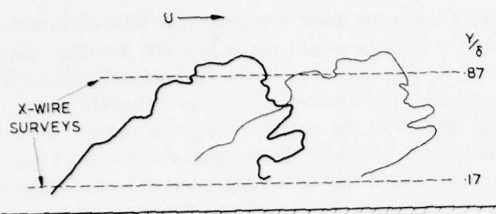
FIG. 5. Tracing of a large scale motion at two positions about δ apart, showing the relatively slow evolution of its shape. The dashed lines indicate the levels where x-wire information was obtained.

their time scales to length scales using the local mean velocity, their bursts sizes at $R_\theta = 4230$ fit over the range indicated in Fig. 4. We are further encouraged by their single point measured at $y^+ = 265$ at $R_\theta = 38\,000$ which shows an increase similar to the "typical eddy" increase. Considering the strong Reynolds number dependence of C_x/δ and $C_y/\delta$, the correspondence is very good. While it is clear from examination of the instantaneous simultaneous smoke/hot-wire records that "typical eddies" are the cause of the outer region bursts at low R_θ, this scaling suggests that "typical eddies" produce the large uv peaks at moderate and perhaps even high Reynolds numbers. Furthermore, if this correspondence is valid, we see that these outer region bursts have length scales which are strongly Reynolds number dependent.

B. Large scale motions

Observations of the visualized boundary layer as the Reynolds number is increased show that it is necessary to reach R_θ of 1000 or more before the "typical eddies" become small enough to (on average) identify in the bulges of the layer features other than "typical eddies." Because of the limitations of the tunnel, we were forced to work at $R_\theta \simeq 1000$ although it would clearly be desirable to examine large scale motions at higher R_θ. Large scale motions are defined in the smoke technique by the existence of smoke free regions or concentration gradients which extend deep into the layer on both the upstream and downstream side of the bulges (see Fig. 1). The concentration gradients and the large scale motions bounded by them as a whole evolved slowly. Using the simultaneous smoke/hot-wire technique, the signals produced when a large scale motion passed the wire could be obtained in exactly the same way as for the "typical eddies." This has been done for two positions at $y/\delta = 0.87$ and $y/\delta = 0.17$, which is $y^+ = yu_\tau/v = 67$; the orientations relative to a large scale motion are indicated in Fig. 5 which also shows tracings of an actual large scale motion after convecting a boundary layer thickness. We see that the large scale motion evolved slowly. The hot-wire results obtained in the outer region showed great variation among the large scale motions. Generally, significant Reynolds stress was associated with any "typical eddies" that were present in the large scale motion, and sometimes whole smoke filled regions would pass and no significant uv signal would result. Further documentation of large

scale motion behavior in the outer region will have to await a higher Reynolds number experiment, where typical eddies are a smaller fraction of the large scale motions scale, but it appears that large scale motions do not represent large scale burst-like features of high Reynolds stress content at $R_\theta \simeq 1000$, in the outer part of the layer. Results near the wall were carried farther along. Here, although a large variation was also observed, one quite regular feature encouraged us to see the digitization through even for this low R_θ data. This feature is the high streamwise velocity found at the back of the large scale motions.

The sampling criteria were (a) find a bulge; (b) trace the upstream and downstream boundaries of the bulge deep into the layer; (c) follow the large scale motion so defined over the field of view (approximately 3.5δ) to confirm that the overall shape remained the same. Thus, we avoided the misinterpretations possible from the observation of a single picture, and avoided sampling a large scale motion that was about to break up, or move laterally. If these conditions were met, the large scale motion was added to the ensemble. It is important to emphasize that the sampling criteria were not based on the observations of the hot-wire signals (which were simultaneously recorded). Furthermore, it is important to emphasize that the aspects of the sampling criteria which utilized Lagrangian observations made it possible to specifically avoid sampling large scale motions which were interacting with each other, at least as far as the interaction was observable in the light plane.

For all of the large scale motions sampled, an upstream and downstream boundary was defined at the wire level $y/\delta = 0.17$ ($y^+ = 67$). For most motions, the boundaries at wire level were simply defined by the intersection of the concentration gradients and the line of measurement. However, in a significant number of cases, the concentration gradients did not extend down to the wire level. In these cases, the boundaries were determined by extrapolation of a least squares fit of a straight line to the existing concentration gradient. Since the average length of the large scale motions was 1.6δ, and the average length of the extrapolation was approximately 0.1δ, the errors in defining the boundaries of the large scale flow fields were considered acceptable.

The zone averaged streamwise velocity within the large scale motions was first examined. These results showed that approximately one half of the large scale motions had a zone average, u, greater than the local mean, and one half had a streamwise zone average less than $\bar{U}$. Thus, there appeared to be two different kinds of large scale motions which we call type 1 and type 2. Type 1 has a zone average u less than the local mean. What both types of large scale motions have in common is a region of high streamwise velocity at their upstream boundary. Furthermore, the average length of both types was approximately 1.6δ. Figures 6 and 7 show the ensemble averages. Here, as with the "typical eddies," the large scale motions have been stretched or compressed to the length between the vertical lines.

FIG. 6. Ensemble averaged u, v, and uv signals for large scale motion-type 1, i.e., large scale motions which have a negative zone averaged streamwise velocity perturbation at $y^+ \approx 67$. There are 26 large scale motions in the sample.

Large scale motions of type 1, shown in Fig. 6 (zone averaged $u < 0$ at $y^+ = 67$) on average have a significant large scale normal velocity contribution coupled with their negative streamwise velocity.

Looking at the signature of u we see a significant contribution on the scale of the motion, with a stronger gradient at the back than at the front. In the immediate vicinity of the upstream boundary a strong positive peak exists. The normal component of velocity indicates downflow at the back and front and upflow in the body of the large scale motion. The ensemble-averaged Reynolds stress shows positive peaks in the back, middle, and front of approximately twice the time-averaged values. It also shows regions of very low stress. The appearance of the peaks and valleys of Reynolds stress at $y^+ = 67$ suggests that the passage of approximately half of the bulges over the wall is associated with the production of Reynolds stress in the log-region, on a scale considerably smaller than the large scale motions which are partly defined by the bulges.

Furthermore, the peak value of $\langle uv \rangle$ in the middle of the motion is approximately equal to $\langle u \rangle$ times $\langle v \rangle$, indicating a high degree of coherence over a limited region around the middle, this is true to a lesser extent near the back. The flow in the middle of large scale motion-type 1 is a large scale burst since here the uv contribution results from the outward movement of low speed fluid. A second important region of flow exists at the back, where a large scale wallward movement of high speed fluid occurs, resulting in a sweep.

Figure 7 shows the ensemble averages for large scale motions of type 2 (zone average $u > 0$ at $y^+ = 67$). The ensemble-averaged positive streamwise values found in

the center are considerably higher and extend over a larger scale than the positive u peaks found upstream of the backs of either type 1 or type 2 motions. The positive peak found upstream of the back is similar in magnitude and width to the one found upstream of the type 1 motion. Type 2 motions have an antisymmetric ensemble averaged v signature, which shows wallward moving fluid in the downstream half and motion away from the wall in the upstream half. The peak magnitudes of $\langle v \rangle$ are similar to those of type 1 motions. From Fig. 7 we can also see that the normal velocity component undergoes similar variations upstream of both types of large scale motion. An important difference under the bulge is the lower magnitude of the $\langle uv \rangle$ signature for type 2 motions; the zone average of the $\langle uv \rangle$ is somewhat less than the long time average $\overline{uv}$. The motion in the front half of type 2 motions appears to be a weak large scale sweep at $y^+ = 67$.

Although roughly half of the large scale motions were of type 1, it should not be assumed that the type 1 motions were followed by type 2 motions and so on. This was sometimes true, but a regular pattern was not apparent.

Since the large scale burst in the middle of large scale motion-type 1 occurs when the streamwise velocity is low and decreasing, i.e., the criteria used by Willmarth and Lu,[14] in the inner region to detect bursts, it appears that the large (length) scale bursts they have detected may occur under large scale motions of type 1. A further check indicated roughly the same peak values at the same value of nondimensional threshold levels (our thresholds were at $y^+ = 67$ and theirs at $y^+ = 16$). Estimates of the widths of their $\langle uv \rangle$ peaks also are close to the width of the $\langle uv \rangle$ peak under large scale motion-type 1, although the experiments were performed at quite different Reynolds numbers.
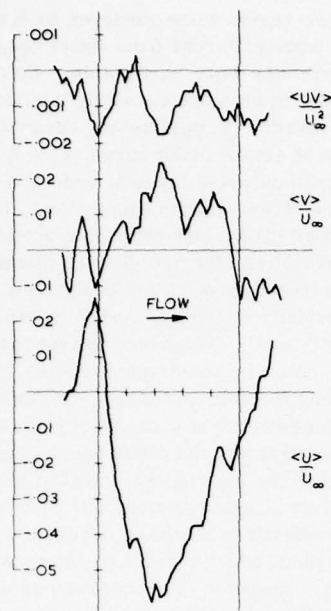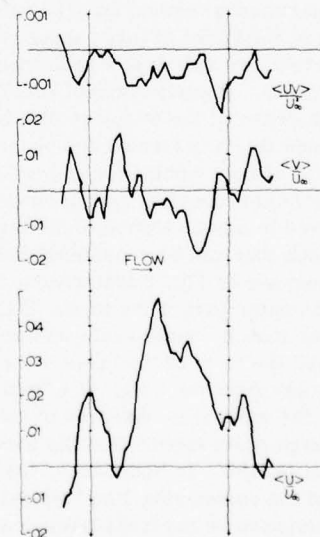

FIG. 7. Ensemble averaged u, v, and uv signals for large scale motions of type 2, i.e., large scale motions which have a positive zone averaged streamwise velocity perturbation at $y^+ = 67$. There are 29 motions in the sample.
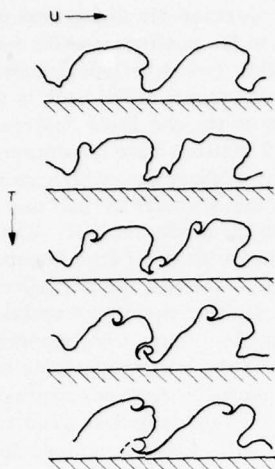
FIG. 8. Evolution of log region and outer region "typical eddies." Because of the relative convection velocities, outer region "typical eddies" convect downstream with respect to the center of the large scale motions they form on, while the log-region "typical eddies" rapidly find themselves in the large scale motions immmediately upstream.

C. The relationship between "typical eddies" and large scale motions

The suggestion of the visual and of the conditionally sampled anemometry signals is that the two families of motion represent important coherent flow modules in low and moderate Reynolds number turbulent boundary layers. Thus, it is interesting to consider the relationship between them. The basic observation is that when "typical eddies" are observed at the upstream boundary of large scale motions they produce the largest fluctuations in the u, v, and uv signals and they are most sharply defined visually. Furthermore in the Lagrangian experiments "typical eddies" have been observed to form at the backs of large scale motions. It appears that their formation is a fundamental part of the cascade process. Clearly "typical eddy" formation results in a contortion of the boundary of a large scale motion. But once they are formed and become identifiable as a result of the combination of smoke marked and smoke free fluid present in their formation region, they are observed to move relative to the large scale motions, and thus they can be considered independent motions. We can see in Fig. 8 that when a "typical eddy" forms in the outer part of the layer, it is observed to convect faster than the large scale motion and thus it will move toward the front of the large scale motion. It also moves away from the wall. If a "typical eddy" forms close to the wall, it is observed to convect from the back of a large scale motion into the front of the adjacent upstream feature. In both cases, the self-induced motion of the vortex ring-like "typical eddies" must be superimposed on the local large scale perturbation. When a "typical eddy" forms near the wall, vortex image effects also influence the observed motion.

The "typical eddies" which formed in, or just above,

the logarithmic region were observed to determine whether they were different from those seen farther out. No differences were observable. However, the technique needs to be more carefully applied to study inner region events. In particular, because of the dense concentration of smoke under large scale motions of type 1, we could only see "typical eddies" emerge from the back of the large scale motions; thus, it was not possible through direct observation to ascertain whether these "typical eddies" formed directly from sublayer bursts or whether they were the result of a re-distribution of the vorticity in the log-region by the *large scale flow fields* previously discussed; the mechanism of formation of the outer region "typical eddies." This is a point that needs further research. Although, Offen and Kline[4] have suggested that coalescence of sublayer ejections is responsible for the disturbances they found which formed in the log region, and then moved down toward the wall and caused another burst, certainly several sublayer ejections would be necessary to produce a feature of "typical eddy" size, i.e., approximately 100 cubic y^+ units. However, the observed sublayer burst period[2] is $5\delta/U_\infty$ which indicates that there just are not enough sublayer ejections available.

The other question is do "typical eddies" which are observed in the log region produce sublayer ejections? Certainly, the sweep motion that is associated with a burst as described by Offen and Kline[4] looks exactly like a "typical eddy," and its normal scale is $\simeq 100 y^+$ units as is the average "typical eddy" scale. This question also cannot be conclusively answered without further investigation; however, two additional crucial correspondences have been observed. First, is the fact that when "typical eddies" emerge from the large scale motions in the log region, they are generally observed to be convected towards the wall. This is consistent with the direction of the conditionally sampled normal velocity at the backs of both types of large scale motion (at $y^+ = 67$). In fact, the large majority of "typical eddies" which are observed in the log region remain associated with the log region, as opposed to being convected farther out. When "typical eddies" move toward the wall, they will be sweep motions. The fact that "typical eddy" scales, when made dimensionless by u_τ and ν, vary very little with Reynolds number over the decade of R_θ between 10^3 and 10^4, and the fact that their scales are close to $z^+ = 100$ in the inner region which, of course, is the sublayer streak spacing[9] suggests that "typical eddies" may be responsible for this lateral scale, and thus by implication responsible for sublayer bursts. Observations of the interaction of "isolated" "typical eddies" with a laminar boundary layer, i.e., ones which form in the overhang of turbulent spots, strongly support this hypothesis. If the hypothesis is true, then the "typical eddy" may be an intermediate structural link between the inner and outer layers of the boundary layer.

We consider the features just described to represent the essential features of the normal modes of transfer in the outer region of a turbulent boundary layer, at low and intermediate Reynolds numbers.
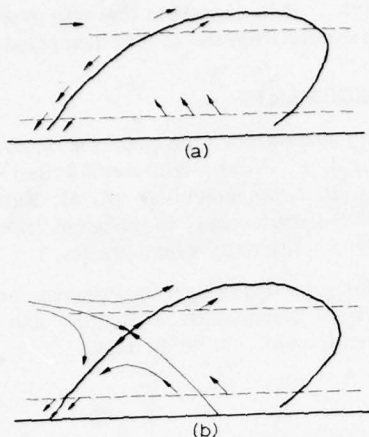
FIG. 9. (a) Flow field in regions of considerable motion within large scale motions of type 1 at $R_\theta \approx 1000$, as seen by an observer moving with the convection velocity of the upper back. (b) The model of large scale motion type 1; observer moving with the velocity of the saddle point. Note the upflow in the middle and downflow at the back.

IV. A STRUCTURAL MODEL

A simplified model of the outer flow will now be presented. First, both visual observations of evolving smoke patterns, and combined visual/hot-wire information suggest that approximately one-half of the large scale motions have a flow pattern indicated in the top half of Fig. 9, as seen by an observer moving with the convection velocity of the back of the large scale motion. This is modeled by a *saddle point* at the upper back of the large scale motion-type 1, which results in large scale wallward flow at the back and upward flow in the middle (we are convecting at $U_c \approx 0.9U_\infty$ and $V_c = 0$). Little importance is given to the downstream part. In these respects, the model is essentially different from the conceptual picture proposed by Laufer.[15] "Typical eddies" are modeled as deformed thick cored laminar vortex rings. Figure 10 shows a simplified relationship between "typical eddies" and large scale motions, which is consistent with the major features described herein. The model explains two seemingly contradictory observations. It shows that the average frequency of occurrence of outer region bursts (the "typical eddies") scales on outer layer parameters, i.e., on δ and U_∞, while at the same time the average burst length scales on u_τ and ν (see Fig. 4). Furthermore, it explains the observation that the frequency of occurrence of bursts is approximately constant across the outer region of the boundary layer.[1,3,6] Both types of large scale motion have streamwise velocity defect in the outer part of the layer, so the period of occurrence of bursts in the outer region should be approximately equal to that of the bulges, which is $2.5\delta/U_\infty$.[2] In the inner region, although large scale motions of type 2 (which occur about 50% of the time) less frequently show "typical eddies" at their lower backs, the large scale bursts which develop under large scale motion-type 1 will begin to be counted. Thus, there is a transition region in which bursts of different kinds exist. However, in the

sublayer, we should see a longer period between bursts if sublayer bursts are due to inner region "typical eddy"-wall interactions. In the model it is assumed that they are produced only, on average, every other large scale motion. This results in $U_\infty T_B/\delta = 5$, which is the sublayer bursting period.[2] It should also be noted that if these log region "typical eddies" are responsible for the sublayer bursts, then the phasing of the "typical eddies" and the large scale motions provides an explanation of the findings of Blackwelder and Kaplan[16] that a large scale velocity excess existed above and immediately after a burst. Furthermore, the positioning of the newly formed "typical eddies" on the backs of large scale motions explains the skewness in the results of Ref. 13 compared with the "typical eddy" signatures (see Fig. 3).

Finally, we wish to comment briefly on a relatively rare event in low and intermediate Reynolds number boundary layers. We call this the superburst. Superbursts are first seen in the log region, usually in a valley between two large scale motions. There are four essential differences which we can detect between the superbursts and the two burst-like motions previously discussed, even in the low R_θ movies. These are (a) the large scale of these events, at $R_\theta \approx 1000$ superbursts are several times the "typical eddy" scales; (b) the complicated internal structure, superbursts often have "typical eddies" within them and on their boundaries; (c) the very rapid evolution compared with large scale motions; and (d) they appear much less frequently than the motions described previously. Unlike those "typical eddies" which form in or just above the log region, within a few δ, superbursts have convected across the layer and have grown into new large scale motions. Coalescence with adjacent "typical eddies" is an important mechanism of superburst growth. The new large scale motions that result, at least initially, have an overall rotation in the streamwise light planes.

The complicated internal structures of the superbursts suggest that they are Reynolds number independent events. Still photographs at higher R_θ appear to show similar events, as indicated in Fig. 1. Superbursts most closely correspond to the mixing jets proposed by Grant.[17] Although superbursts may result in very large contributions to the Reynolds stress ($uv > 50$
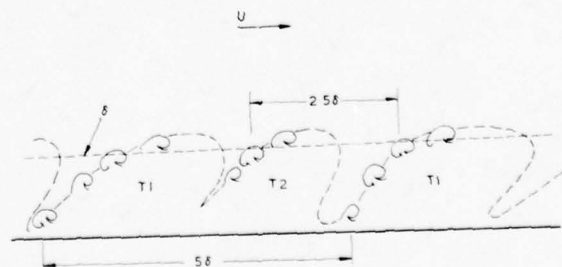
FIG. 10. A model of the flow in the outer region of turbulent boundary layers, showing the relationship between "typical eddies" and large scale motions; the ratio of "typical eddy" scale to large scale motion scale is for a moderate Reynolds number layer.

$\overline{uv}$ has been measured at $y/\delta = 0.17$), they occur relatively rarely at least in low Reynolds number boundary layers, so their overall contribution to the Reynolds stress may not be very significant. We have not observed a sufficient number of superbursts to estimate their period, however it is at least an order of magnitude greater than wall layer or outer layer burst periods. Thus, the burst frequencies measured by other investigators do not relate to these events, although they may be contaminated by them. The question of the role played by superbursts in the generation of large scale motions clearly warrants further investigation.

V. CONCLUSIONS

In conclusion a conceptual framework has been provided which ties up many of the structural results found in turbulent boundary layers. It is based on the existence of both Reynolds number dependent "typical eddies" and Reynolds number independent large scale motions.

It appears that outer layer strong intermittent bursts of instantaneous Reynolds stress are produced by "typical eddies." Since "typical eddy" scales are strongly Reynolds number dependent, these outer layer bursts decrease in scale as indicated in Fig. 4. The "typical eddy" frequency of occurrence scales on outerlayer parameters because they are produced on the backs of large scale motions. The constancy of burst frequency across the outer region is a result of the uniform distribution of the average production of "typical eddies" across the outer region. The "typical eddy" nondimensional length scale which is approximately independent of Reynolds number over a decade may set the sublayer streak spacing. Examination of the effects of the passage of a bulge on the flow at $y^+ = 67$ showed that two different types of flow fields occurred. At this position, in addition to the "typical eddy" scale bursts, the large scale motions result in both burst and sweeps events.

A violent, relatively rare event is briefly described which can transport fluid across a large fraction of the boundary layer. It is suggested that this event be considered *separately from the events described herein.*

[1]K. N. Rao, R. Narashima, and M. A. Badri Narayanan, J. Fluid Mech. **48**, 339 (1971).
[2]J. Laufer and M. A. Badri Narayanan, Phys. Fluids 14, 182 (1971).
[3]S. S. Lu and W. W. Willmarth, J. Fluid Mech. 60, 481 (1973).
[4]G. R. Offen and S. J. Kline, J. Fluid Mech. 70, 209 (1975).
[5]H. Eckelmann, S. G. Nychas, R. S. Brodkey, and J. M. Wallace, Phys. Fluids 20, S225 (October, Part II, 1977).
[6]H. Ueda and J. O. Hinze, J. Fluid Mech. 67, 125 (1975).
[7]S. Corrsin and A. K. Kistler, NACA Report 1244 (1955).
[8]P. Bradshaw, J. Fluid Mech. 29, 625 (1967).
[9]H. T. Kim, S. J. Kline, and W. C. Reynolds, J. Fluid Mech. **50**, 133 (1971).
[10]L. S. G. Kovasznay, V. Kibens, and R. F. Blackwelder, J. Fluid Mech. **41**, 283 (1970).
[11]R. E. Falco, presented at the AIAA 12th Aerospace Sciences Meeting, Washington, D. C., (1974), paper 74-99.
[12]R. E. Falco and G. R. Newman, Bull. Am. Phys. Soc. **19**, 1152 (1974).
[13]R. A. Antonia, J. Fluid Mech. 56, 1 (1972).
[14]W. W. Willmarth and S. S. Lu, J. Fluid Mech. 55, 65 (1972).
[15]J. Laufer, in *Annual Review of Fluid Mechanics*, edited by M. Van Dyke, W. G. Vincenti, and J. V. Wehausen (Annual Reviews, Palo Alto, Calif., 1975), Vol. 7, p. 316.
[16]R. F. Blackwelder and R. E. Kaplan, in *Turbulent Shear Flows* (Advisory Group for Aerospace Research and Development, North Atlantic Treaty Organization, Neuilly sur Seine, France, 1972), p. 5-1.
[17]H. L. Grant, J. Fluid Mech. 4, 149 (1958).

Spatial structure of the viscous sublayer in drag-reducing channel flows

D. K. Oldaker and W. G. Tiederman

School of Mechanical and Aerospace Engineering, Oklahoma State University, Stillwater, Oklahoma 74074

The effect of dilute, long-chain, polymer solutions upon the spatial structure of the viscous sublayer in fully developed, turbulent, two-dimensional channel flows was determined. The longitudinal, low-speed streaks characteristic of the sublayer were made visible by seeping dye through a transverse slot in one wall. Motion pictures yielded a detailed description of the streak formation process and revealed two major differences in the sublayer structure when drag reduction occurs. At a given nondimensional distance from the wall, the average transverse spacing of the streaks increases as the amount of drag reduction increases. The average streak spacing within the viscous sublayer is not a function of the distance from the wall in water flows and flows at lower levels of drag reduction. At high levels of drag reduction, the average spacing varies within the sublayer increasing as the wall is approached.

I. INTRODUCTION

The fundamental purpose of this experimental study was to gain a more thorough understanding of how drag-reducing additives affect the turbulent flow processes, particularly those in the region very near the wall. Emphasis was placed on this near-wall region because it is within this region that both the production and dissipation of turbulent kinetic energy reach sharp maxima[1] and because the additives must be in this region before drag reduction can occur.[2]

Experiments by various investigators[3,4] have shown that the dominant feature of the viscous sublayer part of the near-wall region is a longitudinal *streaky structure* that is associated with spanwise variations in the streamwise velocity component. The low-speed streaks of this structure are a crucial part of the turbulence production process because they periodically lift away from the wall, oscillate, and then burst violently away from the wall region into the outer flow.[3,5] This bursting process accounts for a large portion of the total production of turbulent kinetic energy.[6–8]

The structural characteristics of the viscous sublayer have been studied extensively and well reviewed for Newtonian flows.[9,10] These studies have yielded information about the average spanwise spacing of the streaks, the average bursting rate and the duration of the bursts, the average production of turbulent kinetic energy during a bursting period and the interaction of the outer flow with these near-wall processes. In contrast, there have been relatively few studies of the near-wall flow structure in drag-reducing flows. Those that are particularly relevant to this study are the streak-spacing studies of Eckelman *et al.*,[11] Achia and Thompson,[12] and Donohue *et al.*[13]

These three studies have each shown that the nondimensional spanwise spacing of the low-speed streaks increases as the amount of drag reduction increases. While all three investigations yielded the same nondimensional spacings for flows with less than 35% drag reduction, the three sets of results diverged as the amount of drag reduction increased. Therefore, the initial objective of this study was to conduct streak-

spacing experiments that would yield an explanation for these differences at the higher levels of drag reduction.

The flow processes in the near-wall region were made visible by seeping dye through a transverse slot into the viscous sublayer of fully developed, turbulent flows in a large aspect ratio, two-dimensional channel. Motion pictures of the flow processes marked by the dye were made and analyzed to determine the spanwise spacing of the low-speed streaks and some details of the process by which the streaks form. The latter is a particularly important part of the study because it appears that the dilute polymer solutions reduce drag by inhibiting the formation of low-speed streaks. The movies also yield some additional qualitative information about the near-wall flow processes.

Measurements were made in 8 water flows and 16 dilute polymer flows at various levels of drag reduction ranging from 13% to 61%. Two polyacrylamides (Separan AP-273 and Magnifloc 837A) and one polyethylene oxide, (Polyox WSR-301) were used at several different concentrations to produce the drag-reducing flows. However, an unequivocal explanation of why the observed changes occur does not yet exist.

II. EXPERIMENTAL APPARATUS AND PROCEDURES

A. Flow facility

This experimental study was conducted with the two-dimensional channel[13] and flow system[14] shown in Fig. 1. The clear Plexiglas channel is 2.54 m long and 38.1 mm wide, with an aspect ratio of 11.9 and a hydraulic diameter of 71.7 mm. The upstream settling chamber has a perforated plate followed by a screen that evenly redistributes the inlet flow before it enters the channel through a two-dimensional bellmouth entrance. Prior to these latest experiments the side walls were reinforced and realigned and pressure taps were added.[15]

All flow visualization experiments were made by pressurizing the stainless steel, 13.63 m³ upstream storage tank to force fluid through the channel. After passing through the channel and over a weir, the fluid passed through the 2.27 m³ catch tank and on to the drain. The large volume of the upstream storage tank allowed us to
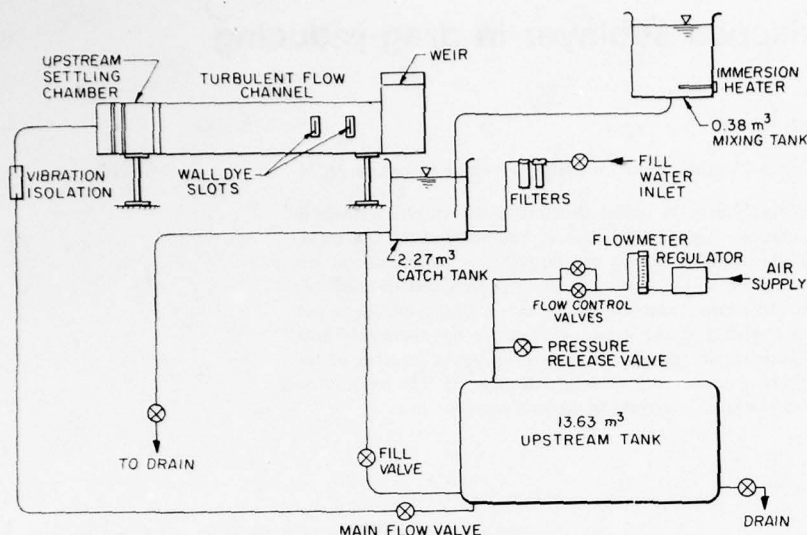
FIG. 1. Flow system and two-dimensional channel.

conduct experiments for as long as 30 to 45 min in this blow-down mode of operation. Consequently, photographs of the flow processes are clear because dyed fluid was not recirculated.

B. Dilute polymer solutions

Each batch of polymer solution was prepared from a concentrated solution (1000–2000 wppm) that was mixed in a separate 0.38 m³ stainless steel tank. The concentrated solutions were held in this tank for two hours to provide time for hydration. Dilution and thorough mixing to the desired 50 to 200 wppm concentration was done in the 2.27 m³ catch tank. This method of mixing yielded clear homogeneous solutions without any visable agglomerations.

The viscosity of each freshly mixed dilute solution was measured over a range of shear rates from 15 to 1022 sec⁻¹ using two Couette viscometers. The wall shear rates in the drag reducing flows were within this range as they varied from 94 to 654 sec⁻¹. Since the polyacrylamide solutions were slightly shear dependent, the wall shear rate in the channel flows was used to determine the viscosity needed to obtain nondimensional variables.

C. Flow rate and wall shear measurements

Mass-average velocities were calculated from flow rates which were obtained during each run by timing the collection of a quantity of fluid caught in a graduated 0.152 m³ rectangular container. The stainless steel container was mounted on wheels and placed in the catch tank where it could be quickly rolled under the weir for fluid collection and removed when full. Generally, two to four flow-rate measurements were taken during each run, with the average of those measurements taken as a final estimate of the channel flow rate.

The wall shear and shear velocities used throughout this study were calculated from measurements of the pressure difference between two 3.18 mm diam wall

taps. The upstream tap was 46.8 channel widths downstream of the entrance while the downstream tap was about 8 channel widths upstream of the exit. A two-fluid micromanometer consisting of water above carbon tetrachloride was used to measure the pressure drop and the average wall shear stress, τ_w, was calculated directly from the pressure drop measurements. The wall-shear velocity $v^* = (\tau_w/\rho)^{1/2}$ was computed from its definition using the density of the experimental fluid, ρ.

Using the pressure drop between the two pressure taps for the dilute polymer flows, ΔP_p, and the pressure drop for the same flow rate of water at the same temperature as the solution ΔP_s, the percentage drag reduction, D_r was determined for each drag-reducing flow using the equation

$$D_r = 100 \times (1 - \Delta P_p/\Delta P_s). \tag{1}$$

To verify the accuracy of the two-fluid manometer, solvent pressure drop measurements were made in a long 62.2 mm diam plastic pipe as well as the channel. The 6.1 m long pipe was temporarily connected between the upstream storage tank and the inlet of the channel. The pressure drop and flow rate measurements were made in the same manner as they were made in the channel flows. Results of water experiments in both the pipe and the channel are shown in Fig. 2 where the friction factor

$$f = (-dP/dz)D_h(\tfrac{1}{2}\rho U_m^2)^{-1} \tag{2}$$

is plotted as a function of the Reynolds number based upon the mass-average velocity U_m and hydraulic diameter, D_h. The well known Prandtl universal law of friction for smooth pipes is also shown in Fig. 2. Both the pipe and channel data are in good agreement with the circular tube correlation. These results agree with those of Hartnett et al.[16] who have shown that the circular tube correlation accurately predicts the friction coefficient for flow through rectangular channels of any aspect ratio, provided that the Reynolds number based upon hydraulic diameter is between 6×10^3 and 5×10^5.

D. K. Oldaker and W. G. Tiederman   S134

FIG. 2. Friction correlation for water flows in the channel.

D. Flow visualization tecnhiques

Visualization of the near-wall region was accomplished by seeping dyed fluid (either water or dilute polymer solution depending upon the fluid in the channel) through either of the two wall dye slots located 1.78 m and 2.06 m downstream from the two-dimensional entrance. The slot dimensions are 0.127 mm in the streamwise direction and 147 mm in the spanwise direction. It should be pointed out that since the channel walls were constructed from a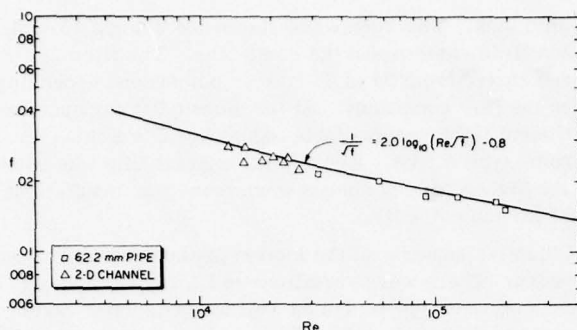 single continuous sheet of Plexiglas and the slots made free of any burrs, disturbances produced by the wall were minimized. This was clearly demonstrated in a series of experiments that were conducted for the purpose of identifying the Reynolds number for laminar-to-turbulent transition in this channel. In laminar flow the dye sheet from the slot was very uniform, and it remained undisturbed and adjacent to the wall all of the way to the channel exit. During the later stages of transition the dye sheet was intermittently partially "laminar-like" and partially "streaky." The appearance and location of these disturbances appeared to be random. Most importantly, they frequently originated well downstream of the slot. In addition to showing that the slot did not cause flow disturbances, these experiments also indicated that both the water and drag-reducing flows were fully turbulent for Re ≥ 10 000. All of the streak spacing results reported in this study were obtained at Re > 10 000.

In this study one of the most critical elements involving the wall dye slot technique is the injection rate of the dye. For this reason volumetric dye injection rates, $\dot{Q}_d$, were monitored using a series of three Matheson rotameters capable of measuring flow rates ranging from 0.004 ml/sec to 2.0 ml/sec. The rotameters were calibrated with dyed solutions of each polymer type at the same concentration and temperature as the solution flowing in the channel.

In order to more clearly interpret the results from this study, it was necessary to estimate that portion of the near-wall flow marked by the dye. This thickness is denoted as y_d. Estimates were made from continuity considerations by assuming that the dye remains next to the wall in a laminar sheet and by assuming that the velocity profile of the dyed fluid is the same as the velocity profile in the undisturbed viscous sublayer. Therefore, the volume flow rate of dye is related to the thickness of the dye sheet by

$$\dot{Q}_d = b \int_0^{y_d} \overline{U}\, dy = b(v^* y_d)^2/(2\nu) . \tag{3}$$

Here, b is the spanwise length of the dye siot, y is the coordinate normal to the wall, $\overline{U}$ is the mean streamwise component of the velocity, and ν is the kinematic viscosity. Obviously, the y_d estimates are not precise; however, they do indicate the relative thickness of the dyed region which must increase as the dye flow rate increases.

A more precise indication of the relative amount of dyed fluid in the sublayer is given by M, the ratio of the dye flow rate to the flow rate in the sublayer passing over the dye slot. The thickness of the viscous sublayer was assumed to be equal to $y^* = yv^*/\nu = 8$ because the measurements of Reischman and Tiederman[14] have shown that the nondimensional thickness of the sublayer is essentially the same for both water and drag-reducing flows. Therefore, the operational relationship for M is

$$M = \dot{Q}_d \left/ \left(b \int_0^{8\nu/v^*} \overline{U}\, dy \right) \right. . \tag{4}$$

Two types of dye were used during this study. The first which was used in only two water flow experiments was a 0.25% aqueous solution of methylene blue. The second dye was a 0.12% solution of rhodamine B(practical), a water soluble fluorescent dye that is an Eastman Kodak Company product. In the drag-reducing experiments, the dye solution was prepared from the same batch of polymer solution used in the experiment. Moreover, the dye solutions were maintained at the same temperature as the solution in the storage tank to insure that the viscosity of the dye solution was the same as the fluid in the channel.

Two different lighting schemes were employed to aid in visualizing the near-wall streaks. The first was a silhouette or back-lighting arrangement shown in Fig. 3(a). This is the same technique that was used in the experiments of Runstadler et al.[17] and Donohue et al.[13] When using this technique, the streaks appear as longitudinally oriented dye structures which are much darker than the surrounding dye between the streaks.

During the course of this study a fluorescent dye lighting technique was developed. The lighting and viewing arrangements for this technique, shown in Fig. 3(b), differ in several ways from the well known silhouette lighting technique. The most obvious difference is that the light orientation is 90° to the observer, hence, the term "side-lighting technique" will also refer to this lighting arrangement using fluorescent dye. The major effect resulting from this change in light orientation is that the dye now fluoresces light toward the observer and the near-wall structure appears self-illuminating. In turbulent flow the dye collects into longitudinal structures which bulge out from the wall a small amount. Disturbances to the dye or variations in displacement of the dye from the wall are accentuated by this side lighting and appear quite distinctively as "protrusions" or "depressions" on the surface of the dye. The observer thus has a three-dimensional view of the dye marked near-wall structure. Another important feature of the side-lighting technique is that the observer can see
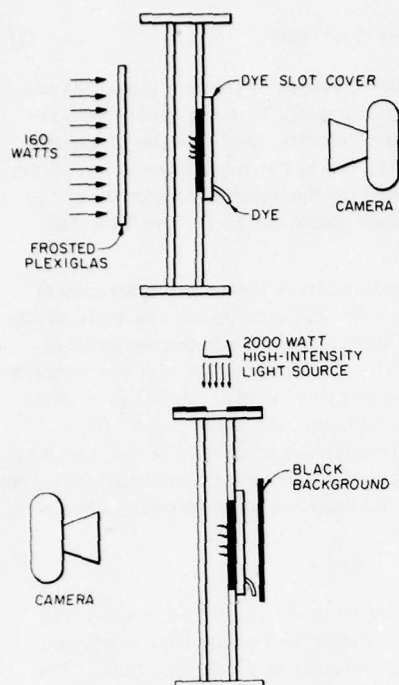
FIG. 3. End-view of channel showing the arrangement of the camera and lighting: (a) silhouette, back lighting, (b) fluorescent dye, side lighting.

lower concentrations of the fluorescent dye than he can see with the back-lighting technique which naturally "washes out" the regions of low dye concentration.

E. Motion pictures and their analysis

The majority of the motion pictures were made with a Super 8 mm Beaulieu camera equipped with a f-1.8,

25 mm lens. Two runs were also made using a 16 mm Bolex H-16 camera and the same lens. The filming speed varied from 24 to 36 frames per second depending upon the flow conditions. At the slower filming speed sufficient light was available to use Kodak's Ecktachrome type A film. Kodak 4-x Reversal film was used at the higher filming speeds when there was insufficient light for the color film.

Objective analysis of the motion pictures was a major concern. There were variations in film type, lighting technique, and type of dye as well as systematic variations in the dye flow rate. There were also more subtle variations that occurred in the processing of the film and minor day-to-day variations in the side-lighting technique which is sensitive to the position of the overhead lights. It was possible to conduct experiments where all of the conditions except dye flow were held constant and this was done to isolate the effect of this variable. However, for each observer there are some ambiguities about what should be counted as a streak. Consequently, a reduction scheme was developed using multiple observers that yielded statistically reproducible results from the various types of motion pictures.

The basic scheme involves counting, from the motion pictures, the number of streaks in a number of statistically independent frames and deducing an average spanwise streak spacing, $\bar{\lambda}$, from

$$\bar{\lambda} = b/\bar{N}_s . \tag{5}$$

Here, $\bar{N}_s$ is the average number of streaks per frame. As can be seen from Table I, part of the dye slot was occasionally masked off so that b was not always 147 mm.

Prior to reducing data from a film the observers were prepared in the following manner. They were reminded that a streak was defined to be a clearly identifiable,

TABLE I. Summary of experimental conditions.

Run number	Type of solution	Concentration of solution (wppm)	Temperature (°C)	Lighting S—side B—back	Type of dye R—Rhodamine MB—methyl blue	Type of film	Length of dye slot (mm)
SL-1	water	0	12.8	B	MB	C 8mm	109
SL-3	water	0	9.4	B	R	C 8mm	102
SL-4	water	0	9.6	S & B	R	C 8mm	102
SL-5	water	0	23.6	S	R	B & W 8mm	102
SL-6	water	0	29.0	B	MB	C 8mm	102
MG-1	837-A	100	26.7	S	R	C 8mm	147 & 122
PL-3	WSR-301	100	26.7	S	R	C 8mm	147
HB-4	Coagulant	50	20.8	S	R	B & W 8mm	94
AP-2	AP-273	100	13.2	S	R	C 8mm	147
AP-3	AP-273	100	13.0	S & B	R	C 8mm	147
AP-9	AP-273	100	14.0	S	R	C 8mm	147
AP-12	AP-273	100	23.4	S	R	C 8mm	147
AP-14	AP-273	50	23.8	S	R	C 8mm	147
AP-16	AP-273	100	26.7	S	R	C 16mm	147
AP-18	AP-273	200	26.7	S	R	C 8mm	147
AP-19	AP-273	100	27.2	S	R	C 16mm C 8mm	147
AP-20	AP-273	50	28.0	S	R	C 8mm	102
AP-21	AP-273	100	8.9	S	R	B & W 8mm	147
AP-22	AP-273	100	9.4	S	R	B & W 8mm	102
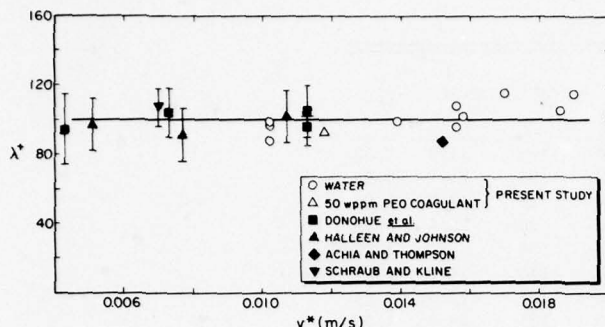
FIG. 4. Comparison of nondimensional streak spacing for non-drag-reducing liquid flows from various techniques.

single longitudinal structure which has a streamwise length of at least four times the apparent average spanwise spacing. There was no constraint placed upon a minimum spanwise spacing between streaks. Streaks were always counted at a nondimensional distance downstream of the dye slot of $x^+ = xv^*/\nu \approx 1000$ because Oldaker[15] has shown that in this region, the dye marks the flow such that $\lambda^+ = \bar{\lambda}v^*/\nu$ is independent of x^+. This distance was calculated and identified on the screen by a thread which crossed the entire picture. The projector and screen were always arranged so that the projected pictures were about 1 m×1 m and the observers were all located 3 to 4.5 m in front of the screen. The same room was used for all of the data reduction and the room lighting conditions were the same for each film. All exterior and artificial light sources were eliminated. At each session the observers were instructed to be as independent and internally consistent as possible. Finally, each film was previewed by the group for about 30 to 60 sec before reduction began.

The observers watched the movie at the normal projection rate of 18 frames per second. The movies were stopped at approximately equal time intervals that were sufficiently long to insure statistically independent counts and the streaks on that frame were simultaneously and independently counted and tabulated by each observer. The projectionist did not watch the movie so the counted frames were randomly selected. Depending upon the flow conditions a single frame would contain from 2 to 20 streaks. The number of frames counted from each movie were varied so that not less than 100 nor generally more than 300 streaks were counted for each flow condition.

The average number of streaks per frame were calculated for each observer and then the mean and standard deviation of these averages was used to determine $\bar{\lambda}$ and the 95% confidence intervals for $\bar{\lambda}$. Five to eight observers counted streaks for most of the films. When replicate reductions were made, the final mean was based upon all of the data. In two cases, an average from a single observer was rejected from the computation because it did not meet the modified 3σ test.[18] However, this was rare and the replicate reductions along with the fact that new inexperienced observers when mixed into an experienced group gave counts that were well within the scatter of the group, showed that

the reduction technique was statistically reproducible.

III. SPATIAL STRUCTURES

A. Streak spacing measurements

A summary of the experimental conditions is given in Table I while a summary of the quantitative results appears in Table II. None of the results was found to depend upon either the type of dye or lighting technique. However, the side-lighting technique with the fluorescent dye was used in a majority of the experiments because it allowed visualization of the wall structure at much lower dye concentrations than the back-lighting technique. This feature allowed systematic variations of the dye flow rate and hence systematic variations, over a wide range, in the amount of the viscous sublayer marked with dye without loss of structural detail or spatial resolution.

Streak spacing results obtained from the water flows in this study are presented in Fig. 4 where they are compared to streak spacing results deduced from other flow visualization experiments.[12,13,19,20] For all cases in this study, the ratio of dye to sublayer flow rate remained less than 1/7. The slightly larger spacings at two of the higher shear velocities are believed to be the result of poor spatial resolution due to the relatively close physical spacing of the streaks. The average nondimensional streak spacing for this water data from all the investigations is $\lambda^+ = 100 \pm 15$ (20:1 odds). It should be noted that a value of $\lambda^+ = 93$ was obtained for the single non-drag-reducing polymer flow shown. The agreement between investigations is quite good considering the wide variety of detection and data reduction schemes employed. These results also agree well with the hot-wire results of Gupta et al.[4] and the electrochemical results of Eckelman et al.[11]

The effect of M (ratio of dye to sublayer flow rate) on the nondimensional streak spacing is shown in Fig. 5 for both water and drag-reducing flows. Note that the scale for M is nonlinear. Approximate y_d^+ estimates, representing the region normal to the wall where dye marks fluid are also shown. All measurements shown in Fig. 5 were obtained using the multiple observer techniques described earlier. The measurements shown in Fig. 5 indicate that for the range $\frac{1}{7} > M > \frac{1}{27}$ the nondimensional streak spacing in flows of water has not
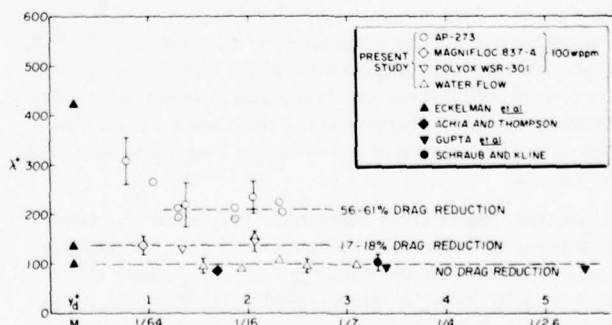

FIG. 5. Variation of nondimensional streak spacing within the viscous sublayer.

TABLE II. Summary of streak spacing results.

Run & film number	Average velocity (m/s)	Shear velocity (m/s)	Drag reduction (%)	$\nu \times 10^6$ (m²/s)	$\bar{\lambda}$ (mm)	λ^*	$1/M$	y_d^*
SL-4-1	0.287	0.0156	0	1.32	9.20	108	11.9	2.32
SL-6-1	0.174	0.0102	0	0.82	7.75	96	26.7	1.55
SL-6-2	0.174	0.0102	0	0.82	7.08	88	16.7	1.96
SL-6-3	0.174	0.0102	0	0.82	7.75	96	9.5	2.59
SL-6-4	0.174	0.0102	0	0.82	7.91	99	6.7	3.10
MG-1-1	0.238	0.0125	17	1.11	13.70	153	14.9	2.07
MG-1-2	0.238	0.0125	17	1.11	12.22	137	72.0	0.94
PL-3-1	0.248	0.0129	18	1.11	11.40	131	34.8	1.36
PL-3-2	0.248	0.0129	18	1.11	12.60	147	14.9	2.07
AP-12-1	0.311	0.0124	44	1.63	22.20	170	17.4	1.92
AP-12-2	0.465	0.0164	54	1.58	21.50	223	16.9	1.95
AP-14-1	0.334	0.0157	24	1.30	14.60	177	11.5	2.36
AP-19-2	0.474	0.0165	57	1.49	21.20	234	15.2	2.05
AP-20-1	0.401	0.0165	40	1.25	12.30	162	11.6	2.35
AP-20-2	0.557	0.0286	56	1.25	13.60	205	11.6	2.35
AP-21-1	0.485	0.0170	60	2.23	40.40	308	108	0.78
AP-21-2	0.485	0.0170	60	2.23	34.96	266	58	1.05
AP-21-3	0.485	0.0170	60	2.23	28.7	219	34	1.37
AP-21-4	0.485	0.0170	60	2.23	28.3	215	18.4	1.87
AP-21-5	0.485	0.0170	60	2.23	25.05	191	18.4	1.87
AP-22-1	0.536	0.0183	61	2.18	25.28	212	37.3	1.31
AP-22-2	0.536	0.0183	61	2.18	23.10	194	37.3	1.31
AP-22-3	0.536	0.0183	61	2.18	26.90	225	11.8	2.33

The following films were analyzed by 1 or 2 observers

Run & film number	Average velocity (m/s)	Shear velocity (m/s)	Drag reduction (%)	$\nu \times 10^6$ (m²/s)	$\bar{\lambda}$ (mm)	λ^*	$1/M$	y_d^*
SL-1-1	0.260	0.0158	0	1.21	7.77	102	13.0	2.22
SL-3-1	0.335	0.0186	0	1.33	7.49	105	15.3	2.05
SL-4-2	0.287	0.0156	0	1.32	8.14	96	11.9	2.32
SL-5-1	0.360	0.0190	0	0.92	5.61	116	7.7	2.88
SL-5-2	0.311	0.0170	0	0.92	6.30	116	7.7	2.88
SL-5-3	0.250	0.0139	0	0.92	6.58	99	7.7	2.88
SL-5-4	0.180	0.0106	0	0.92	7.67	89	7.7	2.88
HB-4-1	0.169	0.0118	0	1.08	10.21	93	9.8	2.56
AP-2-1	0.360	0.0140	52	1.86	23.51	177	19.9	1.80
AP-3-1	0.445	0.0165	55	1.95	22.82	192	20.8	1.75
AP-3-2	0.445	0.0165	55	1.95	22.43	189	20.8	1.75
AP-9-1	0.575	0.0188	59	1.86	20.08	204	19.9	1.80
AP-14-2	0.232	0.0123	13	1.30	12.62	119	11.5	2.36
AP-16-1	0.481	0.0166	57	1.49	19.47	216	6.5	3.13
AP-19-1	0.474	0.0165	57	1.49	19.21	213	15.2	2.05

changed from the characteristic value of 100. This is consistent with the measurements of Gupta et al.[4] that were made with a hot-wire array located at $y^* = 3.4$, 5.4, and 7.8 as well as the measurements of Schraub and Kline[20] made with a hydrogen-bubble wire located at $y^* = 3.3$. The measurements of Eckelman et al.[11] are representative of the structure in the region $0 < y^* < 0.5$, since the high Schmidt number mass transfer boundary layer formed by their electrochemical technique is within these limits. Consequently, the streak spacing in the near-wall region of a Newtonian flow is constant for $y^* \lesssim 8$.

Measurements from flows near the 18% drag reduction level indicate that the nondimensional streak spacing is constant for the range $\frac{1}{15} > M > \frac{1}{72}$. These estimates along with the interpolated value from the measurements of Eckelman et al.[11] suggest that λ^* is constant across the viscous sublayer for flows in the 20% drag reduction range.

In the 60% drag reduction range the value of M was found to have a pronounced influence on the nondimensional streak spacing. The measurements indicate a "plateau" region where the mean spacing ($\lambda^* \approx 200$) is unaffected by the value of M. At this level of drag reduction the region extends essentially over the range $\frac{1}{12} > M > \frac{1}{34}$. However, for values of M less than $\frac{1}{34}$, λ^* was found to increase toward the value, $\lambda^* \approx 400$, interpolated at 60% drag reduction from the measurements of Eckelman et al.[11]

The 60% drag reduction results shown in Fig. 5 are from a series of replicate experiments that were suggested by some shorter preliminary experiments.[15] These initial experiments show the same trend of λ^* increasing as M decreases. However, since the initial experiments were short, the 95% confidence intervals were large. Moreover, the lighting and film exposures varied somewhat in these initial experiments. Consequently, the replicate experiments were longer and very
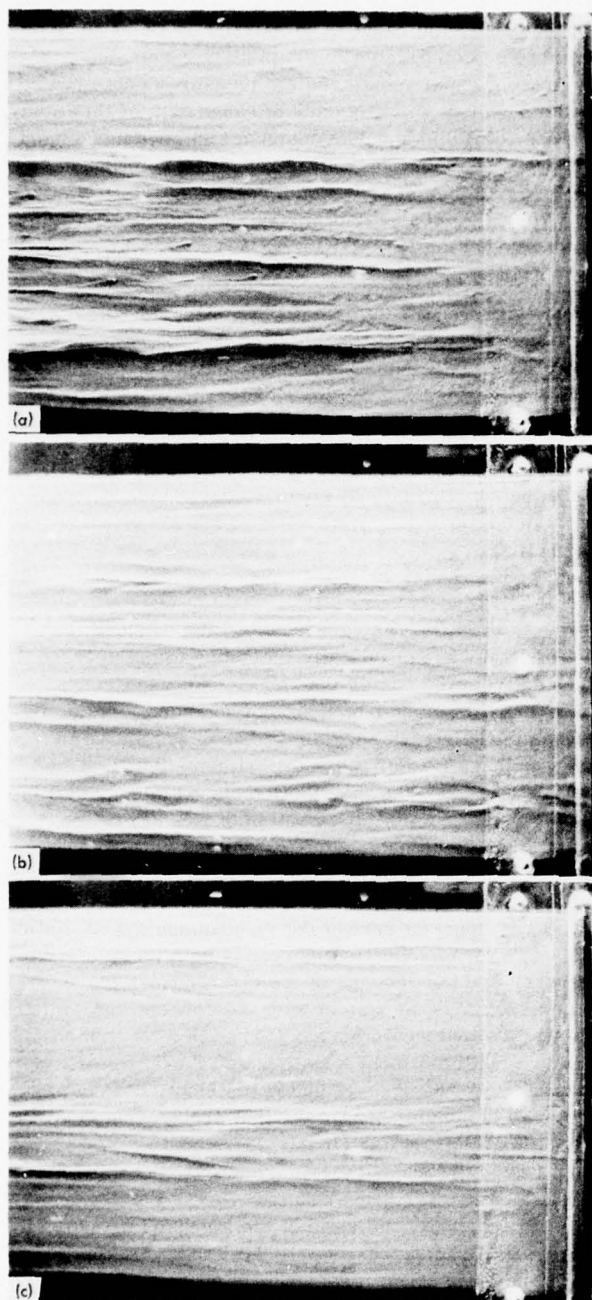
FIG. 6. Typical photographs of streak structure in a 56% drag-reducing flow. (a) $M = 1/18$, $y_d^+ = 1.9$, dye concentration of 0.12%. (b) $M = 1/18$, $y_d^+ = 1.9$, dye concentration of 0.025%. (c) $M = 1/108$, $y_d^+ = 0.8$, dye concentration of 0.12%.

carefully constrained so that there was no change in any of the experimental variables except the dye flow rate.

Since there was a concern that this increase in λ^+ could be due to an insufficient concentration of dye in the viscous sublayer, two experiments were conducted where the only difference was the concentration of the dye. In both cases, M was set equal to $\frac{1}{18}$ and the polymer solution, flow, lighting, and filming conditions re-

mained unchanged. However, in one case the dye was made up at its regular 0.12% concentration while in the second case the dye was diluted by a factor of 5. For the regular dye concentration (run number AP-21-4) $\bar{N}_s = 5.19 \pm 0.63$ and for the diluted dye (run number AP-21-5) $\bar{N}_s = 5.86 \pm 0.80$. There is only a 10% probability that these two averages are statistically different at the 95% confidence level. Photographs that are representative of the average structural features seen in these two experiments are shown in Figs. 6(a) and 6(b).

These results are strikingly different from the comparison that can be made between the experiments at the regular dye concentration for $M = \frac{1}{18}$ and $M = \frac{1}{108}$. In this case there is a 99.9% probability (95% confidence level) that the $\bar{N}_s = 3.63 \pm 0.66$ obtained at $M = \frac{1}{108}$ is statistically different from the $\bar{N}_s = 5.19 \pm 0.63$.

Figure 6(c) is a representative photograph of the streak spacing in the $M = \frac{1}{108}$ experiment. From the photograph it is apparent that sufficient dye is present to identify all of the streaks in the region marked by the dyed fluid. This as well as the other photographs that were made with the side-lighting, fluorescent dye technique also illustrate that the dye collects into streaks. Dye is not simply washed out of the region in between the streaks.

It is also highly unlikely that the observed increase in streak spacing at the higher values of drag reduction was caused by an insufficient volume of dyed fluid. The 60% drag reduction experiments were conducted with relatively cold fluid. As a result the volumetric flow rate of dye for the 60% drag reduction results shown in Fig. 5 was about twice the dye flow rate for the warmer water and 17% drag reduction flows at the same value of M.

There are additional experimental results[21,22] that support the conclusion that one can visualize different zones within the viscous sublayer by varying the dye flow rate. The object of these experiments was to measure bursting rates in water and in drag-reducing flows by counting ejections and bursts of dyed fluid downstream of a dye slot. The dye flow rate was varied for a given flow condition and histograms of the number of ejections per unit time and per unit area $\dot{N}_e''$ were constructed downstream of the dye slot. In these fully developed flows, $\dot{N}_e''$ must be constant; however, not all of the ejections downstream of the slot are marked by the dye. The dye must collect into streaks and these marked streaks must thicken and lift away from the wall and into the buffer region before dyed fluid is ejected from the wall region. That is, the dye must mark events at the outer edge of the sublayer and in the buffer region before the observer can see ejections. Therefore, it was not surprising that the maximum value for $\dot{N}_e''$ was obtained some distance downstream of the dye slot for values of $M \leq \frac{1}{9}$. What is important here, is that as the value of M increased from $\frac{1}{29}$ to $\frac{1}{9}$ the upstream edge of the maximum magnitude region of $\dot{N}_e''$ moved upstream toward the slot from an x^+ value of about 3800 to an x^+ of 1600 in a 17% drag-reducing flow. The maximum magnitude of $\dot{N}_e''$ did not change and therefore, it is reasonable to conclude that the changes in the histo-
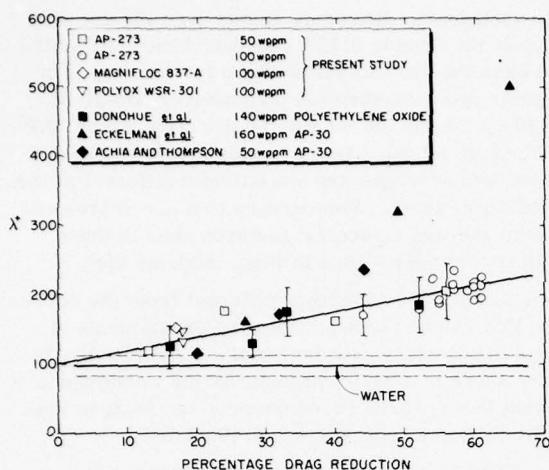
FIG. 7. Comparison of nondimensional streak spacing for $\frac{1}{12} > M > \frac{1}{37}$ with other drag-reducing data.

grams resulted from marking different regions within the viscous sublayer.

Consequently, all of the data indicate that the observed changes in streak spacing at the 60% level of drag reduction are the result of marking regions of different thickness within the sublayer. The exact y^+ location where λ^+ begins to increase is not known because the estimates of the marked region given by y_d^+ are not precise. The reported values for y_d^+ are very likely too low. However, it is clear that the increase occurs in the viscous sublayer. The important conclusion is that λ^+ increases as y^+ decreases at the higher levels of drag reduction while λ^+ does not vary within the viscous sublayer of either solvent flows or flows with small amounts of drag reduction.

This variation of λ^+ with y^+ at the higher levels of drag reduction explains the difference between the previously reported results of Eckelman et al.[11] and Donohue et al.[13] Their data are compared to data from the present study in Fig. 7. Here, the only data shown from the present study are from experiments where $\frac{1}{12} > M > \frac{1}{37}$ and consequently, the flows were marked by dye out to y^+ values of at least $1\frac{1}{2}$ or more. The present results which include data from experiments with two concentrations of Separan AP 273 (polyacrylamide), one concentration of Magnifloc 837-A (polyacrylamide), and one concentration of Polyox WSR-301 (polyethylene oxide), show a nearly linear increase in λ^+ with drag reduction which is independent of either polymer type or concentration. The solid line through the polymer data in Fig. 7 is a least squares fit of this present data. The equation for this line is

$$\lambda^+ = 1.9 D_r + 99.7 . \tag{6}$$

Figure 7 also shows the 140 wppm Polyox data of Donohue et al.,[13] the 50 wppm AP-30 data of Achia and Thompson,[12] and the 160 wppm AP-30 data of Eckelman et al.[11] Donohue et al.[13] indicated that in their measurements the dye flow rate always remained less than 10% of the sublayer flow rate. It is also believed that this ratio was greater than 3% in all those experiments.

Consequently, the range of y^+ marked by Donohue is believed to be comparable to the plateau range shown in the present experiments and the measurements show good agreement with the plateau range data of this study. The data of Achia and Thompson are in good agreement except for the single 44% drag reduction point. The data of Eckelman et al.[11] which represent the flow structure for $y^+ < 0.5$, are also in good agreement for values of drag reduction less than about 35%.

For one water and two drag-reducing experiments the streak spacing was determined by measuring the distance between each of the adjacent streaks, λ_i. Therefore, the average nondimensional spacing was calculated from

$$\lambda^+ = \frac{1}{N} \sum_{i=1}^{N} \lambda_i^+ \tag{7}$$

while the nondimensional standard deviation, s_λ^+, was estimated from

$$s_\lambda^+ = \frac{1}{N-1} \sum_{i=1}^{N} (\lambda_i^+ - \lambda^+)^2 . \tag{8}$$

Here, $\lambda_i^+ = \lambda_i v^*/\nu$. The average spacing deduced from this method was statistically the same as the average deduced from the easier method of counting streaks. However, this more laborious method does yield distributions of the streak spacings. These are shown in Figs. 8(a)–8(c). For these experiments $\frac{1}{16} < M < \frac{1}{11}$ and therefore $y_d^+ > 2$. The distribution shown in Fig. 8(a) is very similar to the λ^+ distribution of Lee et al.[23] obtained from electrochemical transverse velocity correlations in a water flow. This is further evidence to support the previous suggestion that the Newtonian streak spacing is constant across the viscous sublayer. Notice that as the drag reduction increases both the standard deviation and the average of the distributions increase. This behavior is consistent with the concept that some of the streaks that would have occurred in a Newtonian flow are inhibited from forming, and therefore are missing from the drag-reducing distributions. In particular, the number of streaks that are separated by λ^+ values less than 50 has clearly decreased in the 24% drag-reducing flow and there are no streaks this close together in the 57% drag-reducing flow. For these three distributions the ratio of the standard deviation to the average was approximately 36%. This is very similar to the ratio of 30% reported for a zero-pressure gradient boundary layer in water by Schraub and Kline.[20]

B. Observations of streak formation, growth and breakdown

Due to the increased spatial and temporal scales in the drag-reducing flows and to the visual clarity of the side-lighting, fluorescent dye technique, it was possible to observe a sequence of events which appears to be associated with the formation of low-speed streaks. These events were typically observed downstream of the dye slot in a small region of the dye sheet that was uniform because it had not yet been distorted by turbulent events. The formation sequence begins when the undistorted surface is distorted by a small crater-like depression as indicated by the shadows cast by the side-
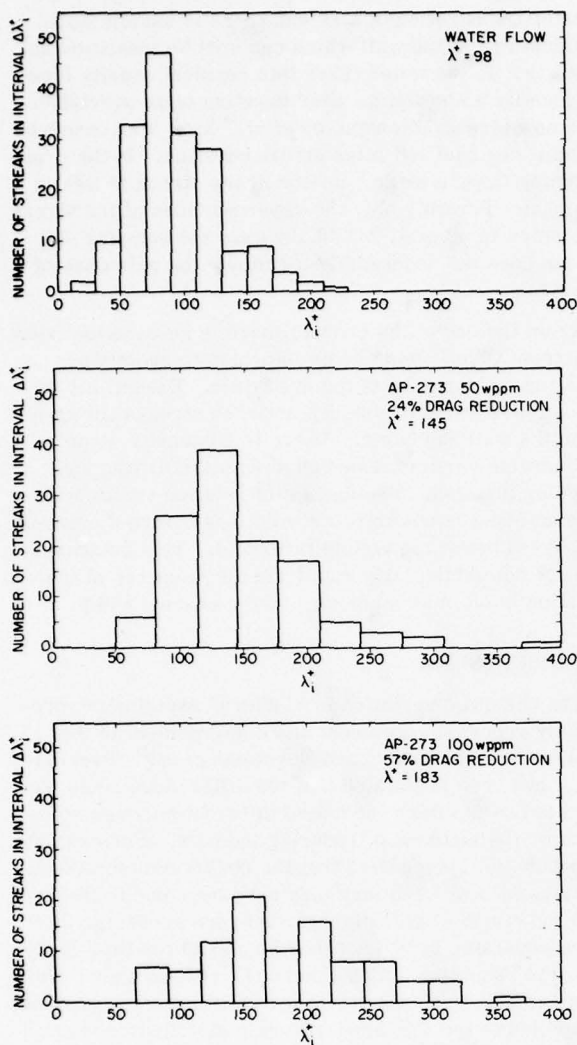
FIG. 8. Histograms of nondimensional streak spacing: (a) water flow, (b) 24% drag reduction, (c) 57% drag reduction.

lighting technique. The major axis of this oval shaped crater is aligned in the flow direction. This initial depression elongates in the downstream direction with the longitudinal sides rising up above the surrounding dye to become more brightly lit than the surrounding dye. The elongation continues forming a valley between the streak pair as they begin to grow. Similar depressions or disturbances may occur within the valley between this initial streak pair as they grow.

Figures 9(a)–9(j) show the formation and growth of a typical streak pair in a 56% drag reducing flow. The developing sequence in Fig. 9 is the outline of the high lit ridges of dye during the development of a pair of streaks. All of the sequences in Fig. 9 are shown at their correct relative locations downstream of the dye slot. Sequences 9(h), 9(i), and 9(j) have been shifted downward for visual clarification. The initial depression shown in Fig. 9(a) occurred 32 mm downstream of the dye slot. The initial growth of this disturbance is shown in sequences 9(a)–9(g). A second depression initially shown by 9(e) occurred at the time when the first depression had grown to the position indicated by 9(d). These two depressions continued to grow and then coalesced so that in Fig. 9(h) the first two depressions appear as a streak pair. Also shown in 9(h) are the locations of a third and fourth depression that occurred almost but not quite simultaneously. The continued growth of the streaks is shown in Figs. 9(i) and 9(j). Notice that the downstream end of the upper streak has disappeared in Fig. 9(j) and that there has been a slow downstream convection of the upstream end of the streaks during this 0.280 sec time period.

Using the time and downstream location of the initial appearance of each of the four depressions and by assuming that each of these depressions was caused by a single event in the outer flow, this outer-flow event would have been traveling in the downstream direction at approximately 75% of the mass average velocity. Applying the velocity profile predictions of Tiederman and Reischman[24] this convection velocity is the same as the

Scale : 3 mm per division

LOCATION OF THE THIRD AND FOURTH DEPRESSIONS

LOCATION OF DYE SLOT
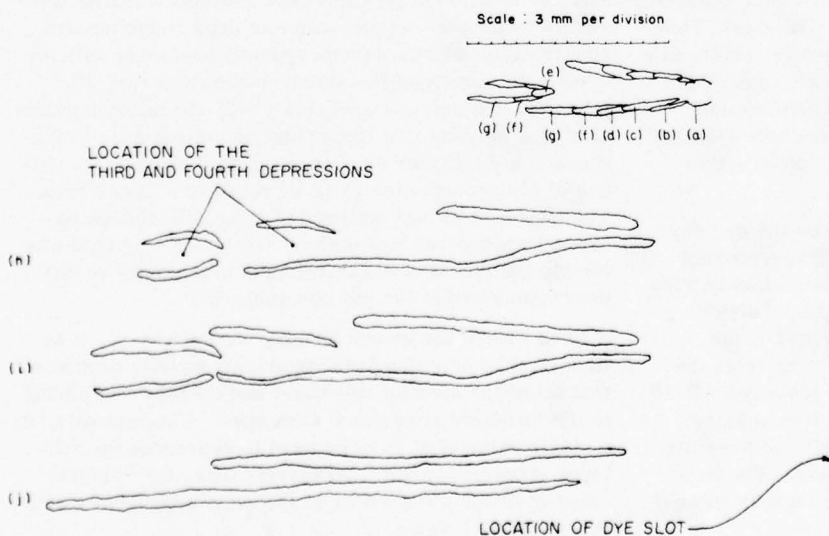
FIG. 9. Formation and growth of a streak pair in a 56% drag-reducing flow: (a) $t = 0$, initial crater-like depression; (b) $t = 0.028$ sec; (c) $t = 0.056$ sec; (d) $t = 0.084$ sec; (e) $t = 0.084$ sec, second depression; (f) $t = 0.112$ sec; (g) $t = 0.140$ sec; (h) $t = 0.196$ sec; (i) $t = 0.224$ sec; (j) $t = 0.280$ sec.

D. K. Oldaker and W. G. Tiederman   S141

mean velocity at $y^+ \approx 40$. The initial rate of elongation of these streaks occurs at approximately half this velocity.

Obviously, caution must be exercised in generalizing too much from the detailed analysis of this single streak formation sequence. However, similar formation events appear to occur in the water flows suggesting that the streak formation process could be the same for both drag-reducing and non-drag-reducing flows. Moreover, all the observations clearly indicate that the dye sheet is responding to either a wallward moving eddy or a locally intense pressure field moving at a speed considerably above the local streamwise velocity. Several such initial disturbances appear to occur at about the same time within a local region, resulting in the formation of several streaks at nearly the same time. When the back-lighting technique is used, a local accumulation of dye is usually seen, indicating a local fluid deceleration in the vicinity of the dye slot, preceding the depressions which led to streak formation. While the formation sequence just described seems to generally yield a pair of streaks, one of the most predominant characteristics of the drag-reducing movies is the appearance of large, significantly thicker, single streaks. Although it is more difficult to pick out these dominant streaks in a still photo, there appear to be three such structures in Fig. 6(a). In the water flows there is some variation in the size of the streaks, but the variation is small compared with the variations seen in the drag-reducing flows.

The average length of the drag-reducing streaks was much longer than the average streak length in a water flow at equal v^*. The streak length appears to increase with both the percentage drag reduction and the solution viscosity. At higher values of drag reduction some streaks extended from the dye slot to the channel exit 760 mm downstream from the dye slot.

In both water and drag-reducing flows the streaks periodically sweep from side to side with a small amplitude lateral waving motion. The drag-reducing streaks show an attenuation of this waving motion when compared to a water flow at the same v^*. This feature was also noted by Donohue[13] for Polyox solutions. This lateral movement of the streaks occasionally results in the combination of two or more streaks into one. By observing the films through a window of approximately 3λ in width, two adjacent streaks combined into a single one for approximately 15% of the streaks observed in both the water and drag-reducing flows.

In the water flows all streaks marked by the dye slot burst within the field of view. For the drag-reducing flows, some streaks that formed lose their identity without bursting while some were seen to form, subside, reform, and burst. Within the field of view, some streaks were also seen to gradually lift away from the wall without bursting. Movies analyzed from run AP-19 revealed that approximately 63% of the streaks had burst within the field of view, 14% left without bursting, and 23% lost their identity without bursting. The dominant streaks generally did not lose their identity without bursting.

After the bursting of a streak there is usually some residual dye at the wall which can still be identified as a streak. In the water flows this residual usually loses its identity a short time after bursting or is overtaken by a new streak. Runstadler et al.[17] have also observed a small residual left after streak bursting. In the drag-reducing flows a larger portion of the streak is left as a residual. Possibly only the upper portions of the streak is ejected in a burst, but in any case the bursting of a streak does not necessarily terminate the existence of the streak.

From the end of the channel there is an excellent view upstream which yields some information about the streamwise vorticity of the dyed fluid. Essentially no streamwise vorticity is seen until the streaks lift away from the wall and burst. There is frequently some streamwise vorticity associated with this lifting and bursting process. The amount of rotation varies but seldom exceeds one to two revolutions before the dye is dispersed below the visible threshold. This rotation is usually not particularly rapid and the diameter of the rotation is often as much as $\frac{1}{5}$ of the channel width.

IV. DISCUSSION

The observed variation in λ^+ with y^+ explains the previously reported agreement and disagreement in the data of Donohue et al.[13] and Eckelman et al.[11] Previously, it had been postulated that the differences could have resulted from either the use of different polymer solutions or the methods of reducing the data. For example, Donohue et al. suggested that the observed discrepancy with the data of Eckelman may have been due to the fact that Eckelman et al.[11] disregarded zero crossings that were separated by z^+ less than 50 and 60 for flows having drag reductions of 49% and 60%, respectively. However, if Eckelman's criteria for omitting zero crossings is applied to the 57% drag-reducing distribution [Fig. 8(c)], the average streak spacing is increased by about 12%. Similarly, all of the data from the three previous studies[11–13] and this study show that neither polymer type nor concentration directly affect the streak spacing. Any combination of polymer type and concentration necessary to produce a given value of drag reduction will apparently produce a streak spacing consistent with the structural picture of the sublayer shown in Fig. 10. When the dye marks the region $y^+ > 2$, the nondimensional streak spacing is a linear function of the drag reduction while for higher amounts of drag reduction the values of λ^+ measured for $y^+ < 2$ increase at a faster rate. Therefore, it is now believed that the differences between Donohue and Eckelman's streak spacing data was simply the result of measurements being made in different regions within the viscous sublayer.

Even though the streak spacing varies with y^+, it is important to note that it is apparently equally probable that all of the streaks will burst and thereby contribute to the turbulent momentum transport. Consequently, if a single value of λ^+ is to be used to represent the sublayer structure in a drag-reducing flow, the "plateau" value of λ^+ for $y^+ > 2$ would be the most appropriate and representative value.
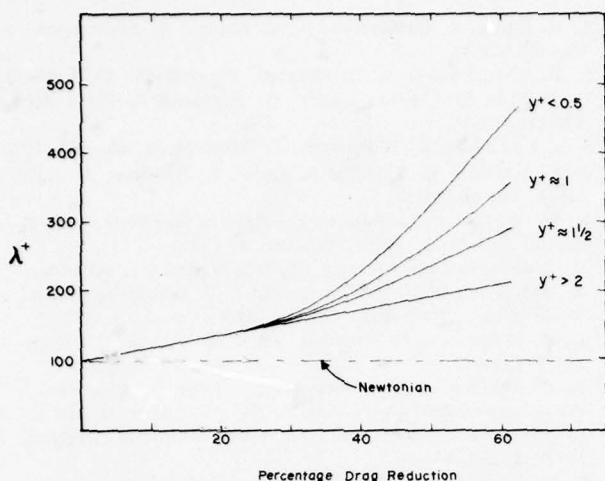
FIG. 10. Schematic of apparent variation of nondimensional streak spacing in viscous sublayer as a function of drag reduction.

It has been hypothesized that the increased streak spacing in drag-reducing flows is due to the resistance of the dilute polymer solution to vortex stretching which inhibits the formation of streaks.[13] The hypothesis of inhibited streak formation has been strengthened because now three studies[12,13,22] have shown that the time between bursts of a streak is essentially unchanged in a drag-reducing flow. The nature of the inhibiting mechanism has not been clarified. However, whether or not one adopts a vortex stretching representation for the streak formation process is not crucial to the hypothesis of inhibited formation. The solutions have a high resistance to axisymmetric strains and these are clearly present in the streak formation sequence described in Fig. 9.

While some streaks are apparently inhibited from forming by the polymer additive, there were streaks in all of the drag-reducing flows. Moreover, some of these streaks were essentially adjacent to the wall even in the flows with high values of drag reduction where λ^+ varied with y^+. This variation could be due to variations in the amplitude or strength of the event which causes the streaks to form. The weaker less intense interactions may be successfully resisted by the viscoelastic properties of the dilute polymer solutions while the more intense interactions cannot be damped and these lead to sublayer streaks.

A major unresolved question concerns the connection between the observed wall disturbances, which appear to initiate streak formation, and some other flow module which causes the disturbance. The presence of an initial crater-like depression in previously undisturbed dye suggest that the disturbance is caused by a small finite volume event which has a velocity component toward the wall. As noted earlier this event is convected much faster than the local mean velocity in the dye marked region, suggesting that the disturbances are associated with a "sweep" type event. If one postulates that the streaks are initially formed by a downward

moving eddy, then the strains created by this eddy would increase as the eddy approached the wall. The size, the trajectory, and the magnitude of the normal velocity component, V, of the eddy would contribute to the apparent strength of the streak formation event. In dilute polymer flows the resistance to axisymmetric strains could be such that the eddies with shallow trajectories and/or small V components would be less likely to form streaks at $y^+ < 1$ than at $y^+ > 1$ whereas the eddies with steep trajectories and large V components would still form streaks at $y^+ < 1$. The non-drag-reducing flows are Newtonian and without this large resistance to axisymmetric strains all eddies would have approximately the same effect upon the sublayer and λ^+ would not vary with y^+.

A somewhat different explanation for the variation of λ^+ with y^+ has been offered by Lumley.[25] His explanation is based upon an enlarged streamwise eddy structure in the drag-reducing flows that is geometrically similar to the large eddy structure described by Bakewell and Lumley.[26] The increased scale of the streamwise eddy structure, which has an average spacing consistent with the λ^+ values reported for $y^+ > 2$, is a natural consequence of the thickening of the near-wall region that Lumley discussed earlier.[27] He now suggests that the larger scales would yield small but significant variations in the location of these eddies with respect to the wall and that these variations could be large enough that some of the "footprints" of the eddies (the streaks) would not be seen when only a thin region of the sublayer is marked by dye. The results of this study cannot confirm either this hypothesis or the one based upon a downward moving eddy. In both cases the proposed mechanisms are consistent with both the larger streak spacing and the variation in λ^+ with y^+ observed in the drag-reducing flows.

This study also does not conclusively confirm or deny any of the other previously proposed interactions between the viscous sublayer and the outer flow. The description of the streak formation event is basically consistent with the intense small scale pressure fluctuation data reported by Emmerling[28] and the interaction of the sublayer with these regions of high pressure proposed by Willmarth.[9] The observations of this study are also consistent with the proposals of Offen and Kline.[29] In this case, it is important to remember that not every burst-sweep interaction may yield new streaks because some formations may be inhibited. However, it is also plausible that some burst-sweep interactions may yield more than one new streak. Similarly, some aspects of the formation events are consistent with the conceptual model proposed by Laufer.[10] He proposes a model where the relatively large scale sweep event described by Corino and Brodkey[5] contains regions of small-scale vorticity that are the size of the streak formation events. In Laufer's proposed model of the interaction, streaks would be formed in groups. There is some indication of this in the movies. However, this apparent tendency of the streaks to form in groups must be considered as a tentative result because it has not yet been confirmed by an objective statistical analysis. Moreover, the nondimensional width of our two-dimensional channel based

upon wall parameters is on the order of 400 and therefore, the large scale events may be somewhat different in these channel flows than they are in a high Reynolds number boundary layer.

This study does verify and yield new evidence to support the earlier conclusion that a significant mechanism by which a dilute polymer solution achieves drag reduction is by inhibiting the formation of streaks. At equal flow rates, the smaller number of streaks in the drag-reducing flow yields a lower spatially averaged bursting rate, less turbulent momentum transport, and hence a reduced wall shear stress. One should note that at equal wall shear stress, there are also fewer streaks in a drag-reducing flow than in the comparable solvent flow. Thus, if the mechanism for turbulent production and transport is the same in both flows, there must be more momentum transport per burst in the drag-reducing flow. This is possible because the scale of the burst appears larger and there is a larger velocity difference between the wall layers and the center portion of the channel. However, the dominant physical impression you receive from comparing movies of drag-reducing and solvent flows at equal shear stress is that the transport has been reduced in the drag-reducing flow because there is a considerable increase in the quantity of dye that remains adjacent to the wall.

It is now apparent that a drag-reducing flow has the same basic structural features as a non-drag-reducing flow. While some of the structural features are altered, none are eliminated. It is also apparent from the scale of the eddies that are altered during drag reduction that it is the viscoelastic properties of the solution which are responsible for reducing the momentum transport and thereby the drag.

ACKNOWLEDGMENTS

[1] J. Laufer, NACA Report 1174 (1954).

[2] C. S. Wells and J. G. Spangler, Phys. Fluids 10, 1890 (1967).

[3] S. J. Kline, W. C. Reynolds, F. A. Schraub, and P. W. Runstadler, J. Fluid Mech. 30, 741 (1967).

[4] A. K. Gupta, J. Laufer, and R. E. Kaplan, J. Fluid Mech. 50, 493 (1971).

[5] E. R. Corino and R. S. Brodkey, J. Fluid Mech. 37, 1 (1969).

[6] H. T. Kim, S. J. Kline, and W. C. Reynolds, J. Fluid Mech. 50, 133 (1971).

[7] S. S. Lu and W. W. Willmarth, J. Fluid Mech. 60, 481 (1973).

[8] J. M. Wallace, H. Eckelmann, and R. S. Brodkey, J. Fluid Mech. 55, 65 (1972).

[9] W. W. Willmarth, in *Advances in Applied Mechanics* (Academic, New York, 1975), Vol. 15, p. 159.

[10] J. Laufer, in *Annual Review of Fluid Mechanics*, edited by M. Van Dyke, W. G. Vincenti, and J. V. Wehausen (Annual Reviews Inc., Palo Alto, Calif., 1975), Vol. 7, p. 307.

[11] L. D. Eckelman, G. Fortuna, and T. J. Hanratty, Nature 236, 94 (1972).

[12] B. U. Achia and D. W. Thompson, in *Proceedings of the First International Conference on Drag Reduction* (British Hydromechanics Research Association, Cranfield, England, 1974), p. A2–23.

[13] G. L. Donohue, W. G. Tiederman, and M. M. Reischman, J. Fluid Mech. 56, 559 (1972).

[14] M. M. Reischman and W. G. Tiederman, J. Fluid Mech. 70, 369 (1975).

[15] D. K. Oldaker, M. S. thesis, Oklahoma State University (1974).

[16] J. P. Hartnett, J. C. Koh, and S. T. McComas, J. Heat Transfer (Trans. ASME) 84, 82 (1962).

[17] P. W. Runstadler, S. J. Kline, and W. C. Reynolds, Thermosciences Division, Department of Mechanical Engineering, Stanford University, Report MD-8 (1963).

[18] C. Lipson and N. J. Sheth, *Statistical Design and Analysis of Engineering Experiments* (McGraw-Hill, New York, 1973), p. 90.

[19] R. M. Halleen and J. P. Johnston, Thermosciences Division, Department of Mechanical Engineering, Stanford University, Report MD-18 (1967).

[20] F. A. Schraub and S. J. Kline, Thermosciences Division, Department of Mechanical Engineering, Stanford University, Report MD-12 (1965).

[21] A. J. Smith, M. S. thesis, Oklahoma State University (1975).

[22] W. G. Tiederman, A. J. Smith, and D. K. Oldaker, in *Proceedings of the Symposium on Turbulence in Liquids*, edited by G. K. Patterson and J. L. Zakin (to be published).

[23] M. K. Lee, L. D. Eckelman, and T. J. Hanratty, J. Fluid Mech. 66, 17 (1974).

[24] W. G. Tiederman and M. M. Reischman, J. Fluids Eng. (Trans. ASME) 98, 563 (1975).

[25] J. L. Lumley, Phys. Fluids 20, S64 (October, Part II, 1977).

[26] H. P. Bakewell, Jr., and J. L. Lumley, Phys. Fluids 10, 1880 (1967).

[27] J. L. Lumley, J. Polymer. Sci. Macromol. Rev. 7, 263 (1973).

[28] R. Emmerling, Max-Planck-Institut für Strömungsforschung, Göttingen, No. 56 (1973).

[29] G. R. Offen and S. J. Kline, J. Fluid Mech. 70, 209 (1975).

Polymer solution and fiber suspension rheology and their relationship to turbulent drag reduction

Arthur B. Metzner

University of Delaware, Newark, Delaware 19711

It is shown that the rheological behavior of dilute polymeric solutions can be described, at least semi-quantitatively, by means of an equation containing a single viscosity coefficient and a single time constant. This expression and the Batchelor equation for suspension rheology are used to predict the major drag-reduction phenomena observed experimentally. It is shown that mixed polymer-fiber systems may be much more effective in their drag reduction capabilities than is either kind of additive when used alone. This latter prediction finds its qualitative verification in drag coefficients which are *several-fold* lower than those observed *at the asymptote of "maximum"* drag reduction in polymer solutions.

I. INTRODUCTION

Approximately a decade has passed since publication of the first hypothesis linking drag reduction processes to the unusually high resistance of viscoelastic media to the extensional deformations[1-3] which characterize the roll waves or turbulent bursts in the wall region of turbulent shear flows.[4,5] In the interval, a second mechanistic explanation of drag reduction has also been advanced,[6,7] one which notes that viscoelastic media may be easier to deform in shearing processes of short duration than are Newtonian fluids.

Mechanistic analyses of phenomena responsible for drag reduction in dilute polymeric solutions should, presumably, also serve to explain the corresponding phenomenon in suspensions[8] and the enhancement of drag reduction to especially high levels in mixtures containing both suspended particles (fibers) and dissolved polymers in which drag reductions of over 95% have been observed.[9] This paper will attempt to begin this process by concentration on the responses to be expected rheologically when fiber suspensions, polymer solutions, and mixtures of the two are deformed in shearing and in elongational flow processes.

II. RHEOLOGICAL BEHAVIOR OF DILUTE POLYMER SOLUTIONS AND FIBER SUSPENSIONS

A. Dilute polymer solutions

Several previous papers[1,2,10] have utilized the contravariant Oldroyd–Maxwell model to portray the response of polymeric solutions to deformation; this expression may be written as

$$\mathbf{P} + \theta(\delta\mathbf{P}/\delta t) = 2\mu\mathbf{d}, \tag{1}$$

$$\mathbf{S} = -p\mathbf{g} + \mathbf{P}, \tag{2}$$

and the convected derivative is defined by

$$\frac{\delta P^{ij}}{\delta t} \equiv \frac{\partial P^{ij}}{\partial t} + v^m \frac{\partial P^{ij}}{\partial x^m} - P^{im}\frac{\partial v^j}{\partial x^m} - P^{mj}\frac{\partial v^i}{\partial x^m} \ . \tag{3}$$

Here, $\mathbf{d}$, $\mathbf{P}$, and $\mathbf{S}$ denote the deformation rate, deviatoric and total stress tensors, respectively. The term p is an isotropic pressure (the general level of which is fixed by boundary conditions on the flow process) and $\mathbf{g}$ is the metric tensor. The physical properties of the fluid are given in terms of the viscosity μ and the relaxation time θ; both may be taken as dependent upon the mean deformation rates to which the fluid is subjected.[11]

The use of Eqs. (1)–(3) is based upon the following considerations:

(1) They are known to portray the form of the major stress-time of deformation effects arising in steady shearing flows of both polymeric solutions and melts.[2,12,13]

(2) They may be applied to complex flow processes in which the entire upstream deformation history of a fluid element is not known in contrast to integral equations which require a full knowledge of the upstream kinematics.[12]

(3) Conceptually, the introduction of only one new or additional physical property parameter, the relaxation time θ, represents the simplest possible manner in which "strong flows" characterized by high levels of the Weissenberg and Deborah numbers may be described. (An excellent discussion of the dimensionless groups required in models of flow processes involving viscoelastic media has recently been provided by Tanner.[14])

(4) The contravariant derivative used in Eq. (3) gives rise to high levels of the stress in rapid extensional flow processes.[15]

Equations (1)–(3) do not predict the existence of a finite second normal stress difference in steady shearing flows nor of the overshoot in stress levels in shearing deformations started from a rest state.[16] The first of these limitations appears to be of importance when stability calculations are carried out[17] but neither appears to be serious in the context of modeling well-developed turbulent flow processes. An important early limitation of these equations was their unproven ability to model the behavior of the very dilute solutions of interest in drag reduction and good data have only recently become available. Figure 1, taken from Baid and Metzner,[18] compares the predictions of several constitutive equations with the stress levels measured in an elongational flow field for a 100 ppm solution of polyacrylamid in a glycerine-water mixture. The experiment used to obtain these data is one in which a filament of the solution is "spun" by applying an axial tension to
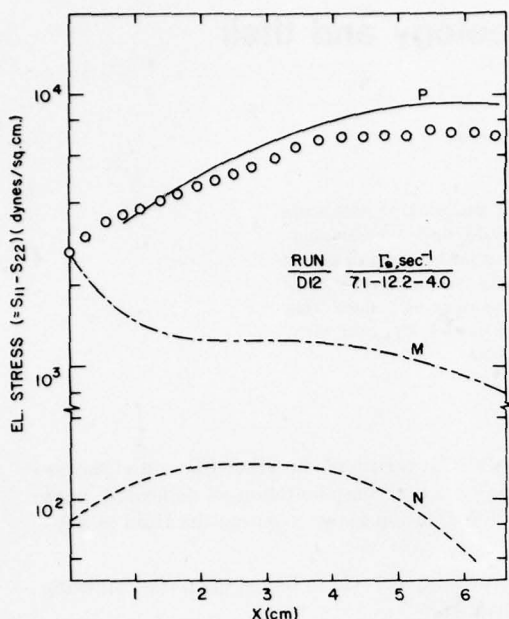
FIG. 1. Elongational stresses as a function of position in an extending fluid filament. Fluid: 100 wppm of Separan AP30, a polyacrylamide, dissolved in a glycerin–water mixture. Data taken from Baid and Metzner.[18]

a jet of fluid emerging from a small nozzle or spinneret. The stress levels in the deforming jet are plotted in this figure as a function of axial distance downstream from the spinneret. The several aspects of this figure which are of importance to the modeling of the behavior of drag-reducing fluids are as follows:

(1) The stress-position profile predicted for a Newtonian fluid having the same viscosity as the 100 ppm polymer solution is given by the curve labeled N. It is seen that these Newtonian stress levels fall below those encountered in the polymeric fluid by 1–2 orders of magnitude. This discrepancy is not as great as earlier approximate data[19] would have indicated, possibly due to the use of a very viscous solvent (to increase the accuracy of shearing measurements) for the results shown in Fig. 1. However, the experimental stress levels in the polymer solution are still enormously greater than those exhibited by the comparable Newtonian fluid and would, therefore, appear to be capable of inhibiting momentum transport in processes involving elongational kinematics, as in turbulent bursts. The elongational deformation rates in the experiment depicted in Fig. 1 varied from 4.0 to a maximum of 12.2 sec^{-1}; as these fall below those expected within a burst, and as the stress levels depend exponentially upon deformation rate, Fig. 1 does confirm the general expectation of very high stress levels in polymer solutions subjected to extensional deformations.

(2) The curve labeled P describes the prediction of Eqs. (1)–(3) using, for the viscosity parameter, the value measured separately in a shearing experiment at the identical deformation rate levels. The relaxation time θ has, however, been adjusted to a "best-fit" value

for the several independent experiments involving the 100 ppm solution. The curve labeled M is the prediction of Eqs. (1)–(3) when both parameters μ and θ are obtained from measurements in steady shearing flows.

The ability of model P to portray all the extensional flow results obtained by Baid and Metzner (a total of 43 runs using 100, 200, and 300 ppm solutions) confirms the general applicability of Eqs. (1)–(3) to processes involving extensional as well as shearing deformation processes. The fact that the material property parameter θ is dependent on the flow process being considered is disquieting but not debilitating; Denn and Marrucci[20] have shown that more precise quantitative predictions may be made by replacing the single time constant θ of Eq. (1) with a spectrum of relaxation times. However, for our purposes, it is much more convenient to retain the single term and to adjust its numerical value to the flow process being considered since spectral information on dilute solutions is not yet available. Further, there is some evidence that a part of the difference between curves M and P of Fig. 1 may be due to crystallization of some of the polymer in purely extensional flow processes,[18,21] a difficulty which has only been encountered in modeling the extensional behavior of crystallizable polymeric systems.[13] In any event Fig. 1 and the other data obtained by Baid and Metzner all confirm the applicability of Eqs. (1)–(3) to extensional flow processes provided the physical property parameters μ and θ are evaluated appropriately.

In summary, the applicability of Eqs. (1)–(3) for the portrayal of rheological behavior of dilute solutions is excellent *qualitatively*. Because the physical property parameter θ has not been shown to be independent of the kind of deformation process being considered, the *quantitative* applicability of these equations to flows of arbitrary complexity has not been proven. There are good reasons for believing that the microstructure of the fluid used to obtain the results shown in Fig. 1 may differ in shearing flows from that developed under well-defined extensional flow fields—a difficulty which might not arise in the more random kinematics of turbulent flows. Until these questions are resolved we can only be confident of the qualitative or semi-quantitative applicability of Eqs. (1)–(3), but as this may suffice for the following we shall proceed to embrace all of the qualitative predictions of Eqs. (1)–(3) and apply these to the drag reduction phenomenon.

Since the kinematics of the extensional flow processes in Bakewell–Lumley–Townsend rolls are of short duration, the time-dependent resistance to deformation predicted by Eqs. (1)–(3) may be of primary interest. It is given by

$$\mu_e = \mu\left[\frac{2}{(1-2\theta\Gamma_e)}[1-\exp-(1-2\theta\Gamma_e)t/\theta]\right.$$

$$\left. + \frac{[1-\exp-(1+\theta\Gamma_e)t/\theta]}{(1+\theta\Gamma_e)}\right] \qquad (4)$$

for the special case in which a virgin (unstressed) element of fluid is subjected to an extension at a constant rate Γ_e for time t.

Considering the Ruckenstein[6]–Hansen[7] arguments concerning the importance of shearing deformation processes, we should note, first, that Eqs. (1)–(3) predict the exponential rise of shearing stresses to their steady-state values, the rise-time being characterized by the time constant θ of the fluid. Thus, for deformation processes which begin with an unstressed fluid element and which occur on a time scale comparable to, or smaller than, θ, the stress levels required to sustain the deformation will be smaller than in Newtonian fluids. Second, in the presence of both shearing and elongational deformation modes Eqs. (1)–(3) predict the steady-state shearing stress to be

$$S_{12} = \mu\Gamma_s/(1 + 2\theta\Gamma_e), \tag{5}$$

for deformation of a two-dimensional sheet of fluid with a shearing deformation rate of Γ_s and an extensional deformation rate of Γ_e. Thus, the presence of elongational deformation processes in the Bakewell–Lumley–Townsend rolls would appear to reduce the dissipation rates in the fluid in the wall region.

Before leaving this discussion of polymer solution rheology we must emphasize that any model of viscoelastic fluid properties introduces, as a matter of principle, the concept of fluid history as a significant parameter. Thus, its quantitative application to turbulent shear flows is only possible if the kinematic history of the fluid elements involved in the flow process are also known quantitatively. At the present time there is a dearth of such kinematic information and a completely convincing and precise modeling of the drag reduction phenomenon will not be possible until this deficiency is resolved. Thus, it will be difficult to ascertain with certainty whether rheological arguments related to extensional deformation processes or to shearing are more nearly correct.

B. Fiber suspensions

Under conditions of steady extensional flows of long duration the extensional deformation resistance is given by [22–24]

$$\mu_e = 3\mu(1 + \tfrac{4}{9}\{c(L/D)_f^2[\ln(\pi/c)]^{-1}\}), \tag{6}$$

Here, μ denotes the viscosity of the suspending fluid, c is the volumetric concentration of fibers, and $(L/D)_f$ is their length to diameter ratio.

C. Mixed fiber-polymer systems

If a polymer solution containing suspended fibers is subjected to extensional deformations, the polymer solution will be sheared, as well as stretched, as fluid elements move axially along the fiber particles. It is easy to show that under steady state conditions the presence of a shearing deformation rate of magnitude Γ_s, imposed upon a steady extension rate of magnitude Γ_e, increases the stresses in a sheet of deforming fluid by the ratio

$$\frac{\mu_{es}}{\mu_e} = 1 + \frac{\theta\Gamma_e}{2}\left(\frac{\Gamma_s}{\Gamma_e}\right)^2. \tag{7}$$

Here, μ_{es} denotes the ratio of stress to strain rate ("extensional viscosity") in an element subjected to both ex-

tensional and shearing deformations whilst μ_e is the corresponding extensional viscosity in the same material element when it is being extended only. Using a "cell" model of the system containing the suspended fibers the ratio Γ_s/Γ_e in Eq. (7) may be related to the concentration of the fibers and to their geometry (length to diameter ratio) as

$$\Gamma_s/\Gamma_e = 2\sqrt{c}(L/D)_f. \tag{8}$$

Thus, as a first approximation the ratio of the extensional viscosity of a polymeric solution containing suspended fibers to that of the polymer solution itself is obtained by combining Eqs. (7) and (8) to give

$$\frac{(\mu_e)_{pf}}{(\mu_e)_p} = 1 + 2\theta\Gamma_e c\left(\frac{L}{D}\right)_f^2. \tag{9}$$

This viscosity ratio expressed by Eq. (9) may be of very great magnitude: If the fibers are present in a volumetric concentration of 500 ppm and their length-to-diameter ratio is of the order of 10^3–10^4, one obtains

$$(\mu_e)_{pf}/(\mu_e)_p = O(10^3-10^5)$$

when reasonable values of θ^{18} and Γ_e^2 are chosen.

In the case of the Lagrangian unsteady state kinematics of interest in drag reduction, one finds that the equations describing the stress evolution are somewhat more complex than the linear combination of Eqs. (4) and (9) owing to the fact the fluid properties are, of course, being described by non-linear relationships. However, Lorntson[25] has shown that the principal terms are similar to the result obtained by simply multiplying these equations. Thus, the primary feature of Eq. (9) is carried over into the unsteady state behavior of the system.

The actual increment in the stress levels developed in an element of polymer solution upon addition of fibers to it may not be, at a given deformation rate level, as great as indicated by Eqs. (6)–(9) because turbulent flows subject the solution to shearing as well as stretching even in the absence of added fibers. However, the addition of fibers insures the continual presence of shearing motions in any deforming eddy whilst the turbulent flow itself, in the absence of any suspended fibers in the fluid, presumably only shears the fluid elements in a random, time-dependent manner.

III. RELATIONSHIP OF RHEOLOGICAL PROPERTIES OF THE FLUID TO DRAG REDUCTION

A. Onset phenomena and the "maximum drag reduction" asymptote

The stretch rate Γ_e in the Bakewell–Lumley–Townsend rolls, before the onset of drag reduction, is given by [2]

$$\Gamma_e = Ku^*/\nu, \tag{10}$$

in which K is a scaling constant, u^* is the friction velocity, and ν is the kinematic viscosity of the fluid. Thus, the kinematics of the extensional flow processes in the roll waves appear to conform to the constant stretch-rate kinematics presumed in the derivation of Eq. (4). This expression suggests, in view of the rapid rise of

the extensional viscosity as the dimensionless stretch rate $\theta\Gamma_e$ approaches a value of one half, that the onset will be an abrupt rather than a gradual one and that, for a given fluid, it will occur at a fixed value of the friction velocity in view of Eq. (10). These suggestions are in qualitative accord with observation as indicated by any of the several reviews of the drag reduction process[26-28] as well as with the recent study of Poreh and Hassid.[29]

Under very strong flow conditions the dimensionless stretch rate $\theta\Gamma_e$ of Eq. (4) may be expected to be much greater than unity. Additionally, a fluid element in a roll wave will not enter it in a virgin unstressed condition as assumed in the development of Eq. (4), but will be at some initial or residual stress level S_0. Under these conditions all terms in Eq. (4) except the first exponential term will be small and, as an approximation, may be neglected. Carrying out this simplification and considering the additional influence of the initial stress term one obtains

$$\mu_e(t) \approx [(\mu + \theta S_0)/\theta\Gamma_e] \exp(2\Gamma_e t), \quad (\theta\Gamma_e \gg 1). \tag{11}$$

Thus, the rate of rise (in time) of the extensional viscosity of a fluid element as it traverses a roll is independent of the fluid properties and is very great: The work of Bakewell[4] suggests that the exponent in Eq. (11) may rise to a numerical value of order 10. Baid and Metzner's results[18] also suggest that $\theta S_0 \gg \mu$ for dilute solutions. Employing Eq. (10) to define the kinematics the pre-exponential term of Eq. (11) then becomes approximately equal to $(S_0 \nu/Ku^*)$. Qualitatively, S_0 would be expected to increase as the friction velocity u^* increases. Since the kinematic viscosity is close to 10^{-2} cm²/sec for most fluids studied, these arguments make a plausible case for considerable similarity among all drag-reducing fluids under such limiting conditions of very strong flows and a common asymptote would be predicted for the maximum drag reduction obtainable. These arguments also, however, indicate that a large number of rather tenuous postulates are required to develop the case for a common asymptote and that this should break down if substantial changes are made in fluid properties. All of this is in accord with observation: The data for a majority of dilute polymer solutions fall into a narrow band in the limit of "strong flows" or high stress levels,[26,27] but substantial deviations from this asymptote are revealed by a few systems.[9,30]

B. Comparison of polymeric and fibrous additives as drag reducing agents

The resistance of polymeric fluids to extensional deformations is governed to a large degree by the dimensionless deformation rate term $\theta\Gamma_e$, [see Eq. (4)] as noted in the previous section. Since Γ_e, the extension rate of fluid elements in the rolls, is determined by the friction velocity [Eq. (10)], these considerations lead one to expect the rapid diminution of drag reduction levels as the friction velocity is decreased, as by considering, at a given Reynolds number, flow through a series of tubes of progressively larger diameters. Such adverse effects of increases in system scale upon the performance of polymeric drag reduction additives have been well-documented.[1,2,9,10,26-28,31] In contrast, Eq.

TABLE I. Independence of drag reduction levels of tube diameter in fiber suspensions. (Data taken from Lee *et al.* (Ref. 9).

Nominal tube diam, cm	Additive	Fiber conc., wppm	Reynolds number	% Drag reduction
2.4	3T12[a]	800	10^5	21
4.9	3T12	800	10^5	18
7.0	3T12	800	10^5	22
2.4	TB[b]	200	10^5	17 ± 5
4.9		200	10^5	22 ± 7
2.4	Nylon[c]	1,000	5×10^4	17
4.9		1,000	5×10^4	17

[a]Chrysotile asbestos fibers manufactured by Johns Manville.
[b]Chrysotile asbestos fibers supplied by Turner Brothers.
[c]Nylon fibers having an aspect ratio of 100.

(6) suggests the independence of the extensional viscosity of a suspension of any stress-, deformation rate- or scale-related parameters. Table I confirms this independency of the drag reduction levels upon pipe diameter for fiber suspensions.

Use of Eq. (6) is predicted upon the sufficiently long residency of an element of the fluid in an extensional velocity field in order to align all particles in the direction of flow. The fact that the Bakewell data, as noted earlier, show evidence of total extensional deformations $\Gamma_e t$ of as great as 5 means that the deformations are much more than sufficient to insure such relatively complete alignment of particles in the absence of any disturbances due to either the main shear flow or of the turbulent velocity fluctuations.

Finally, we should note that there is no analog of Eq. (5) for fiber suspensions and that if, mechanistically, the action of both polymeric and fibrous additives is identical, we must focus on their resistance to extensional deformations rather than on the characteristics of shear flows of short duration.

C. Characteristics of drag reduction in mixed systems containing both polymeric and fibrous additives

The calculations summarized in Eqs. (7)–(9) suggest that:

(a) Mixed systems might inhibit the rolls in turbulent shear flows, and hence reduce the turbulent drag, to a *far* greater extent than does either kind of additive by itself.

The importance of this prediction is quite substantial: In several of the mixed systems studied by Lee *et al.*[9] drag coefficients which were as little as 30% of those predicted by the "maximum drag-reduction asymptote" of Virk for polymeric fluids were observed. Further, the highest level of drag reduction noted by Lee and co-workers, 96.5%, was observed in a 2.4 cm tube. While earlier students of drag reduction in polymer solutions occasionally observed drag reduction levels somewhat in excess of 80% (see, for example, Hoyt[26]), the highest levels were usually obtained in such small tubes as to

TABLE II. Comparison of drag reduction levels obtained using polymeric and fibrous additives. Polymer: Separan AP30; 150 wppm. Fibers: JM Asbestos 3T12.

| Nominal tube diam, cm | Reynolds number | Fiber conc., wppm | Percentage reduction in drag obtained using | | |
			Fiber additive only	Polymeric additive only	Both additivies
2.6	4×10^4	200	4.9	34	47
		400	8.8	34	57
		800	17.7	34	70
	6×10^4	200	5.3	41	54
		400	9.8	41	63
		800	17.8	41	76
2.4[a]	2×10^5	800	19	64	92.5
Polymer: as above Fiber: Nylon particles; aspect ratio = 100					
2.4[a]	10^5	1000	15	36	63
4.9[a]	5×10^4	1000	17	0	36
Polymer: as above but undegraded Fiber: Turner Bros. asbestos					
2.4[a]	2×10^5	200	21 ± 7	91	94

[a]Data from Lee et al.[9]

be of little interest pragmatically. The availability of an analysis which predicts such major effects, even if qualitative or only semi-quantitative, is important.

(b) The basic elements of the modeling process embodied in Eqs. (7)–(9) are the same for mixed systems as for dilute solutions of polymer alone. Correspondingly, one should expect that mixed systems will show at least some of the same adverse effects of system scale which the polymer does when it is present alone.

Table II shows both of these expectations to be fulfilled in systems in which the total drag reduction levels are not especially high; when very high levels of drag reduction are obtained using either additive alone then addition of the other has only a modest effect.

IV. CONCLUDING COMMENTS

The writer notes that this manuscript is less quantitative and much more speculative than desirable. However, the basic tenets of solution and suspension rheology appeared to be worth compiling.

Several recommendations may be made for further work. No data at all appear to be available to evaluate Eq. (9) and the rheological data available for dilute solutions are much less extensive than desired. Moreover, a major omission which prevents a precise and quantitative, hence convincing, modeling of the effects of system rheology is the still-primitive state of our knowledge of the *quantitative* kinematic features of turbulent flows.

[1]F. A. Seyer and A. B. Metzner, in *Proceedings of the 6th Symposium on Naval Hydrodynamics* (Office of Naval Research, Washington, D. C., 1966), p. 19.
[2]F. A. Seyer and A. B. Metzner, AIChE J. **15**, 426 (1969); see also F. A. Seyer, Ph.D. thesis, University of Delaware (1968).
[3]J. L. Lumley, J. Poly. Sci. Macromol. Rev. **7**, 263 (1973).
[4]H. P. Bakewell, Ph.D. thesis, Pennsylvania State University (1966); see also H. P. Bakewell and J. L. Lumley, Phys. Fluids **10**, 1880 (1967).
[5]A. A. Townsend, *The Structure of Turbulent Shear Flow* (Cambridge University, Cambridge, 1956), Chap. 9.
[6]E. Ruckenstein, Chem. Eng. Sci. **26**, 1075 (1971).
[7]R. J. Hansen, J. Fluids Eng. (Trans. A.S.M.E.) **95**, 23 (1973).
[8]I. Radin, J. L. Zakin, and G. K. Patterson, AIChE J. **21**, 358 (1975).
[9]W. K. Lee, R. C. Vaseleski, and A. B. Metzner, AIChE J. **20**, 128 (1974).
[10]A. B. Metzner and M. G. Park, J. Fluid Mech. **20**, 291 (1964).
[11]J. L. White and A. B. Metzner, J. Appl. Polym. Sci. **7**, 1867 (1963).
[12]J. A. Spearot and A. B. Metzner, Trans. Soc. Rheol. **16**, 495 (1972).
[13]P. K. Agrawal, W. K. Lee, J. M. Lorntson, C. I. Richardson, K. F. Wissbrun, and A. B. Metzner, Trans. Soc. Rheol. (to be published).
[14]R. I. Tanner, AIChE J. **22**, 910 (1976).
[15]M. M. Denn and G. Marrucci, AIChE J. **17**, 101 (1971).
[16]W. R. Leppard and E. B. Christiansen, AIChE J. **21**, 999 (1975).
[17]M. M. Denn, *Stability of Reaction and Transport Processes*, (Prentice-Hall, Englewood Cliffs, N. J., 1975), p. 135.
[18]K. M. Baid and A. B. Metzner, Trans. Soc. Rheol. **21**, 237 (1977).
[19]A. B. Metzner and A. P. Metzner, Rheol. Acta **9**, 174 (1970).
[20]M. M. Denn and G. Marrucci, J. Non-Newt. Fluid Mech. (to be published).
[21]F. A. Kanel, Ph.D. thesis, University of Delaware (1972).
[22]G. K. Batchelor, J. Fluid Mech. **46**, 813 (1971).
[23]T. E. Kizior and F. A. Seyer, Trans. Soc. Rheol. **18**, 271 (1974).
[24]J. Mewis and A. B. Metzner, J. Fluid Mech. **62**, 593 (1974).
[25]J. M. Lorntson, M.Ch.E. thesis, University of Delaware (1975).
[26]J. W. Hoyt, J. Basic Eng. (Trans. A.S.M.E.) **94**D, 258 (1972).
[27]P. S. Virk, AIChE J. **21**, 625 (1975).
[28]R. C. Little, R. J. Hansen, D. L. Hunston, O. K. Kim, R. L. Patterson, and R. Y. Ting, Ind. Eng. Chem. Fundam. Q. **14**, 283 (1975).
[29]M. Poreh and S. Hassid, presented at the Symposium on Structure of Turbulence and Drag Reduction, Washington, D. C. (1976).
[30]A. Rollin and F. A. Seyer, Can. J. Chem. Eng. **50**, 714 (1972).
[31]J. G. Savins and F. A. Seyer, Phys. Fluids **20**, S78 (October, Part II, 1977).

Effects of roughness on the intermittent maintenance of Reynolds shear stress in pipe flow

J. Sabot, I. Saleh, and G. Comte-Bellot

Laboratoire de Mécanique des Fluides, associé au Centre National de la Recherche Scientifique, Ecole Centrale de Lyon, 69130 Ecully, France

The presence of a rough wall does not fundamentally alter the intermittent maintenance of Reynolds shear stress as found for turbulent flows over a smooth wall, be it boundary layers or pipe flows. Ejections, and to a lesser extent sweeps, are still the dominant events contributing to the shear stress. The mean period of occurrence of the violent ejections (those whose amplitude exceeds a characteristic threshold) is, however, larger for the rough pipe than it is for the smooth pipe at the same Reynolds number. A scaling based on specific parameters of the largest scale motions is proposed. The mean length scale of the violent ejections is larger than those encountered for a smooth pipe, but still seems to be of the order of the integral length scale of the transverse component of the velocity fluctuation.

I. INTRODUCTION

The intermittent maintenance of the Reynolds shear stress is a problem of current interest for wall turbulent flows. It is usually investigated by means of visualizations or hot-wire conditional analysis of the instantaneous shear stress, and a recent and extensive list of references is given in Ref. 1. The visualizations (either hydrogen bubbles, dye, or smoke) are suitable at low Reynolds numbers and have provided visual evidence for the existence of a deterministic sequence of discrete events which takes place in the flow. In the conditional analysis of $u_1 u_2(t)$, which can be applied to a wide range of flow conditions, attention is paid to the contributions brought to the Reynolds shear stress (the Reynolds shear stress is $-\rho \overline{u_1 u_2}$ by definition; however, the notation $\overline{u_1 u_2}$ is used hereafter, for simplicity) by the four quadrants of the u_1, u_2 plane (u_1, component of the velocity fluctuation in the mean streamwise direction; u_2 component of the velocity fluctuation along the normal to the wall) as a function of the parameter $H = u_1 u_2/ u_1' u_2'$ (u_1' and u_2', rms values of u_1 and u_2). For $H = 0$, and in the inner part of wall turbulent flow, it is found that approximately 80% of $\overline{u_1 u_2}$ is associated with ejections (events related to the second quadrant and such that $u_1 < 0$ and $u_2 > 0$) and 55% to sweeps (events related to the fourth quadrant and such that $u_1 > 0$ and $u_2 < 0$). The excess percentage over 100% is compensated for by contributions related to the other quadrants. For $H \leq H_c = -4.5$ only ejections contribute to $\overline{u_1 u_2}$. Later, these strong ejections will be designated as "violent."

Such ejections are characterized by two properties: their mean period of occurrence and their mean duration. The first property is best measured at the characteristic threshold H_c (so that the values obtained can be noted $\overline{T}_{c, \text{II}}$ to remind one of both H_c and the second quadrant of the u_1, u_2 plane in which $u_1 < 0$, $u_2 > 0$. It is then found that $\overline{T}_{c, \text{II}}$ keeps an almost constant value across the flow (except in the core region of completely wall-bounded flows[1]). This suggests that the most violent ejections are created with the same probability across the flow or that they originate in the wall region and move outward during their downstream convective mo-

tions. Even in the core region of completely wall bounded flows, such as pipe flow in the fully developed regime, violent ejections related to one half of the pipe are detected beyond the pipe axis. In addition, the relevant scales for $\overline{T}_{c, \text{II}}$ seem to be the outer parameters of the flow (boundary layer thickness or pipe radius and external or mean velocity on the pipe axis) rather than the inner parameters (friction velocity and kinematic viscosity). Some links therefore exist between the large scale motions of the flow and the ejections. The exact mechanism is not yet well known, but the ejections could stem from an overall flow instability.[2] On the other hand, the mean duration $\overline{\Delta T}_{0, \text{II}}$ of the violent ejections which are best determined at their base (i.e., by extrapolation down to $H = 0$ of the mean durations obtained for $H \leq H_c$), seem to be such that the associated longitudinal length scale (obtained from the mean duration by means of the Taylor hypothesis) is of the same order of magnitude as the integral length scale $L_{22}^{(1)}$ of the normal velocity component u_2 with a longitudinal separation. This shows that although the violent ejections appear during a short period of time, their mean scale is not necessarily associated with the fine turbulent structures. In wall shear flows the integral scale $L_{22}^{(1)}$ is only an order of magnitude smaller than the integral length scale $L_{11}^{(1)}$ associated with the longitudinal velocity components. The coherence of the normal velocity component u_2 can then be mainly provided by the violent ejections whereas the space coherence of the longitudinal velocity component u_1 would presumably be due to the longitudinally decelerated or accelerated fluid motions which take place for a long time before an ejection.[3]

These results have been obtained for turbulent boundary layers or pipe flows over *smooth* walls. The case of a *rough* wall, which provides drastic changes in the wall conditions, and also in the whole flow, does not seem to have been considered, except for the visualizations of Grass[4] which already gave evidence of the existence of a sequence of events similar to those observed over a smooth wall. Quantitative information was nevertheless needed so that the present investigation has been undertaken. Here, pipe flow has been chosen be-
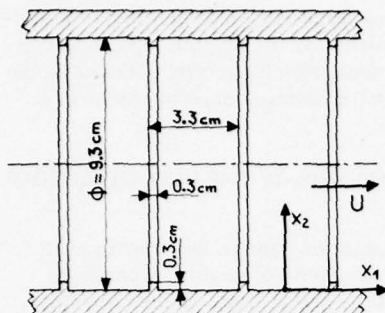
FIG. 1. Geometry of the roughness.

cause of the previous detailed investigation already done in that flow with a smooth wall.[1]

II. EXPERIMENTAL CONDITIONS AND OVERALL CHARACTERISTICS OF THE FLOW

Experiments were carried out in a very rough pipe. The roughness, Fig. 1, was made of ring-shaped slats with a 3×3 mm square section and a longitudinal spacing of 33 mm. The hydraulic diameter $D_h = 2R_h$ (i.e., the diameter of a smooth pipe which would have the same volume by unit of length as the actual rough pipe) was 92.5 mm. All measurements reported here were taken at 95 diam from the pipe inlet. At this distance and for the Reynolds number investigated (Re $= 2R_h U_{max}/\nu = 135\,000$), the flow was fully developed and representative of the fully rough regime. There was, however, a streamwise inhomogeneity near the wall due to the discrete roughness elements. Mean velocity and turbulence intensity profiles taken at different locations downstream of one of the slats have shown that this inhomogeneity does not extend beyond $x_2/R_h \simeq 0.30$ (x_2, distance from the wall). In view of the present objective (comparison of the shear stress structure between a very rough pipe and a smooth pipe) only the flow region not affected by the streamwise inhomogeneity was considered. Finally, the experimental methods used in this study were the same as those previously described for smooth pipe flow.[1,3]
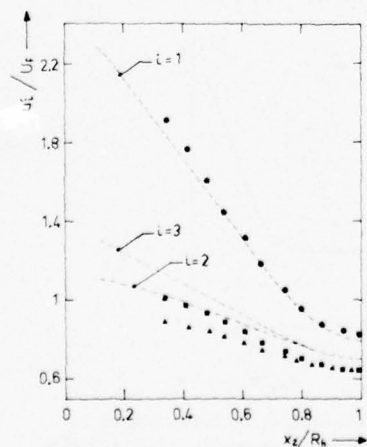

FIG. 2. Turbulence intensity profiles: ($\ast$, u_1'/U_f; $\blacktriangle$, u_2'/U_f; $\blacksquare$, u_3'/U_f), rough pipe; (----), smooth pipe.
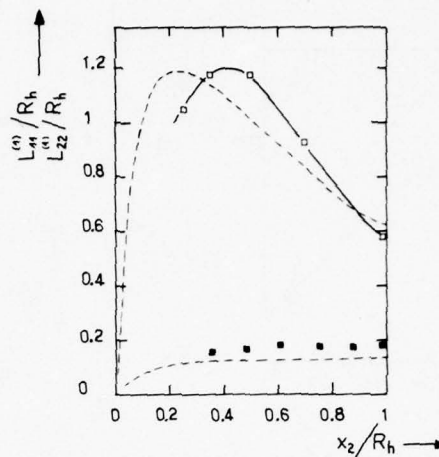

FIG. 3. Integral length scales of the velocity components as a function of the distance from the wall: ($\square$, integral length scale $L_{11}^{(1)}$ of the streamwise velocity component u_1 in the streamwise direction; $\blacksquare$, integral length scale $L_{22}^{(1)}$ of the radial velocity component u_2 in the streamwise direction), (———) rough pipe; (-----), smooth pipe.

The essential overall characteristics of the flow in the rough pipe were as follows: friction velocity, $U_f = 2.0$ m sec^{-1}; relative bulk velocity, $\bar{U}/U_{max} \simeq 0.70$; friction factor, $8U_f^2/\bar{U}^2 = 0.135$. For comparison, the corresponding characteristics for the smooth pipe are 0.78, 0.83, and 0.0173, respectively, at the same Reynolds number, so that the chosen roughness alters the flow very strongly.

A. Turbulence intensities

The profiles of u_1'/U_f, u_2'/U_f, and u_3'/U_f are given in Fig. 2 for $x_2/R_h \gtrsim 0.30$. Compared with those obtained in the smooth pipe, the u_1'/U_f profile is the same, whereas the u_2'/U_f and u_3'/U_f profiles are systematically located at a slightly lower level. The turbulence anisotropy is then larger for the rough pipe than for the smooth pipe, even in the core region. This suggests that the coherent structures associated with the wall side of the core region[1] could be affected by the nature of the wall and hence mark all the properties of the flow.

B. Integral length scales

Two major integral length scales have been obtained to describe the large scale motions: $L_{11}^{(1)}$ and $L_{22}^{(1)}$ which are respectively related to the downstream velocity component and a downstream separation, and to the velocity component normal to the wall and a downstream separation. Results are reported in Fig. 3. As in the smooth pipe, it can be observed that $L_{22}^{(1)} \ll L_{11}^{(1)}$ and that $L_{22}^{(1)}$ increases monotonically toward the pipe axis whereas $L_{11}^{(1)}$ increases, attains a maximum, and then decreases.[1,3] The maximum occurs at about $x_2/R_h = 0.40$, slightly farther from the wall then in the smooth pipe.

C. Integral time scales

Values of the integral time scale $\Theta_{11}^{(1)}$ of the longitudinal velocity component (obtained from the envelope of
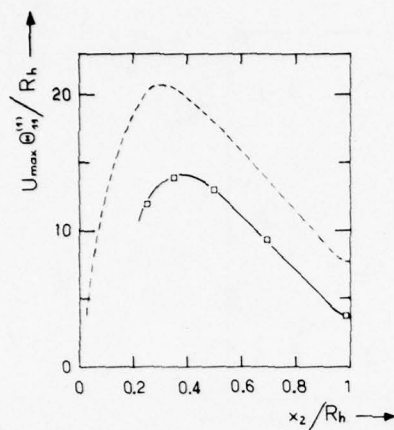
FIG. 4. Integral time scale $\Theta_{11}^{(1)}$ of the streamwise velocity component in a convected frame as a function of the distance from the wall: □, rough pipe; ----, smooth pipe.

the optimal space-time correlations with downstream separation) are given in Fig. 4. All across the rough pipe this memory time is noticeably shorter than in the smooth pipe (at the same Reynolds number), a fact which expresses the fast production and renewal rates of turbulence in the rough pipe. However, as in the smooth pipe, the relative integral time scale $U_{max}\Theta_{11}^{(1)}/R_h$ presents a maximum at nearly the same location as $L_{11}^{(1)}/R_h$. The region in which the space and time coherences of turbulence are the largest is important in view of the largest scale structures. Its location with respect to the wall probably results from a balance between two contrary effects related to the existence of a velocity gradient: (i) the generation of longitudinally decelerated or accelerated coherent fluid motions (see Sec. I), and (ii) the renewal of turbulence. Near the wall, the high level of production precludes the existence of long lifetime coherent motions, so that $\Theta_{11}^{(1)}$ is small. Near the pipe axis, the renewal effect (ii) is negligible, but $\Theta_{11}^{(1)}$ cannot be large because the velocity gradient is small and the ordering effect (i) is weak. Between these two regions a location can exist where the balance between (i) and (ii) leads $\Theta_{11}^{(1)}$ to reach its maximum value [concerning this behavior, it should be noted that for a porous pipe with aspiration, the maximum of the integral length scale $L_{11}^{(1)}$ occurs closer to the wall as the aspiration rate increases[5]]. As a result, the distance from the wall where $\Theta_{11}^{(1)}$ and $L_{11}^{(1)}$ are maxima appears to be a relevant parameter of the large scale motions in the context of the flow which permits their development. This parameter along with the convection velocity limit hereafter defined will be used in Sec. IV.

D. Convection velocity

Measurements of optimal space-time double velocity correlations $R_{11}^{opt}(r_1, 0, 0; \tau_m)$ for large streamwise separation r_1 allow one to define a lower convection velocity limit U_{cl} independent of r_1 and characteristic of the largest scale structures.[6] The profile of U_{cl} across the flow is shown in Fig. 5. The constant value U_{cl}/U_{max}

= 0.60 observed over a large region of the flow is smaller than the value obtained for the smooth pipe, because of the more pointed mean velocity profile obtained in the rough pipe and the spatial average done by the largest coherent structures.

III. AMPLITUDE ANALYSIS OF THE INSTANTANEOUS SHEAR STRESS

The various investigations done in the smooth wall pipe[1] have shown the necessity of dealing separately with the wall side of the core region, where $\overline{u_1 u_2}/u_1' u_2' = -0.45$ (a zone similar to the inner part of the boundary layers with events organized by a velocity gradient which has a constant sign) and the core region (where events belonging to opposite halves of the flow, with opposite signs of the mean velocity gradients, exist).

In the wall side of the core region, Figs. 6(a)–(b) show the amplitude analysis of the instantaneous shear stress, for every quadrant J of the u_1, u_2 plane ($J = $ I, II, III, IV). The mean frequency $\overline{N}_J$ is the mean number of times per second the amplitude of $u_1 u_2$ is equal to or exceeds a given threshold $|H|u_1' u_2'$. The main result is that ejections (quadrant II, $u_1 < 0$, $u_2 > 0$) and, in a lesser extent, sweeps (quadrant IV, $u_1 > 0$, $u_2 < 0$) are still the events providing the largest amplitudes of $u_1 u_2$. The intermittent maintenance of the Reynolds shear stress, therefore, seems to be due to the same types of events in the rough and in the smooth wall pipes. However, the largest negative peaks of $u_1 u_2$ associated with ejections are much larger than those observed in a smooth pipe [approximately in the ratio of $(u_1' u_2')$ rough$/(u_1' u_2')$ smooth]. It can also be noted that the frequency laws $\overline{N}_J = f_J(H)$ do not appreciably depend on the distance from the wall.

In the core region, Figs. 6(c)–(d) show that in addition to the ejections related to one half of the flow, there exist ejections related to the opposite half (i.e., quadrant III, $u_1 < 0$, $u_2 < 0$; see Ref. 1 p. 780 and Table 2). The core region is therefore marked, as in the
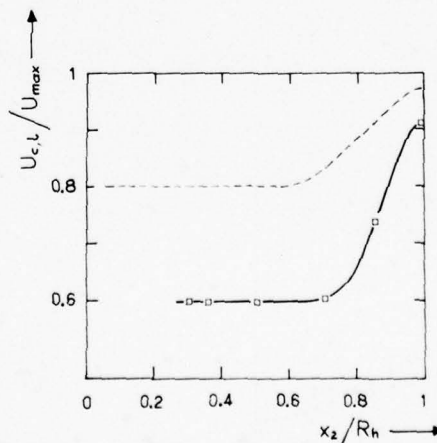

FIG. 5. Convection velocity limit U_{cl} as a function of the distance from the wall (deduced from double velocity space-time correlations for large streamwise separations): □, rough pipe; ----, smooth pipe.
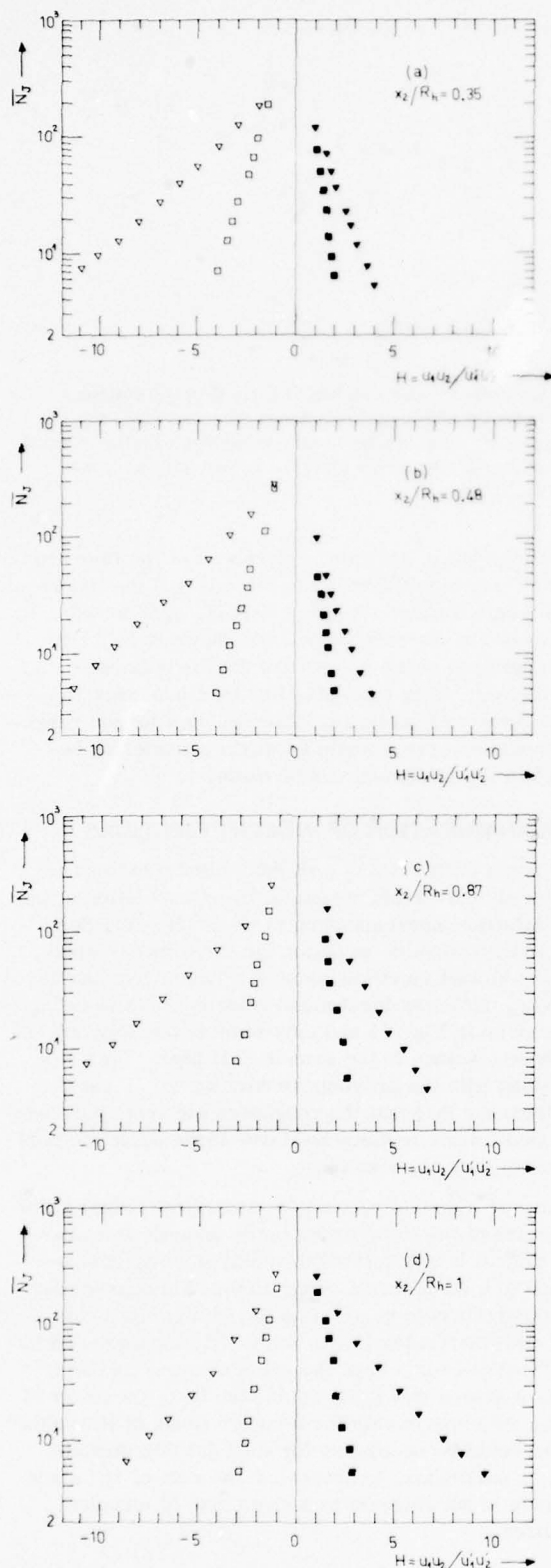
FIG. 6. (a), (b), (c), (d) Frequency distribution of u_1u_2 as a function of the threshold $H = u_1u_2/u_1'u_2'$ in the four quadrants of the u_1, u_2 plane for several distances from the rough wall. ■, $J = I(u_1u_2 > 0,\ u_2 > 0)$; ▽, $J = II(u_1u_2 < 0,\ u_2 > 0)$; ▼, $J = III(u_1u_2 > 0,\ u_2 < 0)$; □, $J = IV(u_1u_2 < 0,\ u_2 < 0)$.
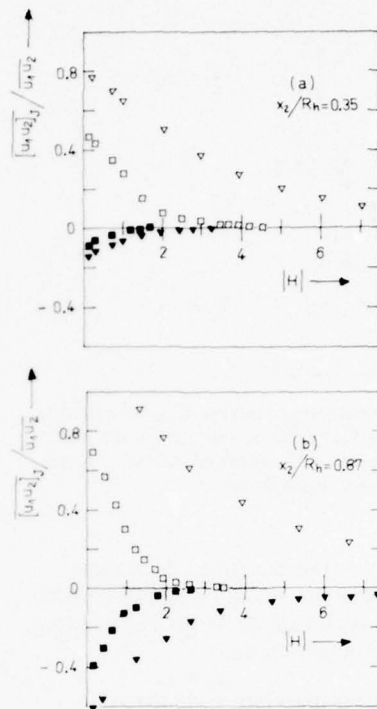

FIG. 7. (a), (b) Contribution to $\overline{u_1u_2}$ from the four quadrants of the u_1, u_2 plane in the rough pipe. ■, $J = I(u_1u_2 > 0,\ u_2 > 0)$; ▽, $J = II(u_1u_2 < 0,\ u_2 > 0)$; ▼, $J = III(u_1u_2 > 0,\ u_2 < 0)$; □, $J = IV(u_1u_2 < 0,\ u_2 < 0)$.

smooth wall pipe, by ejections related to various azimuthal directions of the pipe.

IV. DETECTION OF THE VIOLENT EJECTIONS

As recalled in Sec. I, the "*violent*" ejections are those whose amplitude exceeds the threshold $|H_c|\,u_1'u_2'$ such that only the ejections contribute to the Reynolds shear stress. Two examples are given in Fig. 7, one for the wall side of the core region $(x_2/R_h = 0.35)$, the other for the core region itself $(x_2/R_h = 0.87)$. In each case a characteristic threshold can be obtained (for instance, $-4.5 \le H_c \le -4$ for $x_2/R_h = 0.35$). Figure 8
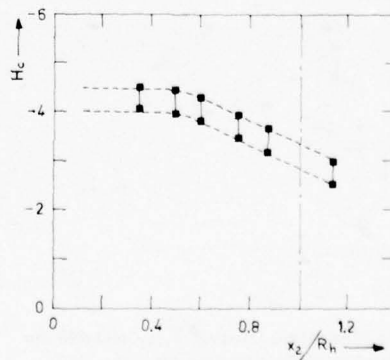

FIG. 8. Characteristic value H_c of the threshold H used for the detection of the violent ejections across the flow: ■, rough pipe; ----, smooth pipe.
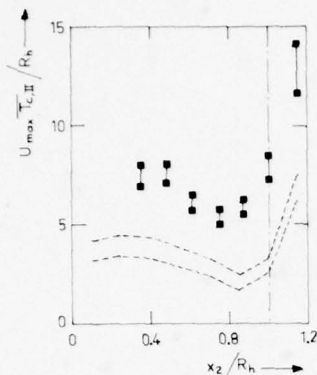
FIG. 9. Characteristic mean time interval $\overline{T}_{c,\mathrm{II}}$ between the violent ejections as a function of the distance from the wall. The scaling of $\overline{T}_{c,\mathrm{II}}$ is based on the outer parameters of the flow. ■, rough pipe; (----), smooth pipe.

FIG. 11. Mean streamwise length scale l_0^1 of the violent ejections as a function of the distance from the wall (▼, rough pipe; ▽, smooth pipe), and comparison with the integral length scale $L_{22}^{(1)}$ (■, rough pipe; □, smooth pipe).

shows the profile of H_c across the flow. It is quite similar to that obtained in the smooth wall pipe, which supports a confident comparison of the characteristics of the violent ejections in both flows.

V. CHARACTERISTIC MEAN TIME INTERVAL BETWEEN VIOLENT EJECTIONS

The characteristic mean time interval $\widetilde{T}_{c,\mathrm{II}}$ can be obtained from the frequency law $\tilde{N}_{\mathrm{II}} = f_{\mathrm{II}}(H)$ for $H = H_c$, since evidently $\overline{T}_{c,\mathrm{II}} = 1/\overline{N}_{\mathrm{II}}(H_c)$. The scaling of $\overline{T}_{c,\mathrm{II}}$ with the outer parameters of the flow has first been used as shown in Fig. 9, since these parameters have been found appropriate for smooth walls, be it boundary layers[7,8] or pipe flow[1] ($U_* \overline{T}_{c,\mathrm{II}}/\delta$ or $U_{\max} \overline{T}_{c,\mathrm{II}}/R$ independent of Reynolds number). For the rough wall pipe the values of $U_{\max} \overline{T}_{c,\mathrm{II}}/R_h$ are, however, distinct from the previous values. At the same Reynolds number, it appears that $\overline{T}_{c,\mathrm{II}}$ is greater in the rough than in the smooth wall pipe. Another scaling, based on the features brought out in Sec. II for the largest scale motions has, therefore, been attempted. The limit U_{cl} of the convective velocity and the distance δ^* from the wall
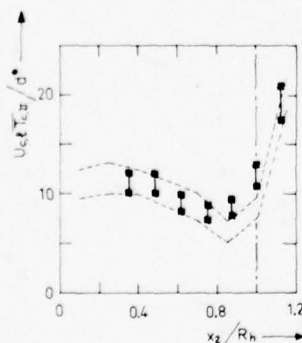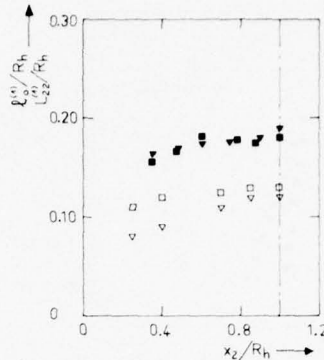
at which the space and time coherences of the flow are maximal, are now used for the velocity and the (transverse) length scales. Profiles of $U_{cl} \overline{T}_{c,\mathrm{II}}/\delta^*$ across the smooth and the rough pipes are shown in Fig. 10. A good collapse of the two sets of data is obtained. Nevertheless, other examples (for instance, flow in porous pipes with suction or blowing, or a larger range of Reynolds numbers) would be worth considering before a definite statement can be made.

VI. MEAN DURATION OF VIOLENT EJECTIONS

The mean duration $\overline{\Delta T_{0,\mathrm{II}}}$ of the violent ejections is considered at $H = 0$ and measured by extrapolation of the mean durations corresponding to $|H| \geqslant |H_c|$ (cf. Sec. I). It is then possible to obtain the streamwise length, l_0, of the violent ejections using the Taylor hypothesis: $l_0 = U \Delta T_{0,\mathrm{II}}$ (U is the local mean velocity). Values of l_0/R_h are given in Fig. 11 and they seem noticeably larger than those obtained in the smooth wall pipe. This result, along with the previous results for $\overline{T}_{c,\mathrm{II}}$, could stem from the fact that the roughness elements preclude some small scale motions but favor large scale motions as soon as they can take place.

Figure 11 also compared l_0/R_h and $L_{22}^{(1)}/R_h$ since these lengths are of the same order in the smooth wall pipe[1] ($L_{22}^{(1)}$ integral length related to radial velocity component and to a streamwise separation). This agreement seems to again hold here. Finally, if a comparison is made[3] with the Taylor length scale $\lambda_{11}^{(1)}$, as suggested by Falco[9] (indices for λ have the same meaning as those for L), it seems that l_0/R_n would also be of the order of $\lambda_{11}^{(1)}/R_h$, but experiments for a larger range of Reynolds number would be necessary for such definite conclusions, in particular, to determine the role of $\lambda_{11}^{(1)}$ since this scale is not relevant to a given size of turbulent structures.

FIG. 10. Characteristic mean time interval $\overline{T}_{c,\mathrm{II}}$ between the violent ejections as a function of the distance from the wall. The scaling of $\overline{T}_{c,\mathrm{II}}$ is based on parameters related to the large coherent structures of the flow. ■, rough pipe, (----), smooth pipe.

VII. CONCLUSION

From the numerous experiments already done with smooth boundaries and from the present investigation in a rough wall pipe, ejection events appear to be a uni-

versal dominant mode of maintenance of the mean shear stress across wall turbulent shear flows. In addition, results for the rough wall pipe enhance the belief that the wall region responds to perturbations created farther out from the wall.

Compared to the smooth wall pipe, the violent ejections observed for the rough wall pipe ($|u_1 u_2| \geq |H_c| u_1' u_2'$, $u_1 < 0$, $u_2 > 0$) present, for the same Reynolds number: (i) larger mean periods of occurrence, (ii) larger mean time duration and length scale, and (iii) larger negative peaks of $u_1 u_2$.

Two sets of length and velocity scales have been used to make the mean time interval between the violent ejections dimensionless: (i) the usual outer scales, i.e., the mean velocity on the pipe axis and the pipe radius; (ii) features of the largest scale motions in their mean flow environment as pointed out in the analysis of the space-time coherence of turbulence, i.e., the convection velocity limit U_{c_l} and the distance δ^* from the wall at which the integral time scale and the integral length scale of the longitudinal component of the velocity fluctuations are maxima. It appears that only the latter

set would collapse the data obtained in the rough and smooth wall pipes.

Finally, the mean streamwise length of the violent ejections seems to be of the order of the integral length scale of the radial component of the velocity fluctuations. Hence, ejection could be the main agent for the space coherence of this component.

[1]J. Sabot and G. Comte-Bellot, J. Fluid Mech. 74, 767 (1976).

[2]G. L. Brown and A.S.W. Thomas, Phys. Fluids 20, S243 (October, Part II, 1977).

[3]J. Sabot, Dr. ès Sci., Université Claude Bernard, Lyon (1976).

[4]A. J. Grass, J. Fluid, Mech. 50, 233 (1971).

[5]M. Elena, Dr. ès Sci., Université Aix-Marseille (1975).

[6]J. Sabot and G. Comte-Bellot, C. R. Acad. Sci. A 273, 628 (1971).

[7]K. N. Rao, R. Narasimha, and M. A. Badri Narayanan, J. Fluid Mech. 48, 339 (1971).

[8]S. S. Lu and W. W. Willmarth, J. Fluid Mech. 60, 481 (1973).

[9]R. E. Falco (to be published).

Structure of sheared turbulent fields

Carl H. Gibson,[a] Carl A. Friehe,[a] and Steven O. McConnell[b]

Department of Applied Mechanics and Engineering Sciences, University of California, San Diego, La Jolla, California 92093

Small scale turbulent temperature and velocity measurements were made in a variety of turbulent shear flows in the atmosphere and laboratory, in air and in water. Nonzero skewness values of the streamwise temperature gradient were observed in every case, with a sign equal to that of the gradient dotted with the cross product of the mean temperature gradient and mean shear vectors. Large temperature jumps were found across sharp shear zones at the outer boundaries of large scale eddies rotating with the mean vorticity of the shear flow, giving a distinctive ramp-like structure to the temperature signals which seems to be a characteristic feature of scalar fields mixed by sheared turbulence. The streamwise gradient of the vertical velocity in the atmospheric boundary layer over the ocean was found to have positive skewness. Thus, both velocity and temperature fields are locally anisotropic in the same sense as the anisotropic mean quantities.

I. INTRODUCTION

The concept of local isotropy introduced by Kolmogoroff[1] states that probability laws describing velocity differences between neighboring points in high Reynolds number turbulence should become invariant to either translations in space-time or rotations and reflections of the coordinate axes. Local isotropy is a necessary condition for Kolmogoroff's universal similarity hypothesis describing the small-scale structure of the velocity field and for related universal similarity hypotheses describing scalar fields such as temperature mixed by turbulence. Universal similarity hypotheses provide powerful tools in many practical applications, but as experimental and data processing techniques improve, at some point the accuracy of estimates of statistical parameters might be expected to exceed the reliability of the assumptions of universal similarity and local isotropy which might be applied.

A variety of statistical parameters has been used to test for local isotropy, and conflicting results have been obtained. For the velocity field, a common measure is the ratio of the power spectra of the components of the velocity vector. In the inertial subrange, the ratio of the spectra of the vertical or transverse components to that of the streamwise component should be 4/3. In atmospheric flows at large Reynolds numbers under a variety of stability conditions, the ratio 4/3 has been found by Busch and Panofsky[2] and Kaimal *et al.*[3] while Miyake *et al.*,[4] Stewart,[5] Weiler and Burling,[6] McBean,[7] and Smith *et al.*[8] reported lower values, ranging from 0.6 to 1.2. In laboratory flows, Gibson[9] obtained the ratio of 4/3 in a round turbulent jet flow, as did Champagne *et al.*[10] in a low Reynolds number homogeneous shear flow.

Another test for local isotropy of the velocity field is the measurement of the skewness of the streamwise spatial derivative of the fluctuating vertical velocity component, $S(\partial u_3/\partial x_1)$, which should be zero if the field

is isotropic $[S(\xi) \equiv \langle(\xi - \langle\xi\rangle)^3\rangle/\langle(\xi - \langle\xi\rangle)^2\rangle^{3/2}]$. It is often assumed that $S(\partial u_3/\partial x_1) = -S(dw/dt)$ by Taylor's hypothesis (t is time and w is the *measured* fluctuating vertical velocity component, which we distinguish from u_3, the fluctuating velocity component in the x_3 direction), for example, see Wygnanski and Fielder.[11] Freymuth and Uberoi[12,13] reported measurements of $S(dw/dt) \simeq 0$ as evidence of local isotropy in the wake flows of a sphere and cylinder at low Reynolds numbers. However, we shall show that, in general, $-S(dw/dt)$ is not equal to $S(\partial u_3/\partial x_1)$ because of a rather subtle failure of the usual application of Taylor's hypothesis to the measured quantity dw/dt. The present results, taking this difficulty into account (Sec. IIID), indicate that $S(\partial u_3/\partial x_1)$ was, in fact, significantly different from zero in the atmospheric boundary layer over the ocean.

Evidence for anisotropy of turbulent scalar fields in shear flows has also been reported. From measurements in the atmospheric boundary layer (heated from below) Stewart,[5] Gibson *et al.*,[14] and Boston[15] found values of $S(\partial T/\partial x_1)$ which were consistently positive rather than the isotropic value of zero, where the temperature gradient $\partial T/\partial x_1 \simeq -(\partial T/\partial t)/\overline{U}$ using Taylor's hypothesis. For the wake of a heated sphere, Freymuth and Uberoi[13] also found that $-S(\partial T/\partial t) = S(\partial T/\partial x_1)$ was positive.

Wyngaard[16] has shown that positive $S(\partial T/\partial x_1)$ values can be obtained in a locally isotropic field due to contamination of the measured temperature skewness by a term due to the finite velocity sensitivity of the small resistance wire sensors. Boston[15] estimated the corrections to his results, and while there were effects, the nonzero skewness values remained. In the atmospheric boundary layer experiments reported herein, precise corrections were made for the velocity sensitivity, and the final results indicated local anisotropy. Further, the skewness of the temperature derivative was measured in two laboratory flows, jets and sphere wakes and again nonzero values were obtained. In fact, it was found that the signs of $-S(\partial T/\partial x_1)$ were consistently negative for the heated jets and the wake of the cooled sphere. A negative value of $S(\partial T/\partial x_1)$ cannot be caused

---

[a] Also Scripps Institution of Oceanography.
[b] Present address: Applied Physics Laboratory, Seattle, Wash. 98195.

TABLE I. Experimental conditions and statistical parameters.

	Atmospheric boundary Layer		Large jet	Small jet	Hot sphere wake	Cold sphere wake
Reynolds number, $U(D,x_3)/\nu$	4.9×10^6	5.1×10^6	7.0×10^5	1.1×10^5	1.5×10^4	1.5×10^4
$\overline{U}_1$(cm/sec)	610	636	424	423	48	48
ϵ(cm²/sec³)[a]	16.6	14.7	1.54×10^4	5.52×10^4	120	120
χ(°C²/sec)[b]	6.3×10^{-4}	1.3×10^{-4}	1.42×10^{-1}	1.63×10^{-2}	⋯	⋯
x/D or height	12 m	12 m	50	40	4	4
$S(\partial T/\partial x_t)$	+0.85	+0.75	−0.87	−0.72	+0.81	−1.08
$K(\partial T/\partial x_1)$	98	109	55	23	14.6	20.5
Number of samples	2.15×10^6	2.31×10^6	1.19×10^6	0.204×10^6	1.02×10^6	1.02×10^6
Cold wire current (μA)	400	400	130	400	⋯	⋯

[a] $\epsilon = (15\nu/\overline{U}_1^2)(\overline{du/dt})^2$.

[b] $\chi = (6D/\overline{U}_1^2)(\overline{\partial T/dt})^2$.

by velocity-sensitivity contamination, according to Wyngaard's analysis.

Evidence for local anisotropy of turbulent velocity and scalar fields is disconcerting, since the most successful theoretical framework for analysis has been based on the assumption of an approach to local isotropy at large Reynolds numbers, e.g., Kolmogoroff,[1] Obukhov,[17] and Corrsin.[18]

A clue to the cause of the observed skewness values and their signs may lie in an anisotropic feature of the various flows which is easily observed by inspection of the time series of the temperature signal. Characteristic ramp-like or sawtooth structures can be distinguished and are oriented in a way consistent with the orientation of the mean vorticity and temperature gradient vectors as described by Gibson et al.[19] for a heated sphere wake in water. Such structures have also been observed in the atmospheric boundary layer, but are usually attributed to convective plume motion. Monji[20] shows simultaneous ramp temperature structures at several heights in the atmospheric surface layer, from 0.01 to 15 m for unstable conditions. Tillman[21] shows similar traces, also for unstable conditions. However, Laufer[22] cites a study by Chen[23] in a stable heated boundary layer under a flat plate in which ramp structures were observed with the same sense as those found in the unstable cases. Thus, although buoyant plumes may produce isolated and very distinctive ramp-like features in an unstable turbulent boundary layer, it appears that buoyancy is a sufficient but unnecessary factor in producing this characteristic large scale anisotropy in sheared turbulent scalar fields.

In the following sections, the atmospheric boundary layer, jet and sphere wake experiments are described. Results of the skewness of the temperature derivative for the various flows are presented, and corrections for Wyngaard's velocity sensitivity effect are discussed. Observations of the ramp structures are shown, together with a model developed to aid in interpreting the skewness results. Finally, results of the measurement of dw/dt from the atmospheric boundary layer experiment and analysis of the interpretation of $S(dw/dt)$ are presented.

II. EXPERIMENTAL ARRANGEMENTS

As indicated, fine-scale turbulence measurements were made in three shear flows: the atmospheric boundary layer over the ocean, axisymmetric heated air jets, and heated and cooled sphere wakes. The mean conditions for the experiments and other information are given in Table I.

A. Atmospheric boundary layer

Turbulent velocity and temperature fluctuations were measured from the Scripps Institution of Oceanography Floating Instrument Platform (FLIP) as a part of a series of experiments about 75 km off the coast of Mexico. (A description of such experiments is given by Friehe et al.[24]). Probes were attached to, or suspended from, booms mounted on FLIP, from 5 to 12 m above the sea surface. For the results presented here, the micrometerological conditions were typical of open ocean conditions: the boundary layer was slightly unstable with respect to buoyancy forces, with positive (upward) heat and moisture fluxes.

Temperature fluctuations were measured with fine platinum resistance wire sensors, 0.4 to 0.7 mm long and 0.63 μ diam, operated in a low noise battery-powered ac bridge designed in our laboratory by T. Deaton. Bandwidth was estimated to be from dc to about 1.5 kHz for the conditions of the experiment.[25]

Measurements of the instantaneous vertical velocity component were obtained using an X-wire anemometer probe. The probe was about 5 m above the water attached to a cable suspended from a boom on the floating platform. A 90 kg mass was on the end of the cable about 20 m under water to provide cable stiffness and act

as a damped pendulum to isolate the probe from the slight pitching motion of the floating platform. A vertical gyroscope (provided by R. E. Davis) was also attached to the cable and indicated that residual pitching motions were a few tenths of a degree. The X-wire probe was directly calibrated in the laboratory on the floating platform in a small calibration jet before the experiment.

B. Jets in air

Two axisymmetric heated air jet flows were used for temperature measurements: a small jet for preliminary studies and a larger jet for high Reynolds number conditions. The small jet consisted of an axial fan with a 500 W hot air heater positioned at the fan inlet. The Reynolds number was about 1.1×10^5, based on the jet diameter (6.4 cm). Sensors were placed on the jet centerline, 40 diam downstream of the exit. Temperature measurements were made with a 1.3 mm length $\times 0.6~\mu$ diam platinum wire operated in an ac Wheatstone bridge using a Tektronix 3C66 carrier preamplifier. Several wire currents were used to investigate the effect of velocity sensitivity, which is proportional to the square of the current. Velocity fluctuations were measured using a constant temperature anemometer and a TSI hot-wire probe, 1.25 mm length $\times 3.8~\mu$ diam. From the measured dissipation rate, ϵ, the Kolmogoroff scale $(\nu^3/\epsilon)^{1/4}$, was estimated to be about 0.15 mm (ν is kinematic viscosity). Thus, wire length attenuation effects are possible,[26,27] but are not believed to affect the sign of the skewness of dT/dt. [It has been found that low pass filtering has no effect on the sign and little effect on the magnitude of $S(dT/dt)$ except at very low frequencies.]

To alleviate the wire length attenuation problems and to obtain measurements at a greater Reynolds number, an experiment with a much larger jet was performed (with the aid of J. C. LaRue, J. T. Park, and F. H. Champagne). The jet diameter was 30 cm and the Reynolds number was about 7×10^5. An array of 30 kW heaters was placed at the entrance of the jet blower (a 5 hp vane-axial fan). In order to obtain measurements at a sufficiently large distance downstream (50 diam) the experiment was performed in the university gymnasium with the jet 5 m above the floor. The probe was positioned on the jet centerline with a laser alignment system. The temperature sensor was an extremely small platinum wire (fabricated by J. C. LaRue) with length 0.2 mm and diameter 0.25 μ. The value of ϵ was estimated to be 1.54×10^4 cm^2 sec^{-3}, giving a Kolmogoroff length of 0.22 mm, from the conditions of the experiment and the semi-empirical dissipation rate correlation of Friehe et al.[28]

C. Sphere wakes in water

To investigate the changes in sign of the temperature derivative skewness with the change of sign of the mean temperature gradient the heated and cooled wakes of a sphere in a university water tunnel were used as the shear flow. Details of the tunnel and sphere arrangement are given by Gibson et al.[19] Hot or cold water was injected from the upstream stagnation point of the 3.81

cm diam sphere, and temperature fluctuations were detected 4 diam downstream on the wake axis using a 0.1 mm diam conical wedge hot film anemometer probe as a resistance thermometer. The sphere Reynolds number for the flow was about 1.5×10^4 based on diameter and external velocity. Velocity sensitivity was found to be less than the system noise observed with the probe in the isothermal wake, and is therefore considered negligible.

Special precautions are necessary to accurately measure kurtosis and skewness values of high Reynolds number temperature gradients because of the large dynamic range of the signal.[29] Temperature signals were differentiated before analog recording on FM tape recorders in order to preserve the high signal-to-noise ratios.

The appropriate signals were digitized on playback with a 14 bit analog to digital converter, and analyzed on an IBM 1130 laboratory computer.

III. RESULTS

A. Local anisotropy of temperature gradient skewness $S(\partial T/\partial x_1)$

The results of measurements of the skewness of streamwise temperature gradients in the three sheared turbulent flows are summarized in Table I. The magnitudes of the skewness values are substantially different from zero, ranging from 0.7 to 1.1 over the wide range of Reynolds numbers, 1.5×10^4 to 5×10^6. It would appear that local anisotropy of the temperature field is a characteristic feature of shear turbulence. Positive values occur for the heated boundary layer over the ocean and for the hot sphere wake; negative values for the hot jets and the cold sphere wakes. Kurtosis values $[K(\xi) \equiv \langle (\xi - \langle \xi \rangle)^4 \rangle / \langle (\xi - \langle \xi \rangle)^2 \rangle^2]$ were found to increase substantially with Reynolds number, from about 15 to over 100. It was necessary to digitize a very large number of derivative samples from the analog tapes to obtain convergence of the S and K values, especially for the higher Reynolds number flows as discussed by Tennekes and Wyngaard.[29] For the atmospheric flows, the data were sampled at approximately 2000 Hz for a 15 min period which gave 2×10^6 samples for the statistical calculations. This corresponds to sampling once every 3 Kolmogoroff lengths over 7 km of air. For the large jet flow, 10^6 samples were taken at about 3000 Hz for 5 min, equivalent to sampling once per 6 Kolmogoroff lengths over 1.3 km.

In order to assess the statistical stability of the skewness values given in Table I and to determine if the dynamic range of the instrumentation was adequate, plots were made of the skewness density function per unit gradient, defined as the third moment of the probability density function $(X/\sigma)^3 p(X)$ versus X/σ, where X is the random variable $[X = (-1/\overline{U}_1)(dT/dt) = \partial T/\partial x_1$; $\overline{U}_1$ is the mean velocity in the x_1 direction] and σ is the standard deviation. The area under the curve described by the data is the skewness of X, which implies odd symmetry of $p(X)$ about $X/\sigma = 0$ if the flow is locally isotropic. Figure 1 shows the skewness density for the temperature derivative measured in the wake of the
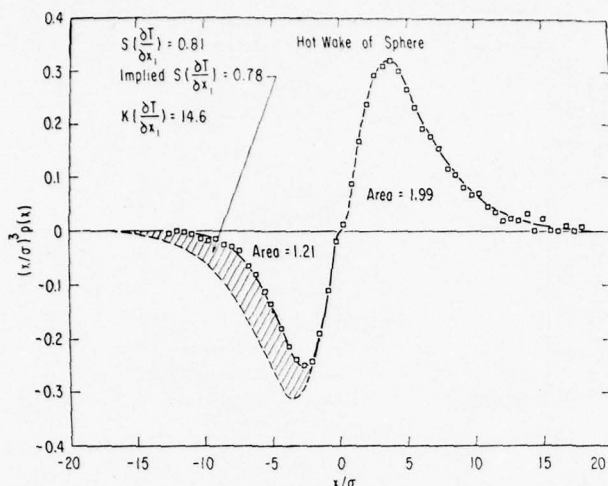
FIG. 1. Skewness probability density function per unit gradient for heated wake of sphere in water tunnel (see Table I). Shaded area shows deviation from symmetry and skewness value.

FIG. 3. Skewness function for large heated jet (see Table I).

heated sphere. There is an obvious asymmetry, as indicated by the difference between the shaded portion on the left (which is the reflected and inverted positive lobe) and the values of the negative lobe. The area under the curve through the measured skewness distribution gave 0.78 compared with 0.81 determined by direct computation from the derivative samples. Even for this low Reynolds number flow, samples to $\pm 10\sigma$ are needed to achieve convergence of S. The skewness density for the cooled wake of the sphere is presented in Fig. 2, and shows the shift of the $\partial T/\partial x_1$ values to the negative lobe, giving $S = -1.08$. Apparently the magnitude of S is insensitive to Prandtl number, since these measurements were made of temperature gradients in water with Prandtl number 7 rather than 0.7 for air.

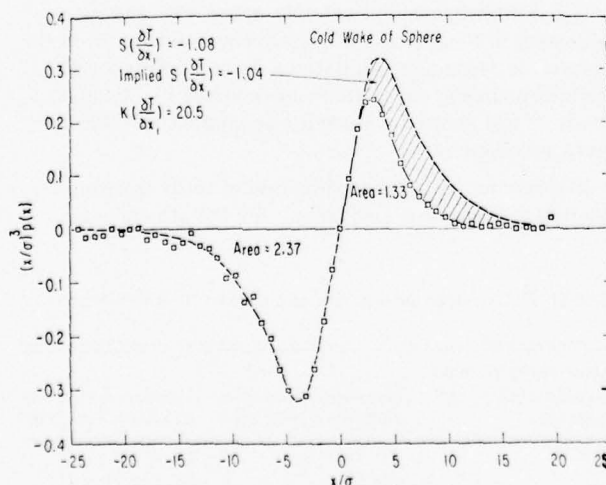Figure 3 shows the skewness density for the large jet

flow, which is also quite well defined and indicates adequate dynamic range requires $\pm 25\,\sigma$. A plot of the kurtosis density per unit gradient $(X/\sigma)^4 p(X)$, also indicated good convergence to $K = 55$ for the heated jet.

The data for the temperature derivative in the atmospheric boundary layer are presented in Figs. 4 and 5 and illustrate that the requirements for convergence are much more severe. Scatter in the data is substantial despite the fact that the 2×10^6 samples were used in estimating the density function, although the scatter is not so great that the asymmetry is in doubt. Again, in both Figs. 4 and 5 the S values implied by the shaded portion are in good agreement with the values calculated directly from the derivative time series. Values of X to nearly 50 standard deviations were required to achieve convergence: i.e., a very large dynamic range. Similarly, plots of the kurtosis density $(X/\sigma)^4 p(X)$ were made and indicated satisfactory (20%–40%) agreement with the direct calculations.

FIG. 2. Skewness function for cooled wake of sphere in a water tunnel (see Table I). Note change in sign of $S(dT/dx_1)$ from Fig. 1.
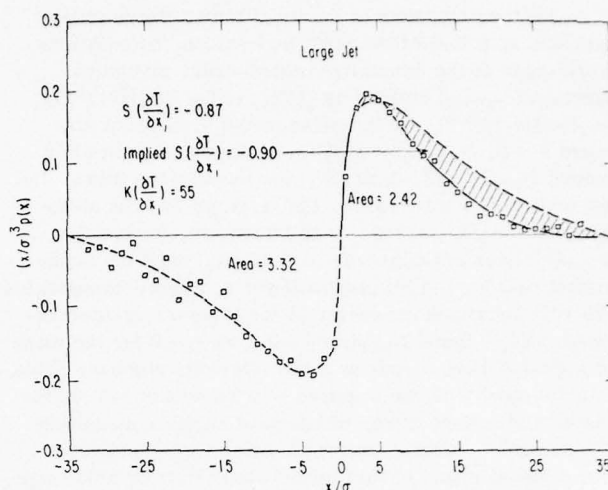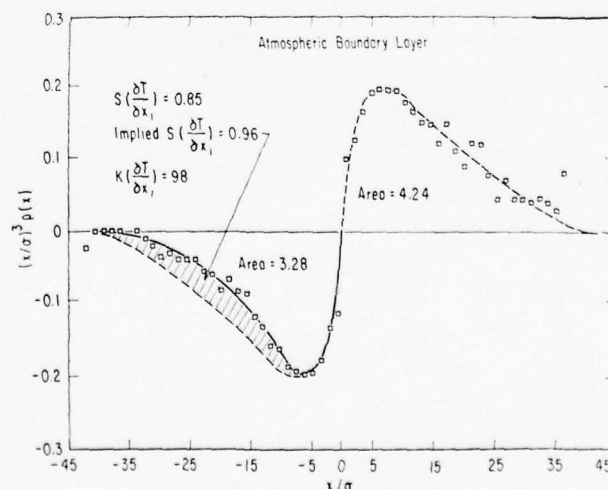

FIG. 4. Skewness function for atmospheric boundary layer over warm ocean (see Table I). $\chi = 6.3 \times 10^{-4}\,°C^2/sec$.

As another measure of the local temperature structure and as a test of the $S(\partial T/\partial x_1)$ values, calculations were made of the normalized third-order structure function $D_{TTT}(r_1)$ defined as $\langle[T(x_1 + r_1) - T(x_1)]^3\rangle/\langle[T(x_1 + r_1) - T(x_1)]^2\rangle^{3/2}$. As the streamwise separation distance $r_1 \to 0$, $D_{TTT}(r_1) \to S(\partial T/\partial x)$. Figure 6 shows that indeed $D_{TTT}(r_1 \to 0) \simeq S(\partial T/\partial x_1)$ for the various flows: the hot and cold sphere wakes, the large jet and the atmospheric boundary layer. It is interesting to note that $D_{TTT}(r_1)$ does not converge to $S(\partial T/\partial x_1)$ until the separation reaches the Kolmogoroff scale, which demonstrates the very localized character of the temperature derivatives. Yeh[30] found $D_{TTT}(r_1) \to -0.2$ as $r_1 \to 0$ for the wake of a grid of heated rods at a low Reynolds number. This is consistent with the negative S in Table I of -1.08 for the heated sphere wake, although of smaller magnitude. Presumably, the interaction of the rod wakes reduces the residual effect of this initial shear flow on $S(\partial T/\partial x_1)$.

B. Velocity sensitivity corrections

Wyngaard[16] has shown that in isotropic turbulence the measured skewness of the temperature derivative can be in error due to a contamination term arising from the finite velocity sensitivity of the temperature resistance wire sensor. The result of Wyngaard's analysis was

$$S\left(\frac{\partial T}{\partial x_1}\right)\bigg|_m = S\left(\frac{\partial T}{\partial x_1}\right) - 3c\left(\frac{6\mathcal{D}\epsilon}{15\,\nu\chi}\right)^{1/2}\Sigma$$

where $\mathcal{D}$ is the thermal diffusivity, c is the velocity sensitivity of the wire (deg K/msec^{-1}), χ is the dissipation rate of the temperature fluctuations,

$$\Sigma = \frac{\langle(\partial u_1/\partial x_1)(\partial T/\partial x_1)^2\rangle}{\langle(\partial u_1/\partial x_1)^2\rangle^{1/2}\langle(\partial T/\partial x_1)^2\rangle} \quad,$$

u_1 is the fluctuating streamwise component of velocity, $S(\partial T/\partial x_1) = 0$ by isotropy and the subscript m denotes a measured value. Σ is the strain rate-scalar dissipation rate correlation which Wyngaard estimated to be -2. Σ has been measured by Clay[31] in several flows and found
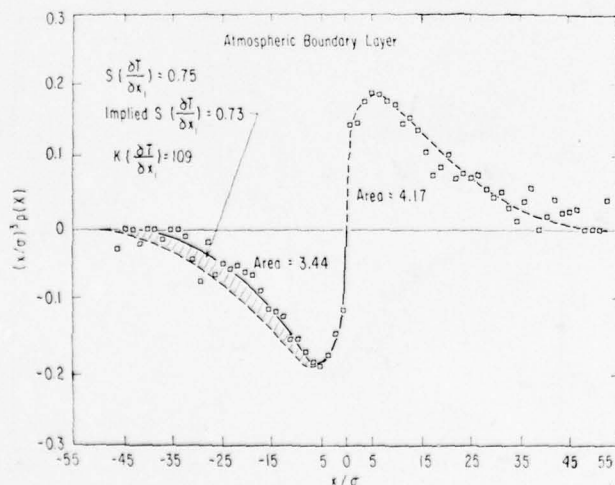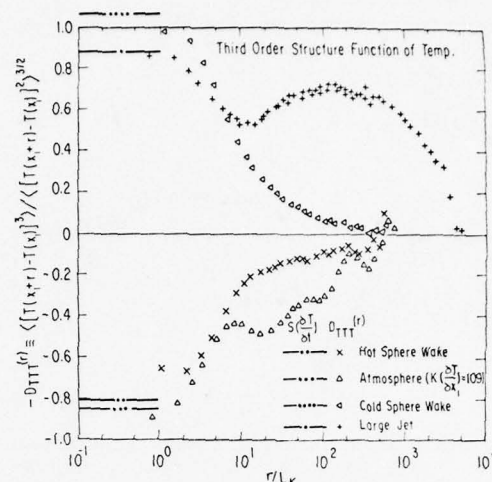

FIG. 6. Third order structure functions for temperature difference in streamwise direction: hot and cold wakes, large jet, atmospheric boundary layer over the ocean. Values $\to S(\partial T/\partial x_1)$ as $r \to 0$.

to be about -0.5. The velocity sensitivity c is a function of the heat transfer between the wire and the fluid, and is proportional to the square of the sensing current through the wire. To determine the effect of c on the measured value of S, the current through the temperature wire in the small jet experiment was varied over a 12:1 range. The results are presented in Table II and show that the values of S and K were about the same for sensing currents of 226 and 715 μA whereas for a current of 2500 μA the value of the skewness of the temperature derivative changed sign and the kurtosis value decreased substantially. The results for the highest current indicate that the sensor is acting as a hot wire anemometer, and those at the lower currents indicate no significant differences and hence, no significant velocity effect. Wyngaard's analysis predicts that $S(\partial T/\partial x_1)|_m > 0$ because Σ is always expected to be negative, whereas the jet results gave $S(\partial T/\partial x_1)|_m < 0$. A more detailed investigation of velocity sensitivity and measurement of S carried out subsequent to this work at the Institut de Mécanique Statistique de la Turbulence in various boundary layer flows is reported by Mestayer et al.,[32] and showed S behavior consistent with the results reported here.

In order to avoid the assumption of local isotropy leading to Wyngaard's equation, for the atmospheric

FIG. 5. Skewness function for atmospheric boundary layer over warm ocean (see Table I). $\chi = 1.3 \times 10^{-4}\,^\circ\text{C}^2$ sec.

TABLE II. Velocity sensitivity of cold wire in small heated jet.

Alternating current through cold wire[a] (rms μA)	Measured skewness $S(\partial T/\partial x_1 + c\partial u_1/\partial t)$	Measured kurtosis $K(\partial T/\partial x_1 + c\partial u_1/\partial t)$
226	-0.73	26.8
715	-0.79	21.6
2500	$+0.37$	6.5

[a]Wire diameter 0.62μ, length = 1 mm.

HEATED SMALL JET , $S\left(\frac{\partial T}{\partial x_1}\right) = -0.7 = |S| \, \mathrm{sgn} \, [x_1 \cdot (\nabla \bar{T} \times \underline{\omega})]$

a.

WIND OVER WARM OCEAN , $S\left(\frac{\partial T}{\partial x_1}\right) = +0.8 = |S| \, \mathrm{sgn} \, [x_1 \cdot (\nabla \bar{T} \times \underline{\omega})]$
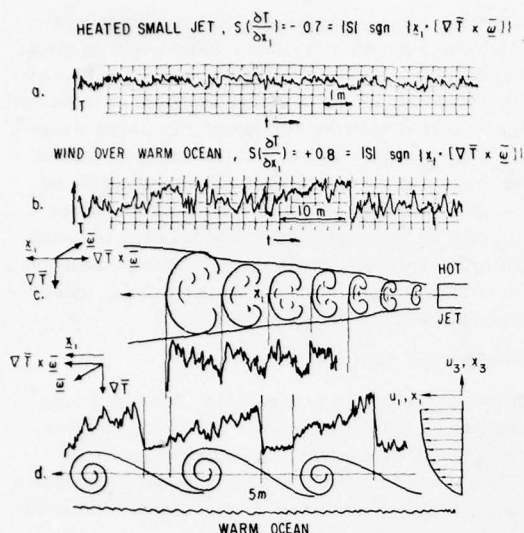
b.

c.

d.

WARM OCEAN

FIG. 7. Ramp model for gradient skewness in shear flows. (a) Temperature record for heated jet-ramps face downstream $S(\partial T/\partial x_1) = |S| \, \mathrm{sgn}[x_1 \cdot (\nabla \bar{T} \times \underline{\omega})] = -0.7$. (b) Temperature record for heat boundary layer—ramps face upwind $S(\partial T/\partial x_1) = |S| \, \mathrm{sgn}[x_1 \cdot (\nabla \bar{T} \times \underline{\omega})] = +0.5$. (c) Ramp model for heated jet. (d) Ramp model for heated boundary layer.

flow an attempt was made to measure c and correct the instantaneous measured temperature derivative samples using

$$\left(\frac{\partial T}{\partial x_1}\right) = \left(\frac{\partial T}{\partial x_1}\right)\bigg|_m - c\left(\frac{\partial u_1}{\partial x_1}\right)\bigg|_m .$$

The $\partial u_1/\partial x_1$ values were obtained from du_1/dt from a hot-wire placed less than 1 mm (approximately the Kolmogoroff scale) away from the temperature sensor. It was found that the corrections to $S(\partial T/\partial x_1)|_m$ were less than 20%.

The conclusion from these tests is that the nonzero skewness values for dT/dt are not due to velocity sensitivity contamination.

C. Ramp model for $S(\partial T/\partial x_1)$

An interesting feature of the temperature signals measured in the jet and the boundary layer over the ocean is shown by strip chart records in Fig. 7. Both demonstrate the peculiar ramp-like anisotropy mentioned previously. The sign reversal in Taylor's hypothesis, $dx_1 = -\bar{U}_1 dt$, is illustrated by the sketches at the bottom of the figure for x_1 positive in the streamwise direction. The sharp temperature decrease at the end of the ramps occurs in the direction of the wind for the jet, but against the wind for the boundary layer.

The same sort of ramplike signal was observed by Gibson *et al.*[19] in the heated wake of a sphere: the ramps faced the sphere, opposite the direction of fluid motion. It was proposed that the feature is due to sharp thermal interfaces that develop on the sides of large eddies rotating with the mean vorticity of the shear flow which brings hot fluid up from the wake axis. The same explanation will account for the ramps in the jet and boundary layer flows, as illustrated by the sketches at the bottom of Fig. 7.

Ramplike or sawtooth behavior in temperature and humidity signals has previously been noted in the meteorological literature[33–39] for measurements in buoyantly unstable atmospheric boundary layers. This sawtooth structure has been attributed to either convective plumes maintained by buoyant acceleration[33,34,36] or horizontal roll vortices[40,41,39] or a combination of the two.[37] Although buoyant plumes produce dramatic ramp-like features in the temperature signals, the present evidence suggests that buoyancy enhances rather than causes such features. The present measurements indicate that the ramp-like structure is a characteristic feature of sheared turbulent scalar fields: A large scale feature which may result in small scale anisotropy.

To pursue the apparent connection between the ramp structure in the temperature and the nonzero skewness values of the derivative, simultaneous strip chart records were made of T and dT/dt. Qualitative examination of these records did not give a particularly convincing conclusion that the ramps cause the skewness. Sometimes, a spike in dT/dt with the right sign would occur at a ramp cutoff, sometimes not. Even though ΔT for the cutoff might look large from the T record, the excursion might not occur in a small enough time to make an extreme value for dT/dt. Often large dT/dt spikes occur in the body of the ramp, and with either sign.

1. Ramp model

Figure 8 shows a model temperature distribution in which the extreme values of the gradient are confined to the ramp interfaces with preferred sign, giving maximum anisotropy [i.e., maximum skewness magnitude for a given intermittency (kurtosis value)]. The temperature derivative is taken to be a square wave with both amplitude and switching frequencies equal to 1 unit. Occasional large excursions of amplitude $a \gg 1$ and period 1 occur at an average period $y \gg 1$. The corresponding temperature consists of ramps of period y with a small amplitude, high frequency triangle wave added, as shown in Fig. 8 along with the corresponding derivative. It can be shown that the kurtosis of such a signal is approximately $K \simeq (a^4/y + 1)/(a^2/y + 1)^2$, and the skewness $S \simeq (a^3/y)/(a^2/y + 1)^{3/2}$.

Physically, the unit period in x_1 corresponds to the Batchelor length L_B and the unit temperature change corresponds to the scalar scale Σ_B where $L_B \cong (\nu D^2/\epsilon)^{1/4}$ and $\Sigma_B \cong (\nu \chi^2/\epsilon)^{1/4}$.[42]

The ramp period or "macroscale" of the temperature field is thus $y L_B$ and the height of the ramp "jump" is $a \Sigma_B$. Using the expressions for $K(a, y)$ and $S(a, y)$, Fig. 8 shows $|S|$ versus K values calculated compared with the measured values from Table I. Clearly, the measured values of $|S|$ are much less than those inferred from the anisotropic model. Therefore, we may conclude that although the measured S values are not zero, they are much smaller than expected from complete local anisotropy.

$$K(\partial T/\partial x_1) \doteq (a^4/y+1)/(a^2/y+1)^2$$
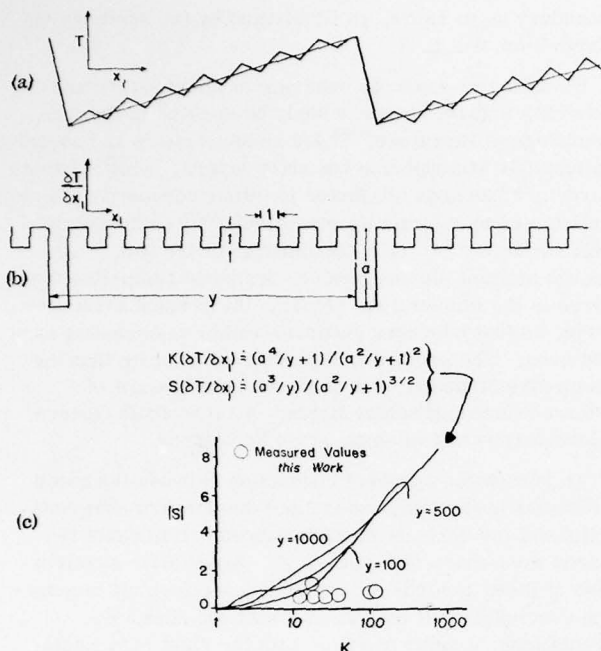$$S(\partial T/\partial x_1) \doteq (a^3/y)/(a^2/y+1)^{3/2}$$

FIG. 8. Local anisotropy test. (a) Temperature distribution $T(x_1)$: Batchelor length and temperature scales. (b) $\partial T/\partial x_1$ (c) $|S|(a,y)$ versus $K(a,y)$ for $\partial T/\partial x_1$ of anisotropic model compared to measured values of Table I. Comparison suggests approach to local isotropy with increasing Reynolds number (large K).

For example, if we take $y = 200$ for the small jet corresponding to the energy to viscous length scale ratio, we find a is about 11 to give the measured $K(\partial T/\partial x_1)$ value of 26, but, $|S|$ calculated from the model under these conditions is 3.5, rather than only 0.7 as measured. Similarly, taking 1000 for y as appropriate for the atmospheric boundary layer implies a is about 16 to give K about 40, but this also implies $|S|$ is about 3.0, compared with the measured values around 0.6. All reasonable values for y and a lead to the same conclusion: the measured non-zero skewness magnitudes could easily be accounted for by extreme one-sided derivative spikes in only a moderate fraction of the observed ramps with preferred direction. This shows why the connection was not obvious from the strip chart records discussed in Sec. III C. We conclude that if the observed local anisotropy of $\partial T/\partial x_1$ is due to the ramp structure of T, it must be interpreted as a relatively small residual effect.

2. The sign of the skewness

The different shear flows have indicated a relationship between the sign of $S(\partial T/\partial x_1)$ and the sense of the ramps with respect to the mean flow direction. Whether the steep face of the ramp is in the direction of the mean fluid motion (jet) or opposed to the mean flow direction (wake, boundary layer) appears to depend on the mean vorticity $\overline{\omega} = \nabla \times \overline{u} = \hat{x}_1(\partial \overline{U}_1/\partial x_3)$, where $\hat{x}_1$ is the mean flow direction and $\hat{x}_3$ is the direction away from the surface in the boundary layer or away from the jet or wake

axis ($\hat{x}_3 = \hat{x}_1 \times \hat{x}_2$, i.e., a right-handed coordinate system). The wake and boundary layer have positive mean vorticity and the jet negative. The sign of $S(\partial T/\partial x_1)$ also depends on the mean temperature gradient as indicated by the sign reversal between hot and cold sphere wakes (Table I). The boundary layer, heated jet, and heated wake flows have negative mean temperature gradients and the cooled wake has a positive mean temperature gradient. This suggests the following relation between the sign of temperature derivatives in shear turbulence with mean vorticity $\overline{\omega}$, and mean temperature gradient $\nabla \overline{T}$ and the sign of their cross product

$$\text{sgn}[S(\partial T/\partial x_1)] = \text{sgn}[\hat{x}_1 \cdot (\nabla \overline{T} \times \overline{\omega})] .$$

This expression correctly predicts the signs of all the nonzero skewness values measured in sheared scalar fields discussed in this paper. An extension of this work by Mestayer et al.[32] has confirmed this expression for various combinations of stability and mean temperature gradient in boundary layers.

D. Local anisotropy of velocity: $S(\partial u_3/\partial x_1)$

As another test for local anisotropy in the atmospheric boundary layer, and to further test the model previously described connecting the anisotropy of $\partial T/\partial x_1$ with the ramp interfaces, an attempt was made to measure the skewness of the derivative of the vertical velocity component with respect to the streamwise direction x_1, $S(\partial u_3/\partial x_1)$, from X-wire data obtained on the floating platform (FLIP). For locally isotropic turbulence, $S(\partial u_3/\partial x_1)$ should be zero since $(\partial u_3/\partial x_1)^3$ changes sign when x_1 is reflected.

However, the measurement is complicated by the fact that a perfectly calibrated X-wire anemometer indicates a velocity component perpendicular to the probe axis, w, rather than the x_1 direction, u_3. The output of the anemometer is a function of time, and we wish to relate it to the spatial derivative $\partial u_3/\partial x_1$. The common method is to apply Taylor's hypothesis as $(dw/dt)^3 = -\overline{U}_1^3(\partial u_3/\partial x_1)^3$.[11,12] However, it is necessary to examine the interpretation of $(dw/dt)^3$ in detail to be sure that there are no residual contamination terms due to higher-order corrections to Taylor's hypothesis.

In order to determine the proper interpretation of the skewness of the dw/dt signal from an X-sensor anemometer, let us consider the more general problem of determining what a velocity probe measures in a fluid. Corrsin[43] considers the problem of a probe which measures a scalar quantity θ while moving in an arbitrary trajectory $\mathbf{P}(t)$ through the fluid. The output of the probe is $m = k\theta$, where k is the (known) sensitivity. In a fluid where θ varies with space $\mathbf{x}$ and time, the output is

$$m(t) = k\theta[\mathbf{P}(t), t] , \tag{1}$$

The time derivative of the measured signal is shown by Corrsin to be

$$\frac{1}{k}\left(\frac{dm}{dt}\right) = \left[\left(\frac{\partial \theta}{\partial t}\right) + V_j \frac{\partial \theta}{\partial x_j}\right]_{\mathbf{P}} , \tag{2}$$

where $V_j = dP_j/dt$ is the velocity of the probe. We can extend Corrsin's analysis to the case of the measure-

ment of the velocity vector from a moving probe. For the case of velocity, however, we note that most probes (e.g., anemometers) measure velocity components relative to the probe motion through the fluid:

$$m_i = k_i S_i \quad \text{(no summation)}, \tag{3}$$

$$S_i = U_i - V_i, \tag{4}$$

where S_i is the measured velocity component relative to the probe, U_i is the velocity component in the fluid, and k_i is the sensitivity to component i (it will be assumed that $k_i = k$; $i = 1, 2, 3$). Therefore,

$$(1/k)m_i = S_i[\mathbf{P}(t), t] \tag{5}$$

and

$$\frac{1}{k}\left(\frac{dm_i}{dt}\right) = \left[\left(\frac{\partial S_i}{\partial t}\right) + V_j\left(\frac{\partial S_i}{\partial x_j}\right)\right]_{\mathbf{P}}. \tag{6}$$

Equations (4) and (6) give

$$\frac{1}{k}\left(\frac{dm_i}{dt}\right) = \left[\left(\frac{\partial U_i}{\partial t} - \frac{\partial V_i}{\partial t}\right) + V_j\left(\frac{\partial U_i}{\partial x_j} - \frac{\partial V_i}{\partial x_j}\right)\right]_{\mathbf{P}} \tag{7}$$

which is a general expression relating time derivatives of anemometer output signals to fluid and platform velocity gradients and accelerations. We restrict the probe to travel without acceleration ($\partial V_i/\partial t = \partial V_i/\partial x_j = 0$),

$$\frac{1}{k}\left(\frac{dm_i}{dt}\right) = \left[\left(\frac{\partial U_i}{\partial t}\right) + V_j\left(\frac{\partial U_i}{\partial x_j}\right)\right]_{\mathbf{P}}, \tag{8}$$

which is analogous to Corrsin's scalar equation.

To proceed further, we note that $(\partial U_i/\partial t)_{\mathbf{P}}$ is the rate of change of fluid velocity at the probe (at position $\mathbf{P}$). This is related to the acceleration of the fluid following the fluid motion by

$$\left(\frac{\partial U_i}{\partial t}\right)_{\mathbf{P}} = \left(\frac{DU_i}{Dt} - U_j\frac{\partial U_i}{\partial x_j}\right)_{\mathbf{P}}, \tag{9}$$

where DU_i/Dt is often termed the substantial derivative. With Eq. (9), Eq. (8) becomes

$$\frac{1}{k}\left(\frac{dm_i}{dt}\right) = \left(\frac{DU_i}{Dt} + (V_j - U_j)\frac{\partial U_i}{\partial x_j}\right)_{\mathbf{P}}. \tag{10}$$

From (8) and (10), it appears that measurements of $\partial U_i/\partial x_j$ can be made by making V_j arbitrarily large (using an airplane, for example) so that

$$\frac{1}{k}\left(\frac{dm_i}{dt}\right) = V_j\frac{\partial U_i}{\partial x_j}.$$

The case of most practical importance is for fixed probes, so that $\mathbf{V} = 0$ and Eq. (10) becomes

$$\frac{1}{k}\left(\frac{dm_i}{dt}\right) = \left(\frac{DU_i}{Dt} - U_j\frac{\partial U_i}{\partial x_j}\right)_{\mathbf{P}}. \tag{11}$$

At this point we propose a generalized Taylor's hypothesis that $(DU_i/Dt)_{\mathbf{P}}$ is small compared with $U_j(\partial U_i/\partial x_j)$, which reduces Eq. (11) to

$$\frac{1}{k}\left(\frac{dm_i}{dt}\right) = -U_j\frac{\partial U_i}{\partial x_j}. \tag{12}$$

We do not make the usual Taylor's hypothesis assumption that $(1/k)(dm_i/dt) = -\overline{U}_1(\partial u_i/\partial x_1)$ (u_i are the fluctuat-

ing velocity components) however, since the relationship between dm_i/dt and $\partial u_i/\partial x_j$ may depend crucially on the deviation of U_j from $\overline{U}_1$ through the cross-product terms in Eq. (12).

Alternatively, Heskestad[44] wrote

$$\frac{Du_i}{Dt} \equiv \frac{\partial u_i}{\partial t} + \overline{U}_1\frac{\partial u_i}{\partial x_1} + u_j\frac{\partial u_i}{\partial x_j}$$

which was assumed to be zero, and, for vanishingly small intensities, gave $\partial u_i/\partial t = -U_1(\partial u_i/\partial x_1)$. If the mean flow field is homogeneous and $\overline{U}_2 = \overline{U}_3 = 0$, the difference between DU_i/Dt and Du_i/Dt is zero. However, there is a considerable conceptual difference between obtaining the space-time transformation from Eq. (11) under the assumption that DU_i/Dt is negligible, and from the approach Heskestad used.

We will apply Eq. (11) to the measurement of the skewness of the streamwise derivative of the vertical velocity component. Denoting $(1/k)(dm_3/dt)$ as dw/dt, we have

$$\frac{dw}{dt} = -U_j\frac{\partial U_3}{\partial x_j}. \tag{13}$$

If we consider a turbulent flow field where $U_1 = \overline{U}_1 + u_1$, $U_2 \approx u_2$, $U_3 = u_3(\overline{U}_2 = \overline{U}_3 = 0)$, it follows from (13) that

$$\frac{dw}{dt} = -\overline{U}_1\left[\left(1 + \frac{u_1}{\overline{U}_1}\right)\left(\frac{\partial u_3}{\partial x_1}\right) + \frac{u_2}{\overline{U}_1}\left(\frac{\partial u_3}{\partial x_2}\right) + \frac{u_3}{\overline{U}_1}\left(\frac{\partial u_3}{\partial x_3}\right)\right] \tag{14}$$

and

$$\left(\frac{dw}{dt}\right)^3 = -\overline{U}_1^3\left[\left(1 + \frac{u_1}{\overline{U}_1}\right)^3\left(\frac{\partial u_3}{\partial x_1}\right)^3 + \frac{3u_2}{\overline{U}_1}\left(1 + \frac{u_1}{\overline{U}_1}\right)^2\left(\frac{\partial u_3}{\partial x_2}\right)\left(\frac{\partial u_3}{\partial x_1}\right)^2\right.$$
$$\left. + \frac{3u_3}{\overline{U}_1}\left(1 + \frac{u_1}{\overline{U}_1}\right)^2\left(\frac{\partial u_3}{\partial x_3}\right)\left(\frac{\partial u_3}{\partial x_1}\right)^2 + O\left(\frac{u_3^2}{\overline{U}_1^2}, \frac{u_2 u_3}{\overline{U}_1^2}\cdots\right)\right]. \tag{15}$$

Equation (15) indicates that there are many terms which may modify the relationship between the instantaneous values of $(dw/dt)^3$ and $-\overline{U}_1^3(\partial u_3/\partial x_1)^3$. These can be eliminated by conditionally sampling $(dw/dt)^3$ when $u_1 = u_2 = u_3 = 0$. The average of this conditionally-sampled statistic is

$$\left\langle\left(\frac{dw}{dt}\right)^3, u_1 = u_2 = u_3 = 0\right\rangle = -\overline{U}_1^3\left\langle\left(\frac{\partial u_3}{\partial x_1}\right)^3\right\rangle \tag{16}$$

which gives the desired measure of $\langle(\partial u_3/\partial x_1)^3\rangle$. The interpretation of Eq. (16) is that an X-sensor probe aligned in the x_1 direction measures $(\partial u_3/\partial x_1)$ only when the instantaneous total velocity vector coincides with the probe axis and the streamwise turbulent intensity is zero which occurs only when $u_1 = u_2 = u_3 = 0$. Clearly, the interpretation of dw/dt according to Eq. (16) is a difficult task, and therefore, we should seek approximations to Eq. (15), examine the residual terms and determine their significance.

If the streamwise intensity u_1/U_1 is small, Eq. (15) becomes

$$\left(\frac{dw}{dt}\right)^3 = -\overline{U}_1^3\left[\left(1 + \frac{3u_1}{\overline{U}_1}\right)\left(\frac{\partial u_3}{\partial x_1}\right)^3 + \frac{3u_2}{\overline{U}_1}\left(\frac{\partial u_3}{\partial x_2}\right)\left(\frac{\partial u_3}{\partial x_1}\right)^2\right.$$
$$\left. + \frac{3u_3}{\overline{U}_1}\left(\frac{\partial u_3}{\partial x_3}\right)\left(\frac{\partial u_3}{\partial x_1}\right)^2\right] \tag{17a}$$

and the conditioned average (assuming independence of the velocity and its gradient) is

$$\left\langle\left(\frac{dw}{dt}\right)^3, u_i\right\rangle = -\bar{U}_1^3\left[\left\langle\left(1+\frac{3u_1}{\bar{U}_1}\right)\left(\frac{\partial u_3}{\partial x_1}\right)^3\right\rangle + \frac{3}{\bar{U}_1}u_2\left\langle\left(\frac{\partial u_3}{\partial x_2}\right)\left(\frac{\partial u_3}{\partial x_1}\right)^2\right\rangle\right.$$

$$\left.+\frac{3}{\bar{U}_1}u_3\left\langle\left(\frac{\partial u_3}{\partial x_3}\right)\left(\frac{\partial u_3}{\partial x_1}\right)^2\right\rangle\right] . \tag{17b}$$

Of the terms in Eq. (17b), the first and second approach zero by local isotropy, whereas the last does not. Therefore, we may expect that the main contamination term in the interpretation of $\langle(dw/dt)^3\rangle$ is from $(u_3/\bar{U}_1)$ $\times\langle(\partial u_3/\partial x_3)(\partial u_3/\partial x_1)^2\rangle$. The quantity $\langle(\partial u_3/\partial x_3)(\partial u_3/\partial x_1)^2\rangle$ represents the tendency for $\partial u_3/\partial x_1$ gradients to

be steepened by strain in the x_3 direction. It is not obvious what the average value of this correlation will be, although it seems doubtful that it will be zero since such interactions between local strain and velocity gradients are important terms in the mean-square vorticity production equation. [45]

However, we recently learned that Wyngaard and Tennekes[46] have found that $\langle(\partial u_3/\partial x_3)(\partial u_3/\partial x_1)^2\rangle$ should be $(2/3)\langle(\partial u_3/\partial x_3)^3\rangle$ based on the isotropic relations of the sixth order tensor $\langle(\partial u_i/\partial x_j)(\partial u_k/\partial x_l)(\partial u_m/\partial x_n)\rangle$, and therefore negative since $\langle(\partial u_3/\partial x_3)^3\rangle$ is negative. Details of the derivation were sent to the authors by Wyngaard[47] and have been independently verified by Champagne and Nearing[48]. It was found that

$$\langle(\partial u_i/\partial x_j)(\partial u_k/\partial x_l)(\partial u_m/\partial x_n)\rangle = a_1\delta_{ij}\delta_{kl}\delta_{mn} + a_2\delta_{ij}\delta_{km}\delta_{ln} + a_3\delta_{kn}\delta_{lm} + a_4\delta_{il}\delta_{kn}\delta_{jm} + a_5\delta_{il}\delta_{kj}\delta_{nm} + a_6\delta_{il}\delta_{km}\delta_{jn} + a_7\delta_{in}\delta_{kl}\delta_{jm}$$

$$+ a_8\delta_{in}\delta_{km}\delta_{lj} + a_9\delta_{in}\delta_{kj}\delta_{lm} + a_{10}\delta_{ik}\delta_{lm}\delta_{jn} + a_{11}\delta_{ik}\delta_{lj}\delta_{mn} + a_{12}\delta_{ik}\delta_{ln}\delta_{jm} + a_{13}\delta_{im}\delta_{jl}\delta_{kn} + a_{14}\delta_{im}\delta_{jk}\delta_{ln} + a_{15}\delta_{im}\delta_{jn}\delta_{kl} ,$$

where

$$a_4 = a_9 = -3/4a_1 , \quad a_3 = a_5 = a_7 = -1/6a_1 , \quad a_2 = a_{15} = a_{11} = -4/3a_1 , \quad a_{12} = a_{10} = a_{14} = a_{13} = a_6 = a_8 = a_1 ,$$

so that

$$\langle(\partial u_3/\partial x_1)^2\partial u_3/\partial x_3\rangle = a_8 + a_{11} + a_{13} = 2/3a_1 = 2/3\langle(\partial u_3/\partial x_3)^3\rangle.$$

Isotropic relations have recently been discovered for the components of the eighth order tensor $\langle(\partial u_i/\partial x_j)$ $\times(\partial u_k/\partial x_l)(\partial u_m/\partial x_n)(\partial u_o/\partial x_p)\rangle$ by Nearing using numerical techniques. [49] As referred to in Sec. IIIB, Clay[31] measured the term Σ which is similar to $\langle(\partial u_3/\partial x_3)(\partial u_3/\partial x_1)^2\rangle$ when suitably normalized and obtained the value -0.5. Hence, we conclude that substantial contribution to $S(dw/dt)$ can result from terms other than $S(\partial u_3/\partial x_1)$. It should be pointed out that similar contamination terms do *not* arise in the approximation $S(dT/dx_1) = -S(dT/dt)$.

In this work, since u_2 was not measured and since the contribution of the u_2-term in Eq. (17) is expected to be small, we approximate $(\partial u_3/\partial x_1)$ by a conditioned sampling of dw/dt with only $u_3 = 0$ and neglecting the u_1 term

$$\left\langle\left(\frac{\partial u_3}{\partial x_1}\right)^3\right\rangle = -\frac{1}{\bar{U}_1^3}\left\langle\left.\left(\frac{dw}{dt}\right)^3\right|_{w=u_3=0}\right\rangle. \tag{18}$$

For the calculation of $S(\partial u_3/\partial x_1)$, the quantity $\langle(\partial u_3/\partial x_1)^2\rangle^{3/2}$ is required, which may also be obtained from $\langle(dw/dt)^2\rangle$. An analysis similar to that of Eq. (18) can be done for $\langle(dw/dt)^2\rangle$, and the result indicates that there are no significant contamination terms. Heskestad[44] found for $\langle(du_1/dt)^2\rangle$ that the higher order corrections were approximately given by

$$\left\langle\left(\frac{du_1}{dt}\right)^2\right\rangle = \bar{U}_1^2\left\langle\left(\frac{\partial u_1}{\partial x_1}\right)^2\right\rangle\left(1+\frac{\langle u_1^2\rangle}{\bar{U}_1^2} + \frac{2\langle u_2^2\rangle}{\bar{U}_1^2} + \frac{2\langle u_3^2\rangle}{\bar{U}_1^2}\right) , \tag{19}$$

which indicates that approximation $\langle(du_1/dt)^2\rangle = \bar{U}_1^2\langle(\partial u_1/\partial x_1)^2\rangle$ is valid in low-intensity turbulence. For our present measurements in the atmospheric boundary layer over the ocean, the intensities are small $(\langle u_i^2\rangle/U_1^2)^{1/2}$ $\sim 10\%$; therefore, we used

$$\left\langle\left(\frac{\partial u_3}{\partial x_1}\right)^2\right\rangle = \frac{1}{\bar{U}_1^2}\left\langle\left(\frac{dw}{dt}\right)^2\right\rangle . \tag{20}$$

Figure 9 shows measured conditioned skewness values of the quantity $-(1/\bar{U}_1)(dw/dt)$ for different magnitudes of w, $|w| \le \Delta w/2$ where Δw is the width of the w "window." As indicated in Fig. 9, the quantity $S(-(1/\bar{U}_1)dw/dt; |w| \le \Delta w/2)$ is between 0 and -0.03 for large values of $|w| > 1.2\sigma_w$, where σ_w is the standard deviation of w. This corresponds to the interpretation of using the unconditional skewness of dw/dt as the skewness of $(\partial u_3/\partial x_1)$, and is consistent with the results of Wygnanski and Fiedler[11] and Freymuth and Uberoi. [12] For smaller $|w|$ values, however, the conditioned skewness becomes large and positive, approaching about $+0.5$ as $|w|$ goes to zero. From (18) we see this implies that $S(\partial u_3/\partial x_1)$
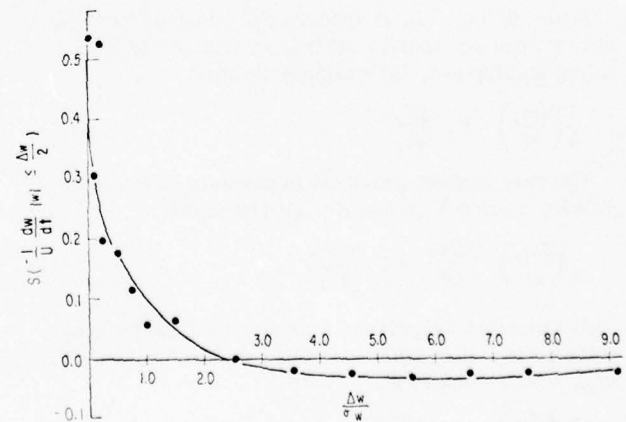

FIG. 9. Conditional skewness of vertical velocity derivative versus width of sampling window. Note that $S(-1\bar{U}_1\cdot dw/dt; |w| \le \Delta w/2)$ versus $\Delta w/\sigma_w \to +0.5$ as $\Delta w \to 0$ indicating local anisotropy of $\partial u_3/\partial x_1$.
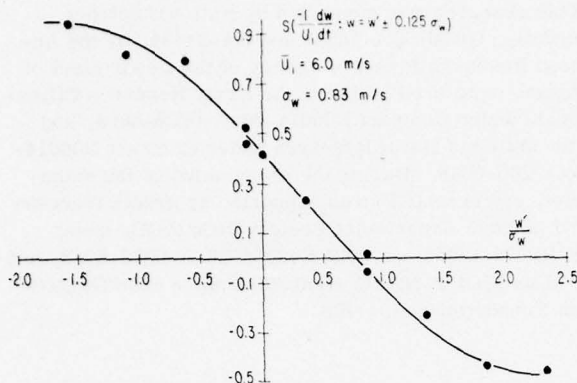
Gibson, Friehe, and McConnell

FIG. 10. Conditional skewness of vertical velocity derivative versus vertical velocity for constant window width. $S(-1/\bar{U}_1 \cdot dw/dt: \ w=w' \pm 0.125\,\sigma_w)$ versus $w'/\sigma_w \to +0.4$ as $w' \to 0$, also indicating local anisotropy. Slope near $w'=0$ implies value of $\Sigma_{3,1} = -1.3$.

is $+0.5$, which we can compare with laboratory values of $S(\partial u_1/\partial x_1)$ of about -0.4. This large positive value implies local anisotropy of $\partial u_3/\partial x_1$. The sign is consistent with the model previously developed to account for the measured anisotropy of $\partial T/\partial x_1$ assuming the local vorticity on the ramp surface tends to be in the same direction as the mean. Crossing the interfaces of the ramps in the streamwise direction would correspond to passing from a downdraft to updraft, giving a large positive $\partial u_3/\partial x_1$ whose residual might give a positive $S(\partial u_3/\partial x_1)$.

If the u_2 term is neglected in Eq. (17a), the equation states that the conditioned statistic $(dw/dt)^3|_{w=w'}$ should be a linear function of $u_3 = w$ with slope proportional to the strain rate-squared shear rate correlation

$$\left(\frac{dw}{dt}\right)^3 \bigg|_{w=w'} = \left(\frac{dw}{dt}\right)^3 \bigg|_{u=0} - 3\bar{U}_1^2 \left(\frac{\partial u_3}{\partial x_3}\right)\left(\frac{\partial u_3}{\partial x_1}\right)^2 w \big|_{w=w'}, \quad (21a)$$

or

$$S\left(-\frac{1}{\bar{U}_1}\frac{dw}{dt}\right)\bigg|_{w=w'} = S\left(-\frac{1}{\bar{U}_1}\frac{dw}{dt}\right)\bigg|_{w=0} + \frac{3}{\bar{U}_1}\left\langle\!\left\langle\left(\frac{\partial u_3}{\partial x_3}\right)\left(\frac{\partial u_3}{\partial x_1}\right)^2 w\right\rangle\!\right\rangle\bigg|_{w=w'}\left\langle\!\left\langle\left(\frac{\partial u_3}{\partial x_1}\right)^2\right\rangle\!\right\rangle^{-3/2}.$$
$$(21b)$$

If we assume that large scale and small scale structures of the flow are independent, then the numerator of the last term of Eq. (21b) is

$$\left\langle w\left(\frac{\partial u_3}{\partial x_3}\right)\left(\frac{\partial u_3}{\partial x_1}\right)^2\right\rangle\bigg|_{w=w'} = \langle w\rangle\left\langle\!\left\langle\left(\frac{\partial u_3}{\partial x_3}\right)\left(\frac{\partial u_3}{\partial x_1}\right)^2\right\rangle\!\right\rangle\bigg|_{w=w'}$$
$$= w'\left\langle\!\left\langle\left(\frac{\partial u_3}{\partial x_3}\right)\left(\frac{\partial u_3}{\partial x_1}\right)^2\right\rangle\!\right\rangle. \quad (22)$$

Figure 10 is a plot of measured values of the conditional skewness $S[(-1/U_1)(dw/dt): \ w=w' \pm 0.125\,\sigma_w]$. For values of w' greater than $2\sigma_w$ the conditional skewness approaches an asymptotic value of -0.5. For values smaller than -1.5, it approaches $+1.0$.

For intermediate values of w', $S[(-1/U_1)(dw/dt); \ w']$

varies linearly with w', as expected from Eqs. (21b) and (22). The slope of the linear portion of Fig. 10 and Eq. (21b) gives a value of $-0.18\, U_1/\sigma_w$ for the quantity $\langle(\partial u_3/\partial x_3)(\partial u_3/\partial x_1)^2\rangle/\langle(\partial u_3/\partial x_1)^2\rangle^{3/2} \equiv \Sigma_{3,1}$. Therefore, $\Sigma_{3,1}$ should be about -1.3 for the atmosphere over the ocean. From the isotropic relations between components of $\langle(\partial u_i/\partial x_j)(\partial u_k/\partial x_1)(\partial u_m/\partial x_n)\rangle$ discussed previously,[46] $\Sigma_{3,1}$ should be $S(\partial u_1/\partial x_1)/3\sqrt{2}$. Since $S(\partial u_1/\partial x_1) = -0.6$, we see the value of $\Sigma_{3,1}$ implied by Fig. 10 has the right sign, although with ten times the magnitude of the predicted isotropic value of -0.14. The intercept of the curve with the ordinate in Fig. 10 is about $+0.4$ which should be the value of $S(\partial u_3/\partial x_1)$ according to Eq. (10), compared to about $+0.5$ indicated by Fig. 9. It is possible that some reduction in magnitude occurs due to the finite window width used in the calculations of Fig. 10. Both values of $S(\partial u_3/\partial x_1)$ are quite different from zero required by local isotropy.

It should be noted that the calculations of conditioned skewness in Figs. 9 and 10 require very large quantities of data samples to achieve statistical convergence, and that our attempts to reproduce these results with other data sets have so far been frustrated by problems of X-wire calibration drift and the sensitivity of the statistics to small errors. Therefore, the present evidence for local anisotropy of the velocity field, as well as the magnitudes of $S(\partial u_3/\partial x_1)$ and $\Sigma_{3,1}$ is tentative and should be measured in other sheared turbulent flows.

It should also be noted that recent evidence suggests that the temperature signals from the atmospheric boundary layer over the ocean may be somewhat contaminated by relative humidity sensitivity due to sea spray coating.[50] In view of the consistency between the marine and land boundary layer results and the many laboratory tests with uncontaminated sensors it appears that for the conditions of the measurements $S(\partial T/\partial x)$ was relatively insensitive to this effect. Further measurements have been carried out to confirm this hypothesis in the atmospheric boundary layer over land. A recent measurement of $S(\partial T/\partial x_1)$ over land under similar Reynolds number and boundary conditions without sensor contamination effects gave a value of $+0.7$,[51] where the temperature signals were of excellent quality. Recently these data have been subjected to a number of filtering operators by Schmitt[52] who finds the K/S ratio increases with filtering frequency, suggesting an approach to local isotropy.

IV. CONCLUSIONS

Measurements of the skewness of temperature gradient in the streamwise direction in several sheared turbulent flows show consistent departure from the value of zero expected for perfect local isotropy of the turbulent temperature. This local temperature anisotropy may be a residual effect of the large scale anisotropy in the temperature and vorticity fields. An equation relating the skewness of the temperature gradient to its direction and that of the mean temperature gradient and the mean vorticity expresses this idea and is consistent with all available data; namely,

$$\text{sgn } S(\partial T/\partial x_1) = \text{sgn}\,[\hat{\mathbf{x}}_1 \cdot (\nabla\bar{T} \times \bar{\omega})].$$

Skewness density functions per unit gradient $(X/\sigma)^3 p(X)$ for the flows were also found to be asymmetric, which is further evidence of local anisotropy. The physical mechanism producing the anisotropy is apparently associated with a large scale ramp-like or sawtooth anisotropy of the temperature signal produced by large scale eddies rotating with the mean vorticity of the shear flow. The sign of the temperature gradient skewness was consistent with the sense of the sawtooth structure in all cases tested as though caused by the sharp interfaces at the end of ramps. The magnitudes were small compared with those calculated from a model where extreme gradients are confined to the ramp interfaces. Therefore, *we can interpret the departure from local isotropy as a small residual effect from the large scale anisotropy.*

The possibility that the observed nonzero temperature derivative skewness was due to the effect of velocity sensitivity of the cold wire temperature sensors was examined. It was concluded that a small effect may exist in some of the atmospheric results, but that this could not explain the observed local anisotropy in the heated jet or hot or cold wake. Point by point velocity sensitivity corrections were made for the atmospheric temperature derivative skewness, and a residual positive value was still obtained.

Measurements are also presented of the skewness of $\partial u_3/\partial x_1$ where u_3 is a velocity component perpendicular to x_1. It was found that $-S(dw/dt)$ is not a good approximation to $S(\partial u_3/\partial x_1)$ unless the dw/dt values are sampled only when $w \sim 0$ because of contamination by the quantity $\langle(\partial u_3/\partial x_3)(\partial u_3/\partial x_1)^2\rangle/\langle(\partial u_3/\partial x_1)^2\rangle^{3/2}$. The latter term was measured to be about -1.3 for the atmospheric boundary layer data, although the isotropic value is predicted to be -0.14. The quantity $S(\partial u_3/\partial x_1)$ was about $+0.5$, compared with the isotropic value of zero. The sign is consistent with the hypothesis that this result is also a small residual effect of the large eddy structure that induces local anisotropy in the temperature field since a strong vortex sheet is formed on the upwind sides of the large eddies such that $\partial u_3/\partial x_1$ is positive across the sheet.

It is not known at this time the extent to which the departures from local isotropy of sheared turbulent flows indicated by the present measurements will affect various predictions of universal similarity theories of turbulence and turbulent mixing which rely on this assumption, but it is clear that the possibility should be recognized and efforts made to determine the size of the effects.

ACKNOWLEDGMENTS

The authors would like to express their appreciation to Paul Masiello who reduced the vertical velocity derivative data. The data reported from the large jet experiment was obtained with the aid of John LaRue who constructed the cold wire, F. H. Champagne, J. T. Park, and J. Schedvin. Frank Champagne was particularly helpful in many discussions on Taylor's hypothesis, and brought to our attention Corrsin's analysis and Wyngaard's prediction of the isotropic value of $\Sigma_{3,1}$.

[1] A. N. Kolmogoroff, C. R. Acad. Sci. USSR **30**, 301 (1941).
[2] N. E. Busch and H. A. Panofsky, Q. J. R. Meteorol. Soc. **94**, 132 (1968).
[3] J. C. Kaimal, J. C. Wyngaard, Y. Izumi, and O. R. Coté, Q. J. R. Meteorol. Soc. **98**, 1563 (1972).
[4] M. Miyake, R. W. Stewart, and R. W. Burling, Q. J. R. Meteorol. Soc. **96**, 138 (1970).
[5] R. W. Stewart, Radio Sci. **12**, 1269 (1969).
[6] H. S. Weiler and R. W. Burling, J. Atmos. Sci. **24**, 653 (1967).
[7] G. A. McBean, Boundary Layer Meteorol. **1**, 438 (1971).
[8] S. D. Smith, E. G. Burke, and O. M. Johannessen, J. Geophys. Res. **75**, 2803 (1970).
[9] M. M. Gibson, J. Fluid Mech. **15**, 161 (1963).
[10] F. H. Champagne, V. G. Harris, and S. Corrsin, J. Fluid Mech. **41**, 81 (1970).
[11] I. J. Wygnanski and H. E. Fiedler, J. Fluid Mech. **41**, 327 (1970).
[12] P. Freymuth and M. S. Uberoi, Phys. Fluids **14**, 2574 (1971).
[13] P. Freymuth and M. S. Uberoi, Phys. Fluids **16**, 161 (1973).
[14] C. H. Gibson, G. R. Stegen, and R. W. Williams, J. Fluid Mech. **41**, 153 (1970).
[15] N. E. Boston, Ph. D. thesis, University of British Columbia (1970).
[16] J. C. Wyngaard, Phys. Fluids **14**, 2052 (1971).
[17] A. M. Obukhov, Izv. Akad. Nauk SSSR Ser. Geogr. Geofiz. **13**, 59 (1949).
[18] S. Corrsin, J. Appl. Phys. **22**, 469 (1951).
[19] C. H. Gibson, C. C. Chen, and S. C. Lin, AIAA J. **6**, 642 (1968).
[20] N. Monji, J. Meteorol. Soc. Jpn. **51**, 133 (1973).
[21] J. E. Tillman, J. Appl. Meteorol. **11**, 783 (1972)
[22] J. Laufer, in *Annual Review of Fluid Mechanics*, edited by M. Van Dyke, W. G. Vincenti, and J. V. Wehausen (Annual Reviews, Palo Alto, Calif., 1975), Vol. 7, p. 307.
[23] P. Chen, Ph. D. thesis, University of Southern California (1975).
[24] C. A. Friehe, C. H. Gibson, F. H. Champagne, and J. C. LaRue, Atmos. Tech. **7**, 15 (1975).
[25] J. C. LaRue, T. Deaton, and C. H. Gibson, Rev. Sci. Instrum. **46**, 757 (1975).
[26] J. C. Wyngaard, J. Sci. Instrum. **1**, 1105 (1968).
[27] J. C. Wyngaard, J. Fluid Mech. **48**, 763 (1971).
[28] C. A. Friehe, C. W. Van Atta, and C. H. Gibson, in *Turbulent Shear Flows*, AGARD Conference Proceedings No. 93 (Advisory Group for Aerospace Research and Development, North Atlantic Treaty Organization, Neuilly sur Seine, France, 1972), p. 18.
[29] H. Tennekes and J. C. Wyngaard, J. Fluid Mech. **55**, 93 (1972).
[30] T. T. Yeh, Ph. D. thesis, University of San Diego (1971).
[31] J. Clay, Ph. D. thesis, University of California, San Diego (1973).
[32] P. G. Mestayer, C. H. Gibson, M. F. Coantic, and A. S. Patel, Phys. Fluids **19**, 1279 (1976).

[33]C. H. B. Priestley, Proc. R. Soc. London Ser. A **238**, 287 (1956).

[34]E. K. Webb, Appl. Oct. **3**, 1329 (1964).

[35]G. T. Phelps and S. Pond, J. Atmos. Sci. **28**, 918 (1971).

[36]J. C. Kaimal and J. A. Businger, J. Appl. Meteorol. **9**, 612 (1970).

[37]B. R. Bean, R. Gilmer, R. L. Grossmann, and R. McGavin, J. Atmos. Sci. **29**, 860 (1972).

[38]K. L. Davidson and G. W. Safley, presented at the Fifteenth Conference on Great Lakes Research, Madison, Wis. (1972).

[39]D. A. Haugen, J. C. Kaimal, and E. F. Bradley, Q. J. R. Meteorol. Soc. **97**, 168 (1971).

[40]A. J. Faller and R. E. Kayler, J. Atmos. Sci. **23**, 466 (1966).

[41]M. A. Lemone, J. Atmos. Sci. **30**, 1977 (1973).

[42]C. H. Gibson, Phys. Fluids **11**, 2305 (1968).

[43]S. Corrsin, *Lecture Notes on Introduction to Fluid Mechanics* (The Johns Hopkins University, Baltimore, Md., 1967), Chap. 2.

[44]G. Heskestad, J. Appl. Mech. **32**, 735 (1965).

[45]H. Tennekes and J. L. Lumley, *A First Course in Turbulence* (MIT Press, Cambridge, Mass., 1972).

[46]J. C. Wyngaard and H. Tennekes, Phys. Fluids **13**, 1962 (1970).

[47]J. C. Wyngaard (private communication).

[48]F. H. Champagne and J. Nearing (private communication).

[49]J. Nearing (private communication).

[50]K. R. Schmitt, C. H. Gibson, and C. A. Friehe, Bull. Am. Meteorol. Soc. **57**, 153 (1976).

[51]F. H. Champagne, C. A. Friehe, J. C. LaRue, and J. C. Wyngaard, J. Atmos. Sci. **34**, 515 (1977).

[52]K. F. Schmitt (private communication).

Flow time scales and drag reduction

Neil S. Berman

School of Engineering, Arizona State University, Tempe, Arizona 85281

The effects of the flow time scales on the onset and magnitude of drag reduction in turbulent pipe flow were studied using comparatively low molecular weight samples of water soluble polymers in glycerine-water mixtures and in two different pipe sizes. The results show that onset depends only on the time scale ν/u_τ^2 with no Reynolds number dependence. The magnitude of drag reduction after the molecules are extended was found to increase with pipe diameter. A correlation with the lifetime of large eddies or the mean period of turbulence production is suggested.

INTRODUCTION

High molecular weight polymers can be in random coil or extended conformations in solutions. Both shapes lead to drag reduction in turbulent flow with the random coil form exhibiting an onset. Since the drag reducing materials are mixtures of many different molecular weights and a quantitative relationship between molecular parameters and drag reduction is not known, analyses of all onset data in the literature leads to poor correlations with flow parameters.[1] Experiments can be designed, however, to test the direction of change in flow scales when molecular scales are altered. Previous preliminary experiments on the relationship between molecular time scales and pipe flow drag reduction[2,3] show a definite correspondence of molecular scale to the onset of drag reduction. The object of the present work is to extend these experiments to examine the effect of the large scales in turbulent pipe flow on the onset and magnitude of drag reduction. Random coiling molecules are used to test the onset relationship and expanded polyelectrolytes to test the influence of the lifetime of large eddies.

PRELIMINARY CONSIDERATIONS

Strong evidence for a time scale relationship is found in an experiment shown in Fig. 1 from Berman and George.[3] The curves show an exact correspondence between Pitot tube error and drag reduction onset measured on the same fluid at the same time. These experiments were performed on a degraded polyethylene oxide (Polyox 301) solution which was recirculating in a water tunnel at the Applied Research Laboratory of the Pennsylvania State University. The onset values of $2U/D$ for the Pitot tube error and u_τ^2/ν for the pipe flow are the same!

Molecular theories of dilute polymer solutions show a rapid increase in elongational viscosity as the inverse of the strain rate of the flow is increased beyond about twice the terminal relaxation time of the molecule.[4,5] Almost the same conclusion is reached for a dumbbell model in a two-dimensional flow by Lumley.[6,7] In the near rotation free strain field around the Pitot tube we might expect an onset criterion like $(2U/D)T_1 > A$; where U is the free stream velocity, D is the diameter, T_1 is the molecular time scale, and A is a constant.

In turbulent pipe flow the onset relationship of Lumley is $(u_\tau^2/\nu)T_1 > B$; where u_τ is the shear velocity, ν is the kinematic viscosity, and B is a constant. Figure 1 implies that A and B are the same. This result is somewhat surprising since Polyox 301 has a broad molecular weight distribution and no single characteristic time. Berman and George[3] have shown that a simple molecular distribution model will explain the dependence on a single time scale, and Hunston and Reischman[8] show that qualitative predictions of the model are correct, but a more complex model is needed to explain the detailed behavior of drag reducing polymers. To examine the flow parameters needed in such a model, therefore, it is necessary to keep all properties of the polymer solution except the one to be tested constant, and the one changed must be altered in a known way.

In Lumley's analysis[6] the Lagrangian integral time scale is used as being representative of the persistence of the strain field. Other possibilities are discussed by Lumley[9] leading to an onset dependent on Reynolds number.

Berman and George[2] show that onset does indeed correlate with wall shear rate, u_τ^2/ν, when an experiment
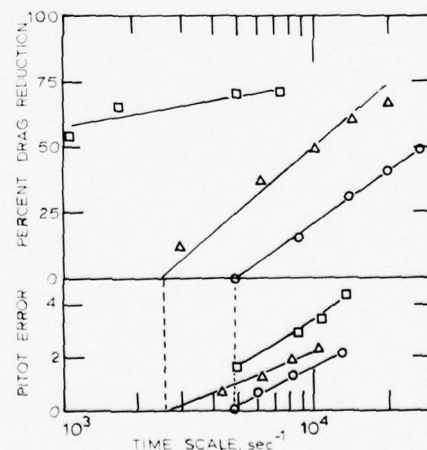

FIG. 1. Comparison of onset of drag reduction and Pitot tube error. Time scales are $2U/D$ for the Pitot tube error, where U is the free stream velocity and D is the diameter, and u_τ^2/ν for the pipe flow drag reduction in a 0.635 cm tube. Pitot error is in units of $\mathrm{dyn/cm^2} \times 10^{-4}$. The same symbols apply to measurements on the same polymer solution, 100 ppm fresh Polyox 301, □ ; after 2 min of degradation, △ ; and after 20 min of degradation, ○ .

is run at constant diameter and ν is changed. This experiment also showed that a polymer length scale correlation was not consistent with the data, but a single pipe diameter experiment does not rule out a Reynolds number dependence since all the scales are related when the diameter is held constant.

Laboratory pipe flow experiments do not always give well defined onsets unless the pipe is large or the polymer molecular weight is relatively low. Also, plots can be made of coordinates similar to Fig. 1, coordinates of Reynolds number, R vs friction factor, f, coordinates of $f^{-1/2}$ vs $Rf^{1/2}$, and others. For low amounts of drag reduction velocity profile measurements show a displacement of the core compared with the solvent.[10] Neglecting the wall and buffer regions the integrated profile becomes

$$f^{-1/2} = a \log(f^{1/2}R) + b; \tag{1}$$

then, plots of $f^{-1/2}$ vs $\log(f^{1/2}R)$ scales will give straight lines. Such plots can be used to define onset as the intersection with the solvent line so that onset is related to all of the points used to define the line based on Eq. (1).

The difficulty of relating onset to the molecular properties is illustrated by Figs. 2 and 3. Each curve, for constant concentration, has a group of points that can be represented by a straight line. These points are a part of the high molecular weight tail of the molecular weight distribution and the straight line forces an artificial extrapolation of this distribution. This imposed distribution is different for each concentration so onset as a
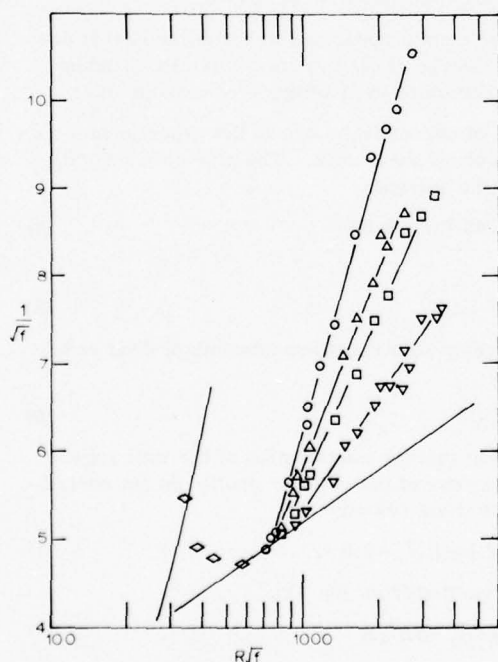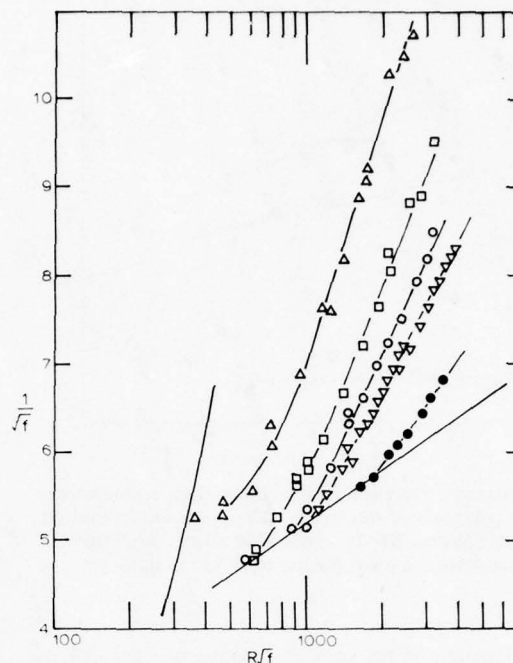

FIG. 3. Concentration dependence of drag reduction for Separan NP-10 dissolved in tap water in a 0.554 cm diam tube. Concentrations are 20 ppm, $\circ$; 50, $\triangledown$; 100, $\circ$; 200, $\square$; and 400, $\triangle$.

function of concentration cannot be analyzed in a simple manner.

The Polyox WSR 205 (intrinsic viscosity 500 cm³/g) was a fresh sample exhibiting an onset independent of concentration and illustrates the behavior of the Polyox N-80 used in the time scale studies to follow. On the other hand, Separan NP-10 in tap water (intrinsic viscosity 750 cm³/g) shows a concentration dependent onset. These polymers are similar in solution, Polyox is a random coil in a good solvent, while Separan is a collapsed polyelectrolyte in a dilute salt solution. Separan NP-10 is a polyacrylamide with a small portion of the amide groups hydrolyzed. The molecular weight is approximately 1×10^6. Polyox WSR 250 is a non-ionic polyethylene oxide with similar molecular weight.[11] The differences in onset behavior are related to the molecular weight distribution and are not fundamental properties of drag reduction or due to the differences in the molecules in solution. We have observed that old samples of Polyox also show a dependence of onset on concentration. If we try to compare different polymer concentrations, we can arrive at entirely different conclusions if onset is a function of concentration or not. In this work the concentration variable is held constant for any studies comparing onset time scales.

Although the polymer solutions contain a distribution of molecular weights, each molecule will have a characteristic time scale. The Zimm–Rouse models of a polymer molecule in dilute solution lead to the relationship for the largest relaxation time

$$T_1 = (\eta - \eta_s)M/cRTS , \tag{2}$$

FIG. 2. Concentration dependence of drag reduction for Polyox WSR 205 in a 0.554 cm diam tube. Concentrations are 10 ppm, $\triangledown$; 20, $\square$; 30, $\triangle$; and 50, $\circ$. The symbol $\diamond$ illustrates points representative of all concentrations.
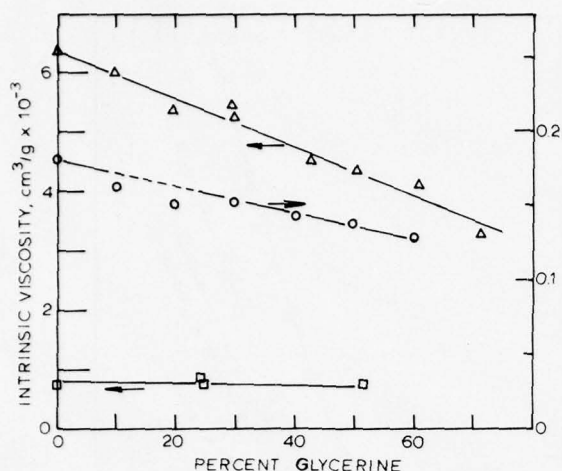
FIG. 4. Intrinsic viscosity as a function of glycerine concentration for polymers of this work. The polymers and initial solvents are Separan NP-10 in distilled water, △; Separan NP-10 in tap water, □; and Polyox N-80 in tap water, ○ .

where S depends on the molecule shape and the hydrodynamic interaction. In Eq. (2), M is the molecular weight, c is the concentration, R is the gas constant, T is the absolute temperature, η is the solution viscosity, and η_s is the solvent viscosity.

At low concentrations

$$(\eta - \eta_s)/c = [\eta]\eta_s \ . \tag{3}$$

Significant changes in T_1 can be obtained by changing the solvent viscosity, if the intrinsic viscosity is relatively unchanged. Equations (2) and (3) refer to infinitely dilute solutions, and the intrinsic viscosity also has a limit of zero shear rate. Measurements at the conditions approaching zero shear are difficult so we can only make comparisons. We use intrinsic viscosity $[\eta]$ to mean $(\eta - \eta_s)/c\eta_s$ measured at similar shear rates in this work.

Figure 4 shows the intrinsic viscosity as a function of glycerine concentrations in glycerine-water solutions for Polyox N-80 and Separan NP-10 in distilled and in tap water. The tap water has a concentration of calcium ions sufficient to collapse the molecule into a random coil. All viscosities were measured in standard Cannon-Fenske capillary tube viscometers numbers 50-100. Then, these data were compared with laminar pipe flow results at low Reynolds numbers to obtain corrections to the lowest shear rates obtainable with 50% glycerine solutions. The procedure is discussed by Yuen.[12] In other tests using distilled water with various concentrations of sodium chloride, Separan NP-10 had intrinsic viscosities of 830, 890, 2100, 4300, and 6300 cm³/g for NaCl molarities of 0.1, 0.01, 0.001, 0.0001, and distilled water, respectively. Similarly, 30% by weight glycerine solutions gave intrinsic viscosities of 810, 1240, 2160, and 3860 cm³/g when the 70% water solutions contained 0.1, 0.01, 0.001, and 0.0001 M NaCl, respectively. In distilled water, the Separan NP-10 is partially extended. In glycerine-water solu-

tions, the Polyox and distilled water Separan assume a tighter conformation than in water alone leading to approximately a linear fall off in intrinsic viscosity with glycerine concentrations up to at least 70% glycerine by weight. This indicates that the Separan is not completely uncoiled if the dimensions of the molecule change with the intrinsic viscosity. In the calcium ion tap water the Separan molecule changes only slightly with added glycerine when the ion influence is dominant.

The comparative intrinsic viscosities show that the time scale for *all* the molecules in the distribution will be approximately increased by factors of up to two in 30% glycerine and from three to five in 50% glycerine compared with pure water. For random coiling molecules in solution which show an onset of drag reduction, a significant change in onset should occur as a function of glycerine concentration. Partially extended molecules should show little change in drag reduction characteristics when no onset is observed. The partially extended molecules provide an opportunity to evaluate the effect of the large scale since *all* of the molecules are changed initially and not as a result of a flow interaction.

EXPERIMENTAL PROCEDURE

The experiments were performed on carefully prepared solutions mixed over a 48 h period. First, 0.1%-1% solutions were prepared in one to two liters of of water. After 24 h dilutions of one order of magnitude were made, and the polymer was left for another 24 h to completely dissolve. The final dilutions and combinations with glycerine were made immediately preceding the once through experimental run. All solutions were discarded after the run and not reused.

The experimental apparatus was similar to that described by George *et al.*[13] Three to ten independent runs were combined to give single continuous plots.

Analysis of curves fit by eye to the experimental data leads to an onset shear rate. The pipe core velocity profile for the solvent

$$U_+^{(s)} = 2.45 \ln y_+ + 5.66 \tag{4}$$

becomes

$$U_+ = U_+^{(s)} + \Delta B \tag{5}$$

for the polymer solution at low amounts of drag reduction. For

$$f = 8 u_\tau^2/\bar{U}^2 \tag{6}$$

and assuming that the contribution of the wall region and buffer layers of the velocity profile do not contribute to the average velocity

$$1/\sqrt{f_s} = 2 \log R\sqrt{f_s} - 0.8 \ . \tag{7}$$

Then, subtracting from Eq. (1),

$$1/\sqrt{f} - 1/\sqrt{f_s} = \Delta B/\sqrt{8} \tag{8}$$

or

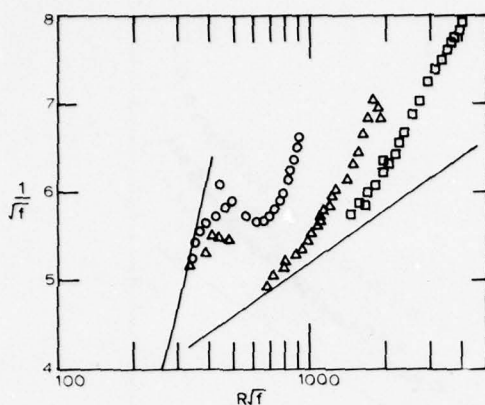$$\bar{U}/u_\tau - \bar{U}_s/u_{\tau s} = \Delta B. \tag{9}$$

Following Virk[1]

FIG. 5. Drag reduction onset for 400 ppm Polyox N-80 in glycerine-water solutions in a 0.553 cm diam tube for no glycerine, □; 31.4% glycerine, △; and 52.5% glycerine, ○.

$$1/\sqrt{f} - 1/\sqrt{f_s} = (a-2)\log R\sqrt{f} - (b-0.8)$$
$$= \delta \log[R\sqrt{f}/(R\sqrt{f})_0], \qquad (10)$$

where the subscript refers to onset.

Therefore, if straight lines are found on $1/\sqrt{f}$ vs $\log R\sqrt{f}$ coordinates

$$1/\sqrt{f} - 1/\sqrt{f_s} = \delta \log u_\tau/u_{\tau 0} . \qquad (11)$$

This analysis tells nothing about the nature of onset, but does provide the method for defining onset. The results of three series of experiments are given in Figs. 5–10 for Polyox N-80, Separan NP-10 in tap water, and Separan in distilled water.

Random coil molecules show definite onsets from the turbulent curve or at some point in the transition regime. Figures 5–8 show the effect of glycerine addition to solutions of random coil polymers in water. Each plot is for a fixed pipe diameter and polymer con-
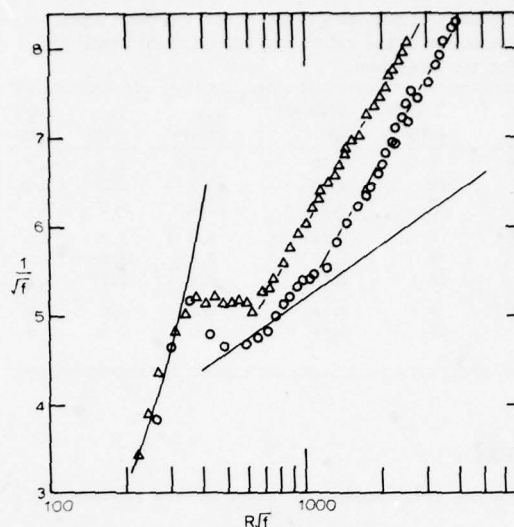
FIG. 7. Drag reduction onset for 50 ppm Separan NP-10 in glycerine-tap water solutions in 0.554 cm diam tube for no glycerine, ○; and 25% glycerine △.

centration. The polymers Polyox N-80 and Separan NP-10 and the concentration were selected so that onset could be observed in the two pipes with 0%–50% glycerine concentrations. The expanded polyelectrolyte curves in Figs. 9 and 10 first show a somewhat constant level of drag reduction, and then a new onset at the same time scale as the collapsed random coil molecules.

Solid lines on the curves are for laminar, $f = 64/R$, and turbulent flow, $1/f^{1/2} = 2 \log R f^{1/2} - 0.8$. In all cases the solvent viscosity was used to calculate the Reynolds number.
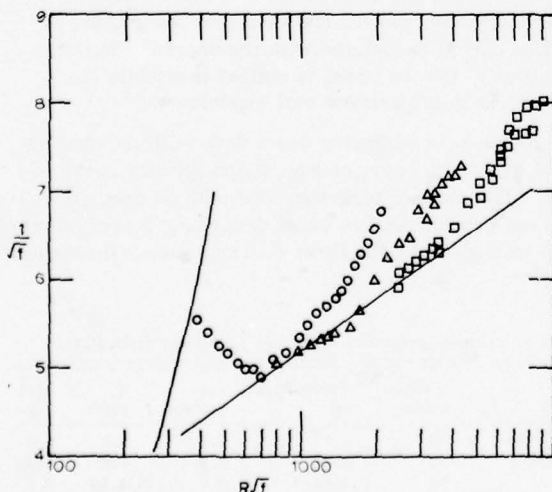
FIG. 6. Drag reduction onset for 400 ppm Polyox N-80 in glycerine-water solutions in a 1.494 cm diam tube for no glycerine, □; 30% glycerine, △; and 53% glycerine, ○.
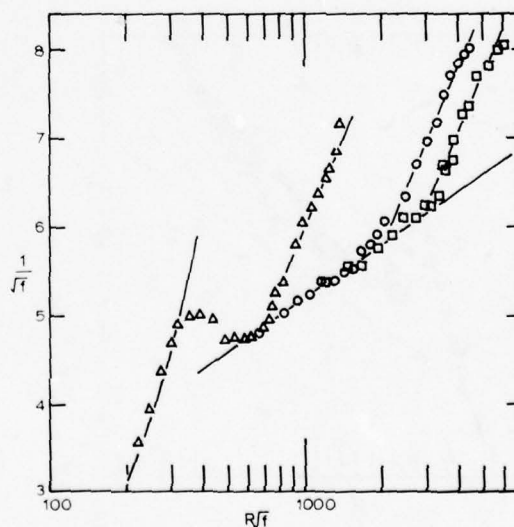
FIG. 8. Drag reduction onset for 50 ppm Separan NP-10 in glycerine-tap water solutions in 1.494 cm diam tube for no glycerine, □; 25% glycerine, ○; and 52% glycerine, △.

TABLE I. Onset comparisons in the 0.554 cm diam pipe. Estimated accuracy of the ratios are ± 15% for the small pipe and ± 25% for the large pipe.

Polymer	% Glyc-erine	Viscosity, cp	$u_{\tau 0}$, cm/sec	T_1 ratio	ν/u_τ^2 ratio
Polyox N-80	0	0.90	8.6	1.0	1.0
400 ppm	30	2.05	9.8	1.7	1.65
	53	5.31	10.5	4.0	3.5
Separan NP-10	0	0.94	8.6	1.0	1.0
20 ppm	25	1.77	8.4	1.9	1.8
Tap water	48	4.28	8.4	4.2	4.2
Separan NP-10	0	0.90	5.6	1.0	1.0
50 ppm	25	1.67	5.5	1.9	1.9
Tap water					

DISCUSSION

To check the relationship of onset to flow time scale we note

$$R\sqrt{f}/\sqrt{8} = Du_\tau/\nu = (D/u_\tau)\,(u_\tau^2/\nu). \quad (12)$$

Two time scales are shown in Eq. (12), and one or the other can be replaced by a molecular time scale at onset. If $T_1 = k_1(\nu/u_\tau^2)_0$, then

$$1/\sqrt{f} - 1/\sqrt{f}_s = \delta \log(u_\tau u_{\tau 0} T_1/\nu k_1) \quad (13)$$

or if $T_1 = k_2 D/u_{\tau 0}$,

$$1/\sqrt{f} - 1/\sqrt{f}_s = \delta \log(Du_\tau k_2/T_1 u_{\tau 0}^2). \quad (14)$$

These possibilities can be tested by comparing the molecular time scales and the flow time scales. A summary of such calculations for the random coils is shown in Tables I and II. The T_1 ratio column is the ratio of $\eta_s\,[\eta]$ to the 0% glycerine value. When polymer concentration and pipe diameter are constant, each individual set of onset points is consistent with a correlation between onset ν/u_τ^2 and T_1. The $u_{\tau 0}$ column can be used to show that a $D/u_{\tau 0}$ relationship to T_1 does

FIG. 10. Drag reduction of Separan NP-10 in distilled water in 1.494 cm diameter pipe for, □, 50 ppm concentration; ●, 20 ppm concentration; and △, 20 ppm with 30% glycerine. The dotted line is the onset for 50 ppm in tap water from Fig. 8 and the dashed line is for 20 ppm in tap water scaled from the smaller pipe of this work.

not exist. At least for the Reynolds numbers of this work a strong Reynolds number dependence is not found; however, the onset value and drag reduction itself appear to be diameter dependent.

Before we examine the diameter effect other qualitative evidence of the time scale-onset relationship can be found from the data. First, the random coil data always show a displacement in the direction of higher time scales as solvent viscosity is increased. Next, we see that the Separan NP-10 in tap water which has only a small change in intrinsic viscosity with glycerine concentration compared with Polyox N-80 shows a greater effect on onset displacement. Finally, glycerine addition to the expanded polyelectrolyte shows two differences from the original solution; at first, the drag reduction is reduced and then it is increased. The reduction can be associated with the decrease in intrinsic viscosity, but the onset is shifted in exactly the same way as in the random coil experiment.

One problem in analyzing onset data is illustrated by the 53% glycerine curve of Fig. 5 and the 25% curve in Fig. 7. The state of turbulent flow with no drag reduction is not reached before onset occurs. If the polymers are all influenced by the flow, extrapolation of the higher
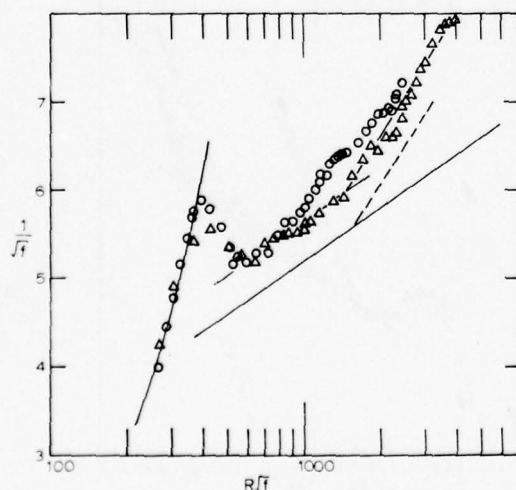

FIG. 9. Drag reduction of 20 ppm Separan NP-10 initially dissolved in distilled water in the 0.554 cm diam tube for no glycerine, △; and 30% glycerine, ○. The dashed line is for 20 ppm Separan NP-10 in tap water after onset.
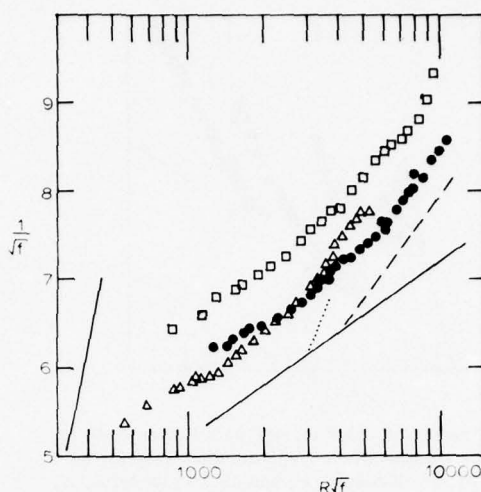
TABLE II. Onset comparisons in the 1.494 cm diam pipe.

Polymer	% Glyc-erine	Viscosity, cp	$u_{\tau 0}$ cm/sec	T_1 ratio	ν/u_τ^2 ratio
Polyox N-80	0	0.9	8.1	1.0	1.0
400 ppm	30	2.13	8.4	1.9	2.0
	53	5.05	9.0	4.1	4.1
Separan NP-10	0	0.9	6.1	1.0	1.0
50 ppm	25	1.65	6.4	1.8	1.6
Tap water	52	4.67	6.8	4.8	3.7

TABLE III. Onset shear rate comparisons at two diameters.

| % Glycerine | Polymer | Onset shear rate $\times 10^{-3}$ sec^{-1} | |
		Small pipe	Large pipe
0	Polyox	8.2	7.3
0	Separan	3.5	4.1
30	Polyox	5.0	3.6
25	Separan	1.9	2.6
53	Polyox	2.3	1.8
52	Separan	(0.7)[a]	1.1

[a]Estimated.

Reynolds number data to get onset is invalid. On the other hand, if only the higher molecular weight molecules (those where $T_1 > k\nu/u_\tau^2$) contribute to drag reduction, an extrapolation procedure is justified. We assume that our method of analysis does relate only to the stretched molecules in turbulent flow regardless of where the extrapolated onset point lies.

If we compare onset in two different pipes, the results in Table III show opposite trends for Polyox and Separan. Polyox degrades more rapidly than Separan and degradation probably occurs for Polyox during the molecular stretching process. Then, we can account for the difference if the length of time the molecules stretch is given by the lifetime of the large eddies, D/U, if Polyox degrades while Separan does not, and if the amount of drag reduction after onset is also related to the time scale D/U. Unfortunately, this means that we cannot use data in two different pipes to examine onset by the procedure outlined in this work. The points after onset which are used to obtain a and b in Eq. (1) would be functions of the number of drag reducing molecules, the pipe diameter, and the degradation along the flow. Increased degradation in a larger diameter pipe leads to a decrease in the slope, a, of Eq. (1) and an apparent decrease in the onset shear rate. If little or no degradation occurs, an increased slope should result in an increase in the onset shear rate. Thus, the most likely effect of pipe diameter on the onset shear rate in the absence of degradation is no effect at all.

Further substantiation of the increase in drag reduction with pipe diameter can be found from the results using the expanded polyelectrolytes. Assuming that all the molecules are now in an extended ellipsoidal shape, onset is no longer a factor. Although there is a trend toward decreasing drag reduction with Reynolds number before the polyelectrolyte curves reach their onset, a line parallel to the Newtonian curve can be placed through the data. For the curves with water as a solvent and 20 ppm Separan NP-10, ΔB is 0.4 in the small pipe and 0.8 in the large one. This represents a diameter dependence to the 0.7 power. Also, there is essentially no dependence of drag reduction for the extended polyelectrolytes on viscosity, and a concentration dependence to the 0.7 power.

The new "onset" observed in the extended polyelectrolyte solutions shows several interesting facets. The striking correlation between onset and time scale is revealed in two ways. The onset occurs at approximately the same u_τ^2/ν in the collapsed or expanded molecules and increased viscosity of the solution leads to decreased onset shear rate. Both effects correlate with the molecular time scales. The time scale of the extended molecules is nearly the same as the random coil. After onset, the large pipe data show a slope similar to that of the small pipe in contrast to the random coil case where the large pipe curves have a higher slope. It appears that the incremental increase in drag reduction due to additional stretching of the large molecules is less than the initial effect, at least for the large pipe.

There is a small but observable decrease in drag reduction as $Rf^{1/2}$ is raised for all the extended polyelectrolytes. If the eddy lifetime is indeed related to the drag reduction amount, such a trend should indeed occur. The existence of onset for extended molecules indicates that higher molecular weight samples of Separan may not show this trend as molecules would be further stretched to counteract the effect. All experiments with the extended polyelectrolytes are, of course, subject to the influence of the large charged molecules in solution which cover a substantial volume perhaps as large as the microscale.

CONCLUSIONS

The onset of drag reduction is dependent only on the inner time scale u_τ^2/ν. After onset and in solutions of extended molecules, drag reduction is related to the lifetime of the large eddies D/U. These results tend to confirm Lumley's analysis[6] that both the mean strain rate and the persistence time of rotation free strain determine the onset relationship between the flow and the molecular time scale. In the absence of degradation, after the onset shear rate is exceeded, drag reduction is increased for larger pipes when the concentration of stretched molecules is constant. Under these conditions the large eddy lifetime is greater for a larger pipe and the polymers effectively spend more time in the drag reducing state. More molecules could be stretched for a longer time.

The relationship between drag reduction ΔB and the time scale D/U is strongly influenced by degradation. Therefore, the 0.7 power dependence found for Separan NP-10 is a lower limit and perhaps a first power dependence is likely. Then, the effectiveness would correlate with the mean period of turbulent production or the bursting process which also scales with D/U.[14]

Expanded polyelectrolytes in distilled water show drag reducing phenomena similar to fibers as first shown by Virk.[15] In addition, the diameter effect and a latent onset appear. Drag reduction was found to be dependent on diameter to the 0.7 power but not dependent on viscosity lending strong support to the relationship of drag reduction to the lifetime of large eddies. Some data reported by Vaseleski and Metzner[16] also show an increase in drag reduction by fibers as diameter is increased.

The results of this work also indicate that compari-

sons of drag reduction data using different pipe diameters should not be made. Polyox results are difficult to interpret because severe degradation is present which increases with pipe diameter. Additional studies are necessary before the diameter effect can be related to turbulence dynamics as only two pipe diameters were used in this work.

ACKNOWLEDGMENTS

[1]P. S. Virk, AIChE J. 21, 625 (1975).
[2]N. S. Berman and W. K. George, Jr., Phys. Fluids 17, 250 (1974).
[3]N. S. Berman and W. K. George, Jr., in *Proceedings of the* 1974 *Heat Transfer and Fluid Mechanics Institute*, edited by L. R. Davis and R. E. Wilson (Stanford University, Palo Alto, Calif., 1974), p. 348.
[4]O. Hassager, J. Chem. Phys. 60, 2111 (1974).
[5]M. C. Williams, AIChE J. 21, 1 (1975).
[6]J. L. Lumley, Symp. Mathematica 9, 315 (1972).
[7]J. L. Lumley, Macromol. Rev. 1, 263 (1973).
[8]D. L. Hunston and M. M. Reischman, Phys. Fluids 18, 1626 (1975).
[9]J. L. Lumley, in *Topics in Applied Physics-Turbulence*, edited by P. Bradshaw (Springer-Verlag, New York, 1976), p. 321.
[10]M. M. Reischman and W. G. Tiederman, J. Fluid Mech. 70, 369 (1975).
[11]R. W. Paterson and F. H. Abernathy, J. Fluid Mech. 43, 689 (1970).
[12]J. Yuen, M. S. Thesis, Arizona State University (1976).
[13]W. K. George Jr., G. B. Gurney, and N. S. Berman, J. Hydronaut. 9, 36 (1975).
[14]J. Laufer and M. A. Badri Narayanan, Phys. Fluids 14, 182 (1971).
[15]P. S. Virk, Nature 253, 109 (1975).
[16]R. C. Vaseleski and A. B. Metzner, AIChE J. 20, 301 (1974).

Rotation of the Reynolds' stress tensor in a decaying grid-generated turbulent flow

J. O. Hinze and P. J. H. Builtjes

Delft University of Technology, Delft, Netherlands

The fully-developed turbulent flow generated by a grid is axisymmetric, the intensity of the axial turbulence component being greater than that of the lateral component. Since the mean-velocity distribution is uniform and consequently, the gradient of the mean velocity is zero everywhere, a local stress-strain relationship is not possible. Measurements of the turbulence structure in a region up to 50 grid mesh-sizes downstream of the grid, have revealed that long-distance memory effects are responsible for a nonlocal relationship. In the local shear layers just downstream of the rods, the principal axes of the stress tensor make an angle of roughly 40 deg with the direction of the main flow. This angle decreases in the developing region, and becomes zero in the fully-developed region. The plane of maximum shear stress then makes an angle of 45 deg with the direction of the main flow. The transport equations for turbulence are transformed to nonhomogeneous linear relaxation equations, which clearly show the long-distance memory behavior of the maximum shear stress.

I. INTRODUCTION

The axisymmetric turbulent flow generated by a uniform grid shows, in the fully-developed region, an intensity of the axial turbulence velocity component that is greater than that of the lateral components. In this region the mean-velocity distribution is uniform, so that the mean-velocity gradients in all directions are zero. In the main-flow direction and perpendicular to it the turbulence shear stress is zero, but, in the planes making an angle between 0 and 90 deg with the main-flow direction, the shear stress is nonzero, with a maximum value in the planes making an angle of 45 deg with this direction.

A local stress-strain relationship, therefore, cannot account for these shear stresses. Since shear stresses are generated in the local shear layers just downstream of the rods, it is logical to attribute the shear stresses in the fully-developed region to the long-distance memory behavior of the turbulence.

In order to investigate this behavior an experimental study has been made of the turbulent flow in the developing region just downstream of a uniform square-mesh grid.

II. EXPERIMENTS

The bi-plane grid with a total area of 0.28×0.38 m^2, consisted of straight rods with a diameter $d = 1.88$ mm, and spaced at a distance $M = 10$ mm. With $M/d = 5.3$, the grid has a free area of 66%, which is just sufficient to avoid instabilities of the flow.[1,2] The grid has been manufactured with great precision (maximum deviation in M is 0.001 mm, and that in d is 0.002 mm). In the cross section at $x_1 = 24\ M$, the fully developed region showed deviations in the mean velocity, U_0, within 0.3 percent, while the variations of the turbulence intensities were within the accuracy of the turbulence measurements.

The experiments reported here, have been made with a mean velocity $U_0 = 10.28$ m/sec in the fully developed region. The turbulence measurements were carried out with a hot-wire anemometer with two wires in X ar-ray, and operating at constant temperature. Platinum-coated tungsten wires of 5 μm diam and a length of 1 mm of the sensitive part, were used. The measurements refer to $\bar{U}_1$, $\overline{u_1^2}$, $\overline{u_2^2}$, and $\overline{u_2 u_1}$.

Figure 1 shows the transverse distribution of $\bar{U}_1$ in a plane of symmetry (x_1, x_2 plane) at three distances $x_1/M = 1.4$, 3.75, and 8.25.

In general, the mean-velocity gradient $\partial \bar{U}_1/\partial x_2$, and the turbulence shear stress ($-\overline{u_2 u_1}$) had a maximum along the line $x_2 = \pm 2.5$ mm, $x_3 = 0$.

Figures 2 and 3 show, respectively, the axial distribution of $\bar{U}_1$ along the line $x_2 = -2.5$ mm, $x_3 = 0$, and the axial distributions of $U_0^2/\overline{u_1^2}$, $U_0^2/\overline{u_2^2}$, and u_1'/u_2' along the same line $[u_1' = (\overline{u_1^2})^{1/2}]$.

In the region $15 \gtrsim x_1/M \gtrsim 40$, $U_0^2/\overline{u_1^2}$ and $U_0^2/\overline{u_2^2}$ follows the "linear" decay law, with $u_1'/u_2' \simeq 1.19$. A constant value of this ratio will be maintained as long as u_1' and u_2' follow the same decay law. The two figures seem to show that a uniform, fully-developed, flow condition has
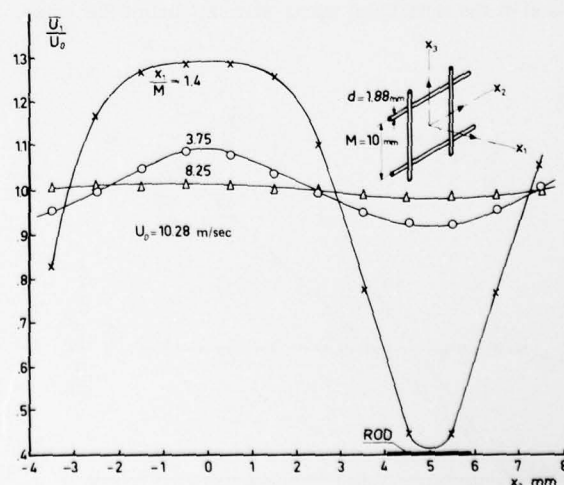

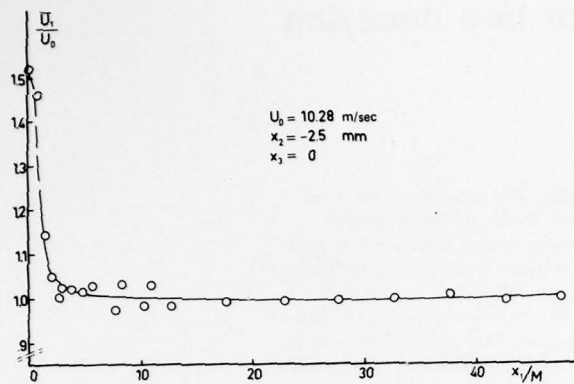FIG. 1. Transverse distributions of U_1 in a plane of symmetry.

FIG. 2. Axial distribution of $\bar{U}_1/U_0$.

FIG. 4. Axial distributions of $(-\overline{u_2 u_1})$ and R_{21}.

been obtained after $x_1/M \gtrsim 10$. However, the shear stress $(-\overline{u_2 u_1})$ and the correlation coefficient $R_{21} = -\overline{u_2 u_1}/u_2' u_1'$ appear to become zero not earlier than $x_1/M \approx 20$. This is clearly shown in Fig. 4. For $x_1/M > 20$, the (x_2, x_3) plane and planes through the x_1 axis are principal planes. Since $\overline{u_1^2} > \overline{u_2^2}$, there is a shear stress in any other plane. The maximum value of the shear stress is given by the relation

$$(-\overline{u_2 u_1})_{max} = \left[\tfrac{1}{4}(\overline{u_1^2} - \overline{u_2^2})^2 + (-\overline{u_2 u_1})^2 \right]^{1/2} . \qquad (1)$$

The corresponding maximum correlation coefficient is defined by

$$(R_{21})_{max} = (-\overline{u_2 u_1})_{max}/(u_2' u_1')_{max} .$$

Since $(u_1^2)_{max} = (u_2^2)_{max} = (u_1^2 + u_2^2)/2$, the maximum correlation coefficient can be calculated from

$$(R_{21})_{max} = 2(-\overline{u_2 u_1})_{max}/(u_1^2 + u_2^2) . \qquad (2)$$

Let α_p be the angle between the principal coordinate, x_{1p} and the coordinate, x_1. This angle satisfies the relation

$$\tan 2\alpha_p = 2(-\overline{u_2 u_1})/(\overline{u_1^2} - \overline{u_2^2}) . \qquad (3)$$

The plane of maximum shear stress makes an angle $45\deg$ with the x_1 direction. Figure 5 shows the distribution of the maximum shear stress, and of the max-
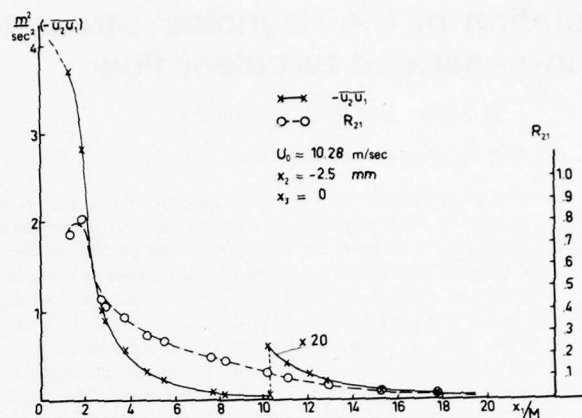
imum correlation coefficient. Figure 6 shows the distribution of the angle α_p. All distributions are along the line $x_2 = -2.5$ mm, $x_3 = 0$.

The angle, α_p, decreases gradually from approximately 40 deg to zero at $x_1/M \gtrsim 20$. Also, the maximum correlation coefficient $(R_{21})_{max}$ decreases, but seems to obtain a constant value of 0.2 in the fully-developed turbulent region. The plane of maximum shear stress then makes an angle of 45 deg with the x_1 direction. In the developing region, the principal axes rotate counterclockwise, until x_{1p} coincides with x_1.

III. THEORETICAL CONSIDERATIONS

As mentioned in the introduction, we believe that long-distance memory effects in the main-flow direction are present all the way downstream, and may account for the occurrence of shear stresses in the absence of mean-velocity gradients.

It is reasonable to consider the transport equations for u_1^2, u_2^2, and $l = u_2 u_1$. Since, except very close to the peak, $\overline{U}_2 \ll \overline{U}_1$, we have $\overline{U}_2 \partial/\partial x_2 \ll \overline{U}_1 \partial/\partial x_1$, so that the effect of the transverse mean velocity on the transport may be neglected. With the usual boundary-layer sim-

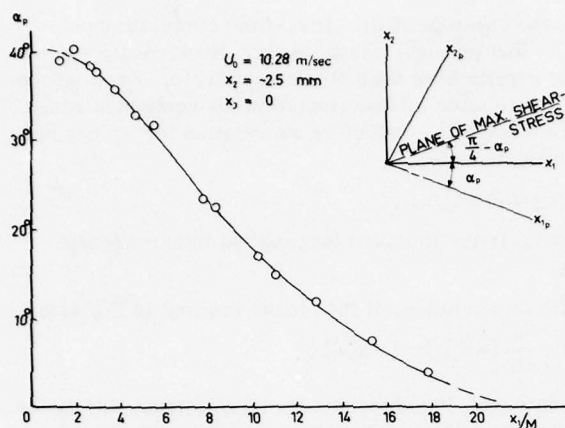FIG. 6. Rotation of the principal axes through a decrease of α_p in axial direction.

plifications, the transport equation for $\overline{u_1^2}$ may be reduced to

$$\overline{U}_1 \frac{\partial}{\partial x_1} \overline{u_1^2} \simeq - 2 \overline{u_2 u_1} \frac{\partial \overline{U}_1}{\partial x_2} + \frac{2}{\rho} \overline{p \frac{\partial u_1}{\partial x_1}} - \frac{2}{3} \epsilon , \qquad (4)$$

where ϵ is the viscous dissipation, and a sufficient degree of local isotropy is assumed so that

$$2\nu \overline{\frac{\partial u_1}{\partial x_k} \frac{\partial u_1}{\partial x_k}} \simeq \frac{2}{3} \nu \overline{\frac{\partial u_i}{\partial x_k} \frac{\partial u_i}{\partial x_k}} \simeq \frac{2}{3} \epsilon .$$

Similarly,

$$\overline{U}_1 \frac{\partial}{\partial x_1} \overline{u_2^2} \simeq \frac{2}{\rho} \overline{p \frac{\partial u_2}{\partial x_2}} - \frac{2}{3} \epsilon \qquad (5)$$

and

$$\overline{U}_1 \frac{\partial}{\partial x_1} (- \overline{u_2 u_1}) \simeq \overline{u_2^2} \frac{\partial \overline{U}_1}{\partial x_2} - \frac{1}{\rho} \overline{p \left(\frac{\partial u_1}{\partial x_2} + \frac{\partial u_2}{\partial x_1} \right)} . \qquad (6)$$

Equation (6) does not contain a viscous dissipation term, since we assumed a sufficient degree of local isotropy to make

$$\overline{\frac{\partial u_1}{\partial x_2} \frac{\partial u_2}{\partial x_1}} = 0 .$$

The neglect of this viscous dissipation term is not essential for the final results.

The pressure p may be considered to consist of two parts, one p_s due to the interaction with the mean-velocity gradients, and the other p_t due to the interaction with the turbulence velocity gradients.

time. As will be made clear later it may be interpreted as the reciprocal of a relaxation time. Now, the experiments showed that the relaxation time for $(-\overline{u_2 u_1})$ is different from those for $\overline{u_1^2}$ and $\overline{u_2^2}$. Since the relation (8) is intended as an approximation only, we accept a violation of Eq. (8) by making a distinction between a value $c_2^{(21)}$ for $-\overline{u_2 u_1}$, and c_2 for $\overline{u_1^2}$ and $\overline{u_2^2}$.

Thus, the pressure terms in Eqs. (4), (5), and (6) become

$$\frac{2}{\rho} \overline{p \frac{\partial u_1}{\partial x_1}} \simeq \frac{2}{\rho} \overline{p_t \frac{\partial u_1}{\partial x_1}} = - c_2 \frac{q'}{L} (\overline{u_1^2} - \tfrac{1}{3} \overline{q^2}) ,$$

$$\frac{2}{\rho} \overline{p \frac{\partial u_2}{\partial x_2}} \simeq \frac{2}{\rho} \overline{p_t \frac{\partial u_2}{\partial x_2}} = - c_2 \frac{q'}{L} (\overline{u_2^2} - \tfrac{1}{3} \overline{q^2}) ,$$

$$\frac{1}{\rho} \overline{p \left(\frac{\partial u_1}{\partial x_2} + \frac{\partial u_2}{\partial x_1} \right)} = c_1 \overline{q^2} \frac{\partial \overline{U}_1}{\partial x_2} + c_2^{(21)} \frac{q'}{L} (- \overline{u_2 u_1}) .$$

Furthermore, we may put

$$\epsilon \simeq \nu \overline{\frac{\partial u_i}{\partial x_k} \frac{\partial u_i}{\partial x_k}} = c_3 \frac{q'^3}{L} . \qquad (9)$$

We thus obtain for Eqs. (4), (5), and (6), respectively,

$$\overline{U}_1 \frac{\partial}{\partial x_1} \overline{u_1^2} = - 2 \overline{u_2 u_1} \frac{\partial \overline{U}_1}{\partial x_2} - c_2 \frac{q'}{L} (\overline{u_1^2} - \tfrac{1}{3} \overline{q^2}) - \frac{2}{3} c_3 \frac{q'^3}{L} , \quad (10)$$

$$\overline{U}_1 \frac{\partial}{\partial x_1} \overline{u_2^2} = - c_2 \frac{q'}{L} (\overline{u_2^2} - \tfrac{1}{3} \overline{q^2}) - \frac{2}{3} c_3 \frac{q'^3}{L} , \qquad (11)$$

$$\overline{U}_1 \frac{\partial}{\partial x_1} (- \overline{u_2 u_1}) = (\overline{u_2^2} - c_1 \overline{q^2}) \frac{\partial \overline{U}_1}{\partial x_2} - c_2^{(21)} \frac{q'}{L} (- \overline{u_2 u_1}) . \qquad (12)$$

In the fully developed turbulent part of the flow, the occurrence of a maximum shear stress $(-\overline{u_2 u_1})_{max}$ is of interest. This shear stress is determined by Eq. (1). Consequently, we also have to consider the transport equation for $(\overline{u_1^2} - \overline{u_2^2})$.

Subtraction of Eq. (11) from Eq. (10) then gives

$$\overline{U}_1 \frac{\partial}{\partial x_1} (\overline{u_1^2} - \overline{u_2^2}) + c_2 \frac{q'}{L} (\overline{u_1^2} - \overline{u_2^2}) = - 2 \overline{u_2 u_1} \frac{\partial \overline{U}_1}{\partial x_2} . \qquad (13)$$

When $\partial \overline{U}_1 / \partial x_2 = 0$, we conclude from these equations that:

(a) $\overline{u_1^2}$ and $\overline{u_2^2}$ change due to pressure velocity-gradient correlations, and due to viscous dissipation;
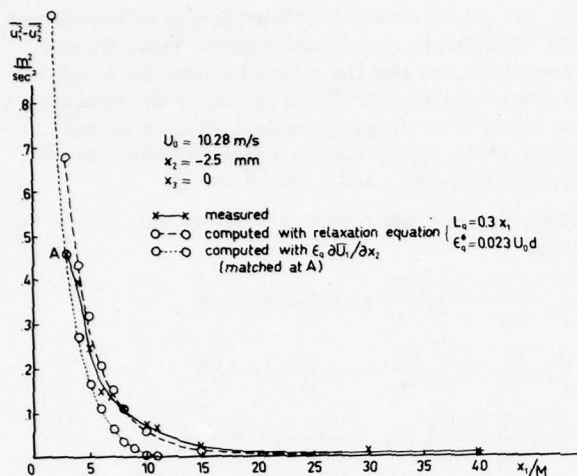
FIG. 7. Axial distributions of $\overline{(u_1^2 - u_2^2)}$, measured and computed.

$$L_m \frac{\partial}{\partial x_1}(-\overline{u_2 u_1}) + (-\overline{u_2 u_1}) = (\overline{u_2^2} - c_1 \overline{q^2}) T_m \frac{\partial \overline{U_1}}{\partial x_2} = \in_m^* \frac{\partial \overline{U_1}}{\partial x_2} , \tag{16}$$

and

$$L_q \frac{\partial}{\partial x_1}(\overline{u_1^2} - \overline{u_2^2}) + (\overline{u_1^2} - \overline{u_2^2}) = -2 \overline{u_2 u_1} T_q \frac{\partial \overline{U_1}}{\partial x_2} = \in_q^* \frac{\partial \overline{U_1}}{\partial x_2} , \tag{17}$$

where $L_m = \overline{U_1} T_m$, $L_q = \overline{U_1} T_q$, and $\in_m^*$ and $\in_q^*$ are eddy diffusion coefficients.

The relaxation or memory distances, L_m and L_q, may still be functions of x_1. In self-preserving flows the functions are linear.

Other studies of the memory behavior in free turbulent shear-flows have revealed that $\in_m^*$ is independent of x_1.[5] We may assume the same to be true for $\in_q^*$.

When the first term on the left-hand side of Eqs. (16) and (17) are neglected, the equations reduce to the Boussinesq relations.

A major difficulty is presented by the fact that neither the relaxation or memory distances, L_m and L_q, are known, nor the eddy diffusion coefficients, $\in_m^*$ and $\in_q^*$. The relaxation times, T_m and T_q, may be determined from the envelope of the space-time correlations of $(-\overline{u_2 u_1})$ and $\overline{(u_1^2 - u_2^2)}$, respectively. No accurate and reliable results have been obtained hitherto. From space-time correlation measurements in the restricted range where $-\overline{u_2 u_1} \neq 0$, a rather crude relation for T_m has been obtained, namely,

$$T_m \simeq 0.17 \Lambda_f / u_1' ,$$

where Λ_f is the Eulerian longitudinal integral length scale.

With this relation, it then turns out that in Eq. (16)

$$L_m \frac{\partial}{\partial x_1}(-\overline{u_2 u_1}) \ll (-\overline{u_2 u_1}) .$$

Consequently, the shear-stress $(-\overline{u_2 u_1})$ must satisfy the Boussinesq relation. Indeed, a satisfactory agreement is obtained between measured values of $(-\overline{u_2 u_1})$, and values computed with $\in_m^* \simeq 0.06 U_0 d$. If the convective term is not neglected, then the eddy diffusion coefficient $\in_m^*$ must have a slightly smaller value.

Because values of L_q and $\in_q^*$ were lacking, in order to see whether the relaxation equation (17) does give a satisfactory description of the behavior of $(\overline{u_1^2} - \overline{u_2^2})$, and thus of $(-\overline{u_2 u_1})_{max}$, this equation has been solved for various values of L_q and $\in_q^*$. The best result was obtained with

$$L_q \approx 0.3 x_1 \quad \text{and} \quad \in_q^* = 0.023 U_0 d .$$

Figure 7 shows this result, from which it may be concluded that the relaxation equation (17) does describe the behavior of $(\overline{u_1^2} - \overline{u_2^2})$ and $(-\overline{u_2 u_1})_{max}$ satisfactorily.

In the same figure, $(\overline{u_1^2} - \overline{u_2^2})$, calculated with the neglect of the convective term, is shown. For $\in_q$, a value has been taken such that computed and measured values agree at the point $x_1/M = 3$. Since, in contrast to the results of the complete relaxation equation $\overline{u_1^2} - \overline{u_2^2} \to 0$ when $x_1/M \gtrsim 10$, the long distance memory effect on $\overline{u_1^2} - \overline{u_2^2}$ is well demonstrated.

[1] P. G. Morgan, J. R. Aeronaut. Soc. **64**, 359 (1960).

[2] P. Bradshaw, J. R. Aeronaut. Soc. **68**, 198 (1964).

[3] B. E. Launder, G. J. Reece, and W. Rodi, J. Fluid Mech. **68**, 537 (1975).

[4] J. Rotta, Z. Physik **129**, 547 (1951).

[5] J. O. Hinze, Z. Angew. Math. Mech. **56**, T 403 (1976).

Behavior of a turbulent flow, strongly out of equilibrium, at supersonic speeds

Jean Gaviglio, Jean-Paul Dussauge, Jean-François Debieve, and Alexandre Favre

Institut de Mécanique Statistique de la Turbulence, Université d'Aix-Marseille II, Laboratoire Associé au Centre National de la Recherche Scientifique, 13003 Marseille, France

A study is presented of the mechanisms occurring in a turbulent near wake flow at supersonic speed, in which there exist strong pressure and velocity gradients. The role played by the "production" of turbulent kinetic energy is shown. It is influenced by compressibility and anisotropy. The analysis indicates that compressibility increases production when a sheared flow develops in a positive pressure gradient, and decreases it in the case of an expansion. The experiments give the mean and turbulent characteristics of a near wake flow. The results show that: the levels of vorticity and entropy modes verify the relationship given by the strong Reynolds analogy; the correlation coefficient between modes is not significantly altered by strong gradients and rates of strain; negative production occurs in the expansion zone; as a consequence, there exists a decrease in turbulence measured downstream of this region.

I. INTRODUCTION

The structure of turbulent flows at supersonic speeds for moderate nominal Mach numbers ($M_\infty < 4$) is well known in the case when the evolution of the flows is slow. This can be derived from results given, for example, by Kovasznay,[1] Laufer,[2] Morkovin,[3] Kistler,[4] and others, in the case of boundary layers, and from those given by Demetriades[5-7] for wakes. These results made it possible to relate the properties of supersonic flows to those of subsonic flows containing sources of heat, as shown by Morkovin,[3] Crocco,[8] Laufer.[9] The available information is not as complete when considering flows which are strongly out of equilibrium. Results given by Sternberg,[10] Morkovin,[11] Lewis and Behrens,[12] Page and Sernas,[13] Rose and Childs,[14] Sirieix[15] ... show important differences between the two types of flow.

The results presented here concern the study of a steady flow, strongly out of equilibrium, in which important pressure gradients and strains exist, as well as the effects of compressibility. This type of flow belongs to "complex" turbulent flows as defined by Bradshaw.[16] Difficulties arise in the interpretation of the experiments. The analysis is mainly developed in terms of the production of turbulence, which greatly influences the development of the flow, and for which theoretical considerations are given in Sec. II. The experimental arrangements are described in Sec. III, while the results are given and discussed in Sec. IV. Finally, an attempt is made in Sec. V to draw conclusions that take into account the results obtained by other authors.

The flow considered is the near wake flow downstream of a nearly streamlined model placed in a supersonic nozzle, at the nominal Mach number $M_\infty = 2.3$, Fig. 1. The section at the end of the model is circular with a diameter of 40 mm.

The configuration of the flow, which has already been described,[17-19] is indicated in Fig. 2, obtained from a schlieren picture. The initial boundary layer is fully turbulent, it leaves the model from the edge AA, is accelerated through an expansion fan, then develops as a mixing layer which is subjected to compression and

a shock wave, and finally transforms into a wake. The mixing layer encloses a recirculating "dead air" zone which is separated from the mixing layer by a randomly fluctuating interface. The average location of the interface is called the "dividing surface"; its trace in a radial plane is the "dividing streamline". The present measurements mainly concern the boundary layer and the flow developing around and downstream of the recirculation zone, the latter not having been extensively studied here.

II. ANALYTICAL CONSIDERATIONS

Let $\mathbf{u}$, p, θ, and ρ be the instantaneous values of the velocity, pressure, temperature, and specific mass; u_i and θ are separated into their mean mass averaged values denoted by the tilde (~) and fluctuation denoted by the prime (') such as

$$\overline{\rho u_i} \equiv \bar{\rho}\tilde{u}_i \Rightarrow \overline{\rho u_i'} \equiv 0 \ , \quad \overline{\rho \theta} \equiv \bar{\rho}\tilde{\theta} \Rightarrow \overline{\rho \theta'} \equiv 0 \ .$$

In addition,

$$p \equiv \bar{p} + p' \Leftrightarrow \overline{p'} \equiv 0 \ , \quad \rho \equiv \bar{\rho} + \rho' \Leftrightarrow \overline{\rho'} \equiv 0 \ .$$

The overbar (—) indicates an ensemble average which here is equal to the time average because of stationarity. The corresponding statistical equations are simpler than those based on the Reynolds separation: $w = \bar{w} + w''$ $\Leftrightarrow \overline{w''} = 0$ and the physical interpretation of the terms is
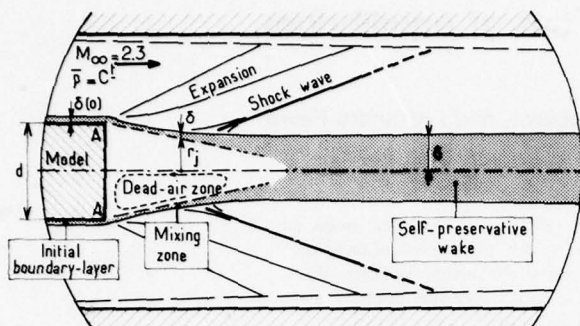
FIG. 2. Sketch of the flow.

clearer, as shown by Favre.[20,21] Using tensor notation, the statistical equation giving the rate of variation $D/Dt = \partial/\partial t + \bar{u}_j \partial/\partial x_j$ of turbulent kinetic energy $\overline{\rho u_i' u_i'}/2$ per unit volume, which will be called the kinetic energy of turbulence, may be written as

$$D(\overline{\rho u_i' u_i'}/2)/Dt + (\overline{\rho u_i' u_i'}/2)\partial \bar{u}_k/\partial x_k = \mathbf{Pr} + \mathbf{D} + \overline{\varphi'} \quad (1)$$

where $\mathbf{Pr}$, $\mathbf{D}$, and $\overline{\varphi'}$ represent the rates of production, of diffusion and of dissipation, respectively. The streamwise evolution of the flow depends on these rates. In the case of supersonic flows, only the production may be submitted to a detailed analysis and to meaningful measurements. The other terms are extremely difficult to measure and are usually estimated by comparison with incompressible flows. In addition, such a comparison shows that production plays an important role in separated flows. Consequently, an attempt is made to analyze it precisely.

The total production term is

$$\mathbf{Pr} = (-\overline{\rho u_i' u_j'}\partial \bar{u}_i/\partial x_j) + (\overline{-u_i' \partial p/\partial x_i}) = \mathbf{Pr}_c + \mathbf{Pr}_p . \quad (2)$$

The term $\mathbf{Pr}_c = -\overline{\rho u_i' u_j'}\partial \bar{u}_i/\partial x_j$ may be called "kinetic production." It appears with opposite signs in Eq. (1) and in the kinetic energy of the mean flow, so that it describes an exchange between the latter and the turbulent kinetic energy. The term $\mathbf{Pr}_p = -\overline{u_i' \partial p/\partial x_i}$ may be called "enthalpic production." It appears with opposite signs in Eq. (1) and in the mean enthalpy $C_p \bar{\rho} \bar{\theta}$, thus describing

an exchange between the latter and the averaged turbulent kinetic energy. It can be separated into the following three terms.

$$-\overline{u_i' \partial p/\partial x_i} = (\overline{\rho' u_i'}/\rho)\partial \bar{p}/\partial x_i + \overline{p' \partial u_i'/\partial x_i} - \partial(\overline{p' u_i'})/\partial x_i . \quad (3)$$

The first term on the right-hand side may be important, especially in the case of expansion or compression; in geophysics, this term corresponds to buoyancy production. The second term on the right-hand side may be different from zero when the fluctuating field is not incompressible, but the condition $\partial u_i'/\partial x_i \simeq 0$ is often satisfied at moderate Mach numbers. It follows that, according to Rotta,[22] there is a redistribution of energy between the three components, and a tendency toward isotropy. The third term expresses the diffusion of mean turbulent kinetic energy by pressure fluctuations or sound waves. Since it remains unmeasured or estimated at supersonic speeds, it is often analyzed together with the other diffusion terms in the modeling problems[23,24] so that it will not be considered in the present analysis. Nevertheless, it may be remarked that each separate component of the term $\overline{p' \partial u_i'/\partial x_i}$ and $\partial(\overline{p' u_i'})/\partial x_i$ is probably influenced by compressibility at an unknown rate, although it has the same form as in incompressible flow.

A. Analysis of kinetic production $\mathbf{Pr}_c$

The interpretation of $\mathbf{Pr}_c = -\overline{\rho u_i' u_j'}\partial \bar{u}_i/\partial x_j$ has to be cleared up in the case of volume changes. To take into account these effects, Favre[25] proposed to separate, from $\mathbf{Pr}_c$, the "isotropic" term $\frac{1}{3}\overline{\rho u_i' u_i'}\partial \bar{u}_k/\partial x_k$ the sign of which changes as the rate of volume variation, so that

$$\mathbf{Pr}_c = -[\overline{\rho u_i' u_j'} - (\overline{\rho u_i' u_i'}/3)\delta_{ij}]\partial \bar{u}_i/\partial x_j - (\overline{\rho u_i' u_i'}/3)\partial \bar{u}_k/\partial x_k . \quad (4)$$

Then, Debieve[26] separated the Reynolds tensor $\overline{\rho u_i' u_j'}$ into its anisotropic part d_{ij}' and its isotropic part s_{ij}', and, in addition, considered the mean velocity gradient $\partial \bar{u}_i/\partial x_j$ as the sum of: (i) a spherical part S_{ij} representing the dilatation rate; (ii) a symmetric part D_{ij} corresponding to the isovolumetric part of the deformation rate; (iii) an antisymmetric part R_{ij} describing rotation. These separations are both classical and unique (for example, see Refs. 27 and 28).

$$\overline{\rho u_i' u_j'} = s_{ij}' + d_{ij}' \begin{cases} d_{ij}' = \overline{\rho u_i' u_j'} - \frac{1}{3}\overline{\rho u_i' u_i'}\delta_{ij} , \\ s_{ij}' = \frac{1}{3}\overline{\rho u_i' u_i'}\delta_{ij} . \end{cases} \quad (5)$$

$$\partial \bar{u}_i/\partial x_j = S_{ij} + D_{ij} + R_{ij} \begin{cases} S_{ij} = \frac{1}{3}(\partial \bar{u}_k/\partial x_k)\delta_{ij} = -(D\bar{\rho}/Dt)\delta_{ij}/3\bar{\rho} , \\ D_{ij} = \frac{1}{2}[(\partial \bar{u}_i/\partial x_j) + (\partial \bar{u}_j/\partial x_i)] - \frac{1}{3}(\partial \bar{u}_k/\partial x_k)\delta_{ij} , \\ R_{ij} = \frac{1}{2}[(\partial \bar{u}_i/\partial x_j) - (\partial \bar{u}_j/\partial x_i)] . \end{cases} \quad (6)$$

The full expression for $\mathbf{Pr}_c$ includes six terms, four of which are zero, while only two terms may be different from zero and correspond to the terms of the right-hand side of expression (6).

The properties of the separation are summarized in

Fig. 3. The kinetic production of turbulent energy is exclusively due to the terms [1] and [2]. Term [1] expresses the interaction between the isovolumetric part of the mean mass-weighted deformation strain and the anisotropic part of the Reynolds stresses; it may be called the "isovolumetric deformation part of kinetic

FIG. 3. Kinetic production of turbulence.

production", or simply, the isovolumetric production. Term [2] corresponds to the interaction between the dilatation in the mean mass-weighted movement and the isotropic part of the Reynolds stresses.

B. Explicit effects of compressibility on turbulence production

It might be useful to characterize the effects of compressibility on the turbulence production by comparing it with the term for the isovolumetric production Pr_{iv} which is formally free from such effects, the term for kinetic production Pr_c, for enthalpic production Pr_p, and for total production Pr Eq. (2)

$$Pr_c = Pr_{iv} + (\overline{\rho q'^2}/3\bar{\rho})\, D\bar{\rho}/Dt \, , \tag{7}$$

$$Pr_p = (\overline{\rho' u_i'}/\bar{\rho})\,\partial \bar{p}/\partial x_i \, , \tag{8}$$

where $\overline{q'^2} = \overline{u_i' u_i'}$.

The sign of the term $(\overline{\rho q'^2}/3\bar{\rho})\, D\bar{\rho}/Dt$ is that of $D\bar{\rho}/Dt$. So, if the particle of fluid is submitted to an expansion such as $D\bar{\rho}/Dt < 0$, the kinetic production is lower than the isovolumetric deformation production. In the particular case of isotropy, where Pr_{iv} is zero, even in compressible flows,[17] the total kinetic production would be negative. The situation would be the opposite in a compression.

Dealing with the effect of compressibility on total production, the role of the pressure gradient must be studied in each case. An application of this was made[29] to an axisymmetric flow having longitudinal curvature (Fig. 2). A new system of curvilinear coordinates is used (Fig. 4). s is the direction of the mean streamline, on which the mean mass-weighted velocity is measured; y is the normal direction to s in a radial plane.

$$Pr_p \text{ is } (\overline{\rho' u_s'}/\bar{\rho})\,\partial \bar{p}/\partial s/(1+y/R_c) + (\overline{\rho' u_y'}/\bar{\rho})\,\partial \bar{p}/\partial y \, . \tag{9}$$

It is assumed that the correlations $\overline{\rho' u_s'}$ and $\overline{\rho' u_y'}$ are, respectively, positive and negative, as in a self-preserving boundary layer. The measurements show that in the near wake $\overline{\rho' u_s'}$ is positive (Sec. IVC 2), there is also

some evidence that $\overline{\rho' u_y'}$ is negative (Sec. IVB 2). The role of the longitudinal and radial components of the pressure gradients is shown. The radial component $\partial \bar{p}/\partial y$ often expresses the centrifugal forces: $\partial \bar{p}/\partial y \simeq (\bar{\rho}\tilde{u}_s^2)/R$. Then, in the case of the expansion provoking a convex curvature $1/R$ of the mean streamlines, the terms of (9) are negative. The other pressure fluctuation terms remain unmeasured; if they are small enough, the total production Pr is less than the kinetic and the isovolumetric production Pr_{iv} and may become locally negative. It should be noted that Pr_{iv} itself may be negative, but although this situation can lead to a reverse transition even in subsonic flows[30] (see the references in Ref. 31), it does not have to be negative for relaminarization because the latter may be associated with a decrease in Reynolds number[32] or with an increase in dissipation. The situation would be the opposite for a compression.

Consequently, the following inequalities may be written:

for an expansion:

$$Pr \leqslant Pr_c \leqslant Pr_{iv} \, ;$$

for a compression:

$$Pr \geqslant Pr_c \geqslant Pr_{iv} \, .$$

From this analysis, it can be deduced that Morkovin's hypothesis, according to which, as a first approximation, the properties of the turbulent field of compressible flows are not very different from those of low speed flows with heat sources, would imply that, from the point of view of the explicit effects of compressibility, the total production not be much different from the isovolumetric production. This condition is fulfilled for self-preserving flows, at moderate Mach numbers, but, if rapid expansions or compressions exist, a second approximation may be necessary to take their effects into account.

III. EXPERIMENTAL EQUIPMENT AND MEASUREMENT CHECKING

The flow which is described in Sec. I was explored by means of pressure probes moderately sensitive to yaw,
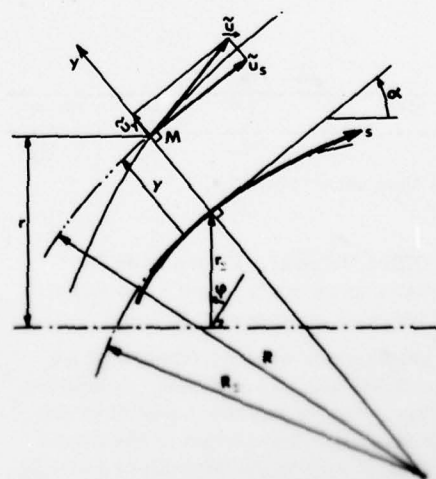

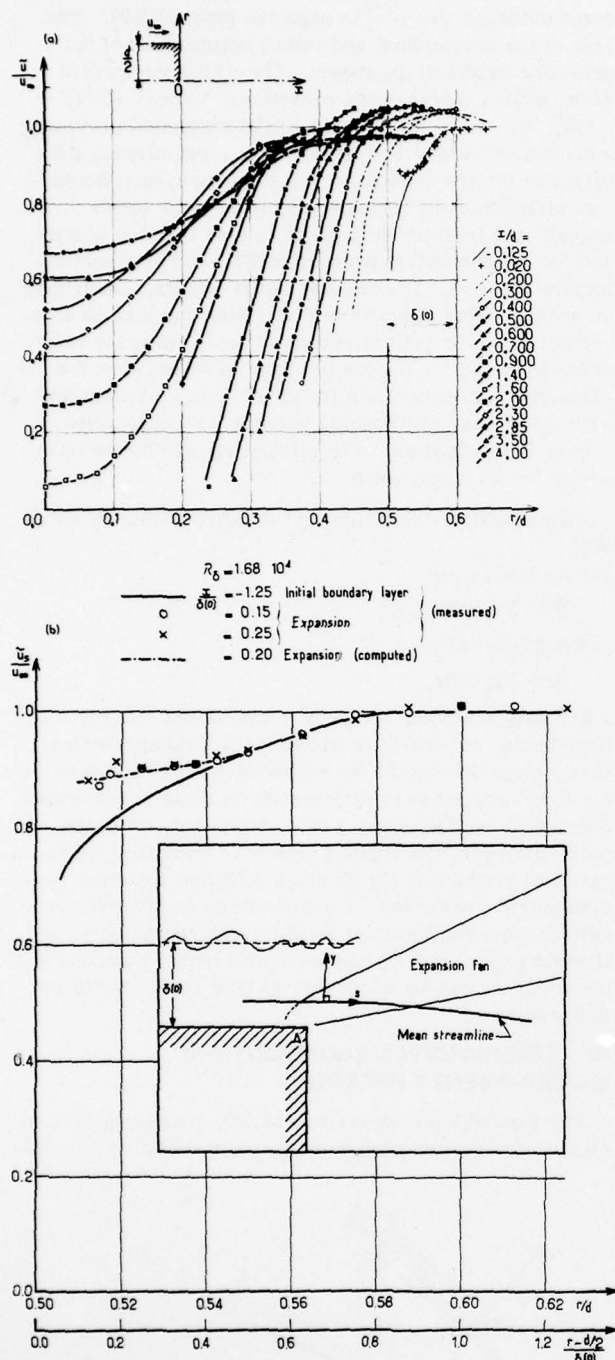FIG. 4. Orthogonal curvilinear coordinate system.

FIG. 5. (a) and (b) Mean velocity profiles.

nolds numbers $\bar{\rho}\bar{u}\delta(0)/\mu$, where μ is the viscosity taken at the temperature $\bar{\theta}$, are 16 800 and 33 600, respectively, and those based on the momentum thickness δ^{**} are 2000 and 1000.

The mean velocity profiles [Fig. 5(a) and (b)] and the mean streamlines [Fig. 6(a)], have been deduced from pressure measurements assuming a constant stagnation temperature, $\bar{\theta}_t$. It has been verified that the results are not changed significantly if the measured values of $\bar{\theta}_t$ are used. The streamlines were determined by two approximations in order to take into account their obliqueness. They correspond to constant values of mass flow $Q = 2\pi \int_{r_j}^{r} r\bar{\rho}\bar{u}\,dr$, calculated from the dividing surface which is defined through the relation $Q_j = 0 = 2\pi \int_0^{r_j} \times r\bar{\rho}\bar{u}_s\,dr$. The radius r_j coincides with that of the cylinder upstream of the wedge AA, and is equal to zero downstream of the dead air zone (Fig. 2). Each streamline corresponds to the marked value of the ratio Q/Q_*, where Q_* is the mean streamwise mass flux through the displacement thickness of the initial boundary layer. It is recalled that the mean transverse turbulent mass flux through these streamlines is zero, according to the definition of mean mass-weighted velocity given in Sec. IIA.

The length l and the diameter Φ of the hot wire probes are 0.9 mm and 3.8 μ, respectively. The wire is made of tungsten plated with platinum and calibrated following a method proposed by Gaviglio[33] to take into account a large part of the energy losses at the wire ends. The sensitivities $F(a'_w, \mathcal{R}_{dT})$ and $G(a'_w, \mathcal{R}_{dT})$ to mass flow and to local stagnation temperature depend on the conventional overheating of the wire.[34,35] F is supposed to depend little on the Reynolds number $\mathcal{R}_{dT} = \bar{\rho}\bar{u}\Phi/u_t$, as shown in Ref. 33, where μ_T is the viscosity at the stagnation temperature $\bar{\theta}_T$; and not to depend on the local Mach number M in the range $1.2 < M < 5$, a result which is commonly admitted. In addition, the recirculation region was not investigated by hot-wire anemometry. The sensitivity G is determined for each wire. The computation is based on the simplified formulae[35] giving F and G and expressing G as a function of F and other parameters. The fluctuating signal delivered by the hot-wire anemometer is interpreted according to Kovasznay's method.[1] Since the Mach number is low, the vorticity mode and the entropy mode will hereafter be called velocity and temperature fluctuations, respectively.

Mean local stagnation temperatures (Reynolds number $\approx$ 33 600) were measured according to a method initially proposed by Bissonette and Burnage[36] and derived from Laufer and McClellan's method.[37]

Dealing with the turbulence measurements by hot wires (Reynolds number 16 800), it should be noted that the levels of velocity and temperature fluctuations are often underestimated. This is due to the well known imperfections[38] in the anemometer, such as the inadequacy of spatial resolution of the probes, or the limitation of the amplifier bandwidth. These sources of error are often weak in the case of low speed flows, when short enough wires are used and when the characteristic frequency is weak if compared with the upper frequency

manufactured by Office National d'Etudes et de Recherche Aérospatiales and using a Shapiro and Edwards constant-current hot-wire anemometer.

Two series of experiments were performed, at a total pressure $p_T = 0.375$ atm and 0.75 atm, respectively. In the first case, roughnesses were placed on the lateral surface of the model downstream of the nozzle (Fig. 1). In each case, the initial boundary layer was fully turbulent, and its thickness was $\delta(0) \approx 4$ mm. The Rey-
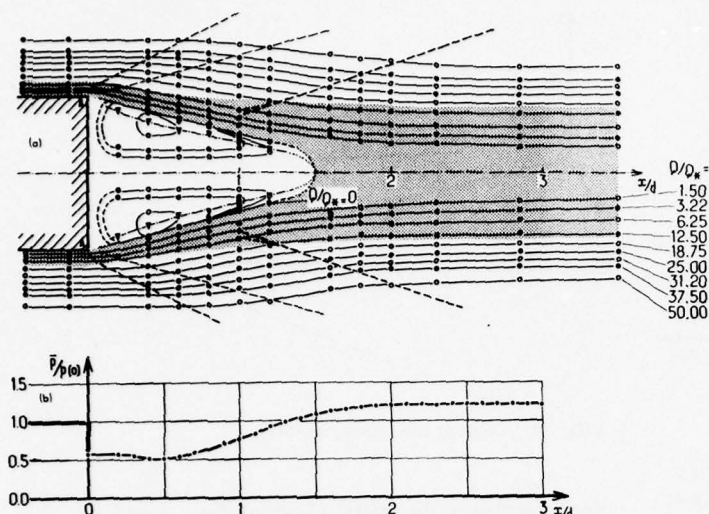
FIG. 6. (a) Mean streamlines. (b) Mean pressure.

limit of the apparatus. At supersonic speeds, however, the situation is quite different, and these errors may be much more important. In the present case, the bandwidth of the uncompensated amplifier has been limited to 210 kHz (3 dB) to avoid perturbations due to radio-electrical interference; this reduces the measured energy of the turbulent signal, especially in the initial boundary layer. It has been shown that this reduction is mainly due to the fact that the energy transfer function of the network compensating for the effects of thermal lag is lower than the theoretical definition. This also reduces the bandwidth, but, the damping law is well determined, so corrections are possible. They were computed from autocorrelation curves. They are apparently adequate, as shown in Fig. 7, since the corrected results obtained in a case where the corrections are important, agree well with measurements made by other authors in favorable cases. Note that results given by Johnson and Rose were obtained with a laser and a constant temperature hot-wire anemometer.

IV. EXPERIMENTAL RESULTS–DISCUSSION

A. Mean characteristics of the flow

Figure 5(b) shows the evolution of the dimensionless mean pressure $\bar{p}/p(0)$ measured at a distance $r_j(x/d)$ from the axis. $p(0)$ is the pressure in the external flow upstream of the expansion; $\bar{p}/p(0)$ is strongly reduced through this region; it remains approximately constant along the recirculation zone; it then grows downstream, the maximum longitudinal gradient being located at the distance $(x/d) \approx 1.4$, where it reaches the value $\partial[\bar{p}/\rho(0)]/\partial[x/\delta(0)] \approx 0.08$. The mean mass weighted velocity profiles are given in Figs. 5(a) and (b). Figure 5(b) corresponds to the Reynolds number 16 800 at which the hot-wire measurements were performed. It compares the velocity distributions measured in the initial boundary layer, $(x/d) = -0.125$ {equivalent to $[x/\delta(0)] = -1.25$} and in the region of expansion, $[x/\delta(0)] = 0.15$ and $[x/\delta(0)] = 0.25$ where the mean streamlines may be assumed parallel to the generators of the model. Figure 5(b) also gives a velocity distribution computed for the

distance $[x/\delta(0)] = 0.20$ using a method given by Sternberg.[10] The method is based on the fact that the total friction force by unit volume is smaller than the pressure force $\partial \bar{p}/\partial s$ by at least an order of magnitude. As for the application, the momentum equation takes the simple form $\bar{\rho}\bar{u}_s(\partial\bar{u}_s/\partial s) \simeq -\partial\bar{p}/\partial s$, valid along each streamline on which $\bar{u}_s$ is measured; the distribution $\bar{p}[r/d, x/\delta(0) = 0.20]$ is replaced by a linear one, estimated from a schlieren picture [Fig. 5(b)] and from the knowledge of the initial pressure and of the pressure after expansion (base pressure). The measured and computed profiles fit suitably [Fig. 5(b)]. The computation explicitly shows that the low density particles, i.e.,

FIG. 7. Measurement checking.

Gaviglio, Dussauge, Debieve, and Favre
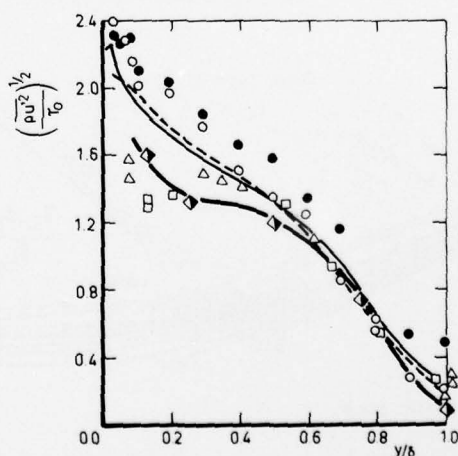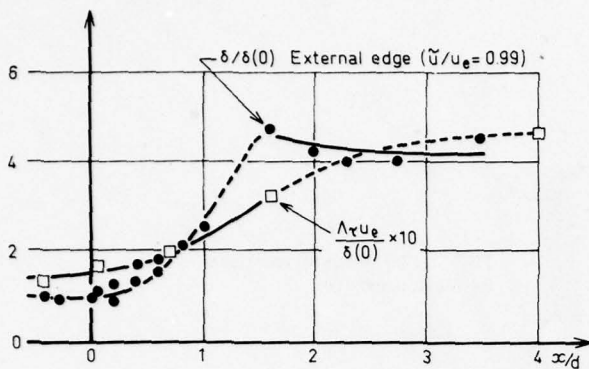
FIG. 8. Thickness of the turbulent flow—integral length.

FIG. 10. Conical coordinate system.

those coming from a region near the wall, are more accelerated than those which come from the outer part of the initial boundary layer. A striking fact is that in the expansion, there is a region the thickness of which is about $\delta(0)/4$, where the transverse velocity gradient $\partial \bar{u}_s /\partial y$ is less than the longitudinal gradient $\partial \bar{u}_s /\partial s$. This result will be used in Sec. IV D 2. (A nearly constant velocity region has been already found in the case of an accelerated turbulent boundary layer on a flat plate, at supersonic speeds.[39])

Figure 8 shows the evolution of the ratio $\delta/\delta(0)$ of the part of the shear layer $r > r_j$ which is external to the dividing streamline [see Fig. 6(a)]. The thickness $\delta(x/d)$ is defined by the condition $(\bar{u}/u_e) = 0.99$, where u_e is the mean velocity out of the turbulent flow, at the distance x/d. It seems that δ is not significantly altered by the expansion. Then, it increases rapidly, reaches a maximum in the re-attachment zone, and then decreases slightly. The evolution of the displacement δ^* and of the momentum δ^{**} thicknesses are qualitatively similar. The values of the integral scale of turbulence $\Lambda_\tau u_e /\delta(0)$ are given in the same figure. Λ_τ is $\int R \, dT$ and R is the autocorrelation function. The results will be noted in Sec. IV C 3.

The distributions of mean stagnation temperature $\bar{\theta}_T$ were also determined. Contours of the ratio $(\bar{\theta}_T - \theta_{T_\infty})/\theta_{T_\infty}$ are drawn in Fig. 9, where θ_{T_∞} is the value of $\bar{\theta}_T$
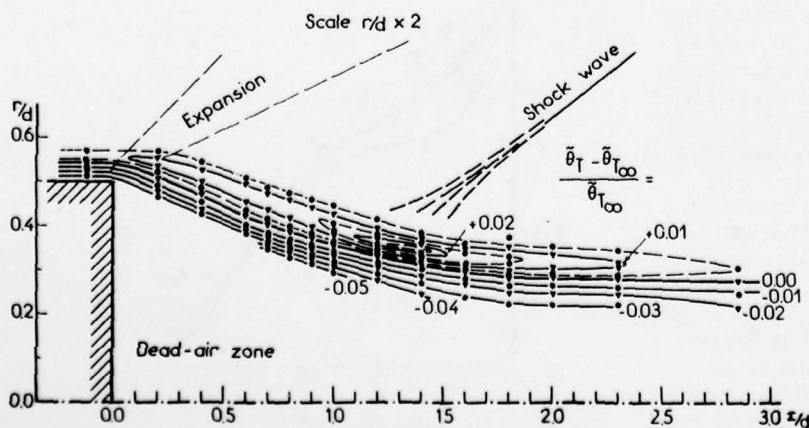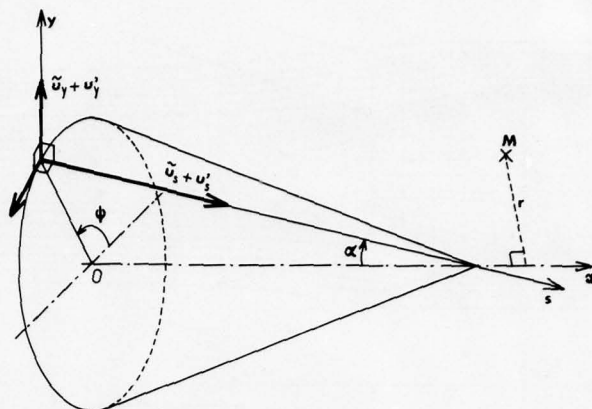
as measured in the initial external flow, upstream of the base. Note that departures from θ_{T_∞}, of several percent, seem to be slightly higher inside the detached flow than inside the initial boundary layer.

B. Distributions of turbulent momentum flux and of heat flux through mean streamlines

1. Method

The shear stress $\tau = -\overline{\rho u_s' u_y'} + \mu (\partial \bar{u}_s /\partial y)$ was computed by Dussauge[40] using the statistical equation of momentum.

The application is limited to the regions of the flow where the mean streamlines are quasi-parallel, that is, in the initial boundary layer, in part of the mixing layer, and in the wake at some distance downstream of the base. A system of conical coordinates was chosen (Fig. 10). The s direction coincides with the trace of the dividing surface. The statistical equation of momentum becomes

$$\bar{\rho}\bar{u}_s(\partial \bar{u}_s /\partial s) + \bar{\rho}\bar{u}_y(\partial \bar{u}_s /\partial y)$$
$$\simeq -\partial \bar{p}/\partial s - [\partial (\overline{r\rho u_s'^2})/\partial s]/r + [\partial (r\tau)/\partial y]/r . \quad (10)$$

Computations were performed by first assuming that the term $[\partial (\overline{r\rho u_s'^2})/\partial s]/r$ is negligible; the validity of this assumption was checked later. Then, it follows that
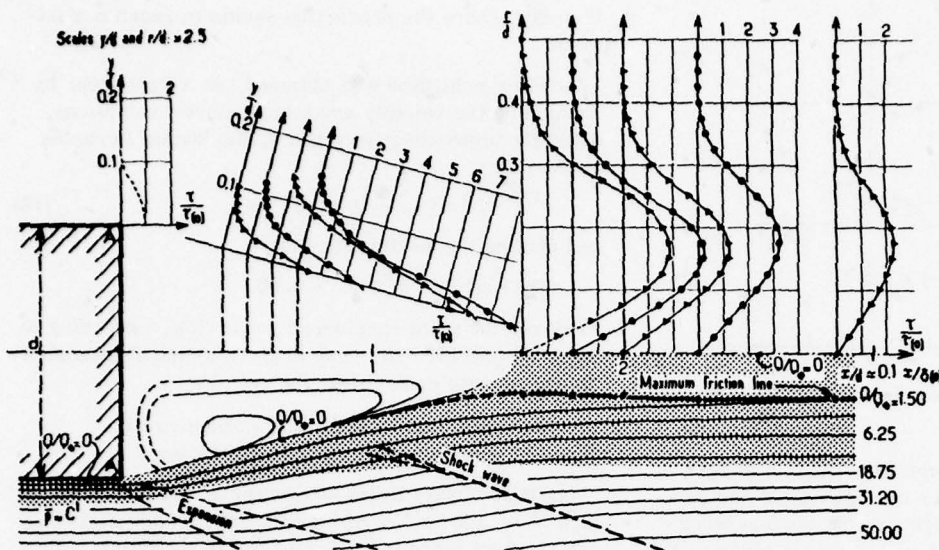

FIG. 9. Iso-contours of dimensionless mean-stagnation. temperature.

Scales y/d and r/d = 2.5

FIG. 11. Total friction stress.

$$\tau = \left\{ \int_{1.25}^{y} r[\overline{\rho}\overline{u}_s(\partial \overline{u}_s/\partial s) + \overline{\rho}\overline{u}_y(\partial \overline{u}_s/\partial y) + \partial \overline{p}/\partial s] \, dy \right\} / r \quad (11)$$

with $\rho \tilde{u}_y = -\left\{ \int_0^y [\partial(r\overline{\rho}\overline{u}_s)/\partial s] \, dy \right\} / r$ from the continuity equation. The application of the method requires a great number of measurements and intermediate graphical computations. The results are significant only when the sum of the terms on the right-hand side of Eq. (11) is not small compared with each of these terms. Following these considerations, results were obtained only for the regions where the pressure gradient is low enough, so that is $0.4 \leqslant x/d \leqslant 0.7$ and $x/d > 1.6$. The order of magnitude of the errors may reach about 30%.

For the initial boundary layer, the distribution of τ is assumed to be given by Maise and McDonald's method.[41]

An attempt was made to obtain the turbulent heat flux $c_p\overline{\rho\theta'u'}$ using a balance method similar to the previous one. It is based on the statistical equation of total enthalpy.[9,26] The sources of errors are important here, more than in the case of expression (4b) because the expression for the heat flux includes errors in τ.

2. Results

Profiles of $\tau/\tau(0)$ are given in Fig. 11. $\tau(0)$ is the value of the wall friction. $\tau_{max}(0)$ was computed by using a method developed by Michel,[42] and also deduced from measurements of velocity profiles.[19,40] For Reynolds number 33 600, both methods give the value $\tau_{max}(0) \simeq 58.5$ N/m^2. The friction coefficient is

$$C_f = \tau_{max}(0)/(\rho_\infty u_\infty^2/2) \simeq 0.0025$$

a value which is consistent with those published by Coles.[43] For Reynolds number 16 800, $\tau_{max}(0)$ is 32.8 N/m^2 and C_f is 0.0029. Dealing with the mixing layer, the maximum values of τ were not reached in the profile measurements, but a reasonable extrapolation of graphical computations shows that they are located in the vicinity of the dividing streamline where the velocity gradient is a maximum, as in subsonic flows.[44] Down-

stream of the dead air zone, τ has maxima approximately where $\partial \tilde{u}_s/\partial y$ have maxima. At relatively large distances, $(x/d) > 2.5$, distributions of τ are not far from those of an incompressible self-preserving wake[18,45] (Fig. 12). Departures come partly from differences in mean density.

Along the flow, τ_{max} increases in the mixing layer and apparently reaches an absolute maximum, several times greater than the initial value $\tau_{max}(0)$, at a distance $x/d \leqslant 1$ where the pressure gradient is a maximum. Then, it decreases rapidly, Fig. 11. With respect to modeling the turbulent flows, first, it may be noticed that in the mixing layer, between the two stations $x/d = 0.4$ and $x/d = 0.7$, τ_{max} increases up to 4–6 times, although $\partial \tilde{u}_s/\partial y$ decreases slightly, about (30%), and $\overline{\rho}$ does not change appreciably along the line of the maxima of τ. So, the increase in τ_{max} is essentially due to that of $-\overline{u_s'u_y'}$. These results show that using a simple gradient type assumption would not be justified.

Then, attention is paid to the evolution of the ratio $\tau_{max}/\overline{\rho}\Delta U^2$ which makes it possible to compare it with a term involving the velocity scale ΔU of the mean flow,
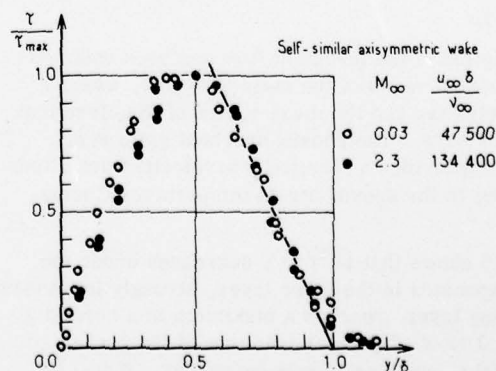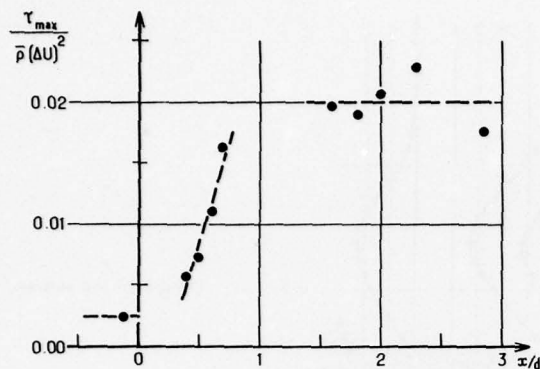

FIG. 12. Test of similarity.

FIG. 13. Dimensionless maximum friction.

the typical value τ_{max} of turbulent friction. $\bar{\rho}$ is the density at the location where τ is a maximum and $\Delta U = u_e - (\bar{u})_{r=0}$ is the velocity defect, at the section being considered. The evolution of $\tau_{max}/\bar{\rho} \Delta U^2$ is given in Fig. 13. Its value is expected to vary from the initial boundary layer to the wake. Indeed, measurements show that it increases monotonically along the mixing layer. In the wake, no important evolution is discerned, but this could be due to the scattered results and to the lack of information downstream. Figure 14 gives an indication about the evolution along the flow of the dimensionless heat flux $C_p \overline{\rho \theta' u_y'}/\rho_\infty u_\infty i_\infty$ and that of the momentum flux $\tau/\rho_\infty u_\infty^2$, as determined along a mean streamline, here $Q/Q_* \simeq 2.25$, where i_∞ is the enthalpy per unit volume in the initial outer flow. Both quantities suggest a similar qualitative behavior, apparently reaching a maximum in the recompression zone. Although these values cannot be accurate, it is reasonable to think that these results give a correct idea of the phenomena.

Results for the behavior of a boundary layer subjected to compression were published by Rose[46] and by Rose and Childs,[14] in the case of a shock wake boundary without separation. They found that the fluxes $-\overline{\rho u_s' u_y'}$ and $C_p \overline{\rho \theta' u_y'}$ were multiplied at least by a factor of five while the velocity gradient was increased by only a factor of two.

C. Velocity and temperature fluctuations autocorrelations. Integral scale

1. Description of the turbulent flow through hot-wire measurements

A description of the turbulent flow has been obtained through measurements of the ratio $(\overline{e'^2})^{1/2}/\bar{e}$, where e' are the fluctuating and the mean values of the electrical signal of the wire. The chosen overheat ratio is $a_w' = 0.20$ which provides a sensitivity to velocity fluctuations almost equal to the sensitivity to temperature fluctuations.[26]

Figure 15 shows that $(\overline{e'^2})^{1/2}/\bar{e}$ decreases under the effect of expansion in the inner layer, strongly increases in the mixing layer, reaches a maximum in a core at a distance $1.3 < x/d < 2$ greater than that of the presumed maximum of τ, and then slowly decreases. It will be further seen (Sec. IV D 3) that this distance is larger

than that where the production seems to reach a maximum.

Another indication was obtained, as a first step, by separating the velocity and temperature fluctuations, using the approximation given by the strong Reynolds analogy:

$$(\overline{\theta'^2})^{1/2}/\bar{\theta} \simeq (\gamma - 1)M^2(\overline{u_s'^2})^{1/2}/\bar{u}_s \qquad (12)$$

and making the assumption that

$$r_{\theta u} = \overline{\theta' u_s'}/(\overline{\theta'^2 u_s'^2})^{1/2} = -0.80.$$

whatever the point considered in the flow, according to Figs. 16 and 17. The results given by more extensive measurements do not alter the results.

2. Distribution of "modes" and normal stress. Velocity-temperature correlation coefficient

(a) The velocity fluctuations may be characterized by $(\overline{u_s'^2})^{1/2}/u_\infty$ and $\overline{\rho u_s'^2}/\rho_\infty u_\infty^2 \simeq \overline{\rho u_s'^2}/\rho_\infty u_\infty^2$, where ρ_∞ and u_∞ are constant since they correspond to the initial potential flow. Distributions of these ratios are given in Figs. 18 and 19 with respect to the dimensionless distance $(r - r_J)/\delta(0)$, where $\delta(0)$ is the thickness of the initial boundary layer. For the expansion fan, they both decrease along streamlines. At a distance $x/d \simeq 0.1$ in the region $(r - r_J)/\delta(0) \ll 1$ which is expected to be slightly affected by intermittency, the maximum observed reduction of $(\overline{\rho u_s'^2})/2$ exceeds 50% while $\bar{\rho}$ decreases about 25%; farther from the dividing streamline, $(r - r_J)/\delta(0) > 0.6$, a slight increase in the levels occurs. In the re-attachment zone, where the recompression acts, at a distance downstream from the base $0.7 < x/d < 1.6$, there is an important increase in the two terms, as shown in Figs. 18 and 19. As for the term $\overline{\rho u_s'^2}$, its maximum is about three times that of the greatest value measured downstream of the expansion; despite the strong increase in mean pressure, the contribution of $\bar{\rho}$ to the observed increase of $\overline{\rho u_s'^2}$ is small.

These results confirm the large effect associated with dilatation, and more generally with other extra strain rates, such as streamwise curvature or lateral divergence, as emphasized by Bradshaw.[16] An attempt to relate the evolution of the fluctuation velocity level to that of its production will be made in Sec. IV D.

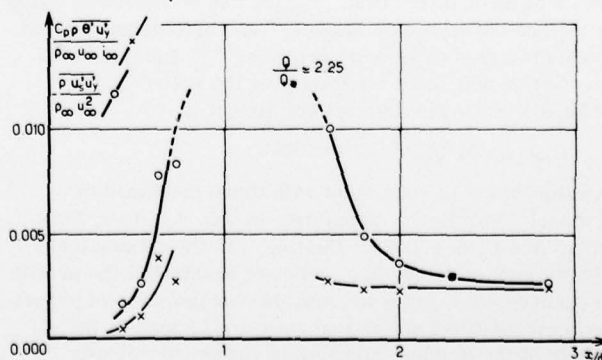(b) The temperature fluctuations are characterized
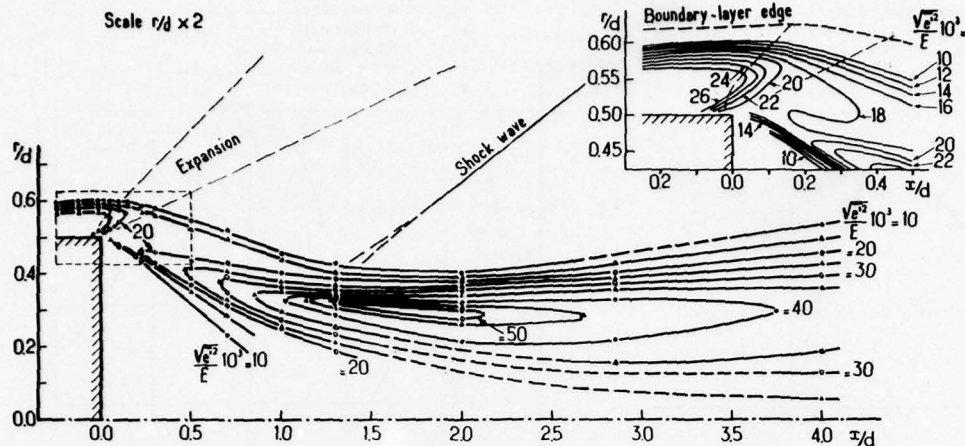

FIG. 14. Heat- and momentum turbulent fluxes.

Gaviglio, Dussauge, Debieve, and Favre

Scale r/d × 2

FIG. 15. Iso-contours of dim dimensionless rms output voltage of the hot-wire anemometer (uncorrected values).

here by the ratio $\overline{(\theta'^2)}^{1/2}/\theta_\infty$. Its evolution along the flow can be seen in Fig. 20; it seems to be smaller than that of $\overline{(u_s'^2)}^{1/2}/u_\infty$. Indeed, the relationship (12) which expresses the strong Reynolds analogy applies in this case, as indicated by Fig. 16, although its demonstration[47] requires that there be no pressure gradient. From (12) it may be seen that the evolutions along the flow of M^2 explain the fact that the relative variations of the temperature fluctuations are smaller than those of the velocity.

(c) In Fig. 17, measured values of the correlation coefficient $r_{\theta u}$ between θ' and u_s' are plotted for various sections. Whatever the location of the point, $r_{\theta u}$ being considered does not differ much from the usual values found in self-preserving flows. These results suggest that important accelerations and pressure gradients do not strongly affect the mechanism by which the temperature fluctuations are diffused by velocity fluctuations.

3. Spectral distributions of energy. Autocorrelations. Integral length scales

Some measurements of the spectral distribution of energy were made in order to insure that the initial
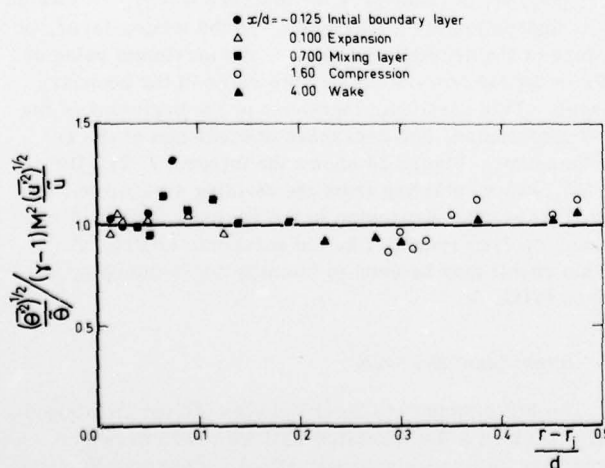
boundary layer is fully turbulent, and to check the possible existence, after expansion, of intermittency provoked by reverse transition. Such a phenomenon was not found, at a first approximation. This conclusion is confirmed by the shape of the autocorrelation curves [Figs. 21(a) and (b)] the measurements of which were performed for $a'_w = 0.20$.

Distributions of the integral scales of times $\Lambda_\tau = \int_0^\infty R(T)dT$ were obtained directly from [Figs. 21(a) to (e)]. Then, the results were corrected as indicated in Sec. IIC. They are presented in Fig. 22. Λ_τ is given as a function of the distance $(r - r_j)/\delta$ to the dividing streamline, where δ is the local thickness of the flow. In the regions $(r - r_j)/\delta < 0.6$ where the intermittency is expected to be weak, whatever the distance to the base (except, that in the fluctuating part of the dead air for $x/d < 0.6$), Λ_τ depends slightly on the distance $(r - r_j)/\delta$. The evolution of the integral length scale $\Lambda_x = u_e \Lambda_\tau$ as

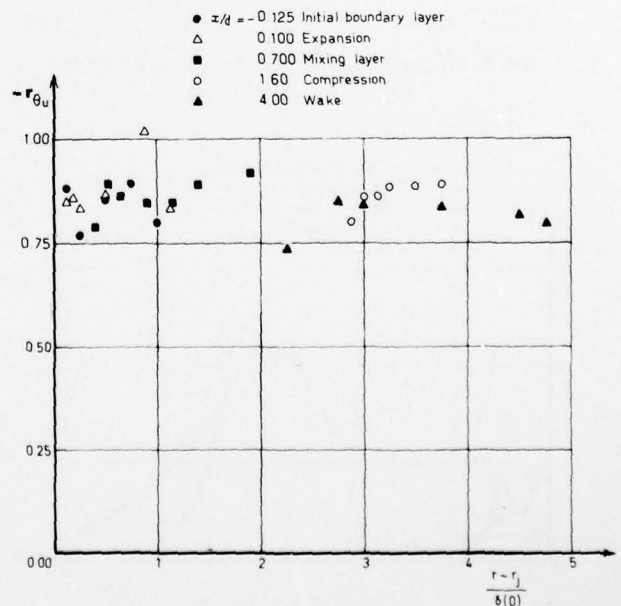FIG. 16. Test of application of the strong Reynolds analogy.

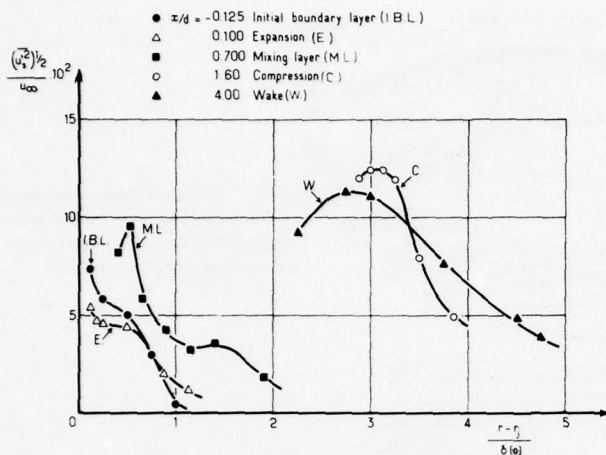FIG. 17. Velocity-temperature correlation coefficient.

FIG. 18. Distributions of velocity fluctuation level.

determined for $(r - r_j)/\delta = 0.5$, and the thickness $\delta(x/d)$, are compared in Fig. 8. They both increase along the flow. A rough estimate gives $\Lambda_x \simeq 0.1 \delta$.

D. Turbulence production. Role discussion

As noted in Sec. IIA, the streamwise evolution of the flow depends on production, diffusion, and dissipation. Since the latter two cannot be safely measured or estimated, attention is mainly focused on production, which plays an important role in the development of incompressible separated flows.[48] Both production of kinetic energy of turbulence $\overline{(\rho u'_i u'_i)}/2$ and production for that part of the energy $\overline{(\rho u'^2_s)}/2$ which has been measured, will be considered. Using the coordinate system of Fig. 4, they are

$$\mathbf{Pr} \simeq (-\bar{\rho}\,\overline{u'_s u'_y}\,\partial \tilde{u}_s / \partial y) + (-\bar{\rho}\,\overline{u'^2_s}\,\partial u_s / \partial s) + \bar{\rho}\,\overline{u'^2_y}\,\partial \tilde{u}_s / \partial s$$

$$+ \bar{\rho}\,\overline{u'_s u'_y}\,\tilde{u}_s / R + (\bar{\rho}\,\overline{u'^2_y}/\bar{\rho})\,D\bar{\rho}/Dt + (\overline{\rho'\,u'_s}/\rho)\,\partial \bar{p} / \partial s$$

$$+ (\overline{\rho'\,u'_y}/\bar{\rho'})\,\partial \bar{p} / \partial y \, , \tag{13}$$

$$\mathbf{Pr}_s \simeq -\bar{\rho}\,\overline{u'_s u'_y}\,\partial \tilde{u}_s / \partial y + (-\bar{\rho}\,\overline{u'^2_s}\,\partial \tilde{u}_s / \partial s) + (\overline{\rho'\,u'_s}/\bar{\rho})\,\partial \bar{p} / \partial s \, , \tag{14}$$

FIG. 19. Distributions of $\bar{\rho}\,\overline{u'^2_s}$.
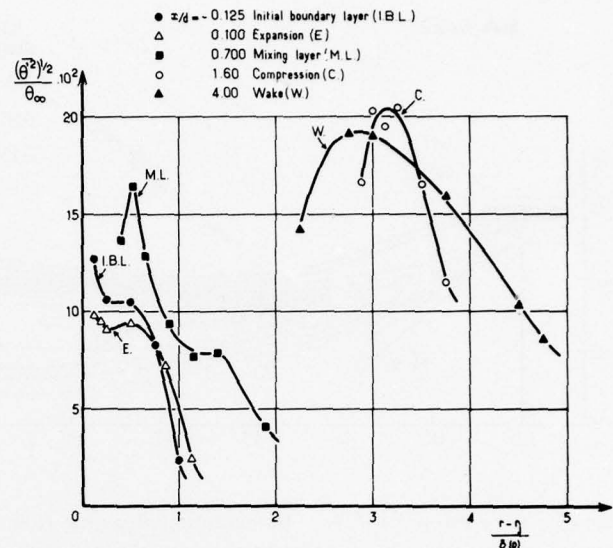

FIG. 20. Distributions of temperature fluctuation level.

where $\overline{\rho u'_i u'_j}$ is approximated by $\bar{\rho}\,\overline{u'_i u'_j}$. The different terms of $\mathbf{Pr}_s$ are measured or estimated and compared to each other. Estimations are made using the following assumptions: the temperature fluctuations are essentially isobaric,[9] such as $\rho'/\bar{\rho} \simeq -\theta'/\bar{\theta}$; the levels of velocity and temperature fluctuations verify the strong Reynolds analogy (12); the correlation coefficients are not changed very much by the effects of gradients. As for the special effect of the expansion, the ratio $\overline{u'^2_s}/\overline{u'^2_y}$ which is related to the anisotropy of the turbulent field is changed little, since "the full effect of dilatation on the turbulence structure is not felt as soon as the dilatation begins".... [16]

The conventional term $\mathbf{Pr} \simeq \tau\,\partial \tilde{u}_s / \partial y$ has been studied extensively. Distributions of this term are given in Fig. 23. $\mathbf{Pr}$ is divided by the maximum value $\mathbf{Pr}_{max}(0) \simeq \tau^2(0)/4\mu$ of this term reached in the initial viscous part of the boundary layer. [In Refs. 18, 19, and 40, $\mathbf{Pr}$ was compared to $\tau^2(0)/\mu$.] Whatever the section, the maximum of $\tau(\partial \tilde{u}_s / \partial y)$ is reached at the distance $(r - r_j)/\delta$ for which τ is approximately a maximum. In the mixing layer, because of the decrease in $\partial \tilde{u}_s / \partial y$, the maximum value of $\mathbf{Pr}$ is not far from the maximum value in the boundary layer. This maximum increases at the beginning of the recompression, and decreases downstream of the reattachment. Figure 24 shows the integral $I = 2\pi\int_0^\delta [r\tau \times (\partial \tilde{u}_s / \partial y)]\,dy$ starting from the dividing streamline. It decreases after expansion in the region $x/\delta(0) < 0.1$ and then, evolves roughly like the maximum of $\mathbf{Pr}(x/d)$. This result may be used to simplify the comments, in Sec. IVD3.

1. Initial boundary layer

The initial boundary layer behaves almost as a boundary layer on a flat insulated wall with zero pressure gradient (thin layer approximation). The term $\mathbf{Pr} \simeq \tau\partial \tilde{u}_s / \partial y$ is the most important of all.
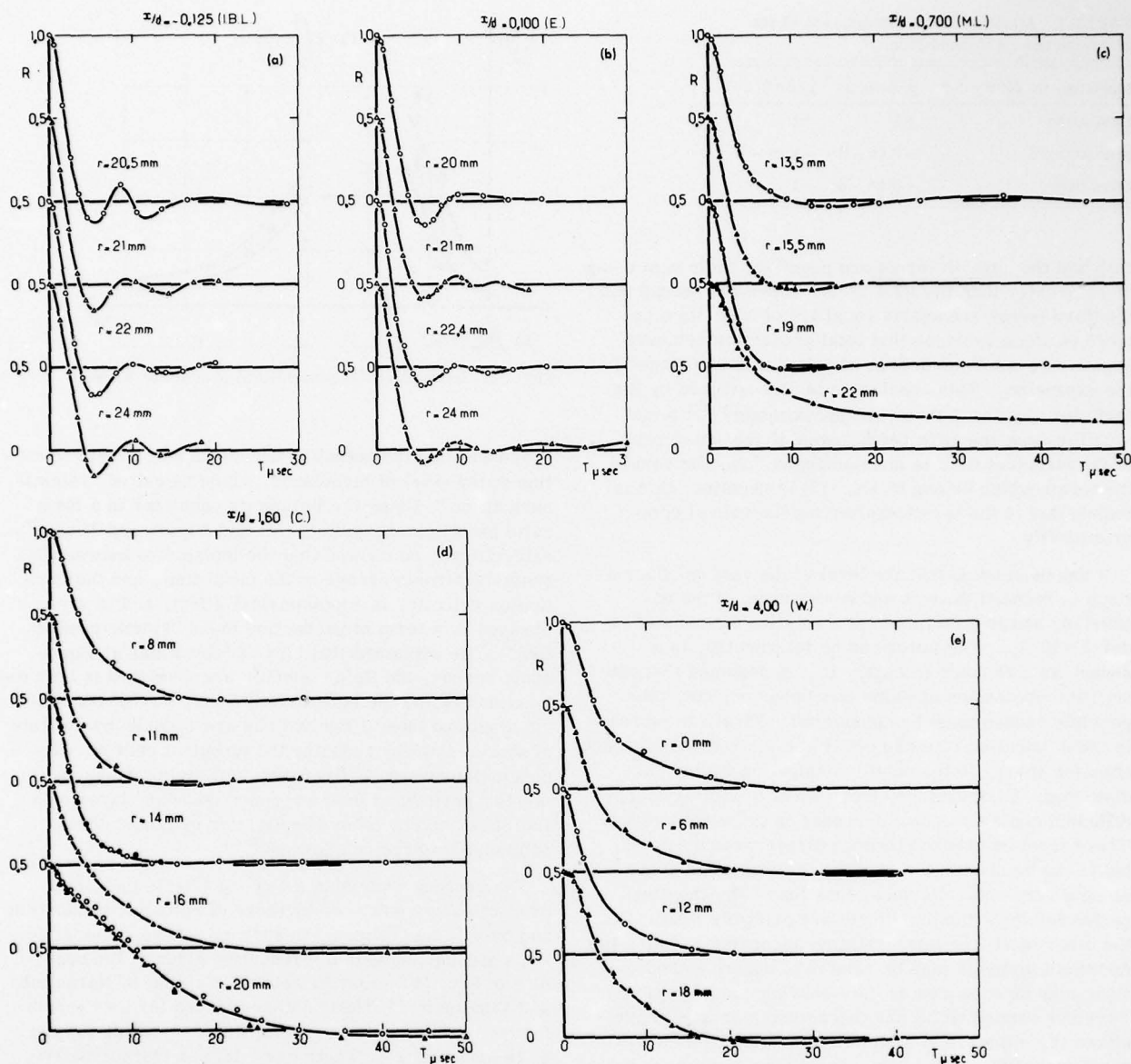
FIG. 21. (a)–(e). Autocorrelations.

2. Expansion region

At small distances from the dividing streamlines, say $y/\delta < 0.4$, a strong longitudinal acceleration takes place and the velocity gradient $\partial \bar{u}_s / \partial y$ is small [see Fig. 5(b) and Sec. IVA]. Both expressions (13) and (14) of the production seem to be negative. For instance, in the expansion fan, at the streamwise distance $[s/\delta(0)] = 0.2$, and for the two distances $[y/\delta(0)] = 0.2$ and 0.3 in the radial direction, reasonable comparisons of the terms on the right-hand side of Eq. (14) give the results presented in Table I.

Some comments may be made, about the production of kinetic energy of turbulence **Pr**, under the assumptions made in Sec. IVD 1. Only the first and the third terms on the right-hand side of Eq. (13) are positive. The

FIG. 22. Integral time scale.

TABLE I. Equation (14)—Comparison of the terms on the right-hand side.

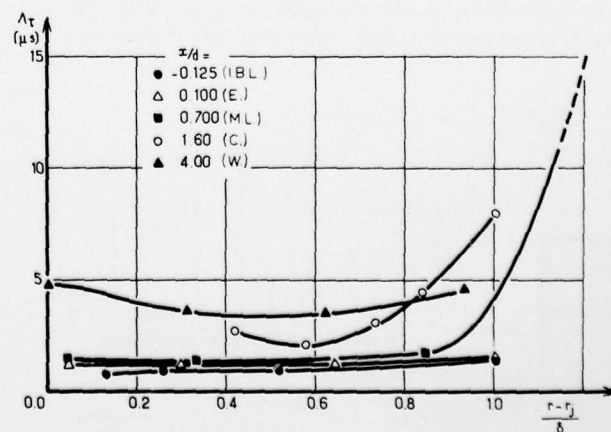| location:	$[s \ \delta(0)] = 0.2$	$y/\delta = 0.2$	$y/\delta = 0.3$
first term		$+1$	$+1$
second term		-3 to -6	-1 to -2
third term		-3 to -6	-1

fifth and the seventh terms are negative; their sum being much greater than the first term. Since the second and the third terms are nearly equal but of opposite sign, there is some evidence that total production remains negative, even if the degree of anisotropy is changed in the expansion. This conclusion is strengthened by the fact that the third term is approximately M^2 times smaller than the fifth term, even if the anisotropy of the turbulent field is much changed. So, the sum of the terms which belong to Eq. (13) is negative; this is mainly due to the terms expressing the role of compressibility.

It has been noted that the level of the vortical fluctuations is reduced through and downstream of the expansion, and is a minimum at a relative distance of order $\delta \simeq 10 \ \Lambda_x$. The latter can be interpreted, in a sense, as a relaxation length, if it is assumed that the negative production explains this behavior; but, other possible causes must be considered. First, an increase in the dissipation rate can occur if the large eddies which transfer energy to the small, dissipating eddies, are distorted. Furthermore, local effect of lateral energy diffusion could produce a decrease in turbulent energy. This cannot be checked through direct measurements, but it can be observed that since the expansion acts along a very short distance, less than $\delta(0)$, the dissipation and the diffusion effects are probably weak. On the other hand, the interpretation according to which the decrease in levels may be related to negative production, may be enhanced by the following considerations. Previous experimental and theoretical works[10,11] have shown the influence of a high acceleration on a supersonic turbulent shear layer. Sternberg studied the behavior of such a layer which develops on the surface of a cone and is subjected to a rapid expansion fan, without separation, at Mach numbers of 3 and 3.5. Visualizations and boundary layer recovery-factor mea-
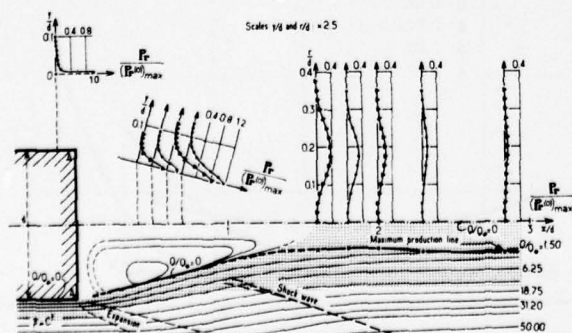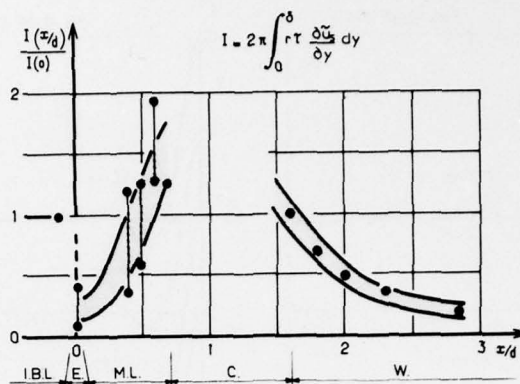
FIG. 23. Conventional production term.

FIG. 24. Integral of the conventional production term.

surements led the author to deduce an important reduction in the level of turbulence, which he called "relaminarization." Using the Helmholtz equations in a form valid for a compressible fluid, and Ribner and Tucker's calculations, he showed that the interaction between the quasi-isentropic change in the mean flow, and the fluctuation velocity, is a geometrical effect, and is expressed by a term of production (here "kinetic production"). He explained that, for accelerations at supersonic speeds, the fluid elements are stretched in both the longitudinal and the lateral directions, so that the longitudinal and lateral fluctuations are reduced by the rate of strain, thereby reducing the turbulent energy. His conclusions were confirmed by Morkovin's measurements[11] performed in an expanded boundary layer on a flat plate, and by other results, for instance, those published by Page and Sernas.[13]

The present study shows how the effects of kinetic production are enhanced by those of enthalpic production and by volume changes. In addition, these considerations and the analysis of production given at the beginning of Sec. IVD, may be related to a study by Narasimha and Viswanath.[49] These authors looked for a criterion for the occurrence of turbulent flows reverting toward a "laminar state". Their basic idea is that during reversion the Reynolds stresses have little influence in a large part of the flow. They consider the total pressure drop $\Delta \bar{p}$ over the expansion. They compare many available experiments, and conclude that the occurrence of reversion is governed by the expression $(- \partial \bar{p} / \partial s)/[\tau_{max}(0)/\delta] \sim \Delta \bar{p}/\tau_{max}(0)$ and is likely whenever this ratio is greater than about 70. In the present analysis, the role played by the mean pressure gradient and by the tangential stresses, respectively, appears when, for instance, expression (14) is transformed as follows: The second and third terms may be grouped. Using the simplified equation $(\partial \tilde{u}_s / \partial s) \simeq - (\partial \bar{p} / \partial s)/\overline{\rho} \tilde{u}_s$, the sum of these terms is

$$- \overline{\rho u_s'^2} \ \partial \tilde{u}_s / \partial s + (\overline{\rho' u_s'}/\overline{\rho}) \partial \bar{p}/\partial s$$
$$\simeq (\overline{u_s'^2}/\tilde{u}_s)(\partial \bar{p}/\partial s) [1 - (\gamma - 1) M^2 r_{\theta u}] < 0 .$$

Then, $\mathbf{Pr}_s$ reads

$$\mathbf{Pr}_s = (\overline{u_s'^2}/\tilde{u}_s^2) \tilde{u}_s (\partial \bar{p}/\partial s) [1 - (\gamma - 1) M^2 r_{\theta u}]$$

$$\times \left[1 + \frac{(\tau/\bar{u}_s)\,\partial \bar{u}_s/\partial y}{(u_s'^2/\bar{u}_s^2)\left[1 - (\gamma-1)M^2 r_{\theta u}\right]\partial \bar{p}/\partial s} \right] \qquad (15)$$

The expression for $\mathbf{Pr}_s$ is negative if the absolute value of the ratio $(\partial \bar{p}/\partial s)/\left[(\tau/\bar{u}_s)\,\partial \bar{u}_s/\partial y\right]$, which is of the order of $\Delta \bar{p}/\tau_{max}(0)$, is great enough. This ratio varies from point to point in the flow, but, since the interaction of the expansion fan with the layer takes place over a length which is of order δ, it increases with increasing $-\Delta \bar{p}/\tau_{max}(0)$. Correspondingly, when this parameter is great enough, the production is negative, and reversion occurs, a fact which emphasizes the role of the production in the behavior of a flow subjected to an expansion. In the case of the present experiments, $-\Delta \bar{p}/\tau_{max}(0)$ has the value 46 which, following the detailed results given by Narasimha and Viswanath, seems to correspond to the beginning of the reversion occurrence.

3. Mixing layer and recompression region

The conventional term $\tau\,\partial \bar{u}_s/\partial y$ is the most important of all in expressions (13) and (14). This is due to the fact that the absolute value of the pressure gradient $\partial p/\partial s$ is less than in the expansion, at least by an order of magnitude. Therefore, as a first approximation both $\mathbf{Pr}$ and $\mathbf{Pr}_s$ evolve like the conventional production term. The maximum value of this term and its integral $I(x/d)$, taken in sections orthogonal to the mean flow, rapidly increase in the mixing layer; each seems to be a maximum at a distance $x/d \lesssim 1$, as may be inferred from Figs. 23 and 24. Correspondingly, the measured term $\overline{(\rho u_s'^2)}/2$ is a maximum downstream, at the abscissa $x/d \simeq 3$. In a sense, the distance $2\delta \simeq 20\Lambda_x$ from the section where the production seems to be a maximum appears as a relaxation distance.

However, production alone is not a sufficient guide to the behavior of turbulent energy in the disturbed flow, since other phenomena may contribute to the increase in the level of turbulence in the mixing layer. The dissipation may be decreased in this region where the integral scale increases (Fig. 8). On the contrary, a local increase in transverse diffusion related to that in kinetic turbulent energy would tend to moderate the increase of the levels, but these terms of dissipation and diffusion are not measurable. So, other experimental investigations are needed to explain the whole story of the flow.

V. CONCLUSIONS

Our aim was to follow the development of the kinetic turbulent energy in a flow strongly out of equilibrium, at supersonic speed, and to get information about the turbulent mechanisms. This has been done by analyzing the behavior of the flow mainly through turbulence production which can be known in a relatively accurate way. The experimental configuration is the near wake which develops downstream of a truncated longitudinal cylinder

Physical and analytical considerations have shown that, in the presence of dilatation, the total production of kinetic turbulent energy may be separated into kinetic production and enthalpic production. The kinetic pro-

duction involves an isovolumetric part and a dilatation part; the enthalpic production is due to the density-velocity correlation interacting with the mean pressure gradient. The isovolumetric production often seems to be positive, as in subsonic flows; the dilatation and the enthalpic productions are either positive or negative. When the level of temperature fluctuations increases with Mach number, it can be expected that the importance of the enthalpic production also increases. It has been useful to consider the effects of compressibility, by making a difference between the total production and the isovolumetric production. That difference involves the dilatation production related to mean density changes, and the enthalpic production related to mean pressure gradients.

The analysis of the experimental results, and comparison with those obtained by other authors for the behavior of compressible flows strongly out of equilibrium, exhibit two complementary but opposite features, which can be helpful in understanding such phenomena and their calculation.

(a) Some properties do not seem to be altered much by the presence of strong velocity and pressure gradients. This may be considered as a possible extent of the well known Morkovin's hypothesis about the essential dynamics of self-preserving supersonic flows and may be supported by the following results. In the mixing layer surrounding the recirculating zone, the maxima of Reynolds stresses are located in the vicinity of the dividing streamline, as in low-speed flows. The momentum and heat-fluxes through the mean mass-weighted streamlines seem to have an analogous development along the flow. The spatial integral scale and the thickness of the flow evolve in a comparable way. The velocity-temperature correlation coefficient is not noticeably changed by a rapid expansion or by a compression. In addition, the ratio of the levels of velocity and entropy fluctuations is approximately that given by the strong Reynolds analogy, although the latter has been established under the assumption that the pressure gradient is zero.

(b) Conversely, important departures from the properties of incompressible flows are noted, which are characteristic of expanded or compressed flows. With respect to prediction methods, discrepancies from gradient type assumptions may be noted, particularly in the mixing zone.

More generally, a strong negative pressure gradient, for example in an expansion fan with important accelerations, may provide a negative production. As for the part of the production related to the longitudinal velocity fluctuations, the conventional term is reduced and the absolute value of the other terms, which are usually negligible in self-preservative flows, are increased. Such supplementary terms are negative, so that this production may also be negative. As a consequence, a decrease in the velocity fluctuation level is found at some relaxation distance downstream. The production of the total kinetic energy of turbulence, i.e., involving the three components, is negative whenever the previously mentioned part of the production is negative.

This is due to the terms which express the explicit effects of compressibility. Taking into account results given by other authors, there is some evidence that production plays a very important role in the interaction of a sheared layer and of a strong negative pressure gradient.

In addition, in free mixing layers developing in a positive adverse pressure gradient, a large increase in production is found, which is essentially related to the *conventional* term of production. Correlatively, although production does not tell the whole story of the flow, an increase in the velocity fluctuation level is found at some relaxation distance downstream.

Finally, the results show that a theoretical and an experimental study of the production of turbulent kinetic energy may provide useful information about the turbulent mechanisms in flows strongly out of equilibrium, at supersonic speeds.

ACKNOWLEDGMENTS

[1] L. S. G. Kovasznay, J. Aeronaut. Sci. **20**, 657 (1953).
[2] J. Laufer, AIAA J. **7**, 706 (1969).
[3] M. V. Morkovin, in *Mécanique de la Turbulence* (Centre National de la Recherche Scientifique, Paris, 1962), p. 367; see also *The Mechanics of Turbulence* (Gordon and Breach, New York, 1964), p. 367.
[4] A. Kistler, Phys. Fluids **2**, 290 (1959).
[5] A. Demetriades, Phys. Fluids **11**, 1841 (1968).
[6] A. Demetriades, AIAA J. **6**, 432 (1968).
[7] A. Demetriades, Phys. Fluids **12**, 24 (1969).
[8] L. Crocco, AIAA J. **1**, 2723 (1963).
[9] J. Laufer, in *Proceedings of Compressible Turbulent Boundary Layers Symposium*, NASA SP 216 (1969), p. 1.
[10] J. Sternberg, Ballistic Research Laboratories Report 906, U. S. Army, Aberdeen Proving Ground (1954).
[11] M. V. Morkovin, in *Proceedings 1955 Heat Transfer and Fluid Mechanics Institute* (Stanford University, Stanford, Calif., 1955), p. 6.
[12] J. E. Lewis and W. Behrens, AIAA J. **7**, 664 (1969).
[13] R. H. Page and V. Sernas, AIAA J. **8**, 189 (1970).
[14] W. C. Rose and M. Childs, J. Fluid Mech. **65**, 177 (1974).
[15] M. Sireix, in *Flow Separation*, AGARD CP 168 (Advisory Group for Aerospace Research and Development, North Atlantic Treaty Organization, Paris, 1975), Paper 12.
[16] P. Bradshaw, J. Fluid Mech. **63**, 449 (1974).
[17] J. Gaviglio, P. Tchepidjian, and J. P. Dussauge, C. R. Acad. Sci. Paris Sér. A **275**, 853 (1972).
[18] J. P. Dussauge, J. Gaviglio, and A. Favre, C. R. Acad. Sci. Paris Sér. B **278**, 953 (1974).
[19] J. P. Dussauge and J. Gaviglio, Recherche Aérospatiale 3, (1975), p. 145.
[20] A. Favre, C. R. Acad. Sci. Paris Sér. A **246**, 2576 (1958); **246**, 2723 (1958); **246**, 2839 (1958); **246**, 3216 (1958).
[21] A. Favre, *Problems of Hydrodynamics and Continuum Mechanics* (Society for Industrial and Applied Mathematics, Philadelphia, 1969), p. 246.
[22] J. C. Rotta, Z. Phys. **131**, 51 (1951).
[23] P. Bradshaw and D. H. Ferries, J. Fluid Mech. **46**, 83 (1971).
[24] D. C. Wilcox and I. E. Alber, in *Proceedings* 1972 *Heat Transfer and Fluid Mechanics Institute* (Stanford University, Stanford, Calif., 1972), p. 231.
[25] A. Favre, C. R. Acad. Sci. Paris Sér. A **273**, 1087 (1971).
[26] J. F. Debieve, Thèse de Doctorat de Spécialité, Université II, Marseille (1976).
[27] G. Gontier, *Mécanique des Milieux Déformables* (Dunod, Paris, 1969), Chap. 1.
[28] H. Tennekes and J. L. Lumley, *A First Course in Turbulence*, (MIT Press, Cambridge, Mass., 1972), p. 60.
[29] J. Gaviglio, J. P. Dussauge, J. F. Debieve and A. Favre, C. R. Acad. Sci., Paris Sér. B **282**, 445 (1976).
[30] I. Wygnanski, M. Sokolov, and D. Friedman, J. Fluid Mech. **69**, 283 (1975).
[31] R. F. Blackwelder and L. S. G. Kovasznay, J. Fluid Mech. **53**, 61 (1972).
[32] M. A. Badri Narayanan and V. Ramjee, J. Fluid Mech. **35**, 225 (1969).
[33] J. Gaviglio, C. R. Acad. Sci., Paris Sér. A **273**, 634 (1971).
[34] L. S. G. Kovasznay, J. Aeronaut. Sci. **17**, 565 (1950).
[35] M. V. Morkovin, AGARDograph 24 (1956).
[36] L. R. Bissonnette and H. Burnage, C. R. Acad. Sci. Paris, Sér. A **273**, 928 (1971).
[37] J. Laufer and R. Mc Clellan, J. Fluid Mech. **1**, 276 (1956).
[38] G. Comte-Bellot, in *Annual Review of Fluid Mechanics* (Annual Reviews, Palo Alto, Calif., 1976), Vol. 8, p. 209.
[39] R. Michel, C. Quemard, and M. Elena, Recherche Aérospatiale No. 128 (1969), p. 33.
[40] J. P. Dussauge, Thèse de Docteur-Ingénieur, Université de Provence, Marseille (1974).
[41] G. Maise and H. Mc Donald, AIAA J. **6**, 73 (1968).
[42] R. Michel, *Couches Limites Frottement et Transfert de Chaleur*, Ecole Nationale Supérieure de l'Aéronautique, Paris (1963).
[43] D. Coles, J. Aeronaut. Sci. **21**, 433 (1954).
[44] H. Rouse, in *Proceedings of the International Association for Hydraulic Research*, Dubrovnik, Yugoslavia, 1961, paper 94; also in *Selected Writings of Hunter Rouse*, edited by J. F. Kennedy and E. O. Macagno (Dover, New York, 1971), p. 396.
[45] M. S. Uberoi and P. Freymuth, Phys. Fluids **13**, 2205 (1970).
[46] W. C. Rose, Ph.D. Thesis, University Washington (1972).
[47] A. D. Young, College of Aeronautics, Cranfield, England, Report 42 (1951).
[48] H. M. Hieu, Thèse de Docteur ès Sciences, Institut National Polytechnique de Toulouse (1976).
[49] R. Narasimha and P. R. Viswanath, AIAA J. **13**, 693 (1975).

Mean velocity and turbulent energy closures for flows with drag reduction

M. Poreh and S. Hassid[a]

Technion-Israel Institute of Technology, Haifa, Israel

Earlier models for flows with drag reduction are reviewed and compared with a new energy-dissipation closure which describes the observed effects of drag reduction on the mean velocity, turbulent energy, and turbulent length-scale distributions, and suggests a new maximum drag reduction law related to the onset of drag reduction.

INTRODUCTION

The advance of semi-empirical models for turbulent flows with drag reduction closely resembles the evolvement of models for turbulent, Newtonian flows, although the latter had been considerably developed when the study of drag reduction started. Initially, simple laws were proposed for describing the distinct gross effect of drag reduction on different regions. These were followed by mean velocity closures capable of describing the mean transfer of momentum, and predicting heat and mass transfer. Finally, turbulent-energy closures were investigated in an attempt to describe the change in the structure of turbulence associated with drag reduction. No Reynold-stress closures have been proposed for flows with drag reduction, but some work in this direction has already begun.

Of course, use has been made at each stage of knowledge, experience, and insight which had been accumulated earlier. Since models for flows with drag reduction should be valid in the limiting case of zero drag reduction, researchers primarily attempted to extend known successful models to the more general case and to form universal models for turbulent flows with and without drag reduction. In so doing it was found that some empirical models could be extended to the general case in a simple and logical way, whereas others, which gave almost identical results in Newtonian flows, could not.

The basic inherent limitations and inadequacies of semi-empirical theories and models for turbulent flows are well known. So is their extreme usefulness in systemizing experimental data, in predicting results of similar experiments, in describing the structure of the flows, and in advancing the development of more rigorous theories. The usefulness and limitations of semi-empirical models for flows with drag reduction are expected to be similar.

We shall briefly review various closures for flows with drag reduction, and discuss their merits and limitations.

TWO- AND THREE-LAYER MODELS

Meyer[1] has proposed a two-layer model, later modified by Elata *et al.*[2] who divided the flow into a viscous

[a]Present address: Department of Aero-Space Engineering, Pennsylvania State University, University Park, Pa. 16802.

sublayer, where $u^+ = y^+$, and a log region, where $u^+ = A \ln y^+ + B + \Delta u^+$. The term Δu^+ represents the observed shift of the straight line describing the log profile in the conventional law-of-the-wall representation and notation. This model suggested that the thickness of the viscous sublayer is increased in flows with drag reduction.

Virk[3] assumed that the thickness of the viscous sublayer remains constant but introduced between the two layers an additional layer which he termed the elastic sublayer. He described the velocity profile in the elastic sublayer by a universal log profile $u^+ = D \ln y^+ + E$. Virk's model thus describes a limiting regime of maximum drag reduction which occurs when the elastic layer replaces the entire log region.

Neither model explains the observed effect of drag reduction on the sublayer which is manifested by the reduction of heat transfer at high Prandtl numbers.

MEAN VELOCITY CLOSURES

Several mean velocity closures[4-6] have been proposed to describe flows with drag reduction. Particularly useful has been the mixing length model of Van Driest: $L = ky[1 - \exp(-y^+/A^+)]$, in which A^+ was assumed a function of drag reduction. When using the constant shear stress approximation, this model gives a shifted log profile in the outer region. However, later it was found necessary to abandon the constant shear stress approximation since it gives, at the limit of very large drag reduction, a velocity profile which approaches the line $u^+ = y^+$ throughout the pipe, rather than the parabolic laminar profile.[5]

This mean velocity closure has been used in the analysis of heat and mass transfer in flows with drag reduction. Using the Reynolds analogy and assuming a turbulent Prandtl number $Pr_t = 1$, an implicit relation has been obtained by Dimand and Poreh[7] which does not contain any empirical coefficients, $Nu = Nu (Re, f, Pr, T_w/T_b)$, for established heat transfer in pipe flows, as well as for the thermal entrance region. (In this relation Nu is the Nusselt number, Re is the Reynolds number, f is the friction coefficient, Pr is the Prandtl number, and T_w/T_b is the wall-to-bulk temperature ratio.) Note that the performance of such a model at different Pr numbers is an indicator of its ability to describe the transport processes in different regions of the flow. The
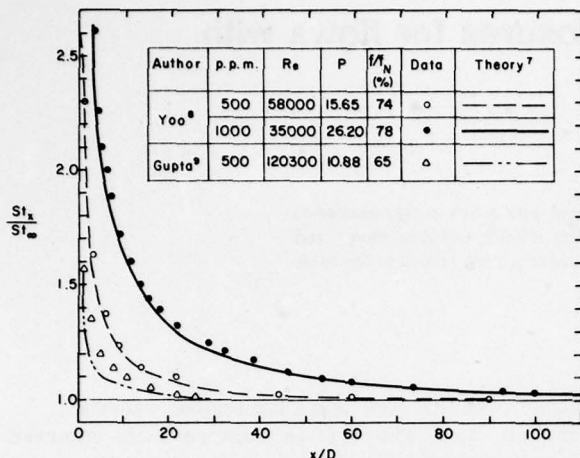
FIG. 1. Comparison of calculated and measured values of St_x in the entrance region (from Dimant and Poreh[7]).

calculated results were found to be in very good agreement with almost all the available experimental data. The model has pointed out unknown important characteristics of heat transfer in turbulent flows with drag reduction which are also found in laminar flows:

(1) In flows with high drag reduction it is necessary to distinguish between the boundary conditions of constant wall temperature and constant wall heat flux. Such a distinction is possible only if one does not use the constant shear stress and constant heat flux approximations.

(2) The thermal entrance region in turbulent flows with drag reduction can be many times longer, as shown in Fig. 1, which compares the theoretical calculations of the relative variation of the Stanton number at a given distance from the beginning of the thermal region with data taken from Yoo[8] and Gupta.[9]

(3) The effect of temperature dependent fluid properties in flows with drag reduction is larger than in turbulent Newtonian flows.

Earlier models, which had not taken these effects into consideration, could not explain the differences between the data in "almost similar" experiments.

A TURBULENT-ENERGY CLOSURE

The effect of drag reduction on the turbulent quantities is of considerable interest. Measurements of the longitudinal rms fluctuating velocity u indicate, for example, that u^* decreases slightly very close to the wall, but increases significantly elsewhere. A turbulent-energy closure which can describe this change might also reveal the effect of drag reduction on other turbulent quantities. It could be used, for example, to examine whether additional transfer of turbulent energy from the wall region, by the polymer molecules, can be the primary cause of drag reduction as suggested by some investigators.[10,11]

Hassid and Poreh[12] investigated the following one-equation turbulent-energy model:

$$-\overline{uv} = \nu_t \frac{\partial U}{\partial Y} \tag{1}$$

$$\frac{Dk}{Dt} = \frac{\partial}{\partial Y}(\nu + \nu_t)\frac{\partial k}{\partial Y} - \overline{uv}\frac{\partial U}{\partial Y} - 2\frac{(\nu + \nu_t)k}{L^2}, \tag{2}$$

where k is the turbulent energy and ν_t is the eddy viscosity. The damping effect near the wall was related to the turbulent Reynolds number of the turbulence $R_k = k^{1/2}L/\nu$ as follows:

$$\nu_t = C_\mu k^{1/2} L [1 - \exp(-A_\mu R_k)] . \tag{3}$$

The value of C_μ in the model is a universal constant (0.225), whereas A_μ is a function of drag reduction. The length scale L for pipe flow was set equal to the length scale used by Prandtl[13]

$$L = y[1 - 1.1(y/R) + 0.6(y/R)^2 - 0.15(y/R)^3] .$$

The model is capable of reproducing the measured velocity profiles as well as the main features of the turbulent-energy distribution. This work indicated that an increase in the transport term in the turbulent-energy equation cannot reproduce the observed features of the phenomenon correctly. The model suffers, however, from the limitation that it is necessary to specify the distribution of the length scale of the turbulent motion. Recent measurements indicate that drag reduction drastically affects this scale.

A TURBULENT-ENERGY-DISSIPATION CLOSURE

In order to overcome the shortcoming of the one-equation turbulent-energy model, an energy-dissipation model, similar to the model of Jones and Launder,[14] has been proposed by Hassid and Poreh.[15] The equations of the model are

$$-\overline{uv} = \nu_t(\partial U/\partial y) , \tag{4}$$

where

$$\nu_t = C_1(k^2/\epsilon)[1 - \exp(-A_m R_k)] \tag{5}$$

and where $R_k = k^2/\epsilon\nu$ is the Reynolds number of turbulence.

$$\frac{Dk}{Dt} = \frac{\partial}{\partial y}\left[(\nu + \nu_t)\frac{\partial k}{\partial y}\right] - \overline{uv}\frac{\partial U}{\partial y} - \epsilon - \frac{2\nu k}{y^2}, \tag{6}$$

$$\frac{D\epsilon}{Dt} = \frac{\partial}{\partial y}\left[\left(\nu + \frac{\nu_t}{C_2}\right)\frac{\partial \epsilon}{\partial y}\right] - C_3\overline{uv}\frac{\epsilon}{k}\frac{\partial U}{\partial k}$$

$$\qquad - C_4\frac{\epsilon^2}{k}[1 - 0.3\exp(-R_k^2)] - 2\nu\left(\frac{\partial \epsilon^{1/2}}{\partial y}\right)^2 . \tag{7}$$

The only parameter in this model which varies with drag reduction is the coefficient A_m in the damping term in the expression for the eddy viscosity. Its value for Newtonian flows is 0.0015.

Once the drag reduction at a particular Reynolds number is known, the value of A_m is determined and the distributions of the mean velocity, the turbulent energy, and the dissipation can be calculated by the model. In addition, it is possible to define a length scale Λ related to the turbulent motion, by the equation

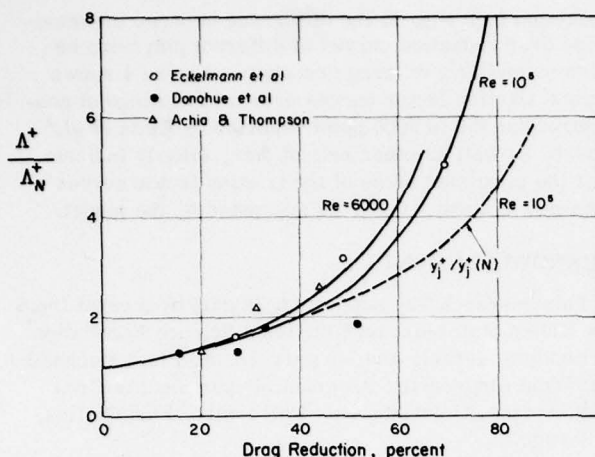$$\Lambda \propto k^{3/2}/\epsilon \tag{8}$$

FIG. 2. Calculated and measured increase of length scales in flows with drag reduction.

and determine its distribution.

The predictions of the model for turbulent Newtonian flows and for flows with drag reduction are similar to those predicted by the simpler models and in good agreement with the observed changes.[15]

Of particular interest is the predicted effect of drag reduction on the length scale of the motion which cannot be predicted with the simpler models. The solid lines in Fig. 2 show the calculated average change in the ratio Λ^+/Λ_N^+, where Λ_N is the value of the length scale in a Newtonian fluid at the same Reynolds number. The broken line in this figure shows the change in the dimensionless thickness of the viscous sublayer y_j^+ in the two-layer models, defined by $y_j^+ = A \ln y_j^+ + B + \Delta u^+$ for $Re = 10^5$. The change in the two length scales is identical for small drag reductions. When the drag reduction is large, the parameter y_j^+ becomes meaningless since the outer velocity profile is no longer described by a log profile.

The effect of drag reduction on different measurable length scales has been reported in the literature.[16-18] The experimental data are shown in Fig. 2. Clearly, the predicted increase in the dimensionless length scale is consistent with these data.

DISCUSSION

Several mean velocity and turbulent energy closures which assume that the effect of drag reducing additives is to decrease the magnitude of the eddy viscosity near the wall have been reviewed. None of the models attempts to explain the mechanism by which the drag reducing molecules decrease the eddy viscosity. Nevertheless, one observes that in all three models the change in the empirical parameters which determine the magnitude of the drag reduction is equivalent to an increase in the effective viscosity acting on the turbulent eddies in the buffer zone. This equivalent viscosity is proportional to $A^+ \nu$ in the mean velocity closure and to ν/A_u and ν/A_m in the turbulent energy and turbulent energy dissipation models, respectively.

In spite of the inherent limitations of the phenomenological models as a means for studying the mechanism of drag reduction, their success in describing and relating the observed flow characteristics makes them a valuable tool in drag reduction research. The turbulent energy dissipation model, for instance, makes it possible to deduce a new maximum drag reduction law for a given polymer pipe system. It has been established that drag reducing polymers are effective only when the shear stress exceeds a critical value. It was therefore hypothesized that drag reduction can occur only when $t_1 V^{*2}/\nu$ or $\lambda_1 V^*/\nu$ exceed critical values, where t_1 and λ_1 are characteristic time and length scales of the molecules. Thus, if Re_0 and f_0 are the values of the Reynolds number and the friction factor at the onset of drag reduction, (see Fig. 3) the curve $f/f_0 = (Re/Re_0)^{-2}$, on which $V^* = V_0^*$ is constant, would be a maximum drag reduction curve according to this hypothesis. Note that this curve crosses the laminar friction factor curve. Such curves have never been observed.

A more plausible conclusion from the observation of the onset phenomenon is that drag reduction is possible only when $t_1 k^{1/2}/\Lambda$ or λ_1/Λ exceed certain critical values which can be determined by the onset conditions. These hypotheses will be referred to as the time-scale hypothesis and length-scale hypothesis, respectively. Since Λ increases rapidly and $k^{1/2}$ decreases at high values of drag reduction, maximum values of drag reduction are imposed by these requirements well before the laminar friction factor curve is reached: A rough estimate of the initial form of such a maximum drag reduction curve follows. It is noted, from Fig. 2, that the ratio Λ^+/Λ_N^+ can be very roughly approximated, up to 70% drag reduction, by $(V_N^*/V^*)^3$, or $\Lambda/\Lambda_N = (f_N/f)^2$. In this region $f_N \propto Re^{-0.25}$ or $\Lambda_N \propto Re^{-0.875}$ (assuming that $\nu = const$). The locus of the points where $\lambda_1/\Lambda = \lambda_1/\Lambda_0$, where Λ_0 is the value at Re_0, is thus described by the curve

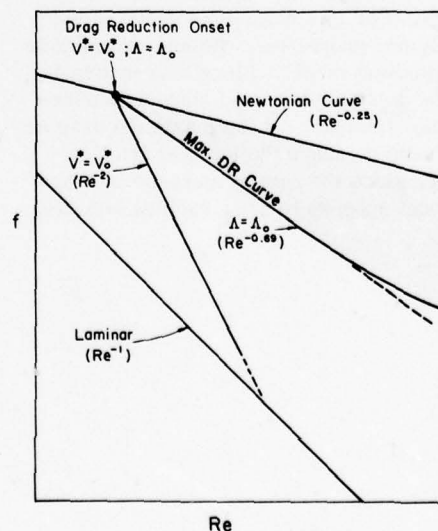$$f/f_0 = (Re/Re_0)^{-m} , \qquad (9)$$

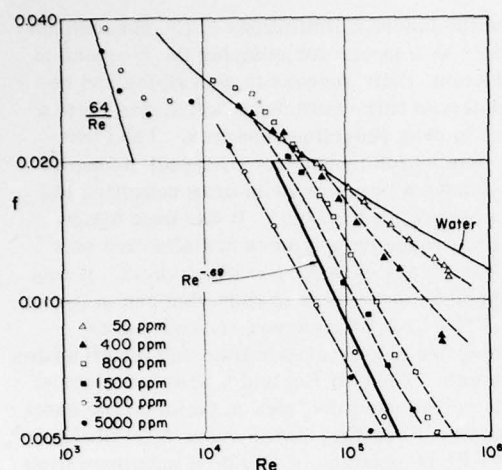FIG. 3. Maximum and onset of drag reduction (log-log scales).

FIG. 4. Typical drag reduction curves.[2]

where $m = -0.6875 \sim 0.69$. Larger values of m are expected in pseudo-plastic solutions. Thus, according to the length-scale hypothesis drag reduction is approximately limited to the region above Eq. (9) as shown in Fig. 3. The time-scale hypothesis seems more plausible physically. Unfortunately, the curve of maximum drag reduction which it defines cannot readily be calculated. However, since the change in $k^{1/2}$ at small values of drag reduction is small; the two hypotheses should initially define close maximum drag reduction curves. At higher values of drag reduction the slope of these curves should be milder due to the decrease in $k^{1/2}$.

It should be stressed that these maximum drag reduction curves, like the onset points, depend on the polymer properties as well as on the pipe diameter and should not be confused with Virk's maximum drag reduction curve. Virk's curve does not describe the limit of drag reduction which can be obtained by a given polymer solution in a given pipe, but rather the envelope of all maximum drag reduction curves obtained so far by the most efficient polymers. For this reason his curve is independent of the polymer properties. Another conclusion follows from the present model. Since Λ is inversely proportional to the dissipation ϵ, and since ϵ vanishes as the flow becomes laminar, all the maximum drag reduction curves should be above the laminar friction curve. Moreover, since the rate of increase in Λ according to the model appears to grow rapidly with drag

reduction (see Fig. 3) the difference between the maximum drag reduction curves of different polymers becomes smaller with drag reduction. Figure 4 shows typical friction factor curves over a wide range of concentrations (50 to 5000 ppm) reported by Elata et al.[2] These, as well as other sets of data, clearly indicate that the maximum slope of the friction factor curves obtained is about -0.69, as suggested by the model.

ACKNOWLEDGMENTS

[1]W. A. Meyer, AIChE J. **2**, 522 (1966).
[2]C. Elata, J. Lehrer, and A. Kahanowitz, Isr. J. Tech. **4**, 87 (1966).
[3]P. S. Virk, J. Fluid Mech. **45**, 417 (1971).
[4]N. G. Vasetskaya and V. A. Ioselevich, Izv. Akad. Nauk. SSSR Sr. Mekh. Zhidk. Gaza **5**, 136 (1970) [Fluid Dyn. **5**, 289 (1970)].
[5]M. Poreh and Y. Dimant, in *Proceedings of the Ninth International Symposium Naval Hydrodynamics* (Office of Naval Research, Washington, D. C., 1972), p. 1305.
[6]D. B. Spalding, in *Progress in Heat Transfer* (Pergamon, New York, 1972), Vol. 5, p. 275.
[7]Y. Dimant and M. Poreh, in *Advances in Heat Transfer* (Academic, New York, 1976), Vol. 12, p. 77.
[8]S. A. Yoo, Ph.D. thesis, University of Illinois (1974).
[9]M. K. Gupta, M. S. thesis, University of Delaware (1966).
[10]M. A. Walsh, Ph.D. thesis, California Institute of Technology (1967).
[11]M. S. Kohn, J. Polym. Sci. **2**, 2339 (1973).
[12]S. Hassid and M. Poreh, J. Fluid Eng. **97**, 234 (1975).
[13]L. Prandtl, Nachr. Akad. Wiss. Göttingen, Math.-Phys. Kl. Sec. 6 **19**, 874 (1945).
[14]W. P. Jones and B. E. Launder, Int. J. Heat Mass Transfer **15**, 301 (1972); and **16**, 1119 (1973).
[15]S. Hassid and M. Poreh, Technion-Israel Institute of Technology, Civil Engineering Department Report No. 215 (1975).
[16]L. P. Eckelmann, G. Fortuna, and J. J. Hanratty, Nat. Phys. Sci. **236**, 94 (1972).
[17]G. I. Donohue, J. J. Tiederman, and M. M. Reischman, J. Fluid Mech. **56**, 559 (1972).
[18]B. V. Achia and D. W. Thompson, in *Proceedings of the International Conference on Drag Reduction* (British Hydrodynamics Research Association, Cranfield, England, 1974), p. A 2.

Turbulent boundary layer bearing silt in suspension

Jacques C. J. Nihoul[a]

Institut de Mathématique, Université de Liège, 4000 Liège, Belgium

Essential characteristics of a turbulent boundary layer, bearing silt flocks in suspension, are described and interpreted with the help of a simple steady state model calibrated for the test region of the Math Modelsea project off the Northern Belgian Coast under near critical conditions : no net flux of particles through the bottom boundary. The model emphasizes the existence between the viscous sublayer and the classical Prandtl–Kármán logarithmic layer, of an "elastic sublayer" where gravity acting on the suspended load provides the necessary restoring force.

I. INTRODUCTION

An extensive survey of the eastern part of the Southern Bight of the North Sea was made, between the years 1970 and 1976, in the scope of the Belgian National Environment Program (Math Modelsea Project).

The mathematical model of the residual circulation in the Bight predicted the existence of a gyre off the eastern Belgian coast and a resulting long-shore southerly current entraining the very turbid waters of the Scheldt estuary to the region of Zeebrugge and Ostend before turning off-shore and merging with a branch of the North Atlantic current flowing north through the Straits of Dover[1] (Fig. 1).

Although intensive tidal currents are superimposed on the residual flow, moving suspended sediments back and forth, in the long run, muds from the Scheldt river are transported and deposited along the Belgian coast.[2,3]

The predictions of the model are confirmed by the observations which reveal a large area of muddy bottom sediments persisting near the coast (Fig. 2).

Suspended matter in this region is not dispersed into its elementary particles but aggregated into flocs.[4] Flocculation is produced by electrolytes in sea water as well as by biological factors such as aggregation of mud around diatoms' frustules by excreted mucous.

The dynamic equilibrium which seems to be maintained, in the mean, between bottom and suspended sediments may be regarded as the result of successive deposition and bottom erosion. The observations indicate that there is a critical friction velocity u_*^c below which suspensions, entrapped in a fairly stable viscous sublayer, are sedimented. For friction velocities larger than u_*^c but smaller than a second critical value u_*^e, the downward flux of sedimenting flocs appear to be compensated for by turbulent scavenging of the viscous sublayer and upward entrainment of depositing sediments. For friction velocities larger than u_*^e, the turbulence is able to erode the bottom and return freshly deposited sediments into the water column. (Typically, one finds $u_*^e \sim 2u_*^c$ with $u_*^c \sim 10^{-2}$ m/sec, in agreement with similar

observations in the Thames estuary[5] and in the Dutch tidal waters[6]).

Tide and storm surge velocities in the area can exceed 1 m/sec and one expects, over a tidal cycle, successive deposition and erosion separated by fairly long intervals where the friction velocity is intermediate between u_*^c and u_*^e, a mean tidal velocity of 0.5 m/sec gives $u_* \sim 1.5 \times 10^{-2}$ m/sec and the net flux of matter through the lower boundary is zero.

During one of these intervals, considering that the mean tidal current varies very little over times characteristic of turbulent eddies and turbulent bursts in the bottom layer, one may presumably apply a steady state model in a first attempt to elucidate the characteristic features of the turbulence in the bottom boundary layer and the effects of the suspended load on the turbulent structures.

In the following, essential characteristics of a turbulent boundary layer, bearing slit flocs in suspension, are described and interpreted with the help of a simple steady state model calibrated for the test region of the Math Modelsea Project, off the Northern Belgian Coast, under rear critical conditions ($u_* \sim 10^{-2}$ m/sec: no net flux of particles through the bottom boundary; diameter of flocs $d \sim 2 \times 10^{-5}$ m; specific mass of sediments $\rho_1 \sim 2700$ kg/m^3, volume concentration of sediments in the water column $s \sim 4 \times 10^{-6}$, sea bed volume concentration of sediments $s_0 \sim 4 \times 10^{-1}$).

The model emphasizes the existence, between the viscous sublayer and the classical Prandtl–Kármán logarithmic layer, of an "elastic sublayer" where gravity acting on the suspended load provides the necessary restoring force.

II. RECENT OBSERVATIONS OF BOTTOM TURBULENCE IN SHALLOW TIDAL SEAS

Experimental evidence of the intermittent nature of the turbulent transport of momentum in the bottom boundary layer, in a shallow tidal sea, has recently been reported by several authors.[7-9]

According to Heathershaw,[8] up to 57% of the Reynolds stress is contributed in 7% of the time by events outside 2 standard deviations from zero.

Sedimenting particles in the viscous sublayer and freshly deposited sediments are thus presumably submitted to peaks of very high stress provoking their recirculation in the water column. According to

---

[a] Also at the Institut d'Astronomie et de Géophysique, Université de Louvain, Belgium.
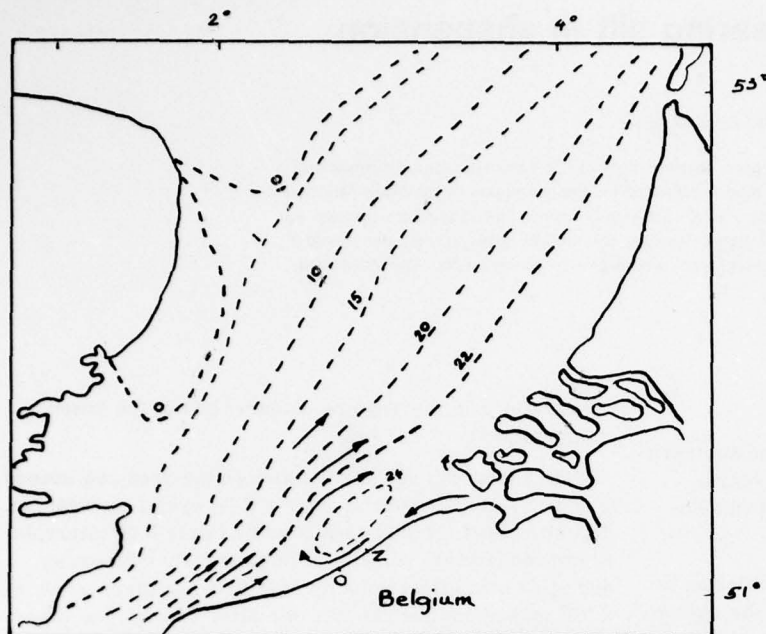
FIG. 1. Residual circulation in the Southern Bight Streamlines $\psi = $ const (in 10^3 m^3/sec).

McCave,[10] suspended sediments tend to move in low velocity streaks in the region $y^+ = x_3 u_*/\nu < 10$ and are periodically ejected with low momentum fluid when these streaks become unstable.

A feedback effect of the suspended load on the turbulent motion has been identified by different authors.[10,11] The effect was associated with the observed reduction of the von Kármán constant in the vicinity of the sea bed; the velocity profile near the bottom fitting a logarithmic law with a value of the von Kármán constant about one-half the classical 0.4 value (Vanoni and Brooks[11] find $k \sim 0.21$; McCave,[10] quoting Runstadler[12] proposes $k \sim 0.18$; compilation of data in the scope of the Math Modelsea Project suggests the typical value $k \sim 0.2$ with illusory possible refinements).

Analyzing field observations in a tidal channel and laboratory experiments performed with the same clay-mineral suspension and bottom sediment, Gust[9] concluded that the friction velocity u_*, determined from measurements in the viscous sublayer was reduced by as much as 40% when compared with values using Prandtl's formula in the logarithmic layer.

This effect, which cannot be explained by a 5‰ modification of the viscosity by the suspensions, was attributed by Gust to "non-Newtonian turbulent drag reduction caused by the suspended clay mineral." Pursuing the analogy with the effect of macromolecules on turbulent structures,[13] Gust conjectured the existence, between viscous sublayer and Prandtl logarithmic layer, of an additional layer possessing viscoelastic properties resulting from the, admittedly unknown, "mechanical interaction between aggregates of the suspended clay minerals and the high wave number part of the turbulence."
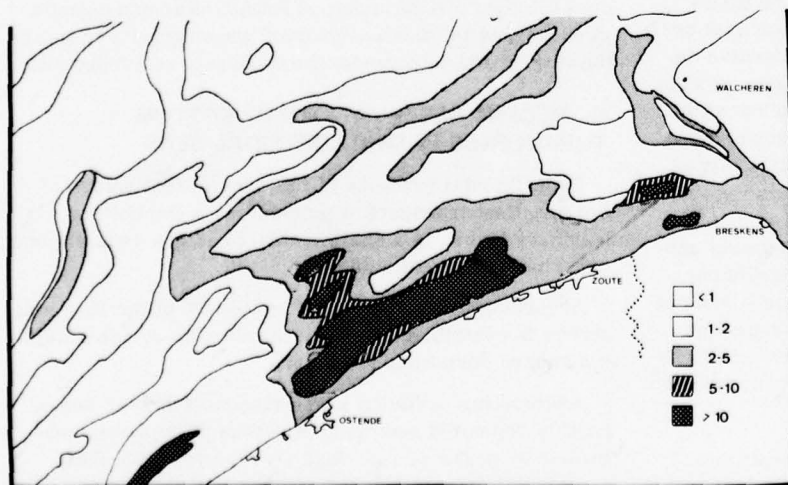

FIG. 2. Distribution of silt in the bottom sediments off the Belgian Coast.

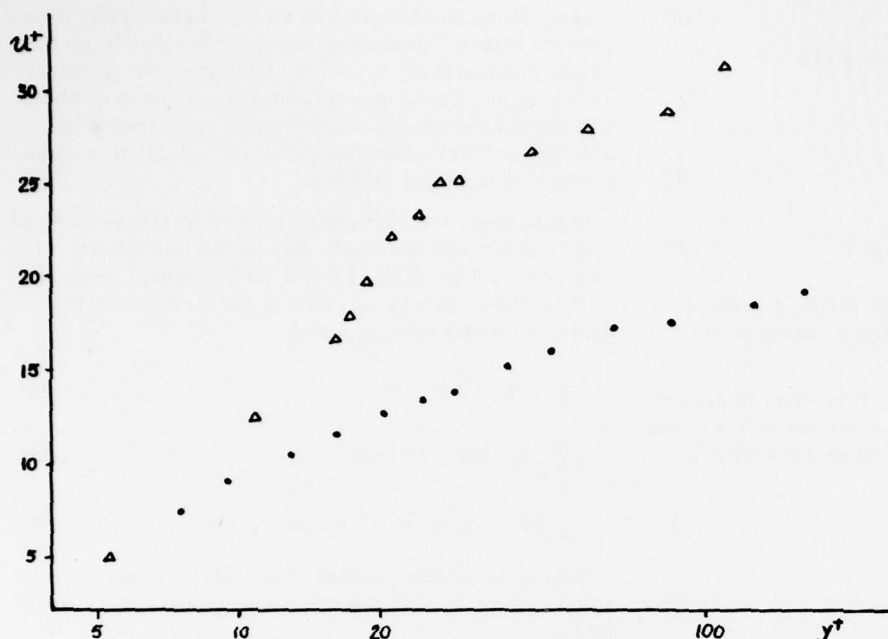|	
☐	< 1
☐	1-2
▦	2-5
▨	5-10
■	> 10

FIG. 3. Nondimensional velocity profiles in a turbulent boundary layer bearing clay in suspension: ● fresh water; ▲ clay suspension.

Nondimensional velocity profiles derived from some of Gust's measurements (Fig. 3) show striking analogies with results obtained with solutions of polymers in water. [13]

The region of steeper velocity profile ($10 \lesssim y^+ \lesssim 25$) may be related to the long-observed higher velocity gradient layer associated with a reduced value of the von Kármán constant.

The reduction of the friction velocity by as much as 40%, as claimed by Gust, may seem rather excessive, but it may be due to the artificial conditions of the experiments using fairly high clay-mineral concentrations (~ 0.5 kg/m^3). In the test area of the Math Modelsea Project (concentration of suspension < 0.05 kg/m^3), there are indications of a reduction of maybe 20% for friction velocities of the order of 10^{-2} m/sec.

With $u_* \sim 10^{-2}$ m/sec and the kinematic viscosity $\nu \sim 10^{-6}$ m^2/sec, one expects the viscous sublayer to be little more than 10^{-3} m thick. The elastic sublayer presumably extends to 10^{-2} m or less. [9,10] Thus, reduction of the friction velocity is limited to a region near the bottom which is also characteristic of the bursting process.

While this suggests interesting interactions between the suspended load and the turbulent structures, it also indicates that, whatever new understanding is gained of the structures of bottom turbulence, empirical formulas widely used in sedimentation engineering will probably not be invalidated. In most cases, they are indeed based on the friction velocity which can be estimated by extrapolating downward the velocity profile inferred from velocity measurements taken at heights above the bottom rarely less than 1 m. That friction velocity is the one that fits the classical logarithmic profile; it may be called the Prandtl friction velocity, and engineers have

learned, through repeated experimentation, to relate the Prandtl friction velocity to such phenomena as deposition of sediments, bottom erosion, bed-load transport, etc. Whether these result effectively from the application of a local stress intermittently much higher than the mean or partially reduced by turbulence inhibition, is not important, in practice, as the empirical formulas presumably integrate, through long-established parameterization, the possible relationship between close-to-bottom events and Prandtl friction velocity in the classical logarithmic layer.

When interpreting experimental results in the light of a modern conception of turbulent structures, one should remember that observations are generally scaled with the Prandtl friction velocity. For instance, as already mentioned, the velocity profile in the elastic sublayer is approximated by a logarithmic profile with a factor of proportionality which is equal to the Prandtl friction velocity, a scaling appropriate to the layer above, divided by a constant approximately equal to one-half the von Kármán constant.

III. A SIMPLE STEADY STATE MODEL

If ρ_0, v_0, and ρ_1, v_1 are, respectively, the specific mass and the velocity of sea water and the specific mass and the velocity of the sediment and if s denotes the volume concentration of the sediment, one can define bulk flow variables as:

(i) specific mass ρ:

$$\rho = \rho_0(1 - s) + \rho_1 s = \rho_0(1 + \alpha_0 s) = \rho_0 \delta \quad , \qquad (1)$$

where

$$\alpha_0 = (\rho_1 - \rho_0)/\rho_0 \qquad (2)$$

$$\delta = 1 + \alpha_0 s; \qquad (3)$$

(ii) momentum ρv:

S199   Phys. Fluids, Vol. 20, No. 10, Pt. II, October 1977

Jacques C. J. Nihoul   S199

$$\rho \mathbf{v} = \rho_0 (1-s)\mathbf{v}_0 + \rho_1 s\mathbf{v}_1 \quad . \tag{4}$$

Conservation of mass and momentum gives

$$\frac{\partial}{\partial t}[\rho_0(1-s)] + \nabla \cdot [\rho_0(1-s)\mathbf{v}_0] = 0 \quad, \tag{5}$$

$$\frac{\partial}{\partial t}(\rho_1 s) + \nabla \cdot (\rho_1 s\mathbf{v}_1) = 0 \quad, \tag{6}$$

$$\rho \frac{\partial \mathbf{v}}{\partial t} + \rho \mathbf{v} \cdot \nabla \mathbf{v} + 2\rho \boldsymbol{\Omega} \Lambda \mathbf{v} = \rho \mathbf{g} - \nabla p + \mu \quad, \tag{7}$$

where $\boldsymbol{\Omega}$ is the rotation vector of the earth, g is the acceleration of gravity, p is the pressure, and μ is the dynamic viscous stress.

In suspended sediment problems, it is usual to assume that the sediment velocity is equal to the velocity $\mathbf{v}$ of the sediment-water mixture plus the settling velocity σ of the sediment:

$$\mathbf{v}_1 = \mathbf{v} + \sigma \tag{8}$$

with

$$\sigma = -\sigma \mathbf{e}_3 \; ; \tag{9}$$

the $\mathbf{e}_3$ axis pointing upward.

Equation (9) assumes negligible horizontal slip between particles and water. Although this may be an important effect for problems with drag reduction due to dust in gas, it is undoubtedly very small in this case, especially under the quasi-steady conditions on which the forthcoming model is based.[11]

For small particles and slit flocs of moderate size ($\lesssim 5 \times 10^{-5}$ m), the Stokes formula applies and

$$\sigma = (gd^2/18)\alpha \tag{10}$$

where d is the diameter of the floc and where

$$\alpha = (\rho_1 - \rho)/\rho \neq \alpha_0 = (\rho_1 - \rho_0)/\rho_0 \quad . \tag{11}$$

Indeed, the sedimentation velocity being referred to the velocity $\mathbf{v}$ of the sediment-water mixture, the submerged weight of the flocs must be referred to the specific mass ρ of the mixture. Thus, σ is not a constant, but a function of the suspended load concentration.

Combining Eqs. (5), (6), (7), and (8), one obtains the equivalent system of equations:

$$\frac{\partial \delta}{\partial t} + \nabla \cdot (\delta \mathbf{v}) = 0 \quad, \tag{12}$$

$$\nabla \cdot \mathbf{v} = \nabla \cdot [\sigma(\delta - 1)] \quad, \tag{13}$$

$$\frac{\partial}{\partial t}(\delta \mathbf{v}) + \nabla \cdot (\delta \mathbf{v}\mathbf{v}) + 2\delta \boldsymbol{\Omega}\Lambda\mathbf{v} = \delta \mathbf{g} - \nabla\left(\frac{p}{\rho_0}\right) + \nu \quad, \tag{14}$$

where $\nu = \rho_0^{-1}\mu$ is the kinematic viscous stress.

Separating each variable into a mean part and a fluctuating part, let

$$\mathbf{v} = \mathbf{u} + \mathbf{w}; \qquad \langle \mathbf{w} \rangle = 0, \tag{15}$$

$$p/\rho_0 = q + r; \qquad \langle r \rangle = 0, \tag{16}$$

$$\delta = \eta + \xi; \qquad \langle \xi \rangle = 0, \tag{17}$$

where the angular brackets $\langle \; \rangle$ denote an ensemble average.

Restricting our attention to steady, horizontally homogeneous bottom turbulence, one assumes that (i) mean values are functions of x_3 only, (ii) horizontal pressure gradients and Coriolis accelerations may be neglected, (iii) vertical accelerations are small compared with gravity, and (iv) molecular diffusion is negligible compared with turbulent diffusion.

In this case, the vertical component of (14) reduces to a hydrostatic balance which may be left aside here. The averages of Eqs. (12), (13) and the horizontal component of (14), the x_1 axis being taken in the direction of the mean horizontal velocity, give

$$\frac{d}{dx_3}(\eta u_3 + \langle \xi w_3 \rangle) = 0 \quad, \tag{18}$$

$$\frac{d}{dx_3}[u_3 + \langle \sigma(\delta - 1) \rangle] = 0 \quad, \tag{19}$$

$$\frac{d}{dx_3}[(\eta u_3 + \langle \xi w_3 \rangle)u_1 + \langle (\eta + \xi)w_1 w_3 \rangle] = 0 \quad. \tag{20}$$

Taking the scalar product of Eq. (7) by w and averaging, one gets, with the same approximations as before,

$$\frac{d}{dx_3}[u_3\langle (\eta + \xi)\tfrac{1}{2}w^2 \rangle + \langle w_3(\eta + \xi)\tfrac{1}{2}w^2 \rangle] + \left\langle w_3 \frac{\partial r}{\partial x_3} \right\rangle$$
$$= \langle -(\eta + \xi)w_3 w_3 \rangle \frac{du_3}{dx_3} + \langle -(\eta + \xi)w_1 w_3 \rangle \frac{du_1}{dx_3} - g\langle \xi w_3 \rangle - \epsilon \quad, \tag{21}$$

where ϵ is the rate of dissipation of the turbulent energy.

The first terms on the left- and right-hand sides may reasonably be neglected because the vertical velocity u_3 is considerably smaller than the horizontal velocity u_1. The second and third terms on the left-hand side are less easy to evaluate, but they are commonly considered negligible in the turbulent energy budget of the surface layer.[14]

If one considers a steady state situation where there is no inflow of suspensions from above (through the free surface, say) and no net deposition on the bottom (sedimentation being counter-balanced by vertical advection and turbulent diffusion), it is reasonable to expect high silt concentrations near the bottom, tending to bed concentrations values for very small x_3, and fairly clear water ($s \ll 1$, $\eta \sim 1$) in the water column above. (This is observed in the test region of the Math Modelsea Project and other areas where a similar type of silt is found. In other situations and in the case of noncohesive sediments the concentration profile seems to remain very flat down to the bottom with a discontinuity at the bottom.)

For $y^+ = x_3 u_*/\nu$ sufficiently large, the classical boundary layer results should apply yielding the Prandtl logarithmic profile with the Prandtl friction velocity given by

$$\langle -w_1 w_3 \rangle = u_*^2 \tag{22}$$

and the von Kármán constant equal to

$$k = 0.4 \quad . \tag{23}$$

S200   Phys. Fluids, Vol. 20, No. 10, Pt. II, October 1977

Jacques C. J. Nihoul   S200

Integrating Eqs. (18), (19), and (20), one requires that asymptotically (for sufficiently large y^+) the suspended load concentration be negligibly small ($\eta \sim 1$), the total flux of suspended matter (vertical advection + sedimentation + turbulent diffusion) tend to zero, and the vertical velocity tend to zero. One thus obtains

$$\eta u_3 + \langle \xi w_3 \rangle = 0 , \tag{24}$$

$$u_3 + \langle \sigma(\delta - 1) \rangle = 0 , \tag{25}$$

$$\langle -(\eta + \xi) w_1 w_3 \rangle = \text{const} , \tag{26}$$

while Eq. (21) reduces to

$$\langle -(\eta + \xi) w_1 w_3 \rangle (du_1/dx_3) - g\langle \xi w_3 \rangle - \epsilon = 0 . \tag{27}$$

For y^+ sufficiently large, (26) tends to (22) as expected and one can set the constant, on the right-hand side of (26) equal to u_*^2. The Prandtl friction velocity can then be used as a scaling factor throughout the water column, in agreement with common engineering practice.

Equation (27) indicates that

$$\tau = \rho_0 \langle -(\eta + \xi) w_1 w_3 \rangle \tag{28}$$

is the effective Reynolds stress and Eq. (26) determines that τ is a constant ($\tau = \rho_0 u_*^2$).

If the friction velocity is defined as $\tau^{1/2} \langle \rho \rangle^{-1/2}$, it is identical to u_* in the Prandtl logarithmic layer, but differs from it in the elastic sublayer below and, in particular, near the bottom

$$u_*^0 \sim u_* \eta_0^{-1/2} . \tag{29}$$

(For typical values of the Math Modelsea test region, $\alpha_0 \sim 1.62$; $s_0 \sim 0.4$; $\eta_0 \sim 1.65$; $u_*^0 \sim 0.8 u_*$; the friction velocity at the top of the viscous layer is reduced to about 80% of the Prandtl friction velocity.)

Since τ is the same all over the water column, however, one should not expect noticeable effects of the friction velocity reduction on well-established threshold for sediment deposition and erosion.

The first critical friction velocity u_*^c (corresponding to a critical value τ_c of τ) may be interpreted as the value for which regular sedimentation through the viscous sublayer is, in the mean, exactly balanced by turbulent disruption and scavenging of the viscous layer, associated with intermittent peak values of the Reynolds stress reducing the viscous layer thickness to almost grain diameter.

In the "clear water" region (y^+ sufficiently large), Eqs. (24), (25), and (26) can easily be solved if one introduces an eddy diffusivity and an eddy viscosity such that

$$\langle -w_1 w_3 \rangle = \bar{\nu} (du_1/dx_3) , \tag{30}$$

$$\langle -\xi w_3 \rangle = \bar{\lambda} (d\eta/dx_3) , \tag{31}$$

with

$$\bar{\nu} \sim \bar{\lambda} \sim k x_3 u_* . \tag{32}$$

One finds

$$\eta \sim 1; \quad d\eta/dx_3 \sim 0 \tag{33}$$

$$u_3 \sim 0, \tag{34}$$

$$u_1 = (u_*/k) \ln(x_3/z_0) , \tag{35}$$

where z_0 is the rugosity length.

In the turbid bottom layer, an eddy diffusivity approach might also be appropriate, but the question arises as to whether eddy coefficients can be parametrized on the model (32). One might expect a similar equation to hold for $\bar{\nu}$ but not necessarily for $\bar{\lambda}$. Indeed, one generally observes that the ratio $\bar{\nu}/\bar{\lambda}$ decreases significantly in stably stratified water and in the turbid bottom layer one should expect this ratio to be a function of the concentration gradient of the suspended load.

One notes that, if (32) is used, (24) and (25) give

$$k u_* x_3 (d\eta/dx_3) = -\eta \langle \sigma(\delta - 1) \rangle; \tag{36}$$

i.e.,

$$x_3 \frac{d\eta}{dx_3} = -\beta \left\langle \frac{\eta(\eta - 1 + \xi)(1 - s)}{\eta + \xi} \right\rangle \sim -\beta(\eta - 1) , \tag{37}$$

where

$$\beta = g d^2 \alpha_0 / 18 \nu k u_* \sim O(10^{-1}) . \tag{38}$$

Thus, the sediment concentration profile, to a first approximation, would be of the type

$$\eta = 1 + (\eta_0 - 1)(z_0/x_3)^\beta . \tag{39}$$

Although the solution (39) gives $\eta = \eta_0$ at $x_3 = z_0$ and η tending to 1 at large distance from the bottom, it does not seem to be appropriate to describe the rapid decrease of the sediment concentration which is observed in the case of silt in the vicinity of the sea bed and the related uniformly negligible concentration in the rest of the water column. (With $\beta \sim 10^{-1}$, η is still 75% of η, at 1 m). The failure of (39) to reproduce the observations indicates that the eddy diffusivity approximation (32) is not valid near the bottom where much smaller values of $\bar{\lambda}$ presumably prevail as a result of the strong stratification associated with the suspended load.

IV. VELOCITY AND SEDIMENT CONCENTRATION PROFILES IN THE ELASTIC LAYER

Combining (24) and (25), one obtains, after multiplication by g,

$$\begin{aligned} \langle g\xi w_3 \rangle &= -g\eta u_3 = -g(\eta - 1)u_3 - gu_3 \\ &= g\langle (\sigma - u_3)(\delta - 1) \rangle = \mathbf{g} \cdot \langle \mathbf{v}_1(\delta - 1) \rangle \\ &= g \frac{\rho_s - \rho_0}{\rho_0} \langle s(\sigma - u_3) \rangle . \end{aligned} \tag{40}$$

The expression on the right-hand side represents the mean power required per unit mass of sea water to counterbalance the effective downward motion of the sediments. That power is provided by the turbulent motion and one may argue that, in a steady situation, it must scale with the turbulent energy available per unit time, i.e.,

$$g \frac{\rho_s - \rho_0}{\rho_0} \langle s(\sigma - u_3) \rangle = c u_*^2 \frac{u_*}{k x_3} , \tag{41}$$

where $u_*/k x_3$ is the characteristic frequency of the energy containing eddies and where c is a nondimensional
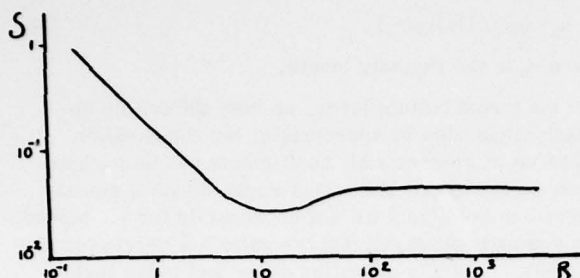
FIG. 4. Shields diagram.

function, hopefully of order 1 at the viscous interface, taking into account possible modifications of the turbulent fluctuation field near the bottom.

Information concerning the limit value of c may be obtained by considering the equality (41) at the interface with the viscous sublayer. Substituting

$$x_3 \sim 12\,\nu/u_*^0 \sim 12\,\eta_0^{1/2}\nu/u_* \tag{42}$$

and

$$\sigma = gd^2/18\nu; \tag{43}$$

$$\alpha_0 = \delta\alpha/(1-s) \, , \tag{44}$$

one gets

$$c = 0.27\bigl[s_0\eta_0^{5/2}/(1-s_0)\bigr]S^{-2} \, , \tag{45}$$

where

$$S = u_*^2/g\alpha d \tag{46}$$

is the Shields number.[15]

The steady state situation considered here corresponds to critical conditions at the bottom (neither deposition nor erosion). An impressive series of experimental data have established that, in that case, the Shields number is a universal function of the floc Reynolds number $R = u_* d/\nu$ (Fig. 4).[11]

Under the conditions of the test region of the Math Modelsea Project, one has

$$u_* \sim 10^{-2}\ \text{m/sec}; \quad d \sim 2\times10^{-5}\ \text{m}; \quad s_0 \sim 0.4$$

$$\eta_0 \sim 1.65; \quad R \sim 0.2; \quad S \sim 0.8$$

and thus

$$c \sim 1 \, . \tag{47}$$

The limit value 1 of the function c, confirming the estimate of the turbulent power made in (41), suggests that turbulent fluctuations are not much different near the bottom and in the Prandtl logarithmic layer.

Hence, one may assume

$$\epsilon \sim u_*^3/kx_3 \tag{48}$$

and Eq. (27) may be written, using (41), (47), and (48)

$$u_*^2\frac{du_1}{dx_3} - \frac{u_*^3}{kx_3} - \frac{u_*^3}{kx_3} = 0 \, . \tag{49}$$

Integrating, the logarithmic velocity profile is once more obtained but with $k/2$ instead of k in the role of the von Kármán constant

$$u_1 = 2(u_*/k)\ln(x_3/z_0) \, . \tag{50}$$

Taking $c = 1$, one can write Eq. (41), in the form

$$g\eta\langle\sigma(\delta-1)\rangle = \frac{g^2 d^2}{18\nu}\alpha_0^2\eta\left\langle\frac{s(1-s)}{\delta}\right\rangle = \frac{u_*^4}{ky^+\nu} \, ,$$

i.e., neglecting small order terms

$$\langle s(1-s)\rangle \sim s_0(1-s_0)z^{-1} \, , \tag{51}$$

where z is equal to x_3 divided by the thickness of the viscous sublayer.

At a distance from the bottom equal to six times the thickness of the viscous sublayer, the volume concentration s, is already reduced by a factor of 10. Thus, the variation of the suspended load is extremely rapid as one expected and the elastic sublayer affected by the suspensions is confined to about 1 cm above the bottom in agreement with the observations.

[1] J. C. J. Nihoul and F. C. Ronday, Tellus 27, 5 (1975).
[2] J. C. J. Nihoul, Pure Appl. Geophys. 113, 577 (1975).
[3] O. Beckers, R. Wollast, and J. C. J. Nihoul, in Modélisation des Systèmes Marins, edited by J. C. J. Nihoul (Ministry for Science Policy, Belgium, 1976), p. 95.
[4] Math Modelsea, Fisheries Improvement and Hydrography Committee, International Council for the Exploration of the Sea, E:9, (1973).
[5] Thames Estuary floor Prevention Investigation (Mathematical Silt Model Studies), Rpt. EX479, Hydraulic Research Station Wallengford, England (1970).
[6] J. H. J. Terwindt and N. N. C. Breusers, Sedimentology 19, 85 (1972).
[7] M. C. Gordon, Nature 248, 392 (1974).
[8] A. D. Heathershaw, Nature 248, 394 (1974).
[9] G. Gust, Ph. D. dissertation, Universität Kiel, Germany (1976).
[10] I. N. McCave, J. Geophys. Res. 75, 4151 (1970).
[11] M. S. Yalin, Mechanics of Sediment Transport (Pergamon, New York, 1972).
[12] S. J. Kline, W. C. Reynolds, F. A. Schraut, and P. W. Runstadler, J. Fluid Mech. 30, 741 (1967).
[13] P. S. Virk, AIChE J. 21, 625 (1975).
[14] A. S. Monin and A. M. Yaglom, Statistical Fluid Mechanics (The MIT Press, Cambridge, Mass., 1971), Vol. I, pp. 412–416.
[15] A. Shields, Mitter. Preuss. Versuchsanst. Wasserbau Schiffbau 26, 1 (1936).

Influence of molecular aggregates on drag reduction

E. H. Dunlop[a] and L.R. Cox

Department of Pure and Applied Chemistry, University of Strathclyde, Glasgow G1 1XL, Scotland

Methods of detecting and characterizing molecular aggregates in solution are discussed and it is shown that several polymer/solvent systems of interest in drag reduction also form aggregates. Drag reduction results obtained with a spinning disk apparatus can most readily be explained by an aggregation hypothesis, as can a number of other results reported in the literature. The relevance of molecular aggregates to the development of drag reduction theory and investigations is considered.

I. INTRODUCTION

The study of the phenomenon of drag reduction, whereby minute quantities of polymer dissolved in a liquid can bring about dramatic reductions in the frictional resistance when it moves over a surface, usually has three objectives. The first is to obtain an understanding of why the effect occurs from a fluid dynamic point of view, explanations being sought in terms of eddy frequencies, burst cycles, sublayer thickening, etc.[1] Secondly, an explanation may be sought of how the polymer molecules can interact with the flow to produce drag reduction.[2] Thirdly, methods of exploiting the effect for commercial and technical reasons are pursued.[3]

Drag reduction has been of interest to the hydrodynamicist and engineer rather than the polymer chemist or physicist and the assumption behind most experiments has been that more was known about polymer molecules in solution than about the structure of turbulent flow. Unfortunately, the polymers most widely used in drag reduction studies are those whose nature in solution is most in doubt and while this does not necessarily invalidate the conclusions drawn when using these polymers, it does throw doubt on some of them.

Although it has long been suspected that there might be molecular entanglements present in certain drag reducing situations, most workers have assumed that polymer molecules in dilute solution exist as isolated random or slightly extended coils. In this paper we show that molecular aggregates are a common feature of polymer solutions, that their presence has been demonstrated by physico-chemical means in solutions of poly(ethylene oxide) and other drag reducing agents, and that they can sometimes be produced by shearing such solutions. We describe experiments using poly(ethylene oxide) and polyacrylamide in which an enhanced drag reduction effect can most reasonably be ascribed to the presence of molecular aggregates. Lastly, we consider the implication for drag reduction theories and investigations of these supermolecular structures.

---

[a]Present address: Imperial Chemical Industries Ltd., Agricultural Divison, Research and Development Department, Billingham, Cleveland TS23 1LD, United Kingdom.

II. PHYSICO-CHEMICAL METHODS OF DETECTING AND CHARACTERIZING MOLECULAR AGGREGATES IN SOLUTION

Although molecular aggregates and entanglements have received little more than a passing mention in drag reduction literature, they have received considerable attention in the polymer literature. The aggregation of polymer molecules in solution has been reviewed by Elias[4] and Rehage.[5] One fairly recent review[6] is devoted to aggregates in just one substance, poly(vinyl chloride). Among organic polymers which form aggregates or associates in one solvent or another are polyethylene, polypropylene, polystyrene, polyacrylamide, poly(vinyl chloride), poly(methyl methacrylate), nylon 6.6, poly(ethylene oxide), poly(dimethyl siloxane), various polysaccharides, and proteins.[4]

In the terminology used by Elias, association is defined as the equilibrium phenomenon and aggregation as the nonequilibrium process. We shall not differentiate between the two processes but use the term aggregate to describe any group of polymer molecules bound together by physical forces, e.g., hydrogen bonding.

Aggregates may, in principle, be detected by the same methods as are available for the determination of molecular weight and size. These include those based on colligative properties (ebulliometry, cryoscopy, membrane osmometry, and vapor phase osmometry), light scattering, viscosity measurement, and sedimentation. More recently, scanning electron microscopy has come into use.[7]

Methods based on colligative properties are not suitable for the determination of high molecular weights and are therefore of limited use for studying aggregation.

Measurement of intrinsic viscosity has been widely used in drag reduction work for obtaining molecular weights and has also been used to infer the presence of aggregates. However, it is not an absolute method and is known to be only weakly sensitive to the presence of aggregates.[8]

Intrinsic viscosity[9] is a measure of molecular volume and is related to molecular weight M by a law of the type

$$[\eta] = K M^a ,$$

where the constants K and a have to be determined by using polymer samples whose molecular weights have been determined by other means, e.g., light scattering or end group determination. If the polymer aggregates in the solvent used, intrinsic viscosity determinations made to characterize the sample will lead to a false conclusion about its molecular weight in that solvent, since the values of K and a used will be based on the polymer in a nonaggregated state.

Probably the most satisfactory methods for showing the presence of aggregates are light scattering and scanning electron microscopy.

In light scattering the intensity of the light scattered by a series of dilute solutions of the polymer of concentration c is measured as a function of the scattering angle Θ. The data are correlated by plotting Kc/R_Θ vs $[\sin^2(\Theta/2) + kc]$, where R_Θ is the measured excess scattering intensity of the solution over that of the pure solvent, K is an optical constant depending on the particular system, and k is an arbitrary constant. In simple cases this results in a parallelogram-shaped grid (Fig. 1). The data are extrapolated to $\Theta = 0$ and $c = 0$ and the value of the ordinate at this point gives the reciprocal of the weight average molecular weight. In the case of systems which form aggregates the so-called Zimm plot is very much distorted, but deductions about aggregation may be made from its shape.

Richardson[10,11] showed that scanning electron microscopy could be used to determine the molecular weights of high polymers. The specimen is prepared by spraying a dilute solution of the polymer onto a supported carbon film, evaporating off the solvent, and shadowing the residue with a metal at a low angle. Under the electron microscope the polymer appears as a collection of small particles, each casting a long shadow; if

FIG. 2. Scanning electron micrograph of polystyrene, $\overline{M}_v = 1.5 \times 10^6$, sprayed from 1 ppm solution in a benzene/n-butanol mixture. Each sphere is a single molecule. The better solvent has evaporated first leaving the polymer in a tightly coiled compact form. (Courtesy of M. J. Richardson[11] and The Royal Society, London.)

the solution is sufficiently dilute each particle is an individual polymer molecule.

Polymer molecules deposited in this way more or less retain the same form as they had in solution. If a good solvent is used, the molecules collapse into flat disks or shapeless masses which are of little use for measurement purposes. If, however, a mixture of a good solvent with a less volatile poor solvent is employed, the good solvent evaporates off first and the molecules contract into compact spheres of the same density as the bulk polymer (Fig. 2). The diameter and hence the molecular weight may be calculated from the length of the shadow tail.

Richardson noted that careful choice of solvents and polymer concentration was necessary to prevent the formation of aggregates, which could occur at concentration levels as low as 1 ppm.

III. PHYSICO-CHEMICAL EVIDENCE FOR AGGREGATES IN PARTICULAR DRAG REDUCING SUBSTANCES

A. Poly(ethylene oxide)

The literature relating to this polymer is made more confusing by the different nomenclatures used. It can be made by the condensation polymerization of ethylene glycol by the removal of one water molecule per mono-
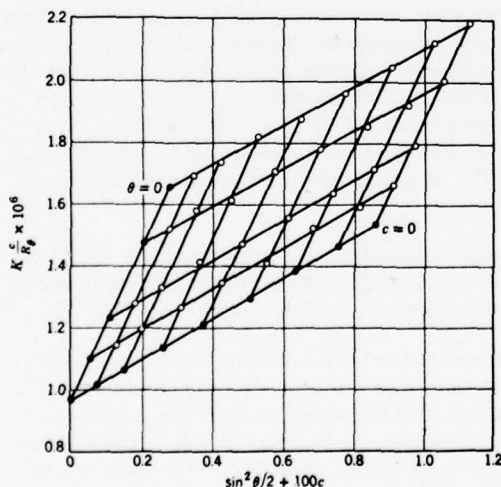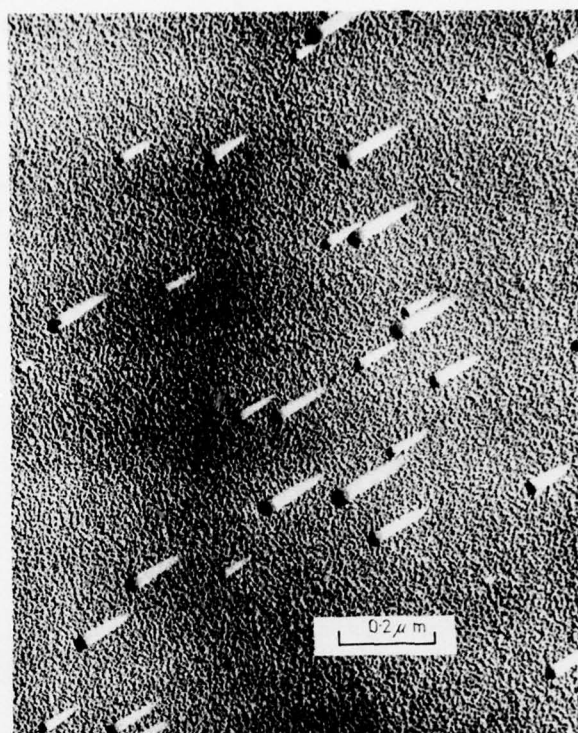

FIG. 1. Zimm plot showing the light scattering from a sample of polystyrene in a good solvent, butanone. Extrapolation to zero concentration and zero scattering angle gives the intercept on the vertical axis, which is equal to the reciprocal of the molecular weight. $\overline{M}_w = 1.03 \times 10^6$. (Courtesy of F. W. Billmeyer[9] and J. Wiley & Sons, Inc., New York.)

mer unit when it is usually referred to as poly(ethylene glycol) and is invariably of low molecular weight. High molecular weight polymer is usually made by addition polymerization of ethylene oxide, when it is named poly(ethylene oxide) or polyoxyethylene.

Delmas[12] fractionated a poly(ethylene oxide) of $\bar{M}_w$ about 400 000 and characterized the fractions by gel permeation chromatography, infrared spectroscopy, viscometry, and dialysis. She observed that the hydroxyl content of the various fractions increased in proportion to their molecular weight and that the number average molecular weight of the whole sample was only 14 000 giving a $\bar{M}_w : \bar{M}_n$ of 29, an extremely broad distribution of molecular weights. The highest molecular weight fraction contained only about 1% of polymer of molecular weight 3500 and had a $\bar{M}_w$ of 500 000, yet 20%–30% passed through a dialysis membrane known to exclude molecules of molecular weight greater than 5000. Gel permeation chromatography showed that the maximum in the molecular weight distribution remained virtually unchanged by dialysis with peaks occurring at 360 000 and 3500. Low molecular weight poly(ethylene oxide) prepared especially for calibration indicated only two terminal hydroxyl groups. Delmas concluded that the high molecular fractions were aggregates of low molecular weight (about 3500) which were stable but dissociated sufficiently reversibly to pass through a membrane. The aggregates were considered to be held together by intermolecular hydrogen bonds between ether groups and hydroxyl end groups. The possibility of degradation was considered but regarded as very unlikely in view of the gel permeation and other data.

Strazielle[13] studied the light scattering produced by a poly(ethylene oxide) solution of molecular weight around 130 000 in methanol. He concluded that molecular aggregates were present whose molecular weight could be computed as being between 6×10^6 and 14×10^9

FIG. 4. Scanning electron micrograph of poly(ethylene oxide), $\bar{M}_v = 2.2 \times 10^5$, sprayed from a 0.18% solution in water. Note the compact form and wide variation in size. Each sphere has a diameter six to ten times that expected for single molecules and thus is an aggregate of many hundreds of molecules. (Courtesy of C. Cuniberti[16] and I. P. C. Science and Technology Press Ltd., Great Britain.)

depending on the way the data were interpreted. The aggregates were resistant to temperatures up to and exceeding the melting point of the polymer.

Cuniberti[14,15] studied the cystallization of poly(ethylene oxide), $\bar{M}_w$ 1.8×10^5 and 6.65×10^5, from dimethyl formamide and from water. From light scattering, viscosity and crystallization measurements she concluded that molecular aggregates were present and that these were resistant to dissociation even at high temperatures and were in equilibrium with the dissolved polymer molecules. The complex behavior of poly(ethylene oxide) in solution can be inferred from her light scattering data which produced the skewed form of the Zimm plot shown in Fig. 3, which should be contrasted with the regular behavior of polystyrene (Fig. 1).

Cuniberti and Ferrando[16] produced scanning electron micrographs of these particles (Fig. 4); their size indicates that they could contain up to several thousand molecules.

Carpenter et al.[17] in light scattering studies of two poly(ethylene oxide) samples (nominal $\bar{M}_w$ 3×10^6 and 6×10^5, respectively), found large aggregates of up to 10^3 chains in benzene and chloroform but not in methanol or dioxane (the cyclic dimer of ethylene oxide). They showed these aggregates to be stable in benzene but that water reduced the aggregation in chloroform solu-
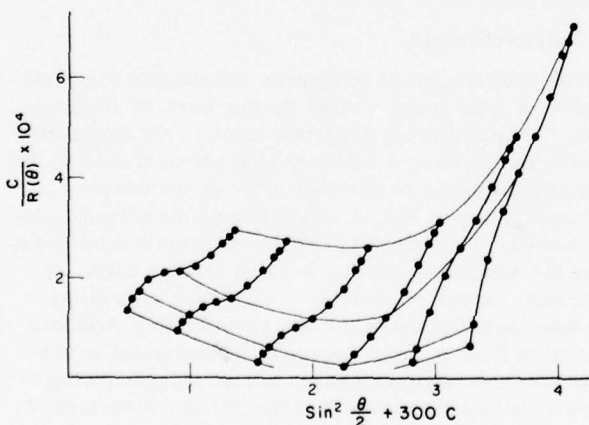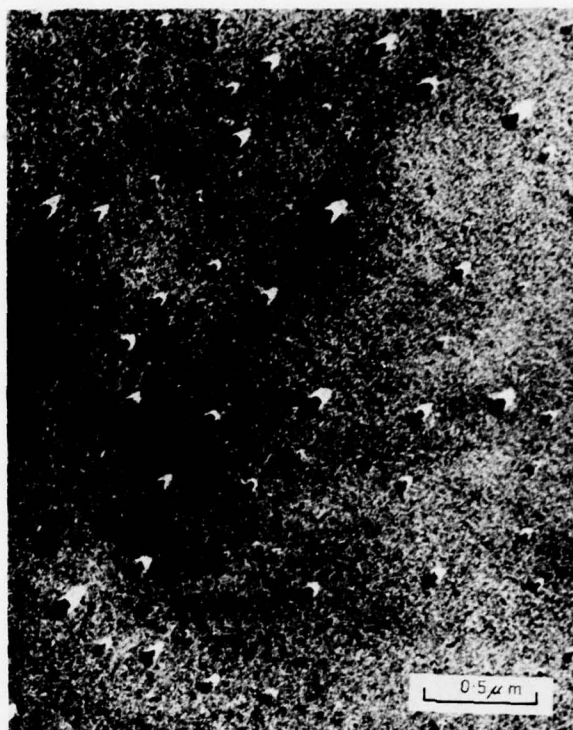
FIG. 3. The grossly distorted Zimm plot obtained from the light scattering by poly(ethylene oxide), $\bar{M}_v = 3.4 \times 10^5$, in dimethyl formamide. Extrapolation to zero concentration and zero scattering angle is meaningless. The degree of curvature of the lines can be used to draw inferences about the size of the polymer aggregates present. (Courtesy of C. Cuniberti[15] and Pergamon Press Ltd., Great Britain.)
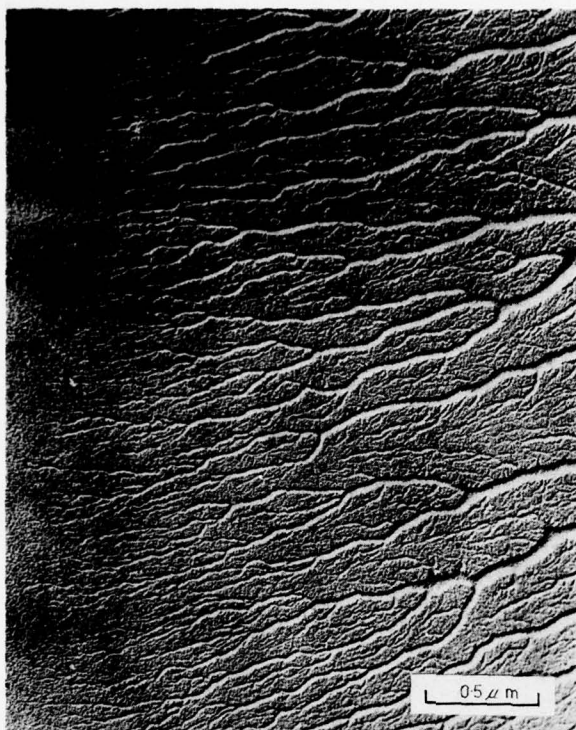
FIG. 5. Scanning electron micrograph of polyacrylamide sprayed from a 10 ppm aqueous solution. The polymer does not disperse as spherical molecules but as long fibrils, some of which are of molecular dimensions. (Courtesy of M. J. Richardson[11] and The Royal Society, London.)

tion. They concluded that the aggregates were stable, compact, extensively branched and anisotropic.

Sarker and Ghosh[18,19] made intrinsic viscosity and light scattering measurements on a low molecular weight poly(ethylene glycol). In water the molecular weight was about 17 000 but if a 5M solution of urea or thiourea was used the molecular weight was 7800. They concluded that poly(ethylene glycol) associates in water and that urea or thiourea prevented this by breaking the hydrogen bonds. However, as we shall show, their observations are capable of a quite different interpretation.

Both Cuniberti and Ferrando, and Sarker and Ghosh used solutions that in some cases were of the same order of concentration as solutions used in drag reduction, which would imply that aggregates are not simply a feature of the more concentrated solutions used in other physico-chemical measurements.

The ability of the ether groups to form hydrogen bonds leads to a further complication. Graham[20] has studied a poly(ethylene glycol) of molecular weight about 6000 both in the pure state and as a cross-linked gel. From calorimetric and other results he has concluded that a relatively stable complex is formed between three molecules of water and the $-CH_2CH_2O-$ unit. Recent work by the authors using mixtures of water and a poly(ethylene glycol) of molecular weight 4000 has shown a discontinuity in both the refractive index and

density curves at the composition corresponding to such a complex. If the trihydrate exists, it would have a molecular weight 2.2 times that of unhydrated poly(ethylene glycol). The results of Sarkar and Ghosh, already quoted, indicate that the molecular weight of poly(ethylene glycol) in water is 2.3 times that in urea or thiourea solution.

A possible structure for a trihydrate is a helix with a core of water molecules. Tadokoro et al.[21] have shown by x-ray crystallography that in the solid state poly(ethylene oxide) crystallizes in a helical configuration. Deryagin[22] has published an electron micrograph of a poly(ethylene oxide) aggregate which shows a spiral structure containing between 8 and 10 threads of polymer per strand of the helix. It is possible that this merely shows his solution process was not as complete as he expected, or that the helix in fact does play some vital role in the drag reduction he observed with this polymer solution.

Maxfield and Shepherd[23] studied the conformation of poly(ethylene oxide) in the solid state, melt and solution by Raman scattering using samples of $\overline{M}_w$ 3×10^6 and 6×10^3 in water and chloroform. The spectral changes on melting were consistent with a helix to coil transition. In both solvents the ordered nature of the solid was largely lost, but some residual ordering was still apparent and the randomly coiled state was attained only above the melting point. They showed that changes in one of the scattered peaks as a function of water concentration was consistent with the formation of a complex involving three water molecules per monomer unit and proposed a simple hydrogen bonding model whereby water molecules were effectively able to form a cross-link between poly(ethylene oxide) molecules resulting in some form of aggregation.

Other evidence for the existence of a trihydrate complex is to be found in the viscosity measurements of Rösch[24,25] and the nuclear magnetic resonance and infrared studies of Liu and Parsons.[26]

B. Polyacrylamide

The complex nature of aqueous solutions of polyacrylamide is well demonstrated by the work of Richardson.[11] If polystyrene deposited from a very dilute solution is examined by a scanning electron microscope, the molecules appear as flattened disks or the compact spheres shown in Fig. 3, depending on the solvent mixture used. This suggests that in sufficiently dilute solution the molecules exist as isolated random coils. By contrast, polyacrylamide sprayed from a very dilute aqueous solution shows the complex fibrillar structure shown in Fig. 5; a high degree of entanglement is evident, but the smallest strands are of molecular dimensions. Richardson noted that the fibrillar structure of polyacrylamide solutions took some time to develop and that an inappropriate method of deposition could result in spherical particles. The opportunity for artifacts resulting from sample preparation is alway high with electron microscopy, but Richardson's results have been confirmed by Audsley and Fursley,[27] who noted that guar gum also forms fibrillar structures.

Narkis and Rebhun[28] studied aging effects in poly-acrylamide solution viscosities. They were able to reverse the decrease in intrinsic viscosity which occurred over 15 days and obtained very similar results whether the aging was carried out under oxygen or nitrogen. They concluded that aging effects could not be attributed to degradation, but were related rather to disentanglement of polymer molecules. Shyluck and Stow[29] continued this investigation and concluded that (a) a high degree of entanglement was established during the polymerization process, (b) the rate constant for the disappearance of viscosity decreased as concentration increased, implying disentanglement of molecules was occurring rather than degradation, and (c) the temperature dependence of the viscosity loss effect was more consistent with the breaking of physical bonds than chemical bonds, again implying disentanglement rather than degradation.

Boyadjian et al.[30,31] used light scattering to study aggregation in polyacrylamide and in two acrylamide/acrylic acid copolymers containing 93% and 73% acrylamide, respectively. They found that aggregates were present in aqueous solution and that aggregation increased with molecular weight and ionic character. The aggregation could be prevented by high salt concentrations.

C. Other drag reducing polymers

Polymer/solvent systems which are known to produce molecular aggregates and also produce drag reduction include polystyrene/toluene[32] if the polymer has been prepared by a redox catalyst leaving sulphate or hydroxyl fragments on the polymer chain, poly(dimethyl siloxane)/toluene,[33] and polyacrylic acid copolymers/water.[34] As noted earlier, many drag reducing polymers are known to form aggregates under certain conditions, but few have been investigated in the same solvents as have been used in drag reduction. If they were, it seems likely that many more polymer/solvent systems would display both effects.

IV. FORMATION OF AGGREGATES BY SHEARING

When solutions of certain drag reducing polymers are subjected to shear, they exhibit peculiar time-dependent behavior and also form aggregates.

Lodge[35] found that prolonged shearing of relatively concentrated (about 2% or 3%) solutions of high molecular weight polystyrene or poly(methyl methacrylate) in dimethyl phthalate resulted in the formation of gel particles between 0.25 mm and 0.5 mm in size. Matsuo et al.[36] used a cone-and-plate viscometer to study the time-dependent shear stress in dilute solutions (0.05%–0.1%) of high molecular weight poly(methyl methacrylate) (M. W. 16×10^6) and polystyrene (M.W. 7×10^6) in a viscous solvent, Arochlor 1248. They found that beyond a certain shear rate rheopexy occurred followed by thixotropy. Light scattering measurements showed the presence of aggregates in their solutions, but since solutions from which aggregates had been removed by quenching from 80 °C showed similar rheological behavior to solutions containing aggregates, they concluded

that these were not responsible for that behavior. Similar rheological behavior was observed with a 0.3% solution of poly(ethylene oxide) (M. W. 3×10^6) in Arochlor,[37] but in this case it was concluded that aggregates were not present in the solutions used. This conclusion is probably incorrect, as the extraordinary stability of poly(ethylene oxide) aggregates revealed by Cuniberti's work[14] was not known at that time.

Laufer et al.[38] repeated some of these experiments using a more sophisticated plate-and-cone viscometer which could accelerate to full speed in less than 0.01 sec and this enabled the initial stages of shearing to be studied; in the previous work observations had been made every 10 sec. When a 1% solution of poly(ethylene oxide) (M. W. 1.5×10^6) in Arochlor was sheared at a constant rate (18 sec^{-1}), it was found that within seconds the shear stress rose to a sharp maximum and then collapsed to a value less than half this over the next minute or so; this was followed by an increase over the next two minutes to a second maximum somewhat less that the first, and then a slight decline to a steady value. Use of lower shear rates or a lower molecular weight poly(ethylene oxide) (M. W. 7.3×10^5) showed similar but less dramatic results.

A 5% solution of polystyrene (M. W. 1.8×10^6) in Arochlor showed somewhat different behavior. There was the same rapid rise in shear stress as had been observed with poly(ethylene oxide) followed by an equally rapid collapse; however, the second rise (the one that Matsuo et al. had observed) only occurred beyond a certain shear rate and was shown to be an artifact caused by a steady uncontrolled rise of temperature. After shearing at high rates (above 100 sec^{-1}) the poly(ethylene oxide) solutions contained particles clearly visible to the naked eye, while the polystyrene solution showed no evidence of inhomogeneities.

The hypothesis put forward by Laufer et al. to explain their results incorporates ideas also used by Matsuo and coworkers. It is assumed that in a solution of poly(ethylene oxide) at rest there exists a network held together by entanglements. When a shear stress is applied, the network behaves like an elastic solid up to a certain point and then ruptures. The entanglements are disentangled, as shown by the decrease of shear stress, but then formation of new entanglements between the oriented and elongated molecules causes an increase in shear stress. These new entanglements have a shorter lifetime than the entanglements at the state of rest, which have been broken at the beginning of the shearing. Since there is a delay between the process of formation of new entanglements and the disentanglement process, the stresses pass through a small maximum. Thus, a stationary process of formation and loosening of entanglements, in accordance with the prescribed rate of shear, gives rise to a steady stress. At high rates of shear only the weaker entanglements, with the shorter lifetimes, have time to disentangle, leaving network particles with longer lifetime intact. These disentangled network particles form aggregates due to the shearing.

All the investigations described here employed poly-

mer solutions of a much higher concentration than are normally used in drag reduction studies and the results are therefore not directly applicable to that field. However, they do suggest the possiblility of the existence or formation of polymer networks or aggregates in turbulent shear flow and that these may play a part in drag reduction.

V. AGGREGATES IN DRAG REDUCTION

A. Observations with a spinning disk apparatus

1. Experimental

The experimental technique involved the addition of solid polymer particles to a tank containing 0.7 m^3 of water in which a disk, 0.23 m diameter, was rotating at a constant speed of between 6 and 20 rps. The torque required to rotate the disk in solution was continuously monitored by a dynamometer as a function of time. Temperature could be controlled from 5 °C to 50 °C by immersion heaters. Full details of the equipment used, including disk roughness profiles, have already been described.[39,40]

Solid polymer powder, sieved into discrete particle size ranges where appropriate, was added either directly to the tank or added below the surface of the water from a suspension of the polymer in a nonsolvent such as isopropyl alcohol.

2. Results obtained

The torque-time curves for the guar gums (Fig. 6) showed a monotonic decrease in the torque required to drive the disk, settling out to a steady value after which no significant changes occurred. However, with poly(ethylene oxide) (Fig. 7), markedly different behavior was observed. An "excess" drag reduction was observed before the torque required to drive the disk
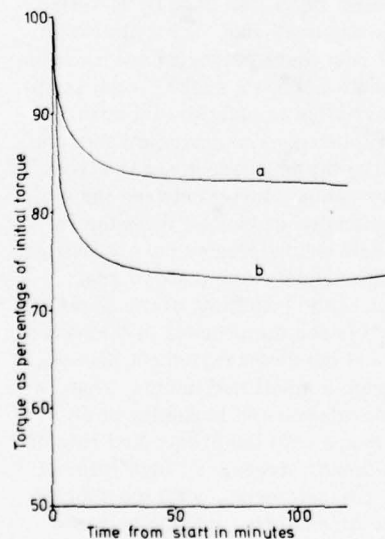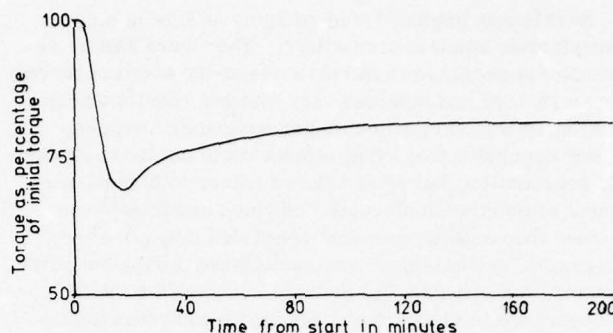
FIG. 7. Typical torque-time curve obtained with poly(ethylene oxide) powder. Polyox coagulent, M.W. $>5 \times 10^6$, 30–36 B.S. mesh, 0.86 ppm, 14 rps, 17 °C.

settled down to a constant value. The excess effect could be made more marked by using polymer powder of smaller mesh size (Fig. 8) although the same steady state drag reduction was observed in all cases.

Increasing the quantity of polymer added to the tank resulted in increased torque reduction until some minimum torque was achieved. The maximum in the excess drag reduction (that is, the minimum in the torque-time curve) reached this limitation first. At higher concentrations, this limitation was also reached by the steady state drag reduction (Fig. 9).

The amount of degradation occurring was seen to be small, as is shown by the almost horizontal torque-

FIG. 6. Torque-time curves obtained for spinning disk on addition of 43 ppm guar gums; (a) Gendriv 162, (b) Gendriv 492S; 14 rps, 17 °C.
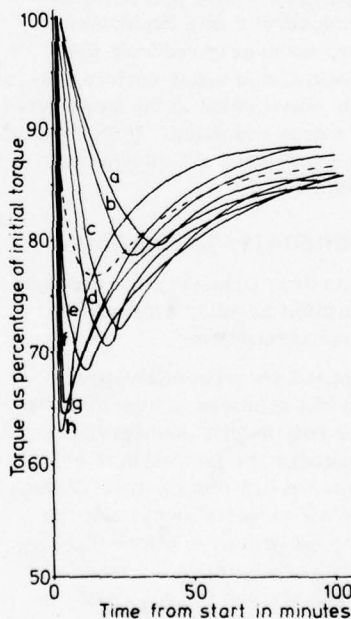
FIG. 8. Torque-time curves obtained with sieved poly(ethylene oxide) powder. The first figures refer to the B.S. sieve sizes, those in brackets to the mean aperture in millimeters: (a) below 22 (over 0.71), (b) 22–25 (0.655), (c) 25–30 (0.55), (d) 30–36 (0.46), (e) 44–85 (0.26), (f) 85–150 (0.141), (g) 150–300 (0.079), (h) over 300 (below 0.053), broken line, unsieved material. Polyox coagulent, 0.86 ppm, 14 rps, 17 °C.
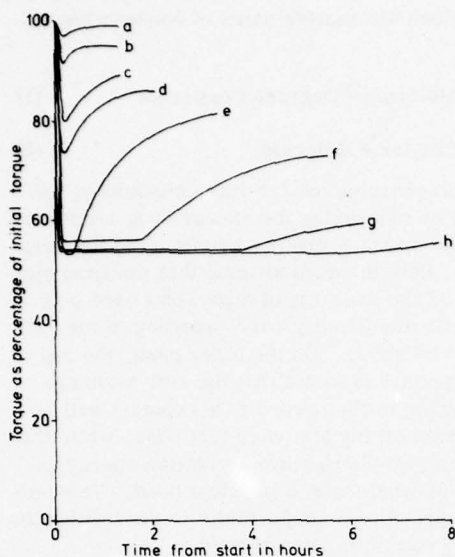
FIG. 9. Effect of polymer concentration (ppm): (a) 0.086, (b) 0.171, (c) 0.43, (d) 0.86, (e) 1.71, (f) 4.30, (g) 8.6, (h) 17.1. Polyox coagulent, 36–44 mesh (0.39 mm), 14 rps, 17 °C.

time line observed once steady state had been achieved (Fig. 7).

Similar effects were observed using polyacrylamide (Fig. 10) where excess drag reduction was noted although the overshoot was not so marked as in the poly(ethylene oxide) case.

The effect of temperature on the excess drag reduction with poly(ethylene oxide) is shown in Fig. 11.

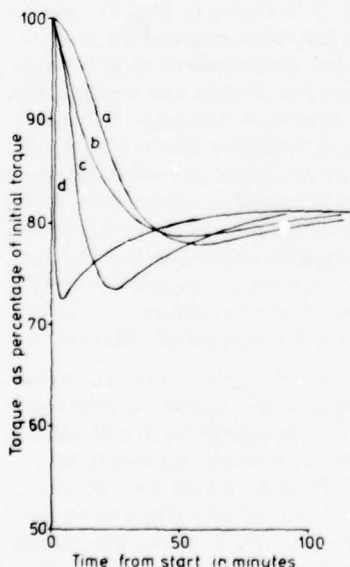The addition of insoluble polymer beads of 30–36

FIG. 10. Torque-time curves for polyacrylamide powder, $\overline{M}_w = 5 \times 10^6$: (a) 22–25 mesh, (b) unsieved (as received), (c) 36–44 mesh, (d) 150–300 mesh. 4.3 ppm, 14 rps, 17 °C.
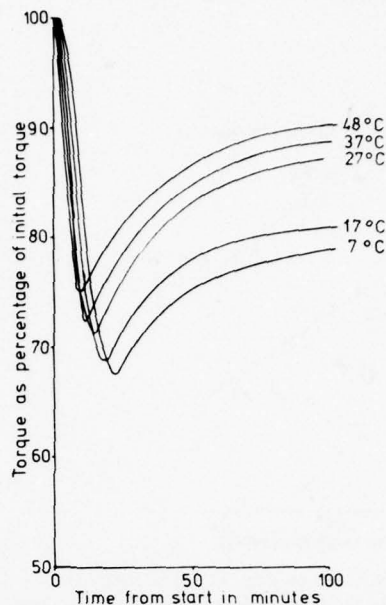

FIG. 11. Torque-time curve for poly(ethylene oxide) as a function of temperature. Polyox coagulent, 30–36 mesh, 0.86 ppm. 14 rps.

mesh and 100–120 mesh size was found to have no effect on the torque-time curve. Visual observation of mixing within the tank using colored dyes showed mixing was complete within 15 sec. Similarly, conductivity probes placed at various positions in the tank showed mixing at every point to be complete within 30 sec after the addition of a slug of salt solution.

3. Interpretation

The observed time to achieve a homogeneous dispersion of dye and salt tracers was short compared with the time scale of the excess drag reduction effect, and allows hydrodynamic anomalies within the tank to be dismissed as an explanation. Likewise, the failure of insoluble polymer spheres of the same particle size as the drag reducing polymers to produce any detectable change in the torque required to drive the disk shows that the effect cannot be attributed to particulate effects similar to the drag reduction observable with fiber suspensions and dust particles.[41] The fact that guar gum behaved in the way one would normally expect in monotonically reducing the torque until steady state was achieved implies that abnormalities in the time-dependent behavior of poly(ethylene oxide) and polyacrylamide must reflect some intrinsic property of these polymers and were not artifacts of the experiment.

To explain these results a hypothesis can be advanced in which the observed behavior is seen as involving the superposition of at least two processes, one of which has a transient existence while the other spans a longer time scale.

The hypothesis assumes the presence in the liquid of three species, each with a different drag reducing ability. The first is solid poly(ethylene oxide) particles of
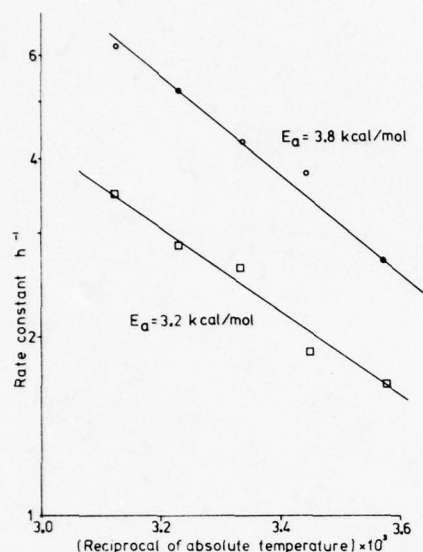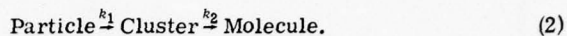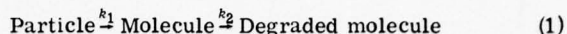
FIG. 12. Arrhenius plot based on Fig. 11. The lower line represents the kinetics of the first process only while the upper line is for the log mean of the rate constants for the two consecutive reactions.

zero drag reducing ability, the concentration of which will monotonically fall from the finite initial value to zero when the particle is totally broken up into free molecules (the second species) of completely dissolved polymer. These free molecules are assumed to be capable of effecting a moderate amount of drag reduction and their concentration will rise from zero to a finite equilibrium concentration. To explain our results, it is necessary to postulate the existence of a third species, an intermediate between the extremes of a solid particle and a free molecule, viz., molecular aggregates or clusters of high drag reducing effectiveness whose concentration will rise from zero, pass through a maximum, and return to zero with time. As the number of these aggregates at any instant must be small yet produce an extra drag reduction, it is necessary to conclude that they are more, rather than less, effective drag reducers than are free molecules. We have previously reported[41] some observations on the time dependent nature of drag reduction as poly(ethylene oxide) particles of different molecular weights dissolve in water, and have also studied the effect of rotation rate. Similar conclusions were also drawn on the basis of these data.

4. Activation energies

It is necessary to differentiate unambiguously these effects from the effects of degradation and this can best be done by measurement of activation energies for the processes concerned. Degradation involves the breaking of chemical bonds, a phenomenon associated with high activation energies (typically 30–100 kcal/mol); on the other hand, the aggregate hypothesis proposed involves only the breaking of physical bonds, i.e., those associated with dissolution where the activation energies involved will be small (typically 2–5 kcal/mol).

Consider the two alternative pairs of consecutive reactions:

$$\text{Particle} \overset{k_1}{\rightleftharpoons} \text{Molecule} \overset{k_2}{\rightleftharpoons} \text{Degraded molecule} \qquad (1)$$

$$\text{Particle} \overset{k_1}{\rightleftharpoons} \text{Cluster} \overset{k_2}{\rightleftharpoons} \text{Molecule}. \qquad (2)$$

The activation energies for the rate constants k_1 and k_2 can be found by measuring the excess drag reduction obtained with the spinning disk as a function of temperature (Fig. 11). Both theories assume that the first step in the reaction is the breaking of a physical bond only and thus the activation energy corresponding to the rate constant k_1 will be small. On the other hand, the degradation hypothesis 1 predicts that the activation energy corresponding to the second rate constant will be high, that of the breaking of a chemical bond, while the cluster hypothesis predicts a low activation energy associated with the breaking of a physical bond. The second stage thus provides an opportunity to distinguish between these two conflicting hypotheses.

To calculate rate constants from the observed torque-time curves it is necessary to assume that drag reduction is directly proportional to concentration, which for the dilute solution used, 0.86 ppm, would appear reasonable. The rate constant for the first process is then the initial slope of the torque-time curve.

For the consecutive reactions $A \rightarrow B \rightarrow C$ the time at which the maximum concentration of B occurs is equal to the reciprocal of the logarithmic mean of k_1 and k_2.[42] In this case the minimum in the torque-time curve is equated with the maximum concentration of the intermediate species. The rate constant, k, is related to the absolute temperature, T, by

$$k = A \exp(-E_a/RT),$$

where E_a is the activation energy, R is the gas constant and A is a pre-exponential probability factor. An Arrhenius plot of $\ln k$ vs $1/T$ is shown in Fig. 12, where the rate constants are as defined herein and the measurements were taken below temperatures at which significant breakdown of hydrogen bonding was taking place. For the first reaction an activation energy of 3.2 kcal/mol was found which clearly indicates that only a physical process is involved, as predicted by both the alternative hypotheses, (and also provides a convenient test of the validity of the assumptions). The second activation energy of 3.8 kcal/mol corresponds to the log mean rate constant for the two processes. As activation energies are additive for consecutive reactions, a value of 0.6 kcal/mol is indicated for the second reaction.

Clearly, with an activation energy this low, the breaking of chemical bonds (degradation) cannot be involved. For comparison, the activation energy for the dissolution of polystyrene in amyl acetate was measured by Ueberreiter and Asmussen[43] as 2.13 kcal/mol while that for the thermal degradation of poly(ethylene oxide) has been measured as 46 kcal/mol.[44] Thus, the results obtained in our experiments cannot be reconciled with the breaking of chemical bonds and the degradation hypothesis 1, but are in accord with those of the disaggregation hypothesis 2.
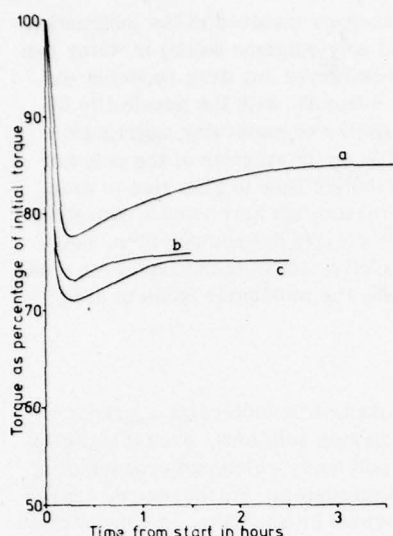
FIG. 13. Stabilization of the aggregates in polyacrylamide (M. W. $= 8 \times 10^6$) with complexing agent ethylenediaminetetraacetic acid (EDTA): (a) polymer alone, (b) polymer plus 2 ppm EDTA, (c) polymer plus 10 ppm EDTA. 5 ppm polyacrylamide, 55–60 mesh, 14 rps, 16.5 °C.

5. Effect of molecular weight

While activation energies provide the most effective method of choosing between the two rival hypotheses, the cluster hypothesis is also more consistent with the observed effect of molecular weight. When different samples of poly(ethylene oxide) were tested at the same concentration under similar conditions, both the excess drag reduction and the equilibrium drag reduction increased markedly with molecular weight.[41] If degradation rather than disaggregation was occurring, one would expect that under the same shearing conditions all samples would degrade to the same equilibrium molecular weight and would therefore show the same equilibrium drag reduction irrespective of the molecular weight of the starting material. The pronounced differences in equilibrium drag reduction are more consistent with undegraded than degraded polymer molecules.

Although for simplicity we have distinguished between an equilibrium species consisting of degraded molecules and one consisting of undegraded molecules, the equilibrium species could also consist of small aggregates. If this were the case no breaking of chemical bonds would be involved and the activation energy for the second process, the breakdown of clusters to smaller clusters, would be similar to that for the breakdown of clusters to individual molecules.

Some support for this idea comes from the behavior of solutions sheared for a long time at different speeds.[41] A solution of poly(ethylene oxide) was sheared for 6 h at 12 rps in the spinning disk apparatus and at the end of this time the drag reduction was quickly measured as a function of disk speed in the same apparatus. When the experiment was repeated using a shearing speed of 7 rps but otherwise identical conditions, the final solution exhibited quite different drag reduction character-

istics from the previous one. The solution sheared at the lower speed would be expected to contain larger aggregates than that sheared at the higher. Not only did the solution sheared at 7 rps show a much greater drag reduction than the other, the drag reduction also showed a greater dependence on disk speed. Since both drag reduction and intrinsic slope increment are known to increase with molecular weight,[45] the results are consistent with the equilibrium species consisting of aggregates rather than individual polymer molecules. More work is, however, required to clarify this point.

6. Aggregate stabilization

An extension of the molecular aggregate hypothesis must be that the excess drag reduction could, in principle, be stabilized by the addition of a suitable crosslinking agent. Such a situation is shown in Fig. 13, where the addition of 2 or 10 ppm of the crosslinking agent, ethylenediaminetetraacetic acid (EDTA) enhances the drag reducing effect of 5 ppm polyacrylamide. It would not be anticipated that this particular agent would permanently crosslink the molecules into clusters, due to the reversibility of the bonding in this case. However, other crosslinking agents are under investigation.

7. Consequences of the proposed model

If some limit exists to the maximum drag reduction obtainable in a particular case, such as Virk's maximum drag reduction asymptote,[46] then at concentrations high enough for the individual molecules to show maximum drag reduction the effect of the transient species will not be obvious. Thus, a solution which shows constant drag reduction with time may still have a molecular structure which is changing with time.

It is generally accepted that drag reduction occurs when some characteristic scale such as length, time, or energy of the polymer molecule becomes of comparable dimensions with the corresponding scale of the turbulence.[2,47] Thus, it can be envisaged that the scales associated with aggregates will be larger than those for individual molecules and aggregates will exhibit drag reduction in flows characterized by lower turbulence scales than those required for molecules. An experiment carried out under sufficiently low shear rates may reveal the presence only of aggregates while at higher shear rates both aggregates and molecules may manifest themselves in reduced drag. The same solution may therefore have quite different characteristics in experiments performed under different shear rates.

The work of Brennan and Gadd[48] is relevant here. They observed that the errors in Pitot tube measurements (low shear) rose with time in a poly(ethylene oxide) solution, went through a maximum, and then fell again to zero. During this time the drag reduction in a tube (higher shear) remained constant. This would be consistent with our hypothesis, with the Pitot tube sensing the presence of aggregates only and the tube experiment sensing both species.

Further evidence for the hypothesis can be inferred from the work of Ellis[49] in which degradation apparently

took place faster in a large diameter tube than in a small one. Using 10 ppm poly(ethylene oxide) solutions the drag reduction was measured immediately and then again after one hour's continuous circulation. In a 0.115 cm diam tube the fresh solution gave 51% reduction and after one hour 50% reduction. A 1.43 cm diam tube, while giving an initial 54% reduction, only gave 1% after one hour. This is readily explainable on the basis that the shear rate in the large diameter tube was sufficiently low to be sensitive to the presence only of aggregates which had virtually disappeared after one hour; the smaller tube, however, was able to respond to the presence of both molecules and aggregates.

Tullis and Ramu[3] injected concentrated poly(ethylene oxide) solution into a pipe and followed the drag reduction as a function of distance down the pipe. They observed that a high initial drag reduction occurred which fell off to a steady state value farther down the pipe. Their graphs could readily be explained on a disaggregation hypothesis.

8. Other evidence for aggregates in drag reduction

The presence of aggregates in drag reducing solutions has long been suspected. Fabula[50] first reported "raggedness" in the response of a hot film anemometer and postulated molecular aggregates as a possible cause. Gadd[51] found that the aging effect in poly(ethylene oxide) solutions on friction reduction was small at high concentrations but became more pronounced as the concentration fell to around 10 ppm. This he thought to imply that large molecular aggregates were initially present but were broken up by aging. White[52] also postulates the presence of clusters to explain the fall-off in effectiveness of an aged solution. Vlasov and Kalashnikov[53] studied the diffusion of turbulent jets and interpreted their results as showing the existence of a lattice of polymer chains with poly(ethylene oxide) but no such structure for guar gum. Granville[54] attempted to distinguish between the viscoelastic nature of poly(ethylene oxide) solutions and their drag reduction on the basis that elasticity disappears with time while drag reduction does not, one explanation being that elasticity is stored in the entanglements which are slowly dispersed by stirring and by time.

A macromolecular entanglement hypothesis has been proposed by Kowalski and Brundrett[55] based on measurements of the turbulent energy spectrum with and without polymer solutions. The measured changes in the dissipative scales of the flow correspond to much larger molecules than were nominally present but could correspond to large intertwined chains which entrap large amounts of the solvent. A formula was developed which related the size of the entanglement to the size of the dissipative eddy.

The overall amount of evidence for the existence of molecular aggregates or entanglements is growing rapidly, particularly with regard to the way in which such species can dominate the behavior of the solution. This does not detract from the considerable amount of evidence for degradation which takes place over and above the effects discussed. The complex physico-chemical processes involved in the interaction of polyacrylamide and poly(ethylene oxide) in water can thus make the interpretation of any drag reducing experiments extremely difficult, with the possibility of this secondary phenomenon of molecular aggregation overshadowing the primary interaction of the polymer molecules with the turbulent flow to give rise to drag reduction. For this reason, we have used a non-polar liquid, toluene, with a clearly defined polymer, polystyrene, known to dissolve totally in the liquid for studies aimed at elucidating the molecular basis of drag reduction.[2]

VI. CONCLUSIONS

There seems little doubt that molecular aggregates commonly occur in polymer solutions, even at high dilutions, and that many polymers which can produce drag reduction also form aggregates. Furthermore, aggregates may often be formed by shearing, in concentrated solutions at least.

We have shown that the results we have obtained using poly(ethylene oxide) and polyacrylamide powder in a spinning dish apparatus are most readily explained by the transient existence of molecular aggregates and that these may be more effective drag reducers than the individual polymer molecules themselves; moreover, the results of a number of other investigators are consistent with the presence in solution of molecular clusters. Despite this, it remains to be shown that the existence or formation of supermolecular structures is necessary for drag reduction, although the fact that three of the most effective polymers, poly(ethylene oxide), polyacrylamide, and guar gum, readily do so is highly suggestive.

The aggregate or entanglement theory has received comparatively little attention because it is thought that the volumetric concentration of polymer molecules in a typical drag reducing solution is too low for such structures to occur. This is not always borne out by the available data. Thus, in one recent review[45] an example is given of a drag reducing solution of poly(ethylene oxide) for which it is estimated that the volume fraction occupied by the polymer coils is 0.1, yet the author then says that the low volume fraction suggests that individual polymer molecules are involved rather than entangled clusters. A volume fraction of 0.1 means that the average separation of the randomly coiled polymer molecules is of the same order as their diameter and in this situation the possibility of intermolecular interactions cannot be dismissed.

The size of polymer molecules in solution is commonly determined by intrinsic viscosity measurements and these are carried out at low shear rates. Since in solution polymer-solvent interactions are preferred to polymer-polymer interactions, one would expect polymer molecules not to interfere with each other under such conditions. This situation is very different from that in turbulent flow, where there may not be time for molecules to get out of each other's way during the formation or propagation of an eddy. The extent which they are able to do so will presumably depend on the relaxation time of the molecule or some related quantity,

and this may be the reason why a number of workers have found correlations between polymer and fluid time scales during drag reduction.[2]

Hitherto most attempts to elucidate the molecular basis of drag reduction have consisted of investigations into how the effect is influenced by gross molecular parameters such as molecular weight and chain flexibility. While these investigations have yielded results of practical value, it is unlikely the phenomenon will be understood until more is known about the way polymers behave in a turbulent field. This will almost certainly involve physico-chemical methods of characterization such as the use of infrared and Raman spectra for the detection of hydrogen bonding. It will also be desirable to use well characterized polymer samples of narrow molecular weight distribution in organic nonpolar solvents, the latter considerably reducing the complexities inherent in using water.

Most workers investigating drag reduction confine themselves to commonly available polymers. However, synthetic polymer chemistry has reached the stage where it is possible to synthesize polymers with precisely defined characteristics,[56-58] particularly stereoregular polymers, which should allow a systemic investigation of the interaction of the polymer with the turbulent flow field.

The potential reward, in practical terms, for a proper understanding of the molecular basis of drag reduction is high, for once this has come about the way will be open for cheaper, more effective, and more stable polymers.

[1]F. H. Bark, presented at Euromech 52, Royal Institute of Technology, Stockholm, Sweden (1974).

[2]L. R. Cox, A. M. North, and E. H. Dunlop, in *Proceedings of the International Conference on Drag Reduction*, Cambridge, 1974 (BHRA Fluid Engineering, Bedford, United Kingdom, 1974), paper G2.

[3]J. P. Tullis and K. L. V. Ramu, in *Proceedings of the International Conference on Drag Reduction*, Cambridge, 1974 (BHRA Fluid Engineering, Bedford, United Kingdom, 1974), paper G3.

[4]H.-G. Elias, in *Light Scattering from Polymer Solutions*, edited by M. B. Huglin (Academic, New York, 1972), Chap. 9.

[5]G. Rehage, Prog. Colloid Polym. Sci. 57, 11 (1975).

[6]Z. Czlonkowska-Kohutnicka, Polimery 19, 517 (1974).

[7]M. J. Richardson, J. Polym. Sci., Pt. C 3, 21 (1963).

[8]W. R. Moore, in *Progress in Polymer Science*, edited by A. D. Jenkins (Pergamon, London, 1967), Vol. 1, p. 38.

[9]F. W. Billmeyer, *Textbook of Polymer Science* (Wiley, New York, 1962), 2nd ed., p. 84.

[10]M. J. Richardson, Nature 198, 252 (1963).

[11]M. J. Richardson, Proc. R. Soc. London, Ser. A 279, 50 (1964).

[12]G. Delmas, J. Appl. Polym. Sci. 12, 839 (1968).

[13]C. Strazielle, Makromol. Chem. 119, 50 (1968).

[14]C. Cuniberti, Polymer 16, 306 (1975).

[15]C. Cuniberti, Eur. Polym. J. 10, 1175 (1974).

[16]C. Cuniberti and R. Ferrando, Polymer 13, 379 (1972).

[17]D. K. Carpenter, G. Santiago, and A. Hunt, J. Polym. Sci. Pt. C 44, 75 (1974).

[18]A. Sarker and K. Ghosh, Kolloid-Z. Z. Polym. 236, 140 (1970).

[19]K. Ghosh, B. C. Chatterjee, and A. Sarkar, Colloid Polym. Sci. 254, 429 (1976).

[20]N. B. Graham, presented at the Faraday Society, Cranfield Institute of Technology, United Kingdom (1976) (to be published).

[21]H. Tadokoro, H. Chatani, and S. Murahashi, J. Chem. Phys. 41, 2902 (1964).

[22]B. V. Deryagin, K. F. Lyashev, and O. G. Novik, Dokl. Akad. Nauk. USSR 218, 100 (1974).

[23]J. Maxfield and I. W. Shepherd, Polymer 16, 505 (1975).

[24]M. Rösch, Kolloid-Z. 147, 78 (1956).

[25]M. Rösch, Fette, Seifen, Anstrichm. 65, 223 (1963).

[26]K.-J. Liu and J. L. Parsons, Macromolecules 2, 529 (1969).

[27]A. Audsley and A. Fursley, Nature 208, 753 (1965).

[28]N. Narkis and M. Rebhun, Polymer 7, 507 (1966).

[29]W. P. Shyluk and F. S. Stow, J. Appl. Polym. Sci. 13, 1023 (1969).

[30]R. Boyadjian, G. Seytre, P. Berticat, and G. Vallet, Eur. Polym. J. 12, 401 (1976).

[31]R. Boyadjian, G. Seytre, D. Sage, and P. Berticat, Eur. Polym. J. 12, 409 (1976).

[32]Q. A. Trementozzi, R. F. Steiner, and P. Doty, J. Am. Chem. Soc. 74, 2070 (1952).

[33]G. Adank and H.-G. Elias, Makromol. Chem. 102, 151 (1967).

[34]V. A. Kargin, Z. Y. Berestneva, E. P. Cherneva, T. D. Ignatovich and G. S. Potapova, Dokl. Akad. Nauk. USSR 175, 1318 (1967).

[35]A. S. Lodge, Polymer 2, 195 (1961).

[36]T. Matsuo, A. Pavan, A. Peterlin, and D. T. Turner, J. Colloid Interface Sci. 24, 241 (1967).

[37]A. Pavan, T. Matsuo, A. Peterlin, and D. T. Turner, J. Colloid Interface Sci. 24, 273 (1967).

[38]Z. Laufer, H. L. Jalink, and A. J. Staverman, J. Polym. Sci. Polym. Chem. Ed. 11, 3005 (1973).

[39]E. H. Dunlop, Ph. D. thesis, University of Strathclyde, Glasgow, Scotland (1973).

[40]L. R. Cox, E. H. Dunlop, and A. M. North, Nature 249, 243 (1974).

[41]R. Pfeffer and R. S. Kane, in *Proceedings of the International Conference on Drag Reduction*, Cambridge, 1974 (BHRA Fluid Engineering, Bedford, United Kingdom, 1974), paper F1.

[42]O. Levenspiel, *Chemical Reaction Engineering* (Wiley, New York, 1972), 2nd ed., p. 60.

[43]K. Ueberreiter and F. Asmussen, J. Polym. Sci. 23, 75 (1957).

[44]S. L. Madorsky and S. Straus, J. Polym. Sci. 36, 183(1959).

[45]P. S. Virk, Am. Inst. Chem. Eng. J. 21, 625 (1975).

[46]P. S. Virk, J. Fluid Mech. 45, 417 (1971).

[47]P. S. Virk and E. W. Merrill, in *Proceedings of the Symposium on Viscous Drag Reduction*, Dallas, 1968 (Office of Naval Research and National Aeronautics and Space Administration, Washington, D.C., 1968), p. 107.

[48]C. Brennan and G. E. Gadd, Nature 215, 1368 (1967).

[49]H. D. Ellis, Nature 226, 352 (1970).

[50]A. G. Fabula, in *Proceedings of the Sixth Symposium on Naval Hydrodynamics*, edited by R. D. Cooper and S. W. Doroff (Office of Naval Research, Washington, D.C., 1966), p. 39.

[51]G. E. Gadd, Nature 217, 1040 (1968).

[52]A. White, in *Viscous Drag Reduction*, edited by C. S. Wells (Plenum, New York, 1969), p. 303.

[53]S. A. Vlasov and V. N. Kalashnikov, Nature 224, 1195 (1969).

[54]P. S. Granville, U. S. Naval Ship Research and Development Center, Hydromechanics Laboratory Technical Note 118 (1968).

[55]T. Kowalski and E. Brundrett, in *Proceedings of the International Conference on Drag Reduction*, Cambridge, 1974 (BHRA Fluid Engineering, Bedford, United Kingdom, 1974), paper C1.

[56]J. Pannell, Polymer 12, 547 (1971).

[57]J. Pannell, Polymer 12, 558 (1971).

[58]J. Pannell, Polymer 13, 1 (1972).

Drag reduction by compliant walls

G. Zimmermann

Max-Planck-Institut für Strömungsforschung, Göttingen, Germany

The turbulent boundary layer flow over a flat plate, smooth and hard except for a finite section, is considered. In this section the plate may be compliant, have a prescribed waviness, or consist of an "active wall", etc. The section thus constitutes a disturbance to the turbulent boundary layer flow over a completely smooth and hard plate. An exact integral equation for the resulting disturbances of the fluid stresses at the plate is derived. To a reasonable approximation, this integral equation reduces to an explicit integral representation of the stress disturbances at the plate in terms of the undisturbed flow and the properties of the disturbing plate section. Further evaluation then requires the use of measured data. For a certain type of compliant wall a drag reduction of 1%–10% is estimated.

I. INTRODUCTION

Among other possibilities the use of compliant coatings has been suggested as a means of reducing the drag of ships, airplanes, etc. Experiments on this problem have so far remained inconclusive, probably due to its great complexity. Another difficulty consists of the wide choice of compliant coatings. In this paper a theoretical estimate of the possible effects of drag of such compliant coatings is given.

To this end the flow over a flat plate, smooth and hard except for a finite section, is considered. This finite section, situated sufficiently downstream of the plate edge so as to be underneath the fully developed turbulent boundary layer, is to consist of some sort of compliant material (or alternatively of an "active wall" etc.).

It is assumed that the compliant material is relatively stiff as compared with the fluid forces exerted on it and that therefore, the presence of the compliant section constitutes a small perturbation only of a basic flow (velocity $\mathring{\mathbf{u}}$, pressure $\mathring{p}$), this being the turbulent boundary layer flow over a plate which is smooth and hard everywhere. It is usual in treating the compliant wall problem to approximately fulfill the coupling condition between flow and compliant material at the mean or undisturbed position of the interface between the two. This is a good approximation only under the small perturbation assumption made herein or a similar assumption, a consequence which is not always stated. Asymptotic expansion with respect to a suitable perturbation parameter breaks the problem down into a series of successive computational steps of which only the first two are considered here. In the first step, the undisturbed pressure $\mathring{p}$ excites the compliant section into motion giving rise to a velocity perturbation on the compliant section. No velocity perturbation is created on the hard section of the plate (nor, as is assumed, in the upstream part of the plate plane). In the second step then, the flow perturbation has to be calculated (in the half-space above the plate plane) from the Navier–Stokes equations linearized about the undisturbed flow and with prescribed velocity perturbations in the plate plane; even though it is linear, this is still a formidable problem. A method to extract approximate information on the resulting perturbations of the wall stresses, especially wall shear stresses, is sketched in the next paragraph.

For an extended discussion of the whole problem the reader is referred to Ref. 1.

In the case of an "active wall", etc., the velocity perturbation at the wall is created in a way different from that described as the first step here. However, as is obvious, this does not affect the second step.

II. FLOW PERTURBATION

The flow perturbation (velocity $\mathbf{u}$, pressure p) has to be calculated from the linearized nondimensional Navier–Stokes equations

$$\frac{\partial \mathbf{u}}{\partial t} - \mu \Delta \mathbf{u} + \nabla p = -\mathbf{q}, \qquad \mathbf{r}_0 \in B, \quad 0 \le z < \infty \tag{1}$$

$$\nabla \cdot \mathbf{u} = 0,$$

$$\mathbf{u} = \mathbf{u}_0, \qquad \mathbf{r}_0 \in B, \quad z = 0,$$

and a suitable decay condition at infinity. Here, $\mathbf{q}$ is an abbreviation for the linearized convective terms, μ is a nondimensional viscosity, the reciprocal of a Reynolds number, $\mathbf{r}_0$ is the position vector in the plate plane B, z is the distance from the plate, and $\mathbf{u}_0$ are the velocity perturbations prescribed at the plate, nonzero only over the finite compliant section.

Because of the presence of the undisturbed basic flow $\mathring{\mathbf{u}}$ in the linearized convective terms $\mathbf{q}$, this problem for the flow perturbation $\mathbf{u}$, p cannot be solved exactly by analytical means. However, with the help of a suitable Green's solution of the left-hand side of Eq. (1), the following equation may be derived from this problem

$$\tau_0^{l3} = \int_{-\infty}^{\infty} \int_B \left[G_l^i u_0^l + \int_0^\infty H_l^i q^l \, dz \right] d^2 \mathbf{r}_0' dt' \tag{2}$$

(implied summation over l). Here, τ_0^{l3} are the values of the stress perturbations at the plate at field point $(\mathbf{r}_0, t)$, u_0^l and q^l are the components of $\mathbf{u}_0$ and $\mathbf{q}$, respectively, at the source point (r_0', t'), q^l also depends on z. G_l^i and H_l^i result from the Green's solution, depending on $(\mathbf{r}_0 - \mathbf{r}_0', t - t')$. H_l^i also depends on z. q^l contains the unperturbed flow and flow perturbation, both determined by the corresponding velocities and stresses at the plate. Thus, Eq. (2) is an integral equation for the stress perturbations at the wall τ_0^{l3}. The unknown terms q^l again constitute the essential difficulty in Eq. (2).

The Green's solution required in Eq. (2) is easily obtained via Fourier transforms (with respect to $r_0 - r_0'$ and $t - t'$). In the Fourier transform version, the z integral in Eq. (2) has the general form

$$\int_0^\infty e^{-\gamma z} \hat{q}^l \, dz \, ,$$

where $\hat{q}^l$ is the Fourier component of q^l at wavenumber $\mathbf{k}$ and frequency ω, and $\gamma = k(=|\mathbf{k}|)$ or $\gamma = (k^2 - i\omega/\mu)^{1/2}$.

There seems to be evidence that the spatial structure of q^l is such that it extends in the direction normal to the wall (z direction) at least to the same degree as in the directions parallel to the wall. This means that the Fourier transform (with respect to the wall plane variables and the time) $\hat{q}^l$ of q^l at wavenumber $\mathbf{k}$ remains essentially constant over an initial distance normal to the wall $0 \leq z \leq \pi/k$. As essentially $\gamma = k$, $\exp(-\gamma z)$ will decrease by one or two orders of magnitude within this distance. Therefore,

$$\int_0^\infty e^{-\gamma z} \hat{q}^l \, dz \approx \int_0^\infty e^{-\gamma z} \, dz \cdot \hat{q}_0^l = \frac{\hat{q}_0^l}{\gamma} \, , \qquad (3)$$

where the right-hand side may also be obtained as the leading term of an expansion of the left-hand side in powers of $1/\gamma$. By retaining higher order terms in this expansion, which is valid under the same conditions as the simplification introduced in Eq. (3), one may approximate the left-hand side of Eq. (3), and thus the right-hand side of Eq. (2), to any degree of accuracy.

On introducing the approximation given in Eq. (3) the integral Eq. (2) reduces to an integral representation for the stress perturbations at the wall in terms of the prescribed velocity perturbations at the wall and the known Green's solution.

In the temporal mean and for the shear stresses this integral representation is

$$\tau_0^{\iota 3} = \frac{-1}{2\pi\mu} \int_B \frac{(r^\iota - r^{\iota\prime})(r_\lambda - r_\lambda')}{|\mathbf{r}_0 - \mathbf{r}_0'|^3} \, \overline{u_0^3 \, \overset{\circ}{\tau}_0^{\lambda 3}} \, d^2 r_0' \, ,$$

where the greek indices are restricted to the values 1, 2 and accordingly, r^ι or r_λ are the components of $\mathbf{r}_0$.

Further evaluation of this requires knowledge of the correlation between the normal component of the prescribed velocity perturbation at the plate u_0^3 and the unperturbed shear stresses, $\overset{\circ}{\tau}_0^{\iota 3}$.

Confining our attention to the case of a compliant wall and assuming the compliant section of the plate to consist of a thin homogeneous elastic layer, the correlation may be reduced to wall pressure-velocity correlations for the unperturbed flow, for which measured data are available. These data, however, only suffice for a rough estimate.

It turns out that for a light fluid such as air a drag reduction on the order of 1% may be expected. For heavier fluids such as water, the density of which is comparable to the density of the compliant material, a reduction in drag on the order of 10% may be obtained. Such estimates obviously depend on the type of compliant section assumed. Other types of compliances may or may not result in reduced drag. Conversely, the integral equation and its derivatives given here, especially in their Fourier transform version, may be used to determine types of compliant walls most suitable for reducing drag.

[1] G. Zimmermann, Max-Planck-Institut für Strömungsforschung, Report 10a/(1974).

Investigation of pressure fluctuations beneath a turbulent boundary layer by means of an optical method

A. Dinkelacker, M. Hessel, G. E. A. Meier, and G. Schewe

Max-Planck-Institut für Strömungsforschung, Göttingen, Federal Republic of Germany

An optical method has been developed by Emmerling, Meier, and Dinkelacker which allows the investigation of the instantaneous structure of the wall pressure field under a turbulent boundary layer. The main component of this method is a pressure transducer consisting of several hundred small elastic membranes, the displacements of which are recorded by interferometric means with a high-speed camera. The method is explained and examples of measurements in a wind-tunnel are presented. The measurements show the development and convection of pressure patterns of a wide range of sizes (from larger than one boundary layer thickness δ down to 0.1 δ) and with a wide range of convection velocities (from about 0.9 U_∞ down to about 0.2 U_∞, with U_∞ the flow velocity outside the boundary layer). Some speculative considerations are made on what sort of flow configurations might be connected with the observed pressure patterns.

I. INTRODUCTION

During recent years in Göttingen, as well as in Southampton, several experimental investigations with flow over compliant walls have been performed. These include three investigations with turbulent pipe flow,[1-3] one with turbulent flow over a flat plate,[4] and one in which an attempt was made to repeat the experiment of Kramer with a rising body technique.[5] For different reasons, these experiments remained inconclusive with respect to the question of drag reduction by means of compliant walls. In our opinion one reason for the difficulties encountered in experiments with compliant walls is that one does not have enough knowledge of the mechanisms in a turbulent boundary layer and especially that one does not have enough knowledge of pressure fluctuations beneath a turbulent boundary layer. Such pressure fluctuations certainly play an important role in the problem of interactions between turbulent flows and compliant walls. So, we have started to investigate turbulent wall pressure fluctuations in some detail.

Usually, wall pressure fluctuations are measured with the help of microphones built flat into one of the flow bounding walls. Such measurements, however, give only the pressure fluctuations at one point on the wall or if several microphones are used, at a few points. Emmerling *et al.*[6,7] have developed a new optical method which allows the investigation of the wall pressure field and of its temporal changes. In the following, the method and the experimental arrangements are briefly explained and some results of experiments performed in a low speed wind tunnel are reported.

II. THE METHOD

The main component of the method is a pressure transducer which consists of several hundred small elastic membranes. The membranes are silvered and the whole transducer forms one mirror of a Michelson interferometer. This transducer is built flat into the wall of a low speed wind tunnel. The turbulent pressure fluctuations in the wind tunnel cause small displacements of the membranes and these displacements are recorded with the interferometer and a high speed camera. No influence of the membrane movements on the flow is to be expected since the displacements are only small fractions of the thickness of the viscous sublayer. The films are evaluated and from each frame a map of the instantaneous pressure distribution over the field of observation (here 50 mm x 30 mm) can be constructed. These maps, which are comparable to the well-known isobaric maps in meteorology, give information on the processes in the turbulent boundary layer without the need to introduce a probe into the flow.

III. THE EXPERIMENTAL ARRANGEMENTS

A. The pressure transducer

Figure 1 shows the pressure transducer. A thin elastic foil (approximately 35 μm thick) is stretched across a rigid base constructed of brass, which has several hundred small holes of 2.5 mm diam. The surface of the base was lapped so that the deviation from
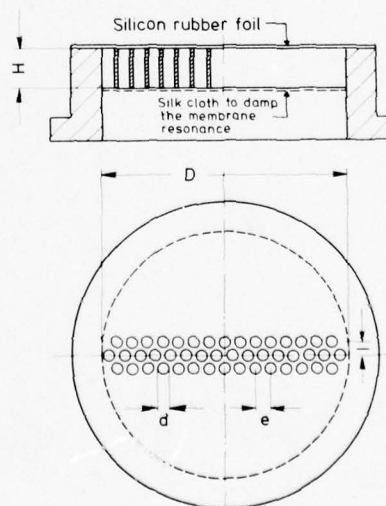

FIG. 1. Pressure transducer ($D = 97$ mm, $H = 6$ mm, $d = 2.5$ mm, $e = 3$ mm, $l = 2.6$ mm).

flatness across the entire surface was reduced to the order of 1 μm. On this base, the thin foil is fixed by means of adhesive. The main problem in producing the transducer is obtaining a thin foil with a low elasticity modulus, and with a smooth surface and uniform thickness, accurate to within a fraction of a light wavelength. This extreme accuracy is necessary because, otherwise even without flow, a dense interference fringe pattern would appear. The foils used here were made of silicone rubber and silvered with the help of a vacuum coating device (for details see Ref. 6). The pressure transducer was fixed in a metal ring and mounted flush in the wall of the wind tunnel. Small holes were drilled in the ring to allow for pressure equalization between the wind tunnel and the chamber behind the membranes.

Static calibration of the transducer was performed by applying a static pressure difference to the membranes. Figure 2 shows that the number of interference fringes (usually concentric rings) occurring on a membrane is very nearly proportional to the static pressure applied. Changes in the fringe pattern of about 0.25 fringes (corresponding to about 1 μbar) can be evaluated. Dynamic calibration was accomplished with a loudspeaker and two calibrated microphones. Figure 3 shows the frequency response of one transducer membrane. It should be noted that this relatively flat frequency response was only achieved after placing a damping layer (silk cloth) at the rear side of the base plate (compare Fig. 1). Without this damping the membranes showed a sharp resonance peak at about 1 kHz. The equality of the different transducer membranes was checked with the help of the interferometer. In fact, the membranes of the transducer used here showed rather low inequalities.

The spatial resolution of the transducer is determined by the diameter of the individual membranes which was $d = 2.5$ mm. With the flow used this diameter corresponds to 0.08 δ or to 57 ν/u_τ, where δ is the boundary layer thickness, ν is the cinematic viscosity, and u_τ is the shear velocity (under certain circumstances one can draw conclusions even on pressure patterns which are smaller than the transducer. These evaluations, however, in which details of the shape of the fringe pattern, e.g., "S" shape, are taken into account only give qualitative results). An additional problem encountered was that the thin rubber foils lose their tension after periods of a month or so. For this reason,
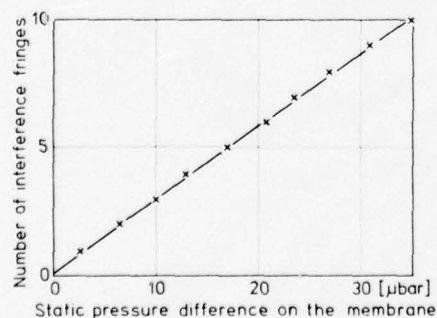

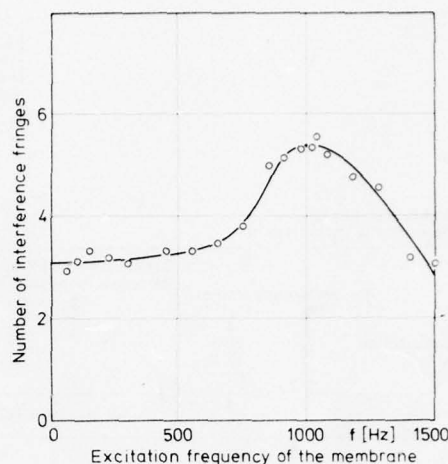FIG. 2. Calibration curve for the membranes (light wave length $\lambda = 0.547$ μm).

FIG. 3. Frequency response of the membranes (transducer with silk cloth for damping).

before each run, the static calibration of the membranes had to be repeated.

B. The wind tunnel

The arrangement is shown in Fig. 4. The test section of the wind tunnel has a cross section of 200 mm × 100 mm and a length of 2.4 m. In the inlet of the tunnel two sets of drinking straws were arranged as flow smoothing devices. The flow is driven by suction and controlled by a sonic nozzle. Great care was taken to reduce noise and vibrations in the whole arrangement. The tunnel is of heavy construction with walls of cast aluminium about 20 mm thick. All the parts lying within the dotted lines shown in Fig. 4 are rigidly connected and elastically suspended on springs. The fundamental frequency of this system is less than 1 Hz. Furthermore, the sonic nozzle was especially designed in order to produce low noise levels. The outside casing of the nozzle is constructed with double walls. A sound absorber is mounted downstream of the nozzle (absorber B in Fig. 4). In principle, a sonic nozzle does not radiate sound upstream, but, in practice, it still produces some noise in the upstream direction (flow noise in the convergent area, transmission in the flow boundary layer, transmission in the walls of the nozzle). To eliminate these influences the sonic nozzle is connected to the test section only with a soft rubber gasket and a specially designed sound absorber (absorber A in Fig. 4). Noise in the laboratory is also reduced as far as possible.

The coordinate system is chosen so that the origin lies in the middle of the transducer surface. The positive x axis points in the flow direction, the positive y axis is normal to the transducer, and the z axis points along the wall in the spanwise direction forming a right-handed system with the other axes.

C. The optical apparatus

The arrangement of the optical apparatus is also shown in Fig. 4. The individual parts of the interferometer
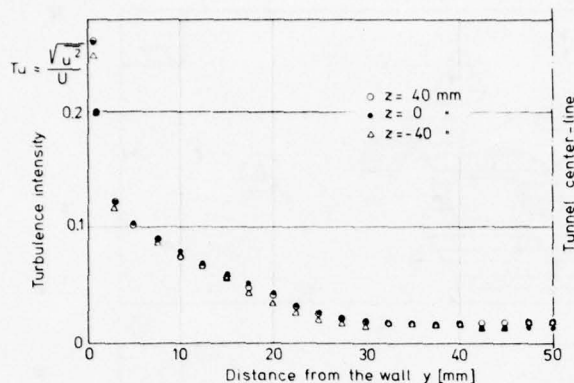
FIG. 4. Experimental facility.

are mounted on a stable steel frame. A 100-W super pressure mercury lamp serves as the light source. Passing through an iris, an interference filter ($\lambda = 0.547$ μm) and a collimator (100 mm diam), the light reaches the beam splitter and from there it goes partly to the pressure transducer and partly to the reference mirror. As can be seen in Fig. 4, one interferometer beam passes through the turbulent flow twice. Since the refractive index of air is dependent upon density, sufficiently large pressure fluctuations in the flow can change the optical path of the beam. This could lead to errors in the evaluation of the membrane displacement. It can be shown, however, that at a flow velocity of 8.5 m/sec, these disturbances are negligibly small. Photographs of the interference patterns were taken with a high-speed camera (Fastax WF-4m). The frame rate at any point on the film can be determined with the aid of timing marks (1 msec) on the edge of the film.

D. The flow

For the experiment reported here the sonic nozzle was adjusted so that the centerline velocity in the tunnel at the position of the transducer was $U_\infty = 8.5$ m/sec. In this case the flow was the "tunnel inlet flow" type with boundaries becoming turbulent immediately after the drinking straws (see Fig. 4). Characteristic qualities of the flow used in this investigation are shown in Figs. 5 to 8. For the position of the pressure transducer the following parameters are obtained: Centerline velocity $U_\infty = 8.5$ m/sec, dynamic pressure $q_\infty = 420$ μbar, shear velocity $u_\tau = 0.34$ m/sec, sublayer length scale $\nu/u_\tau = 44$ μm, boundary layer thickness $\delta = 30$ mm, momentum thickness $\theta = 3.5$ mm, Reynolds number $Re_\theta = 2 \times 10^3$, displacement thickness $\delta^* = 4.6$ mm, pressure gradient -53 μbar per meter or -0.006 q_∞ over the length of the transducer observation field.

FIG. 5. Velocity distributions in the test section of the wind-tunnel (measured with a Pitot tube at $x = -150$ mm, $U_\infty = 8.3$ m/sec).

FIG. 6. Dimensionless velocity distribution (recalculated values from Fig. 5).

S218   Phys. Fluids, Vol. 20, No. 10, Pt. II, October 1977

Dinkelacker, Hessel, Meier, and Schewe   S218

FIG. 7. Turbulence intensity distribution (measured with a hot wire at $x = -150$ mm, $U_\infty = 8.3$ m/sec).

E. Film evaluation

Figure 9 shows one individual frame from a film which was taken at a framing speed of about 7000 frames per second. The field of observation is about 50 mm ×30 mm and contains patterns of about 200 small circular membranes. With the help of the calibration curve (Fig. 2) and with the help of a so-called base fringe pattern, the amplitude and the direction of the membrane displacement can be determined. The base fringe pattern is produced by turning the reference mirror of the interferometer in such a way that with no pressure difference at the membranes (i.e., with no flow in the tunnel) approximately two interference fringes, extending in the lengthwise direction, appear on each membrane. For the evaluation, it is necessary to determine the difference between the instantaneous fringe pattern on a membrane and the base fringe pattern of the same membrane. This part of the evaluation makes the evaluation process rather difficult and time consuming and up to now has made automatic film evaluation unsuccessful. As one can see in Fig. 9 some of the fringes have an S shape which indicates a local pressure gradient on the membrane. Absolute evaluation in this case is difficult because both the calibration
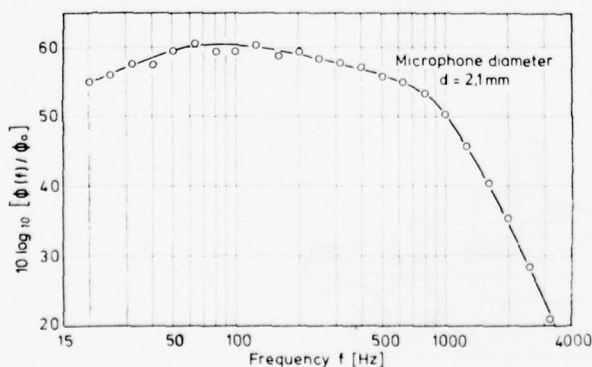
FIG. 8. Spectral density of wall pressure fluctuations relative to a reference spectral density ϕ_0 of $(2 \times 10^{-4}\ \mu bar)^2$/Hz. (Measured with a microphone mounted flush in the tunnel wall at the position of the optical transducer.)
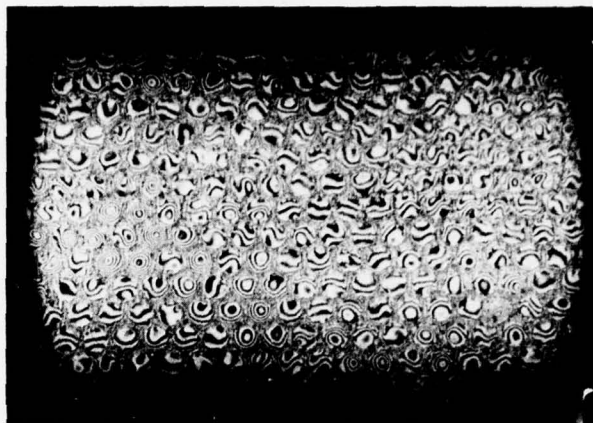
FIG. 9. Interference fringe pattern of one frame of a film taken with $U_\infty = 8.5$ m/sec and a frame rate of 7000 frames per second.

curve and the frequency response curve are only valid for symmetric displacements of the membranes.

The evaluated pressure readings can be represented and processed in different ways. One way is to plot pressure maps as shown in Fig. 10. In these maps the small crosses show the positions of the individual membranes. The lines are isobaric lines connecting points of equal pressure. (The corners of the isobaric lines have no physical significance; they are just a consequence of the plotting process.) Solid lines are lines of overpressure and zero pressure. Dashed lines are lines of underpressure. Zero pressure here is defined so that the average over the 198 membranes of each map is zero. The pressure differences between adjacent lines in Fig. 10 correspond to 0.5 fringes (≈ 1.75 μbar or 0.0042 q_∞).

Two more questions seem to be of importance with respect to the confidence one can have in the pressures evaluated. The first question is whether the movements of the transducer membranes influence the adjacent flow. It is assumed that this is not the case, because the membrane displacements are very small compared with the dimensions of the viscous sublayer (e.g., 6 fringes correspond to a membrane displacement of $y = 1.64\ \mu$m or $y^* = 0.04$). The second question is whether the high frequency parts of the fluctuations are represented properly. If one compares the frequency spectrum measured with the help of the microphone (Fig. 8) and the frequency response curve of the membranes (Fig. 3), it can be concluded that no serious difficulties arise, because the maximum of the electrically measured frequency spectrum is at about 100 Hz and the membranes operate with constant sensitivity up to about 700 Hz.

IV. RESULTS

With the method and experimental arrangements described in the previous sections one can achieve insight into a pressure field beneath a turbulent boundary layer. The evaluation of the fringe patterns, however, is at the present stage still a rather lengthy process. At
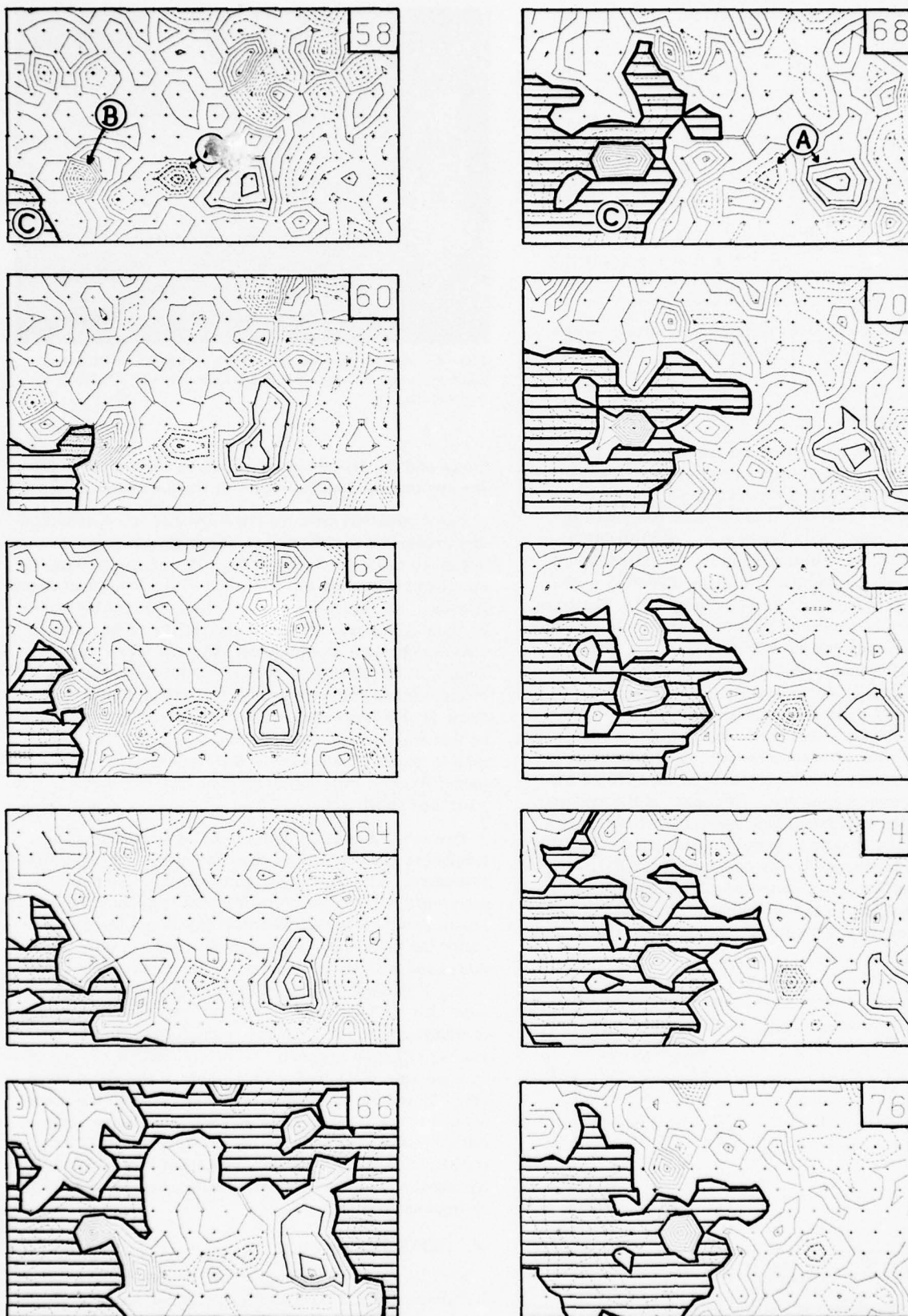
FIG. 10. Sequence of consecutive pressure distributions. (Flow from left to right, flow velocity $U_\infty = 8.5$ m/sec, time between consecutive maps $\Delta t = 0.28$ msec, field of observation 50 mm $\times$ 30 mm.)
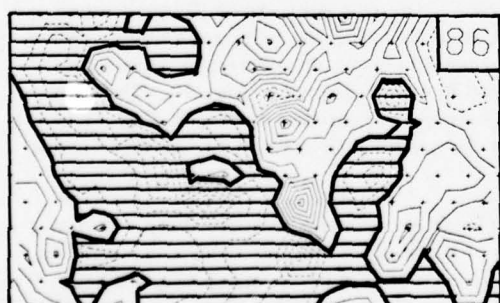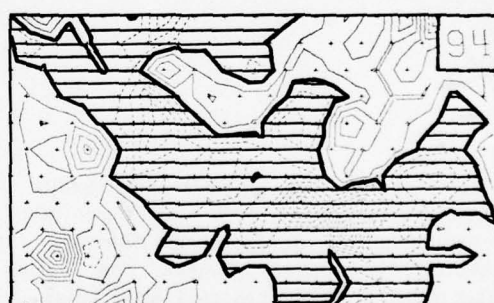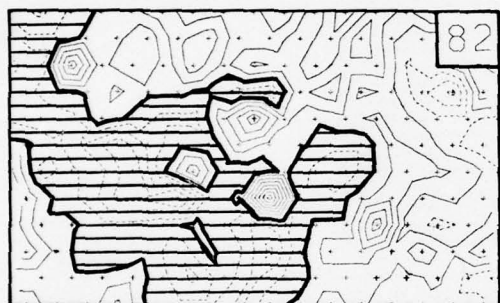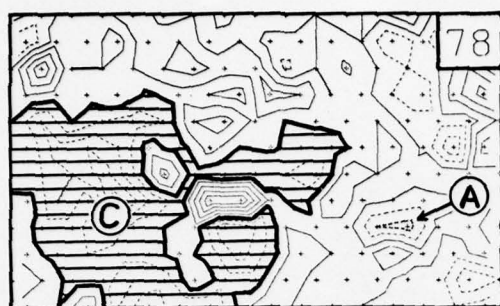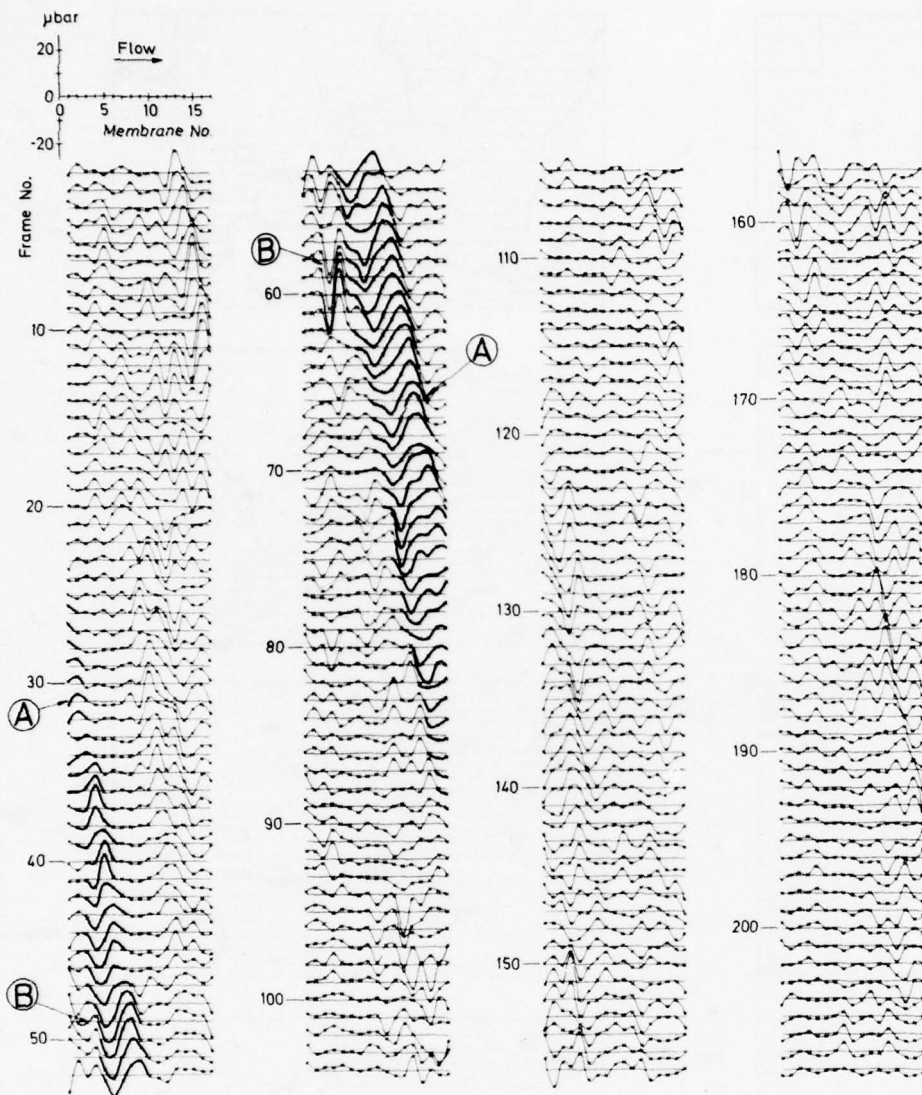
FIG. 10. (Continued).

FIG. 11. Sequence of consecutive pressure distributions along one row of 17 membranes lying in flow direction one behind the other. (Flow from left to right, flow velocity $U_\infty = 8.5$ m/sec, time between consecutive maps $\Delta t = 0.14$ msec.)

present we are still evaluating and processing results of a film taken by Emmerling in 1972. As of now, 208 consecutive frames of this film have been evaluated containing about 40 000 pressure readings. Some examples from this material will be reported in the following text. The examples show clearly that the method works. Furthermore, it is believed that the reported examples are not just arbitrary events in the investigated flow, but that they are typical for turbulent boundary layers. The proof, however, that this is so still has to be established, as the number of observations is still rather small. For this reason, the results reported here have to be regarded as preliminary.

Figure 10 shows 20 consecutive pressure maps. These maps contain the information of frame Nos. 58 to 96 out of the film whereby for brevity only every second map is printed. The time difference between consecutive maps is $\Delta t = 0.28$ msec or $\Delta t^* = 2$, if made nondimensional with ν/u_τ^2. The flow direction is from

left to right. The flow velocity and all other data are as reported in Sec. III D.

Figure 11 shows the spatial pressure distribution of one row of the transducer membranes for 208 temporal consecutive frames of the same film (9th row, frame Nos. 1 to 208). The row consists of 17 membranes lying in the flow direction one behind the other. Some of the represented curves therefore are "cross cuts" through the fields represented in Fig. 10. The time difference between consecutive curves in Fig. 11 is one half that in the previous figures, i.e., $\Delta t = 0.14$ msec or $\Delta t^* = 1$.

In Fig. 11 one can easily recognize the downstream convection of some pressure patterns. Since it is not always clear what should be regarded as a "pattern," for each example we shall explain separately what is meant by the word pattern. Usually, individual patterns can be followed over distances of about half the length
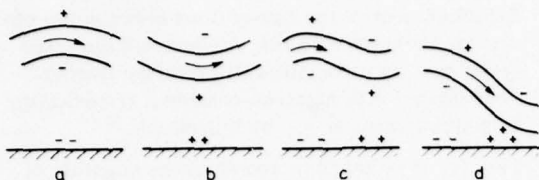
FIG. 12. Relation between bent stream tubes and nearby pressures (+ = overpressure, − = underpressure).

of the observation field. In some cases, however, one can follow individual patterns through the whole field of observation from the first to the last membrane.

The first example (pattern A) is a structure of this type. Pattern A (in Fig. 11 drawn in ink with heavy solid lines) consists of an area of overpressure followed by an area of underpressure. The pattern enters the observation field in frame No. 26 and can be followed until it leaves the observation field in frame No. 89. The convection velocity of this pattern (characterized by the zero between its two parts) is found to be $U_c = 0.76\ U_\infty$. The extensions of pattern A are of the order of 0.5 δ. Furthermore, one can see that the lengthwise extension of the overpressure area of the pattern is increasing with time [e.g., in frame No. 30 the overpressure area of the pattern has a lengthwise extension of 2 membrane distances (= 6 mm) while in frame No. 70 the same extension has grown to 4 membrane distances (= 12 mm)]. In Fig. 10 pattern A also can be observed. In the pressure maps (maps 58 to 80) a few isobars of this pattern are drawn in ink [for the overpressure part of the pattern the + 3.5 μbar line and the + 7.0 μbar line (both heavy solid lines) for the underpressure part the − 3.5 μbar line and the − 7.0 μbar line (both heavy dotted lines)]. In addition to the convection effect in these maps the extensions of the pattern can clearly be seen. The fact that the pattern is observed throughout the field of observation means that this structure exists over a length of at least 1.6 δ or 1100 ν/u_τ.

The second example (pattern B) is again an area of overpressure followed by an area of underpressure. (In frame Nos. 49 and 60 of Fig. 11 pattern B is marked with heavy dotted lines.) As can be seen from Fig. 11 and also from Fig. 10 the extensions of pattern B are only of the order of two membrane distances and the lifetime is rather short (the pattern can be recognized in Fig. 11 from frame 49 to frame 62). Furthermore, one can see that pattern B reaches a rather high pressure amplitude and shows large pressure gradients. In frame No. 61 (Fig. 11) the overpressure of pattern B is 17 μbar (= 0.04 q_∞). Two frames later the pattern has disappeared. For the spatial gradient, a maximum $\partial p/\partial x = 25$ μbar over a distance of 3 mm is found; recalculated, this would be 0.60 q_∞ over a distance of δ. Another interesting fact is that this pattern hardly changes its position while it is observed. Evaluating its shift (from frame 49 to frame 62 it shifts only by 3 mm) a convection velocity as low as $U_c = 0.2\ U_\infty$ is found. The low convection velocity, the small exten-

sions, and the short lifetime of pattern B suggest that pattern B is related to a local flow process of short duration occurring rather close to the wall.

The third example shows the convection of a large area of underpressure (pattern C). In Fig. 10 this area is shaded. The boundaries are zero pressure lines. As can be seen, with increasing frame number, the shaded area moves to the right, i.e., in the flow direction. In the lengthwise direction, the area has an extension of the order of the boundary layer thickness δ and in the spanwise direction the extension must be even larger than δ. (This can be concluded because beginning in frame 80 pattern B touches both lengthwise boundaries of the observation field, these boundaries are at a distance of 30 mm which is equal to δ). The convection velocity of pattern C is about $U_c = 0.85\ U_\infty$. In the maps one can observe how the underpressure area as it travels sometimes joins with or separates from other areas of underpressure (compare maps Nos. 66 and 68) or overtakes smaller, slower moving areas of overpressure which then become peninsulae or islands in the underpressure area. The lifetime of pattern C is evidently considerably larger than the time of its stay in the observation field. The fact that the whole underpressure area is inclined at an angle of about 45° to the flow direction is not believed to be typical. In other evaluations different angles have been obtained. The large extensions of pattern C, the high convection velocity, and the long lifetime suggest that this pattern might be related to a large scale flow process occurring in a region of the boundary layer which is farther away from the wall.

V. SPECULATIONS CONCERNING THE FLOW FIELDS

From the information given in the previous section one can speculate what sort of flows could have generated these pressure patterns. In Fig. 12 a fairly simple model is given in which flow in curved streamtubes is related to nearby pressure fields. According to this model the large scale underpressure area (pattern C) could be related to a spatially extended flow with streamlines bent toward the wall [see Fig. 12(a)]. The medium scale pressure pattern (pattern A) in which an area of overpressure is followed by an area of underpressure could be related to flow with doubly curved streamlines as shown in Fig. 12(c). Pattern B with its very low convection velocity ($U_c = 0.2\ U_\infty$), could also be related to flow with doubly curved streamlines, but occurring very close to the wall [see Fig. 12(d)].

The ideas given in this last section are at present only speculations. However, some numerical calculations performed by Schumann,[8,9] in which turbulent channel flow is simulated with the help of a computer, show pressure fields which are, to some extent, similar to the pressure fields presented in Sec. IV and show fields which are, to some extent, similar to the speculative flow patterns given in this section. Furthermore, it seems to be possible to connect the ideas given here to visual observations of flow fields as given, e.g., by Nychas et al.[10] or by Falco.[11]

Dinkelacker, Hessel, Meier, and Schewe

VI. CONCLUDING REMARKS

(a) The examples show that the method works, and that it is possible to gain, with this method, detailed information on the pressure field beneath a turbulent boundary layer without the need to introduce a probe into the flow.

(b) Large scale pressure patterns are observed which have lengthwise extensions of the order of the boundary layer thickness δ and spanwise extensions larger than δ. Convection velocities of these patterns up to $0.9\,U_\infty$ are found.

(c) Smaller scale pressure patterns are observed which have sometimes extensions right down to the resolution limits of the transducer ($0.08\,\delta$ or $57\,\nu/u_\tau$). The downstream movements of these patterns can sometimes be followed over the whole field of observation which is $1.6\,\delta$ or $1100\,\nu/u_\tau$. Convection velocities of these patterns were observed down to $0.2\,U_\infty$.

(d) The proof that the observed structures are typical for turbulent boundary layers is not yet established. Therefore, the results have to be regarded as preliminary.

(e) Further efforts are now directed toward the following aims:

1. Continuation and improvement of film evaluation.

2. Development of models for the generation of the observed pressure patterns.

3. Examination of these models with the help of conventional techniques (hot wires, electromechanical pressure transducers, computer analysis).

4. Establishment of the connections between the observations made with this method and the large set of data on turbulent wall pressure fluctuations gained with electromechanical transducers as summarized, e.g., by Willmarth.[12]

5. Finally, it is hoped to return to the question of how compliant coatings could influence turbulent boundary layer flow.

[1] A. Dinkelacker, Acustica 12, 341 (1962).

[2] A. Dinkelacker, J. Sound Vib. 4, 187 (1966).

[3] H. R. Carstensen, Acustica 18, 1 (1967).

[4] R. Grosskreutz, Mitteilungen aus dem Max-Planck-Institut für Strömungsforschung und der Aerodynamischen Versuchsanstalt, Göttingen, Nr. 53 (1971), [Navships Translation No. 1320, and in a short version: Univ. Sci. J. (University of Dar es Salaam) 1, 65 (1975)].

[5] A. Dinkelacker, Max-Planck-Institut für Strömungsforschung, Göttingen, Bericht Nr. 2 (1971).

[6] R. Emmerling, Mitteilungen aus dem Max-Planck-Institut für Strömungsforschung und der Aerodynamischen Versuchsanstalt, Göttingen, Nr. 56 (1973), [English translation: Max-Planck-Institut für Strömungsforschung, Göttingen, Bericht Nr. 9 (1973)].

[7] R. Emmerling, G. E. A. Meier, and A. Dinkelacker, in *AGARD Conference Proceedings No. 131 on Noise Mechanisms* (Advisory Group for Aerospace Research and Development, North Atlantic Treaty Organization, Paris, 1973), paper No. 24.

[8] U. Schumann, J. Comput. Phys. 18, 376 (1975).

[9] U. Schumann (private communication).

[10] S. G. Nychas, H. C. Hershey, and R. S. Brodkey, J. Fluid Mech. 61, 513 (1973).

[11] R. E. Falco (to be published).

[12] W. W. Willmarth, in *Annual Review of Fluid Mechanics*, edited by M. Van Dyke, W. G. Vincenti, and J. V. Wehausen (Annual Reviews, Inc., Palo Alto, Calif., 1975), Vol. 7, p. 13.

Vorticity and turbulence production in pattern recognized turbulent flow structures

Helmut Eckelmann and Stavros G. Nychas[a]

Lehrstuhl fur Angewandte Mechanik und Strömungsphysik am Max-Planck-Institut für Strömungsforschung, D 3400 Göttingen, Federal Republic of Germany

Robert S. Brodkey

Department of Chemical Engineering, The Ohio State University, Columbus, Ohio 43210

James M. Wallace

Department of Mechanical Engineering, The University of Maryland, College Park, Maryland 20742

A pattern recognition technique has been applied to data obtained in a turbulent channel flow. The u signal patterns are recognized using several simple criteria, but simultaneously, other signals are processed. A newly designed probe provides, in addition to simultaneous u, v, and w signals, vorticity signals, ω_z and ω_y, and a signal which can be interpreted as the instantaneous turbulence production, $uv(\partial U/\partial y)$. The ensemble averaged results provide insight into the vorticity dynamics and turbulence production characteristics of organized structures. The instantaneous turbulent production results show that ejection-type motions are the principal turbulent energy producers and that the interesting dynamics occur during the acceleration phase of the recognized pattern. A partial model of the flow which explains the results is offered.

I. INTRODUCTION

In a recent paper by Wallace *et al.*[1] a technique was described for detecting and ensemble averaging patterns which repeatedly occur in the streamwise fluctuating velocity signal, u, of a bounded turbulent shear flow. These patterns are characterized by a relatively weak deceleration of the flow followed by a strong acceleration. The acceleration is, on the average, over twice as strong as the deceleration in the region near the wall. In the region where turbulence production is most intense, between y^+ of 10 and 30, this pattern occurs in over 65% of the total sample of the u signal. It is believed that the pattern is the u signal signature of the turbulent bursting process in bounded turbulent shear flows. Research into this process has been extensively described in recent review articles by Laufer[2] and Willmarth.[3]

The pattern recognition technique of Wallace *et al.*[1] recognizes the repetitive pattern that exists in the u signal between maxima in the time derivative of u. The segment of the signal which is accepted as a characteristic pattern by a computer algorithm has a maximum positive time derivative, $\partial u/\partial t$, greater than the absolute value of the minimum time derivative. The lengths of such patterns have a log-normal probability density distribution and vary over quite an extensive range (1 : 25 as seen in Wallace *et al.*[1]). Thus, to obtain a meaningful ensemble average, a normalizing scheme was devised. This scheme normalizes each pattern to an arbitrarily chosen length in time with the maximum and minimum slopes of the pattern fixed at two predetermined points along the time scale. For the time scale, 120 points were used, and all the minimum slopes were matched at

the 35th point and the maximum slopes at the 85th point thus compressing longer patterns and expanding shorter ones. In effect then, all data values at a particular phase location in the recognized patterns are ensemble averaged together. This is an extended form of conditional averaging with the conditions being the various phases of the pattern recognized. During the same signal interval that a u pattern was recognized, the v signal and the product of u and v were also stored, normalized, and ensemble averaged with no predetermined criteria applied to these latter signals. The results showed that the v signal, on the average, was approximately 180° out-of-phase with the u signal, giving insight into how u and v in a bounded shear flow are negatively correlated. Further, it was seen that the sequence of events occurring in the bursting process was particularly evident in the ensemble averaged uv product signal, i.e., the signal which, when averaged, is the principal component of the Reynolds stress tensor. In that signal, the sequence of ejection, interaction, and sweep motions occurred around the period when the flow was highly accelerated.

In the present work, we have applied the same pattern recognition technique to signals obtained with a newly designed probe which gives, in addition to u, v, and uv, the velocity component in the spanwise direction (w), two velocity gradients ($\partial U/\partial y$ and $\partial U/\partial z$), two components of vorticity (ω_z and ω_y), and a term which is an expression of the instantaneous production of turbulent kinetic energy ($uv\, \partial U/\partial y$). This instantaneous production term has been defined and discussed by Brodkey *et al.*,[4] and Bradshaw[5] and the authors[6] have exchanged comments on the concept. Here, we have also studied the traditionally defined turbulent energy production term ($\overline{uv}\, \partial \overline{U}/\partial y$) using the pattern recognition procedure. Our objectives were to gain insight into the vorticity dynamics and turbulence production processes occurring during the bursting events.

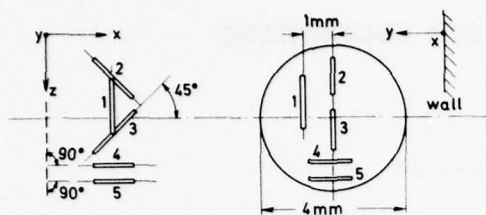[a]Present address: Department of Chemical Engineering, University of Thessaloniki, Thessaloniki, Greece.

FIG. 1. Sketch of five-sensor probe. V probe, 2 and 3; X probe, 4 and 5; U probe, 1.

The newly designed probe was used to obtain data in a fully developed turbulent channel flow whose properties have been thoroughly described in papers by Wallace *et al.*,[7] Eckelmann,[8] and Brodkey *et al.*[9] and will not be further described here. It should be mentioned, however, that the wall region in this channel flow is greatly magnified by using oil as the fluid medium. A measure of this magnification is the thickness of the viscous sublayer which, for this flow, is about 3 mm ($y^+ = 5$).

II. THE PROBE

Figure 1 shows a sketch of the five-sensor probe and its orientation with respect to the coordinates of the flow system. Figure 2 shows a photograph of the probe. The five-sensor probe was built by Thermo Systems, Inc. (model 1294BE-20W). In the x-z plane, parallel to the wall, two sensors are arranged in a V probe configuration with each sensor at an angle of 45° to the mean flow direction. The V probe was used for obtaining the U and w components of the velocity. Directly below this V probe, in the x-y plane, are two sensors in an X probe configuration which were used to obtain the U and v components of velocity. The alignment of the sensors of the X probe is also at 45° to the mean flow direction. The center of the X probe is aligned with the plane of the V probe so that their centers are approximately 2 mm apart. At 1 mm in the positive y direction from the V probe is located a single sensor (U probe) aligned in the z direction to obtain the velocity gradient, $\partial U/\partial y$. The five sensors were used so that the w component could be obtained with sensors unaffected by the mean shear. The X probe was positioned in the x-y plane and is thus affected by the mean shear; both sensors should be equally affected, however, so that the net effect should be zero. By using five sensors, we were also able to obtain the velocity gradient, $\partial U/\partial z$, by taking the difference between the U velocity obtained with the V probe and that obtained with the X probe. All the sensors are quartz-coated platinum films. The sensor diameters are 0.05 mm and have effective lengths of about 1.0 mm giving a length-to-diameter ratio of 20 for each sensor. The sensors are the standard −20 W films produced by TSI. The assembly of all five sensors has a diameter of 4 mm ($d^+ = u_\tau d/\nu \simeq 7$).

All the measurements were made using TSI type 1050 anemomenters, and the signals were linearized with either TSI type 1052 linearizers or DISA type 55D10 linearizers. The sensors were calibrated by towing the probe over a fixed length through the stationary oil as

described by Eckelmann,[8] and the calibrated signals were digitized at a rate of 50 Hz and stored on a magnetic disc using a PDP-15 computer. These data were then transferred to magnetic tape, and all the analysis of the data was accomplished using a UNIVAC 1108. The u, v, and w components were obtained by taking the sums and differences of the voltages obtained from the X probe and the V probe. Tests showed that there was no thermal interference between the sensors. A static calibration of the sensors is adequate, because recent experiments by Hofbauer,[10] where hot-film sensors of the same type were dynamically calibrated in oil, have shown that the static and dynamic frequency responses are identical in the frequency range occurring in the oil channel flow. The spectrum of this flow has a maximum at about 0.1 Hz and contains no significant energy above 20 Hz.

It was discovered, in the course of this work, that measurements of velocity gradients are very difficult where the separation of the sensors giving the two velocities is of the order of the Kolmogoroff microscale. The separation between the probes giving $\partial U/\partial y$ was 1 mm and between the probes giving $\partial U/\partial z$ was 2 mm. One millimeter in this oil channel flow at a Reynolds number of about 8000 corresponds closely to the Kolmogoroff microscale. On the other hand, to obtain true velocity gradients, the separation distance must be about of this order. The problem arises because the gradient is obtained from the small differences of two large numbers, i.e., the U velocities at the two probes. Further, the accuracy of the velocities used depends on the accuracy of the calibrations. It should not be surprising then, that absolute values of velocity gradients measured over Kolmogoroff microscale lengths are difficult to obtain accurately. To test the accuracy of the gradient measurements, several sets of data were taken using a simple gradient probe (two single sensors separated by a distance of 1 mm) and then repeating the measurements using the five-sensor probe. At positions beyond y^+ ~10, the error in measuring the mean velocity gradient, $d\bar{U}/dy$, was very large indeed. However, when these data were processed using the pattern recognition scheme, it was found, for the various sets of data, that the shapes of the patterns for the fluctuating streamwise velocity gradient, $\partial u/\partial y$, were very similar. We therefore added to the instantaneous fluctuating gradient, $\partial u/\partial y$, the mean gradients, $d\bar{U}/dy$, at each y^+ position, calculated from the known velocity profile, to obtain the instantaneous velocity gradient, $\partial U/\partial y$. In Fig. 3, the
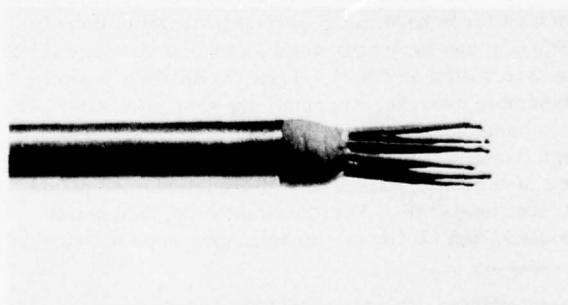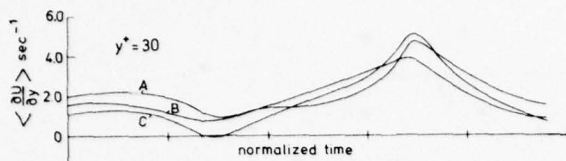

FIG. 2. Photograph of five-sensor probe.

FIG. 3. Pattern recognized $\langle \partial U/\partial y \rangle$ at $y^+ = 30$ for A: 30 000 data pairs from gradient probe, B: same as A, but 60 000 data pairs, C: 128 000 data pairs from five-sensor probe.

$\partial U/\partial y$ patterns recognized are shown for three sets of data at $y^+ = 30$, two of which were obtained with the two-sensor gradient probe and the third with the five-sensor probe. The curve marked A in the figure is based on data taken with the gradient probe for a sample length of approximately 30 000 data pairs, while the curve marked B is based on data from the same probe with a sample length of approximately 60 000 data pairs. The third curve, marked C, was obtained using the five-sensor probe with a sample length of 128 000 data pairs. When the data from all five sensors were obtained with this probe, which is discussed in Sec. IV, 640 000 data points were used. Although at any point along the normalized axis the differences between the ensemble averaged values can be quite large, the shapes of the patterns are very similar. We were thus encouraged to use this technique of adding the calculated mean velocity gradient to the instantaneous fluctuating gradient to obtain the instantaneous velocity gradient, $\partial U/\partial y$. In all the results reported in this work, this is how this gradient was obtained. For such pattern recognition analysis, one is concerned primarily with the shapes of the signals being recognized, because these shapes give us insight into the turbulent bursting process. Errors in the absolute amplitudes are of less concern, since they do not significantly affect the shape of the signals.
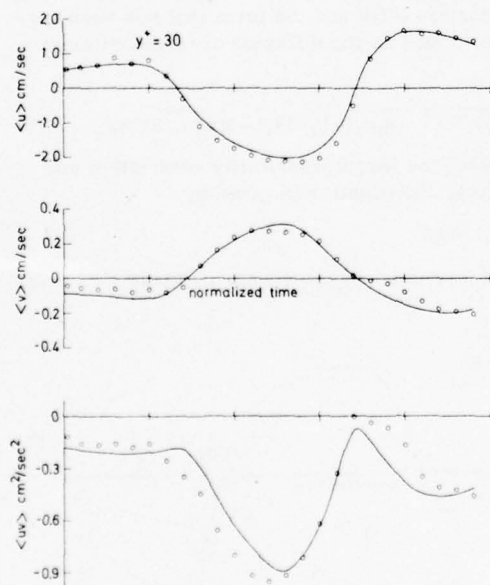
FIG. 4. Pattern recognized $\langle u \rangle$, $\langle v \rangle$, and $\langle uv \rangle$ from five-sensor probe (solid curves) compared to previous X probe results (○).
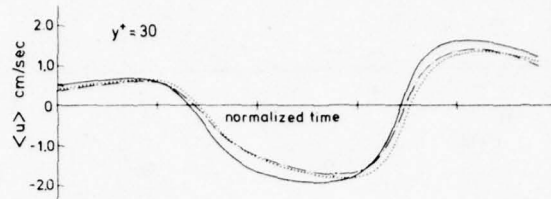
FIG. 5. Pattern recognized $\langle u \rangle$ for three simultaneous u signals available from the five-sensor probe: ———— pattern recognized signal from X probe; ·········· from V probe; —·—·— from single U probe.

III. COMPARISON WITH PREVIOUS RESULTS

Figure 4 compares the pattern recognized u, v, and uv patterns reported by Wallace et al.[1] for $y^+ = 30$ with the same signals obtained with the five-sensor probe and pattern recognized with the same computer algorithm. The data from the five-sensor probe compare well with that obtained earlier with a single X probe. This is strong evidence that the probe functioned satisfactorily and that any major sensor interference did not occur. In Fig. 5, three simultaneously obtained u patterns at $y^+ = 30$ are shown. The two additional u patterns were obtained from the V probe and the U probe signals when the u pattern was recognized from the X probe signal. The patterns are very similar, although slightly shifted in phase, indicating that the probe is small enough so that all the sensors respond to the same structures in the flow.

Figure 6 shows the pattern recognized w signal at $y^+ = 30$ occurring when the u pattern is recognized from the signal of the same V probe. The normalized and ensemble averaged values of w at all points along the time axis are small compared with the u pattern itself. This indicates that the motion, in all its phases, has little preferred direction in the spanwise direction. Wallace et al.[1] mentioned this result but no data were shown because that analysis was done on data obtained from Kreplin[11] with a sample size considered too small.

IV. RESULTS

Our objective was to look at the vorticity dynamics and turbulent production occurring during bursting as detected by our pattern recognition algorithm. To study vorticity dynamics we were able to obtain, from our data, the vorticity components in the spanwise direction $[\omega_z = (\partial v/\partial x) - (\partial u/\partial y)]$ and in the normal direction $[\omega_y = (\partial u/\partial z) - (\partial w/\partial x)]$. The gradients in the x direction were obtained using Taylor's hypothesis $[\partial/\partial x = -(1/\bar{U})(\partial/\partial t)]$. To understand the turbulence produc-
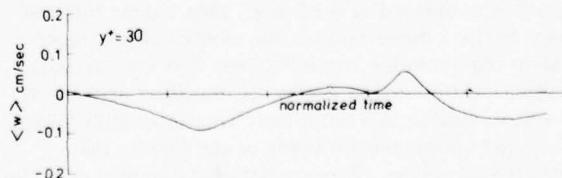

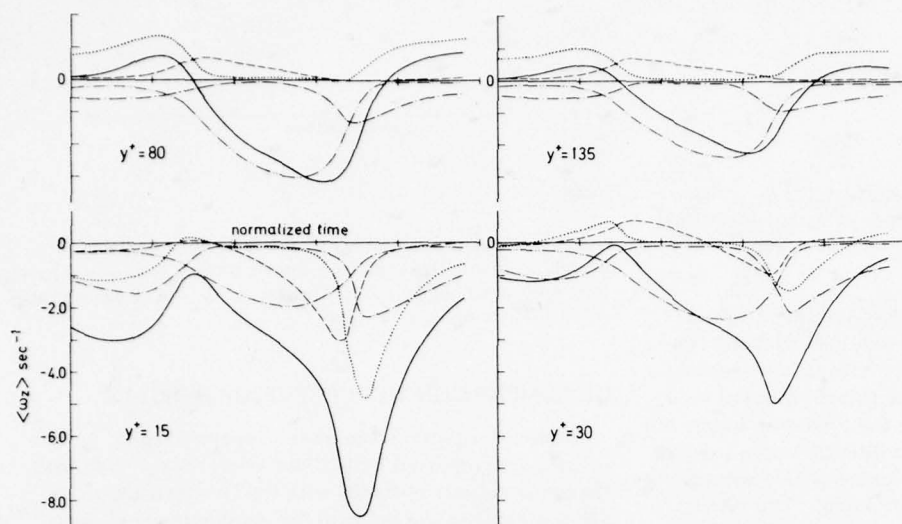FIG. 6. Pattern recognized lateral velocity $\langle w \rangle$ at $y^+ = 30$.

FIG. 7. Quadrant analysis of z vorticity (scale identical at all y^+ values). ·········· sweep; —··—··— ejection; —·—·— interaction outward; ------- interaction wallward; ——— total.

tion results, we also found it necessary to pattern recognize the instantaneous $\partial U/\partial y$ signals.

A. The vorticity components, ω_z and ω_y

The recognized ω_z pattern and its contributions from four quadrants were obtained. The criteria for the quadrant analysis, as in Wallace et al.,[1] were the value of u compared to $\bar{u}_p$ and the sign of v, occurring simultaneously with ω_z. The symbol $\bar{u}_p$ denotes the average value of u over the pattern length so that

$$\frac{1}{N} \sum_{n=1}^{N} \bar{u}_p = 0,$$

where N is the total number of patterns recognized at a particular y^+ position.

These criteria are those used for all quadrant analysis in this paper. The quadrant ensemble averages give the contribution of that quadrant to the total ensemble average at that location along the normalized time scale. The quadrant averages thus contain both occurrence frequency and amplitude information and should not be interpreted as amplitude information alone. The four quadrants associated with visually observed events, as defined in Wallace et al.[7] are $u < \bar{u}_p$, $v > 0$ corresponding to ejection events; $u > \bar{u}_p$, $v < 0$ corresponding to sweep events; $u < \bar{u}_p$, $v < 0$ corresponding to interaction wallward events; $u > \bar{u}_p$, $v > 0$ corresponding to interaction outward events. In Fig. 7, the results of the analysis of ω_z are shown for the entire signal and for the four quadrants at y^+ locations of 15, 30, 80, and 135. If these plots are compared to those for the $\partial U/\partial y$ signals (shown later in Fig. 11), one concludes that almost the entire ω_z signal is composed of $-\partial U/\partial y$. This means that the gradient in the x direction, $\partial v/\partial x$, contributes almost nothing to the spanwise vorticity, and that the vorticity in the spanwise direction during the bursting process is in no sense similar to a solid body rotation. It is entirely due to the instantaneous shear of the flow in the streamwise direction. A more detailed discussion of the flow structure will be deferred to Sec. IVC, where the

pattern recognized gradient, $\partial U/\partial y$, is considered, and a partial flow model is suggested.

Figure 8 shows the pattern recognized ω_y signal at $y^+ = 30$ and the contributions from the four event quadrants. The pattern recognized signal bears remarkable similarity to the pattern recognized u signal. If we make the assumption that the gradient, $\partial w/\partial x$, contributes little to this normal vorticity component, the gradient $\partial u/\partial z$, is very similar to the velocity pattern.

B. Turbulence production

As mentioned in the introduction, the production term in the turbulent energy equation has been redefined by Brodkey et al.[4] to obtain a term which is physically meaningful instantaneously in the flow. For an incompressible flow, this term is the sum of the traditionally defined production term and the term that has been traditionally described as the diffusion of turbulent kinetic energy,

$$\overline{u_i u_j [\partial(\bar{U}_i + u_i)/\partial x_j]} = \overline{u_i u_j}(\partial\bar{U}_i/\partial x_j) + \partial\overline{(u_i^2 u_j/2)}/\partial x_j. \quad (1)$$

Before invoking the incompressibility restriction and time averaging, the equation is given by

$$u_i u_j [\partial(\bar{U}_i + u_i)/\partial x_j]$$
$$= u_i u_j(\partial\bar{U}_i/\partial x_j) + u_i^2(\partial u_j/\partial x_j) + \partial(u_i^2 u_j/2)/\partial x_j. \quad (2)$$
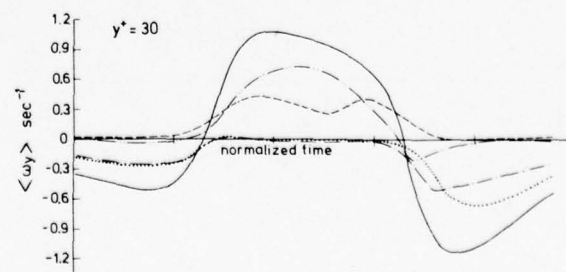

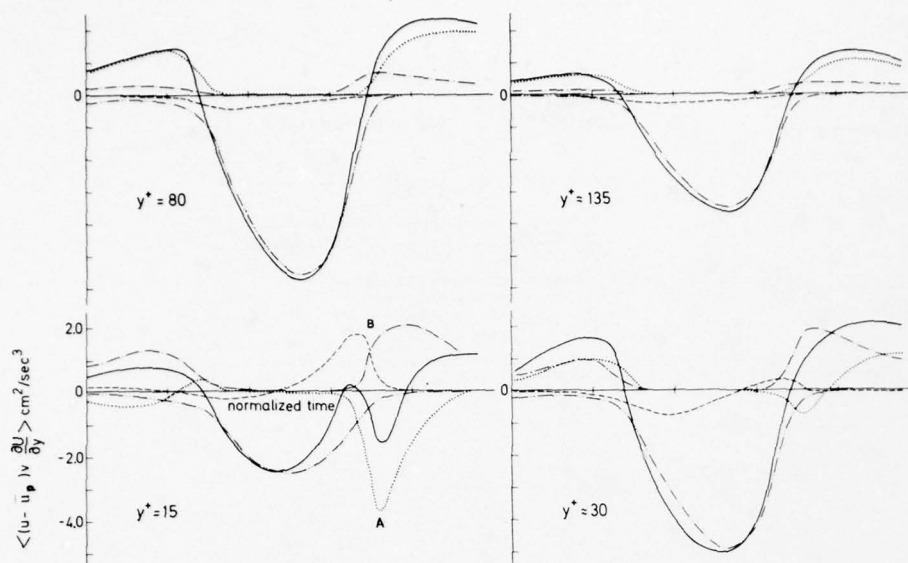FIG. 8. Quadrant analysis of y vorticity at a $y^+ = 30$. Notation as in Fig. 7.

FIG. 9. Quadrant analysis of instantaneous production term (scales identical at all y^+ positions). Notation as in Fig. 7.

By local continuity which will be assumed here, the term $u_i^2(\partial u_j/\partial x_j)$ is zero. Equation (2) can be ensemble averaged, based on conditions occurring in the flow, so that the conditionally ensemble averaged equation is valid at any point along the pattern recognition time axis and is given by

$$\langle u_i u_j \partial(\bar{U}_i + u_i)/\partial x_j \rangle$$
$$= \langle u_i u_j \rangle \, (\partial \bar{U}_i/\partial x_j) + \langle \partial(u_i^2 u_j/2)/\partial x_j \rangle. \qquad (3)$$

In the pattern recognition technique, the conditions applied when ensemble averaging are the various phases of the recognized u pattern.

The same questions and comments[5,6] can be raised about Eq. (3) as have been raised about Eq. (1). If production of turbulence involves deformation of the mean motion by the turbulent stresses,[12] then when the turbulence production associated with an individual event in the flow is considered, it would seem reasonable to ask how the instantaneous stress, $u_i u_j$, interacts with the instantaneous gradient at the same point, $\partial(\bar{U}_i + u_i)/\partial x_j$. The ensemble average of the principal component of the product, $u_i u_j \, \partial(\bar{U}_i + u_i)/\partial x_j$, at the various phases in the recognized u pattern is shown in Fig. 9 for the four y^+ positions of 15, 30, 80, and 135. Negative values of this production term are positive contributors to the energy production, whereas positive values are a form of negative production. At all four positions, the ejection-type motion gives the principal positive contribution to turbulence production. At y^+ positions of 30 and beyond, the absolute contribution of the ejection motion is markedly greater than that of any of the other types of motions. There is a remarkable change in the contribution of the sweep-type motion between $y^+ = 15$ and the region farther out in the channel. At $y^+ = 15$, the sweep-type motion also contributes very heavily to positive production during the acceleration phase of the flow (indicated by the latter A in the figure) counteracting the negative production contributions of the two interaction-type motions (indicated by B). In the outer region of the flow, how-

ever, the sweep motions are also negative contributors to the production process. A similar change occurs with the production contribution of the interaction wallward motions. The region at about $y^+ = 30$ seems to be a transitional region between the types of motion occurring near the wall and those occurring farther out in the flow. To try to explain which flow processes are giving rise to these effects, we decided to pattern recognize the instantaneous gradient, $\partial U/\partial y$; this will be discussed in the next section.

If the pattern recognized Reynolds stress at each point along the normalized time axis is multiplied by the mean velocity gradient at that y^+ position, a conditionally ensemble averaged form of the traditionally defined production term, $\langle uv \rangle (d\bar{U}/dy)$, is obtained. This is the first term on the right side of Eq. (3). These results are shown in Fig. 10 for $y^+ = 30$ together with the newly defined production term results. The difference between the two terms is also shown. This difference is the last term on the right of Eq. (3), i.e., the ensemble average of the diffusion of turbulent kinetic energy as traditionally defined. By comparing the two types of production, one sees that the newly defined production has much larger values, and the contributions of both the sweep and interaction wallward motions have opposite signs over most of the normalized time axis. In traditional terms then, energy is diffusing into the local region during the ejection motions and out of the region during sweep motions. The same characteristics were found to exist at other y^+ positions except that, at $y^+ = 15$, there must be diffusion into the region during the sweep motion. This is a result of the large negative peak at $y^+ = 15$ for the sweep motion of the instantaneous production shown in Fig. 9.

C. A partial model of the flow

Figure 11 shows the pattern recognized gradient, $\partial U/\partial y$, at the same y^+ positions. There are several striking features to be observed. At $y^+ = 15$, the total gradi-
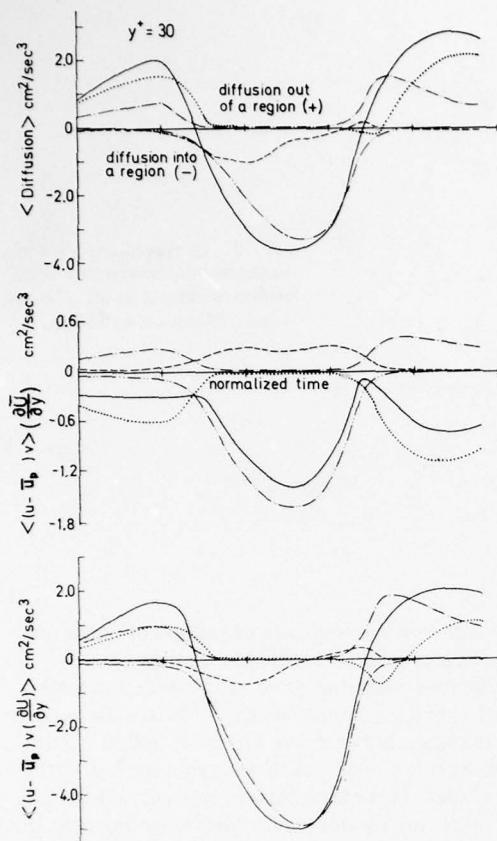
FIG. 10. Quadrant analysis of instantaneous production, production, and diffusion terms. Notation as in Fig. 7.

Note: wall angle emphasized for visualization

idealized instantaneous $\frac{\partial U}{\partial y}$ for three cuts

FIG. 12. Model of turbulence. Notation as in Fig. 7.

ent has a sharp maximum (indicated as A) near the maximum of the gradient in the u pattern, $\partial u/\partial t$. At positions farther out in the flow, this maximum becomes broader, indicating that the velocity interface, passing the probe, is less distinct in that region. This is exactly as reported from the visual results of Nychas *et al.*[13]

Also striking are the negative lobes (B and C) of the $\partial U/\partial y$ pattern near its beginning and its end at the outer positions; these are caused by the sweep motions. On the left of the time sequence (D), the interaction-wallward motions also have negative gradients at these outer positions. In the center of the sequence, during the ejection motions, the ensemble averaged sweep contribution is zero, as would be expected. If these negative average gradients were due to a measurement error, one would expect the whole curve to be shifted upward or downward, so that the sweep motions would not have an ensemble average of zero during the period when ejection motions predominate. Since this is not the case, we believe that negative gradients do occur during the early
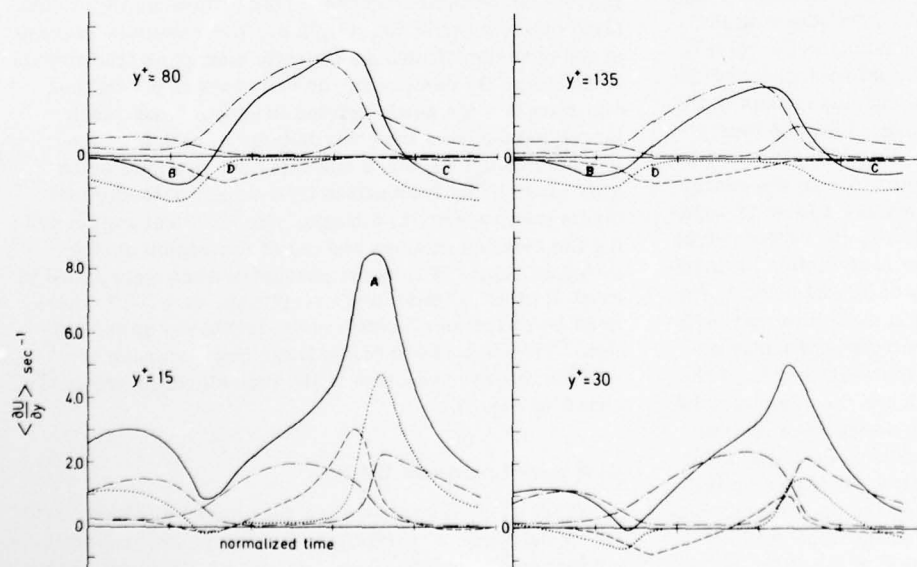
FIG. 11. Quadrant analysis of $\langle \partial U/\partial y \rangle$ (scale identical at all y^+ positions). Notation as in Fig. 7.

and late phases of the pattern sequence in the outer flow. Of course, the overall average gradient will still be positive, as can be seen by time averaging the total gradient shown in the plots of Fig. 11 over the pattern length. The fact that these gradients are negative explains the negative contributions (indicated by A) to the production seen in Fig. 9. In Fig. 11 at $y^+ = 15$, the ensemble average gradient contribution during the sweep phase is highly positive, in fact, having the largest maximum of any of the four quadrants. This maximum is reduced at $y^+ = 30$ and, as observed earlier, becomes negative at the two outer positions.

Figure 12 shows a sketch of the entire flow field during the occurrence of one of these highly accelerated sweeping motions. It moves toward the wall and penetrates into the decelerated flow around it. This is essentially the picture observed by Praturi[14] using stereoscopic visual methods. The lower interface between the accelerated and decelerated fluid is at a shallow angle to the wall $(4°-7°)$ and has been observed in the wall shear stress measurements of Kreplin.[11] Since the whole picture is being convected with the flow, a stationary probe located at $y^+ = 15$ (line A in Fig. 12) would detect ejection motions first and then interaction-wallward motions being forced toward the wall by sweep motions. A strong acceleration in time and a large gradient in space in the y direction would be seen in the u signal as the interface between high- and low-speed fluid passes the probe. Finally at this position, the probe would detect some interaction-outward motion of high-speed fluid moving slightly away from the wall trying to ride over the low-speed fluid at the lower interface and also fluid moving strongly toward the wall from the outer flow as sweep motion. If the stationary probe is at $y^+ = 80$ or 135, the picture can be markedly different. The probe at these positions could, for any individual occurrence of the picture, be either intersecting the lower side (line B) or the upper side (line C) of the interface between high- and low-speed fluid. This will result in different ensemble average pictures. If the probe is intersecting the lower side (line B), the interaction-outward motion will predominate over the sweeping motion. The average gradient, $\partial U/\partial y$, in the ejection and interaction-outward motions will be positive. If the probe is on the upper side of the interface (line C), however, the sweep motions will primarily predominate, with high-speed fluid moving toward the wall and dragging the low-speed fluid on the upper side of the interface toward the wall with it. Here, the average gradient will be negative in the sweep and interaction-wallward motion. Thus, there seem to be

continual large-scale inflows of accelerated fluid that push their way into the surrounding lower-speed fluid nearer the wall, developing a very sharp interface. Kreplin[11] has observed correlation lengths of this interface in the streamwise direction over 1000 x^+ units long. He observed significant correlations in the z direction over only about $z^+ = 30$ ($x^+ = u_\tau x/\nu$ and $z^+ = u_\tau z/\nu$).

One should, therefore, picture these inflows of high-speed fluid approaching the wall, turning downstream in the convected view and penetrating into the surrounding low-speed fluid with long, finger-like motions. Across the high-shear interface, turbulent production is occurring principally during the occurrence of the ejection motions. At the upper side of the finger-like, high-speed motion, negative gradients occur which locally and temporally give rise to negative production of turbulent kinetic energy.

ACKNOWLEDGMENTS

[1]J. M. Wallace, R. S. Brodkey, and H. Eckelmann, J. Fluid Mech. (to be published).

[2]J. Laufer, in *Annual Review of Fluid Mechanics*, edited by M. Van Dyke, W. G. Vincenti, and J. V. Wehausen (Annual Reviews, Palo Alto, Calif., 1975), Vol. 7, p. 307.

[3]W. W. Willmarth, in *Advances in Applied Mechanics* (Academic, New York, 1975), Vol. 5, p. 59.

[4]R. S. Brodkey, S. G. Nychas, J. L. Taraba, and J. M. Wallace, Phys. Fluids 16, 2010 (1973).

[5]P. Bradshaw, Phys. Fluids 17, 2149 (1974).

[6]R. S. Brodkey, J. L. Taraba, S. G. Nychas, and J. M. Wallace, Phys. Fluids 17, 2150 (1974).

[7]J. M. Wallace, H. Eckelmann, and R. S. Brodkey, J. Fluid Mech. 54, 39 (1972).

[8]H. Eckelmann, J. Fluid Mech. 65, 439 (1974).

[9]R. S. Brodkey, J. M. Wallace, and H. Eckelmann, J. Fluid Mech. 63, 209 (1974).

[10]M. Hofbauer, Diplomarbeit, George-August Universität, Göttingen (1975).

[11]H.-P. Kreplin, Dotorarbeit, George-August Universität, Göttingen (1976).

[12]J. O. Hinze, *Turbulence* (McGraw-Hill, New York, 1975), 2nd ed., p. 72.

[13]S. G. Nychas, H. C. Hershey, and R. S. Brodkey, J. Fluid Mech. 61, 513 (1973).

[14]A. K. Praturi, Ph.D. dissertation, The Ohio State University (1975).

On the role of phase information in conditional sampling

Ron Blackwelder

Department of Aerospace Engineering, University of Southern California, Los Angeles, California 90007

Conditional sampling techniques have been studied in order to better understand the phase relationship between the signal used to detect the events and the sampled data signal. It is shown that whenever there is a mean time delay between these two signals or whenever they are obtained from two different spatial locations, a random phase will exist between them if the signals are obtained from a random environment. This randomness is not accounted for in the usual definitions of conditional sampling, and it can cause a serious degradation of the conditionally averaged results. A corrective method is discussed and illustrated with examples from a turbulent boundary layer.

INTRODUCTION

The technique known as conditional sampling or conditional averaging has been an invaluable tool in the study of turbulence. It has been used to investigate coherent structures in turbulent shear flows, the interface between regions of turbulent and nonturbulent fluid, flow fields with imposed perturbations, etc. Without it, much of the quantitative information that has been reported about these phenomena would not exist. The earliest use of this method was apparently that of Townsend[1] in the wake of a cylinder. A general description of the technique is provided by Kaplan,[2] and a brief history is given by Van Atta.[3]

In spite of its broad use, it is not able to solve all of the difficulties associated with experimental studies of turbulence and turbulent structures. The need for better understanding of this and other statistical tools, as well as the development of new techniques, was one of the results of the symposium on "Coherent Structures in Turbulence" as discussed by Davies and Yule.[4] The present paper is concerned with one problem inherent in conditional sampling in a random environment, i.e., the existence of a random phase which is always present between the detection and data signals whenever the detection and averaging are separated by a time delay or are obtained at two different spatial locations. This problem will be outlined, and some examples will be given to illustrate its importance.

CONDITIONAL AVERAGES AT ONE SPATIAL LOCATION

A conditional average can be simply defined as an ensemble average taken over many similar events. Thus, at least two different inputs are required in order to define and obtain a conditional average. One input must contain the information necessary to define the series of events, and the second input must contain the data to be averaged. It is possible that one original signal may satisfy both of these criteria; however, it will need to be processed by two diverse methods to obtain the different information.

Under these conditions, a conditional average may be considered as a special type of generalized cross-correlation. The characteristic property associated with the conditional average is that the input signal defining the events has been processed by a detection network or algorithm. Consider the cross-correlation of two digital signals $f(t_i)$ and $u(t_i)$ given by

$$R(\mathbf{x}, \tau_k) = \frac{1}{L} \sum_{i=1}^{L} f(\mathbf{x}, t_i) u(\mathbf{x}, t_i + \tau_k), \qquad (1)$$

where τ_k is the time delay which may be either positive or negative, L is the number of digital data points to be averaged over, and $R(\mathbf{x}, \tau_k)$ is the correlation function. A similar equation using an integral can be written for the continuous case.

For the conditional averages, one of the signals, say $f(\mathbf{x}, t_i)$, must define the conditions under which averaging is to occur. Usually, $f(\mathbf{x}, t_i)$ is the output of a nonlinear detection algorithm (or circuit, in the analog case) that is explicitly designed to determine when an event has occurred. The design and construction of this algorithm is quite often the most complicated and difficult aspect of conditional averaging. Indeed, it is the sole topic of the field of detection theory in communication enginerring. Its design requires considerable physical insight into the problem being studied, as well as some knowledge of filtering theory and data processing. Obviously, the detection algorithm must be able to find and lock onto some phase relationship that exists between its output signal, $f(\mathbf{x}, t_i)$, and the data signal, $u(\mathbf{x}, t_i)$. In order to accomplish this, the detection scheme must use one or more inputs which may be quite varied. For example, these inputs may be analog signals, their derivatives, visual observations, etc. In a free shear layer, Brown and Roshko[5] and Winant and Browand[6] have found large-scale structures using different visualization techniques. In order to study the pairing process that occurred between neighboring vortices, the latter authors used their visual observations to help design a detection algorithm in order to measure the Reynolds stress associated with this phenomenon.

The flow structures near the wall of a bounded turbulent shear flow have been studied using visual techniques by Kline *et al.*,[7] Corino and Brodkey,[8] and Kim *et al.*[9] They used a Lagrangian velocity field with a visual recognition scheme to identify a series of events which has been called the bursting phenomenon. Lu and Willmarth[10] and Blackwelder and Kaplan[11] used the Eulerian streamwise velocity signal as the basis for detection schemes to study the same phenomenon.

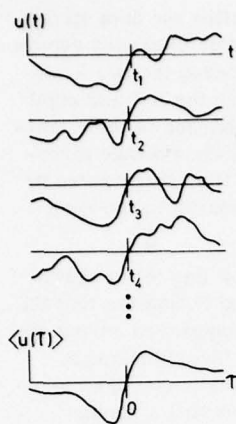Independent of the number and type of inputs to the de-

FIG. 1. Four ensemble members and the conditional average of the streamwise velocity $u(t)$.

tection algorithm, the output is often a series of singular time points that are related to some particular phase of the event under study. In this case the output of the detection scheme can be written as

$$f(\mathbf{x}, t_I) = \sum_{n=1}^{N} w_n(\mathbf{x}) \, \delta(t_n - t_I), \qquad (2)$$

where δ is the Kronecker delta function. The subscript n refers to the nth event, so t_n, $n = 1, 2, 3 \ldots N$, are the time points that mark a phase reference point of the events of interest. A weighting function, w_n, can also be determined by the detection algorithm. It assigns weights to the different events depending upon their importance. For example, if the detection scheme uses a threshold parameter in determining the function $f(\mathbf{x}, t_I)$, it is often possible to assign weights to the different events so that the conditionally averaged results are made independent of the threshold value.

The conditional average is defined as

$$\langle u(\mathbf{x}, \tau_k) \rangle = \frac{1}{N} \sum_{n=1}^{N} w_n(\mathbf{x}) \, u(\mathbf{x}, t_n + \tau_k), \qquad (3)$$

where $\langle u(\mathbf{x}, \tau_k) \rangle$ is the averaged quantity at $\mathbf{x}$ as a function of the time delay τ_k, $w_n(\mathbf{x})$ is the weighting function, and N is the number of events in the ensemble average. By combining Eqs. (1) and (2), the conditional average is seen to be related to the specialized correlation function by $\langle u(\mathbf{x}, \tau_k) \rangle = (L/N)R(\mathbf{x}, \tau_k)$. Although a general comparison between correlation functions and conditional averages cannot be made, the last equation suggests that by properly selecting only those parts of the signal that are directly related to the events of interest, the conditional average can greatly improve the magnitude of the output. Since L/N is usually quite large, the advantages of conditional sampling under these circumstances are quite obvious. An example of the use of this definition is shown in Fig. 1 for the velocity signal, $u(t)$. In this case, the time series, t_n, was obtained by searching for the local temporal regions where the energy associated with the fluctuating velocity signal exceeded the average energy. Thus, a short time average of the variance of the signal was computed for all points in time, and it was compared with the conventional mean variance. If it exceeded the conventional average between times t_x and t_y, the point in the time series was taken as $t_n = (t_x + t_y)/2$,

and the algorithm proceeded to look for the next point, t_{n+1}.

The velocity signals associated with the first four detected events are shown in Fig. 1 with the detection times aligned vertically. The conditional average defined by Eq. (3) with a weighting function of unity is shown in the lower portion of the figure. The main feature of this conditional average is the strong, sharp acceleration of the streamwise velocity. This is preceded and followed by periods of a more gradual deceleration that are seen at the large positive and negative time delays. Approximately 300 different signals were used to obtain the conditional average in Fig. 1. When the features associated with the events are quite strong, the convergence of the average is very rapid, and thus fewer ensemble members could have been used in this case.

A more historical type of conditional average that has been utilized in fluid mechanics is the zone average employed by Corrsin and Kistler[12] Kovasznay et al.,[13] Kaplan and Laufer,[14] and others. In this case, the detection algorithm is only concerned with locating an event and does not attempt to find a particular phase or time reference point within the event. The output from the detection algorithm, $f(\mathbf{x}, t_I)$, is a random square wave which is unity when an event is present and is zero otherwise. Normally, a time delay is not used, and hence, the zone average is a generalized correlation coefficient instead of a correlation function.

CONDITIONAL AVERAGES WITH A SPATIAL VARIABLE

The conditional averages defined and illustrated in the previous section utilized a detection signal and a data signal that were obtained at the same spatial location. It is readily apparent that an extended definition may be desired to include a spatial separation between these two signals. In fact, if one wishes to explore the spatial extent of some event, such as a coherent structure embedded within a turbulent shear flow, the very nature of the problem indicates that information must be taken simultaneously at more than one location.

Analogous to space-time cross correlations, the definition of the conditional average can be expanded so that the point of detection and the location of the data collection are not the same. This is formulated analytically in the same manner as in the previous section and is given by Eq. (4)

$$\langle u(\mathbf{x}, \Delta\mathbf{x}, \tau_k) \rangle = \frac{1}{N} \sum_{n=1}^{N} w_n(\mathbf{x}) \, u(\mathbf{x}, \Delta\mathbf{x}, t_n + \tau_k), \qquad (4)$$

where $\mathbf{x}$ denotes the location of the detection of the event and $\Delta\mathbf{x}$ gives the relative position between $\mathbf{x}$ and the point of data collection. This equation reduces to Eq. (3) when $\Delta\mathbf{x} = 0$, i.e., when the detection and data sampling occur at the same spatial location. The definition given in Eq. (4) can be used for many different configurations of spatial separation in a manner similar to space-time cross correlations. For example, in the study of coherent structures in turbulence, a large-scale eddy is the event and a streamwise separation yields details of the development of this eddy structure as it evolves
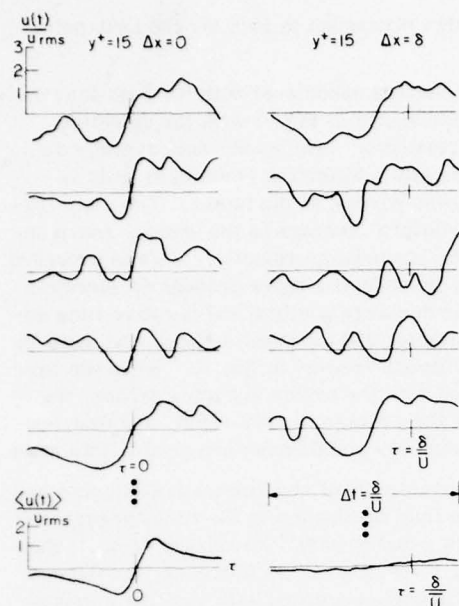
FIG. 2. Data and the conditional average of the streamwise velocity signal in a turbulent boundary layer $y^+=15$. The detection and data sampling occurred at the same location on the left-hand side. The data on the right are from the same eddies after traveling downstream one boundary layer thickness. Note that the sharp accelerations on the right arrive at random times which are generally earlier than the mean velocity predicts.

downstream. On the other hand, if the spatial separation is in the spanwise or normal direction, the conditional average will yield details of the structure in that direction. In any case, a spatial separation between the detector probe and the location of data sampling allows one to gather information about some additional parameter or variable associated with the events. This parameter may be the convection velocity, the spanwise extent, the shape of the structure, etc. Since the flow field is completely turbulent and the coherent structures are not identical, the parameter that is being studied by the conditional averaging technique will always have some randomness associated with it. For example, the convection velocity of the coherent structures will vary from one structure to the next, which introduces a random phase into the conditional average. Their random size, shape, age, etc., will have similar effects on all of the parameters being studied. This randomness can seriously degrade the conditional average of the desired quantity to the point of nonexistence. This is especially important if the parameter being measured is very sensitive to the phase relationship, such as the Reynolds stress, as illustrated by Blackwelder and Kaplan.[11]

An example of this problem is shown in Fig. 2, which again utilizes data from a turbulent boundary layer at $y^+=15$. On the left-hand side, $\Delta\mathbf{x}=0$ so that the detection of the events and data collection were obtained at the same location. Although the individual members of the ensemble were different, the conditional average as shown in the bottom left-hand corner was identical to that shown in Fig. 1. The data on the right-hand side of

Fig. 2 were obtained a short time after the data on the left, and there was one boundary layer thickness separation in the streamwise direction between the two locations. Hence, a comparison between the left and right traces shows how the events have changed in their journey downstream. One would expect the average structure to arrive at approximately the time delay given by $\tau = \delta/\bar{U}$, which is shown by the tick marks in the right-hand set of data in Fig. 2.

The conditional average defined by Eq. (4) is shown at the bottom right-hand corner, and it appears that the structure has almost completely disappeared during its travel downstream of one boundary layer thickness. However, by observing each individual ensemble member, one can see that there is indeed still a strong structure present at the downstream location, as indicated by the strength of the accelerations. The difference between the right-hand side and the left-hand side of Fig. 2 is that, on the left-hand side, all of the strong accelerations have been aligned because the detection and averaging occurred at the same location. However, on the right-hand side, the detection occurred upstream, and the fluctuations in the convection velocity have caused a random distribution of arrival times at the downstream location. Even though the individual amplitudes at the downstream location are not significantly different from those recorded at the upstream location, the magnitude of the conditional average has been drastically decreased. Thus, the problem is not that the magnitude has changed significantly during the journey downstream, but rather that the phase relationship between the data at that location is now random with respect to the detection which occurred at the upstream location. It is expected that this randomness will increase as the separation distance becomes greater. Indeed, the conditional average is expected to go to zero as the separation distance becomes infinitely large. However, the results of Fig. 2 show that the conditional average has grossly exaggerated the demise of the coherent structures associated with the strong accelerations.

AN ILLUSTRATIVE MODEL

An analytical representation of the problem can be obtained by letting the individual members of the ensemble average be identical. Then, any variations in the ensemble averages cannot be attributed to random variations in the amplitude of the signals. Let the members be modeled by the signal given in Eq. (5)

$$u(\Delta\mathbf{x}, t)$$
$$= (a/d)[\, U_c \cdot (t - t_n) - \Delta\mathbf{x}\,] \exp\{(-1/d^2)[\, U_c \cdot (t - t_n) - \Delta\mathbf{x}\,]^2\},$$
$$(5)$$

where U_c is the convection velocity, a and d are the characteristic velocity and length scale of the signal, and $\Delta\mathbf{x}$ is the streamwise separation. The time points, t_n, are the reference times obtained by a detection scheme at $\Delta\mathbf{x}=0$. In this case the reference times, t_n, coincide exactly with the zero crossing of the signal, i.e., $u(0, t_n) = 0$. Thus at $\Delta\mathbf{x}=0$, the signal is centered about $t = t_n$. For nonzero separations, the expected arrival time of the signal, i.e., the zero crossing, is
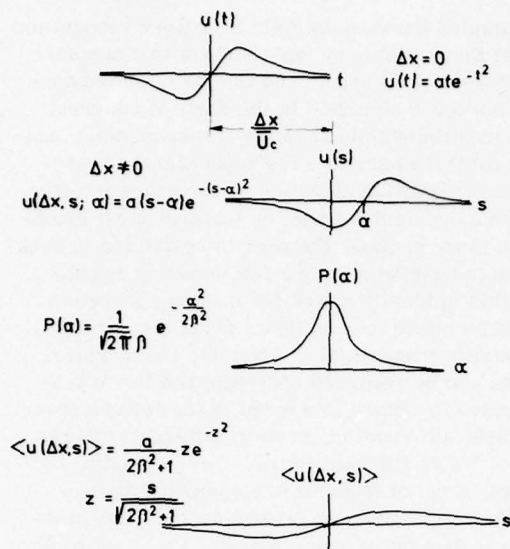
$u(t)$

$\Delta x = 0$
$u(t) = \alpha t e^{-t^2}$

$\dfrac{\Delta x}{U_c}$

$\Delta x \neq 0$ $\quad u(s)$

$u(\Delta x, s; \alpha) = \alpha(s-\alpha)e^{-(s-\alpha)^2}$

$P(\alpha) = \dfrac{1}{\sqrt{2\pi}\,\beta}\, e^{-\frac{\alpha^2}{2\beta^2}}$

$P(\alpha)$

$\langle u(\Delta x, s)\rangle = \dfrac{\alpha}{2\beta^2+1}\, z e^{-z^2}$

$z = \dfrac{s}{\sqrt{2\beta^2+1}}$

$\langle u(\Delta x, s)\rangle$

FIG. 3. A deterministic model that illustrates the effect of the random phase. The basic signal, $u(t)$, is shown at the extreme top. Directly below it is the same signal with $\Delta x = 0$ and a random phase, α, added. If the probability density of α is Gaussian as shown, the resulting conditional average is shown at the bottom.

$t = t_n + \Delta x / U_c.$

In general, the convection velocity associated with a turbulent flow field will be a random variable and can be represented by the sum of a mean and fluctuating component; i.e.,

$U_c = \bar{U}_c + u_c.$

Thus, the time of arrival will also have a randomness associated with it; that is, there will exist a loss of phase between the point of detection and the point of sampling. Thus for $\Delta x = $ const, the measured temporal signal can be represented by

$$u(\Delta x, s; \alpha) = a(s - \alpha)\exp[-(s-\alpha)^2], \qquad (6)$$

where s is the average nondimensional delay variable given by

$$s = [\bar{U}_c \cdot (t - t_n) - \Delta x]/d, \qquad (7)$$

and α is the fluctuating component,

$$\alpha = u_c \cdot (t - t_n)/d. \qquad (8)$$

If the probability density of the random variable, α, is known, the conditional average can be computed using Eq. (4). For a continuous probability density function, $P(\alpha)$, the integral form of Eq. (4) is

$$\langle u(\Delta x, s)\rangle = \int_{-\infty}^{\infty} u(\Delta x, s; \alpha)\, P(\alpha)\, d\alpha, \qquad (9)$$

that is, the ensemble average of Eq. (4) can be replaced by the probability average with each signal weighted by its probability of occurrence.

If the probability density of α is modeled by an analyt-ic function as shown in Fig. 3, the integral in Eq. (9) is easily computed. For a Gaussian distribution, the conditional average is

$$\langle u(\Delta x, s)\rangle = [a/(2\beta^2 + 1)]\, z \exp(-z^2), \qquad (10)$$

where

$$z = s(2\beta^2 + 1)^{-1/2} \qquad (11)$$

and β is the standard deviation of the variable α. This result is shown at the bottom of Fig. 3.

The functional form of Eq. (10) is identical to that of the original signal. However, the characteristic scale of the abscissa has been stretched by the factor $(2\beta^2 + 1)^{1/2}$, that is, the characteristic length is now $d(2\beta^2 + 1)^{1/2}$ instead of d as in the original signal. Secondly, the maximum amplitude of the conditional average has been reduced by $1/(2\beta^2 + 1)$, in spite of the fact that all of the individual ensemble members have identical, and larger, amplitudes. The conclusion is that the randomness has severely distorted the conditional average. Note that as the amount of randomness increases, i.e., as β increases, the amplitude of the conditional average continues to decrease and the characteristic length scale of the conditional average increases monotonically.

In a random environment, such as a turbulent flow field, the effect of this randomness will become more acute as the separation distance, Δx, increases. That is, at a given location in a turbulent flow, the magnitude of the fluctuating convection velocity is a constant, and Eq. (8) shows that α is then proportional to the time delay. As the separation distance, Δx, increases, the time delay must also increase. Hence, the effect of this loss of phase will become more important for larger Δx, independent of the actual shape of the eddy structure.

The phase loss will be more noticeable for those variables that are more sensitive to phase relationships, such as the Reynolds stress. This is represented in the model by the length scale, d. As the region of the eddy responsible for the signal becomes smaller, d decreases. In a Fourier space, this implies a shift to higher wavenumbers. For a smaller d, the same amount of phase jitter will have a larger effect on these signals, as shown by Eq. (8).

Finally, if there were no spatial separations but only a temporal separation between the point of detection and sampling, a similar problem may exist. If all of the events represented by Eq. (5) had the same spatial shapes, but traversed the detection and sampling point with different convection velocities, they would have a different temporal appearance. In this case with $\Delta x = 0$, the independent variable would still have a fluctuating component, as seen by Eq. (8). Hence, the randomness in the convection velocity would cause an apparent stretching or shrinking of the spatial scale. The correct signal could be recovered by a conditional average only if the proper expansion or contraction were applied to the temporal signal. This effect will usually be smaller than that corresponding to a nonzero separation because the time difference in Eq. (8) will be smaller. Even for constant convection velocities, a similar effect

would exist if the shape of the eddies, represented by d in Eq. (7), were fluctuating.

CORRECTION TECHNIQUES

In order to overcome the previous problems, the phase information must be regained while simultaneously allowing for changes in the structure as it varies from point to point in the flow field. Such requirements are not easily met. In any homogeneous direction, for example, the average magnitude of all wavenumbers, and hence frequency components, must remain the same because of the homogeneity. However, the phase relationship between the same frequency component measured at different locations must change; otherwise, the correlation of a single frequency would never approach zero. In nonhomogeneous directions, the magnitudes of all frequency components do change and so does the phase relationship. Thus in essence, there exists a phase-dependent pattern associated with a coherent structure in space and time, and one wishes to explore it at different spatial locations. The problem then becomes one of recognizing a deterministic pattern and defining it in a manner so that it can be followed to other spatial locations while simultaneously allowing it to change somewhat. The philosophy embodied in the methods to be described here attempts to better utilize the existing information rather than to require additional data.

The essential element of the correction scheme is to match two different patterns, such as those associated with velocity signatures from two different locations. Often, characteristic patterns associated with the coherent eddies may easily be seen in visualization studies, such as in Refs. 5 and 6. However, it is usually much more difficult to detect these eddies from signals obtained in an Eulerian coordinate system. It is even difficult to define a pattern in an Eulerian framework, especially if the signals are almost Gaussian with a continuous spectral distribution.

To begin, let us define a "feature" as a characteristic parameter associated with the event of interest. These features are intended to be quite general and may include any combinations of amplitudes, derivatives, filtered signals, etc., from many different input signals. Although, in principle, an infinite number of features can be chosen, only a finite number, M, are used. Following Andrews,[15] one can show that if these features are suitably chosen, they can be used as the basis for defining an M-dimensional feature space with each feature associated with a different axis. That is, the pattern can be characterized by M different features which form an M-dimensional vector. In this manner, an event is represented by a single point in the feature space. If two events have similar features, they will lie in the same proximity of the M-dimensional feature space. Alternatively, if the features do indeed unambiguously characterize the events of interest, then two nearby points in feature space must represent similar patterns. Before a direct quantitative comparison between two patterns can occur, a measure of distance must be defined. In the interest of simplicity, a Euclidean measure will be used.

Most examples found in the field of pattern recognition assume that there are many input signals that measure different aspects of an event, and the features are constructed from these signals. In the study of coherent structures in turbulent shear flows, experimental conditions often limit the user to a few input signals, especially in the streamwise direction where probe interference may be a problem. Since the features must be obtained from these signals, the user is restricted to seeking patterns in time from only a few points in space. However, this is ideally suited for making corrections for the random phase in conditional averages, especially with a streamwise separation. Namely, the temporal eddy pattern can be recorded upstream and the M features computed to record this event in the feature space. At the downstream location, several different patterns can be recorded at different times. Corresponding to each pattern, a set of features are computed and recorded in the M-dimensional feature space. The problem then is to determine which pattern, i.e., set of M features, best matches the original pattern obtained at the upstream location. One of the simplest techniques to determine the "best" correspondence between the patterns is to compute the variance between the original pattern and all of the patterns obtained downstream. This corresponds to finding the Euclidean distance between the points in the M-dimensional space. The minimum variance, i.e., distance, then defines the best match in a least squared sense as will be discussed.

Since the phase is the quantity of interest, one of the most straightforward techniques for selecting the features is to utilize a series of sequential time points. Thus, let the vector $\mathbf{P}(0, t_n)$ represent the pattern at the upstream location as shown in Fig. 4. For the simple case of a sequential series of velocity points in time, the
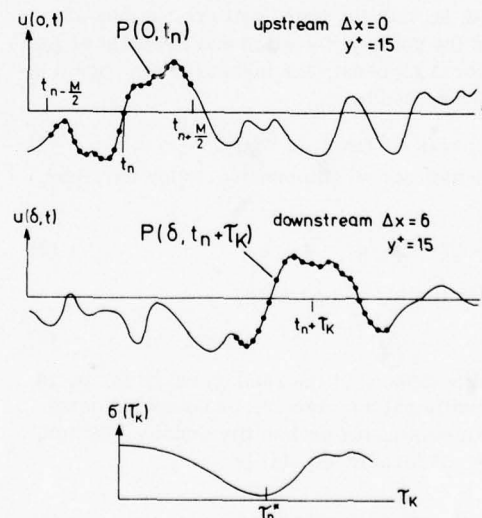

FIG. 4. The upper curve shows the original pattern $\mathbf{P}(0, t_n)$ obtained from the marked individual time points of the $u(0, t)$ signal upstream. The indicated time points of the downstream signal in the middle trace are used to form one of the $\mathbf{P}(\delta, t_n + \tau_k)$ patterns. The variance between the patterns as τ_k is varied is shown at the bottom. The minimum value at τ_n^* corresponds to the "best" match between the patterns.

components of **P** are given by

$$\mathbf{P}_m(0, t_n) = u(0, t_{n+m-M/2}) \qquad (12)$$

for $m = 1, 2, 3 \ldots M$. As seen in Eq. (12), the time series that defines **P** is centered about the point of detection, t_n. Thus, $\mathbf{P}(0, t_n)$ represents a pattern in the M-dimensional feature space that must be compared with similar patterns obtained downstream.

Many different vectors can be chosen at $\Delta \mathbf{x} \neq 0$ by using a different time series for their features. These patterns are denoted by $\mathbf{P}(\Delta \mathbf{x}, t_n + \tau_k)$, where τ_k is the time delay between the point of detection, t_n, and the time point about which P is centered. The relationship between the patterns and the time delay τ_k is illustrated in Fig. 4 for data obtained in a turbulent boundary layer. Any number of patterns may be obtained at the downstream location by varying τ_K. To study the evolution of a turbulent eddy as it moves downstream, the range of τ_k is limited by the physical constraints; namely, the convection velocity must be between zero and U_∞. In any practical problem, only a finite number of patterns, K, are used.

For each of the patterns chosen at the downstream location, the variance between it and the original pattern is given by Eq. (13)

$$\sigma(\tau_k) = \frac{1}{M} \sum_{m=1}^{M} [P_m(0, t_n) - P_m(\Delta \mathbf{x}, t_n + \tau_k)]^2, \qquad (13)$$

where σ is the averaged squared difference between the M components of the vectors. If some features were deemed to be more important than others, a weight function could be assigned to each vector component to obtain a weighted variance. In the present case, the features, i.e., velocity data points, obtained nearer to the original phase reference point, t_n, could be weighted more heavily than those lying at times closer to $t_{n\pm M/2}$. In more general cases when the features are not simple sequential time series, a weighting function is almost always required. For example, if the features have different mean square values along each axis, a weight function is mandatory so that the features with the larger fluctuations do not necessarily dominate the variance in Eq. (13).

The best match in the least squared sense between the set of K patterns, $\mathbf{P}(\Delta \mathbf{x}, t_n + \tau_k)$, and the original pattern, $\mathbf{P}(0, t_n)$, is determined by the minimum value of the set of K variances, $\sigma(\tau_k)$. Let this minimum be denoted by $\sigma(\tau_n^*)$ where the subscript n is still used to denote the nth event. For the case of the vectors being sequential data points, the variance $\sigma(\tau_k)$ is a continuous function and is shown at the bottom of Fig. 4. The time delay associated with the minimum variance, τ_n^*, is the time required for the original pattern to traverse the distance $\Delta \mathbf{x}$ downstream. Note that τ_n^* will vary from one event to the next and hence is a random variable. In fact, it is the temporal representation of the random phase being sought.

Since τ_n^* is not a constant, it is convenient to define a new time series, $t_n^*(\Delta \mathbf{x}, y^+)$, which denotes the corrected arrival time of the events at the new location. Thus,

$$t_n^*(\Delta \mathbf{x}, y^+) = t_n(0, y^+) + \tau_n^*, \qquad (14)$$

where y^+ denotes the position normal to the wall in the boundary layer examples, and $t_n(0, y^+)$ is the original time series that was obtained from the detection algorithm and used in Eq. (2) as simply t_n.

This special case of pattern recognition that utilizes a sequential time series for features is the same as a series of short-time cross correlations taken between the data obtained at the upstream probe and that obtained at the downstream location. That is, under the conditions described here, the M data points associated with the original pattern at the upstream location are cross-correlated with a comparable set of M data points obtained at the $\Delta \mathbf{x}$ location. The correlation for this fixed time delay is obtained by averaging the product over the M data points. This process is then repeated until a correlation has been computed for all K values of the time delay. The maximum correlation obtained in this manner can be shown to be mathematically equivalent to the minimum of the variance discussed earlier. However, in general, the mathematical techniques from pattern recognition described here can be used with many differing features and will not necessarily be equivalent to a cross-correlation method.

The use of the correlation description does have several advantages associated with it. Space-time cross correlations have been used for many years, and thus, there is a considerable amount of familiarity associated with them. The correlation of two signals, each characterized by M data points, provides a more physical description of the mathematical processes that occur in the M-dimensional feature space. In addition, the normalized correlation coefficient is confined to the range -1 to $+1$, and hence, it can be used directly as a weighting parameter in Eq. (4) for the conditional averages. That is, if the pattern has traveled directly downstream, the correlation coefficient should be considerably larger than if it had wandered off in a skewed direction because of the background turbulence. Thus, the larger the correlation coefficient is, the better it should represent the original event at the downstream position, and therefore, a larger weight should be assigned to those members of the ensemble average.

This technique has utilized two different parameters; the number of features, M, and the extent of the temporal domain over which the best pattern was sought, characterized by the number of patterns used, K. Since the technique searches for the maximum correlation coefficient, this coefficient will normally be positive, although this is not guaranteed. The average magnitude of this coefficient will depend upon the parameters M and K. As the number of features, M, is increased, the pattern will be increasingly more difficult to match, and thus the average maximum correlation coefficient will decrease. If one searches for a pattern over a larger temporal domain, the number of patterns, K increases, and the probability increases that a better match between the two patterns $P(0, t_n)$ and $\mathbf{P}(\Delta \mathbf{x}, t_n + \tau_k)$ will be found. Hence, the average maximum correlation coefficient must increase as K is increased. In practice, it is usu-

ally easy to find ranges of these two parameters over which the resulting conditional averages are rather independent.

The effect of varying the parameters M and K can easily be determined experimentally by utilizing data over which one does not expect any agreement between two random patterns. Such data can easily be generated by using filtered random noise to match the characteristics of the signal of interest, as illustrated by Blackwelder and Kaplan,[11] or by using patterns obtained under completely uncorrelated conditions. This procedure, in effect, calibrates the technique for the specific application. It also provides the user with base line data from the underlying probability space so that a statistical significance can be assigned to the results.

The pattern recognition technique described here provides the user considerable freedom in choosing the features. In the illustrated case of the random phase, the temporal aspects of the problem were of the utmost concern, and hence, the series of sequential time points was found to be a very useful set of features. Since the sharp acceleration was the dominating aspect of this event, time derivatives with some smoothing have also proved to be quite reliable features in this problem. However, in a more general case, the M-dimensional vectors could have included weighted combinations of velocity data, derivatives of the velocity, short term averages, Fourier magnitudes, etc.

The user is free to experiment with different features in order to determine which are best suited for the event being studied. Herein lies both the strength and the weakness of the technique. At present, the mathematical theory of pattern recognition cannot offer any guidance in choosing the features originally. However, there are some highly developed mathematical tools available for determining which of the M features contain the most valuable information (see Andrews[15]). For example, in the present example, these tests indicated that the features obtained nearer t_n were more valuable than those obtained at $t_{n+M/2}$. Obviously, it is desirable to reduce the number of required features, M, in order to reduce the computation time. However, the number of features required to properly characterize the pattern will depend strongly upon the definition of the features.

Often it is impossible to obtain signals at two different locations in the flow field because of probe interference and other experimental limitations. However, the technique is not limited by this constraint. If the event being sought has a known characteristic signature associated with it, this can provide the features required for the initial pattern. Even if the characteristics of the event are not known, one may be able to use an initial approximation to the suspected features and iterate until the results converge. This technique has been successfully used by Zilberman et al.,[16] where the initial approximation was a weak conditional average whose magnitude had been diminished by the random convection velocity.

EXPERIMENTAL RESULTS AND DISCUSSION

The sequential time series technique described here was applied to the streamwise velocity signals obtained in a turbulent boundary layer with a Reynolds number of 2500, based upon momentum thickness. The free-stream velocity of the turbulent boundary layer was 4.57 m/sec and the thickness of the layer was $\delta = 8$ cm. The primary data were obtained by using a rake of 10 hot-wires as illustrated in Fig. 5. Each of the hot wires was aligned along the spanwise direction and measured the velocity at ten locations perpendicular to the wall. An additional trigger wire was placed upstream one boundary layer thickness. The original detection of the bursting phenomena was accomplished upstream at $y^+ = 15$ by the algorithm described by Blackwelder and Kaplan.[11] The data were simultaneously recorded, digitized, and stored on magnetic mass storage devices. The previous techniques were assimilated into computer programs which could call the data upon demand. Additional details of the experimental conditions are given in Ref. 11.

Since the detection of the bursting phenomena was accomplished at $y^+ = 15$, the results from these methods were first explored only at that y^+ location. The principal results are seen in Fig. 6. The upper curve is the conditional average of the streamwise velocity taken at $\Delta x = 0$; that is, the detection and conditional averaging were done at the same spatial location, as in Fig. 1. The middle curve shows the conditional average that was obtained at the downstream location when the detection was accomplished upstream. As in Fig. 2, it is seen that the maximum magnitude of the conditionally averaged velocity seems to have decreased to less than 25% of its upstream value. In addition, it has lost its temporal coherence, as indicated by the lack of the sharp acceleration.

The convected arrival times at the downstream locations were then determined by the techniques discussed in the previous section. Between twenty and forty features were used, and the minimum variance was obtained from forty patterns. The conditional average at the downstream location was obtained by Eq. (4) with the
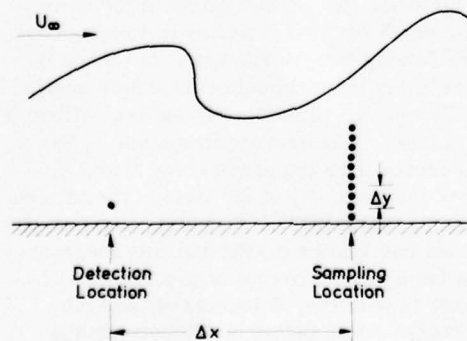

FIG. 5. Experimental configuration with the detector probe located upstream. Data were obtained from the single probe upstream and from the downstream rake of probes.
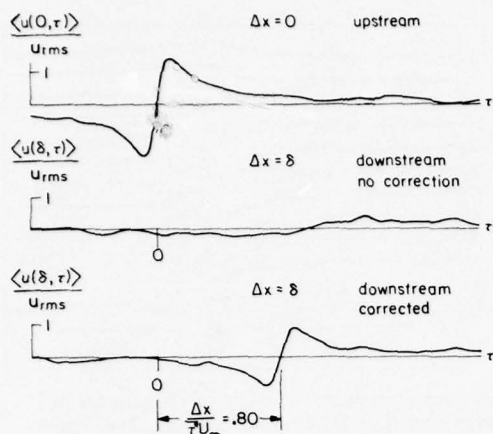
FIG. 6. The upper conditional average was obtained with the detection and sampling occurring at the same spatial location. The middle uncorrected conditional average shows how the random phase degrades the results. The lower curve uses the same data as the middle one but has been corrected for the random phase. All data were obtained at $y^+ = 15$ in a turbulent boundary layer.

time series t_n being replaced by the corrected arrival times of the pattern, $t_n^*(\delta, 15)$, given by Eq. (14). The results are seen in the lower curve of Fig. 6. Note that the data are exactly the same as these used to obtain the middle trace; only the time references are different. As expected, the randomness was responsible for most of the decay that was observed when no corrections were applied.

The time delays, τ_n^*, are now random with respect to the detection times upstream, $t_n = t_n(0, 15)$. Thus, there is no simple means of locating the temporal position of the conditional average downstream with respect to that obtained upstream. However, since an average structure was sought, it was decided to use the average time delay between the patterns obtained at the two locations. The time series used to compute the conditional average at the upstream probe is given by $t_n(0, 15)$ and that used to compute the corrected conditional average at the downstream probe is $t_n^*(\delta, 15)$. Thus, the average time delay is given by

$$\overline{\tau^*} = \frac{1}{N} \sum_{n=1}^{N} t_n^*(\delta, 15) - t_n(0, 15) = \frac{1}{N} \sum_{n=1}^{N} \tau_n^*. \tag{15}$$

This was used to locate the lowermost conditional averate in Fig. 6.

This technique has been able to extract the correlated part of the structure out of the randomness resulting from the fluctuating convection velocity. It is seen that the eddy structure has arrived at the downstream location with a greater coherency than indicated by the uncorrected conditional average. However, the flexibility built into the technique has allowed the structure to change, as can be seen in the lowermost trace of Fig. 6. Namely, the magnitude of the structure has decayed somewhat from its previous value obtained upstream. In addition, the slope of the acceleration measured at the downstream location is seen to be less than that ob-

tained upstream. This is expected because the coherent structure changes as it moves downstream. Definitive statements about the convection velocity cannot be made without knowing the shape and phase relationships of the structure. However, along $y^+ = 15$, the average time delay between similar patterns at $x = 0$ and $\Delta\mathbf{x} = \delta$ corresponded to a convection velocity of $0.8\ U_\infty$. This is considerably faster than the mean velocity at that location, $U \cong 0.5\ U_\infty$. Upon examining the individual realizations in Fig. 2, it is seen that the strong acceleration has traveled faster than predicted by the mean velocity. This indicates that this structure is possibly driven by the outer flow field. It should be noted that the convection velocity of $0.8\ U_\infty$ agrees with that of the large structure associated with the pressure field as reported by Willmarth and Woolridge[17] and Bull.[18]

This technique was also used to study the effects of the random phase when the spatial separation was in a direction normal to the wall. By analyzing only a streamwise separation as done herein, the randomness associated with the convection velocity has been removed. However, another randomness will manifest itself with spatial separations in the normal direction. This results from the slightly different shapes of the coherent structures as they pass the probe. In particular, the cross sections of the coherent structures in the x-y plane will vary because of their three-dimensionality. Even if the eddies were two-dimensional, their cross sections might be different enough to cause a loss of phase. Nychas et al.[19] used visualization techniques to study the shapes of these structures in this plane. Chen and Blackwelder[20] obtained more quantitative information about them by using a slightly heated turbulent boundary layer. They found that the random phase associated with the normal direction was indeed quite large and had to resort to special techniques to overcome this. The same type of pattern recognition technique can also be used to correct this randomness, as will be shown.

In order to study the structure in the direction normal to the wall, the rake was placed at $\Delta\mathbf{x} = 0$ and the detection scheme generated a time series $t_n(0, 15)$. This series was defined when the structure was present at $y^+ = 15$ and is used as a reference time base. Since the structure will have an angle associated with it in the x-y plane, one expects that the structure will not arrive at $y^+ = 20$ simultaneously with its arrival at $y^+ = 15$. By using the procedure outlined earlier and illustrated in Fig. 4, a new time series $t_n^*(0, 20)$ can be defined as

$$t_n^*(0, 20) = t_n(0, 15) + \tau_n^*, \tag{16}$$

where τ_n^* is now the optimum delay time obtained by comparing the M-dimensional pattern at $y^+ = 15$ to those at $y^+ = 20$. That is, the original pattern, $\mathbf{P}$, for each event was obtained at $\Delta\mathbf{x} = 0$ and $y^+ = 15$. For each event, n, several patterns were taken at $\Delta\mathbf{x} = 0$ and $y^+ = 20$ at different points in time, and the best fit was sought by computing the variance. The minimum variance then determined the time delay τ_n^* in Eq. (16) which provided the highest correlation between the neighboring locations. As each one of the coherent eddies passes the hot-wire rake, a new point in each time series, $t_n^*(0, 20)$, was generated. After this time series was generated, the

same technique was used to generate another time series, $t_n^*(0, 30)$, by using the patterns and time series generated at $y^+ = 20$. This procedure was continued in a stepwise fashion out to $y^+ = 100$ and was utilized in a similar fashion from $y^+ = 15$ down to the wall. Forty features were used to compute the variance and approximately fifteen different patterns were compared to find the optimum time delay, τ_n^*. Fewer patterns were needed in this case because no streamwise separation existed and the corresponding time delays were less random.

All of the time series thus generated were random and have probability densities that are shown in Fig. 7. Each of these densities was experimentally obtained from approximately 300 events. The abscissa has been nondimensionalized and represents the time delay between the original detection time of the structure at $y^+ = 15$ and the arrival time at the other nine y^+ locations. Since all of the delay times are referenced to those at $y^+ = 15$, the probability density there is a delta function as shown. For elevations greater than $y^+ = 15$, the eddy structure is seen to arrive at an earlier point in time. As the wall is approached, the opposite is true. As the distance increases from $y^+ = 15$, the probability densities show more dispersion in the arrival times, as expected. Above $y^+ = 15$, the probability densities are skewed negatively, indicating that some of the structures arrive much earlier than the average structure.

The mean values of all of the probability densities have been computed and are indicated by the x's on the absicssas. The average shape indicated by the x's agrees with that obtained by Chen and Blackwelder[20] using a temperature contaminant and by Kreplin[21] using standard correlation techniques. The average length of
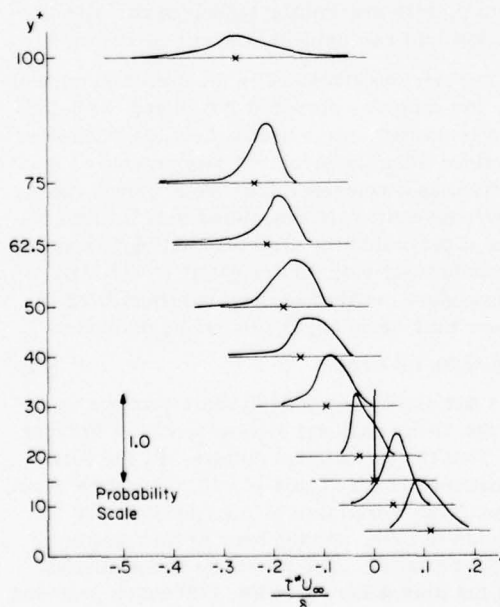
FIG. 7. Probability distributions of the arrival times at the different y^+ locations. Since $\Delta \mathbf{x} = 0$ for this data, the randomness is due to the different shapes and cross sections of the eddies.
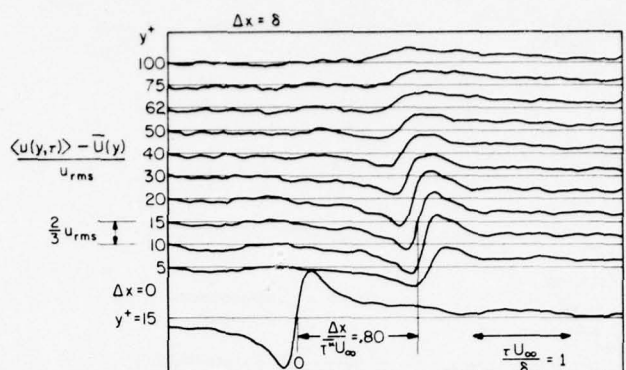
FIG. 8. Conditionally averaged streamwise velocities at ten y^+ locations downstream using phase correction. The detection was obtained at $\Delta \mathbf{x} = 0$ and $y^+ = 15$. The normalizing velocity is the rms velocity at $y^+ = 15$.

this structure in the streamwise direction is seen to be approximately 0.4 δ in this region of the boundary layer. A measure of the randomness of the shape of the structure is given by the standard deviation of the distributions. It increases slowly out to $y^+ = 75$ and then takes a large jump between that location and $y^+ = 100$. This may be due to the larger spatial separation between $y^+ = 75$ and 100 over which the patterns must be compared. However, it may indicate that a more complex phase relationship exists in this region of the flow field.

Separations in both $\Delta \mathbf{x}$ and Δy can be used in order to study the decay of the overall structure as it journeys downstream. The original time series in this case is $t_n(0, 15)$ as obtained by the detector probe at $\Delta \mathbf{x} = 0$. The pattern recognition technique was employed to generate a time series $t_n^*(\delta, 15)$ at the downstream location which corrected for the random convection velocity as before. This series was then used to obtain the corrected times at $y^+ = 20$ by

$$t_n^*(\delta, 20) = t_n^*(\delta, 15) + \tau_n^*$$

in the same manner as described by Eq. (16). This procedure was repeated until a corrected time series had been computed for all of the data.

The results using the corrected time series in Eq. (4) are found in Fig. 8. The lowermost trace is the conditional average obtained at the detector probe upstream using the time series $t_n(0, 15)$. The reference point for the abscissa, i.e., $\tau = 0$, is taken to be the average upstream detection time. The results at $y^+ = 15$ at the downstream location indicate a convection velocity of 0.8 U_∞ as before. The conditional averages obtained at each of the y^+ locations downstream were then displaced by the mean value of the appropriate time delay as computed by Eq. (15). The results show that the structure arrived at the downstream location with a greater strength and coherency than the uncorrected data of Blackwelder and Kaplan[11] indicated. In the outer region, the structure arrived earlier in time than it did at $y^+ = 15$. Closer to the wall, it has arrived correspondingly later. This is clearly indicative of the skewed nature of this eddy, as has been reported in the previous refer-
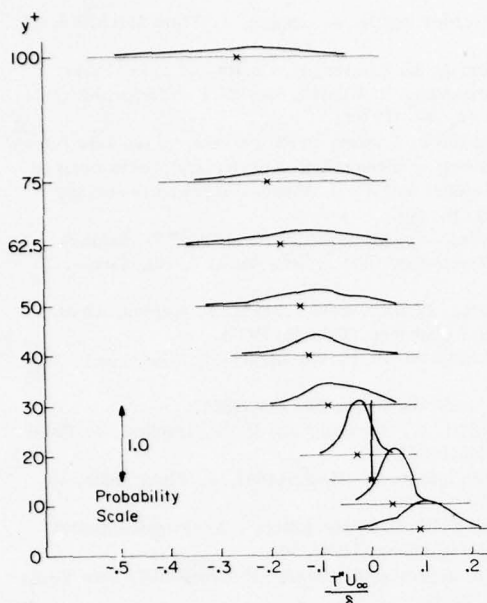
FIG. 9. Probabilty distributions of the arrival times of the characteristic eddies downstream, $\Delta \mathbf{x} = \delta$. The time differences, τ^*, are relative to the arrival time at $y^+ = 15$.

ences. As one proceeds from $y^+ = 15$ outward, the streamwise velocity signature associated with the structure is seen to decay. Although there definitely is a momentum excess at $y^+ = 100$ which is related to the event being detected upstream at $y^+ = 15$, it does not seem to be as strongly correlated with the bursting phenomena as the data obtained in the lower regions is. This suggests that the structure may be more complicated in this region or may experience some interaction with the outer flow field. Similar results were obtained by Chen and Blackwelder.[20]

The probability densities of the arrival times at the downstream locations are shown in Fig. 9. These probability densities were obtained by using $t^*(\delta, y^+)$. All of the arrival times are with respect to $y^+ = 15$ at the downstream location. Hence, the probability density at $y^+ = 15$ in Fig. 9 is a simple delta function as before. Again, one sees that the eddy structure arrives earlier in time at $y^+ > 15$ and later in time below $y^+ = 15$. The main difference between Figs. 7 and 9 is that the standard deviations of the arrival times are much greater at $\Delta \mathbf{x} = \delta$. This is expected because of the randomness in the convection velocity which was not present in the analysis at $\Delta \mathbf{x} = 0$.

The average arrival time with respect to the arrival at $y^+ = 15$ was computed and is shown by the x's in Fig. 9. The mean shape of the structure as indicated by the x's is approximately the same as that at $\Delta \mathbf{x} = 0$ in Fig. 7. This suggests that the whole structure has traveled one boundary layer thickness downstream at a constant velocity and has not been affected by the mean shear.

DISCUSSION

A technique has been described that corrects for the loss of phase between the detection signal and the data

signal in conditional averaging. The random phase was shown to seriously degrade the conditional averages by spreading them out in time so that the results could be in the noise level. The correction method was able to restore the phase of each member of the ensemble average in order to give a more coherent result which indicated a longer lifetime for the eddy structure than that found without the phase correction. Although the results presented here were only for $\Delta \mathbf{x}$ and Δy separations, similar effects are expected for all spatial separation in a random environment.

The correction technique utilized some mathematical methods of pattern recognition. These methods also show some promise for determining better detection algorithms, especially when trying to mate visualization studies with more quantitative techniques using electronic signals. This involves a process called "training", because the algorithm is trained to recognize a set of events, and is described by Nilsson.[22] It proceeds by defining and computing a set of features obtained from various combinations of the input signals. These features are ascribed to an M-dimensional space as described earlier. During training, the different events, e.g., burst, ejection etc., are defined by an additional training input, such as an electronic signal, visual observations, etc. This input determined which event is present and the machine then marks the corresponding features as belonging to that event. The next set of M features is computed and the process repeated. After a sufficient number of sets of features have been so classified, the statistics of the features corresponding to each event, e.g., mean and rms values etc., can be computed.

If the features have been judiciously chosen, each event will occupy a small subspace of the M dimensional feature space. If greater resolution between the events is desired, more and/or different features can be defined and the process repeated.

After training with known events, data corresponding to an unknown event are presented to the algorithm. It then computes the desired features and, depending upon where in the M dimensional space the features lie, the algorithm decides which event has the highest probability of corresponding to the set of features. A new set of data is presented and the process is repeated for another event.

Within this context, the random phase problem is quite simple because the "event" consisted of only one point in the feature space which was defined by the velocity signal at the first spatial location. Thus, the algorithm only had to determine which set of features obtained at the other spatial location lay the closest to the original pattern.

ACKNOWLEDGMENTS

[1] A. A. Townsend, Australian J. Sci. Res. **2**, 451 (1949).

[2] R. E. Kaplan, in *Turbulence in Liquids*, edited by G. K. Patterson and J. L. Zakin (University of Missouri, Rolla, Mo., 1975), p. 274.

[3] C. W. Van Atta, in *Annual Review of Fluid Mechanics*, edited by M. Van Dyke, W. G. Vincenti, and J. V. Wehausen, (Annual Reviews, Inc., Palo Alto, Calif., 1974, Vol. 6, p. 75).

[4] P. O. A. L. Davies and A. J. Yule, J. Fluid Mech. **69**, 513 (1975).

[5] G. L. Brown and A. Roshko, J. Fluid Mech. **64**, 775 (1974).

[6] C. D. Winant and F. K. Browand, J. Fluid Mech. **63**, 237 (1974).

[7] S. J. Kline, W. C. Reynolds, F. A. Schraub, and R. W. Runstadler, J. Fluid Mech. **30**, 741 (1967).

[8] E. R. Corino and R. S. Brodkey, J. Fluid Mech. **37**, 1 (1969).

[9] H. J. Kim, S. J. Kline, and W. C. Reynolds, J. Fluid Mech. **50**, 133 (1971).

[10] S. S. Lu and W. W. Willmarth, J. Fluid Mech. **60**, 481 (1973).

[11] R. F. Blackwelder and R. E. Kaplan, J. Fluid Mech. **76**, 89 (1976).

[12] S. Corrsin and A. L. Kistler, NACA Report 1244 (1955).

[13] L. S. G. Kovasznay, V. Kibens, and R. F. Blackwelder, J. Fluid Mech. **41**, 283 (1970).

[14] R. L. Kaplan and J. Laufer, in *Proceedings of the 12th International Congress of Theoretical and Applied Mechanics*, edited by M. Hetenyi and W. G. Vincenti (Springer-Verlag, Berlin, 1969), p. 236.

[15] H. C. Andrews, *Introduction to Mathematical Techniques in Pattern Recognition* (Wiley, New York, 1972), Chaps. 2 and 4.

[16] M. Zilbermann, I. Wygnanski, and R. E. Kaplan, Phys. Fluids **20**, S258 (October, Part II, 1977).

[17] W. W. Willmarth and C. E. Wooldridge, J. Fluid Mech. **14**, 187 (1962).

[18] M. K. Bull, J. Fluid Mech. **28**, 719 (1967).

[19] S. G. Nychas, H. C. Hershey, and R. S. Brodkey, J. Fluid Mech. **61**, 513 (1973).

[20] C. H. P. Chen and R. F. Blackwelder, J. Fluid Mech. (to be published).

[21] H. -P. Kreplin, Ph.D. dissertation, Max-Planck-Institut für Strömungsforschung (1976).

[22] N. J. Nilsson, *Learning Machines* (McGraw-Hill, New York, 1965), Chap. 3.

Large structure in a turbulent boundary layer

Garry L. Brown and Andrew S. W. Thomas

Department of Mechanical Engineering, University of Adelaide, Adelaide, South Australia

Using an array of hot wires and wall shear stress probes results are presented which support the hypothesis that an organized structure exists in the boundary layer. From the correlation between wall shear stress and velocity it is shown that this structure is at an oblique angle to the free stream. The inferred angle from this correlation is found to agree remarkably with recent flow visualization photographs. Evidence is found that the large scale motion in the organized structure produces a slowly varying component in the wall shear stress and, importantly, a high frequency large amplitude fluctuation occurring near the maximum in the slowly varying wall shear. It is suggested that this latter fluctuation is associated with the bursting phenomenon. A model which accounts for these results is described. It leads to a description of the bursting process in terms of a rotational instability and while too approximate to give more than good order of magnitude estimates, it gives values of the wall streak spacing which are not inconsistent with previous measurements.

I. INTRODUCTION

The structure of the turbulent boundary layer has been the object of an enormous research effort over several decades. No attempt is made here to review this extensive literature; the reader may wish to refer to Willmarth[1] for a recent and excellent review of the progress that has been made. For the present purpose, it is sufficient to note that the structure in the region near the wall, in particular the "bursting" phenomenon (Kline et al.[2] etc.) has been well documented (Willmarth[1] summarizes the many contributions made to build up the present picture), and similarly, the large structure of the outer intermittent flow has been investigated extensively, firstly by space-time correlation techniques and subsequently by conditional sampling techniques (for example, Kaplan and Laufer,[3] Kovasznay et al.[4]). An essential issue which has remained, however, is the connection between the bursting phenomenon near the wall and the large scale motion in the outer part of the layer. Associated with this is the question of the origin of the bursts and the nature of the cyclical regeneration of bursts. Offen and Kline[5] have described a model based on flow visualization studies which attempts to provide a partial answer to these questions. They suggest that a circulatory flow, or vortex, in a burst (or lifted wall streak) can impose an adverse pressure gradient on the wall as it passes downstream, and this adverse pressure gradient acting on a newly forming wall streak stimulates the lift-up of this new streak. A part of this hypothesis as suggested by Offen and Kline is that a pairing of the vortices associated with bursts leads to a return of part of an old burst to form the origin of the new burst. The process is thus regenerative. They further suggest that the large scale motion in the outer part of the layer is a consequence of a repeated "pairing" process as the vortices, associated with bursts, are convected into the outer part of the boundary layer. There is an implication perhaps that the outer part of the boundary layer plays a passive role.

While not of themselves sufficient to contradict these hypotheses, there are several results which are not easily reconciled with them, for example, the important finding of Rao, et al.[6] that the burst rate scales with the outer flow variables. Lu and Willmarth,[7] working with large spikes in the Reynolds stress, also found a rate which scales with outer flow variables. Similarly, the dramatic effect of drag reducing polymers on the flow near the wall and, in general, the considerable difference in scales, at high Reynolds number, between the initial wall streak (mean spacing approximately $100\nu/U_\tau$) and the motions in the outer region of the boundary layer are not easily incorporated in a hypothesis in which the large scale structure, which is very weakly dependent on Reynolds number, is derived from the amalgamation of bursts near the wall.

A quite different point of view from that of Offen and Kline has been taken by Coles and Barker[8] in which it is proposed that a large scale structure, in particular, the turbulent spot, is the building block of the turbulent boundary layer and that the bursting phenomenon is part of the signature of this spot. That the bursting phenomenon may be a signature of such a large scale eddy is also implied in what appears, in the light of the present work, to be a far-sighted speculation by Badri Narayanan et al.[9]

In addition to the extensive literature on the structure of turbulent boundary layers, the authors have obviously been greatly influenced by earlier work[10] and by continuing studies of the large structure in the mixing layer. In fact, the optimistic aim of this work which has guided the planning and carrying out of these experiments was to try and establish whether a similarly significant organized structure exists in the boundary layer.

As "organized" structure has come to mean different things to different people[11] some comment on what is meant by it in the present context is in order. Organized structure is taken here to mean a "recognizable" large scale motion which has its own internal dynamics (a mechanism to generate and transport smaller scale turbulence, for example) and which of itself and through interactions with other similar structures dominates the mechanics of the flow. In some respects this view of

the large structure follows from Townsend's[12] early large eddy hypothesis, but it differs particularly in the way in which the large eddies are formed and the extent to which they are deterministic, in the variety of forms they are expected to take, and correspondingly, in the detailed way in which they dominate the mechanics of the flow, that is, for example, determine the Reynolds stress. (In the results to be discussed, for example, it appears that the Reynolds stress in the mixing layer is essentially determined by the large scale motion of the large structure, i.e., by the two-dimensional motion, whereas a totally different relationship between the large structure and the generation of Reynolds stress is suggested for the boundary layer.)

II. EXPERIMENTAL CONSIDERATIONS

Quite apart from the reality or significance of organized structures in a turbulent flow, what makes any attempt to find them such a difficult problem (fraught with the danger of producing order in chaos as many have recognized) is the randomness in phase between "recognizable" structures, and the "jitter" in the amplitude and the characteristic time scale of these structures. In the boundary layer the problem is made doubly difficult because of the crucial three-dimensionality of the motion and the corresponding randomness in the transverse direction of the slice through any structure obtained at a single measuring station. It is immediately clear, however, that if a large structure exists, there should be some correlation (by definition) between the motion at points throughout the region of the boundary layer which the structure occupies. The experiment was therefore aimed at simultaneous measurements throughout the boundary layer with an array of hot wires and with the intention of using a computer to sort and correlate the data. We were led to build an inexpensive 16 channel analog-to-digital data acquisition system capable of making blocks of 16 000 measurements, at any total rate up to 4 million samples a second and writing them on computer tape. In these experiments this was used to simultaneously sample and record up to seven hot-wire channels.

If, further, there is an organized structure, then it must in some sense be coupled with the bursting phenomenon, but it seemed likely, particularly in view of the somewhat limited results obtained by Blackwelder and Kovasznay[13] using a burst detecting wire at $y^+ \simeq 24$, that the great disparity in scales, the nature of bursting and the general intensity of activity at a y^+ of 24 may make correlations between this region and the outer flow difficult to find. Rather it was felt, more or less intuitively, that the wall shear (ideally, the wall shear measured simultaneously at several points) might be a more suitable indicator of phenomena near the wall with which to correlate measurements in the outer part of the boundary layer. With this in mind extremely small, (0.5 by 0.25 mm) hot-film probes were constructed by the vacuum deposition of nickel on glass. Details of their construction to achieve very accurately repeatable characteristics, the associated high-speed, high-current feed-back bridges used to

operate them, and an analysis of the system time response will be published separately. It is sufficient to note that the response time as measured in a shock tube was less than 50 μsec, that two separate probes side by side in a boundary layer and operated by separate bridges gave indistinguishable spectra, and when calibrated in a laminar flow in the rotating disc apparatus of Brown and Davey[14] the measurement of mean skin friction under a turbulent boundary layer was within 3% of the value determined from Preston tube measurements. From the calibration of the film the "effective" length of the film (in the terminology of Brown[15]) was found to be 2.6 times the measured length (0.25 mm) and in the boundary layer of this study the corresponding value of $U_\tau l_{eff}/\nu$ was 56. The thermal boundary layer of the film therefore extended only to $y^+ \simeq 13$.[15] This, of course, is the thermal boundary layer associated with the mean wall shear; the effective length rapidly reduces to the measured length for fluctuating wall shear[16] so that the thermal boundary layer associated with the fluctuating wall shear is even thinner. Because of the dependence of the effective length on frequency, particularly at low frequencies, the relationship between the fluctuating heat transfer and the wall shear is not simple (of course, for correlation purposes this is not a particular difficulty). Well above a frequency of $\omega l_{eff}^2/\kappa_{glass}$, however, where the effective length has become the measured length, the fluctuating wall shear may be straightforwardly obtained from the steady calibration, (taking into account the different effective lengths). [This, of course, assumes quasi-steady heat transfer, which by simple scaling arguments in the governing heat equation is expected to exist for frequencies $\omega \nu/U_\tau^2$ less than $(U_\tau l/\nu)^{-2/3}$ for Prandtl number 1.]

Since the limits in this experiment for these two frequencies are about 50 Hz and 2.5 kHz which correspond to the relative extremes of velocity fluctuation spectra, the output of the film has been converted to a shear stress fluctuation and the results expressed accordingly. Since it is only correlations which are being compared here, however, the results will be seen to be quite independent of this step. Thus, the experimental arrangement was an array of hot wires arranged initially vertically above a wall shear probe in a zero pressure gradient turbulent boundary layer.

The tunnel used is described by Lim.[17] The free stream velocity was 36 m/sec, the boundary layer thickness approximately 40 mm, the displacement thickness 5.51 mm, and at the measuring station the Reynolds number based on momentum thickness was 10 160. The mean velocity profile was entirely standard and the friction velocity determined from a Preston tube was 1.28 m/sec. The aspect ratio of the boundary layer is unavoidably low in this tunnel (tunnel width: boundary layer thickness = 5.8 in the first set of experiments); however, the experiments have been repeated at distances farther upstream in the working section (aspect ratio = 8.5, Re_θ = 4, 930) and properly scaled with U_0 and δ there is no apparent difference between the two sets of results.
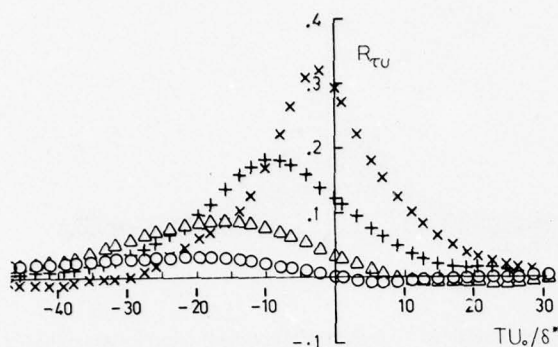
FIG. 1. Long time averaged correlations between the wall shear stress and the velocity at various points directly above the hot film. ×, $y/\delta = 0.05$; +, $y/\delta = 0.25$; △, $y/\delta = 0.50$; ○, $y/\delta = 0.75$.

III. RESULTS

A. Velocity, wall shear correlations

In the first experiment an array of four hot wires was placed immediately above the wall shear probe (at $x = 0$) with the wires located at $y/\delta = 0.05$, 0.25, 0.5, 0.75. The long time correlation coefficient defined by

$$R_{\tau u}(T) = \lim_{T_s \to \infty} \frac{1}{T_s} \int_0^{T_s} \tau(t)\, u(t + T)\, dt$$

(where the wall shear τ and the velocity u were non-dimensionalized by their rms values) was determined for the four wires. The results are shown in Fig. 1.

Several points are worth noting. Firstly, there is a quite perceptible correlation between the wall shear and the velocity even at $y = 0.75\delta$. (The absolute magnitude of this correlation is determined by the rms values of τ and u. As will become clear, the high frequency large amplitude wall shear fluctuations contribute more to the rms value than to the correlation so that the magnitude of the correlation appears unnecessarily small.) As remarked in the introduction this correlation at large distances is especially significant given the relatively high Reynolds number; $y = 0.75\delta$ corresponds to approximately 25 wall-streak spacings, for example. Secondly, and not surprisingly, the correlation peaks at increasing time delay as the point of velocity measurement is moved farther from the wall. Both of these results are consistent with measurements reported by Blackwelder and Kovasznay[13] using a wire at a y^+ of 24 instead of a wall shear probe. Their correlations are similar at the same y/δ but extend, interestingly, only to $y/\delta = 0.5$ which by comparison, at their Reynolds number corresponds to only four wall-streak spacings. Perhaps the most important question which these results raise is whether this correlation is due to events at the wall being convected out into the flow along the trajectory implied by the increasing time delay with distance from the wall, or, alternatively, due to some organized structure at an oblique angle to the wall which produces a characteristic response in the wall shear as it passes by. As a first step toward establishing whether either of these views is correct the rake of wires was moved downstream (i.e., chang-

ing x) keeping the same values of y/δ. It was intended to find, experimentally, the points where $R_{\tau u}$ was a maximum at zero time delay ($T = 0$). This was quite straightforward. As a first estimate for x it was assumed that the convection speed was $0.7U_0$ and x followed from the values of T at which the $x = 0$ correlations peaked. The hot wire was then placed at this value of x, the correlation was found to peak not quite at $T = 0$, and the process repeated. Only a few iterations were required. The resulting correlations having a maximum at $T = 0$ are shown in Fig. 2. The conclusion that can hardly be avoided on this evidence alone is that of the two hypotheses only the second could account for these results. The correlations which peak at $T = 0$ are (within the error bars) practically indistinguishable from those at $x = 0$ (with the appropriate shift in time delay). It must be true, given the velocities in a boundary layer, that the probes at this oblique angle are nearer to the trajectory of a burst convected from the wall than when the probes are vertical and if the first hypothesis were correct, then they should give a higher correlation at this oblique angle. Alternatively, one could argue that the same maxima in the correlation but one at zero time delay and the other at a time delay TU_0/δ^* of approximately 25, which is considerably larger than measured correlation time scales in the sublayer,[18] is inconsistent with the first hypothesis.

The location of the probes which gave correlation maxima at $T = 0$ is shown in Fig. 3. Evidently, the curve which is a good fit to these four points is very nearly a straight line at an angle of 18° to the wall (free stream). Coincidentally and independently, results from a flow visualization study using smoke were presented at the same meeting as the present results.[19] By courtesy of Dr. Falco a tracing of the outline of the smoke in one of his pictures (selected without knowledge of these results) is shown in Fig. 4. The agreement between the inferred angle obtained by wall shear velocity correlation and an apparent angle in the flow visualization study is quite remarkable.

It is interesting to note that the velocity determined from the time delay of the maxima in the correlation at
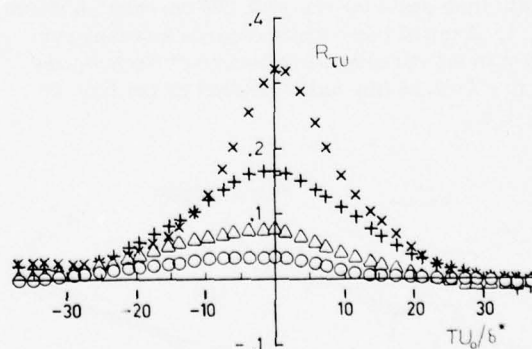
FIG. 2. Long time averaged correlations between the wall shear stress and the velocity at various positions downstream of the film such that the correlations peak at zero time delay. ×, $x/\delta = 0.24$, $y/\delta = 0.05$; +, $x/\delta = 0.89$, $y/\delta = 0.25$; △, $x/\delta = 1.55$, $y/\delta = 0.50$; ○, $x/\delta = 2.13$, $y/\delta = 0.75$.
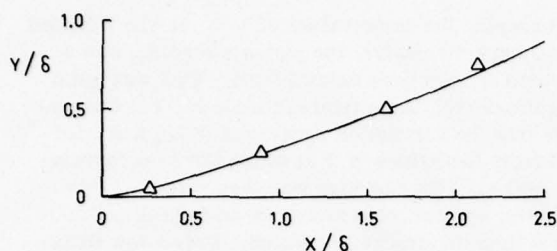
FIG. 3. Positions of the hot wires used to obtain the results in Fig. 2.

$x = 0$ and the value of x for the maxima at $T = 0$ ranges from $0.65\,U_0$ at $y = 0.05$ to $0.75\,U_0$ at $y = 0.75\delta$. (These velocities are more accurately given than might be expected from Figs. 1 and 2; they were obtained from the more accurately defined "enhanced" correlations to be discussed.) These velocities are all smaller than the local mean velocities which, if one point in the structure moves with the local mean velocity (see Sec. IV), suggests that the structure is not frozen but is, presumably, slowly growing and simultaneously very slowly rotating. This result and conclusion is not inconsistent with reported pressure fluctuation measurements[1] and space-time correlation results.[13]

Having concluded that an organized structure could account for these initial results more stringent tests of the hypothesis were now sought. Further progress appeared to require some technique for recognizing the particular pattern in the signals which could be associated with the structure and for the reasons given in the introduction this is the difficult and hazardous step. The approach adopted in this work is as follows. All pattern recognition is in essence a question of correlation, and it was argued that if the large structure accounted for the observed long-time wall-shear velocity correlations, then there should be short periods of time when the correlation is much greater than this long time correlation.

The output of the shear stress probe was therefore broken up into a large number (400) of short records each $T_s (= 7.5)$ milliseconds long. This length of time, i.e., $T_s U_0 / \delta^* = 50$ corresponds to about twice the characteristic time scale for the $y = 0.25\delta$ correlation shown in Fig. 1. Each of these short records was then correlated with the corresponding record of the hot-wire output at $y/\delta = 0.25$ (the latter delayed by the time delay T), i.e.,
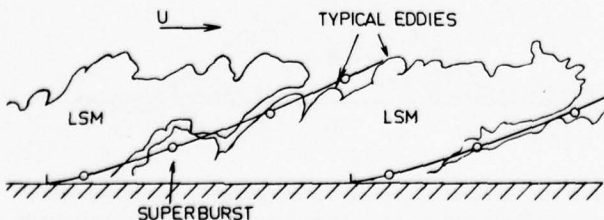
FIG. 4. Comparison of the wire positions required for correlations to peak at zero time delay (shown -o——o—) with a tracing of a smoke picture from Falco.[13]
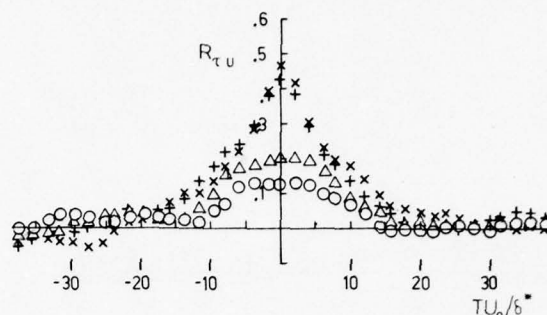
FIG. 5. "Enhanced" correlations obtained from an ensemble of various short time correlations taken at those times when the correlation between the wall shear stress and velocity at $y/\delta = 0.25$ is greater than 0.3 at zero time delay. The symbols are as in Fig. 2. Note the change in ordinate scale from Figs. 1 and 2.

$$R_n(T) = \frac{1}{T_s} \int_{t_n}^{t_n + T_s} \tau(t)\, u(t + T)\, dt.$$

Thus, a set of 400 short time correlations was obtained, the ensemble average of which was, of course, the $y = 0.25\delta$ curve in Fig. 2. These short time correlations were now compared with the ensemble average, and it was argued that if any supposed large structure was well represented in any 7.5 msec of output the short time correlation for this short record of data would be similar in shape but very much larger than the long time correlation. This was the basis of the pattern recognition. That is, from the set of 400, a subset (in fact, of 117) was obtained in which the criterion that the maximum value of the short time correlation be *twice* the long-time average (i.e., exceed 0.3) at zero time delay was satisfied. Obviously, the ensemble average of this subset of 117 had a maximum greater than twice the long-time average but apart from this greater amplitude the two correlations had the same general shape and the same time scale. (This will be clear from Fig. 5.)

A test of the organized structure hypothesis is now self-evident. For this subset of times, the correlation between the wall shear and velocity at 0.25δ is much greater than the long-time correlation and if this enhanced correlation results from a discrimination against those times when an organized structure is less evident, then for this *same* subset of times the correlations between the wall shear and the velocity at other points across the layer must also be larger than the long-time average. Figure 5 shows the result of this test, that is the ensemble average of the short-time correlations at other points based on the subset of times determined by the wire at 0.25δ. It is quite clear that an increased correlation at 0.25δ gives a correspondingly increased correlation throughout the layer, and this the authors suggest is significant evidence for the existence of some organized structure. (It should be added that this increased correlation is not due to a discrimination on the basis of amplitude). Although it made no essential difference in the results, in finally finding the subset of times of large short-time correlation at $y = 0.25\delta$, each short-time correlation was
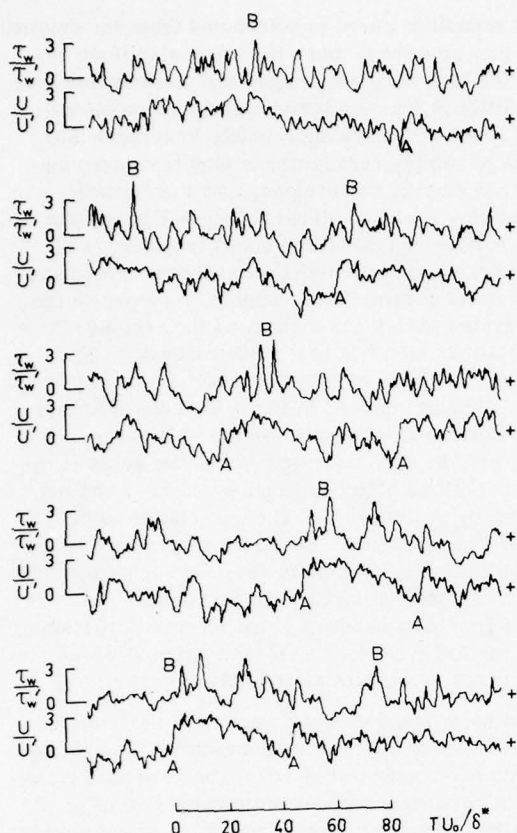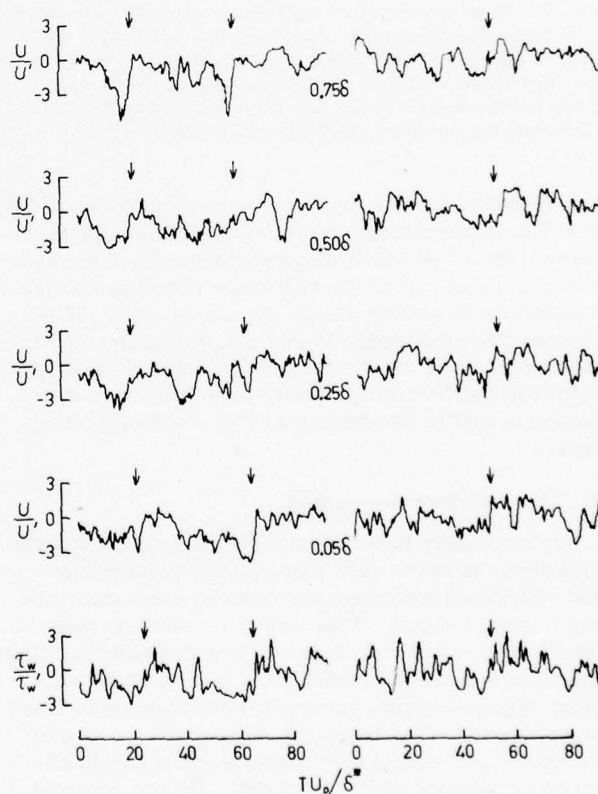
FIG. 6. Time records of the wall shear stress and velocity at $y/\delta = 0.25$ at those times when the detection criterion of Fig. 5 was satisfied.

nondimensionalized by the rms values of the signals during this short-time (thus discriminating entirely on the basis of correlation and not amplitude). For the subset of times of large correlation, the rms value of the signal taken over the whole subset of times was used to nondimensionalize the ensemble average of the corresponding short-time correlations. It is important to note, however, that these rms values obtained for this subset of times were all within 10% of the usual, long-time average rms values.)

We also note in passing that the criterion used to obtain the subset (i.e., the required value of the maximum correlation) was varied. Increasing this value to three and four times the long-time correlation reduced the percentage of records satisfying the criteria to 15% and 7%, respectively, but in every other way only substantiated the result. It is felt, however, that the large number of records in which the short-time correlation has a crudely similar shape, but very much greater correlation than the long-time average, is an indication that whatever accounts for this correlation is not in any sense an exceptional or rare event which might therefore make it insignificant in the mechanics of the flow, but rather it is a basic element of which the flow is composed.

Our attention was then turned toward finding some of

the characteristics of this apparent structure. Careful observation of the long-time signal records of all five probes led to little, but it is clear that the place to look for these characteristics is in the short records of data in which the short-time correlation is the same *shape* as the long-time correlation, but the maximum value is much larger than that of the long-time correlation. Figure 6 shows a sample of a number of these records selected by computer on this basis. The correlation between the wall shear and the velocity at 0.25δ is now overwhelmingly clear (by turbulence standards!). Several features in these signals are of interest. Firstly, the velocity trace frequently shows a relatively sharp "step" from a lower value to a higher value (marked by A in Fig. 6) followed by a slow decrease in velocity. That this is typical is supported by the skewness in the time derivative of the velocity. This feature is even more apparent at larger y/δ as is clear in Fig. 7 which shows the outputs of the five probes for a similar period. The characteristic sudden change in velocity may be seen to frequently extend across the full boundary layer. Laufer[20] shows an example of exactly this characteristic found in the output of an array of temperature probes in a slightly heated boundary layer. As will be discussed, it appears that this feature occurs on the "back" or trailing surface of the large structure. Laufer[20] arrived at the same conclusion.

FIG. 7. Time records of the wall shear stress and velocity at $y/\delta = 0.05$, 0.25, 0.50, and 0.75 at those times when the detection criterion of Fig. 5 was satisfied.
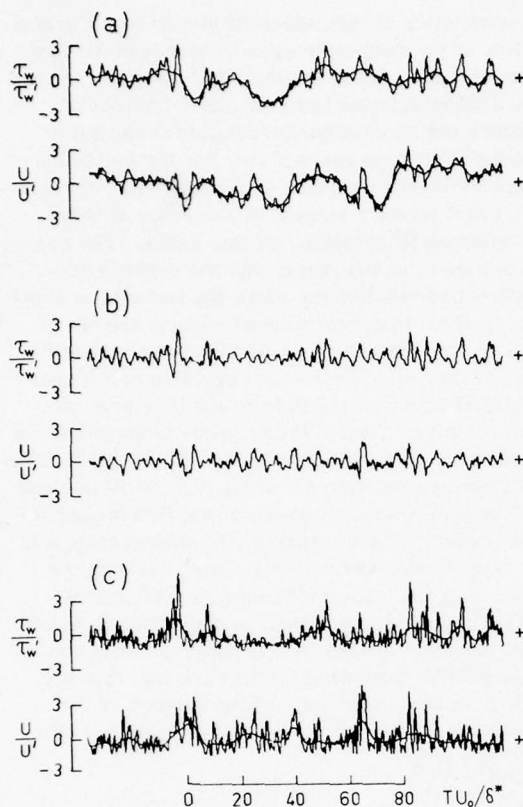
FIG. 8. Time records of the wall shear stress and velocity at $y/\delta = 0.25$ when subjected to smoothing and rectifying. (a) Unfiltered signals with low pass filtered signal superimposed. (b) The high frequency signal obtained by taking the difference between the two signals in (a). (c) The rectified high frequency signal and the smoothed rectified high frequency signal.

A second feature in Fig. 6 which it seemed important to notice is the apparent large fluctuations in the wall shear (marked B) which frequently occur when the more slowly varying part of the wall shear is relatively high. A technique to quantify this is discussed in Sec. III B. The possible implication is that the slowly varying part of the wall shear results from the passage of the large structure and this characteristic high frequency fluctuation is part of the dynamics of the organized structure.

B. The wall shear fluctuations

The qualitative ideas mentioned here suggest that the wall shear signal be split into a slowly varying part and a high frequency part representing large scale and small scale motions. This was done, more or less intuitively, as follows: A zero-phase delay digital filter was used to smooth the wall shear (and velocity) signals. Figure 8 shows the original and smoothed curves superimposed. The frequency of the filter cutoff was varied to give "acceptable" smoothing and was finally set at a frequency of $f\delta*/U_0 = 0.068$. [It may be noted that this frequency corresponds to roughly twice the bursting frequency ($TU_0/\delta \simeq 30$) of Rao et al.[6]] Figure 8 shows the remaining high frequency part of the signal

after the smoothed curve is subtracted from the original signal. Any attempt to mark the large amplitude regions of the high frequency signal and obtain some sort of intermittency function would clearly be problematical, and it seemed more appropriate to achieve the same end by simply rectifying the high frequency signal and then placing an envelope, more accurately, smoothing this rectified signal. Figure 8 shows the result (the nondimensional filter cutoff frequency was again 0.068). Qualitatively, this whole process clearly achieves the original aim, namely, to separate the slowly varying part of the signal and the regions of large amplitude high frequency fluctuations. The resulting low frequency and rectified high frequency smoothed signals (marked in Figs. 8 (a) and (c)] were now correlated and the result for the wall shear is shown in Fig. 9. The time delay is in the sense of the smoothed rectified high frequencies at time t and the low frequency at time $t + T$. The correlation is evidently very large indeed. (The rms levels used to normalize the correlations are those of each smoothed signal.) It is interesting that the correlation peaks at a nonzero time delay implying that there is a particular phase in the low frequency wall fluctuation at which the high frequency activity is most likely to occur.

This same process was now applied to the velocity signals obtained at various distances from the wall and the results are shown in Fig. 10. These results reflect what could perhaps have been anticipated from Fig. 7, namely, the increasing appearance of the sharp step in velocity (discussed in Sec. III A) with distance from the wall. It is interesting to note that substantial correlations exist between the rectified high frequency content of the velocity signals even at $y = 0.75\delta$ and the low frequency content of the wall shear. From the time delay in the peaks in this correlation, it is concluded that the sharp velocity step occurs on the "back" or trailing surface of the large structure. [That this technique did not generate a correlation when none existed was demonstrated by applying it to random noise and various pseudo turbulence signals (similarly skewed). In all cases a negligibly small correlation was obtained].

Without wishing to cloud the picture, there does seem some point in the following digression. Given the
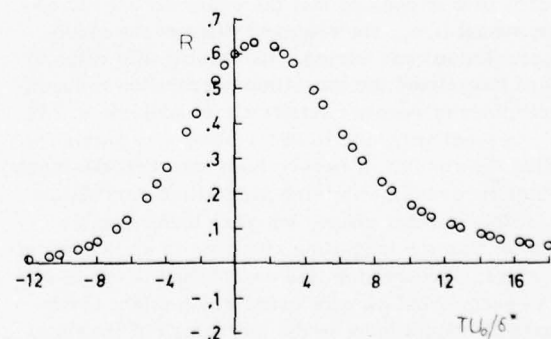
FIG. 9. Correlation between the low pass filtered wall shear stress and the smoothed, rectified high frequency component of the wall shear stress.
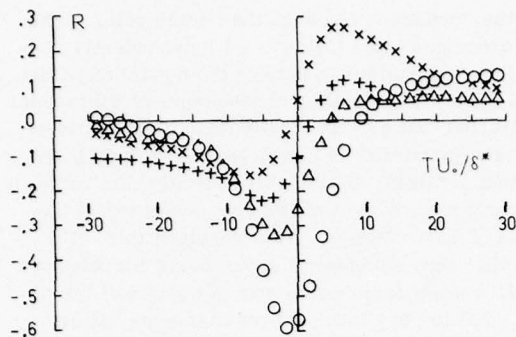
FIG. 10. Correlation between the low pass filtered velocity and the smoothed, rectified high frequency component. The symbols are as in Fig. 1.

correlation between low frequency and high frequency components of the wall shear it seemed appropriate to only correlate the low frequency (slowly varying) part of the wall shear [i.e., signal (a) in Fig. 8] with the similarly obtained low frequency component of the velocity signal at various distances from the wall. From the setting of the filter and the appearance of the signals it seemed that only the smoothed signals would make up the major part of the correlation between the two. This is indeed the case. Taking the correlation between the two smoothed signals and using the original rms values to nondimensionalize the correlation produced no apparent change to the correlation. It is then clear, however, that only the rms value of the smoothed signals should be used in correlating the two. The point of this is more than simply a trivial question of scaling, or a scandalous attempt to produce a correlation of 1. One is interested in the extent to which the large structure produces a correlated large scale motion in the boundary layer and this should be done without including the small-scale "hash" so to speak. (It contributes little or nothing to the correlation and it is sensible to not include it when nondimensionalizing the correlation). Thus, when the smoothed shear and velocity curves and the rms values for these smoothed curves are used to compute the results shown in Fig. 5, the results shown in Fig. 11 are obtained. A direct comparison can now be made between Figs. 2, 5, and 11. The extent to which the organized structure does produce a highly correlated large scale motion in the boundary layer can now clearly be assessed.

IV. DISCUSSION

All of these results taken together suggest that there is an organized structure in the boundary layer. The structure appears to be at an oblique angle to the wall and the most probable value of this angle from these measurements is $18°$. From the time scale of the wall shear velocity correlations, the structure is of the order 2δ long at the wall. There seems strong evidence that a part of the dynamics of this organized structure is a relatively small scale large amplitude wall shear fluctuation which occurs just before the local maximum in the "slowly varying" part of the wall shear. This slowly varying part of the wall shear is itself caused

by the large structure and is on the same scale as the large structure. Alternatively, it could be said that the passage of the large structure gives rise to a characteristic response in the region near the wall and this response is observed as a high frequency large amplitude wall shear fluctuation.

It seems likely that this wall shear fluctuation is directly connected with the bursting phenomenon. In fact, the cycle of bursts and sweeps, the generation of new streaks and all of the present results can be shown to be consistent with the following model of the organized structure. For the present authors, the origin of this model was the suggestion by Coles and Barker[8] that the turbulent spot may be the building block of a turbulent boundary layer. The ideas that led to the description of the burst cycle had their origin in recent work by Konrad and Brown.[21] In this work, it has been found that the large structure in the mixing layer has its own internal instability at a particular Reynolds number and above this Reynolds number there is a very marked increase in small scale mixing and a quite apparent cellular structure in the basic large structure of the flow [see Brown and Roshko[10] Fig. 8(b) for some indication of this]. The explanation for this instability offered by Konrad and Brown is that it is a result of a local rotational instability $[d(\Gamma^2)/dr < 0]$ that is a continuously recurring condition due to the formation and amalgamation of large structures.

(Before discussing the present model we add that further experiments have been undertaken with several wall shear probes, with an array of hot wires spaced in the transverse direction and with crossed wires spaced across the layer. The final results of this work, particularly the streamline pattern are not yet at hand, but they do not appear to contradict the qualitative features of the model described.)

A schematic for the model of the organized structure in the boundary layer is shown in Fig. 12. In a coordinate system fixed in the large structure, that is a coordinate system in which the streamlines are changing only slowly, the organized structure appears as a
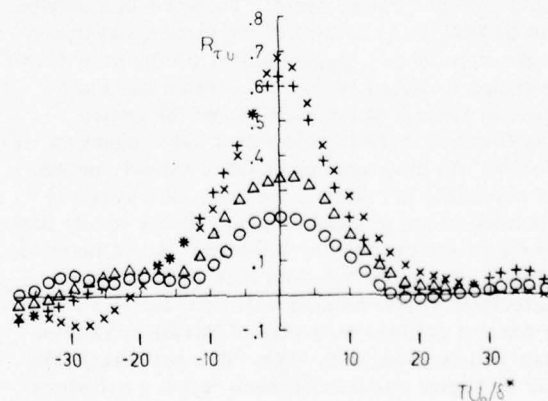

FIG. 11. Enhanced correlations that are similar to those in Fig. 5 except that low pass filtered signals have been used. The symbols are as in Fig. 2.
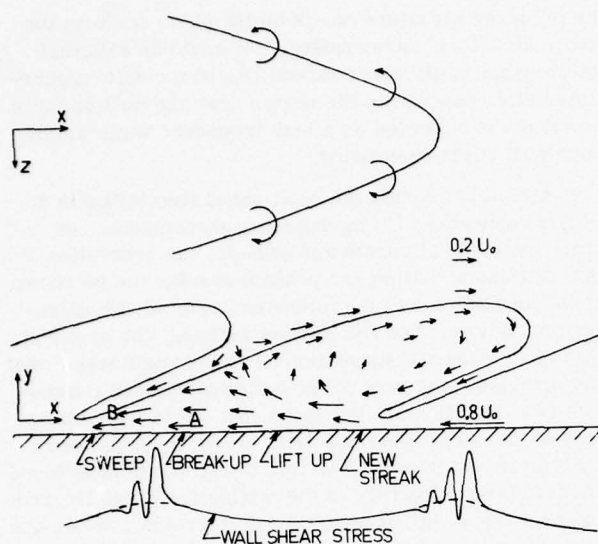
FIG. 12. Proposed flow pattern that might be seen by an observer moving at a speed of $0.8\ U_0$, and the associated wall shear stress distribution.

horseshoe vortex which then gives rise to the velocity field sketched in Fig. 11 in the center-line plane of the vortex. It is expected from the present results (Sec. IIIA) and from pressure fluctuation measurements, that in this coordinate system the wall moves with a velocity of approximately $0.8\ U_0$. The stagnation point is then on the rear surface of the large structure and on or near this surface it is readily believable that the sharp step in velocity discussed in Sec. IIIA occurs. Such a local shear layer is very likely to give rise to the "typical" eddies marked by Dr. Falco in the tracing of Fig. 4. The expected low frequency variation in wall shear due to the velocity field generated by this large structure is also shown in Fig. 11. Marked on this figure is the most probable position for the observed large fluctuations in shear stress and in addition the approximate locations of where the formation of a "new streak," "lift-up," and "break-up" have been observed[22,23] in the "burst" cycle. These results may be seen to fit well in the context of the present organized structure hypothesis. In particular, attention is drawn to the region marked A where the stream lines are convex with respect to the surface and the region marked B where there is evidently a longitudinal straining motion. As discussed more quantitatively in Sec. V it is noted that in region A the mean flow vorticity and circulation are of opposite sign. For a steady flow this is the criterion given by Rayleigh[24] for an inviscid instability. For a viscous fluid it is expected that a characteristic Taylor number will exist for this region above which a cellular structure of Taylor or Görtler vortices will be generated. (That is a secondary flow similar to Taylor vortices between rotating cylinders[25] or Görtler vortices in a boundary layer on a concave wall.[26]) This, it is suggested, is the origin of the longitudinal vortices or streaks in the wall region and at higher Reynolds numbers this basic instability as-

sists in the "breakup" phase of the burst cycle. (The authors understand that Coles[27] has independently considered this mechanism as part of the dynamics of the turbulent spot. As a further consequence of this model it is suggested that as this longitudinal vorticity arising from the instability is convected into region B the longitudinal straining motion will intensify this vorticity and return it toward the wall thereby assisting in the formation of a new streak. As a result of this, it is possible that very substantial streamwise correlations in the wall region could exist over distances of the order of δ, that is very much longer distances, at high Reynolds number, than characteristic wall scales. This too is in accord with experiment. It is also noteworthy that the model would account for the sensitivity of the turbulent boundary layer to radius of curvature of the wall, particularly to concave surfaces. (Care is required in attempting the Galilean transformation.)

Lastly, it is interesting to speculate whether the dramatic effect of drag reducing polymers is due to the ability of the polymer to resist the formation of this longitudinal vorticity in the "unstable" region in which it would otherwise be generated. Within the context of the present model it might be expected that for very small concentrations of polymer the large structure would itself not be greatly affected by the polymer, but the response of the wall region to the passage of the structure could be greatly modified due to this resistance. There would, correspondingly, be a marked reduction in Reynolds stress near the wall and a not very greatly changed external flow in the boundary layer.

A question which naturally arises is what is the origin of this large structure. It is quite plausible that it arises as a turbulent spot as Coles and Barker[8] suggest and that the spots interact, amalgamate, etc., and form a relatively stable and not rapidly growing structure. It is likely, however, that such a structure will not be the building block of fully developed pipe flow and it is curious that the flow near the wall is so similar to that in a boundary layer. We note, however, that the flow near the wall requires only a slowly varying shear stress due to a passing larger scale motion to give rise to the instability described, and it is not difficult to imagine such a large scale motion in pipe or channel flow.

V. ESTIMATES FOR THE INSTABILITY IN THE ORGANIZED STRUCTURE MODEL

It is worth pursuing the discussion of Sec. IV in an endeavor to put the justification for the burst cycle, in terms of a Taylor–Görtler instability, on a more quantitative basis.

Assuming that the velocity near the wall depends on the local wall shear then in the coordinate system of approximately *steady* flow the velocity is

$$u = -U_c + U_\tau f(y U_\tau / \nu),$$

where U_c is the convection speed of the large structure. The stream function at a height δ is then given by

$$\psi = - U_c \delta + \nu \int_0^{\delta^+} f(y^+) \, dy^+,$$

where as usual $\delta^+ = \delta U_\tau / \nu$. It follows that for any ψ if U_τ varies with x, then

$$\delta(x) = \frac{\nu}{U_\tau(x)} F\left(\frac{\psi}{\nu}, \frac{U_\tau(x)}{U_c} \right).$$

The radius of curvature R of the stream line at $y = \delta$ is given by

$$1/R = d^2 \delta / dx^2.$$

For the boundary layer profile near the wall simple functions may be used to approximate $f(yU_\tau/\nu)$. As a quite accurate representation for ψ (within 3%) in the range $15 < \delta^+ < 45$ we obtained

$$\psi + 95\nu = (13 U_\tau - U_c)\delta$$

from which we straightforwardly find, for small variations in U_τ, an expression for $1/R$. Using $U_c = 0.8 \, U_0$, $U_\tau = 0.035 \, U_0$, and $0.1 \, U_\tau$ for the amplitude of a sinusoidal variation in U_τ with $2\delta_0$ (where δ_0 is the boundary layer thickness) the wavelength of this variation, we obtain

$$1/R \simeq \tfrac{4}{3} (\delta / \delta_0^2).$$

The rotational instability criterion found by Taylor[25] can be written in the form

$$\overline{\Omega} \, \overline{\zeta} \leq - \nu^2 / 2L^4,$$

where $\overline{\Omega}$ is the characteristic angular velocity, $\overline{\zeta}$ is the local vorticity, and L is a characteristic viscous dissipation scale for the secondary motion. This result follows directly from orders of magnitude estimates in the linearized vorticity equations and has been expressed in this way by Coles.[28] In using this result he has based estimates for L on the values of L in flows of known instability (i.e., the flow between rotating cylinders). In applying this inequality in the present context we take the angular velocity to be u/R, the vorticity to be $U_\tau^2 / \nu f'(y^+)$ and, based on Coles results, L equal to $2\delta/5$. With this estimate for R, the known function $f(y^+)$, and typical values for U_τ / U_0 and δ^*/δ_0 the inequality reduces, approximately, to

$$\delta^+ \geq 1.2 \, (U_0 \delta^* / \nu)^{2/5}$$

which for the present experiment requires $\delta^+ \sim 53$. The wall region is thus unstable by an inviscid Rayleigh criterion and for a viscous fluid is also unstable with the center of the instability estimated at a height of $\delta^+ \sim 50$. This is, of course, nothing more than an order of magnitude estimate and a demonstration of the plausibility of the qualitative discussion. Changing the ratio between L and δ will have an almost linear effect on the estimate of δ. Reynolds number has a weak effect although it is stronger than might have been hoped for. Nevertheless, the authors feel that these estimates support the model and are not inconsistent with a measured streak spacing of 100 wall units.

VI. CONCLUSION

The results presented point very strongly to the presence of an organized structure in the boundary layer. This structure is on the scale of the full boundary layer. Previous correlations in the outer part of the boundary layer are consistent with this structure and the bursting process near the wall, as inferred in this study from measurements of high frequency wall shear fluctuations, is shown by correlation techniques to be a direct response of the region near the wall to the large scale motion of the organized structure. The techniques employed to recognize organized structure and to then conditionally sample and improve correlations for the purpose of clarifying the properties of this structure are thought to be more widely applicable. A model for the organized structure which is consistent with the present results is presented. While speculative at this stage, it attempts to account for the bursting phenomenon near the wall by demonstrating that the slowly varying wall shear imposed by the large structure gives rise to sufficient streamline curvature, in a steady flow coordinate system, to produce a Taylor–Görtler type of instability. It is shown that this instability may be centered at a δ^+ of the order of 50 in the present experiments so that a streak spacing of the order of 100 wall units is not inconsistent with the model.

[1] W. W. Willmarth, in *Advances in Applied Mechanics* (Academic, New York, 1975), Vol. 15, p. 159.
[2] S. J. Kline, W. C. Reynolds, F. A. Schraub, and P. W. Rundstadler, J. Fluid Mech. **30**, 741 (1967).
[3] R. E. Kaplan and J. Laufer, in *Proceedings of the Twelfth International Congress of Applied Mechanics*, edited by M. Hetenyi and W. G. Vincenti (Springer-Verlag, Berlin, 1969), p. 236.
[4] L. S. G. Kovasznay, V. Kibens, and R. F. Blackwelder, J. Fluid Mech. **41**, 283 (1970).
[5] G. R. Offen and S. J. Kline, J. Fluid Mech. **62**, 223 (1974).
[6] K. N. Rao, R. Narasimha, and M. A. Badri Narayanan, J. Fluid Mech. **48**, 339 (1971).
[7] S. S. Lu and W. W. Willmarth, J. Fluid Mech. **60**, 481 (1973).
[8] D. Coles and S. J. Barker, in *Turbulent Mixing in Non-reactive and Reactive Flows*, edited by S. N. B. Murthy (Plenum, New York, 1975), p. 285.
[9] M. A. Badri Narayanan, S. Rajagopalan, and R. Narasimha, Indian Institute of Science, Fluid Mechanics Report No. 74 FM 15 (1974).
[10] G. L. Brown and A. Roshko, J. Fluid Mech. **64**, 775 (1974).
[11] P. O. A. L. Davies and A. J. Yule, J. Fluid Mech. **69**, 513, (1975).
[12] A. A. Townsend, *The Structure of Turbulent Shear Flow* (Cambridge University, Cambridge, 1956).
[13] R. F. Blackwelder and L. S. G. Kovasznay, Phys. Fluids **15**, 1545 (1972).
[14] G. L. Brown and R. F. Davey, Rev. Sci. Instrum. **42**, 1729 (1971).
[15] G. L. Brown, in *Proceedings of the 1967 Heat Transfer and Fluid Mechanics Institute*, edited by P. A. Libby, D. B. Olfe, and C. W. Van Atta (Stanford University, Stanford, 1967), p. 361.
[16] B. J. Bellhouse and D. L. Schultz, J. Fluid Mech. **24**, 379 (1966).
[17] K. B. Lim, Ph.D. thesis, University of Adelaide, South Australia (1971).
[18] A. K. Gupta, J. Laufer, and R. E. Kaplan, J. Fluid Mech. **50**, 493 (1971).

[19]R. E. Falco, Phys. Fluids 20, S124 (October, Part II, 1977).

[20]J. Laufer, in *Annual Review of Fluid Mechanics*, edited by M. Van Dyke, W. G. Vincenti, and J. V. Wehaysen (Annual Reviews, Palo Alto, California, 1975), Vol. 7, p. 307.

[21]J. H. Konrad and G. L. Brown (to be published).

[22]H. T. Kim, S. J. Kline, and W. C. Reynolds, J. Fluid Mech. 50, 133 (1971).

[23]E. R. Corino and R. S. Brodkey, J. Fluid Mech. 37, 1 (1969).

[24]Lord Rayleigh, Proc. R. Soc. Ser. A 93, 148, (1916).

[25]G. I. Taylor, Philos. Trans. R. Soc. Ser. A 223, 289 (1923).

[26]H. Görtler, Nachr. Ges. Wiss. Göttingen, Math. Phys. Kl., Fachgruppe 2, 250 (1940).

[27]D. Coles (private communication).

[28]D. Coles, J. Appl. Mech. (Trans. ASME, Ser. E)34, 529 (1967).

Turbulence structure in a water jet discharging in air

J. W. Hoyt[a] and J. J. Taylor

Naval Ocean Systems Center, San Diego, California 92152

Special purpose high-speed cameras have been developed which enable the detailed visualization of turbulent water jets discharging in air. The laminar-turbulent transition and initial turbulent formation on the surface of the jet is followed by amplified disturbances which result in spray detachment. A very large modification to this process is observed when polymers are added to the water.

INTRODUCTION

An intensive study of water jets discharging into air is being made in order to develop improved fire-fighting equipment for U.S. Navy ships and shore installations. As part of the research, a detailed study is underway of the mechanism of jet formation, and resultant air entrainment. Through reduction of spray formation and air entrainment it is believed that more compact, coherent, and longer-range fire-fighting streams will result.

High-speed photography has been utilized in studies of water jets to estimate mass transfer and gas adsorption into turbulent liquid jets[1,2] and to estimate air entrainment by jets.[3] Firefighting jets have also been examined photographically.[4]

The preceding studies have dealt with photographs of liquid jets which have lacked sufficient resolution to ascertain the details of transition. The recent development of specialized cameras[5] has permitted examination of the fine structure of turbulent jets in much more detail than previously possible.

EXPERIMENTAL

In the course of this work, two novel high-speed cameras have been developed especially for water-jet photography. Both utilize the principle of compensating for the primarily one-dimensional motion of a water jet either by moving the film at the image speed or by optically deflecting the image to "stop" the motion. If the image motion can be essentially compensated for in the camera, f–16 to f–22 apertures can be used with 4–8 μsec electronic flash exposure to give exceptionally detailed photographs. All photographs were taken on Pan-X or Tri-X ASA 320 (DIN 26) black and white film. The rotating mirror camera is configured for macrophotography at 5 to 8×. A sketch of each camera is given in Fig. 1.

The water jets were produced by a nozzle having a conical convergence at 14° total included angle from 5.08 to 0.635 cm (2 to 0.25 in.) diam, followed by a straight section one diam (0.635 cm) in length as shown in Fig. 2. All photos were taken at a nozzle base pressure of 343 kN/m² (50 psi), supplied from a large pressure tank containing either water or polymer solutions. The inlet piping to the nozzle incorporates a 122 cm

[a]Present address: Department of Naval Systems Engineering, U. S. Naval Academy, Annapolis, Md. 21402.

(4 ft) run of straight pipe with honeycomb flow straighteners. The nozzle contours are representative of standard fire-fighting hose nozzles.

The polymer solutions were mixed in a separate tank and transferred to the pressure tank by gravity. Owing to uncertainties in estimating the quantities of water in the various tank elements, the polymer concentrations were set at a nominal value only. Samples were taken before and during each run, tested in the laboratory on the turbulent-flow rheometer[6] and compared with a calibration curve for laboratory-mixed solutions from the same sample.

RESULTS

Laminar turbulent transition

Initially, the jet emerging from the nozzle is laminar, due to the strong positive pressure gradient in the nozzle. High-speed photographs show that almost imperceptible waves on the laminar surface suddenly appear as a train of greatly magnified surface waves which are regularly spaced (for a nozzle pressure of 345 kN/m²) at a wavelength $\lambda \simeq 0.08D$, where D is the nozzle exit diameter. Although the distance X_1 from the end of the nozzle to the first large wave fluctuates widely with time, a value of $X_1 = 0.25D$ seems representative.

As many as six to eight discrete waves may be identified before they merge into a less well-defined flow. An interesting feature of these waves is that secondary waves appear on their surface, corresponding to the primary and secondary instabilities described theoretically by Landahl.[7] These had not been observed previously on water jets, even with high definition photography,[5] and macrophotography is necessary to resolve these secondary waves. A considerable effort was made to insure that their appearance in the photographs was not an illumination artifact; their existence has been tentatively confirmed since it is believed that crests of
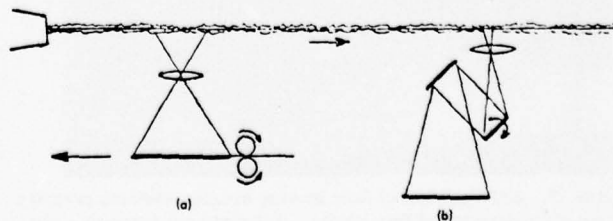
FIG. 1. Camera configurations. (a) Moving-film camera, (b) rotating-mirror camera.
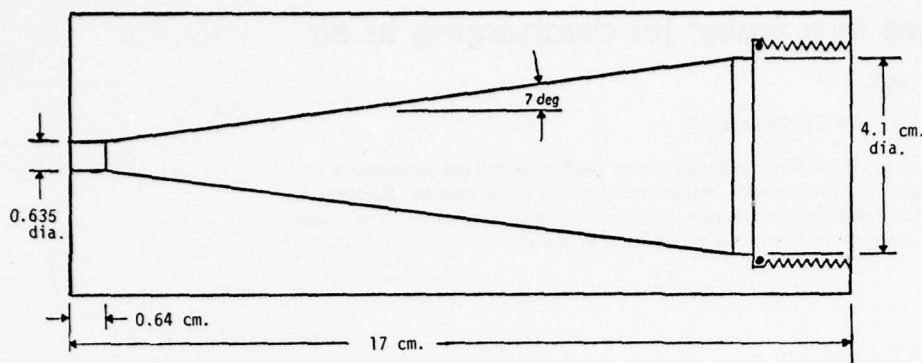
FIG. 2. Dimensions of flow nozzle.

the secondary waves have been observed in profile. Figure 3 shows a view of the wave structure, focusing on the secondary waves.

The regions of secondary waves are shown by arrows in Fig. 3. Landahl has shown that secondary waves, traveling with a group velocity near the phase velocity of the primary wave, are focused on the crest of the primary wave. Amplification of the secondary waves and their interaction with the primary wave are believed to result in flow breakdown into turbulence and subsequent amplified disturbances. In the case of water jets, these amplified disturbances may lead to spray formation and droplet detachment.

Brennan[8] has drawn attention to the surface waves which form on gas or vapor cavities shed from bluff objects in high-speed water flow. Figure 4 shows a cavitating ogive which sheds a wake remarkably similar in appearance to the jet flow from the nozzle. Brennan also developed a linearized stability analysis, based upon the boundary layer developing on the surface of the bluff body, which predicts the wavelength and wave breakup distance for the separated cavity. Brennan's analysis is also applicable to the inverse situation of nozzle flow for water jets discharging in air.

By assuming that a laminar boundary layer begins at the parallel part of the nozzle following the conical convergence (see Fig. 2), a momentum thickness, δ_2, of 0.0012 cm was estimated, leading to a Reynolds number based on momentum thickness, $R\delta_2$, of about 225. En-

tering Brennan's test data chart (reproduced as Fig. 5) of nondimensional frequency, γ, as a function of $R\delta_2$, a nondimensional frequency of about 0.17 is shown by the cavity test data, while the theory indicates 0.175. Thus, a wavelength of 0.043 cm on the jet surface is predicted from both the cavity test data and the theory. Actual measurement of nine different photos gives an average wavelength of 0.046 cm, in good agreement, considering the assumptions made as to boundary-layer growth in the nozzle, with both theory and cavity measurement.

The stability analysis also predicts, for the $R\delta_2$ involved in the jet photos, a nondimensional distance from end of nozzle to wave breakup of $x = X/\delta_2 \simeq 250$, where X is the actual distance. The actual measurement of the same photographs as before gives an average x of 214, in excellent agreement with both theory and cavity-wave data.

Amplified disturbances

The next phase of jet flow is still poorly defined; these are processes of vortex formation and coalescence with consequent entrainment and spray ejection. Initially, the amplified waves accompanying transition overturn and become partially circumferential vortex elements rolling on the jet surface; these may coalesce into pairs which entrain air.[9] The combined energy of the vortices then ejects a mass of water radially outward. An alternative hypothesis follows from boundary-layer instability theory,[7] in which water particles lift off as bursts of "hairpin" shaped vortices from the jet surface. Either of these types of behavior can be inferred from the jet photographs (Fig. 6). As the water particles are de-
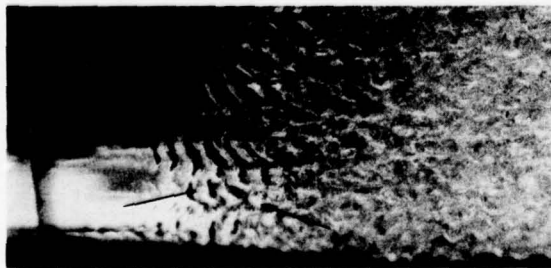
FIG. 3. Enlargement of flow leaving nozzle, showing primary and secondary instability waves. Approximate primary wave spacing, 0.046 cm. Arrows indicate regions of prominent secondary waves.
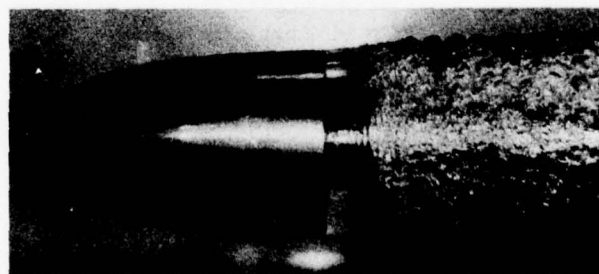
FIG. 4. Photo of cavitating ogive (from Brennan[8]).
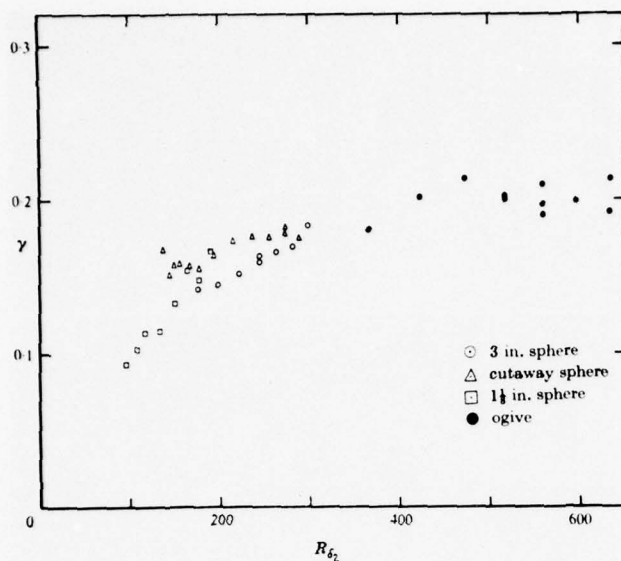
FIG. 5. Chart of nondimensional instability frequencies as function of $R\dot{\delta}_2$ for cavitating spheres and ogives (from Brennan[8]).
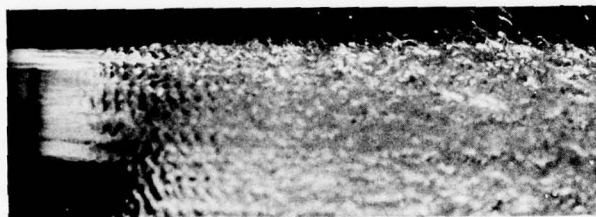
FIG. 6. Edge view of jet leaving nozzle, showing instability waves and vortex rollup.
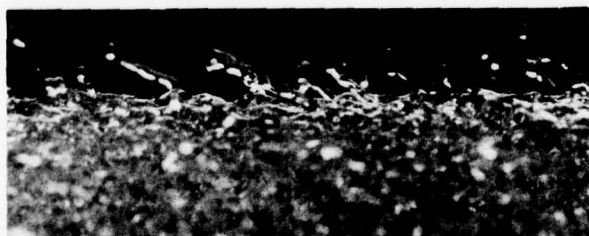
FIG. 7. Edge view of jet, 2.54 cm from end of nozzle, showing spray droplet formation.
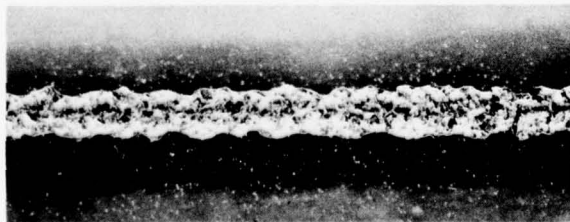
FIG. 8. The jet 45.7 cm from end of nozzle, with air bubble entrainment resulting from spray formation.
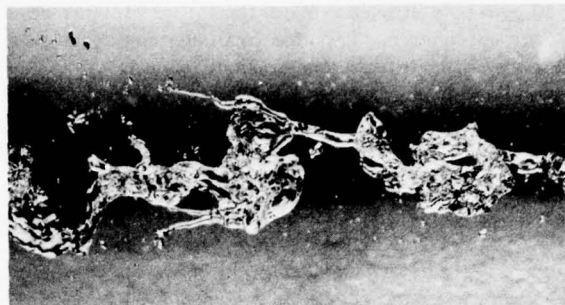
FIG. 9. Jet about to break into droplets, 198 cm from end of nozzle.

tached radially, an attachment point remains in the jet surface. Surface tension subsequently pinches off spray droplets as can be seen in Fig. 7. The returning end of the spray filament then acts as a re-entrant jet, carrying with it an air bubble. Shortly downstream, the surface of the jet is almost completely impregnated with air bubbles as shown in Fig. 8.

These air bubbles are characteristic of jets which produce spray droplets near the nozzle. The air bubbles persist in the jet surface layer until the jet breaks up.

Final state of air entrainment

As the jet moves through the air, viscous forces and large-scale instabilities cause the jet to break up. As it breaks up, it must carry with it a substantial quantity of entrained air. Figure 9 shows the nature of the jet just before complete break-up into drops. These larger-scale motions appear to be helical-type instabilities as contrasted to the axisymmetric instabilities seen near the nozzle exit.

Effects of polymers

Large changes occur in the surface of the jet when polymers are present in the fluid. As shown in Fig. 10,
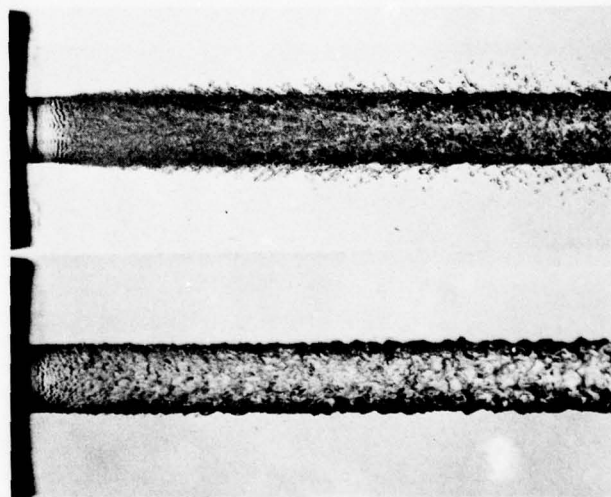
FIG. 10. Flow at exit of nozzle. (a) water, (b) 50 ppm poly (ethylene oxide).

J. W. Hoyt and J. J. Taylor

with 50 ppm poly(ethylene oxide) the initial laminar region does not appear. The effect can be considered as earlier transition to turbulence. In addition to this change, there is a substantial reduction in spray-droplet formation.

At polymer concentrations of 50 ppm and above, spray formation ceases. If the spray formation is due to hairpin vortex eruption, it is evident that this type of boundary flow is greatly inhibited. Since these polymer solutions have a greatly reduced friction in pipe flow compared with water, the reduction in spray formation may be analogous to the drag reduction mechanism, which seems to involve a reduction of turbulent bursts[10] in the wall boundary layer.

Figures 11 and 12 show the appearance of jets from the nozzle at distances of 1 and 2 m from the nozzle exit, respectively. Again, it is clear that the addition of only trace quantities of polymer causes a major reduction in the spray droplets produced by the jet.

The elimination of spray droplet formation also eliminates air bubble entrainment as a result of the spray formation process; the resulting jets are clear and glass-like as shown in Fig. 11. The external surface of the jet is much smoother with polymers than in the pure water case. The effect of the polymer is thus to reduce, dampen, or eliminate the small-scale surface disturbances while not reducing and in some cases even amplifying the larger scale motions.

The most striking changes in appearance come with the highest polymer concentration (200 ppm), where jet breakup is accompanied by filament formation linking all drops together. The formation of filaments ("pituitousness") is a characteristic of compounds of high molecular weight in solution; its occurrence in the jet is evidence of high strain rates, presumably those produced by the large-scale instabilities of the jet.

Figure 12 shows that even at breakup, the polymer jet remains much more transparent than the corresponding water jet. Both jets seem to break up due to large-scale helical instabilities.

FIG. 12. Appearance of jet 2 m from nozzle exit. (a) water, (b) 200 ppm poly(ethylene oxide).

CONCLUSIONS

By detailed study of the fluid mechanics of jet formation, the details of surface turbulence in liquid jets can be outlined. The transition from laminar to turbulent flow is accompanied by instability waves which in turn form vortices. These roll up, pair, and eject a water filament as a "hairpin" vortex. Spray drops detach due to surface tension, while the remaining segment re-enters the jet, bringing with it an air bubble which rides in the jet surface. Additionally, air is physically entrained and carried along as the jet breaks up.

An early transition to turbulence is promoted, and the spray droplet formation is inhibited by polymer solutions. The effect of the polymer is to reduce, dampen, or eliminate small-scale surface disturbances in the jet, while not reducing but even amplifying larger scale motions. The initial laminar zone present in the jet efflux with water is eliminated with trace quantities of polymer. When substantial quantities of polymer are present (200 ppm), the jet breakup is accompanied by filament formation linking all the drops together.

FIG. 11. Appearance of jet 1 m from nozzle exit. (a) water, (b) 200 ppm poly(ethylene oxide).

[1]J. T. Davies and S. T. Ting, Chem. Eng. Sci. **22**, 1539 (1967).

[2]J. T. Davies and A. A. Young-Hoon, Chem. Eng. Sci. **29**, 1115 (1974).

[3]E. Van de Sande and J. M. Smith, *Chem. Eng. Sci.* **28**, 1161 (1973).

[4]P. F. Thorne, in *Proceedings of the Conference on Drag Reduction* (BHRA Fluid Engineering, Cranfield, 1975), p. H-1.

[5]J. W. Hoyt, J. J. Taylor, and C. D. Runge, J. Fluid Mech. **63**, 635 (1974).

[6]J. W. Hoyt, in *Symposium on Rheology* (American Society of Mechanical Engineers, New York, 1965), p. 71.

[7]M. T. Landahl, J. Fluid Mech. **56**, 775 (1972).

[8]C. Brennan, J. Fluid Mech. **44**, 33 (1970).

[9]J. Laufer, in *Annual Review of Fluid Mechanics*, edited by M. Van Dyke, W. G. Vincenti, and J. V. Wehausen (Annual Reviews, Palo Alto, Calif., 1975), Vol. 7, p. 307.

[10]G. L. Donohue, W. G. Tiederman, and M. M. Reischman, J. Fluid Mech. **56**, 559 (1972).

Transitional boundary layer spot in a fully turbulent environment

M. Zilberman, I. Wygnanski, and R. E. Kaplan[a]

School of Engineering, Tel-Aviv University, Ramat Aviv, Israel

A spark was used to initiate and mark in time a turbulent spot in an initially laminar boundary layer. This marked spot of turbulence merged and interacted with the natural turbulent boundary layer generated by a row of spherical trips. By using a digital technique to align individual spot signatures, thus correcting for variations in the transit time to a given measurement station, a structure was tracked over a streamwise extent of 70 average turbulent boundary-layer thicknesses. The scale of the structure is of the order of 10δ in the streamwise direction becoming $2-3\delta$ in the interface region of the boundary layer and is less than 4δ in the spanwise direction, in spite of the fact that no spanwise alignment was performed. The structure is characterized by a convection speed of $0.9\,U_\infty$. It exhibits features in detailed agreement with those at the outer region of the turbulent boundary layer (interface region) and is consistent with existing two- and three-point space-time correlations.

INTRODUCTION

The turbulent boundary layer has been subjected to numerous intensive investigations which explored the hypothesis of a large, coherent structure in some detail. Although significant contributions were made using visual techniques and conditional sampling procedures, the coherent structures have remained rather vaguely described.[1-3] There are ambiguities in defining the signal used to identify the large eddy structure, and to date there are no consistent methods for identification which are independent of the techniques and the observer. Part of the difficulty stems from the fact that we are concerned with a quasi-cyclic process of repeatable events which occur randomly in space and time inbedded in an environment of finer scales. We cannot unambiguously define the signature of an eddy without *a priori* knowledge of its shape and its location relative to the observation station, and cannot map such an eddy because we do not have a proper criterion for pattern recognition.

Some ideas about the size of an eddy and its general trajectory have been obtained from two- and three-point space-time correlations. Kovasznay *et al.*[4] observed that the signal in the streamwise direction remains correlated over three boundary-layer thicknesses, δ, and in the spanwise direction over approximately one δ. Blackwelder and Kaplan[5] studied the bursting phenomenon near the wall and estimated the average trajectory of the burst by using a two-point correlation method. Again, the coherence of the fluctuations did not extend past 3δ even along the path of maximum correlation. We cannot deduce the scale of the large eddies from these correlations because the eddy structure may be distorted by interaction with other eddies. In order to reduce the dispersive effect of the random walk of an eddy about some mean trajectory, Kovasznay[6] measured three point triple correlation signals in the boundary layer. The triple correlation contours were much narrower in the spanwise direction than the double correlation contours, suggesting that the large eddy does not extend beyond 0.4δ in the z direction. The triple velocity correlation eliminates one effect which contributes to smearing of previous experimental results, but helps very little to define the size and shape of the large eddy.

Coles and Barker[7] created a synthetic boundary layer consisting of an array of turbulent spots [one such spot is shown in Fig. 1(a)] generated periodically in a laminar boundary layer by a row of disturbances which were intermittently activated. The underlying assumption in this experiment is that a turbulent spot in a laminar boundary layer is analogous to the large eddy in the turbulent boundary layer. Since it is further assumed that such spots do not interact, the synthetic turbulent boundary layer is no more than a superposition of the basic structures. However, this model does not provide for the generation of new spots farther downstream. It is thus implicit that an eddy generated in the transition process maintains its identity.

There are others (for instance, Landahl[8]) who suggest that large eddies are generated by local instabilities within the turbulent boundary layer. The basis for this assumption is the fact that instantaneous velocity profiles which are associated with bursts contain inflection points and are thus unstable even in an inviscid fluid.

We undertook the present experiment for the following three reasons:

(1) To map the structure of the large eddy in a typical turbulent boundary layer;

(2) to establish a characteristic distance over which such an eddy generated during transition maintains its identity in the fully turbulent boundary layer;

(3) to explore the existence of a possible regeneration process for the large eddy.

---

[a]Present address: Department of Aerospace Engineering, University of Southern California, Los Angeles, Calif. 90007.
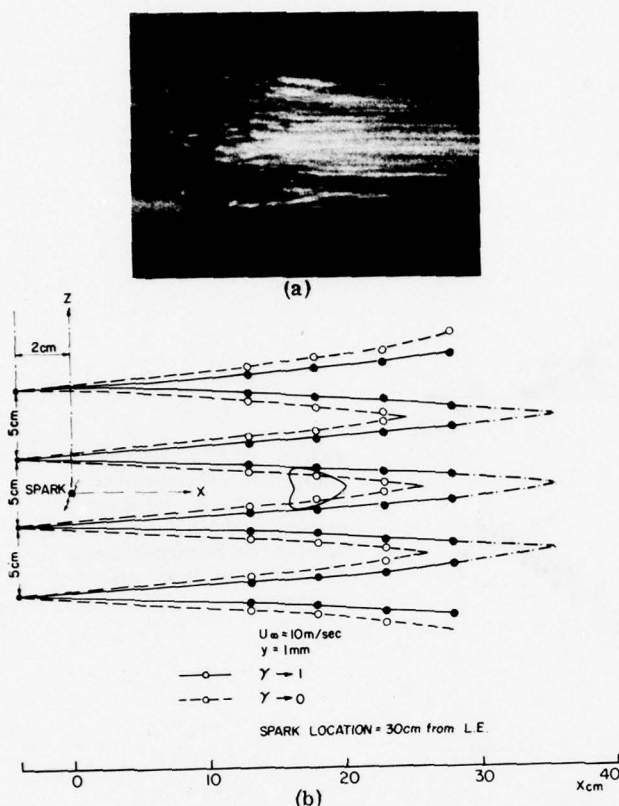
FIG. 1. (a) Plan view of an individual spot in a water channel (courtesy of Professor D. Coles). (b) Plan view of experimental configuration showing a) location of tripping spheres, b) spark, c) contours of intermittency factor indicating extent of turbulent flow.

DESCRIPTION OF THE EXPERIMENT AND THE TURBULENT BOUNDARY LAYER

All measurements were made on a 3.6 m long aluminum plate mounted in a low speed wind tunnel. The apparatus is described in detail elsewhere.[9] At a velocity of 10 m/sec the boundary layer on the plate is laminar and two dimensional over most of its 3.6 m length. The velocity profile was compared with the theoretical profile of Blasius and the pressure gradient was effectively zero.[9]

For the purpose of the present experiment, the boundary layer was tripped by a row of spheres 0.15 cm in diameter ($D/\delta^* = 1.8$) 28 cm downstream of the leading edge. The Reynolds number based on displacement thickness for the laminar boundary layer at this streamwise location was $R_{\delta*} = 500$. Each sphere created in its wake a conical region of turbulent flow. Thus, the spacing between the spheres determined the streamwise coordinate at which the boundary layer became completely turbulent. Approximate contours of the intermittency factor, $\gamma \to 1$, and $\gamma \to 0$, are shown in Fig. 1(b). When the spheres in the row were spaced 5 cm apart, the boundary layer at a free stream velocity U_∞ of 10 m/sec became fully turbulent 40 cm downstream (i.e., 68 cm from the leading edge). Changes in spacing between spheres, in free-stream velocity, and to some extent in diameter of the spheres would alter this

distance, but for the present experiment this configuration remained fixed.

The turbulent boundary layer was surveyed quite extensively in order to establish its universality and two dimensionality. Mean velocity profiles measured at various distances from the row of spheres at $z = 0$ (i.e., on the centerline between two adjacent spheres) are shown in Fig. 2. The profiles are similar with the possible exception of the profile measured at $x = 50$ cm, which deviates slightly but consistently from the rest. The profiles were replotted on a logarithmic scale and compared with the universal relation given by the law of the wall.[10] The skin-friction velocity used to collapse the data onto the universal equation is given by $U_\tau/U_\infty \sim 0.042$. The skin-friction velocity was obtained independently, using the momentum-integral equation, in the following way:

(1) The momentum thickness θ was calculated for each measuring station and plotted in Fig. 3.

(2) The slope $d\theta/dx$ was calculated for every station using Shultz–Grunow's[11] relationship: $C_f = 0.37 \log(R_x)_{le}^{-2.584}$ (where x_{le} is the streamwise distance from the leading edge of the plate).

(3) A simple curve which approximately fits the calculated value of θ, its slope, and the skin friction derived from these quantities at every measuring station was drawn in Fig. 3, and from it was calculated the skin friction to give $0.0416 < U_\tau/U_\infty < 0.045$.

Since we are interested in the large scale structure of the turbulent boundary layer, it is important to establish that the outer part of the boundary layer is also universal. For this purpose, the velocity profiles are replotted in Fig. 4 in the coordinates of the "law of the wake" and compared with the empirical relation suggested by Coles.[10] The experimental results agree very well with the equation $W(\eta) = 1 + \sin(2\eta - 1)\pi/2$, where $\eta = (y/\delta)$. Similarly, the intermittency factor was established with relatively unsophisticated circuitry and the data are shown in Fig. 2(a). The intermittency factor γ is fairly well represented by an error function with the mean position of the interface being at 0.82δ and a standard deviation $\sigma = 0.16\delta$. The intermittency distribution measured by Klebanoff[12] gives 0.78δ and $\sigma \approx 0.14\delta$ while the intermittency distribution measured by Corrsin and Kistler[13] gives 0.8δ and $\sigma = 0.14\delta$. The differences among the three sets of experiments are not large and are attributed partly to the difficulty of measuring γ in the boundary layer and partly to differences in Re.

The longitudinal component of the turbulent intensity u' at three distances from the trip line is shown in Fig. 5. The results agree fairly well with Klebanoff's measurements[12] for $0 < y/\delta < 0.5$. In the outer part of the boundary layer the present results show a higher intensity, but they are still in agreement with the results of Corrsin and Kistler.[13] The present results thus span the other two sets of measurements. The difference may be attributed to the way in which the respective boundary layers were tripped, but they may also be at-
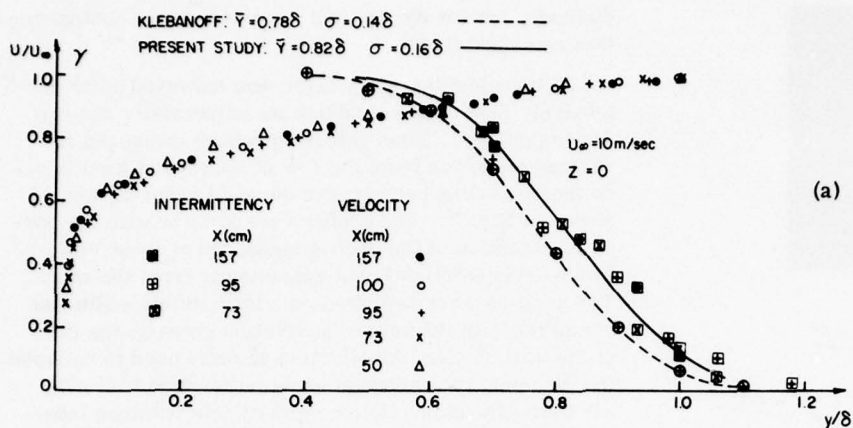
FIG. 2. (a) Mean velocity and intermittency distributions at several stations. (b) Mean velocity profiles of center line between two adjacent tripping spheres in law of the wall coordinates.
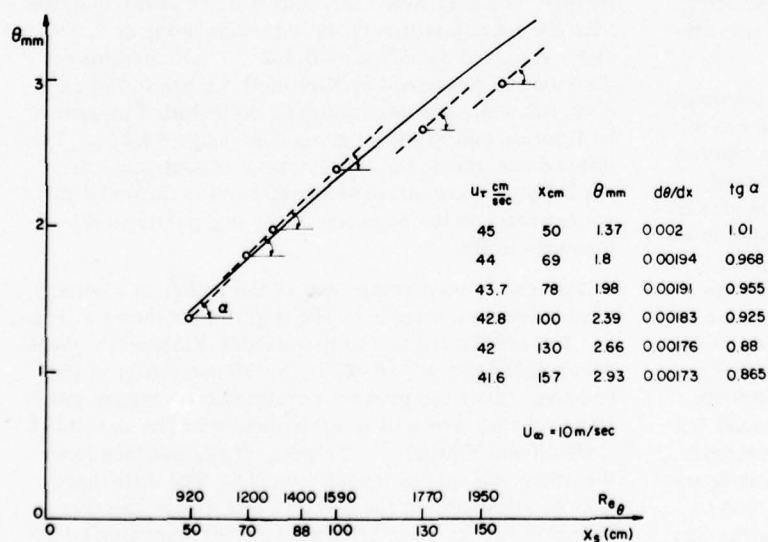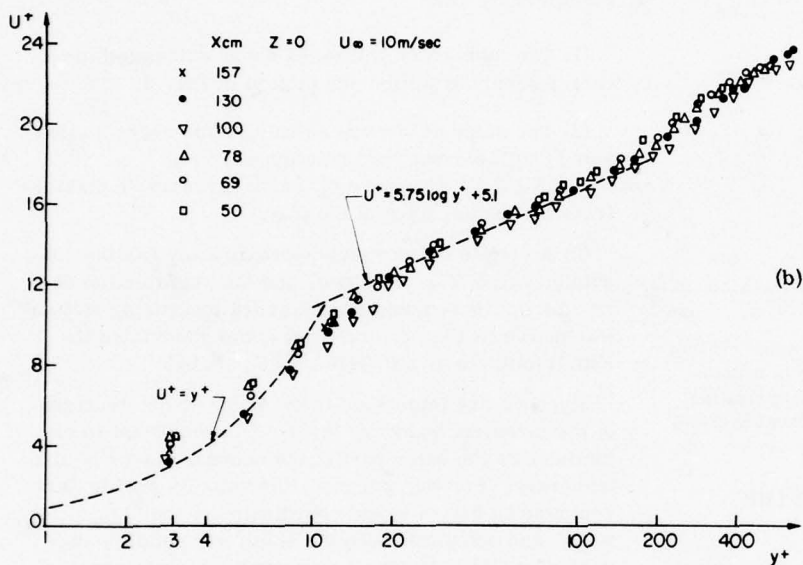

FIG. 3. Distribution of momentum thickness for tripped turbulent boundary layer.
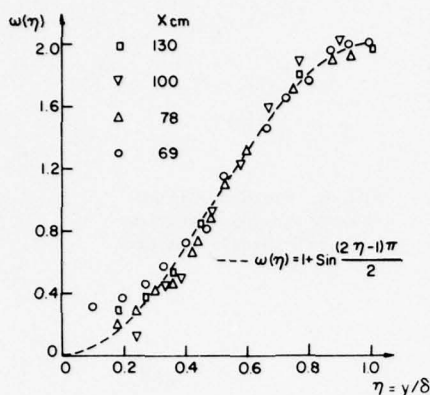
FIG. 4. Comparison of measured mean velocity profile with the law of the wake.

tributed to the frequency response of the hot-wire equipment. We are using linearized constant temperature sets, while the previous experiments were carried out with nonlinearized constant current equipment.

In view of the regularity in the tripping method, we expected a wavy spanwise variation of the boundary layer parameters. Velocity and intensity profiles (Figs. 6 and 7) measured 73 cm downstream of the trip indicate that the boundary layer is two dimensional irrespective of the spanwise position of the measuring station in relation to the spheres. The boundary layer thickness δ does retain some wavy character, being thickest directly downstream of a sphere and thinnest in the midsection between two adjacent spheres. The maximum spanwise variation in δ is about 6% about the mean at this particular section.

Having satisfied ourselves that we had a typical turbulent boundary layer, we proceeded to generate turbulent spots at regular intervals[9] in the laminar region of the flow, observing them as they were swallowed by the surrounding turbulence. The proper location of the spark in relation to the trip was established by comparing the time scale of the signature of the artificially created spot with bulge signatures at the outer part of the boundary layer. When the spark was located upstream of the trip, the time scale of the spot was larger than the average scale of the natural bulges; when it was located close to the line where the boundary layer became fully turbulent, we were unable to educe any large scale perturbation of the flow. The obvious choice for the spark is, thus, at the same streamwise coordinate as the trip. The spot induced by the spark initially develops in a laminar boundary layer until it starts to interact with the conical regions of turbulence which are produced by the spheres adjacent to it. In the given configuration the signal becomes completely turbulent during the passage of the spot about 20 cm downstream of the trip. Thus, the interaction between the spot and the surrounding turbulence starts at the spanwise extremities of the spot. This also occurs in the final stages of natural transition when adjacent spots or cones of turbulence start to interact.

DATA ACQUISITION AND PROCESSING

The complete sequence of data acquisition and processing was performed on a Varian 620/i digital computer connected on-line to the experiment. The spot was initiated by a spark, which also generated the trigger signal used as a basic time reference. An acquisition program was activated by this trigger, and a time delay was programmed to allow the nominal spot signature to reach the center of the data window. After this delay, 1024 12-bit analog/digital conversions were acquired at regular time intervals (usually 100 μsec, for a total sample duration of 102.4 msec). A typical experiment sampled between 200 and 800 sparks per elevation. These data were educible in place (for a fixed time reference with respect to the spark, and were also written on digital tape). The educible average of 1024 time points was written on a disk file, one record per measurement station. The measurement station (usually the vertical coordinate) was then changed, and the process continued until a survey of the layer was completed. All stations were measured with the same hot wire. The time average velocity without artificial spots was calculated by the digitizing system, recorded on tape, and subtracted from each data point before eduction. This value was used to reconstruct the mean velocity profile during the experiment period.

Subsequent processing involved an iterative pattern recognition scheme. The educible average on a fixed time delay from the spark can be regarded as a zero iteration. These averages were, in general, significantly smaller than individual realizations of the spots as seen by playing back individual records. The reason for the poor correspondence between the average and any individual realization was that each spot had a significantly different time of arrival at the measuring station, and hence, there was much cancellation of any coherence present. Additionally, the time duration of this zero iteration seemed significantly longer than that of recognizable individual realizations, again in accord with the interpretation given here. It was clear that in
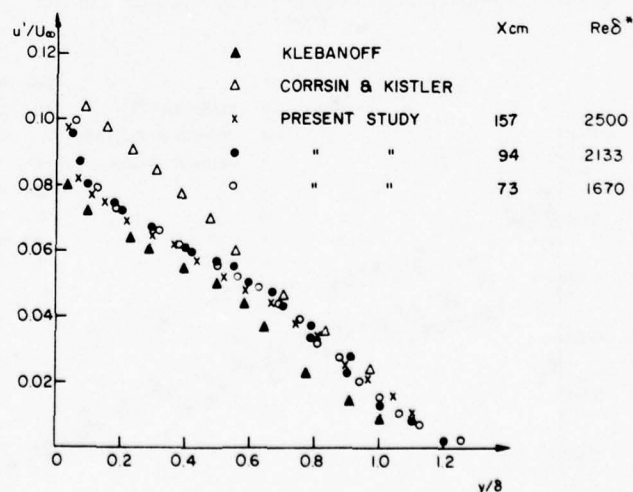

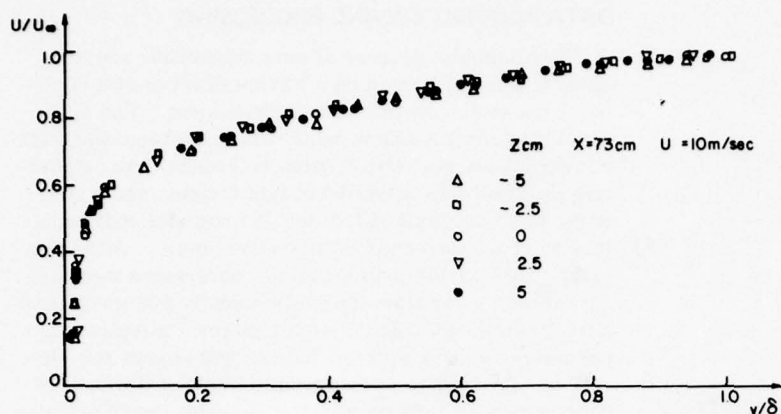FIG. 5. Distribution of longitudinal component of the turbulent fluctuations.

FIG. 6. Profiles of mean velocity in tripped boundary layer at 5 spanwise stations.

order to recover the spot structure more accurately, each record would have to be displaced in time to better align each realization.

As can be seen, the problem seems formidable, because the ambient turbulence in many cases is indistinguishable from individual spot realizations, and any local criteria used to detect the spot signature were also satisfied by similar signatures that could not be the spark-initiated spot. For that reason it was decided to generate a global criterion for the spot structure by using the educible trace as a pattern and cross correlating it with each individual realization.

This pattern-recognition scheme was implemented as follows: The central 512 time points of the test pattern (initially the zero iteration) were extended by 512 null samples and cross correlated with the central 512 points of each individual realization, after digital filtering to remove high frequency fluctuations. This cross correlation was performed by calculation of the discrete Fourier transform of both signals by a fast Fourier transform algorithm implemented by Friedman at Tel-Aviv University for the Varian 620/i minicomputer. Then, the complex transform of the pattern was multiplied by the complex conjugate of the transform of the

filtered individual record, and the product was inverse Fourier transformed.

This process is indicated graphically for two different elevations in Figs. 8 and 9. In these figures, the upper trace represents the central 512 points of an individual data record, while the second trace is the filtered version of that signal. The third trace is the pattern used for the pattern-recognition scheme. In Figs. 8(a) and 9(a), this pattern is the zero iteration; i.e., the result of the eduction based on a fixed time delay from the spark, while in Fig. 8(b) and 9(b), this pattern is the third iteration. The digital cross correlation is taken between the traces shown in lines 2 and 3 of these figures, and is indicated at the bottom of each figure. Note that the complete cross correlation is plotted, and the time span for it is ± 51.2 msec, i.e., double that of the other traces.

These cross correlations are typical of those measured in the outer and inner regions of the turbulent boundary layer. In Fig. 8, the measurement station is located far out in the boundary layer, and the spark-induced structure is easily identified by eye. Also apparent, however, are several natural structures, and indeed, the cross correlation shows local maxima at
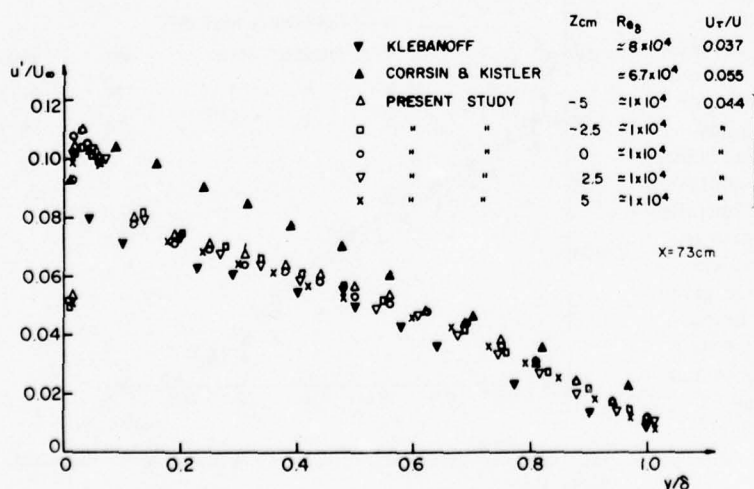
FIG. 7. Distribution of longitudinal component of the turbulent fluctuations at five spanwise stations.
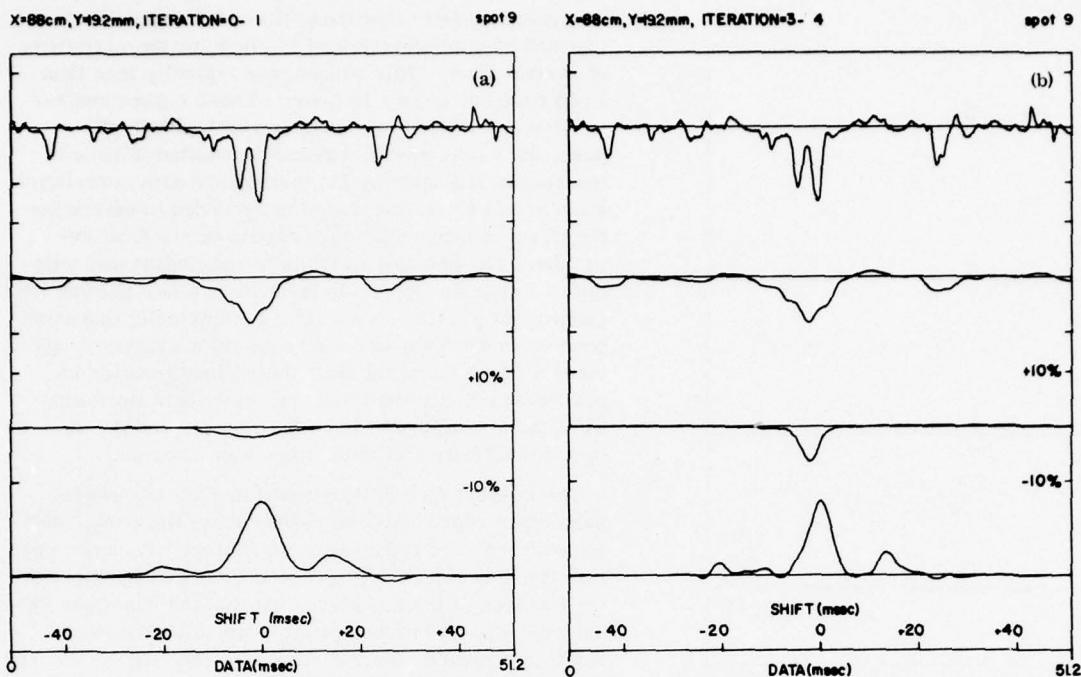
FIG. 8. Illustration of technique to align events in time. Upper trace—digitally obtained velocity history. Second trace—smoothed version of upper trace. Third trace—test pattern for cross correlation. Lower trace—cross correlation of traces 2 and 3. (a) $x = 88$ cm, $y = 19.2$ mm; (a) third trace is pattern from iteration 0 (time educed) (b) third trace is pattern from the third iteration.
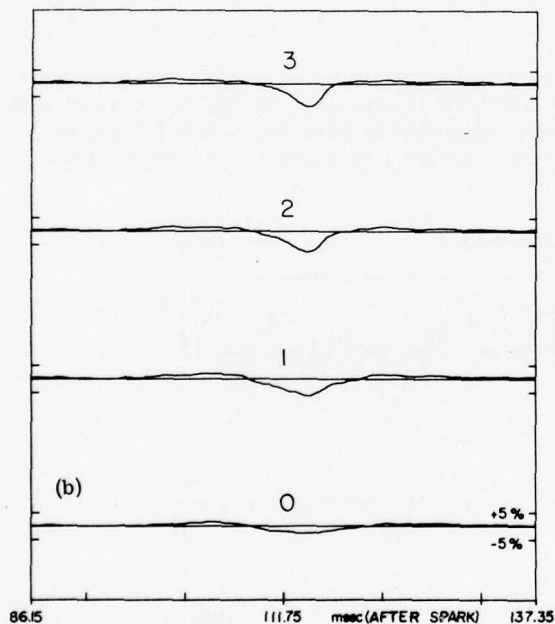
time delays corresponding to these occurrences (recall the factor of two in time on the bottom trace). While the correlation peak is relatively broad for the first iteration [Fig. 8(a)], it quickly sharpens on subsequent

iterations as the pattern becomes more representative of the individual realizations. In Fig. 9, however, it is *virtually impossible* to detect the pattern by eye, but the cross correlation still selects a test signature at
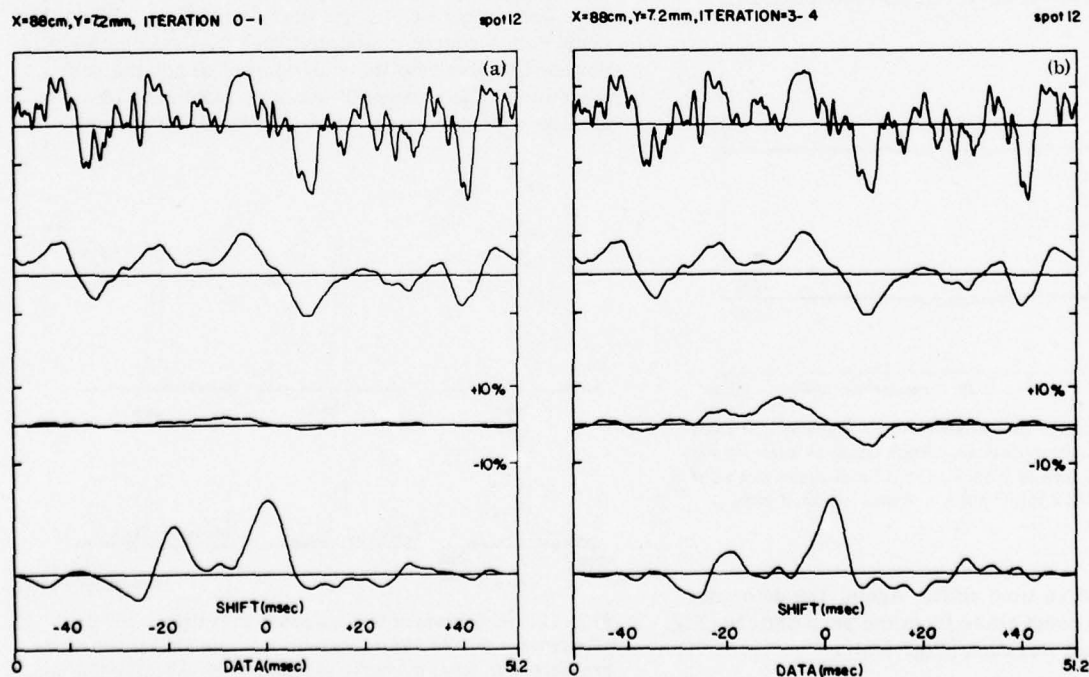
FIG. 9. See Fig. 8 for explanation. $x = 89$ cm, $y = 7.2$ mm; (a) third trace is pattern from iteration 0 (times educed). (b) Third trace is pattern from the third iteration.

X=88cm, Y=19.2mm

(a)

86.15   111.75   msec(AFTER SPARK)   137.35

X=88cm, Y=13.2mm

(b)

86.15   111.75   msec(AFTER SPARK)   137.35
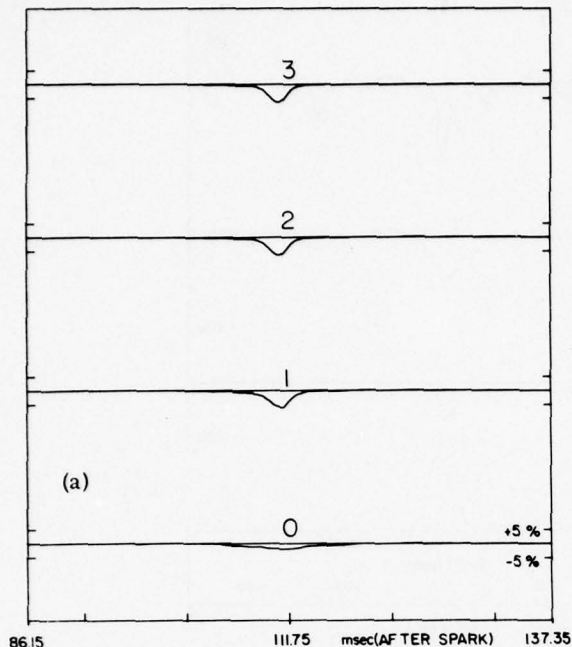
FIG. 10. Development of educed velocity signature at each
stage of the iterative procedure. Each trace is velocity sig-
nature, and departures of $\pm 5\% \, U_\infty$ from local mean are shown.
(a) $x = 88$ cm, $y = 19.2$ mm. (b) $x = 88$ cm, $y = 13.2$ mm.

nearly zero relative time shift. Again, the detection
sharpens as one progresses from the zero pattern [Fig.
9(a)] to the second iteration [Fig. 9(b)].

The time of maximum cross correlation was com-
puted and recorded, and the next iteration of the average

was re-computed using those times within a window
that had been predetermined to allow for the variations
of arrival time. This window was typically less than
± 100 time points or ± 10 msec. These subsequent es-
timates are educed in a manner similar to the first
pass, but each individual record is shifted in time by
the amount indicated by the maximum cross correlation.
Each actual shift time was also recorded to determine
the effect of this windowing process on the final av-
erages. The educible average on conclusion was writ-
ten to a disk file and could be used as a new pattern for
subsequent passes. It was found empirically that this
process converged, and the resultant averaged struc-
tures stopped changing after the second iteration in
most cases (i.e., the third and subsequent iterations
were indistinguishable from the second, and the se-
lected distribution of shift times was invariant).

The convergence is illustrated in Fig. 10, where
each trace represents the results of an iteration, start-
ing with the zero iteration at the bottom. It can be seen
that the first iteration shows a marked enhancement of
the features of the signature, but that the change in sig-
nature decreases as one progresses to higher itera-
tions, and indeed, the variations between the second and
third iterations are quite minor.

We can also construct a histogram of the selected
shift times, shown for various measurement stations
in Fig. 11. The histogram is constructed by grouping
the times in 1.6 msec blocks to generate a smoother
histogram. This figure is referenced to 400 sparks
(i.e., realizations of the pattern). In the outer regions,
the histogram is quite narrow, indicating that the maxi-
mum of the cross correlation corresponds most often
to the spark induced signature, while as one descends
into the layer, the number of samples that could not
have been generated by the spark increases. When this
occurs, the record containing such a false indication is
not used to generate the educible signal for the next
iteration. The number of samples within the 10-msec
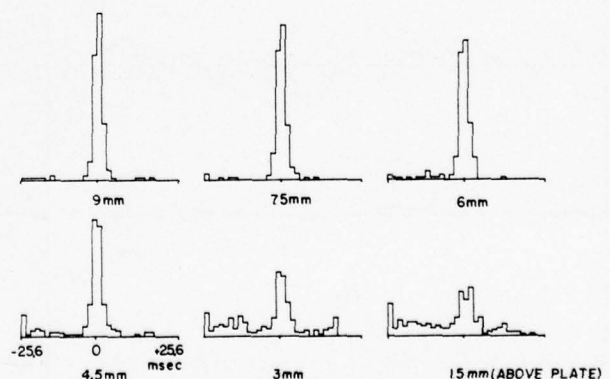window varied but was never less than 200 events.

FIG. 11. Histogram of the computed shift times, for time
axis from -25.6 to $+25.6$ msec in 1.6-msec boxes. Results
presented for different vertical stations, $y = 9$ mm to 1.5 mm,
in 1.5 mm steps. Each histogram represents 600 points.
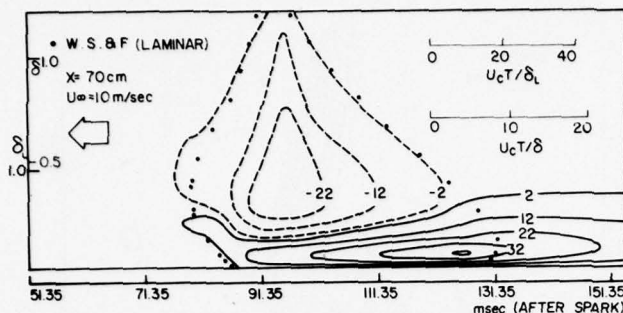Vertical scale arbitrary.

FIG. 12. Contours of *educed velocity difference* of a turbulent spot in a laminar boundary layer. Vertical scale is distance from wall, horizontal scale is time from spark. $x = 70$ cm.

In general, this process produced a signal of greater amplitude and smaller time duration than earlier iterations, and yet the resultant signature was significantly smoother than any individual realization.

RESULTS AND DISCUSSION

A spot check of the method of data processing is provided by re-examining the turbulent spot in the laminar boundary layer. It also enables us to compare the structure observed in a turbulent flow with the universal structure of the spot. In Fig. 12 contours of streamwise velocity perturbation are plotted against time and distance from the wall. The contours representing excess of velocity relative to the mean are shown as solid lines, while contours showing a defect are marked by dashed lines. The spot may thus be represented by a closed loop of velocity defect extending outward from $y/\delta \approx 0.3$; it rides above contours representing an excess velocity, which also trail behind the turbulent region. The borders of the spot, which were determined by detecting the turbulent interface, are shown on this figure. The entire leading interface of the spot is well represented by connecting the perturbation contours of $\pm 2\% \, U_\infty$. The trailing interface is also well represented by the $-2\% \, U_\infty$ contour in the outer part of the boundary layer.

Because the excess velocity decays rather slowly behind the spot, the trailing interface near the wall does not follow any contour of constant velocity perturbation.

A sequence of contours of velocity perturbation generated by the spot after penetrating the turbulent boundary layer along the center line is shown in Figs. 13. Figure 13(a) was deduced from measurements with a single hot wire probe located 40 cm downstream from the spark and roughly at the streamwise position at which the boundary layer becomes fully turbulent. The structure observed still bears a resemblance to the spot in the laminar boundary layer because of the long duration region in which the velocity exceeds the mean velocity. The region of velocity defect, however, extends across the entire boundary layer and actually protrudes above it.

Figure 13(b), which represents measurements taken $x = 47$ cm downstream of the spark, indicates that the

spot in a turbulent environment has an entirely different structure. The region of low velocity did not undergo any significant change after traveling a distance of 7 cm ($\sim 9\delta$). On the other hand, the high velocity region trailing the spot was severely fragmented and weakened and is on the verge of disappearance. A small but coherent region of high velocity now appears near the wall earlier in time.

Measurements made 23 cm farther downstream still show the region of low velocity perturbation appreciably unchanged in size and not distorted or significantly weakened. However, as the boundary layer increases in thickness this region behaves as if it is attached to the outer boundary and remains protruding through the mean position of the interface. It may thus be identified with a bulge which protrudes from the turbulent boundary layer. The velocity in the bulge is lower than in the surrounding fluid.[4] The duration of the bulge (shown here on a time axis) increases as one examines it closer to the wall and corresponds to a spatial extent of $2-3\delta$. It is significant that the velocity defect region no longer extends to the wall along the mean centerline of the structure, and as we proceed downstream this region moves farther and farther away from the surface [Figs. 13(c), (d), (e)].

The region of high velocity perturbation which trailed the spot in the laminar boundary layer disappears entirely [Fig. 13(c)], while the small region of excess velocity which was first observed in Fig. 13(b) triples in size in both t and y coordinates; however, it does not significantly change in its peak velocity excess. Thus, while the velocity defect region remains approximately frozen as it moves downstream, the newly created velocity excess region grows rapidly with downstream distance, displacing the defect region outward and intruding under it along the center line of the spot [see Figs. 13(c), (d), (e)]. Furthermore, at $x = 70$ cm we observe the first sign of a new low velocity region being produced near the wall and growing with downstream distance, although more slowly than the excess velocity region. Thus, we may be seeing a quasi-periodic generation of regions in which the streamwise perturbation velocity alternates in sign. The development of the spot with time is summarized in Fig. 14, where only the $\pm 4\%$ perturbation contours are drawn.

We may track the center of the velocity defect region at $y = \delta_T$ and obtain the convection velocity from the distance between adjacent measuring stations and the time required for the defect region to travel this distance. It is concluded that the pattern is convected downstream at $U = (0.90 \pm 0.01) U_\infty$. Since the region of high velocity does not retain its shape so well, it is much more difficult to assess its convection velocity; nevertheless, the resulting average $U = 0.9 U_\infty$ also seems to characterize its later motion.

The points chosen for the determination of U_c are marked with crosses in Figs. 13(b), (c), (d), (e). Kovasznay *et al.*[4] estimated the convection velocity of the rear interface between the turbulent and nonturbulent fluid (from space time correlations of the intermittency detector function) as $0.9 U_\infty$. Their measurements, and
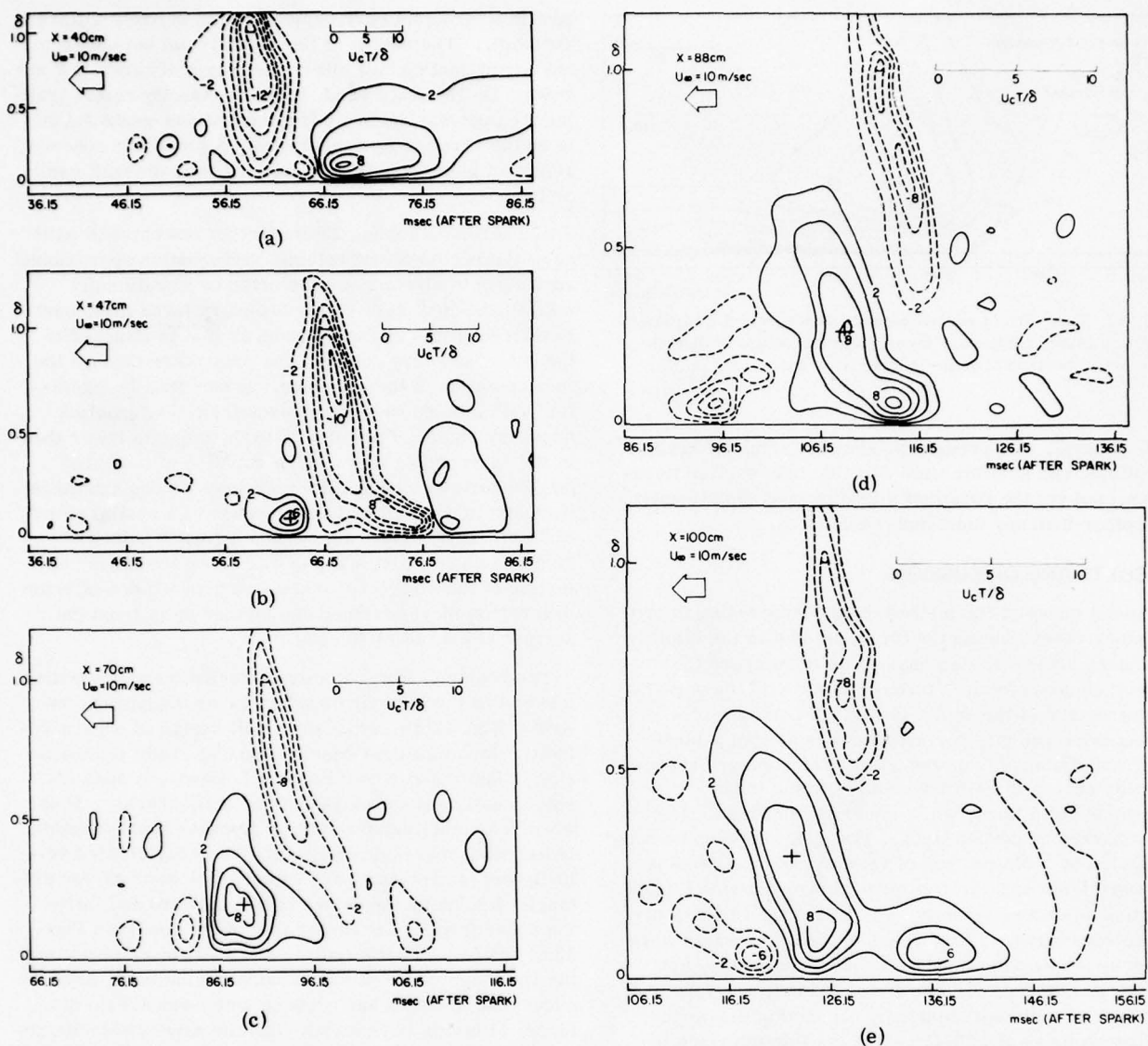
Zilberman, Wygnanski, and Kaplan

FIG. 13. Contours of velocity difference of detected structure from mean velocity profile. Vertical scale is distance from wall, horizontal scale is time from spark. $2\% \, U_\infty$ contours are drawn. (a) $x = 40$ cm, vert = 9 mm. (b) $x = 47$ cm, vert = 14 mm. (c) $x = 70$ cm, vert = 18 mm. (d) $x = 88$ cm, vert = 21.6 mm. (e) $x = 100$ cm, vert = 24 mm.

also those of Kaplan and Laufer,[14] showing that the particle velocities associated with the large outer bulges deviate by up to 6% from the local mean, are in detailed agreement with the measurements as shown here.

Four velocity traverses in the spanwise direction z were taken at a streamwise position located 70 cm downstream of the spark. The velocity perturbation contours are shown in Fig. 15. The velocity-defect region which is detached from the wall at $z = 0$ extends downward and reaches the wall at $z \sim 0.4\delta$. The high velocity region which precedes the defect region at $z = 0$ shrinks with increasing z and disappears at $z = 0.67\delta$. The excess velocity region has a rounded pyramidal shape, tilted forward (downstream) and extending from the wall to approximately 0.7δ in the center. Its base is 6δ long in the direction of streaming and about 1δ
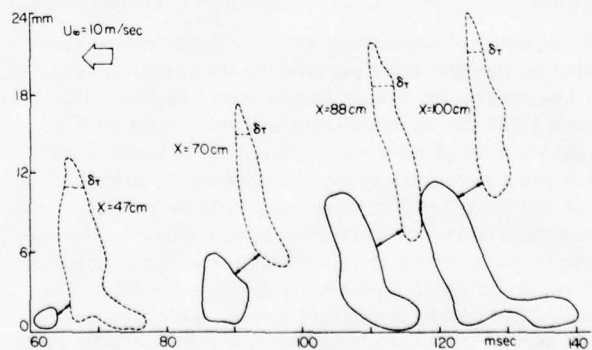
FIG. 14. Time sequence of $4\% \, U_\infty$ velocity perturbation contours for 4 stations $x = 47$, 70, 88, 100 cm. Vertical scale is distance from wall, horizontal scale is time from spark.
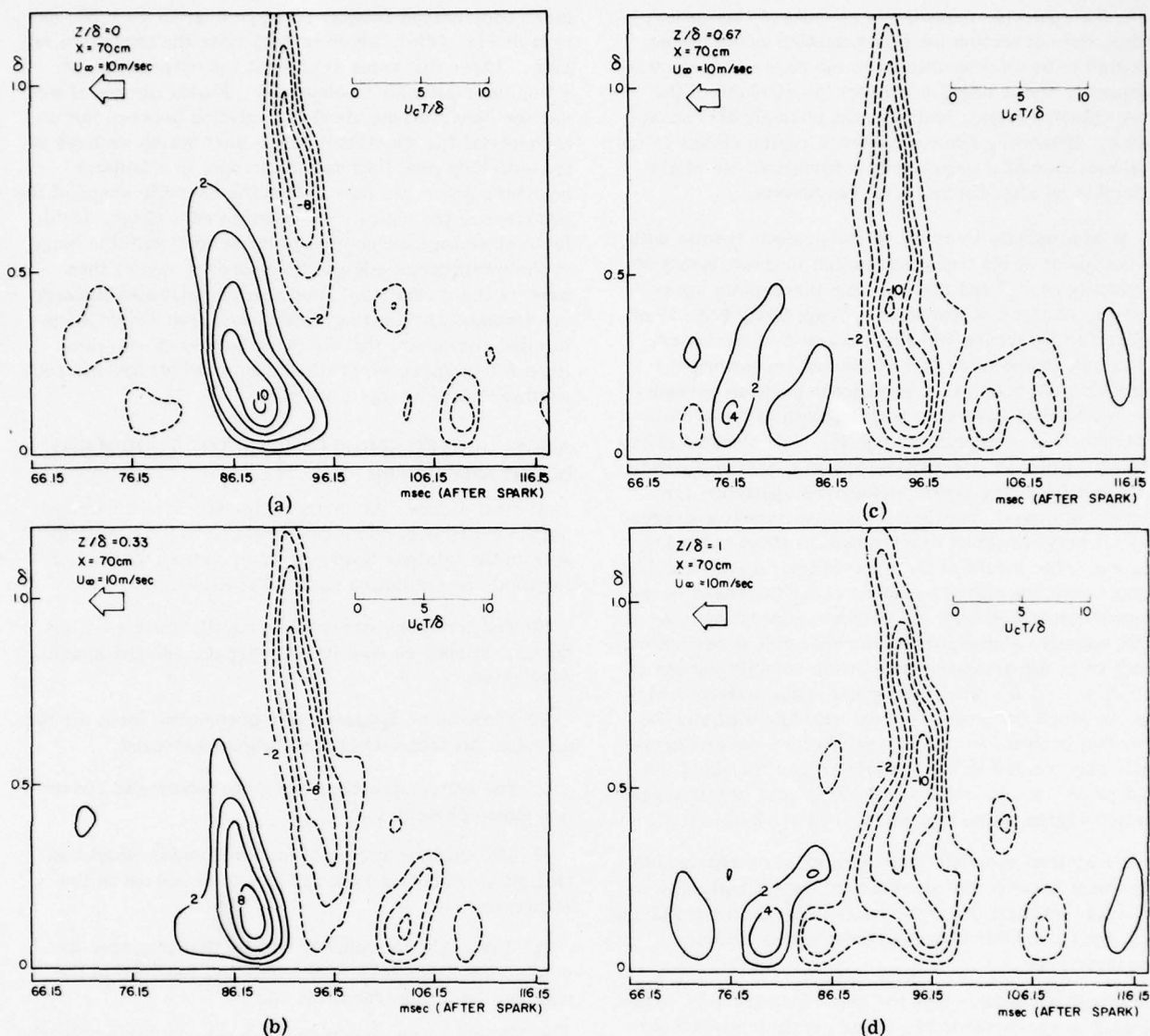
FIG. 15. Spanwise distribution of perturbation velocity history at $x = 70$ cm. (a) $z/\delta = 0$. (b) $z/\delta = 0.33$. (c) $z/\delta = 0.67$. (d) $z/\delta = 1$.

wide in the spanwise direction. Above it and somewhat upstream is the defect region, which has the shape of a spanwise arch, or perhaps a tunnel into which the velocity excess enters. The height of the opening under the arch does not exceed 0.35δ and its width (in the spanwise direction) 0.50δ. The arch itself is 1δ high, $2-6\delta$ long in the direction of streaming, and probably $2-3\delta$ wide. The arch stands erect above the plate with its base spreading upstream. In this respect this description of the spot differs appreciably from the schematic horseshoe models of Offen and Kline,[4] which show the large eddy tilting upstream and being stretched by the mean velocity gradient. The present results in the spanwise direction are probably somewhat smeared by random oscillations of the induced spot from its average path along the centerline of the plate, since in the present experiment the individual events were *only* realigned in the streamwise direction. It must also be stressed that the z traverse was taken only at the 70-cm station,

and it is not clear how this structure develops farther downstream.

We can try to estimate the variation in spanwise position of each individual structure by reference to the streamwise range of shift time. At the 70-cm station, the variation in the arrival times of the spots was ± 5 msec out of a time-of-flight of 90 msec, corresponding to a displacement of 4.5 cm at a convection velocity of 9 m/sec. This displacement is approximately 3δ at this station. If the same order-of-magnitude variation applies to the spanwise displacement, we might expect the centerline of any individual realization to meander by as much as $\pm 3.5°$. While this distance is small compared with the width of the spot in the laminar boundary layer (the spot is 26 cm across at this station), it is large in terms of the spanwise variation in structure apparent in Fig. 15.

Since there were significant changes over a distance

1.5δ, the spanwise meander is at most of this order. Hence, the correction for this variation would not be expected to be as dramatic as in the case of streamwise alignment, and it might not affect the strength of the outer velocity defect, which is not strongly dependent upon z. However, since the excess region closer to the wall does exhibit a pronounced z variation, we might anticipate an intensification of this feature.

It is appropriate to compare the present results with the two-point space time correlation measurements of Kovasznay et al.[4] and the two- and three-point space time correlations of Kovasznay,[6] especially Fig. 17 of the former reference and Figs. 1 and 2 of the latter. Having one probe fixed at $v = 0.5\delta$ and traversing the flow field with another, a significant positive correlation is observed over an average length in the streamwise direction of approximately 3δ. The chances of observing a negative correlation region closer to the wall and 3 to 5 boundary layer thicknesses upstream are very slight indeed, because the measurement averages over all events without discrimination about spanwise location. The height of the correlation region, which extends over the entire boundary layer thickness, corresponds very well with the defect region shown. A slight negative correlation in the spanwise direction will result from the disappearance of the velocity excess region at $z/\delta > 0.6$. The three-point space time correlation, in which one probe is fixed near the wall and the other two probes are moved downstream and are symmetrically located in the spanwise direction about the fixed probe, would result in an arrowhead negative correlation region of the type shown in Fig. 2 of Ref. 6.

We may thus conclude that there exists a reasonable agreement between the structure of the spot in a turbulent environment and the structure inferred for the large eddy from correlation measurements in a turbulent boundary layer.

Although we realize that the observed structure is developing in space and time, we are sufficiently encouraged by the constant convection velocity of its main features to draw pseudo-streamline patterns at 4 streamwise positions (Fig. 16). We refer to the pattern as a pseudo-streamline pattern by virtue of the fact that it is drawn in a v and t coordinate system and under the assumption that at $z = 0$, $\partial W/\partial z = 0$. Since the present structure is much narrower than the spot in the laminar boundary layer (where $\partial W/\partial z$ was measured to be zero[9]) this assumption needs further verification. The streamline pattern for the spot in the laminar boundary layer is shown in Fig. 16 (the time base in Fig. 17 is double the time base in Fig. 16). In fact, the large eddy shown in Fig. 16 appears to be slowly shrinking as the distance from the spark increases.

The circulation in the large eddies is counter clockwise and the free stream flows from right to left. The fluid ahead of the large eddy is being lifted toward the outer part of the boundary layer; this motion is followed by an inrush of flow toward the wall, associated with the direction of circulation of the large eddy. Perhaps, it is significant that the closed contours of the

large eddy extend roughly from $y = 0.4\delta$ to $y = 1.2\delta$, except in Fig. 16(a), which is very near the transition region. These distances represent the extremities at which intermittency is observed. Furthermore, if we use the observations about the relation between the interface and the entrained streamlines which we have in transitioning pipe flow and in the spot in a laminar boundary layer, we may sketch the possible shape of the interface in the vicinity of the large eddy [Figs. 16(b), (c)]. If we thus associate the large eddy with the bulge at the intermittent edge of the boundary layer, then most of the irrotational fluid will be entrained through the downstream (leading) interface. One should keep in mind, however, that we drew the pseudo-stream-lines for the purpose of illustration and we are not yet certain that this step is valid.

A POSTULATED STRUCTURE OF THE TURBULENT BOUNDARY LAYER

At first glance, the large scale structure described herein bears only some resemblance to the turbulent spot in the laminar boundary layer, which we shall refer to as the transition spot. The differences are:

(a) The turbulent structure is significantly smaller than the transition spot in both streamwise and spanwise extent.

(b) There is no apparent self-preserving form for the turbulent structure over the stations surveyed.

(c) The entire structure has a characteristic convection speed close to $0.9U_\infty$.

(d) The calming region of high momentum fluid that trails the transition spot appears to be absent in the structure.

(e) The region of velocity excess that precedes the outer defect region is very small and confined to the wall region in the transition spot.

The present large structure has been regularly referred to as a perturbation about the mean turbulent velocity profile, whereas the transition spot is naturally referred to as a perturbation about the Blasius boundary layer. There is an important distinction between the two mean flows. The Blasius profile represents a mathematical solution of Prandtl's laminar boundary layer equations, which are a rational first approximation to the Navier–Stokes equation. The turbulent boundary layer profile is at best a semi-empirical solution to a set of model equations, involving parameters which have been experimentally deduced. If it is desired to construct a theory for turbulent boundary layer structure, it is necessary to proceed from a more fundamental mean flow than the turbulent profile, no matter how universal its character.
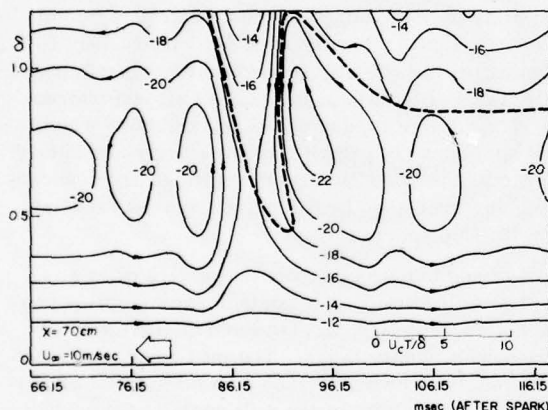
However, the experiment shows that the structure appears to ride in a turbulent boundary layer; i.e., the velocity perturbations of the structure tends to zero as one proceeds in time away from the center of the structure. In fact, when a comparison was made of the total velocity history compared with the Blasius profile at an
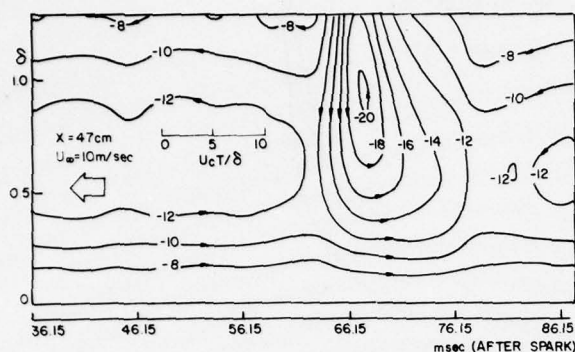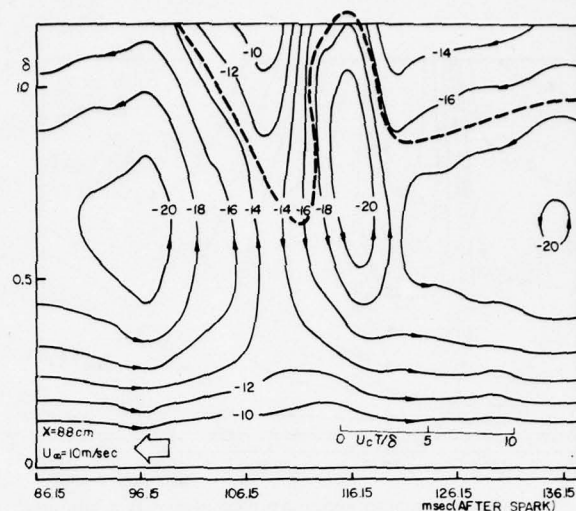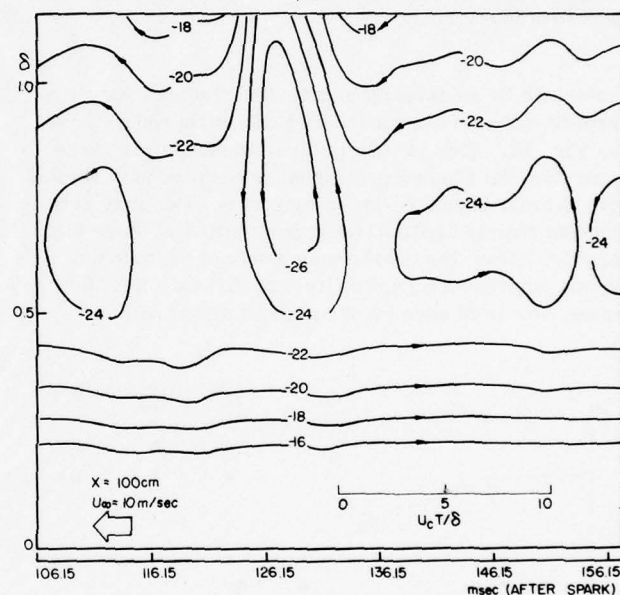
FIG. 16. Pseudo-streamlines: i.e., contours of constant $\int_0^y U \, dy$, as seen in a coordinate system moving with $U_c = 0.9_\infty U$. Vertical coordinate is distance from wall, horizontal coordinate is time from spark. $z = 0$. (a) $x = 47$ cm. (b) $x = 70$ cm. (c) $x = 88$ cm. (d) $x = 100$ cm.

equivalent station it became clear that this was an inappropriate reference field, no matter how theoretically attractive it might be.

If we recall, however, that the transition spot spreads laterally quite rapidly, at an angle of approximately 10°, and that its leading edge (i.e., the interface sampled first by a fixed probe) moves at $0.9 U_\infty$, an alternative explanation of the structure can be constructed.

Referring to the perturbation pattern at 40 cm [Fig. 13(a)], we see a picture quite similar to the transition spot. The major change at 47 cm [Fig. 13(b)] is the relative loss of the high velocity trailing section after a typical turbulent boundary layer mean profile is encountered. This turbulent boundary layer, however, consists primarily of wings of natural transition spots seeded by trip spheres, and the loss of the excess ve-

locity tail can also be interpreted to mean that this part of the flow field in the spot is of the same magnitude as that in the wings of the natural spots.

In fact, it is clear that the leading edge of the transition spot must overtake the wings of other spots, as can be deduced from Fig. 18 (taken from Fig. 10 of Ref. 9). The front central region of the transition spot moves relatively rapidly ($0.9 U_\infty$); the velocity of every other point on the interface moves more slowly. Hence, the front of the spark-generated spot must advance through the stilling region behind natural spots, across their boundaries, and eventually overtake the more slowly moving parts of the leading edges at large spanwise locations (Fig. 18).

The flow field behind the transition spot is of particular interest. It represents a very long tail and is char-
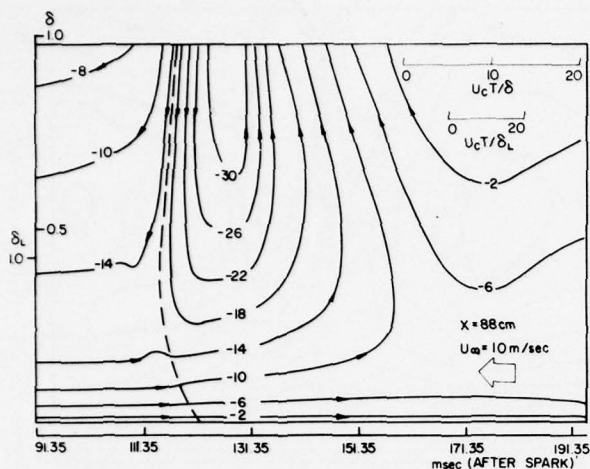
FIG. 17. Pseudo-streamlines for a turbulent spot in a laminar boundary layer as seen in a coordinate system moving with the spot front ($U_c = 0.9U_\infty$).
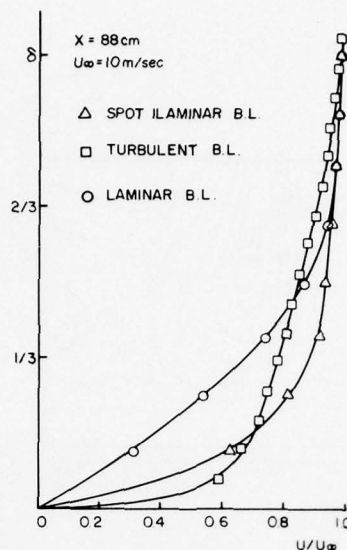

FIG. 19. Representative turbulent and laminar velocity profile and the profile of the tail of a turbulent spot in a laminar boundary layer.

acterized by an absence of turbulent fluctuations. Its profile has also been measured and is reproduced here as Fig. 19. This profile is significantly fuller at the wall than the Blasius profile but resembles solutions of the laminar boundary-layer equations. One may conjecture that an appropriate superposition of these full profiles, from the overlapping wings of surrounding spots, represents a valid first approximation to the mean flow field seen by our marked structure.

If this point of view is valid, the structure educed is very similar to the leading edge and central region of the transition spot, now presented not with respect to the Blasius profile but with respect to the superimposed velocity fields of the wings and tails of all other structures. The concept is also useful in explaining why the marked spot does not exhibit the same degree of lateral coherence as the transition spot; its wings are now constantly being overtaken by natural structures randomly shed by the trip spheres.

There is another benefit from taking this point of view. The wall friction of a laminar superposition profile cannot adequately represent the actual friction of the turbulent boundary layer. The measured spot structure, however, is characterized by a substantial velocity excess in the vicinity of the wall near its center line, and a consequently higher wall shear during passage of the spot. The added friction of the turbulent boundary layer would be due in large part to this velocity excess. Hence, the curve of the skin friction coefficient during transition would depend mainly upon the cumulative probability density of spot passage and display an error-function-like transition from the laminar drag law to the turbulent drag law, depending upon the probability distribution of the spots. Indeed, since spots can be continuously generated over rough surfaces, such a hypothesis is useful as a guide to the effect of wall roughness on both velocity profiles and wall friction.

At this point it cannot be stated that the spot structure is a linear superposition of transition spots without more detailed knowledge of the frequency of spots shed naturally from the tripping spheres, and the nature of the interaction among adjacent spots. This work is obviously planned. In all probability the large structure surviving the interaction of spots is quite similar to the leading edge of the transition spot, but there still appear to be some substantial modifications because of the

FIG. 18. Distribution of propagation velocity of the interface between turbulent and nonturbulent fluid for a turbulent spot in a laminar boundary layer. (Taken from Fig. 10, Ref. 9).

ambient, unsteady pattern. In particular, the appearance of new defect regions close to the wall at the two downstream stations may well be the birth of new structures.

ACKNOWLEDGMENTS

The authors wish to thank Professor D. Coles for the photograph of the transitional spot and for his thorough constructive criticism.

[1]A. R. Offen and S. J. Kline, J. Fluid Mech. **62**, 223 (1974).
[2]R. S. Brodkey, J. M. Wallace, and H. Eckelmann, J. Fluid Mech. **63**, 209 (1974).
[3]W. W. Willmarth and S. S. Lu, J. Fluid Mech. **55**, 65 (1972).
[4]L. S. G. Kovasznay, V. Kibens, and R. F. Blackwelder, J. Fluid Mech. **41**, 283 (1970).
[5]R. F. Blackwelder and R. E. Kaplan, in *Turbulent Shear Flows*, AGARD Conference Proceedings No. 93 (Advisory Group for Aerospace Research and Development, North Atlantic Treaty Organization, Neuilly sur Seine, France, 1972), paper 5.
[6]L. Fulachier, J. P. Giovanangeli, R. Dumas, L. S. G. Kovasznay, and A. Favre, C. R. Acad. Sci. Ser. B **278**, 683 (1974); see also L. S. G. Kovasznay, in *Turbulent Mixing in Nonreactive and Reactive Flows*, edited by S. N. B. Murthy (Plenum, New York, 1974), p. 277.
[7]D. E. Coles and S. J. Barker, in *Turbulent Mixing Nonreactive and Reactive Flows*, edited by S. N. B. Murthy (Plenum, New York, 1974), p. 285.
[8]M. T. Landahl, J. Fluid Mech. **56**, 775 (1972).
[9]I. Wygnanski, M. Sokolov, and D. Friedman, J. Fluid Mech. **78**, 785 (1976).
[10]D. E. Coles, in *Proceedings of the Computation of Turbulent Boundary Layers-1968 AFORS-IFP-Stanford Conference*, edited by D. E. Coles and E. A. Hirst (Thermosciences Division, Department of Mechanical Engineering, Stanford University, Stanford, Calif., 1969), Vol. II, p. 10.
[11]F. Shultz-Grunow, NACA T. M. 986 (1941).
[12]P. S. Klebanoff, NACA Report 1247 (1954).
[13]S. J. Corrsin and A. L. Kistler, NACA Report 1344 (1955).
[14]R. E. Kaplan and J. Laufer, in *Proceedings of the 12th International Congress of Applied Mechanics* (Springer-Verlag, New York, 1969), p. 236.

Dependence of effective slip on wall roughness in dilute polymer solutions

P. G. Saffman

Applied Mathematics, California Institute of Technology, Pasadena, California 91125

A hypothesis is made for the modification of a complete turbulence model to take account of a dilute polymer concentration. The equations are integrated in the wall layer and give the effective slip $u_* \Delta B$ as functions of wall roughness and empirical polymer properties, where u_* is the friction velocity and ΔB is the change of the constant in the logarithmic law of the wall. Results in qualitative agreement with experiment are found.

I. INTRODUCTION

It seems to be generally accepted that the reduction in drag when a dilute polymer solution is in turbulent flow over a wall is due to changes in the turbulence structure close to the wall, i.e., in the logarithmic wall layer, buffer layer, and viscous sublayer. In the outer part of the wall layer, where $y_* = u_* y/\nu \gg 1$ (u_* is the friction velocity, y is the distance from the wall, ν is the kinematic viscosity) the mean velocity $U(y)$ is asymptotic to

$$U(y) \sim u_* \left[\frac{1}{k} \ln\left(\frac{u_* y}{\nu}\right) + B \right], \tag{1}$$

where k is Kármán's constant (≈ 0.42) and B is a function of the wall roughness and the polymer concentration and properties. [1]

For Newtonian flow over rough walls, B can be obtained from Nikuradse's data [2] as a function of $z_* = u_* z_0/\nu$, where z_0 is the equivalent sand roughness; see Fig. 1. For $z_* < 20$ and $z_* > 65$, the following formulas are a good approximation:

$$B = 5.5 - 5.5 z_*, \qquad z_* < 20$$

$$B = 8.5 - (1/k)\ln z_*, \qquad z_* > 65. \tag{2}$$

tion is not known with any degree of certainty. The purpose of the present work is to put forward a hypothesis about the way addition of a polymer may alter a particular complete phenomenological model of turbulence and *then calculate how B depends on roughness*, given the dependence on polymer properties which, in principle, could be determined by experiments on dilute polymer flow over smooth walls.

In Sec. II we shall summarize the turbulence model [3] for Newtonian flow over rough walls. The modifications to incorporate polymer effect and the results are given in Sec. III.

II. TURBULENT NEWTONIAN FLOW OVER ROUGH WALLS

The turbulence model to be employed is that introduced by the present writer. [3] In the wall layer, it reduces to

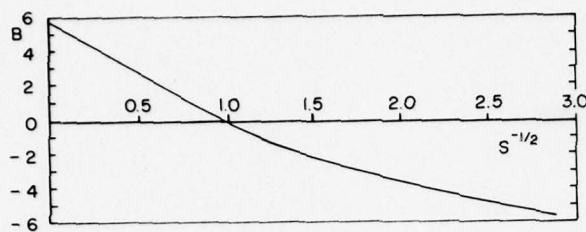$$\left(\frac{A\epsilon}{\omega} + \nu\right)\frac{dU}{dy} = u_*^2, \tag{3}$$

FIG. 2. Values of B vs $S^{-1/2}$ for a Newtonian fluid calculated from Eqs. (3)-(6).

together with Eq. (1). At the wall, $y = 0$,

$$U = 0, \qquad e = 0, \qquad \omega = \alpha''(u_*^2/\nu) S(z_+), \qquad (6)$$

where the quantity S is a function of only the dimensionless wall roughness z_+.

These equations were solved by putting them in dimensionless form with the variables

$$\bar{y} = \frac{ku_* y}{\nu}, \qquad \tilde{e} = \frac{\alpha'' e}{u_*^2}, \qquad \bar{\omega} = \frac{\nu \omega}{\alpha'' u_*^2}, \qquad \bar{U} = \frac{kU}{u_*},$$

then determining the asymptotic behavior as $\bar{y} \to \infty$ which contains two arbitrary constants, one of which can be absorbed into the origin of $\bar{y}$, and then shooting from a large value of $\bar{y}$ (typically 100) toward $\bar{y} = 0$, the wall being placed at the point where $\tilde{e} = 0$. By varying the free arbitary constant, solutions are obtained for various S and by interpolation and extrapolation the functional dependence of B on S is readily obtained.

Theoretical reasons were given earlier[3] (in terms of a "roughness layer") for believing that $S \propto z_+^{-1/2}$ as $z_+ \to 0$, and this is confirmed by the numerical solution. Similarly, the asymptotic behavior $\bar{\omega} \sim \bar{y}^{-1}$ as $\bar{y} \to \infty$ suggests that $S \propto z_+^{-1}$ as $z_+ \to \infty$, and this is also found. Figure 2 shows a plot of B against $S^{-1/2}$ obtained in the way just described. The approximate formulae

gas.[4] A naive picture would be that of elastic bands threading a viscous fluid. We, therefore, make the hypothesis that the change increases or generates pseudo-vorticity, this being a measure of the rotation rate of the eddies which we suppose increased by the elasticity.

Thus, we add a generation term to the pseudo-vorticity rate equation, Eq. (4), leaving the other terms unaltered. Equation (4) is then replaced by

$$\alpha' \omega^2 \frac{dU}{dy} - \beta' \omega^3 + \omega^3 f(e, \omega) + \frac{d}{dy}\left[\left(\frac{A'e}{\omega} + \nu\right)\frac{d\omega^2}{dy}\right] = 0,$$

$$(7)$$

where f is a dimensionless function of the turbulence quantities, e and ω, and also depends on the concentration and properties of the polymer and the viscosity of the fluid. The further hypothesis to be made is that the polymer is characterized by its concentration c and a characteristic time τ, and that the polymer produces pseudo-vorticity when the dimensionless variables $\omega\tau$ and $e\tau/\nu$ are large. For simplicity and definiteness, we take

$$f(e, \omega) = p(c) g(e\omega\tau^2/\nu), \qquad (8)$$

where p is a function only of the concentration, but can also be expected to depend on molecular weight, etc., and g is a step function, $g(\xi) = 0$ for $\xi < 1$, $g(\xi) = 1$ for $\xi > 1$. It follows that the polymer will change the dependence of B on wall roughness only if $\tilde{e}\bar{\omega} > \nu^2/u_*^4\tau^2 = \tau_+^{-2}$.

For a Newtonian fluid, $\tilde{e}\bar{\omega}$ is zero at the wall and vanishes like $\bar{y}^{-1}$ as $\bar{y} \to \infty$. Furthermore, the maximum value, $(\tilde{e}\bar{\omega})_m$, and the value $\bar{y}_m$ at which it occurs, are practically independent of z_+ until $z_+ \approx 20$. It is found that

$$(\tilde{e}\bar{\omega})_m \approx 0.2, \qquad \bar{y}_m \approx 2 \quad \text{for } z_+ < 20.$$

As z_+ increases, $(\tilde{e}\bar{\omega})_m$ decreases leveling off at about 0.05 for $z_+ > 200$. The value of $\bar{y}_m$ increases to about 5 as z_+ increases. Remember that $\bar{y} = ky_+$, where y_+ is the conventional dimensionless distance from the wall. Identifying $\bar{y}_m$ with the thickness of the sublayer, we see that the thickness increases from $5\nu/u_*$ to $12\nu/u_*$ as the roughness increases.
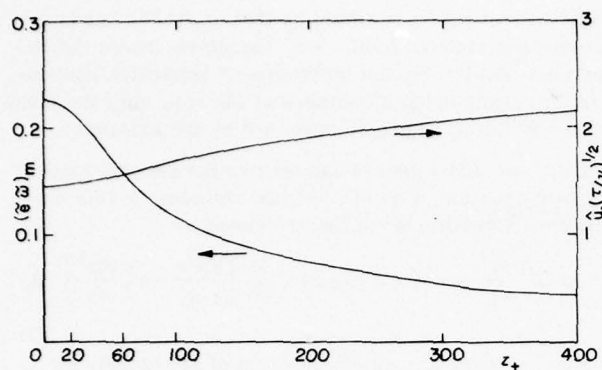
FIG. 3. Maximum value of product $\tilde{e}\tilde{\omega}$ of dimensionless pseudo energy and pseudo vorticity as function of z_+ for Newtonian fluid. Value of onset wall stress $\hat{u}_*$, nondimensionalized with $(\tau/\nu)^{1/2}$, vs z_+.

FIG. 5. B vs $[(u_*^2 - \hat{u}_*^2)\tau/\nu]^{1/2}$ for a dilute polymer solution over a perfectly smooth wall for $p = 0.5$ and $p = 1.0$.

These results appear to be in qualitative agreement with experiment.[1] Thus, dimensionless onset shear stress depends weakly on roughness, increasing from 1.45 when $z_+ = 0$ to 1.7 for $z_+ = 100$. For values of z_+ < 35, the flow is effectively smooth for polymer addition, since ΔU varies by less than 10% in this range. As z_+ increases over this value, the effect of polymer becomes less, eventually disappearing at values of z_+ depending on $u_*^2 \tau/\nu$. Virk[1] reports $z_+ \sim 50$ as the end of the effectively smooth regime, but refers to other workers who found values in the range 20–40. The results shown in Fig. 5 indicate that $p(c)$, the function that measures the effects of concentration, is not linear in c. In fact, the empirical observation that effective slip is proportional to $c^{1/2}$ indicates that $p \sim c^{0.2}$ is appropriate.

A feature of the numerical method employed to obtain the results obtained here was that it failed when p or τ_* became too large, the critical values being just greater than $p = 1$ or $\tau_* = 5$.

The system of equations is not simple, and it remains an open question whether the failure is due to the inadequacies of the numerical scheme or is a genuine mathematical property modeling a real physical phenomena,
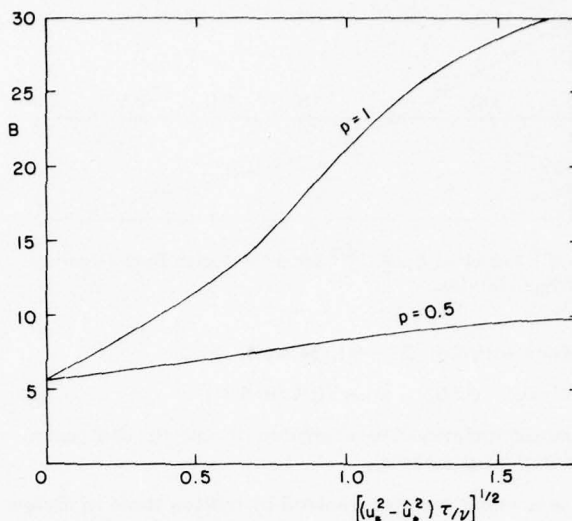
namely, the existence of a maximum drag reduction asymptote. In this connection, we note that if $f \to f_\infty$ for large p and τ_*, then the law of the wall, Eq. (1), is replaced by

$$U \sim u_* \left(\frac{1}{k'} \ln \frac{u_* y}{\nu} + B' \right) \quad k' = (k^2 - \tfrac{1}{2}\alpha'' f_\infty)^{1/2}. \quad (9)$$

The equations were integrated with $f = f_\infty = 1$, and boundary condition (9), corresponding to $k' = 0.09$. B' is found to be approximately constant for $z_+ < 12$ with a value of around -9 and then starts to decrease, reaching -54 at $z_+ = 300$. Virk's[1] maximum drag asymptote for smooth walls is equivalent to experimental values of k' $= -0.08$ and $B' = -12$. The difference between theory and experiment is comparable to the uncertainty in the observed values. Note that under conditions of maximum drag reduction, the drag with large roughness may be comparable to, but will not be exactly equal to, that of the pure solvent; the change in the Kármán constant from k to k' implies a different Reynolds number dependence.

IV. REMARKS

The hypothesis that a dilute polymer increases the generation of pseudo-vorticity is intuitively consistent with the evidence presented at this Symposium that dilute polymer tends to destabilize laminar flows although contrary evidence obtains. Fibrous materials, which also have drag reducing effects, probably act in a way similar to fluid in a gas by increasing the dissipation, and their effect should be modeled by adding an extra dissipation term to the main equation for pseudo-vorticity, Eq. (7). This would be consistent with the observation that drag reduction for a polymer and fibers is never obtained when the two are added in combination; they must counteract each other, and the addition of fibrous fluids disrupts and slows down this interaction at energies of transfer. One of the compounds of pseudo vorticity would be ??? turbulent ??? reduced by a drag

if the addition of fibers tended to stabilize laminar flows.

It should be noted that we have assumed that the surface roughness z_0 is unaffected by the polymer. The surface roughness may, in fact, be smoothed to some extent by polymer, the amount depending on the concentration but not on τ. Then, the polymer drag reduction with a small amount of roughness could actually be greater than for a smooth wall, because of the decrease in roughness in addition to the dynamical changes.

The present model does not describe the changes in turbulent intensity through the wall layer which have been observed.[5] For this purpose, it would be necessary to use a more sophisticated stress relaxation model which calculates all components of the Reynolds stress tensor.[3,6]

An empirical description of drag reduction for dilute polymer solutions in rough pipes has been given by Poreh.[7] The object of the present paper is completely different, being a fundamental investigation to see if the phenomenon of drag reduction can be predicted or included in a complete turbulence model (which does not make *ad hoc* assumptions about the variation of mixing length in the sublayer).

[1]P. S. Virk, J. Fluid Mech. **45**, 225 (1971); **45**, 417 (1971).
[2]J. Nikuradse, N.A.C.A. T. M. 1292 (1933).
[3]P. G. Saffman, Stud. Appl. Math. **53**, 17 (1974), Proc. R. Soc. London Ser. A **317**, 417 (1970).
[4]P. G. Saffman, J. Fluid Mech. **13**, 120 (1962).
[5]M. M. Reischman and W. G. Tiederman, J. Fluid Mech. **70**, 369 (1975).
[6]P. G. Saffman (to be published).
[7]M. Poreh, J. Hydronaut. **4**, 151 (1970).

Polymer additive mixing and turbulent drag reduction

Lars-Göran Stenberg,[a] Torgny Lagerstedt, and E. Rune Lindgren[b]

Department of Mechanics. The Royal Institute of Technology. 100 44 Stockholm 70. Sweden

The turbulent drag reducing abilities of polyethylenoxide polymer additive is shown to depend not only upon the rate of mixing, but upon premixing procedures as well, of parent polymer solution being injected into the water flow at the inlet end of a rectangular experiment pipe via a rotating impeller mixer. Pressure *drop measurements over a downstream measuring section along the pipe, correlated with visual* observations on the presence of polymer strands in the flow by means of a schlieren arrangement indicate that forced mixing, so that all visible polymer strands dissappear, does not impair the drag reducing abilities of the additive until quite high rates of mixing.

INTRODUCTION

In a previous paper[1] experiments were reported on turbulent drag reduction caused by injection of parent polymer solution into pipe flows of water. (Union Carbide, polyethyleneoxide, "Polyox," WSR 301.) The injection was made at the upstream end of a rotational mixer through which the water passed before entering the experiment pipe. The surprising discovery was made that the injected $1\%(0.2\%)$ polymer solution did not readily dissolve in the water flow under a variety of mixing and flow rate conditions. Rather, the injected Polyox suspension formed an elastic string which wound itself around the mixer impeller shaft and propagated between the impeller blades into the test pipe. In passing through the pipe it would gradually split into finer and finer strands with increasing distance downstream (which distance shortened with increasing mixer speed and/or flow rate). The 0.2% parent solution dissolved faster in the flow than did the 1% solution. The parent polymer strings propagating in the flows were observed to possess elastic properties and sustained considerable amounts of stretching in the flow. In addition, it was discovered that there seemed not to be any discrete difference between induced drag reduction (at the same net concentration of polymer in the flow) whether the parent polymer solution was present in the form mainly of long strands, or dissolved into invisibility when passing through the measuring section of the pipe.

The reported observations of polymer strings or strands in the flow were made by dyeing the parent solution to be injected into the flow. Since it cannot be completely excluded that the dye may play a role in the mechanical behavior of the injected Polyox solutions, it was decided to repeat some of the experiments using uncolored Polyox, making visual studies by means of a schlieren arrangement. Also, it seemed desirable to modify the rotational mixer so that, when in operation, it would completely destroy any macroscopic polymer strings before entering the experiment pipe.
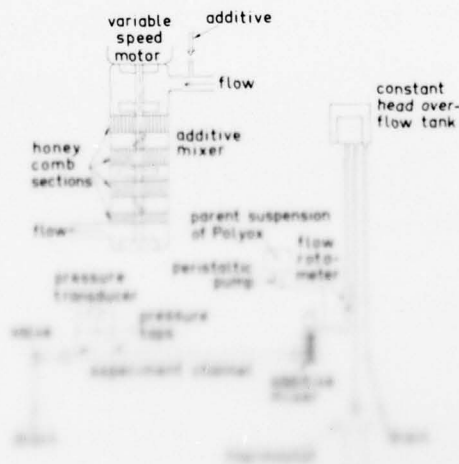
EXPERIMENTAL ARRANGEMENT

The flow apparatus shown in Fig. 1 is essentially the same one as was used and described in the previous

study.[1] However, the schlieren device does not permit the use of pipes of circular cross section. Thus, the flow studies were performed by the use of 3 m long channel of rectangular cross section 5.2 mm by 30.0 mm, the 30 mm sides being made of 5 mm thick optically neutral glass. The measuring section was 0.500 m long (the distance between the pressure taps), the upstream tap being located 2.45 m or 276 hydraulic diam d $[d = 4ab/2(a+b) = 8.86$ mm, $a = 5.2$ mm, and $b = 30.0$ mm] *from the channel inlets.*

Figure 2 illustrates the schlieren arrangement used for the visual studies of the flow in the measuring section of the channel.

The modified rotational mixer is shown schematically by a separate sketch in Fig. 1. With the mixer in operation a general swirl of the flow as well as the propagation of strands of injected polymer parent suspension is prevented by honeycomb sections being attached to the housing of the mixer in between the impeller blades. These honeycomb sections, of some cm in length, are made of 0.1 mm sheet aluminium with individual tube cross dimensions of about 5 mm.

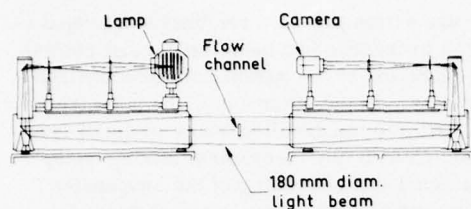The majority of the experiments were run at a temperature of about 15 °C.

FIG. 2. Schlieren arrangement for observing polymer strands in flows of water.

EXPERIMENTAL RECORD

A check on flows of pure water at various mixer speeds, recorded in Fig. 3, shows that at least within the range of turbulent flows there is no observable dependence of the friction factor upon the rotational speed of the mixer. The spread of these and other data, apparent within the range for laminar flows, is explained by the rather low pressure drops recorded here, making the readings very sensitive even to slight imperfections in the bleeding of the pressure transducer.

Figure 3 also contains a record of measurements on flows of water with a 50 ppm net concentration of Polyox WSR 301 maintained by continuous injection of a 1% parent solution. Here, we notice that the drag reduction, at least, is not less when the mixer rotates at 10 r/sec than when it is not in operation, over the whole trubulent flow range investigated. Then, comparing the schlieren photographs shown in Fig. 4, we notice that there are no polymer strands visible in the flow when the mixer is rotating at 10 r/sec, while, when the mixer is not in operation, a large portion of the injected polymer is present in the flow in the flow form of long strands of concentration closer to 1% than to 50 ppm. (No polymer strands are visible in any flow for any operation speed of the mixer reported in this study.) We also notice that even when the rotational speed of the mixer is increased to 20 r/s r/sec, the drag reduction
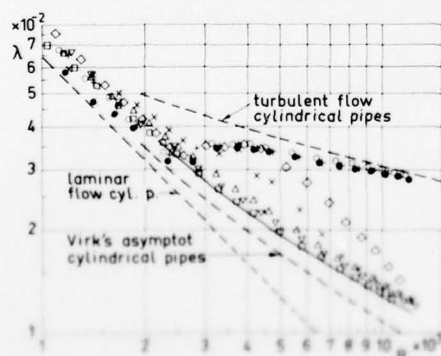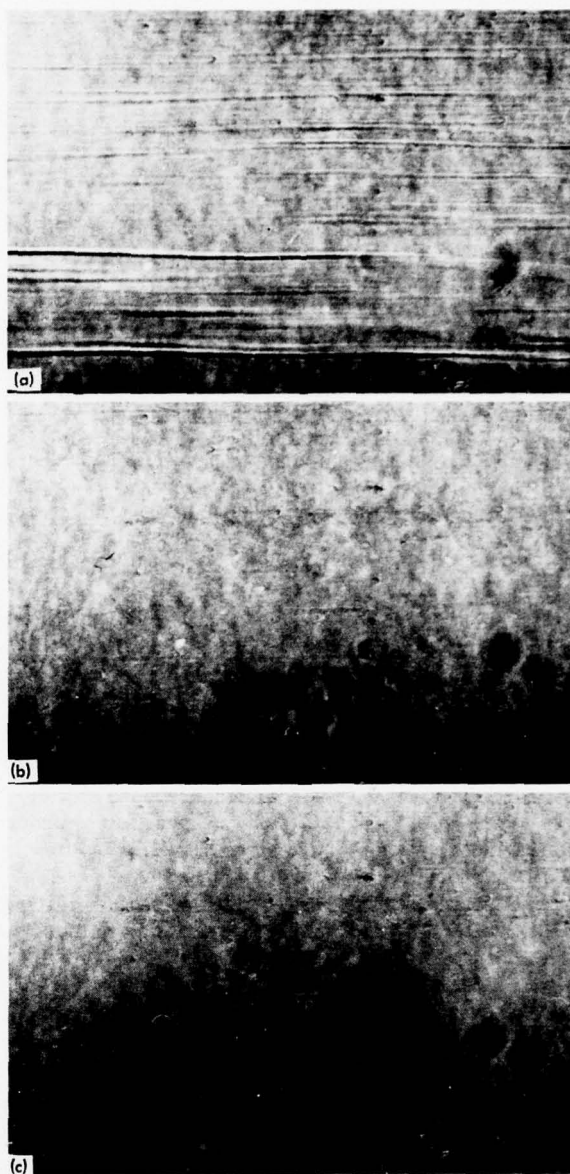

FIG. 4. Schlieren photographs of channel flows. (a) water +50 ppm additive; mixer not in operation $R = 8200$. (b) water +50 ppm additive; mixer working at 10 r/sec $R = 9000$. (c) water, $R = 12\,000$. Each photograph covers the same middle strip of size 22 mm by 35 mm of the flow field within the measuring section of the channel.

is still at least about the same as in the case when the mixer is not in operation. This state of affairs is in variance with the previous study with less effective mixing[1] where at all speeds the mixer was observed to decrease the drag reducing effectivity of the injected polymer solution. Again, the records of Fig. 3 show that further increases in the rotational speed of the mixer to 30 to 40 r/sec suppress the onset of drag reduction to Reynolds numbers of approximately 3500 to 4500 in a fashion similar to that observed in the previous study. Here, the Reynolds number, $R = U d/\nu$, is based on the mean flow velocity, $U = q/a$, and the hydraulic dia-
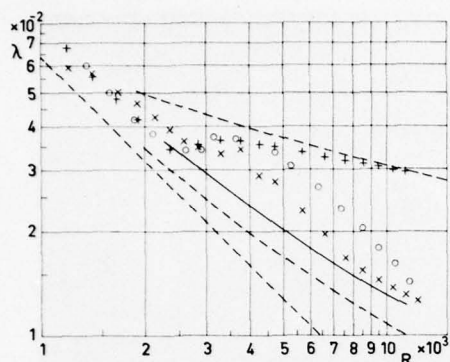
FIG. 5. Comparison of drag reduction effectivity for two 1% parent suspensions of Polyox WSR 301 prepared by different procedures. The flow data have been recorded at a rotational speed of 30 r/sec of the mixer with and without injection of polymer parent suspension to a net concentration of 50 ppm in the flow. × parent suspension prepared by mechanical mixing; two weeks preparation time. o parent suspension prepared without mechanical agitation; three months preparation time. + pure water.

meter d. Q is the volumetric rate of flow, and v is the kinematic viscosity.)

Assuming that the wall shear is uniformly distributed around the channel perimeter, the points of onset for drag reduction at $R = 3500$ and 4500 correspond to wall stress values of 0.7 and 1.2 N/m^2, respectively. Under this same assumption the wall stress at the transition Reynolds number of about 2500 is approximately 0.4 N/m^2. In reality, the stress is, of course, higher along the wider walls and lower along the narrower walls of the channel.

As in the previous study we again notice that, from the point of onset of drag reduction and on, the recorded friction factor λ plotted versus the Reynolds number R (in the standard logarithmic diagram), seems to follow straight lines parallel to each other and the line representing λ for fully developed laminar flow, until some maximum drag reduction limit is reached. While this may be a significant feature, we abstain from any speculations on this matter at present, awaiting results of further experimentation.

Tests were also made in order to examine the sensitivity of polymer drag reducing effects to variations in the procedure of preparation of the 1% parent suspensions of Polyox WSR 301 used for the experiments. For the purpose of carrying out these tests two parent suspensions were manufactured by different methods of preparation.

In the one case, the polymer powder was sifted into the distilled water to the desired concentration during continuous stirring by means of a regular mixer propeller rotating at some 5 r/sec or less in the suspension. The stirring at this low rotational speed is continued on and off (after the addition of all the powder which is completed within an hour or less for a 50 kg batch) until the polymer seems to be homogeneously dissolved

and ready for use within two or three weeks of preparation time. This procedure has been the normal routine followed in preparation of the parent solutions utilized in our experiments. In the other case, the polymer powder was sifted into the distilled water in small fractions day by day without any mechanical mixing except for some occasional gentle shaking of the suspension container. This mixture was kept in a dark storage room for some three months before it was judged homogeneously dissolved and ready for use. Repeated tests had already shown that three months storage of a 1% suspension prepared by normal routine procedure did not noticeably change its drag reducing properties.

Tests performed with the two 1% parent suspensions prepared according to the two different procedures described here, and being of the same age from the simultaneous beginning of their cycles of preparation, are recorded in the diagram of Fig. 5. Here, we notice that the gently prepared suspension is less effective in turbulent drag reduction than is the mechanically agitated suspension. Similar differences were also observed in tests with the same two polymer suspensions at other rotational speeds of the mixer.

The experimental records presented in Fig. 3 for mixer speeds of 10 and 20 r/sec as well as the observations reported in connection with Fig. 5 eliminate any notion that the mechanical mixing at the speeds in question, could possibly be responsible for any mechanical degradation of polymer macromolecules, since such a degradation supposedly should result in less drag reduction contrary to the observations. This fact is also of importance for the proper interpretation of observations reported in the previous paper[1] where there was a consistent decrease in drag reduction effectivity as the rotational speed of the mixer was increased. These observations then cannot be explained as an effect of mechanical degradation of individual polymer macromolecules since the mixing process in the prior experiments, even at the highest attainable speed of the mixer, was much less effective than for the lower mixer speed of 10 r/sec employed in the present experiments.

ADDITIONAL OBSERVATIONS

Additional flow experiments were performed by dyeing the parent additive suspension to be injected (in the same fashion as reported in the previous study) observing the flow through a microscope at one hundred times magnification. The 5 mm thick walls of the channel prevented the microscope from being focused within the flow field at larger magnifications.

The microscope studies revealed the presence of scattered ball shaped polymer agglomerations in the flow up to some 10 μm in diameter at all flow rates and rotational mixer speeds employed in the experiments. While such agglomerations are present in the flow even under forced mixing conditions of the present experiments, their role, if any, in turbulent drag reduction is an open question. They appear to be sparsely and unevenly distributed with distances between each other larger than some 500 μm. On the other hand, there is

the possibility that these agglomerations are but some small part of a spectrum of continuously distributed sizes of agglomerations toward ever smaller dimensions including very thin polymer strands until the limit of individual polymer molecular dimensions reached. This is somehow an impression one gets from the microscope studies. There is also some other experimental evidence in such directions.

For instance, extrusion of a dyed parent suspension of Polyox WSR 301 through a fine tube into water may produce a continuous mould, its diameter being several times that of the extrusion tube due to its viscoelastic properties as depending on the extrusion rate. Bringing the free end of the polymer solution mould into the accelerating flow field close to some orifice so that it gets caught in the orifice out flux, it stretches forming a thin string between the extrusion tube end and the orifice. The diameter of the stretched polymer suspension string depends upon the extrusion rate and the rate of flow through the orifice as maintained by the pressure difference across the orifice. If the extrusion rate or the concentration is too small and the distance between the extrusion mouth piece and the orifice is too long, the polymer string breaks. While the strength of such polymer suspension strings decreases with decreasing polymer concentration, it is, nevertheless, possible to maintain several centimeter long polymer suspension strings of 200 ppm or less concentration of Polyox WSR 301 in an accelerated flow field their thickness being only a fraction of a millimeter (~ 0.1 mm). On the other hand, if such weak suspensions are "extruded" into nonaccelerating flows of water the emerging polymer string flails and dissolves in a stringy fashion within some relatively short distance (of the order of centimeters) from the location of "extrusion." Considering the mechanical strength and the persistence that is exhibited by the rather thin strings of 200 ppm (or less) suspensions against disintegration under stretched conditions, it appears that freshly formed microscopically thin polymer strands also of weaker concentrations could possibly persist in flow fields under the action of high strain rates.

ACKNOWLEDGMENT

[1]L. G. Stenberg, T. Lagerstedt, O. Selén, and E. R. Lindgren, Phys. Fluids 20, 858 (1977).

Onset and saturation limit of polymer effects in porous media flows[a]

E. Naudascher and J. M. Killen

University of Karlsruhe, D 75 Karlsruhe 1, Federal Republic of Germany

The non-Newtonian features of onset, saturation, and degradation exhibited by the flow of dilute water solution of linear polymers through a porous medium are described. A physical model for the non-Newtonian behavior is presented as arising from the gradual extension of the polymer molecules, acting as elongated particles, and their alignment in the direction of flow. Comparisons are made with data from measurements in idealized porous-media configurations.

Resistance to laminar flow of dilute Polyox solutions through a porous medium increases markedly above the Newtonian values for the solvent after a critical flow rate is exceeded (onset). With a further rise in flow rate, this increase eventually reaches a maximum (saturation). In all cases observed so far, the same polymer additives, when applied to turbulent shear flows, produce drag reduction with similar onset and saturation characteristics. One may speculate that similar internal processes are involved in both cases and that a better insight gained in one case will aid in understanding the other. Indeed, a laminar flow environment must also exist on a molecular scale in turbulent flow, and the essential extensional strain field is present both within the converging flow passages of the porous medium and within the bursting and stretching motion in the wall-layer region.

In the following, an interpretation of the phenomena of onset and saturation is proposed which supports and extends the well-known physical model of polymer molecules as a collection of independent, highly deformable fibers. If one postulates that the polymer molecules in solution exist as very long strands of entangled fibers comprising one or more molecules which assume an elongated shape of aspect ratio A and align themselves in predominantly extensional type of flows, then it should be possible to use a functional relationship as derived by Batchelor[1]

$$\frac{\lambda}{3\mu} = 1 + \frac{4}{9} \frac{c_v A^2}{\ln(\pi/c_v)} \tag{1}$$

for describing, as a first approximation, the influence of the volume concentration c_v of polymer particles on the ratio λ/μ of the extensional to the Newtonian shear viscosity and, thus, on the onset and saturation limit of polymer effects on resistance. Once the strain rate G in the flow (which tends to extend the polymer particles) becomes large enough compared with the internal "restoring forces," the polymer particles will start to stretch and A will grow. In terms of the relaxation time τ of the effective polymer particles, this condition can be written as $\tau G > (\tau G)_{cr}$, where $(\tau G)_{cr}$ is of the order

1.0. In order for this polymer effect to become experimentally observable, the expansion process on the molecular level must have been carried beyond its beginning far enough so that $\lambda/(3\mu)$ exceeds its Newtonian value of unity by a certain finite amount, say ϵ. Consequently, Eq. (1) yields, as a condition for onset,

$$\frac{9}{4} \frac{c_v A^2}{\ln(\pi/c_v)} \geq \epsilon. \tag{2}$$

Since ϵ is independent of concentration and $\ln(\pi/c_v)$ does not vary appreciably within the c_v range of interest, this condition demands that the aspect ratio A of the extended polymer particles must attain values at onset that are almost inversely proportional to $\sqrt{c_v}$. For the purpose of obtaining an estimate, A can be assumed to be proportional to the effective relative strain rate τG. Hence, the onset condition may also be written $A \sim 1/\sqrt{c_v} \sim \tau G$ or

$$\tau G \sqrt{c_v} = \text{const}, \tag{3}$$

where $G \sim V/D$ for a given boundary geometry with D denoting the diameter of the beads in the porous bed and V is the average or superficial velocity.

In accordance with the physical model, the non-Newtonian increase in resistance is supposed to be gradual. More specifically, $A \sim \tau G \sim V/D$ in conjunction with Eq. (1) prescribes that the viscous part of flow resistance for a given polymer solution grows in proportion to V^2 near onset.

As A continues to grow, the non-Newtonian effects will increase until A has reached a limiting value A_{max} which will depend on limitations to further extension of the polymer molecules or the pulling apart of molecular entanglements as well as on the breakage of molecular and intermolecular bonds. For any one series of experiments for which the influences affecting the value of A_{max} are held invariable, Eq. (1) would predict a maximum increase in λ/μ, and hence viscous resistance, which is a nearly linear function of c_v or, more precisely, proportional to $c_v/\ln(\pi/c_v)$.

To test the applicability of these interpretations, various porous-media experiments will be examined. The experimental apparatus used consisted of a Plexiglas cylinder of 5.2 cm diam and 25 cm length packed with nearly uniform glass beads between stainless steel screens and provided with pressure taps along its length. As seen from a typical result shown in Fig. 1, the flow
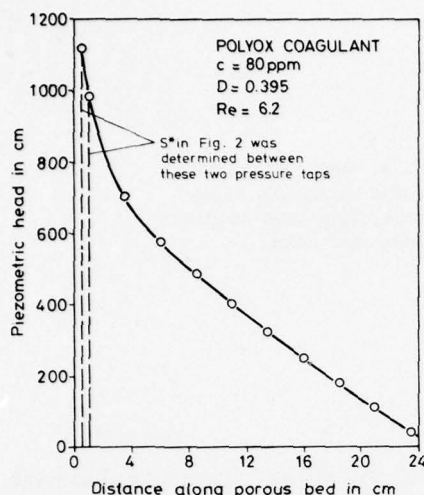

FIG. 1. A typical result of the piezometric-head line obtained by Käser for porous-medium flow of a dilute Polyox solution.

FIG. 3. Replot of data from Fig. 2 and similar diagrams in terms of parameters which do not include ρ. (The lines were drawn for $D = 0.187$ mm.)

resistance is not constant along the flow passage, and the location at which it is determined must be clearly stated. The resistance factor $f*$ plotted in Fig. 2 is based on the slope $S*$ of the piezometric-head line between the first two pressure taps, located 0.5 and 1 cm from the entrance section. Although it was recognized that the initial slope would have been a more meaningful quantity, measurements near the entrance to a porous bed are so susceptible to errors that it was decided to use $S*$ as a best approximation to the initial magnitude. In Fig. 3 a replot of the data is shown in terms of parameters that appear to be more relevant to a flow phenomenon at extremely low Reynolds numbers. Since it is reasonable to assume that this phenomenon is unaffected by inertia and thus independent of density ρ, the latter was eliminated from the resistance factor by cross multiplication
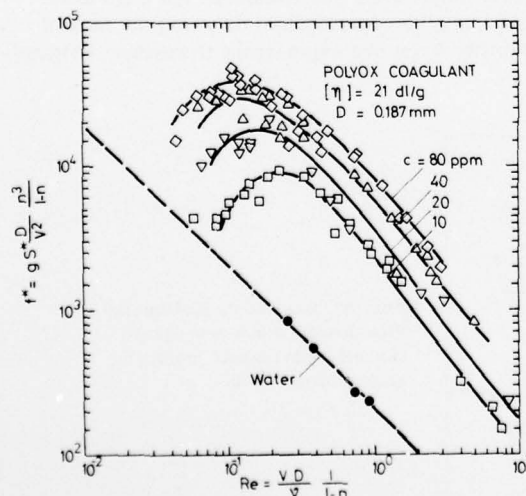

FIG. 2. Resistance factor versus Reynolds number as determined from measurements within the first 10 mm of the porous-medium column.
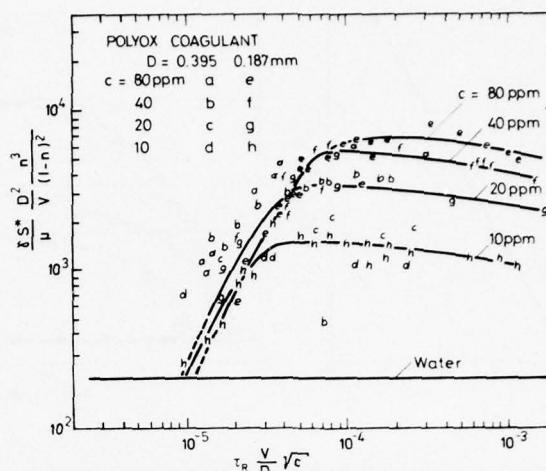
$$f*\mathrm{Re} = \frac{\gamma S*}{\mu}\ \frac{D^2}{V}\ \frac{n^3}{(1-n)^2} \tag{4}$$

(where γ is the specific weight of the solvent and n is the bed porosity) and Re was replaced by a Deborah number De $= \tau_R\ V/D$. In order to facilitate verification of Eq. (3), the factor $\sqrt{c}$ was added in the abscissa of Fig. 3. Use of the dimensionless polymer concentration c (weight of polymer per weight of solution) in place of c_v appears to be justified here, since it is consistent with the concept underlying Eq. (1) to represent the volume of the polymer molecules in their extended state by their dry volume, i.e., $c_v = c/s_g$, where $s_g \simeq 1.0$ is the specific gravity of the polymer.

In order to investigate the non-Newtonian effects near the entrance region of a porous medium, an element of of the latter was simulated by a 0.8 mm square Plexiglas channel of 12 cm length, within which glass spheres were inserted with a diameter slightly larger than 0.8 mm so as to hold them in place.[2] The piezometric-head loss ΔH across the N closely spaced spheres was measured by pressure taps upstream and downstream from the spheres, and a resistance factor equivalent to f (Fig. 2) was determined with $S = \Delta H/(ND)$. From tests with water it was found that the number of spheres N had to be larger than 8 in order that the same type of relationship of f versus Re was obtained as for a porous medium. So far as the polymer effects are concerned, the trends of the modified resistance curves for $N = 16$ in Fig. 4 are seen to be quite similar to those in Fig. 3 with the exception of an inertial effect which was absent in the study reported in Fig. 3.

So far as the dependence of onset on concentration given by Eq. (4) and the predicted proportionality between the viscous part of flow resistance and V^2 near onset are concerned, the data in Figs. 3 and 4 appear to be in reasonable agreement with the proposed physical model, independent of the bead size D and the polymer concentration c. The maximum increase in viscous resistance, on the other hand, is found to vary more nearly
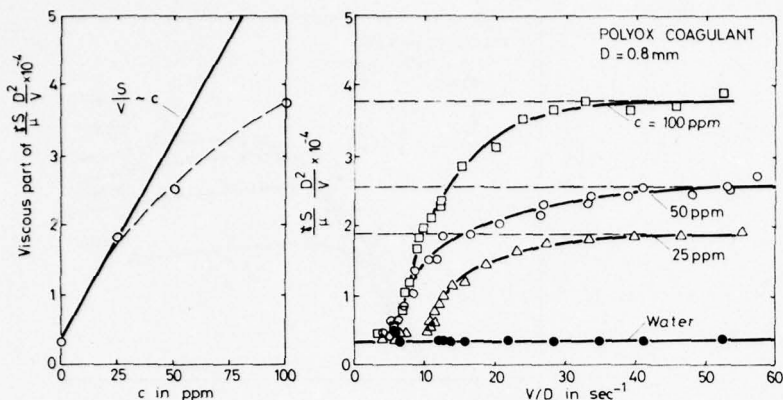
FIG. 4. Resistance plot for the flow through a 0.8 mm square channel with 16 glass sphere obstruction.

in proportion to $\sqrt{c}$ rather than to c as expected from Eq. (1). This was also found by Elata *et al.*[3] The reason for this may lie in the fact that most of the *increased resistance due to the polymer occurs within the* initial few layers of glass beads where the increase in A is not impaired by a breakage of molecular or intermolecular bonds (see Fig. 1), yet the measurements invariably include a flow passage beyond these layers. Because of this breakage, A_{max} is expected to decrease *with distance in the flow direction, and the effective val*ue of A_{max} for the distance over which resistance is measured will be different depending on flow rate and polymer concentration. Only within the first few layers can A_{max} be assumed to be a constant for a given polymer and the linear relation between the maximum increase in the viscous part of the resistance and c as postulated herein be realized.

As can be seen from the rough evaluation of the maximum increase in viscous resistance on the left-hand sides of Figs. 4 and 5, the linear relation is indeed observed for the single but not for the 16 bead obstruction as expected. This evaluation is based on the approximation, frequently used for porous-media flows, that S can be expressed by the sum of two terms: a linear term in V representing the viscous part of the resistance and a term in V^2 approximating the inertially affected residual. The former term, which can be assumed to be directly

proportional to λ/μ, will produce a constant ordinate value in Figs. 4 and 5, whereas the latter will add a deviation that increases linearly with the variable V/D. (This deviation is seen from these figures, Fig. 5 in particular, to be smaller for increased concentration c, which agrees with the fact that inertial effects diminish with the non-Newtonian increase in viscous resistance.)

In order to examine the proposed onset condition of Eq. (3) more closely, values for $\tau G \sqrt{c_v}$ at onset were computed from the data presented by James *et al.*,[4] Elata *et al.*[3] as well as from those reported in this paper The relaxation time was determined from the well-established relationship according to Rouse,[5] G was estimated in accordance with James,[4] i.e., $G = 150 \, V/(nD)$, and c_v was replaced by c/s_g as already explained. As seen from Table I, the scatter in the values of $\tau_R G \sqrt{c}$ is remarkably small for any given polymer despite large variations in bead size and polymer concentration.

The discrepancies with regard to different types of Polyox, it is interesting to note, can be reduced by replacing τ_R by $\tau_R/(\eta)$, where (η) is the intrinsic viscosity. As seen from the last line in Table I, the remaining discrepancies in the values of $\tau_R G \sqrt{c}/(\eta)$ are surprisingly small when one considers the difficulties in securing reliable experimental data and the lack of reproducibility from one experiment to another, original-
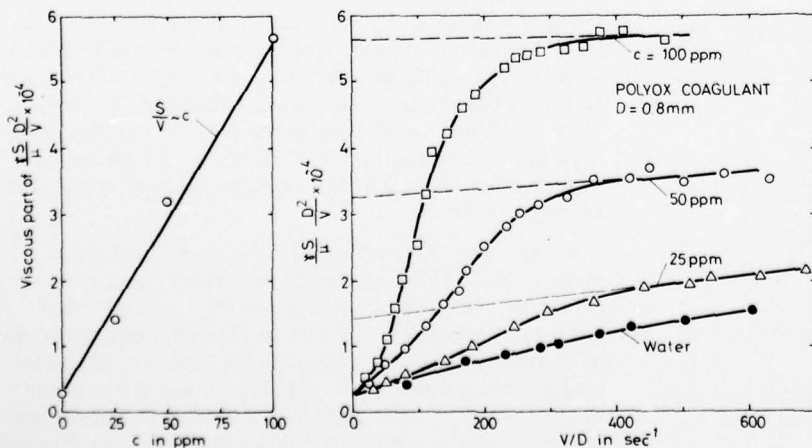

FIG. 5. Resistance plot for the flow through a 0.8 mm square channel with a single glass sphere obstruction.

TABLE I. Values of $\tau_R G\sqrt{c}$ and $\tau_R G\sqrt{c}/(\eta)$ at onset of non-Newtonian effects for flow of Polyox solutions through porous media, where $G = 150\, V/(nD)$.

Reference	James et al.[4]			Elata et al.[3]	Fig. 3
Polymer	WSR 205	WSR 301	FRA	Coagulant	
(η) in cc/g	470	1500	2900	2300	2100
τ_R in sec	9.6×10^{-5}	13.8×10^{-4}	6.1×10^{-3}	4.1×10^{-3}	3.0×10^{-3}
D in mm	0.11 0.22 0.45	0.11 0.22 0.45	0.11 0.22 0.45	0.50 1.0	0.187 0.395
c in ppm	30 to 480	10 to 160	6 to 96	10 to 150	10 to 80
$\tau_R G\sqrt{c}\times10^3$ at onset	>1.7 <2.5	>4.9 <6.7	>11.6 <13.2	>19.8 <21.8	>2.6 <4.4
$\dfrac{\tau_R G\sqrt{c}}{(\eta)}\times10^6$ at onset in g/cc	>3.5 <5.3	>3.3 <4.5	>2.9 <3.3	>8.6 <9.5	>1.2 <2.1

ing from the use of different apparatus, different experimental conditions, and polymer from different batches. One obvious interpretation of this result may lie in the fact that τ_R characterizes polymer particles near their coiled instead of the extended configuration responsible for the polymer effect described. However, the model presented herein contains a number of further gross simplifications, refinement of which will undoubtedly lead to a better understanding. As suggested by Elata, moreover, the agreement is certainly also impaired by the differences in molecular weight distribution for the various types of Polyox.

In summary then, it would seem that the concentration and velocity dependence of the onset and the limit of saturation of the polymer effects in porous-media flows are consistent with the model of polymer molecules of aggregates becoming elongated and aligned in the zones of predominantly extensional flow and give rise to added extensional viscosity in close accord with the Batchelor formula. The non-Newtonian effects on resistance appear to set in and become experimentally observable at a critical value of strain rate times relaxation time the magnitude of which is inversely proportional to the square-root of concentration. As the strain rate is increased beyond these values, the aspect ratio of the polymer particles grows until a limit is reached which is determined by the structure or the breakage point of the molecular or aggregate system (degradation). With the degradation typical for Polyox solutions, the corresponding maximum change in flow resistance is linearly related to the polymer concentration only for the first layer of the porous medium. If the resistance is measured over a larger distance, this limiting value of the increase in resistance becomes more nearly proportional to c^m where $m < 1$. Whether the piezometric head line eventually assumes a constant slope farther downstream has not yet been determined. Elata reports $m = 0.5$ for his experiments,[3] which agrees with the result from our own experiments with the multiple-bead channel (Fig. 4). The latter investigation is being continued.

Although a consistent interpretation has thus been shown to be possible, one must be cautious in concluding that the advanced model gives a complete or concise picture of the mechanism of polymer effects on flow resistance. (To cite just one disquieting result. All experiments reported in this paper were made with fresh Polyox solution. When the solution is aged beyond three days, it was recently observed that almost no change in resistance to flow through the porous medium occurs. It will be recalled that it is the normal-stress effects which are hampered by aging!) However, it is hoped the model presented provides incentive and direction for further research.

ACKNOWLEDGMENTS

[1]G. K. Batchelor, J. Fluid Mech. **46**, 813 (1971).

[2]B. Burkart, E. O. Macagno, and E. Naudascher, Sonderforschungsbereich 80, Universität Karlsruhe, Bericht SFB/E/79 (1976).

[3]C. Elata, J. Burger, J. Michlen, and U. Takserman, Phys. Fluids **20**, S49 (October, Part II, 1977).

[4]D. F. James and D. R. McLaren, J. Fluid Mech. **70**, 733 (1975).

[5]P. E. Rouse, J. Chem. Phys. **21**, 1272 (1953).

PART D

ABSTRACTS OF PAPERS NOT PUBLISHED IN FULL

These papers were either not available at the time of publication of the Proceedings or the reported results are included in papers published (or to be published) elsewhere.

A study of the structure of a plane stationary computer-simulated free-shear turbulence

L. F. Tsen and M. Bouriot

Centre d'Etudes Aérodynamiques et Thermiques, Université de Poitiers, 86000 Poitiers, France

Computer experiments are carried out on a two-dimensional, time-stationary, turbulent free shear flow. The aim is to visualize in a motion picture the time history of the entire field of all variables that are deemed interesting: velocity, pressure, vorticity, dissipation, etc., and to observe the connection between these deterministic motions and the corresponding space-time statistics drawn once the ergodicity is admitted. The simple flow behind a truncated base and confined by frictionless sidewalls is considered. The two-dimensional unsteady Navier–Stokes equations in the stream function form are replaced by their finite difference counterpart, using a centered difference scheme in both the space and time derivative and some artifices to secure numerical stability. Realizations are computed at a nominal Reynolds number referred to the base height of $R_e = 300$, 3000, and 300 000, for a duration of about $T \simeq 800$ in reduced time. The one-point one-signal statistics, including probability density, time-correlation, power spectral density, are drawn from these realizations. The $R_e = 300$ case exhibits a von Kármán vortex street pattern and its statistics are in perfect accordance with a periodic flow. At the two higher Reynolds numbers, the primary vortices break into secondary and higher order vortices. The probability density becomes more and more Gaussian, and, in the power spectrum, more and more energy is transferred from the Strouhal ray and its harmonics to other frequencies. The one-point two-signal statistics are also examined. In particular, the contribution of the successive moving vortices or eddies to the joint probability density of the velocity components u and v shows the way the Reynolds shear stress is generated. Other statistics are also discussed. Despite the notorious inability of a discretized calculation to resolve the ever smaller scale motions at high Reynolds numbers, it is suggested that numerical simulation can cast light on turbulent processes, especially on those that make use of not readily measured variables.

Burst cycle and drag reduction

A. Gyr

Swiss Federal Institute of Technology, Zurich, Switzerland

In two visualization experiments in water, Gyr and Müller[1] showed that the addition of dilute polymer solutions changes the pattern of the flow structures near the wall. They observed a thickening of the viscous sublayer and of the buffer zone, as well as a stabilization of the shear waves in the direction of flow connected with an increase in the formation of transverse vortices. This observation is related to the burst cycle mechanism as described by Offen and Kline.[2] Based upon their burst mechanism a hypothesis is proposed that the drag reduction is the result of a higher alignment of the wall near separation vortices. Such a stabilization of the local pattern would produce a higher number of enrolled vortices, which means more elements of larger coherent motion. At the same time it would reduce the chaotic redistribution in the velocity field. The hypothesis is in good agreement with the observation of higher turbulent intensity u' in the direction of flow in the buffer zone. To describe this higher stabilization it is proposed to use a constitutive relation of the form, $\sigma = 2\mu[E + \theta \hat{x}\hat{x}(\hat{x}E\hat{x})]$ which is based on the concept that the polymer molecules are elongated in the direction of flow ($\hat{x}$) and can support strain forces in this direction.[3] To get an idea of the stabilization process the stability of a plane Poiseuille flow is demonstrated for a fluid with such an anisotropic viscosity, although for a complete investigation at least a two-dimensional flow system should have been taken into consideration. (The full paper is published in Ref. 4.)

[1] A. Gyr and A. Müller, Nature **253**, 185 (1975).
[2] G. R. Offen and S. J. Kline, J. Fluid Mech. **70**, 209 (1975).
[3] D. Jenkel and A. Gyr, Z. Angew. Math. Mech. **28**, 167 (1977).
[4] A. Gyr, Z. Angew. Math. Mech. **27**, 717 (1976).

PRECEDING PAGE NOT FILMED

Free stream turbulence and shear effects on boundary layer and wake structures

R. E. Luxton

University of Adelaide, Adelaide, South Australia

R. A. Antonia

University of Newcastle, Newcastle, New South Wales, Australia

Q. A. Ahmad

University of Sydney, Sydney, Australia

The results of experiments first on a turbulent wake of a cylinder imbedded in a uniformly sheared external turbulent flow,[1] and second on a zero pressure gradient boundary layer developing under an external uniformly sheared turbulent flow with positive, zero, or negative shear,[2] are described and compared. While there are many features which are similar for the wake and for the outer part of the boundary layer, the relative effects of external turbulence level and of free-stream shear are different for the two flows. For the wake it appears that free stream turbulence has little effect on the growth rate, but free stream shear produces a marked asymmetry in the growth rate on the two sides of the wake. (This apparent independence of the two sides of the wake is also evident in the measurements by Fabris[3] of the interaction between the wakes of two neighboring cylinders.) In the boundary layer, by contrast, the free stream turbulence has a major effect on the growth rate, large scale structure and entrainment, whilst the free stream shear effects are relatively small. It is possible that the large scale structure proposed by Brown and Thomas[4] may still exist in the presence of free stream turbulence, but that the external turbulence increases the amount of "jitter" making the coherence more difficult to isolate.

[1]Q. A. Ahmad, R. E. Luxton, and R. A. Antonia, J. Appl. Mech. **97**, 283 (1975).
[2]Q. A. Ahmad, R. E. Luxton, and R. A. Antonia, J. Fluid. Mech. **77**, 369 (1976).
[3]G. Fabris, Ph. D. thesis, Illinois Institute of Technology (1974).
[4]G. L. Brown and A. S. W. Thomas, Phys. Fluids **20**, S243 (October, Part II, 1977).

Temperature dissipation fluctuations in a turbulent boundary layer

K. R. Sreenivasan, H. Q. Danh, and R. A. Antonia

Department of Mechnical Engineering, The University of Newcastle, New South Wales, 2308, Australia

Simultaneous measurements have been made of all three components of the fluctuating temperature dissipation in the inner region of a fully developed turbulent boundary layer at a moderate Reynolds number. Measurements are made with a four-wire arrangement which consists of two parallel vertical wires mounted a small distance upstream of two parallel horizontal wires. Each of the four wires is operated at very low current by a contant current anemometer and is sensitive to only the temperature fluctuation Θ. The separation between wires in each parallel pair is kept small, so that the differences between the outputs of each pair are reasonable approximations to $\partial\Theta/\partial z$ and $\partial\Theta/\partial y$, the temperature derivatives in the transverse and vertical directions, respectively. The streamwise derivative $\partial\Theta/\partial x$ was obtained from the time derivative, through use of Taylor's hypothesis. Mean square and spectral density measurements show that in the inner region local isotropy is not closely approximated $\overline{[(\partial\Theta/\partial z)^2} > \overline{(\partial\Theta/\partial y)^2} > \overline{(\partial\Theta/\partial x)^2]}$. The probability density of the sum $\chi [=(\partial\Theta/\partial x)^2 + (\partial\Theta/\partial y)^2 + (\partial\Theta/\partial z)^2]$ has a lower skewness and flatness factor and is more closely log-normal than the probability densities of the individual components. This is true regardless of whether χ and its components are unaveraged or locally averaged over a linear dimension r, in the Obukhov–Kolmogoroff sense. The variance σ^2 of the logarithm of the locally averaged χ is proportional to log r over a wide range of r ($r_{max}/r_{min} \simeq 30$), in contrast to the individual components where this ratio may be as small as 3. The value of the Kolmogoroff constant μ determined from the slope of σ^2 vs log r is about 0.35. This is consistent with the slope of the spectral density of χ and is also in agreement with previous best estimates of μ obtained at high Reynolds numbers. Using only one component of χ, the evaluation of μ either from the slope of the spectral density or from the slope of σ^2 vs log r seems to be highly ambiguous and can lead to erroneous results.[1]

[1]More complete discussion will be found elsewhere [Phys. Fluid **20**, 1238 (1977)].

Influence of drag reducing polymers on the turbulent boundary layer of a body of revolution

B. Lang

Versuchsanstalt für Wasserbau und Schiffbau, Berlin (Berlin Model Basin), Germany

In the application of polymers for the drag reduction of ships, the study of outer boundary layer flows is a pre-requisite. The static pressures and the velocity profiles in the boundary layer of a body of revolution at 24 static pressure holes and six Pitot tube rakes with five tubes each are measured by means of differential pressure transducers in connection with electronic data acquisition and processing. A comparison is made between water and homogeneous solutions of Polyox Coagulant in eight concentrations from 0.5 to 100 ppmw at Reynolds numbers from 10^6 to 8×10^6. Comparing the static pressure coefficients, a shift to higher values is observed especially behind the front pressure minimum with increasing polymer concentrations. The calculated specific pressure resistance coefficients C_{PV} show smaller values with higher concentrations indicating the influence of drag reducing polymers on boundary layer development. From the velocity profiles measured with the Pitot tube rakes the boundary layer thicknesses are calculated. They become smaller with higher polymer concentrations up to a limiting concentration and then they grow sharply by some hundred percent. The limiting value increases with flow velocity. Some of these effects may depend on the measuring method, i.e., Pitot tube errors in drag reducing liquids, degradation, and the turbulence in the circulating water tank, although these influences were checked. Therefore, interpretation of the measured values may not be quite conclusive.

Model of drag reduction by compliant walls

Steven A. Orszag

Massachusetts Institute of Technology, Cambridge, Massachusetts 02139

Dennis M. Bushnell and Jerry N. Hefner

NASA Langley Research Center, Hampton, Virginia 23665

A numerical model of the effect of compliant walls on turbulent boundary layer flows, has been investigated. The model is based on Burton's[1] observation that turbulent bursts produce large pressure fluctuations that tend to produce low speed "streaks" near the wall. These streaks undergo space-time retardation and a new burst appears when the velocity profile becomes highly inflectional. The idea of the model is that the compliant wall motion interrupts this feedback loop of burst formation and that short wavelength wall motions can possibly delay burst formation long enough for the favorable gradient part of the pressure pulse caused by previous bursts to effect a decrease in the burst frequency. The numerical model involves solution of the two-dimensional time-dependent Navier–Stokes equations in a rectangular geometry. A typical calculation is performed using 257 grid points in the downstream direction with inflow-outflow boundary conditions applied. In the boundary layer direction 33 Chebyshev polynomials are used; linearized boundary conditions are applied at the compliant boundary and a match is made to a logarithmic velocity profile in the outer region. A large moving pressure pulse is applied in the outer region and it is assumed that the background turbulent Reynolds stress between bursts is a small fraction of the mean stress. This code is used to determine mean velocity profiles and has been checked thoroughly by comparison with the velocity profiles measured by Blackwelder. A stability analysis is then made of the resulting mean velocity profiles. The results of the stability analysis are not yet complete and will be reported in detail elsewhere.[2] The results of our calculations to date indicate that only very small wavelength wall motions have a significant effect upon the stability of the turbulent boundary layer. This result suggests that novel structural dynamics will be an essential component of successful drag reduction by compliant walls.

[1]T. E. Burton, Ph. D. thesis, Massachusetts Institute of Technology (1974).
[2]S. A. Orszag, NASA CR 2911 (1977).

Theories of compliant coating drag reductions

Edward F. Blick

School of Aerospace, Mechanical and Nuclear Engineering, University of Oklahoma, Norman, Oklahoma 73069

Approximately two decades ago, Kramer[1-3] reported skin friction drag reductions of up to 60% for compliant-walled bodies towed in water. Since Kramer's initial experiments, many other investigators have delved into this intriguing area. The results have been mixed. Some have reported drag reductions in water and air with compliant coatings while others found no decrease in drag. Most of those who found decreases have reported that these decreases were found when the compliant wall was immersed in a turbulent boundary layer. Kramer originally stated that he felt the drag reduction was perhaps due to retarding the transition from laminar to turbulent flow. Benjamin,[4] Boggs and Tokita,[5] Landahl,[6] Kaplan,[7] and Gyorgyfalvy[8] were among the early theoreticians who examined the possibilities of retarding transition by compliant walls. Generally, their calculations showed that with the proper compliant wall properties it was theoretically possible to retard transition. A few years later most of the theoretical work was aimed at trying to explain how a compliant coating might respond to a turbulent boundary layer in such a manner so as to reduce the turbulent wall skin friction. Different theories were proposed by Ffowcs-Williams,[9] Blick,[10] Amfilokhiyev,[11] Semenov,[12] Grosskreutz,[13] Ash,[14] and Zimmerman.[15] Most of the theories are somewhat incomplete, some had errors in them, and none have demonstrated that they adequately explain all, or even a sizeable portion of the body of experimental data. However, at the moment Semenov's theory seems to hold the most promise.

[1] M. O. Kramer, J. Aeronaut. Sci. **24**, 459 (1957).
[2] M. O. Kramer, J. Am. Soc. Nav. Eng. **72**, 25 (1960).
[3] M. O. Kramer, J. Am. Soc. Nav. Eng. **73**, 103 (1961).
[4] T. B. Benjamin, J. Fluid Mech. **9**, 513 (1960).
[5] F. W. Boggs and N. A. Tokita, in *Third Symposium on Naval Hydrodynamics*, edited S. W. Doroff (Superintendent of Documents, U. S. Government Printing Office, Washington, D. C., 1960), p. 451.
[6] M. T. Landahl, J. Fluid Mech. **13**, 609 (1962).
[7] R. E. Kaplan, Ph. D. thesis, Massachusetts Institute of Technology (1964).
[8] D. Gyorgyfalvy, J. Aircr. **5**, 186 (1967).
[9] J. E. Ffowcs-Williams, Bolt, Beranek, and Newman, Inc. Report 1331 (1965).
[10] E. F. Blick, in *Viscous Drag Reduction*, edited by C. S. Wells (Plenum, New York, 1969), p. 409.
[11] V. B. Amfilokhiyev, NASA TT F14 (1972), p. 601.
[12] B. N. Semenov, NASA TT F-14 (1972), p. 391.
[13] R. Grosskreutz, Max-Planck Institut fur Stromungsforschung Report 53 (1971).
[14] R. L. Ash, NASA CR-2387 (1974).
[15] G. Zimmerman, Max-Planck Institut fur Stromungsforschung Report 10a/1974 (1975).

The role of large scale structures in turbulent jets

J. Laufer, F. K. Browand, and R. A. Petersen

Department of Aerospace Engineering, University of Southern California, Los Angeles, California 90007

The presence of large scale structures in circular jets is well documented in the literature over a wide range of Reynolds numbers. This presentation explores in more detail the generation and interaction and the role they play in the development of the flow field. It is based on experiments carried out, both in water and air jets, at Reynolds numbers up to 100 000.[1,2] It is found, as reported by others, that the frequency of generation, as well as the various modes of the large scale vortices, can be predicted by linear stability theory. However, their further development as they are convected downstream is most difficult to study in detail. Conventional correlation measurements or sampling techniques have proven to be inadequate. In fact, the purpose for doing parallel water and jet experiments is to enable one to develop an adequate experimental method that could provide better information on the interaction process between adjacent structures. In a qualitative way, the measurements so far suggest that the induced flow field of the structures must play an important role in the interaction process and in the flow development. In the region of the potential core there is apparently an upstream influence due to the induced pressure field. This affects and, perhaps, controls such flow characteristics as the length of the potential core and the passage frequency of the structures at the end of the core. By introducing artificial disturbances into the flow further work is being carried out to clarify the above conjecture.

[1] F. K. Browand and J. Laufer, in *Proceedings of the Fourth Biennial Symposium on Turbulence in Liquids*, edited by J. L. Zakin and G. K. Patterson (Science Press, Princeton, N. J.,1977), p. 333.
[2] R. A. Petersen, Ph. D. Dissertation, University of Southern California (1976).

Anatomy of a turbulent spot

Brian Cantwell, Donald Coles, and Paul Dimotakis

California Institute of Technology, Pasadena, California 91109

Measurements have been made in the plane of symmetry of a turbulent spot to study the issue of entrainment. The mean flow is assumed to be similar in coordinates $(x/t, y/t)$, and laser Doppler velocimeter data at several stations are used to determine the effective origin in x and t and to establish particle trajectories with respect to the stationary interface. Entrainment occurs over most of the rear interface and also close to the wall at the front of the spot. Flow visualization has also been used to obtain additional information about entrainment and sublayer structure. Pictures of the underside of spots, wedges, and boundary layers were taken through a glass wall, using a very heavy concentration of aluminum flakes, so that only motions occurring for y^+ less than about 30 were visible. Sublayer streaks have essentially the same streaky, knotted appearance in all three types of flow. Optical correlations confirm the value $\lambda^+ \sim 100$. An attempt has been made to estimate the strength of sublayer streaks as streamwise vortices, assuming that the streaks are a manifestation of local Taylor–Görtler instability. The results account for many of the phenomena actually observed in the sublayer.

Drag reducing polymer in helicoidal flow

Leslie S. G. Kovasznay and Jing Tzong Kuo[a]

The Johns Hopkins University, Baltimore, Maryland 21218

High polymer additives in low concentration have a rather important effect in turbulent flows, but when using the same concentration in a variety of laminar flows, in general, they have only very small effects, only of the order of the viscosity change. In order to see a flow configuration where a small amount of additive (e.g., 10 to 100 ppm) would cause a large effect comparable to that in the turbulent case, a novel configuration was explored. A screw pump, consisting of a smooth hollow cylinder and inside it a concentrically placed smooth screw with a gap comparable to the dimensions of the screw thread was constructed and the flow variables were measured. The pressure head developed by the screw pump was found to be strongly dependent on the presence of additives (by a factor of 2–3).

[a] Present address: Thayer School of Engineering, Dartmouth College, Hanover, N. H. 03755.

Triggered transition in the pipe flow of dilute solutions of random-coiling macromolecules

P. S. Virk and M. Ohara

Department of Chemical Engineering, Massachusetts Institute of Technology, Cambridge, Massachusetts 02139

Laminar-to-turbulent transition was studied experimentally in the flow of dilute, distilled water solutions of two polyethyleneoxide polymers through three pipes, each 200 diam long and equipped with a "trigger" orifice, of i.d. half the pipe i.d., to provide a strong inlet disturbance. Polymer molecular weights, 0.7×10^6 and 5.0×10^6, and pipe sizes, 0.292, 0.457, 0.945 cm i.d., were chosen to cause transition from the laminar regime (L) into each of three turbulent regimes associated with drag reduction,[1] namely, Newtonian (N), polymeric (P), and maximum drag reduction (M). The corresponding three types of laminar-to-turbulent transitions observed, designated $L \rightarrow N$, $L \rightarrow P$, $L \rightarrow M$, had the following characteristics: (1) $L \rightarrow N$. In this case the transition occurred from laminar flow into a turbulent regime wherein the polymer solutions did not cause drag reduction, and the transition process appeared to be the same as in the usual Newtonian case.[2,3] (2) $L \rightarrow P$. In this case the polymer solutions exhibited drag reduction at the lowest fully turbulent flow rates. The critical Reynolds number, below which turbulent

slugs were not observed, was essentially the same as Newtonian. At a given Re in the transitional regime, the intermittency factor at the pipe axis was distinctly greater than Newtonian, the more so with increasing drag reducing ability of the polymer solution. The greater intermittency factor seemed to result mainly from an increased turbulent slug formation frequency relative to Newtonian; turbulent slug lengths had mean values essentially the same as Newtonian, although the dispersion about the mean was somewhat greater in the polymer solutions. (3) L→M. In this case the transition occurred from laminar flow into the turbulent regime of maximum drag reduction. Velocity fluctuations appeared at Re≃1500, appreciably lower than the Newtonian critical Re≃2000, and the fluctuation amplitude increased by an order of magnitude over the transitional range, $1500 < \text{Re} < 4000$. Intermittency could not be discerned during this type of transition.

[1]P. S. Virk, AIChE J. **21**, 625 (1975).
[2]J. Rotta, Ing. Arch. **24**, 258 (1956).
[3]I. J. Wygnanski and F. M. Champagne, J. Fluid Mech. **59**, 281 (1973).

Influence of polymer solutions on the structure of turbulence in a pipe

O. Scrivener and Ch. Kopp

Institut de Mécanique des Fluides, Strasbourg, France

A study of the alterations in the structure of turbulence due to the presence of PEO 301 dilute solutions was made using two experimental techniques. A photographic method was used to explore the wall region from 0.05 to 1 mm of the wall[1] and laser Doppler anemometry in the core and the buffer layer.[2] It was shown that, even if the velocities are reduced in the vicinity of the wall (in correlation with the fluid characteristics), the reduced coordinate profile remains unchanged in the laminar sublayer ($y^+ < 5$). With very low concentrations (~5 ppm) the mean velocity profile is not strongly affected even if the drag reduction is more than 40%. In the core, the shift of the profile observed by several authors was confirmed. The most important effect of the macromolecules was observed in the buffer layer where both the influence of the Reynolds number and the characteristics of the fluid were noted. The change in the structure of turbulence was observed[3] in measuring the streamwise turbulent intensities. It was shown that the maximum is shifted far from the wall in relation to the increase in the thickness of the viscous sublayer. A spectral analysis of the longitudinal velocity fluctuations by calculation of the probability density functions, the autocorrelation functions, and the power spectrum confirmed the idea of a transfer of energy from high frequency to low frequency turbulence structures. Therefore, it appears that the mechanism of drag reduction has to be found in the change in both the turbulent energy production (increase in the great structures) and dissipation (decrease in the importance of small eddies).

[1]O. Scrivener, in *Polymères et Lubrification* (Editions du Centre National de la Recherche Scientifique, Paris, France, 1975), p. 315.
[2]O. Scrivener, Ph.D. thesis, Université Louis Pasteur de Strasbourg (1975).
[3]O. Scrivener, in *Proceedings of the International Conference on Drag Reduction*, 1974 (BHRA, Fluid Engineering, Cranfield, England, 1974), p. C-66.

APPENDICES

SCIENTIFIC PROGRAM OF THE SYMPOSIUM

The titles of papers are listed here as given at the time of the Symposium. The titles of the papers published in the Proceedings are different in some cases. After each title, the page numbers of the corresponding paper (or abstract) are given. In case of multiple authors, an asterisk (*) indicates the one who presented the paper at the Symposium. (Except when indicated the time available for presentation of a paper was 20 min followed by 10 min for discussion.)

Monday Morning, 7 June, I. Introductory Session [*Chairman:* M. T. Landahl (Sweden)]

W. W. Willmarth* and T. J. Bogar (USA), Survey and new results of the turbulent structure near the wall (35 min.). [pp. S9–S21]

E. J. Hinch (UK), Mechanical models of polymer solutions in strong flows (35 min.). [pp. S22–S30]

Y. Tomita* and T. Jotaki (Japan), Effect of elongational viscosity of polymer solution on Taylor–Görtler vortices. [pp. S75–S77]

J. G. Savins* (USA) and F. A. Seyer (Canada), Drag reduction scale-up criteria. [pp. S78–S84]

Monday Afternoon, 7 June, II. Flow with Additives [*Chairman:* E. Naudascher (Fed. Rep. Germany)]

J. L. Zakin,* C. C. Ni, R. J. Hansen, and M. M. Reischman (USA), Laser Doppler velocimetry studies of early turbulence. [pp. S85–S88]

G. K. Patterson,* J. Chosnek, and J. L. Zakin (USA), Turbulence structure in drag reducing polymer solutions. [pp. S89–S99]

T. Mizushina* and H. Usui (Japan), Reduction of eddy diffusion for momentum and heat in viscoelastic fluid flow in a circular tube. [pp. S100–S108]

M. P. Tulin* and Jin Wu (USA), Additive effects in free turbulent flow. [pp. S109–S111]

L. F. Tsen and M. Bouriot* (France), Study of the structure of plane stationary computer-simulated free shear turbulence. [p. S287]

Additional Discussion Period (30 min.)

Tuesday Morning, 8 June, III. Wall Turbulence [*Chairman:* J. L. Lumley (USA)]

T. J. Hanratty (USA), Details of turbulent fluctuations in the viscous wall region. [pp. S112–S119]

L. H. Gustavsson (Sweden), Drag reduction experiments with polystyrene with some implications on the mean velocity profile. [pp. S120–S123]

A. Gyr (Switzerland), Burst cycle and drag reduction. [p. S287]

R. E. Falco (UK), Bursts, superbursts and their relationship to the larger scale motions of the turbulent boundary layer. [pp. S124–S132]

D. K. Oldaker and W. G. Tiederman* (USA), Spatial structure of the viscous sublayer in drag reducing channel flows. [pp. S133–S144]

R. E. Luxton,* R. A. Antonia, and Q. A. Ahmad (Australia), Free stream turbulence and shear effects on boundary layer and wake structures. [p. S288]

Additional Discussion Period (30 min.)

Tuesday Afternoon, 8 June, IV. Turbulence and Drag Reduction, I. [*Chairman:* J. O. Hinze (Netherlands)]

A. B. Metzner (USA), Drag reduction in dilute fiber suspensions and in mixtures of suspended fibers and dissolved polymers. [pp. S145–S149]

J. Sabot, I. Saleh, and G. Comte-Bellot* (France), Effects of roughness on the intermittent maintenance of Reynolds shear stress in pipe flow. [pp. S150–S155]

C. H. Gibson,* C. A. Friehe, and S. O. McConnell (USA), Structure of sheared turbulent fields. [pp. S156–S167]

K. R. Sreenivasan, H. Q. Danh, and R. A. Antonia* (Australia), Temperature dissipation fluctuations in a turbulent boundary layer. [p. S288]

N. S. Berman (USA), Flow time scales and drag reduction. [pp. S168–S174]

Additional Discussion Period (30 min.)

Wednesday Morning, 9 June, V. Turbulence and Drag Reduction, II. [*Chairman:* C. Elata (Israel)]

J. O. Hinze* and P. J. H. Builtjes (Netherlands), Rotation of the Reynolds stress tensor in a decaying grid generated turbulent flow. [pp. S175–S178]

J. Gaviglio,* J. P. Dussauge, J. F. Debieve, and A. Favre (France), Behavior of a turbulent flow, strongly out of equilibrium, at supersonic speeds. [pp. S179–S192]

Michael Poreh (Israel), Mean velocity and turbulent energy closures for flows with drag reduction. [pp. S193–S196]

J. C. J. Nihoul (Belgium), Turbulent boundary layer bearing silt in suspension. [pp. S197–S202]

E. H. Dunlop* and L. R. Cox (UK), Influence of molecular aggregates on drag reduction. [pp. S203–S213]

B. Lang (Fed. Rep. Germany), Influence of drag reducing polymers on the turbulent boundary layer of a body of revolution. [p. S289]

Additional Discussion Period (30 min.)

Thursday Morning, 10 June, VI. Compliant Wall [*Chairman:* P. S. Klebanoff (USA)]

D. M. Bushnell,* J. N. Hefner, and R. L. Ash (USA), Effect of compliant wall motion on turbulent boundary layers (40 min.). [pp. S31–S48]

S. A. Orszag,* D. M. Bushnell, and J. N. Hefner (USA), Model of drag reduction by compliant walls. [p. S289]

E. F. Blick (USA), Theories of compliant coating drag reductions. [p. S290]

G. Zimmerman (Fed. Rep. Germany), Theoretical consideration of the interaction between turbulent boundary layers and compliant walls. [pp. S214–S215]

A. Dinkelacker,* M. Hessel, G. E. A. Meier, and G. Schewe (Fed. Rep. Germany), Investigation of pressure fluctuations beneath a turbulent boundary layer by means of an optical method. [pp. S216–S224]

Thursday Afternoon, 10 June.

NBS, The Nation's Measurement Laboratory, E. L. Brady, Associate Director for Information Programs

Tour of the Fluid Mechanics Laboratory, National Bureau of Standards, Gaithersburg, Maryland

Friday Morning, 11 June, National Academy of Sciences, Washington, D.C., VII. Orderly Structure [*Chairman:* S. Corrsin (USA)]

H. Eckelmann,* S. G. Nychas (Fed. Rep. Germany), R. S. Brodkey, and J. M. Wallace (USA), Vorticity and turbulence production in pattern recognized turbulent flow structures. [pp. S225–S231]

R. F. Blackwelder (USA), On the role of phase information in conditional sampling. [pp. S232–S242]

J. Laufer,* F. K. Browand, and R. A. Petersen (USA), The role of large scale structure in turbulent jets. [p. S290]

G. L. Brown (Australia), Effects from the large structure in mixing layers and further evidence of the structure in the boundary layer. [pp. S243–S252]

J. W. Hoyt (USA). Turbulence structure in a water jet discharging in air. [pp. S253–S257]

B. Cantwell* and D. Coles (USA), Growth of a turbulent spot in a polymer-filled laminar boundary layer. [p. S291]

M. Zilberman, I. Wygnanski* (Israel), and R. Kaplan (USA), Transitional boundary layer spot in a fully turbulent environment—In search of a coherent structure in a turbulent boundary layer. [pp. S258–S271]

Friday Afternoon, 11 June, VIII. Polymer-Flow Interaction [*Chairman:* G. M. Lilley (UK)]

L. S. G. Kovasznay* and J. T. Kuo (USA), Drag reducing polymer in helicoidal flow. [p. 291]

P. G. Saffman (USA), Phenomenological theory for the calculation of the dependence of the effective slip velocity of a dilute polymer solution on wall roughness. [pp. S272–S275]

P. S. Virk* and M. Ohara (India), Triggered transition in the pipe flow of dilute solutions of random-coiling macromolecules. [pp. S291–S292]

E. R. Lindgren (Sweden), Mechanical structure of drag reducing additives. [pp. S276–S278]

O. Scrivener,* Ch. Kopp, and M. Mondon (France), Influence of polymer solutions on the structure of turbulence in a pipe. [p. 292]

Friday Evening, 11 June, Shoreham Americana Hotel, Symposium Banquet [*Chairman:* F. N. Frenkiel (USA)]

B. A. Toms (UK), Origins of the experiments on drag reduction by polymers. [pp. S3–S5]

Saturday Morning, 12 June, IX. Mechanism of Drag Reduction [*Chairman:* I. Tani (Japan)]

C. Elata,* J. Michlin, and J. Burger (Israel), Dilute polymer solutions in elongational flows (40 min.). [pp. S49–S54]

M. T. Landahl (Sweden), Dynamics of boundary layer turbulence and the mechanism of drag reduction (40 min.). [pp. S55–S63]

J. L. Lumley (USA), Drag reduction in two phase and polymer flows (40 min.). [pp. S64–S71]

General Discussion of Drag Reduction Mechanism (1 hour)

AUTHOR INDEX

Ahmad, Q. A.-S288
Antonia, R. A.-S288
Ash, Robert L.-S31

Berman, Neil S.-S168
Blackwelder, Ron-S232
Blick, Edward F.-S290
Bogar, Thomas J.-S9
Bouriot, M.-S287
Brodkey, Robert S.-S225
Browand, F. K.-S290
Brown, Garry L.-S243
Builtjes, P. J. H.-S175
Burger, J.-S49
Bushnell, Dennis M.-S31, S289

Cantwell, Brian-S291
Chorn, Larry G.-S112
Chosnek, Jack-S89
Coles, Donald-S291
Comte-Bellot, G.-S150
Cox, L. R.-S203

Danh, H. Q.-S288
Debieve, Jean-Francois-S179
Dimotakis, Paul-S291
Dinkelacker, A.-S216
Dunlop, E. H.-S203
Dussauge, Jean-Paul-S179

Eckelmann, Helmut-S225

Elata, C.-S49

Falco, R. E.-S124
Favre, Alexandre-S179
Friehe, Carl A.-S156

Gaviglio, Jean-S179
Gibson, Carl H.-S156
Gustavsson, L. H.-S120
Gyr, A.-S287

Hanratty, Thomas J.-S112
Hansen, R. J.-S85
Hassid, S.-S193
Hatziavramidis, Dimitrios T.-S112
Hefner, Jerry N.-S31, S289
Hessel, M.-S216
Hinch, E. J.-S22
Hinze, J. O.-S175
Hoyt, J. W.-S253

Jotaki, T.-S75

Kaplan, R. E.-S258
Killen, J. M.-S280
Kopp, Ch.-S292
Kovasznay, Leslie S. G.-S291
Kuo, Jing Tzong-S291

Lagerstedt, Torgny-S276
Landahl, M. T.-S55
Lang, B.-S289
Laufer, J.-S290
Lindgren, E. Rune-S276
Lumley, John L.-S64
Luxton, R. E.-S288

McConnell, Steven O.-S156
Meier, G. E. A.-S216
Metzner, Arthur B.-S145
Michlin, J.-S49
Mizushina, Tokuro-S100

Naudascher, E.-S280
Ni, C. C.-S85
Nihoul, Jacques C. J.-S197
Nychas, Stavros G.-S225

Ohara, M.-S291
Oldaker, D. K.-S133
Orszag, Steven A.-S289

Patterson, Gary K.-S89
Petersen, R. A.-S290
Poreh, M.-S193

Reischman, M. M.-S85

Sabot, J.-S150

Saffman, P. G.-S272
Saleh, I.-S150
Savins, J. G.-S78
Schewe, G.-S216
Scrivener, O.-S292
Seyer, F. A.-S78
Sreenivasan, K. R.-S288
Stenberg, Lars-Göran-S276

Takserman, U.-S49
Taylor, J. J.-S253
Thomas, Andrew S. W.-S243
Tiederman, W. G.-S133
Tomita, Y.-S75
Toms, B. A.-S3
Tsen, L. F.-S287
Tulin, Marshall P.-S109

Usui, Hiromoto-S100

Virk, P. S.-S291

Wallace, James M.-S225
Willmarth, William W.-S9
Wu, Jin-S109
Wygnanski, I.-S258

Zakin, J. L.-S85, S89
Zilberman, M.-S258
Zimmermann, G.-S214